

ADVANCED SENSING, MATERIALS AND INTELLIGENT ALGORITHMS FOR MULTI-DOMAIN STRUCTURAL HEALTH MONITORING

EDITED BY: Liang Ren, Gangbing Song, Qingzhao Kong, Chun-Xu Qu,
Yang Zhang and Yunlai Zhou

PUBLISHED IN: Frontiers in Materials and Frontiers in Physics



frontiers

Frontiers eBook Copyright Statement

The copyright in the text of individual articles in this eBook is the property of their respective authors or their respective institutions or funders. The copyright in graphics and images within each article may be subject to copyright of other parties. In both cases this is subject to a license granted to Frontiers.

The compilation of articles constituting this eBook is the property of Frontiers.

Each article within this eBook, and the eBook itself, are published under the most recent version of the Creative Commons CC-BY licence.

The version current at the date of publication of this eBook is CC-BY 4.0. If the CC-BY licence is updated, the licence granted by Frontiers is automatically updated to the new version.

When exercising any right under the CC-BY licence, Frontiers must be attributed as the original publisher of the article or eBook, as applicable.

Authors have the responsibility of ensuring that any graphics or other materials which are the property of others may be included in the CC-BY licence, but this should be checked before relying on the CC-BY licence to reproduce those materials. Any copyright notices relating to those materials must be complied with.

Copyright and source acknowledgement notices may not be removed and must be displayed in any copy, derivative work or partial copy which includes the elements in question.

All copyright, and all rights therein, are protected by national and international copyright laws. The above represents a summary only. For further information please read Frontiers' Conditions for Website Use and Copyright Statement, and the applicable CC-BY licence.

ISSN 1664-8714

ISBN 978-2-88971-991-4

DOI 10.3389/978-2-88971-991-4

About Frontiers

Frontiers is more than just an open-access publisher of scholarly articles: it is a pioneering approach to the world of academia, radically improving the way scholarly research is managed. The grand vision of Frontiers is a world where all people have an equal opportunity to seek, share and generate knowledge. Frontiers provides immediate and permanent online open access to all its publications, but this alone is not enough to realize our grand goals.

Frontiers Journal Series

The Frontiers Journal Series is a multi-tier and interdisciplinary set of open-access, online journals, promising a paradigm shift from the current review, selection and dissemination processes in academic publishing. All Frontiers journals are driven by researchers for researchers; therefore, they constitute a service to the scholarly community. At the same time, the Frontiers Journal Series operates on a revolutionary invention, the tiered publishing system, initially addressing specific communities of scholars, and gradually climbing up to broader public understanding, thus serving the interests of the lay society, too.

Dedication to Quality

Each Frontiers article is a landmark of the highest quality, thanks to genuinely collaborative interactions between authors and review editors, who include some of the world's best academicians. Research must be certified by peers before entering a stream of knowledge that may eventually reach the public - and shape society; therefore, Frontiers only applies the most rigorous and unbiased reviews.

Frontiers revolutionizes research publishing by freely delivering the most outstanding research, evaluated with no bias from both the academic and social point of view. By applying the most advanced information technologies, Frontiers is catapulting scholarly publishing into a new generation.

What are Frontiers Research Topics?

Frontiers Research Topics are very popular trademarks of the Frontiers Journals Series: they are collections of at least ten articles, all centered on a particular subject. With their unique mix of varied contributions from Original Research to Review Articles, Frontiers Research Topics unify the most influential researchers, the latest key findings and historical advances in a hot research area! Find out more on how to host your own Frontiers Research Topic or contribute to one as an author by contacting the Frontiers Editorial Office: frontiersin.org/about/contact

ADVANCED SENSING, MATERIALS AND INTELLIGENT ALGORITHMS FOR MULTI-DOMAIN STRUCTURAL HEALTH MONITORING

Topic Editors:

Liang Ren, Dalian University of Technology, China

Gangbing Song, University of Houston, United States

Qingzhao Kong, Tongji University, China

Chun-Xu Qu, Dalian University of Technology, China

Yang Zhang, Dalian University of Technology, China

Yunlai Zhou, Universidade Lusófona, Portugal

Citation: Ren, L., Song, G., Kong, Q., Qu, C.-X., Zhang, Y., Zhou, Y., eds. (2021).

Advanced Sensing, Materials and Intelligent Algorithms for Multi-Domain Structural Health Monitoring. Lausanne: Frontiers Media SA. doi: 10.3389/978-2-88971-991-4

Table of Contents

- 05 Editorial: Advanced Sensing, Materials and Intelligent Algorithms for Multi-Domain Structural Health Monitoring**
Chun-Xu Qu, Liang Ren, Qingzhao Kong, Yang Zhang, Yunlai Zhou and Gangbing Song
- 07 Model Test of Jacked Pile Penetration Process Considering Influence of Pile Diameter**
Yonghong Wang, Songkui Sang, Xueying Liu, Yongfeng Huang, Mingyi Zhang and Dezi Miao
- 18 Monitoring and Analysis of Pore and Earth Pressure at the Pile Surface Using Piezoresistive Silicon Pressure Transducers**
Yonghong Wang, Yongfeng Huang, Mingyi Zhang and Jiaxiao Ma
- 31 Fatigue Reliability Assessment for Orthotropic Steel Bridge Decks Considering Load Sequence Effects**
Jun-Hong Xu, Guang-Dong Zhou and Tai-Yong Zhu
- 41 Detection of Pipeline Deformation Induced by Frost Heave Using OFDR Technology**
Tao Jiang, Jing-wen Zhu and Yi Shi
- 49 Optimal Design of Negative Stiffness Devices for Highway Bridges Using Performance-Based Genetic Algorithm**
Sun Tong, Zhu Tianqi, Sun Li and Zhang Hao
- 57 Effect of Aftershocks on Seismic Fragilities of Single-Story Masonry Structures**
Hao Zhang, Tong Sun, Shi-Wei Hou, Qing-Meng Gao and Xi Li
- 72 Experimental Study on Influence of Temperature to Control Performance for Viscoelastic Materials Pounding Tuned Mass Damper**
Dehui Ye, Jie Tan, Yabin Liang and Qian Feng
- 83 Mechanical Behavior of the Novel Gradient Concrete Tower of a Cable-Stayed Bridge**
Zuo-Cai Wang, Da-You Duan, Shu-Hang Wang, Ye Mo and Yong-Gao Yin
- 98 Structural Health Monitoring Method of Pantograph–Catenary System Based on Strain Response Inversion**
Sheng Liu, Yibo Wei, Yongxin Yin, Tangzheng Feng and Jinbao Lin
- 105 Structural Health Monitoring for Bridge Crane Based on Low Temperature-Sensitivity FBG Sensors**
Zhang Zhaobo, Liu Sheng, Wei Yibo and Li Hongnan
- 112 Collapse Analysis of a Transmission Tower-Line System Induced by Ice Shedding**
Jiaxiang Li, Biao Wang, Jian Sun, Shuhong Wang, Xiaohong Zhang and Xing Fu
- 120 Distant Relative Genetic Algorithm–Based Structural Reliability Optimization**
Hu Cheng, Xin-Chi Yan and Li Fu
- 126 Quantitative Monitoring of Bolt Looseness Using Multichannel Piezoelectric Active Sensing and CBAM-Based Convolutional Neural Network**
Yixuan Chen, Jian Jiang, Xiaojun Qin and Qian Feng

- 139 ***Analysis of Long-Term Durability Monitoring Data of High-Piled Wharf With Anode-Ladder Sensors Embedded in Concrete***
Hongbiao Liu, Baohua Zhang, Haicheng Liu and Zifan Ji
- 151 ***Analysis of the Mechanical Properties and Parameter Sensitivity of a U-Shaped Steel Damper***
Jinhe Gao, Jiahuan Xi, Yuwen Xu, Jiajun Ding, Junwen Zhu, Yi Chang and Baokui Chen
- 164 ***An Approach of the Maximum Curvature Measurement of Dynamic Umbilicals Using OFDR Technology in Fatigue Tests***
Yuanhao Yin, Peng Yu, Ziguang Jia, Shanghua Wu, Qingzhen Lu, Jun Yan and Qianjin Yue
- 173 ***Seismic Performance and Strengthening of Purlin Roof Structures Using a Novel Damping-Limit Device***
Baokui Chen, Bao Jia, Ming Wen and Xiaodong Li
- 186 ***Holistic Design of Energy Pile Bridge Deicing System With Ontology-Based Multiobjective Decision Making***
Peng Zhang, Chunyi Cui, Chaoji Li, Cheng Zhang and Hailong Liu
- 200 ***Research on the Failure Evolution Process of Rock Mass Base on the Acoustic Emission Parameters***
Xiaohui Liu, Xiaoping Zhao, Shishu Zhang, Ran Congyan and Rui Zhao
- 215 ***A Novel Piezoceramic-Based Sensing Technology Combined With Visual Domain Networks for Timber Damage Quantification***
Haibei Xiong, Lin Chen, Cheng Yuan and Qingzhao Kong
- 227 ***Experimental Evaluation of Miniature Impedance Board for Loosening Monitoring of the Threaded Pipe Connection***
Yabin Liang, Yixuan Chen, Zuocai Zhang and Qian Feng
- 238 ***Old - New Concrete Interfacial Bond Slip Monitoring in Anchored Rebar Reinforced Concrete Structure Using PZT Enabled Active Sensing***
Jian Jiang, Yixuan Chen and Junwu Dai



Editorial: Advanced Sensing, Materials and Intelligent Algorithms for Multi-Domain Structural Health Monitoring

Chun-Xu Qu¹, Liang Ren^{1*}, Qingzhao Kong², Yang Zhang³, Yunlai Zhou⁴ and Gangbing Song⁵

¹School of Civil Engineering, Dalian University of Technology, Dalian, China, ²College of Civil Engineering, Tongji University, Shanghai, China, ³School of Physics, Dalian University of Technology, Dalian, China, ⁴Faculty of Engineering, Universidade Lusófona, Lisbon, Portugal, ⁵Department of Mechanical Engineering, University of Houston, Houston, TX, United States

Keywords: structure health monitoring, sensing, smart materials, intelligent algorithms, engineering

Editorial on the Research Topic

Advance Sensing, Materials and Intelligent Algorithms for Multi-Domain Structural Health Monitoring

Structural health monitoring (SHM) is an effective method to obtain and trace a system's operation state by sensing its responses during its lifecycle. For decades, SHM has been widely applied to many types of systems, such as bridges, buildings, transmission towers, wharves, machines, and equipment. Furthermore, it is helpful to evaluate structural safety, analyze structural collapse or failure, optimize structural design, and implement structural control. This special issue shares the original research and review articles on the topics of novel point/distributed sensing technology for various engineering fields, advanced nanomaterial and smart functional material and applications in SHM systems, intelligent algorithms, Artificial Intelligence algorithms for data compression, mining and fusing technology, mathematical theories and methods for SHM system, and other related aspects.

SHM attracts much research and has many applications in civil engineering. Jiang et al. propose an active sensing technology based on piezoelectric ceramics for monitoring the bond-slip in old-new concrete interfaces in anchored reinforced concrete structures. Liu et al. analyze the long-term durability monitoring data of high-piled wharves with anode-ladder sensors embedded in the concrete and found that the temperature affects the resistance of concrete significantly. Xiong et al. propose a timber beam crack detection method based on the combination of stress wave sensing and computer vision technology, which can effectively identify the crack severity. Jiang et al. used an optic frequency domain reflectometer technology to measure the distributed strain and used the plane curve reconstruction algorithm to calculate the shape of the deformed pipeline, which can realize the detection of pipeline frost heave deformation. Liu et al. study and compared the failure evolution characteristics of intact coal and fractured coal based on the maximum amplitude distribution of acoustic emission. The research of Wang et al., has shown that a piezoresistive silicon pressure transducer would be suitable for monitoring pore pressure and earth pressure on pile surface during jacking.

SHM can be also used to monitor or detect instruments or equipment components. Liang et al. applied a low-cost miniature impedance board to monitor the threaded pipe connection looseness monitoring and verified its practical performance in impedance measurement and structural damage identification. Chen et al. propose a quantitative monitoring method of bolt looseness based on multi-channel piezoelectric active sensing and an improved convolution neural network. Yin et al.

OPEN ACCESS

Edited and reviewed by:

Weihua Li,
University of Wollongong, Australia

*Correspondence:

Liang Ren
renliang@dlut.edu.cn

Specialty section:

This article was submitted to
Smart Materials,
a section of the journal
Frontiers in Materials

Received: 14 October 2021

Accepted: 25 October 2021

Published: 12 November 2021

Citation:

Qu C-X, Ren L, Kong Q, Zhang Y,
Zhou Y and Song G (2021) Editorial:
Advanced Sensing, Materials and
Intelligent Algorithms for Multi-Domain
Structural Health Monitoring.
Front. Mater. 8:795056.
doi: 10.3389/fmats.2021.795056

employed OFDR technology to locate fatigue hot spots by measuring the maximum curvature of dynamic umbilicus in fatigue tests. Liu et al. propose a real-time structural health monitoring method of a pantograph-catenary system based on strain response inversion, which can accurately calculate the magnitude and location of dynamic contact force between catenary and pantograph. Zhang et al. present a fiber Bragg grating strain sensor with low temperature sensitivity, whose strain transferring characteristics were conducted by experiment calibration and reliability tests, and the advantages in precision, reliability, and applicability were verified by on-site tests.

The purpose of SHM is to monitor the structural operation state. To evaluate structural safety and optimize structural design, Cheng et al. present an improved adaptive technology termed the distant relative genetic algorithm for the structural reliability optimization design. Li et al. carried out finite element analysis on the collapse of a transmission tower-line system caused by ice shedding, and systematically studied collapse caused by ice shedding and its influencing parameters. Zhang et al. propose the holistic design scheme of an energy-pile bridge de-icing system based on ontology multi-objective decision making and combined it into an overall design tool. Zhang et al. studied the effect of aftershocks on the fragility of single-story masonry structures using a probabilistic seismic demand analysis model. Xu et al. propose a fatigue reliability calculation method based on the sequential law and the whole-range S-N curve, where the fatigue reliability of rib-to-deck welded joints of an orthotropic steel deck was evaluated with consideration of the effect of load sequence. Wang et al. applied the novel gradient concrete to the tower of the Chizhou Yangtze River Bridge. The finite element analysis results show that the FGC tower has good mechanical properties and durability for the cable-stayed bridge towers. Wang et al. studied the effects of different diameters on pile tip resistance, pile side resistance, pile axial force, and pile force transmission during static pressure pile penetration.

To make structure safes, structural control is another effective method. Chen et al. have designed a novel damping-limit device

to strengthen the purlin roof structure and improve its seismic performance. Gao et al. carried out tensile and compressive tests on a U-shaped steel damper considering different test parameters and derived theoretical calculation formula for its mechanical properties. Sun et al. performed parameter optimization design of a negative stiffness device for highway bridges based on a performance genetic algorithm, which obtained a better shock absorption effect. Ye et al. studied the vibration control performance of viscoelastic materials pounding a tuned mass damper at different temperatures, whose temperature robustness was validated by the experiments.

AUTHOR CONTRIBUTIONS

All authors listed have made a substantial, direct, and intellectual contribution to the work and approved it for publication.

ACKNOWLEDGMENTS

All authors' contributions, and those of the editorial staff of Frontiers, are appreciated to make this special issue possible.

Conflict of Interest: The authors declare that the research was conducted in the absence of any commercial or financial relationships that could be construed as a potential conflict of interest.

Publisher's Note: All claims expressed in this article are solely those of the authors and do not necessarily represent those of their affiliated organizations, or those of the publisher, the editors and the reviewers. Any product that may be evaluated in this article, or claim that may be made by its manufacturer, is not guaranteed or endorsed by the publisher.

Copyright © 2021 Qu, Ren, Kong, Zhang, Zhou and Song. This is an open-access article distributed under the terms of the Creative Commons Attribution License (CC BY). The use, distribution or reproduction in other forums is permitted, provided the original author(s) and the copyright owner(s) are credited and that the original publication in this journal is cited, in accordance with accepted academic practice. No use, distribution or reproduction is permitted which does not comply with these terms.



Model Test of Jacked Pile Penetration Process Considering Influence of Pile Diameter

Yonghong Wang^{1,2*}, Songkui Sang¹, Xueying Liu¹, Yongfeng Huang¹, Mingyi Zhang^{1,2} and Dezi Miao¹

¹School of Civil Engineering, Qingdao University of Technology, Qingdao, China, ²Collaborative Innovation Center for Engineering Construction and Safety of Blue Economic Zone, Qingdao, China

OPEN ACCESS

Edited by:

Liang Ren,
Dalian University of Technology, China

Reviewed by:

Ziguang Jia,
Dalian University of Technology, China
Guang-Dong Zhou,
Hohai University, China

*Correspondence:

Yonghong Wang
hong7986@163.com

Specialty section:

This article was submitted to
Interdisciplinary Physics,
a section of the journal
Frontiers in Physics

Received: 12 October 2020

Accepted: 26 January 2021

Published: 08 April 2021

Citation:

Wang Y, Sang S, Liu X, Huang Y,
Zhang M and Miao D (2021) Model
Test of Jacked Pile Penetration
Process Considering Influence of
Pile Diameter.
Front. Phys. 9:616410.
doi: 10.3389/fphy.2021.616410

In order to investigate the influence of different diameters on pile end resistance, pile side resistance, pile axial force and pile force transmission law of jacked pile penetration, two pairs of embedded sensitized microfiber grating sensors were installed by slotting the pile body. The pile-jacking process of static-pressing viscous foundation soil with different diameters of closed-tube model piles was successfully monitored. The test results show that the pile pressure, pile end resistance and pile side resistance of the two test piles increase linearly with the increase of pile depth. When the pile jacks, the final pressure of the test pile TP1 is higher than that of the test pile. TP2 is 31% higher, pile end resistance is 18% higher, and total side resistance is 57% higher. The results show that increasing the pile diameter can significantly increase the pile side resistance; under different penetration depths, the pile side resistance is from top to end. Continuously exerted, the axial force of the pile body decreases with the depth of the pile and the slope of the distribution curve of the axial force gradually decreases. At the maximum penetration depth, the axial force of the pile TP1 is 18% larger than that of the test pile TP2; As the depth increases, the unit side resistance at the same penetration depth gradually decreases, that is, the side resistance has a “degradation effect”; at the end of the pile jacking, the percentage of the pile end resistance to the pile force exceeds 50%, that is, the pile end resistance bears most of the load. This research can be used as a reference for the study of pile driving mechanism in clayey and layered clayey soils.

Keywords: fiber bragg grating sensor, jacked pile, different pile diameter, force state, model test

INTRODUCTION

Many scholars at home and abroad have conducted field tests [1–3] and indoor tests [4–7], combined with numerical simulation, to study the force state of the pile body in the process of pile jacking. Doherty et al. [1] carried out field tests of open pile and studied the stress during pile jacking. Zhang et al. [2] studied the main influence and effect of soil clogging through field tests, and studied the change rule of pile end resistance. Han et al. [3] conducted a slow-maintaining static load test for closed and open steel pipe piles driven side-by-side, and studied the difference in resistance between the two piles. Paik [4] studied the influence of soil plugs on the bearing capacity of open-ended pipe piles, and quantified it with an incremental filling rate. Combined with indoor model pile tests, they proposed an empirical relationship for the bearing capacity of open-end piles. Zhang et al. [5] monitored the change and displacement of soil around the pile through indoor model tests. Lehane



FIGURE 1 | Large scale indoor model test loading system.

et al. [6] studied the aging effect of pile resistance in sand through new laboratory tests. White et al. [7] used centrifuge model piles equipped with side pressure sensors, and obtained the degradation effect of resistance by referring to other laboratory and field experimental data.

At present, most indoor model tests study the load transfer law of pile body during pile jacking from the aspects of foundation soil layer, pipe pile length and different pile end forms [8–12]. However, there are few studies on the influence of pipe pile diameter on the force state of jacked pile during pile jacking. Traditional test methods mostly use strain gauges attached to the outside of the pile, but the pile jacking process is easily damaged by the resistance of the soil around the pile, which is greatly affected by the environment, low reliability, and low accuracy [13–15]. Fiber grating technology is a new type of test element that has been vigorously developed in recent years. Because of its small size, high sensitivity, good long-term stability, light weight, and strong anti-interference ability, it has gradually replaced strain gauges and has become more popular by most people. It is widely used in practical engineering and model tests [16, 17]. In this paper, the sensitivity-enhancing miniature fiber grating sensor and the pile top pressure sensor have been successfully applied to the indoor jacked pile penetration model test in the silt and clay layer. Analyze and study the difference in load-bearing performance of two closed-end model pipe piles with different pile diameters during the pile jacking process of pile shaft force, pile side resistance, pile end resistance, pile pressure, etc. The test results provide practical value and guiding significance for actual engineering and related academic research.

EXPERIMENT PREPARATION

The test site is located in the Power Experiment Center of Qingdao University of Technology. The instrument used in the test is a large-scale model test system developed by the Qingdao University of Technology.



FIGURE 2 | Close-up view of the ground foundation soil.

Test System

The system mainly includes loading system, data acquisition system and model box. Among them, the size of the model box is $3\text{ m} \times 3\text{ m} \times 2\text{ m}$ (length \times width \times height), which is welded by steel plates. In order to observe the pile jacking process, a tempered glass window is installed on the front of the model box; The instruments used for data acquisition are mainly FS2200RM fiber grating demodulator and DH3816N static strain acquisition instrument; the test loading system is shown in **Figure 1**.

Foundation Soil Production

The soil sample used in the indoor model test was taken from the silty clay layer of a residential project in Qingdao. The close-up view of the soil sample is shown in **Figure 2**. After the soil samples are sent to the laboratory, they are filled in layers, rolled, and mechanical vibrating. The vibrating operations are shown in **Figure 3**. After the soil sample



FIGURE 3 | Grounding of foundation soil.

is evenly vibrated, it is sprinkled with water and covered with mulendle layers of film. After standing for about 30 days, the pile pressure test is officially carried out. Before the indoor pile pressure test, a series of indoor geotechnical tests were carried out according to the “Standard for Geotechnical Test Methods” (GB/T 50123-1999) [18], and the related physical and mechanical parameters were determined. The specific parameters are shown in **Table 1**.

Model Pile

In this indoor test, a total of 2 jacked pile tests with different diameter model piles were carried out. the ends of the two model piles are connected to the ends of the pipe piles with hexagon socket head bolts to form a closed mode.

The two piles are made of aluminum with the same material. According to the existing research, it is feasible to analyze the mechanical characteristics of pile foundation by using aluminum model pile in laboratory test. Duan [19]. simulated the mechanical characteristics of Marine fan pile foundation under vertical load by indoor test of aluminum pile. Tang Shidong [20] studied the influencing factors of pile lateral friction by installing strain gauges in aluminum piles.

In this test, the parameters of model pile are determined by the similarity theory. Large steel piles are 3–6 m in diameter and 30–50 m in length [21]. In this paper, according to the prototype pile, the pile length is 40 m, the pile diameter is 5.6 m, the elastic modulus is 210 GPa, and the Poisson’s ratio is 0.3. In order to satisfy the load similarity ratio, the geometric similarity ratio was determined to be 40, the elastic modulus similarity ratio was 2.9,

and the Poisson’s ratio similarity ratio was 1. The test piles were made of aluminum pipe piles TP1 and TP2 with an elastic modulus of 72 GPa, Poisson’s ratio of 0.3, diameter and length of 140 and 1000 mm, respectively. The specific parameters of the model pipe piles are shown in **Table 2**.

INTRODUCTION AND INSTALLATION OF SENSORS

Introduction of Fiber Grating Sensor

The fiber grating sensor used in the experiment is the JMFSS-04 sensitized miniature fiber grating sensor (hereinafter referred to as FBG sensor) produced by Shenzhen Testing Technology Co., Ltd., which is mainly composed of FC connector, fiber grating, clamping sleeve and pigtail, such as shown in **Figure 4A**. Some specific parameters of the FBG sensor are shown in **Table 3**. The center wavelength of the sensor is not listed in the table.

The Layout of Fiber Grating Sensor

The model piles TP1 and TP2 in this experiment are all grooved and embedded with 6 FBG sensors. The specific installation process is as follows: ① A shallow groove with a width of 2 mm and a depth of 2 mm was opened on the surface of the pipe pile. ② Wipe the installation location of the FBG sensor with alcohol and cotton balls. ③ The FBG sensors are numbered 1#~6# sequentially from the pile end to the pile top, and the distribution form is dense at the end and sparse at the top. The sensor spacing is shown in **Figure 4B**. ④ Pre-tension the FBG sensor for about 2 nm and fix it with 704. The operation process is shown in **Figure 4C**. ⑤ After scrubbing the FC connector of the FBG sensor with alcohol and cotton balls, connect it to the FS2200RM fiber grating demodulator to detect its survival rate. The result shows that all survived. Finally, epoxy resin is used to encapsulate the surface of the pile so that the surface is flush with the pile body.

Pile Top Pressure Sensor

The pressure sensor is mainly used to measure the pile pressure during the pile jacking process. Its specific parameters are shown in **Table 4**. The sensor is easy to install and does not need to be tightly connected with the model pile. It only needs to be aligned before starting the pile jacking. Just place the center of the quasi-pile top horizontally on the top of the pile, as shown in **Figure 5**.

INDOOR PILE JACKING TEST

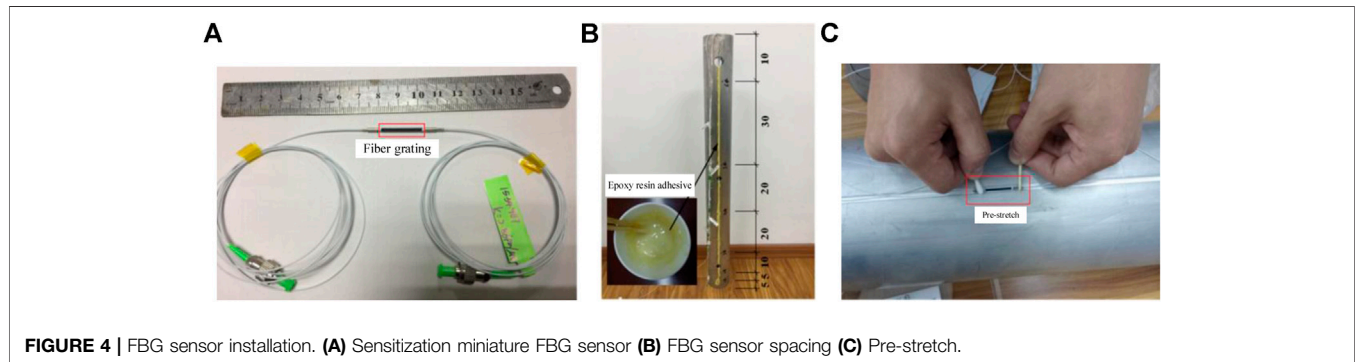
After 30 days of consolidation for the remodeled soil sample of the foundation, the excess pore pressure gradually dissipated and the

TABLE 1 | Physical and mechanical parameters of soil samples.

Relative density d_s	Internal friction angle φ (°)	Cohesion c (kPa)	Severe γ (kN/cm ³)	Moisture content w (%)	Liquid limit w_L (%)	Plastic limit w_p (%)	Plasticity index I_p (%)	Compression modulus E_{s1-2} (MPa)
2.73	8.6	14.4	18.0	34.8	34.8	21.2	13.5	3.3

TABLE 2 | Model pipe pile parameter table.

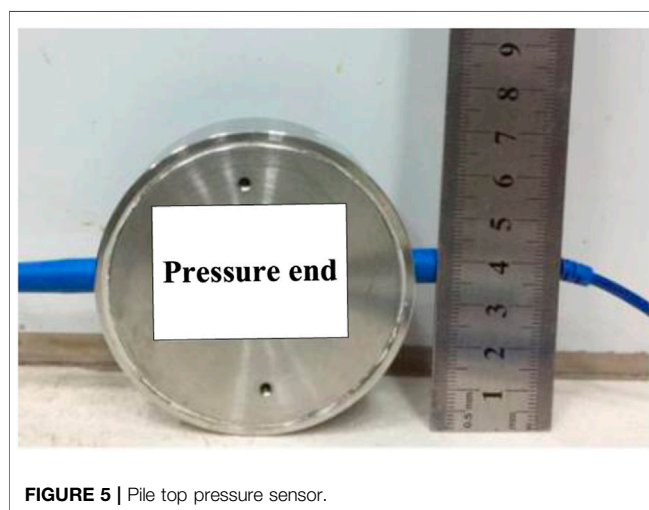
Test pile number	Pile material	Diameter (mm)	Pile length (mm)	Wall thickness (mm)	Pile end form	Elastic modulus (GPa)	Poisson ratio
TP1	Aluminum pipe	140	1000	3	Closed-ended	72	0.3
TP2		100	1000	3	Closed-ended	72	0.3

**TABLE 3** | sensitization micro FBG sensor parameter table.

Parameter type	Wavelength interval (nm)	Center wavelength (nm)	Range ($\mu\epsilon$)	Resolution ($\mu\epsilon$)	Operating temperature ($^{\circ}\text{C}$)
Value size	± 3	1510~1590	± 1500	1	-30~120

TABLE 4 | Pile top pressure sensor parameters.

Pressure sensor	Diameter (mm)	Height (mm)	Range (MPa)	Acquisition equipment
Demodulator	70	25	1	Fiber rating



effective stress increased. Through a series of indoor geotechnical tests, the soil sample has been tested to meet the test requirements, and the pile jacking test can be carried out.

Test Plan

In order to ensure the smooth progress of the test and real-time monitoring of the load change law of the pile jacking process, such as pile pressure and pile end resistance, the following Table 5 test plan is proposed.

Selection of Stake

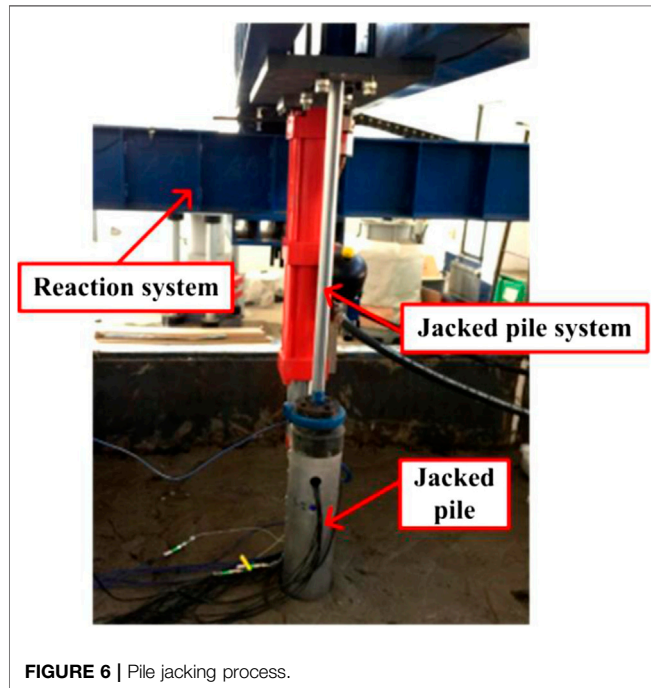
According to the “Technical Specification for Building Pile Foundations” (JGJ 94-2008) [22], the minimum center distance of foundation piles is $4D$ (D : pile diameter), the two sets of model pipe piles in this experiment are all arranged in the center of the model box, and the center of the pile is 1400 mm from the boundary of the model box, which meets the above requirements, and the boundary effect can be ignored [23].

Experimental Procedure

The specific steps of pile jacking test are as follows: ① The hydraulic jack on the loading beam is moved to the designated pile position through the electronic control system. ② Turn on the system host and control the jack to rise to a certain height through the oil pump. Put the test pile upright on the pile to be pressed,

TABLE 5 | Test pile test plan table.

Test pileNumbering	Pile jacking depth (mm)	Pile jacking speed (mm/min)	FBG sensor (pc)	Pressure sensor (pc)
TP1	900	300	6	1
TP2	900	300	6	1

**FIGURE 6 |** Pile jacking process.

and use a magnetic box level to adsorb on the surface of the pipe pile to determine whether the pipe pile is vertical to prevent eccentric compression. ③ After confirming that the pipe pile is upright, pressurize again through the system host to control the oil pump, so that the hydraulic jack is slowly and uniformly lowered until it stops pressurizing when it is about to touch the top of the model pile. ④ Connect the transmission lines of each FBG sensor and pile top pressure sensor to their corresponding collection instruments in turn. ⑤ After confirming that the connection is correct and the parameters have been adjusted, data collection will be carried out before the formal pile jacking test. ⑥ In view of the limited stroke of the hydraulic jack, the entire pile jacking process is completed in two times, with a pause in the middle to increase the falling height of the jack. The pile jacking process is shown in **Figure 6**.

FBG SENSOR DATA PROCESSING

In order to study the influence of different diameters on the pile side resistance, In this sample, the FBG sensor is pasted on the surface of the pile and the wavelength difference of the optical fiber measured by the FS2200RM fiber grating demodulator during the pile jacking process. According to the wavelength

difference, the unit resistance of the pile side is calculated by Eqs 1, 2.

The expression of the strain change value is as follows:

$$\Delta\lambda_B = 1 - P_e \lambda_B \Delta\varepsilon = K_\varepsilon \Delta\varepsilon, \quad (1)$$

where: $\Delta\lambda_B$ is the wavelength difference (nm); P_e is the effective elasticity coefficient of the grating; λ_B is the center wavelength of the light grating (nm); $\Delta\varepsilon$ is the strain change value; K_ε is the sensitivity coefficient (pm/ $\mu\varepsilon$).

The expression of the axial force N during the pile jacking process is as follows:

$$N_i = E_c \Delta\varepsilon A_p, \quad (2)$$

where: N_i is the pile shaft force at the i th FBG sensor position (KN); E_c is modulus of pile concrete (MPa); $\Delta\varepsilon$ is the strain change value of the pile body; A_p is the cross-sectional area of the pile body (mm^2).

The expression of the unit resistance of the pile side during pile jacking is as follows:

$$Q_i = N_i - N_{i+1}, \quad (3)$$

$$q_i = \frac{Q_i}{u l_i} = \frac{N_i - N_{i+1}}{\pi D l_i}, \quad (4)$$

where: Q_i is the side resistance of the i th section (kN); q_i is the unit side resistance of the i th section (kPa); u is the perimeter of the pile (m); l_i is the distance between section i and $i + 1$ (m); D is pile diameter (m).

TEST RESULTS AND ANALYSIS

Analysis of Pile Pressure During Pile Jacking

The pile pressure in the process of pile jacking is mainly measured by the pile top pressure sensor. Aiming at the cohesive soil environment of this experiment, in order to better observe the influence of pile diameter on the pile pressure during pile jacking, plot the curve of the pressure of the test piles TP1 and TP2 with the depth of the pile during the entire pile jacking process, as shown in **Figure 7**.

It can be seen from **Figure 7** that the pile pressure of the two test piles increases approximately linearly with the increase of the pile jacking depth. The pile pressure of the test pile TP1 is always greater than that of the test pile TP2 throughout the pile jacking process, Mainly because the larger the pile diameter, the larger the contact area between the pile body and the clay, the greater the compaction of the soil around the pile, and the compacted pile end soil and the soil around the pile cause the pile pressure to increase continuously. When the pile jacking depth reaches the

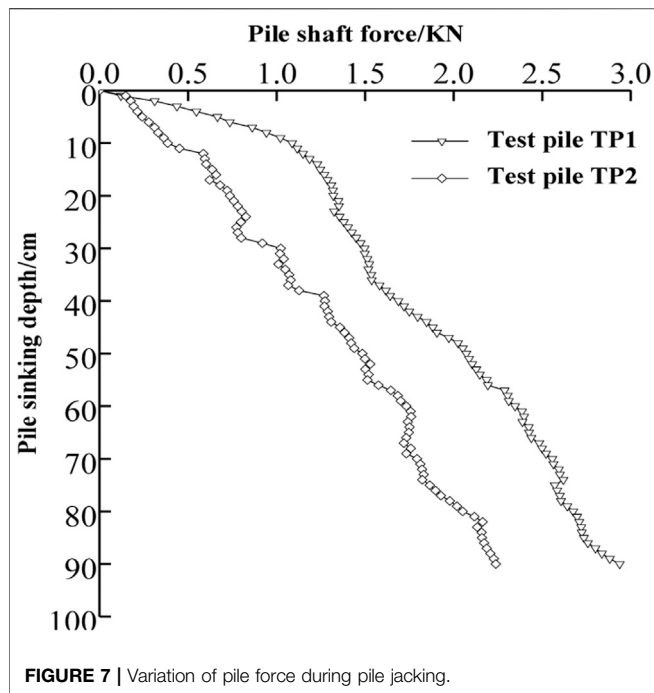


FIGURE 7 | Variation of pile force during pile jacking.

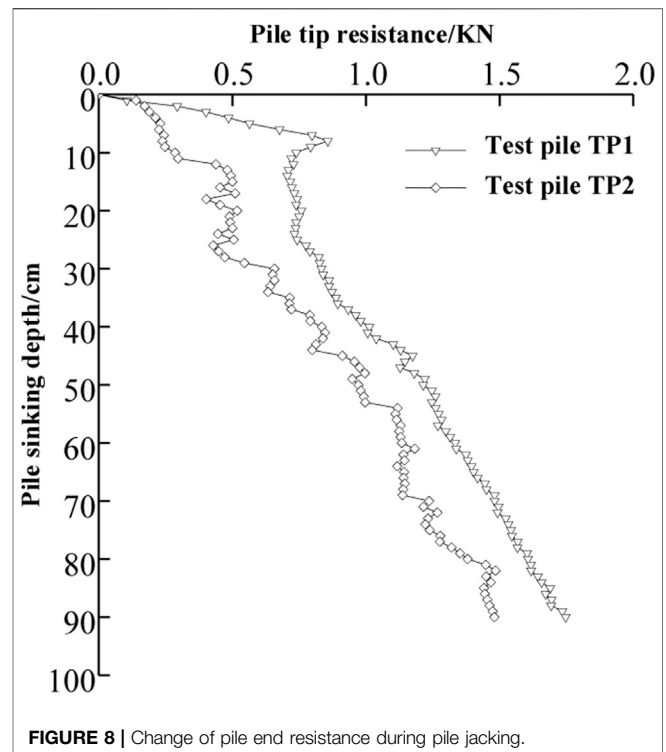


FIGURE 8 | Change of pile end resistance during pile jacking.

maximum, the final pressure of the large-diameter test pile TP1 is 2.94 kN, and the final pressure of the small-diameter test pile TP2 is 2.24 kN. Through comparison, it can be found that the final pressure of the test pile TP1 is 31% higher than that of the test pile TP2, indicating that the pile diameter has a greater influence on the final pressure. The main reason is that different pile diameters affect both the pile end resistance and the pile side resistance.

Analysis of Pile End Resistance During Pile Jacking

The pile end 1# sensor can be used to measure the change law of the pile end resistance of each test pile during the pile jacking process. The change trend of the pile end resistance of different test piles during the pile jacking process reflects the influence of the size of the pile diameter on the load transfer mode. The change in pile end resistance during the process is shown in Figure 8, and the percentage of pile end resistance in the pile pressure at different pile jacking depths is shown in Figure 9.

It can be seen from Figures 8, 9 that during the entire pile jacking process, the pile end resistance of the two pipe piles showed a gradual increase with the increase of the pile jacking depth. When the pile jacking depth is less than 10 cm, the pile end resistance of the two test piles increases rapidly, and the phenomenon of test pile TP1 is more obvious. The value can reach 0.793 kN, accounting for 77.59% of the pile pressure. The pile end resistance of test pile TP2 The growth rate of TP1 is smaller than that of TP1, but the percentage of pile pressure is far more than 65%; The reason for the analysis may be that in the early stage of pile jacking, the test pile disturbs the soil around the shallow pile a lot, the pile body is not in close contact with the surrounding soil, the soil squeezing effect is not obvious, and the

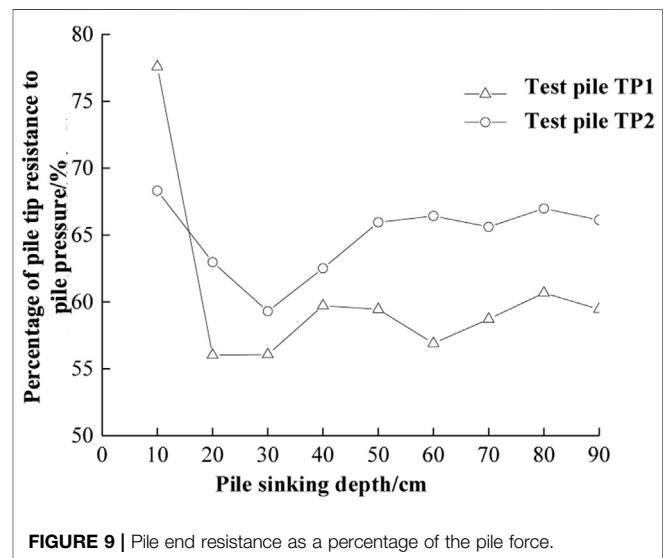
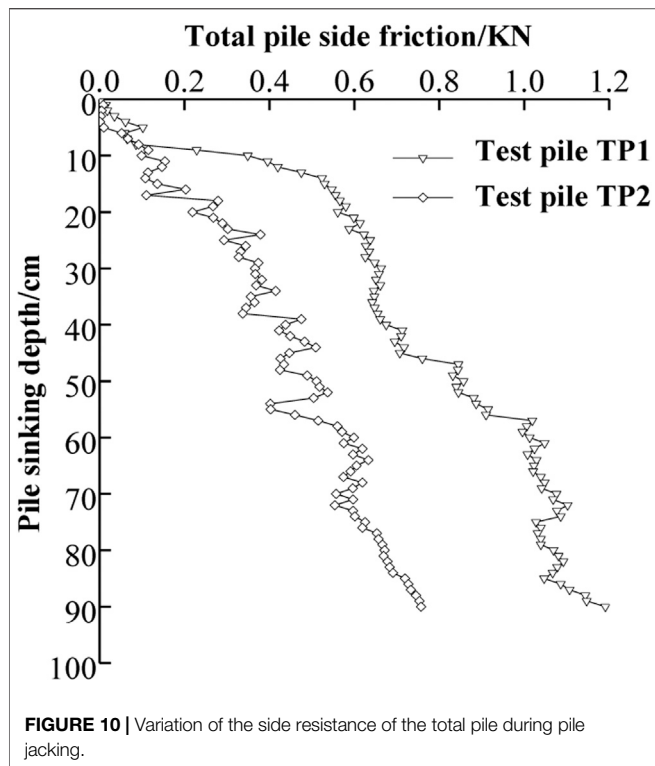


FIGURE 9 | Pile end resistance as a percentage of the pile force.

side resistance of the pile has not been well exerted. Most of the pile pressure is borne by the pile end. Because the pile diameter of the test pile TP1 is large, the disturbance range of the shallow pile surrounding soil is large, and the pile side resistance is small, so the pile end resistance growth rate is large. piles TP1 and TP2 becomes slower, especially in the range of 10 cm~30 cm, the pile end resistance of the test pile TP1 increases from 0.793 kN to 0.827 kN, and the test pile TP2 Increased from 0.248 kN to 0.545 kN, the increase is relatively small, especially when the pile jacking depth is 30 cm, the ratio of the pile end resistance to



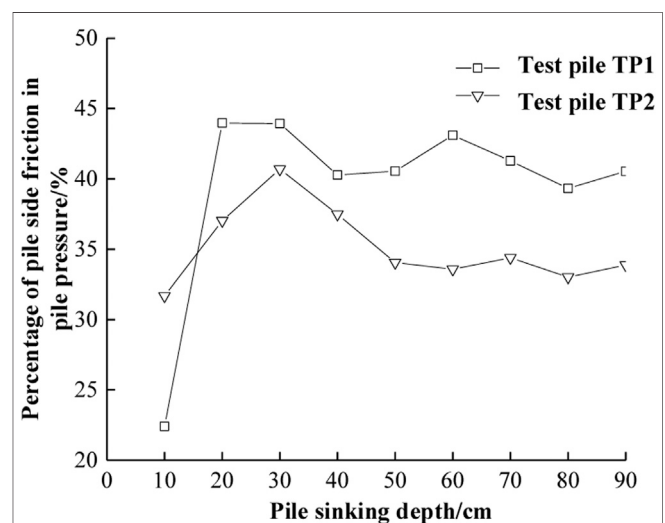
the pile pressure of the two test piles reaches the minimum 56.07% and 59.30%; The reason for the analysis may be that as the penetration depth increases, the contact area between the pile and the soil increases, and the compaction effect of the pile on the surrounding soil makes the side resistance of the pile gradually play from top to end, so the increase rate of the pile end resistance becomes slow. Throughout the pile jacking process, the pile end resistance of the test pile TP2 is always smaller than that of the test pile TP1. The reason is that although the pile end form of the two test piles is the same as the pile length, the test pile TP2 has the smallest pile diameter and the pile-soil interaction area is small. When the pile jacking depth reaches 90 cm, the end resistance of the test pile TP3 is 1.75 kN, the end resistance of the test pile TP2 is 1.48 kN, and the pile end resistance of the test pile TP1 accounts for 59.5% of its pressure. The test pile TP2 The end resistance of the piles accounted for 66.2% of the pile pressure, and the end resistance of the large-diameter test pile was 18% higher than that of the small-diameter pile; It shows that the pile jacking process of cohesive soil, the pile end resistance of the two groups of different pile diameters accounts for a large percentage of the pile pressure force, and the pile end resistance bears most of the load. The side resistance increases within a certain value range.

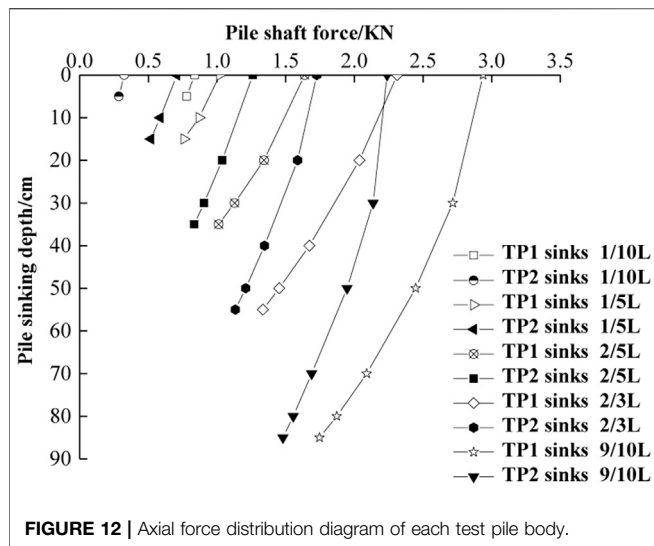
Analysis of Pile Side Resistance During Pile Jacking

Using FBG sensors at different positions of the pile body, using FS2200RM fiber grating demodulator to collect different wavelength differences, using Eqs 1–3 to convert, pile side

resistance of each test pile changes with the pile jacking depth The curve is shown in Figure 10.

It can be seen from Figures 10, 11 that: on the whole, the pile side resistance of each test pile gradually increases with the increase of the pile jacking depth, which is consistent with the research results of Rao et al. [24] and Alawneh et al. [25]. It is analyzed that with the increase of the pile jacking depth, the contact area between the pile body and the soil increases, and the lateral pressure of the soil around the pile gradually increases, which makes the pile side resistance increase. In the range of 10 cm of pile jacking depth, the value of pile side resistance is very small, basically not exceeding 0.1 kN, and the ratio of side resistance to pile pressure is the smallest. This is mainly because the shallow soil body shakes more strongly during the pile jacking process, and the test pile with a larger pile diameter has a larger impact range, resulting in a certain gap between the pile and the soil, and the contact is no longer tight, as a result, the side resistance of pile in shallow soil is small. When the penetration depth is more than 10 cm, the side resistance of large diameter test pile is much greater than that the small diameter test pile at the same pile jacking depth, And at the pile jacking depth of 30 cm, the side resistance accounts for the highest proportion of the pile pressure. The test pile TP1 is about 44%, and the test pile TP2 is about 41%. The ratio of pile side resistance to pile pressure with small pile diameter is about 10% less than that of the test pile with large pile diameter; The reason may be that the diameter of the test pile TP2 is small, the contact area between the pile body and the soil is small, and the degree of side resistance is lower than that of the test pile TP1, which makes the value of the pile side resistance lower. And when the pile jacking depth reaches 90 cm, the side resistance of the test pile TP1 is 1.19 kN, and the ratio of pile side resistance to pile pressure is 40.54%. The side resistance of the test pile TP2 is 0.76 kN and the ratio of pile side resistance to pile pressure is 33.87%. Compared with the test pile TP2, the side resistance of TP1 is





57% higher, and the ratio of pile side resistance to pile pressure is 6.67% higher. It shows that the diameter is an important factor that affects the side resistance of the pile, because the larger the diameter of the pile, the larger the surface area of the pile in contact with the surrounding soil. The more obvious the compaction of the soil around the pile during the pile jacking process, the greater the lateral pressure. The value of pile side resistance is correspondingly large. For piles that rely on friction to carry the load, the effect of increasing the diameter of the pile body is more significant.

Analysis of Axial Force Results of Test Pile

Through Eqs 1, 2, the axial force distribution curves of the two test piles during the entire pile jacking process can be obtained, as shown in Figure 12.

It can be seen from Figure 12 that the axial force distribution of the test piles TP1 and TP2 is similar: at different pile jacking depths, the axial force of the pile body decreases with the increase of the pile jacking depth. The deceleration rate of the test pile TP2 is greater than that of the test pile TP1. And the slope of the axial force distribution curve along the pile body gradually decreases, which is consistent with the research results of Murthy et al. [26] and Cooke et al. [27]; It shows that the side resistance of the pile plays a role from top to end, and the resistance gradually increases along the pile body. The axial force is the smallest at the pile end and the side resistance is the largest. The reason may be: under different penetration depths, as the pile jacking depth gradually increases, the lateral pressure of the soil around the pile gradually increases, Make the bond between the soil particles and the pile body closer, thereby increasing the friction between the pile and the soil, And the process of load transmission down the pile body continuously overcomes the resistance and spreads to the surrounding soil through it. The increase of the pile side resistance makes the axial force decrease larger, so the slope of the pile shaft axial force curve is smaller. In addition, by comparing the two test

piles with different pile diameters at the same jacking depth, it can be found that the axial force of the test pile TP1 is larger than that of the test pile TP2, and the two test piles have increased with the penetration depth, the same jacking The axial force at the depth of the pile gradually increases. The reason for the analysis may be that the greater the pile jacking depth, the greater the gravity stress of the soil on the pile body, so the axial force gradually increases, The smaller the pile diameter and the larger the length of the test pile, the smaller the contact area between the pile end and the soil during the pile jacking process, the smaller the compressive rigidity of the test pile, and the smaller the pressure, so the same pile jacking depth test pile TP2 pile The body axial force is smaller than the test pile TP1. At the maximum penetration depth, the axial force of the test pile TP1 is 1.75 kN, and the axial force of the test pile TP2 is 1.48 kN. The test pile TP1 is 18% larger than the test pile TP2. It shows that the pressure of the pile with a large diameter is large, and the axial force of the pile body is also large.

Analysis of the Unit Resistance Result of the Test Pile Side

Assuming that the side resistance of each test pile is evenly distributed along the pipe pile body, the midpoint between the upper and lower adjacent FBG sensors is intercepted as the unit side resistance corresponding to the depth of the section. The unit side resistance distribution diagram of the test piles TP1 and TP2 As shown in Figure 13.

It can be seen from Figure 13 that the variation trend of unit side resistance of test piles TP1 and TP2 is similar under different penetration depths, That is: the unit side resistance increases unevenly with the increase of the pile jacking depth, and the overall distribution is that the upper soil layer is small and the lower soil layer is large. The reason may be that in the early stage of pile jacking, the pile disturbs the soil greatly, and the contact between the pile and the soil around the pile is not close. At this time, although the unit side increases, the increase is small, and the penetration depth of the pile gradually increases. The horizontal lateral pressure provided by the soil around the pile is large, so the unit side resistance is gradually exerted, the slope of the curve is large, and the axial force of the pile body reaches the maximum value at the maximum penetration depth. By comparing the distribution of unit side resistance at the same jacking depth of each test pile, it can be found that as the penetration depth increases, the unit side resistance gradually decreases, that is, there is a “degradation effect” in the side resistance [28]. The reason for the analysis may be: the greater the penetration depth, the disturbance of the upper soil layer is much greater than that of the lower soil layer, which increases the contact gap between the soil around the upper pile and the test pile, resulting in a gradual decrease in pile side resistance. The other reason is that before the pile is put into the soil, the pile body is relatively rough; after the pile is put into the soil, the relative roughness is reduced due to the fine clay particles filling the convex and concave surface of the pile body, resulting in a reduction in the friction angle, so the pile side resistance is

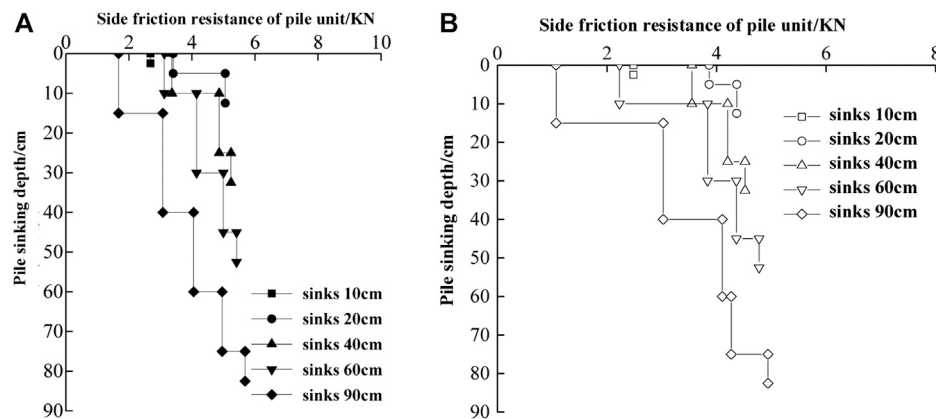


FIGURE 13 | Distribution of side resistance of each test pile body. (A) Test pile TP1 (B) Test pile TP2.

degraded. And at the same pile jacking depth, the unit side resistance value of the test pile TP1 is larger than that of the test pile TP2. The reason is that the pile diameter of the test pile TP1 is large, so the unit friction area between the pile and the soil is large, so the value is larger. By comparing the distribution of unit side resistance of each test pile at the maximum penetration depth, it is found that the value of test pile TP1 is 5.69 kN, the value of test pile TP2 is 4.94 kN, and the unit side resistance of the test pile TP1 is 15% higher than that of the test pile TP2, which means that the pile-soil contact area is small during the process of pile jacking of the small diameter test pile, so the unit side resistance is low.

Analysis of Stress Behavior During Pile Jacking

In order to study and analyze the total stress state of the two model pipe piles in the process of pile jacking, **Figure 14** is drawn.

It can be seen from **Figure 14** that the pile pressure and pile end resistance during the whole process of pile jacking of the two test piles gradually increase with the increase of pile jacking depth, which is consistent with the research results of Chan et al. [28]. And when the pile jacking depth is less than 10 cm, the pile pressure is equal to the pile end resistance; it can also be seen from the figure that the overall change trends of the test piles TP1 and TP2 are similar, but in terms of value, the pile pressure, pile end resistance and the pile side resistance of TP1 are larger than the test pile TP2; the main reason is that the test piles TP1 and TP2 have the same length of 1000 mm, and both are closed pipe piles. At the same pile jacking speed, the two test piles Similar trends; However, due to the large diameter of the test pile TP1, during the pile jacking process, the contact area between the pile body and the soil around the pile is large, and the lateral pressure of the soil is large, resulting in a large proportion of the pile side resistance in the pile pressure.

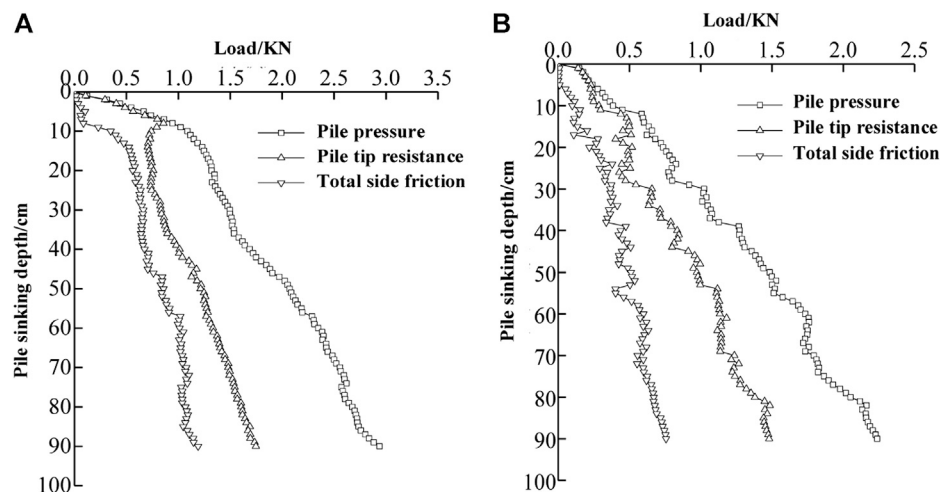


FIGURE 14 | Load curve of the entire pile of test piles. (A) Test pile TP1 (B) Test pile TP2.

CONCLUSION

Aiming at the cohesive soil environment, this paper compares the bearing performance of model test piles with different pile diameters through indoor jacked pile tests, and draws the following conclusions:

- (1) The pressure, end resistance, and side resistance of the two test piles of different diameters increase approximately linearly with the increase of the pile jacking depth; at the end of the pile jacking, the pressure of the test pile TP1 is higher than that of TP2 31%; in terms of pile end resistance, the test pile TP1 accounted for 59.5% of pile pressure, the test pile TP2's pile end resistance accounted for 66.2% of pile pressure, and pile end resistance of the two test piles accounted for the percentage of the pile pressure. Both exceed 50%, that is, the jacked pile of cohesive soil, and the pile end resistance bears most of the load;
- (2) At the end of the pile jacking, the side resistance of the test pile TP1 is 1.19 kN, the pile side resistance of the test pile TP2 is 0.76 kN, and the test pile TP1 is 57% higher than the test pile TP2. It is shown that the diameter is an important factor affecting the exertion of pile side resistance.
- (3) The axial force distribution of the test piles TP1 and TP2 are similar. Under different penetration depths, the pile side resistance continues to play from top to end, which causes the pile shaft axial force to continue to decrease as the pile jacking depth increases and the axial force distribution. The slope of the curve gradually decreases; at the maximum penetration depth: the axial force of test pile TP1 shaft with a larger pile diameter is 18% larger than the test pile TP2 with a smaller pile diameter.

REFERENCES

1. Doherty P, Gavin K, Gallagher D. Field investigation of base resistance of pipe piles in clay. *Proc Inst Civ Eng - Geotech Eng* (2010) 163(1):13–22. doi:10.1680/jeng.2010.163.1.13
2. Zhang LM, Wang H. Field study of construction effects in jacked and driven steel H-piles. *Geotechnique* (2009) 59(1):63–9. doi:10.1680/geot.2008.t.029
3. Han F, Ganju E, Salgado R, Prezzi M. Comparison of the load response of closed-ended and open-ended pipe piles driven in gravelly sand. *Acta Geotech* (2019) 14(6):1785–803. doi:10.1007/s11440-019-00863-1
4. Paik K, Salgado R. Determination of bearing capacity of open-ended piles in sand. *J Geotech Geoenviron Eng* (2003) 129(1):46–57. doi:10.1061/(asce)1090-0241(2003)129:1(46)
5. Zhang Z, Wang YH. Examining setup mechanisms of driven piles in sand using laboratory model pile tests. *J Geotech Geoenviron Eng*. (2015) 141(3):04014114. doi:10.1061/(asce)gt.1943-5606.0001252
6. Lehan BM, Lim JK. Set-up of pile shaft friction in laboratory chamber tests. *Int J Phys Modell Geotech* (2014) 14(2):21–30. doi:10.1680/ijpmg.13.00017
7. Lehan BM, White DJ. Friction fatigue on displacement piles in sand. *Geotechnique* (2004) 54(10):645–58. doi:10.1680/geot.2004.54.10.645
8. Klotz EU, Coop MR. An investigation of the effect of soil state on the capacity of driven piles in sands. *Geotechnique* (2001) 51(9):733–51. doi:10.1680/geot.2001.51.9.733
9. Yuan B, Sun M, Xiong L, Luo Q, Pradhan SP, Li H. Investigation of 3D deformation of transparent soil around a laterally loaded pile based on a hydraulic gradient model test. *J Build Eng* (2020) 28(3):101024. doi:10.1016/j.jobe.2019.101024
10. Gao L, Gong Y, Liu H, Ji B, Xuan Y, Ma Y. Experiment and numerical study on deformation measurement of cast-in-place concrete large-diameter pipe pile using optical frequency domain reflectometer technology. *Appl Sci* (2018) 8(9):1450. doi:10.3390/app8091450
11. Tang L, Wang K, Deng L, Yang G, Chen J, Jin L. Axial loading behaviour of laboratory concrete piles subjected to permafrost degradation. *Cold Reg Sci Technol* (2019) 166:102820. doi:10.1016/j.coldregions.2019.102820
12. Li G, Yu Q, Ma W, Mu Y, Li X, Chen Z. Laboratory testing on heat transfer of frozen soil blocks used as backfills of pile foundation in permafrost along Qinghai-Tibet electrical transmission line. *Arabian J Geosci* (2015) 8(5):2527–35. doi:10.1007/s12517-014-1432-9
13. Tan M, Zhou N, Cheng Y, Wang J, Zhang W, Zou D. A temperature-compensated fiber Bragg grating sensor system based on digital filtering for monitoring the pantograph-catenary contact force. *Proc Inst Mech Eng Part F J Rail Rapid Transit* (2018) 233(2):095440971878614. doi:10.1177/0954409718786143
14. Weng X, Zhan J, Lou Y, Zhan J. Application of fiber bragg grating strain sensors to a centrifuge model of a jacked pile in collapsible loess. *Geotech Test J* (2016) 39(3):20150076. doi:10.1520/gtj20150076
15. Yuan B, Sun M, Wang Y, Zhai L, Luo Q, Zhang X. Full 3D displacement measuring system for 3D displacement field of soil around a laterally loaded pile in transparent soil. *Int J Geomech* (2019) 19(5):04019028. doi:10.1061/(asce)gm.1943-5622.0001409
16. Pei HF, Yin JH, Zhu HH, Hong CY, Jin W, Xu DS. Monitoring of lateral displacements of a slope using a series of special fibre Bragg grating-based in-place inclinometers. *Meas Sci Technol* (2012) 23(2):025007. doi:10.1088/0957-0233/23/2/025007

- (4) As the penetration depth increases, the unit side resistance at the same pile jacking depth gradually decreases, that is, there is a “degeneration effect” in the side resistance.
- (5) The law is found in homogeneous clay soil with specific moisture content. The variation laws of pile compression force, pile tip resistance, pile shaft axial force and pile lateral friction resistance obtained in this paper can provide reference for the study of pile driving mechanism in homogeneous clay and layered clay.

DATA AVAILABILITY STATEMENT

The original contributions presented in the study are included in the article/Supplementary Material, further inquiries can be directed to the corresponding author.

AUTHOR CONTRIBUTIONS

Writing: XL; Methodology: YH; Review: YW and SS; Funding: MZ; Supervision: DM.

FUNDING

This work was supported by the National Natural Science Foundation of China (51708316, 51778312), the China Postdoctoral Science Foundation Funding (2018M632641); the Shandong Provincial Postdoctoral Innovation Program of China (201903043).

17. Kou HL, Yu F, Liu T. Strain monitoring on PHC pipe piles based on fiber bragg grating sensors. *J Perform Constr Facil* (2019) 33(2). doi:10.1061/(asce)cf.1943-5509.0001266
18. People's Republic of China Industry Standards Writing Group. *GB/T 50123-1999 geotechnical test method standards*. Beijing, China: China Planning Press (1999).
19. Duan N. *Mechanical characteristics of monopile foundation in sand for offshore wind turbine*. (Doctoral thesis). London (UK): UCL University College London (2016).
20. Ye ZH, Zhou J, Tang SD. Model test on pile bearing behaviors in clay under different pile tip conditions. *J Tongji Univ Nat Sci Ed* (2009) 37(6): 733–7.
21. Yu J, Huang MS, Zhang CR. Model tests and analysis of single piles with two different diameters subjected to cyclic lateral loadings in clay. *Rock Soil Mech* (2016) 37(4):973–80. doi:10.16285/smj.r.2016.04.009
22. People's Republic of China Industry Standards Writing Group. *Technical specifications for building pile foundation: JGJ 94-2008*. Beijing, China: China Building Industry Press (2008).
23. Elkady A, Lignos DG. Full-scale testing of deep wide-flange steel columns under multiaxial cyclic loading: loading sequence, boundary effects, and lateral stability bracing force demands. *J Struct Eng* (2018) 142(2):04017189. doi:10.1061/(asce)st.1943-541x.0001937
24. Alawneh AS. Modelling load-displacement response of driven piles in cohesionless soils under tensile loading. *Comput Geotechnics* (2005) 32(8): 578–86. doi:10.1016/j.compgeo.2005.11.003
25. Heerema EP. Predicting pile driveability: heather as an illustration of the “friction fatigue theory”. In: *SPE European Petroleum Conference*. London, UK: Society of Petroleum Engineers (1978), Vol. 1:413–22.
26. Murthy DS, Robinson RG, Rajagopal K. Formation of soil plug in open-ended pipe piles in sandy soils. *Int J Geotech Eng* (2018) 1–11. doi:10.1080/19386362.2018.1465742
27. Cooke RW, Price G, Tarr K. Jacked piles in London Clay: a study of load transfer and settlement under working conditions. *Géotechnique* (1979) 29(2): 113–47. doi:10.1680/geot.1979.29.2.113
28. Chan THT, Yu L, Tam HY, Ni YQ, Liu SY, Chung WH, et al. Fiber Bragg grating sensors for structural health monitoring of Tsing Ma bridge: background and experimental observation. *Eng Struct* (2006) 28(5):648–59. doi:10.1016/j.engstruct.2005.09.018

Conflict of Interest: The authors declare that the research was conducted in the absence of any commercial or financial relationships that could be construed as a potential conflict of interest.

Copyright © 2021 Wang, Sang, Liu, Huang, Zhang and Miao. This is an open-access article distributed under the terms of the Creative Commons Attribution License (CC BY). The use, distribution or reproduction in other forums is permitted, provided the original author(s) and the copyright owner(s) are credited and that the original publication in this journal is cited, in accordance with accepted academic practice. No use, distribution or reproduction is permitted which does not comply with these terms.



Monitoring and Analysis of Pore and Earth Pressure at the Pile Surface Using Piezoresistive Silicon Pressure Transducers

Yonghong Wang, Yongfeng Huang, Mingyi Zhang* and Jiaxiao Ma

Department of Civil Engineering, Qingdao University of Technology, Qingdao, China

OPEN ACCESS

Edited by:

Liang Ren,
Dalian University of Technology, China

Reviewed by:

Baoxin Qi,
Shenyang Jianzhu University, China
John Zhanhu Guo,
University of Tennessee, Knoxville,
United States
Qian Feng,
China Earthquake Administration,
China

*Correspondence:

Mingyi Zhang
zmy58@163.com

Specialty section:

This article was submitted to
Smart Materials,
a section of the journal
Frontiers in Materials

Received: 14 November 2020

Accepted: 25 January 2021

Published: 30 April 2021

Citation:

Wang Y, Huang Y, Zhang M and Ma J
(2021) Monitoring and Analysis of Pore
and Earth Pressure at the Pile Surface
Using Piezoresistive Silicon
Pressure Transducers.
Front. Mater. 8:629370.
doi: 10.3389/fmats.2021.629370

The piezoresistive silicon pressure transducers based on the piezoresistive effect have demonstrated their potential in the accurate monitoring of pressure. However, their usage in the pore and earth pressure monitoring at the pile surface under hydraulic jacking has not yet been explored. In this study, two self-made model piles (one is a closed-ended pile and the other is an open-ended pile) were instrumented with piezoresistive silicon earth transducers and pore pressure transducers and then driven into the soil using a hydraulic jack. A comprehensive investigation was first carried out for the structure of the model piles, the installation procedure of the transducers, and the composition of the test system. The pore and earth pressure measurements of the transducers were used for the evaluation of the distribution of the pore pressure, excess pore pressure, radial earth pressure, and radial effective earth pressure. The model test results indicate that the piezoresistive silicon pressure transducers are suitable for monitoring the pore and earth pressure at the pile surface during jacking. In addition, the pore pressure, excess pore pressure, radial earth pressure, and effective radial earth pressure along the test piles were affected by the penetration depth and the pile end form.

Keywords: model test, pore pressure, jacking method, piezoresistive silicon transducers, radial earth pressure

INTRODUCTION

With the rapid development of the economy, many high-rise and ultra high-rise buildings have been built in the cities, and the shallow foundations can no longer meet the bearing capacity and deformation requirements of these buildings. Therefore, precast piles composed of cement (Ghahari et al., 2018; Hou et al., 2018; Liang et al., 2020), sand-gravel aggregates, and steel bars have been widely used in engineering. The common method for pile installation is dynamic driving method and hydraulic jacking method. The hydraulic jacking method is a construction method that uses static pressure to drive precast piles into the soil (Kou et al., 2018). Compared to the dynamic driving method, the hydraulic jacking method has many advantages such as no noise, no vibration, fast construction speed, and little damage to the pile body (Wang et al., 2017a; Wang et al., 2019) and is very popular in many engineering fields.

However, the piles are not only subjected to complex forces during jacking but also generate excess pore pressure and radial soil pressure, adversely affecting the bearing capacity of the piles and adjacent buildings. As early as 1932, Casagrande (1932) found that pile jacking caused clay disturbance around the pile and pointed out that the clay within a certain range around the pile was completely or largely remodeled to maximize the bearing capacity of the pile. Seed and Reese.

(1957) confirmed Casagrande's observations with piles penetration test in the field. The field test shows that the pressure generated by the pile installation is mainly transferred to the soil around the pile with increasing pore water pressure. In the subsequent studies, these findings, indicating the limitations of the hydraulic jacking method, were supported by Bjerrum. (1967) and explained by Roy et al. (1981). More recently, McCabe and Lehane. (2006), Igoe et al. (2011), and Kou et al. (2015) confirmed the importance of monitoring and studying the mechanism of the excess pore pressure and radial earth pressure in the process of pile jacking.

As mankind enters the information age, all social activities of people are centered on information acquisition and information conversion. As an important means of information acquisition and information conversion, sensors are at the forefront of information science and the basis for informatization (Chen et al., 2020; Huang et al., 2020; Su et al., 2020). The common method to measure the pore pressure and earth pressure during the process of pile jacking is to install the pore pressure and earth pressure sensors at different depths within a certain range of the pile diameter. In 1958, Bjerrum et al. (1958) first successfully measured the pore pressure of soil around the pile through a field test. These observations, indicating that the pore pressure reaches the maximum value at the end of pile jacking and the pore pressure is related to the overburden weight, were supported by Orrje and Broms. (1967) and monitored by Airhart et al. (1969) through this measurement method. Randolph et al. (1979) and Steenfelt et al. (1981) installed the earth pressure sensors around the pile and monitored the radial earth pressure during jacking. In the subsequent studies, Pestana et al. (2002) and Li et al. (2018) successfully measured the distribution and variation of the earth pressure around the pile by this method. However, Lo and Stermac. (1965) and Jardine and Bond. (1989) found that the pore and earth pressure decreases rapidly with increasing distance from the pile and is quite different at the pile surface than that around the pile. Therefore, using the pore and earth pressure around the pile as the pore and earth pressure at the pile surface would cause an error, limiting the study of pore and earth pressure characteristics at the pile surface. There are a few reports on the monitoring of the pore and earth pressure at the pile surface (Lehane and Jardine, 1994; Liu et al., 2019), and the sensors used in the experiments are the traditional pressure sensors, which cannot meet the test requirements well. Compared to the traditional pressure sensors, the working principle, material characteristics, and manufacturing process of piezoresistive silicon pressure transducers are different. Compared with piezoresistive silicon sensors, traditional earth pressure cell and hydraulic pressure gauge have low sensitivity, narrow measurement range, low dynamic acquisition frequency, large size, and insufficient linearity stability, which makes it difficult to meet the long-term health monitoring requirements of actual projects (Vaughan and Walbancke, 1973; Lyne and Jack, 2004; Chen et al., 2019). The piezoresistive silicon pressure transducers with high sensitivity, good linearity, good stability, small size, and other advantages have been successfully used in the monitoring of structural health

(Li et al., 2010; Moslehy et al., 2010), concrete strength (Dumoulin et al., 2012), microcracks formation (Xu et al., 2013; Jiang et al., 2017), and interfacial debonding (Feng et al., 2016). However, there are no reports on the use of the piezoresistive silicon pressure transducers to monitor the pore and earth pressure at the pile surface during the pile jacking in the model test.

In this study, the piezoresistive silicon pore pressure transducers and earth pressure transducers were installed in the holes of two self-made model piles: 1) open-ended pile and 2) closed-ended pile. The pore water pressure and earth pressure at the pile surface were tested during pile jacking. The distribution and variation of the pore pressures, excess pore pressure, radial earth pressure, and effective radial earth pressure at the pile surface in the process of jacking were analyzed. In addition, the effects of the pile end form on varying pore and earth pressures were considered. This study provides a reference for subsequent research on the measurement method of the pore and earth pressures at the pile surface.

THE PRINCIPLE OF PIEZORESISTIVE SILICON PRESSURE TRANSDUCER

The Basic Principle

The piezoresistive silicon pressure transducer works on the principle of the piezoresistive effect of monocrystalline silicon. Four equivalent semiconductor resistors are installed in a specific direction of the silicon diaphragm and connected to the Wheatstone bridge. When the diaphragm of the transducer is affected by external pressure and the Wheatstone bridge is out of balance, the output voltage proportional to the measured pressure was obtained by adding the exciting power supply to the Wheatstone bridge.

The output voltage of the bridge V_0 can be expressed as follows (Li et al., 2010):

$$V_0 = \frac{[(R_1 + \Delta R_1)(R_3 + \Delta R_3) - (R_2 - \Delta R_2)(R_4 - \Delta R_4)]}{(R_1 + R_2 + \Delta R_1 - \Delta R_2)(R_3 + R_4 + \Delta R_3 - \Delta R_4)} \times V_1, \quad (1)$$

where V_B is the supply voltage, R_i is the resistance of semiconductor resistors, $i = 1, 2, 3, 4$, and ΔR_i is the resistance variation of semiconductor resistors, $i = 1, 2, 3, 4$.

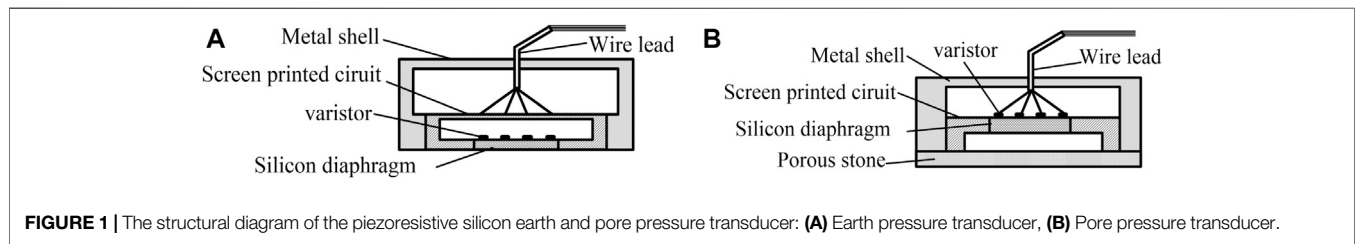
The resistance of semiconductor resistors are equal, $R_1 = R_3 = R_2 = R_4 = R$, and $\Delta R_i = R \cdot G \cdot \varepsilon_i$, $i = 1, 2, 3, 4$; Eq. 5 can be written as follows (Feng et al., 2016):

$$V_0 = \frac{1}{4} G \cdot \frac{\varepsilon_1 + \varepsilon_3 - \varepsilon_2 - \varepsilon_4}{\left[1 + \frac{1}{2}(\varepsilon_1 + \varepsilon_2 + \varepsilon_3 + \varepsilon_4)\right]} V_B, \quad (2)$$

where G is the coefficient of strain and ε_i is the strain value of semiconductor resistance i , $i = 1, 2, 3, 4$.

The strain value of the semiconductor resistance is satisfied, $\varepsilon_1 = \varepsilon_3 = -\varepsilon_2 = -\varepsilon_4$; therefore, the strain value of the diaphragm ε can be expressed as follows (Wang et al., 2017b):

$$\varepsilon = \frac{V_0}{G \cdot V_B}. \quad (3)$$



The Principle of Piezoresistive Silicon Earth Transducer and Pore Pressure Transducer

The piezoresistive silicon earth transducer and pore pressure transducer used in this test are made of polysilicon as the varistor and integrated using a microelectromechanical system. The resistors on the integrated silicon diaphragm of the transducer are connected by the screen-printed circuit, and the transducer is encased in the metal shell. The two transducers are different, as the end of the pore pressure transducer is installed with the permeable stone, and the water enters the transducer through the porous stone and changes the resistance of the polysilicon. **Figure 1** shows the structural diagram of the piezoresistive silicon earth pressure transducer and pore pressure transducer.

EXPERIMENTAL SETUP AND PROCEDURES

The Model Box

The model box used in this test has dimensions of $3,000 \times 3,000 \times 2,000 \text{ mm}^3$ (length \times width \times height) and was welded by a steel plate. The sinking process of the model pile was observed through the toughened glass window ($500 \times 500 \text{ mm}^2$) installed on the front of the model box. The loading system of the model box mainly comprises a reaction frame, a crossbeam, a hydraulic jack, an electric control system, and a static load control system to provide static pressure for the model piles.

The Model Pile

Tang et al. (2002) studied the influencing factors of pile side friction by installing strain gauges on the aluminum pile body. Duan. (2016) simulated the force characteristics of the pile foundation of the marine wind turbine under the vertical load using the aluminum pile indoor test and compared the results with the numerical simulation results. The research of the above scholars shows the feasibility of the indoor model test of the aluminum pile to analyze the pile foundation. In this article, the parameters of the model pile are determined according to the

similarity theory (Chui, 1990; Yang, 2005), and the calculation process is as follows:

1) Geometric similarity ratio

There is a certain relationship between the size and shape of the model and the prototype. The geometric similarity is one of the important indicators to ensure that the model test has a certain practical significance. The geometric similarity is shown in **Eq. 1**.

$$m_b = \frac{L_y}{L_s} = \frac{D_y}{D_s}, \quad (4)$$

where m_b is the model test pile size ratio, L_y and D_y represent the prototype pile size, and L_s and D_s represent model test pile size.

2) Similar modulus of elasticity

$$m_E = \frac{E_y}{E_s}, \quad (5)$$

where m_E is the model test elastic modulus similarity ratio, E_y is the prototype elastic modulus, and E_s is the model test pile elastic modulus.

3) Load similarity ratio

$$m_P = \frac{P_y}{P_s} = m_E \cdot m_b^2, \quad (6)$$

where m_P is the model test load similarity ratio, P_y is the prototype load, and P_s is the model test pile load.

It is very difficult to fully satisfy the similarity theorem when conducting model tests. Approximate similarity methods appear. The approximate similarity method only retains the similarity conditions of the main factors that affect the test results so as to obtain sufficiently accurate similarity (Liu, 2015).

TABLE 1 | Model pipe pile parameter.

Number	Diameter/mm	Length/mm	Thickness/mm	Elastic modulus/GPa	Poisson ratio	Form of pile end
TP1	140	1,000	3	72	0.3	Closed
TP2	140	1,000	3	72	0.3	Open

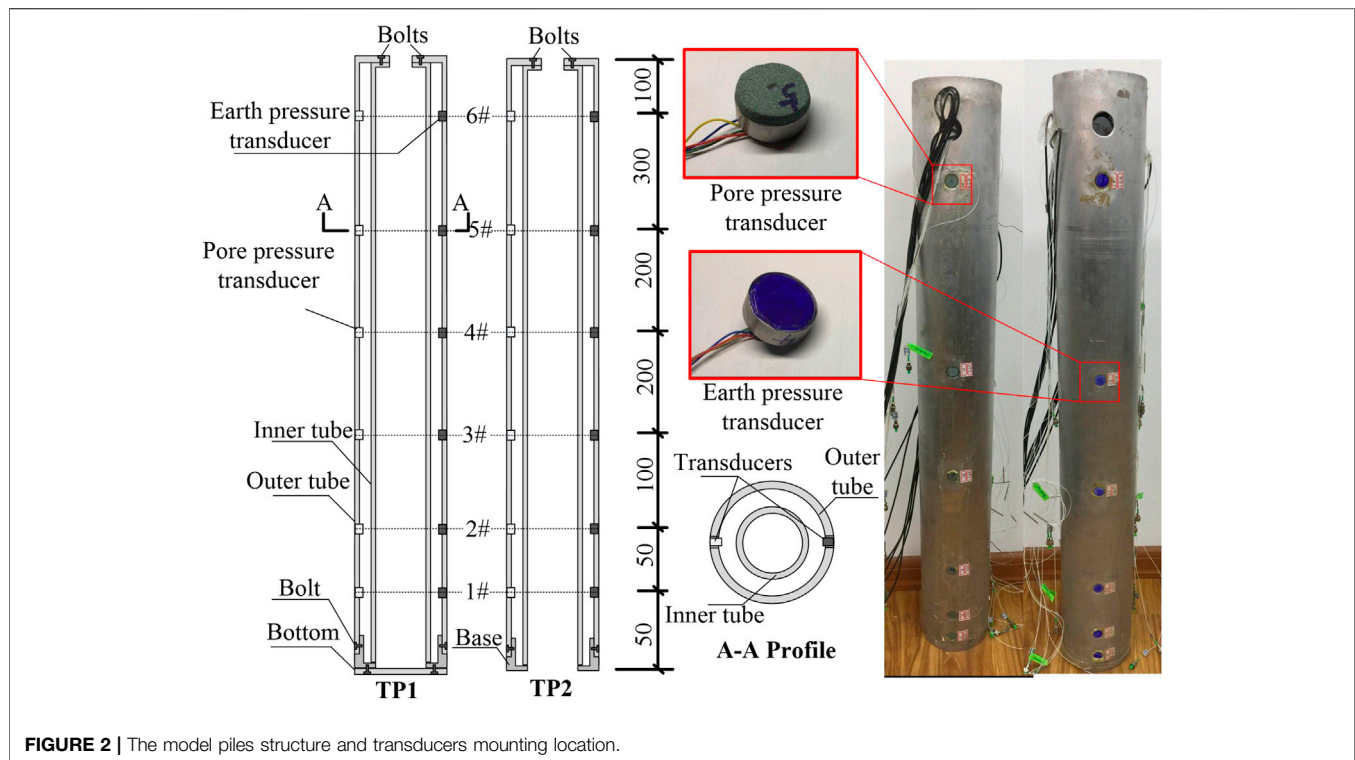


FIGURE 2 | The model piles structure and transducers mounting location.

Generally, the pile diameter of a large diameter single pile is 3–6 m, and the pile length is 30–50 m (Yu et al., 2016). Based on the prototype pile length of 40 m, pile diameter of 5.6 m, elastic modulus of 210 GPa, and Poisson's ratio of 0.3, in order to meet the load similarity ratio, the geometric similarity ratio is determined to be 40 and the elastic modulus similarity ratio is 2.9. The similarity ratio of the loose ratio is 1, and the test piles are made of aluminum material, the elastic modulus is 72 GPa, the Poisson's ratio is 0.3, and the diameter and length are 140 and 1,000 mm for aluminum pipe piles TP1 and TP2, respectively. The thickness of the inner and outer tube of the model pipe piles is 3 mm. In order to facilitate the installation of the transducers, the gap between the inner and outer tubes is 20 mm. The model pile TP1 is a closed-ended pipe pile, and TP2 is an open-ended pipe pile. The model pile parameters are listed in **Table 1**.

The piezoresistive silicon earth pressure transducers and pore pressure transducers were installed on the same cross-section in the model pile body. The excess pore water pressure at the pile-soil interface caused by pile sinking increases linearly with the depth of soil penetration. The average growth gradient of the excess pore water pressure near the bottom of the pile is greater than that of the middle and top of the pile. Therefore, the sensor is arranged with a sparse upper part and a dense lower part. The transducer distances from the pile end are 50, 100, 200, 400, 600, and 900 mm, and the installation location numbers of the transducer from the pile end to the pile top are 1# to 6#. **Figure 2** shows the model piles structure and transducers mounting location.

Transducers Installation

Both transducers were mounted on the model pile in the same way using the following main process:

- 1) The holes were cut in the pile body at the transducer locations, and the metal sleeves of the same diameter as the transducers were welded to the inner wall of the model pile at the transducer mounting location. The holes of the pile are shown in **Figure 3A**.
- 2) The epoxy resin was evenly applied around the transducer, which was then put in the corresponding hole, and the force surface of the transducer shall be flushed with the pile body surface. After the epoxy resin had set, 704 glue was applied to the transducer perimeter to seal it against water, and the data cable was taped to the inside wall of the pile, as shown in **Figure 3B**.
- 3) The transmission line of the transducers was threaded through the reserved hole near the top of the model pile to prevent the damage caused by the direct contact between the jack and the transmission line during driving.

Test Soil Preparation

The silty clay used in the test was taken from an engineering site. The silty clay was dried, crushed, and sieved according to the literature specifications (Ministry of Housing and Urban-Rural Construction of the People's Republic of China, 2019), and then it was layered and compacted by compaction machinery in the model box. The soil was then sprayed with water and covered with a film and left standing for 30 days. The process of the test soil preparation is shown in **Figure 4**. Before the test, the soil was sampled, and its physical and mechanical

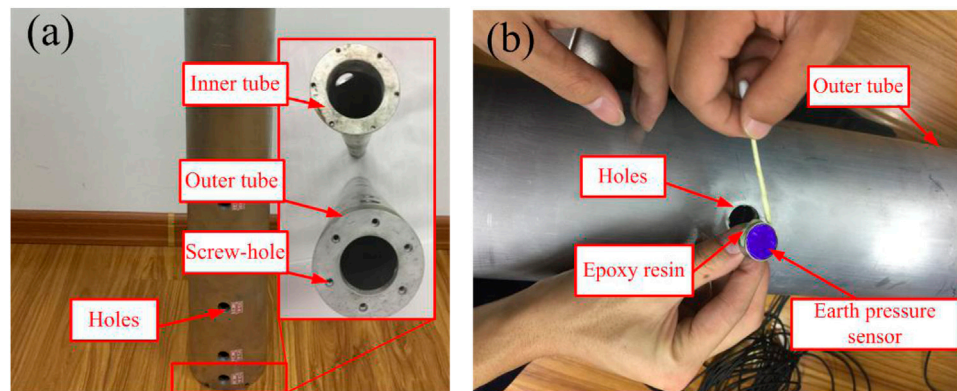


FIGURE 3 | The installation method of transducers: (A) The holes of the pile, (B) Epoxy resin application.

TABLE 2 | The physical and mechanical parameters of the soil.

Relative density d_s	Volumetric weight $\gamma/(\text{kN}/\text{cm}^3)$	Water content $w/\%$	Liquid limit $w_L/\%$	Plastic limit $w_p/\%$	Plasticity index $I_p/\%$	Cohesion c/kPa	Angle of internal friction $\varphi/(^{\circ})$	Modulus of compressibility E_{s1-2}/MPa
2.73	18.0	34.8	43.2	21.2	22.0	14.4	8.6	3.3

parameters were obtained through a series of laboratory tests, as listed in **Table 2**.

Pile Driving and Data Acquisition

Model piles TP1 and TP2 were spaced at 1,000 mm apart (d_1), and model box walls were closer and spaced at 900 mm apart (d_2) (where D is the diameter of the pile). Yegian and Wright. (1973), using finite element analysis, and Rao et al. (1996), through model test studies, demonstrated that the boundary effect can be ignored when the pile distance from the boundary is 6–8 times the pile diameter. The boundary effect of the pile can be ignored in this test.

The model pile was pressed into the test soil using a hydraulic jack, and the sinking speed and pile sinking depth of the pile were controlled using the electric control system. In this test, the

sinking speed and pile sinking depth were 300 mm/min and 900 mm, respectively. The pore pressure and earth pressure at the pile surface during driving were collected using a CF3820 high-speed static signal test analyzer. The composition of the test system is shown in **Figure 5**.

TEST RESULTS AND ANALYSIS

Analysis of the Pore Pressure Results at the Pile Surface

The pore pressure at the surface of the piles under hydraulic jacking was monitored using the piezoresistive silicon pore pressure transducers. The test results of model piles TP1 and TP2 are shown in **Figure 6A,B**, respectively.



FIGURE 4 | The process of soil preparation: (A) Soil filling, (B) Soil compaction.

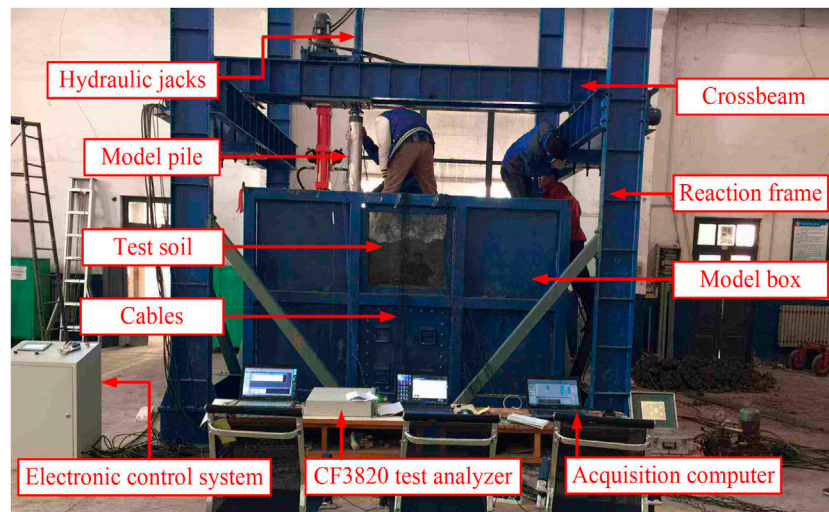


FIGURE 5 | The composition of the test system.

As shown in **Figure 6**, the pore pressure transducers on the model piles survived during the entire test period. The transducer at the top of the test pile did not measure the effective value because of its small penetration depth into the test soil; therefore, the pore pressure curve is not shown in **Figure 6**. The pore pressure measured by each transducer increases gradually and approximately linearly with increasing depth. This is because of the fact that the soil used in this test is homogeneous and the up and down soil layers are uniform, resulting in the more regular pore pressure distribution, different from the distribution of pore pressure in the field test. The pore pressure is caused by the shear force of the pile to the soil, making the pore around the pile too late to dissipate. When the penetration depth of the pile is small, the overburden weight and the horizontal pressure are small,

the pore dissipates quickly, and the pore pressure at the pile surface is small. With increasing penetration depth, the overburden weight and horizontal pressure gradually increase, and the pore pressure at the pile surface increases linearly, and this result is consistent with the results reported by Randolph et al. (1979).

In the process of the pile driving, the variation in the pore pressure at the same depth of the soil is shown in **Figure 7**. With the penetration of the pile, the pore pressure at the same depth decreases slightly because of the greater penetration depth, and the soil layer at the same depth is subjected to the continuous friction of the model pile, causing the pore pressure to rise. However, the continuous perturbation of the soil around the pile also provides a channel for the dissipation of the pore, slightly decreasing the pore

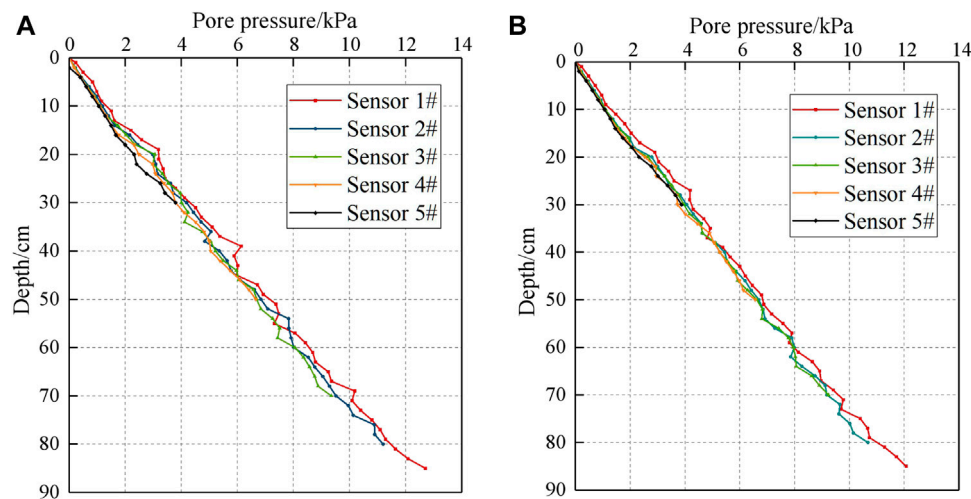
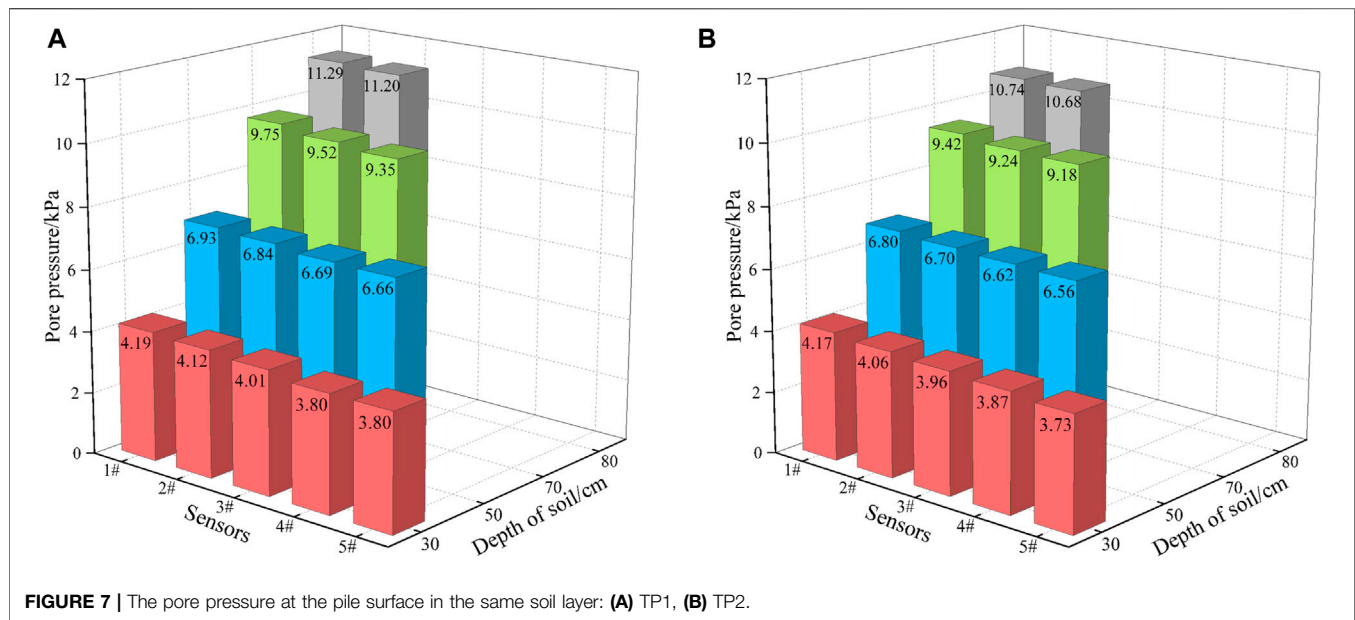


FIGURE 6 | Pore pressure curves at the pile surface with depth: (A) TP1 and (B) TP2.



pressure. At the same penetration depth and the same location, the pore pressure is greater for model pile TP1 than that for model pile TP2, indicating that the compaction effect of the closed-ended pile is greater than that of the open-ended pile and is more pronounced at the end of the pile, because the soil at the end of the pile enters the inner tube of the open-ended pile, forming an earth plug.

Analysis of Excess Pore Pressure Results at the Pile Surface

The curve of the excess pore pressure of model piles TP1 and TP2 with the depth is shown in **Figure 8A,B**, respectively. At the

end of the pile driving, the excess pore pressure with the depth of the model pile TP1 measured by the sensors is 4.21, 3.20, 2.35, 1.66, and 0.79 kPa and that of model pile TP2 measured by the sensors is 3.58, 2.68, 2.24, 1.56, and 0.87 kPa. A comparison of **Figure 8A,B** shows that the excess pore pressure of the closed-ended pile is still greater than that of the open-ended pile, and the maximum difference between the two piles is 0.63 kPa. The excess pore pressure at the pile surface presents a nonlinear increasing trend with increasing depth and is consistent with the excess pore pressure observed at the pile surface, as reported by Tang et al. (2002) and Dash and Bhattacharya. (2015). This is because the distribution of the excess pore pressure at the pile surface is related to the effective overburden weight. The

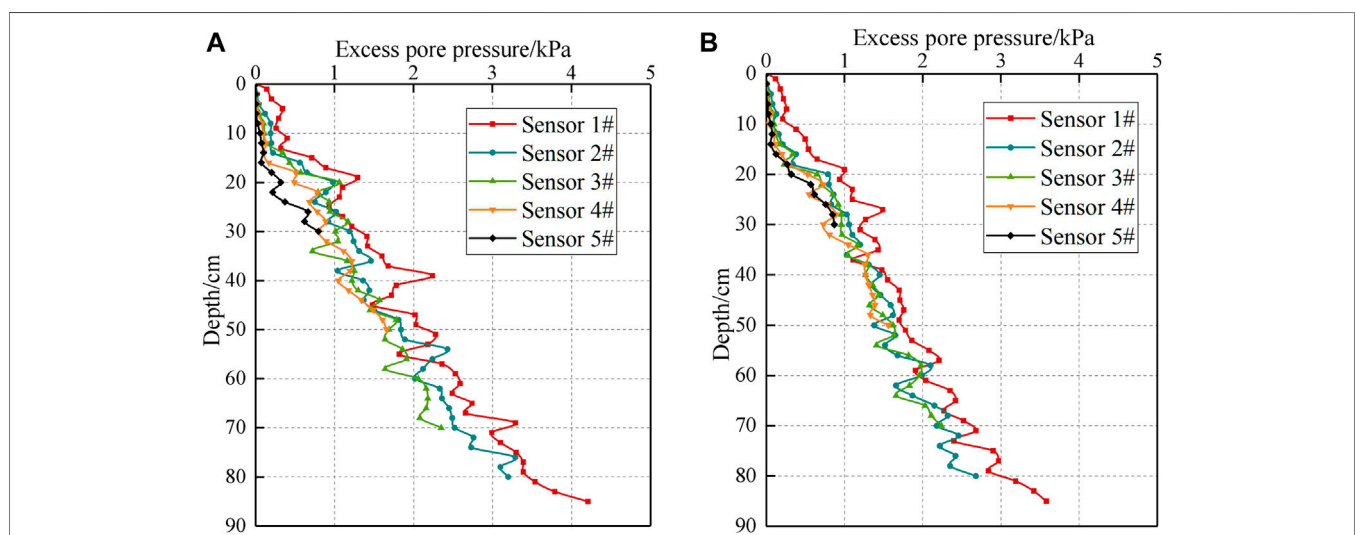
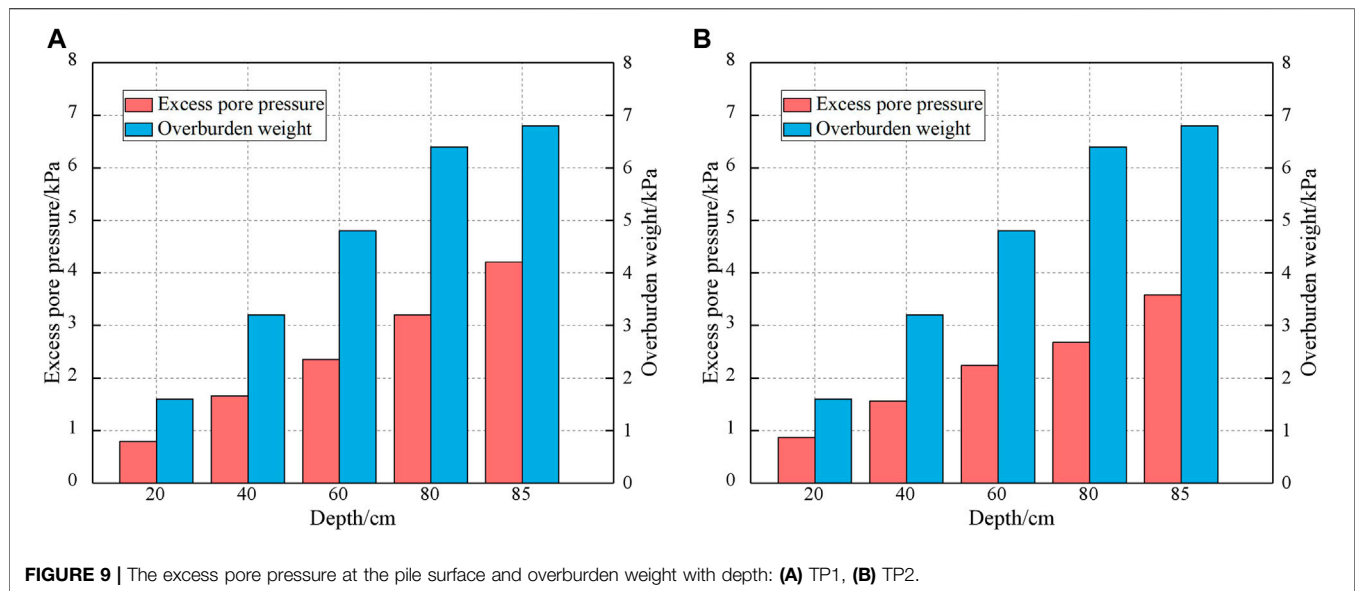


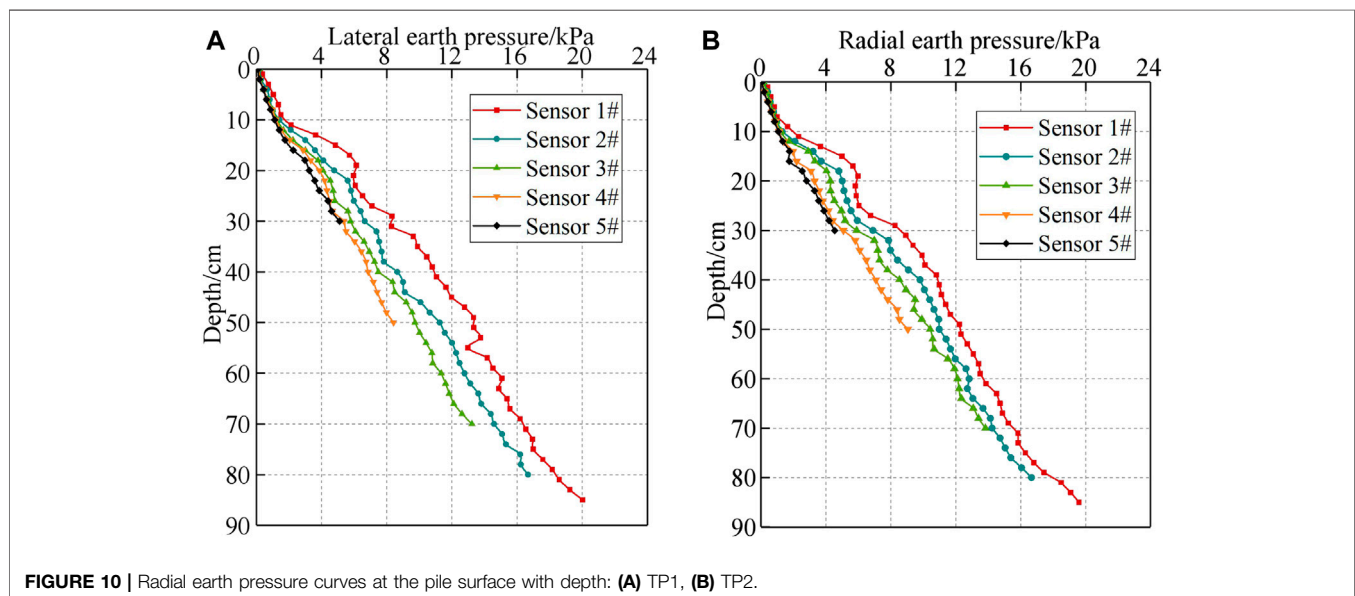
FIGURE 8 | Excess pore pressure curves at the pile surface with depth: **(A)** TP1 and **(B)** TP2.



analysis of excess pore pressure and effective overburden weight is presented in the following section.

At the end of the pile driving, the relationship between the excess pore pressure at different depths of the model piles and the effective overburden weight is shown in **Figure 9A,B**. As shown in **Figure 9**, at the end of the pile driving, the excess pore pressure with the depth of the model pile TP1 measured by the sensors is 0.79, 1.66, 2.35, 3.2, and 4.21 kPa, and that of model pile TP2 is 0.87, 1.56, 2.24, 2.68, and 3.58 kPa. The ratio of the excess pore pressure at the pile surface to the effective overburden weight at the depths 20, 40, 60, 80, and 85 cm of model pile TP1 is 32.9, 47.2, 50.6, 55.6, and 61.2%, and that of model pile TP2 is 36.3, 44.3, 48.3, 46.5, and 52.1%. The ratio of the excess pore pressure at the pile surface and the effective

overburden weight of the two model piles gradually increases with the depth and is consistent with that reported by Seed and Reese. (1957) and Roy et al. (1982). At a depth of 20 cm, the excess pore pressure dissipates rapidly because of the uplift of the surface soil, and the ratio of model piles TP1 and TP2 is 32.9 and 36.3%, respectively. At a depth of 85 cm, the ratio of model pile TP1 to TP2 reached a maximum value of 61.2 and 52.1%, respectively, and the difference of the ratio is 9.1%, indicating that during the pile driving, the excess water pressure is high, adversely affecting the bearing capacity of the pile foundation. Therefore, measures such as vertical drainage channels in the vicinity of piles are needed to reduce the excess water pressure during pile driving in engineering.



Analysis of Radial Earth Pressure at Pile Surface

The radial earth pressure at the surface of the piles under hydraulic jacking was monitored using the piezoresistive silicon earth pressure transducers. The test results of model piles TP1 and TP2 are shown in **Figure 9A,B**, respectively.

As shown in **Figure 10**, the radial earth pressure of model piles TP1 and TP2 basically showed the same pattern in the process of pile driving, both increasing gradually with depth and being consistent with the test results of *Lehane and Jardine. (1994)* and *Bond and Jardine. (1991)*. At the end of pile driving, the radial earth pressure at the depths 40, 60, 80, 90, and 95 mm of model pile TP1 measured by the sensors is 5.10, 8.42, 13.23, 16.68, and 20.03 kPa and that of model pile TP2 measured by the sensors is 4.54, 9.05, 13.83, 16.67, and 19.59 kPa. The radial earth pressure at the pile surface is less affected by the form of the pile end, and the increase in the radial soil pressure further away from the pile end is smaller because of the overburden weight. At the same soil depth, the radial earth pressure of the model piles decreases with increasing penetration depth. This is because increasing penetration of the model pile gradually decreases the adhesion between the pile and soil and increases the gap between the pile and soil, resulting in decreasing the radial earth pressure at the pile interface, and the decrease in the radial earth pressure increases with increasing penetration depth.

Analysis of Effective Radial Earth Pressure at the Pile Surface

The curve of the effective radial earth pressure at the pile surface of model piles TP1 and TP2 with the depth is shown in **Figure 11A,B**, respectively. The effective radial earth pressure and the radial earth pressure at the pile surface vary similarly, both increasing with the penetration depth, and there is also significant degradation at the same soil depth. At the end of pile driving, the

effective radial earth pressure with the depth of the model pile TP1 is 4.31, 6.76, 10.88, 13.48, and 15.82, accounting for 84.5, 80.3, 82.2, 80.8, and 78.9% of the radial earth pressure at the pile interface, respectively. In addition, the effective radial earth pressure of model pile TP2 is 16.01, 13.99, 11.59, 7.49, and 3.67 kPa, accounting for 80.8, 82.8, 83.8, 83.9, and 81.7% of the radial earth pressure, respectively. This indicates that the effective radial earth pressure at both the closed- and open-ended pile is a major component of the radial earth pressure.

To further investigate the contact state of the pile and soil during the pile jacking, as shown in **Figure 11**, the contact coefficient was obtained from **Figure 11** in the following equation:

$$t_c = p' / \sigma_{cx}, \quad (7)$$

where t_c is the contact coefficient, p' is the effective radial earth pressure at pile surface, and σ_{cx} is the self-weight stress.

In the process of the pile driving, the variation in the contact coefficient at the same depth of the soil is shown in **Figure 12**. At a certain penetration depth, the contact coefficient of the model piles first increases and then decreases with increasing depth of the soil and is greater than 1 at large depth. This indicates an obvious compaction effect in the process of pile jacking: effective radial earth pressure at the pile surface is higher than the self-weight stress, the gap between the pile and soil is small, and the pile and soil are in close contact. In the later stages of pile jacking, the contact coefficient decreases because of a faster rise in the excess pore water pressure in the deep soil layer and a lower increase in the effective radial earth pressure at the pile surface. At the same depth of the soil, the coefficient gradually decreases with proceeding jacking pile. This indicates that with the pile jacking, the compaction effect at the same depth decreases, and the gap between the pile and soil increases, resulting in a gradual decrease in the shaft resistances of the piles, and this result is consistent with those reported by *Kou et al. (2019)*. The shallow soils have a smaller coefficient, because they are affected by factors such as

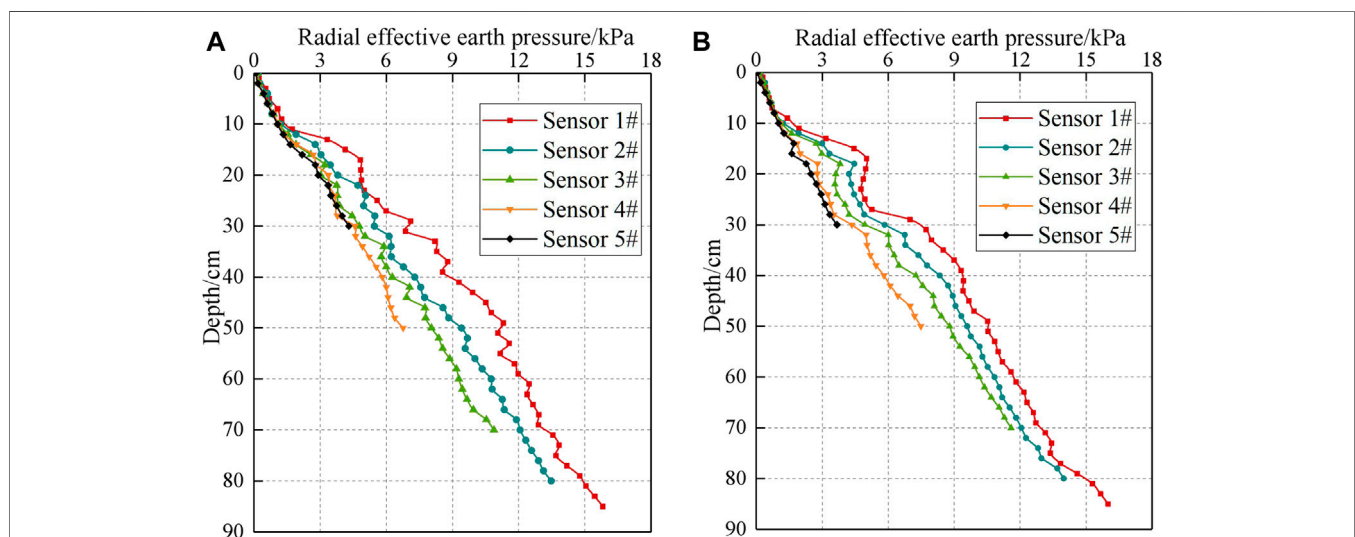
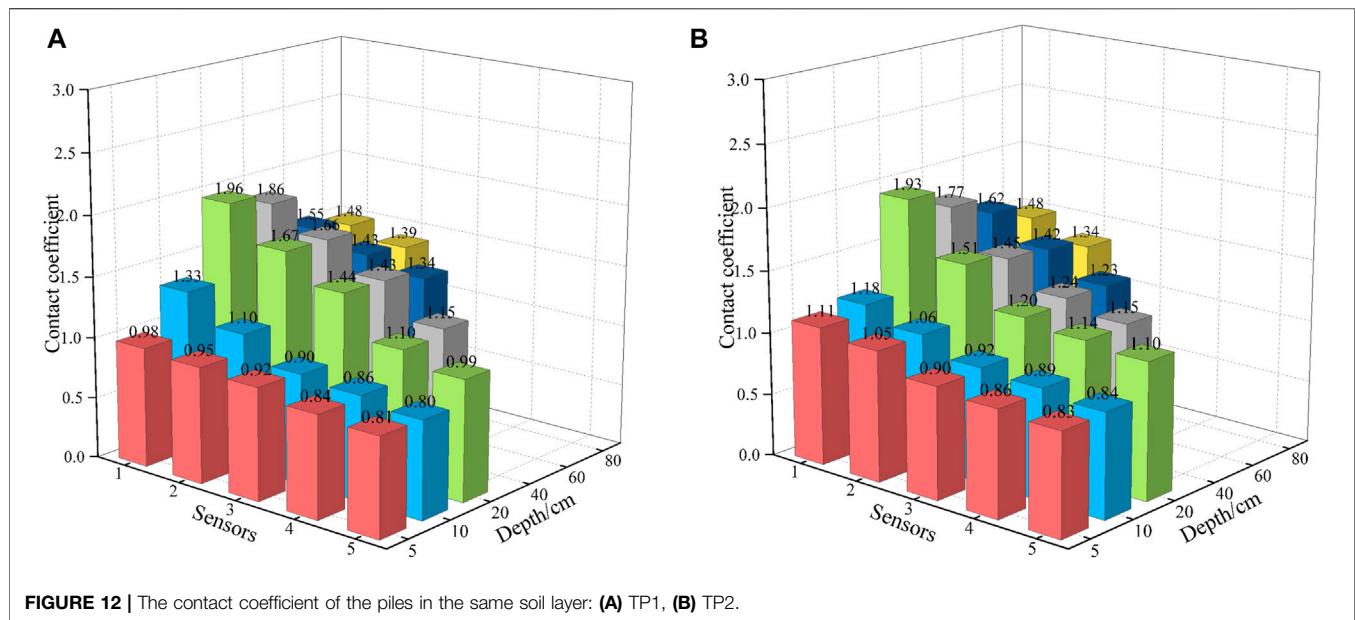


FIGURE 11 | Effective radial earth pressure curves at the pile surface with depth: **(A)** TP1 and **(B)** TP2.



pile body sway during the pile jacking and the pile-soil contact is not tight, reducing the effective radial earth pressure.

NUMERICAL SIMULATION

After the indoor test equipment and test piles are reduced by ten times, the particle flow numerical simulation is carried out. After the reduction, the gravity field will be reduced, which makes the simulation results different from the test results. In order to overcome this drawback, the acceleration of gravity was increased to 10 times the original. The model frame is composed of a wall with a size of 300 mm × 200 mm (length × height).

Peng et al. (2017) considered that for materials such as concrete and stronger rocks, the contact relationship between particles adopts a parallel bonding model; for soft soils with lower strength, the contact relationship between particles adopts a contact bonding model. The simulated foundation soil is homogeneous clay soil, so the contact relationship of particles adopts the contact bonding model, the maximum particle radius is 0.51 mm, and the minimum particle radius is 0.3 mm. The initial porosity of the foundation soil is 0.3, and the total particles are 45,000. The microscopic parameters of the soil layer are shown in **Table 3**. The soil layer is generated and attached with color as shown in **Figure 13** to better observe the movement of the soil during the pile driving process. It can be seen from the figure that after ten layers of soil were formed, the test tank is not completely filled.

The model pile is composed of particles with a radius of 0.5 mm, including the top of the pile, the pile wall, and the end of the pile. The particles overlap each other. The distance between two adjacent particles is 0.1 mm. The scale of the model test is 10 times. In this article, a total of two model piles are simulated for pile sinking, which are closed piles with a diameter of 14 mm and open piles with a diameter of 14 mm. The pile lengths are both 100 mm, and the numbers are M1 and M2, respectively.

Figure 14 is the normalized comparison of experimental and simulated radial earth pressure.

It can be seen from **Figure 14** that the normalized curve form of the experimental and simulated radial earth pressures is basically the same, indicating that the experimental and simulated radial earth pressures are basically consistent with the penetration depth, which also explains the use of silicon. The piezoresistive silicon pressure transducers are feasible to monitor the radial earth pressure on the surface of the pile, but the two curves

TABLE 3 | Mesoscopic parameters of soil layer.

Soil layer	Density/ kg·m ⁻³	kn/ N·m ⁻¹	ks/ N·m ⁻¹	n-bond/ N	s-bond /N	Coefficient of friction
1-10	2730	1×10 ⁷	1×10 ⁶	500	150	0.25

In the table, kn: Normal contact stiffness; ks: Tangential contact stiffness; n-bond: Normal bond strength; s-bond: Tangential bonding strength

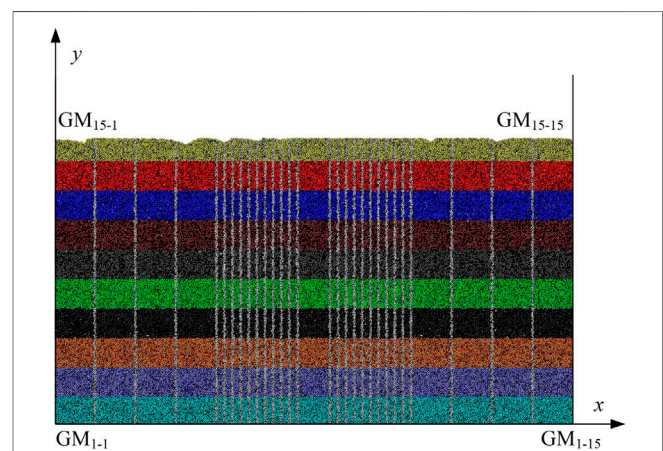


FIGURE 13 | The foundation soil is formed.

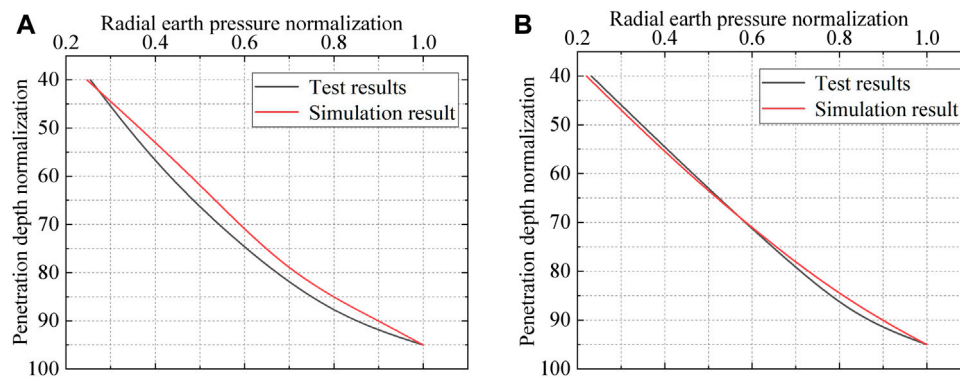


FIGURE 14 | Normalized comparison of experimental and simulated radial earth pressure. **(A)** M1 and TP1. **(B)** M2 and TP2.

still have certain differences. The reasons are as follows: 1) There are many external interference factors during the test; 2) the simulated foundation soil parameters cannot be completely equivalent to the parameters of the foundation soil in the test, and the foundation soil is composed of particles. During the pile driving process, the interaction between soil particles and the pile and the interaction between particles and particles cannot be completely consistent with the indoor test. 3) During the test, the foundation soil may have unevenness somewhere in the layered vibration time. The above reasons lead to the difference between simulation and indoor experiments.

CONCLUSION

In conclusion, a new method was developed for monitoring the pore and earth pressure at the pile surface using the piezoresistive silicon earth transducers introducing pore pressure transducers. Two model piles were instrumented with the piezoresistive silicon pressure transducers and installed using the hydraulic jack in the model box. The experimental results of this study lead to the following conclusions:

- 1) The piezoresistive silicon pressure transducers were proved to be feasible to measure the pore and earth pressure at the pile surface during pile jacking, indicating that the pore and earth pressure on the pile wall can be measured successfully using these transducers.
- 2) The transducers installation method used in this test is feasible, and 12 earth pressure transducers and 12 pore pressure transducers all survived in the test. The small size of the transducers used in the test makes their installation easy.
- 3) The self-made model pile used in this experiment is a double-tube structure. The gap between the inner and outer tubes of the pile can not only provide space for the installation of transducers but also provide protection for the cables of the transducers.
- 4) The pore pressure, excess pore pressure, radial earth pressure, and effective radial earth pressure at the same pile position all increase with increasing penetration depth. At the same penetration depth and the same pile position, the pore pressure and excess pore pressure at the pile surface of the closed-ended pile are greater than those of the open-ended pile.

- 5) The radial earth pressure and effective radial earth pressure at the same soil depth all decrease with the penetration depth, the decrease in value increases with the penetration depth. In addition, the effective radial earth pressure is the main component of the pile surface earth pressure.
- 6) The experimental and simulated radial soil pressure changes with the penetration depth are basically the same. The silicon piezoresistive pressure sensor can be used to monitor the radial soil pressure on the pile surface, especially the pile with an open end.
- 7) In practical applications, after the groove is carved on the pile body, the bottom surface of the groove is leveled with the adhesive, and then the sensor is installed to make the sensor surface parallel to the bottom surface of the groove. In addition, the piezoresistive silicon pressure transducer should be embedded in the groove to avoid exposure outside the groove. The sensor should be prevented from being knocked during the pile pressing process, affecting the survival rate of the sensor.

DATA AVAILABILITY STATEMENT

The original contributions presented in the study are included in the article/Supplementary Material; further inquiries can be directed to the corresponding author.

AUTHOR CONTRIBUTIONS

JM and YH: Data curation; YW: Formal analysis; MZ: Funding acquisition; YH: Methodology; YW: Supervision; YH: Validation; YW: Writing—original draft; YH: Writing—review and editing; All authors have read and agreed to the published version of the manuscript.

FUNDING

This research was financially supported by the National Natural Science Foundation of China (51708316, 51778312, and 51809146).

REFERENCES

- Airhart, T. P., Coyle, H. M., Hirsch, T. J., and Buchanan, S. J. (1969). Pile-soil system response in a cohesive soil. *Performance of Deep Foundations*, Pennsylvania. 444, 264–294. doi:10.1520/STP47289S
- Bjerrum, L., Brinch Hansen, J., and Sevaldson, R. (1958). Geotechnical investigations for a quay structure in Horten. *Norwegian Geotechnical Institute, Publ. Norway*. 28, 1–18.
- Bjerrum, L. (1967). Engineering Geology of Norwegian normally-consolidated marine clays as related to settlements of buildings. *Géotechnique* 17 (2), 83–118. doi:10.1680/geot.1967.17.2.83
- Bond, A. J., and Jardine, R. J. (1991). Effects of installing displacement piles in a high OCR clay. *Géotechnique* 41 (3), 341–363. doi:10.1680/geot.1991.41.3.341
- Casagrande, A. (1932). The structure of clay and its importance in foundation engineering. *J. Boston Soc. Civil Eng.* 19 (4), 168–209.
- Chen, F., Xu, Q., and Zhang, J. (2019). Long term working performance of vibrating wire piezometers in vacuum preloading engineering. *Port Waterway Eng.* 01, 185–190. doi:10.16233/j.cnki.issn1002-4972.20190107.009
- Chen, J. W., Zhu, Y. T., Guo, Z. H., and Nasibulin, A. G. (2020). Recent progress on thermo-electrical properties of conductive polymer composites and their application in temperature sensors. *Engineered Sci.* 12, 13–22. doi:10.30919/es8d1129
- Chui, G. T. (1990). *Similarity theory and model test*. Xuzhou, China: China University of Mining and Technology Press.
- Dash, S. R., and Bhattacharya, S. (2015). Pore water pressure generation and dissipation near to pile and far-field in liquefiable soils. *Inter. J. Geom.* 9 (2), 1454–1459. doi:10.21660/2015.18.4253
- Duan, N. (2016). *Mechanical characteristics of monopile foundation in sand for offshore wind turbine*. London, United Kingdom: University College London.
- Dumoulin, C., Karaiskos, G., Carette, J., Staquet, S., and Deraemaeker, A. (2012). Monitoring of the ultrasonic p-wave velocity in early-age concrete with embedded piezoelectric transducers. *Smart Mater. Struct.* 21, 047001. doi:10.1088/0964-1726/21/4/047001
- Feng, Q., Kong, Q., and Song, G. (2016). Damage detection of concrete piles subject to typical damage types based on stress wave measurement using embedded smart aggregates transducers. *Measurement* 88, 345–352. doi:10.1016/j.measurement.2016.01.042
- Ghahari, S., Ghafari, E., Hou, P. K., and Lu, N. (2018). Hydration properties of cement pastes with Al-zinc oxide and zinc oxide nanoparticles. *ES Mater. Manufacturing* 2, 51–59. doi:10.30919/esmm5f172
- Hou, P. K., Li, R., Li, Q. F., Lu, N., Wang, K. J., Liu, M. L., et al. (2018). Novel superhydrophobic cement-based materials achieved by construction of hierarchical surface structure with FAS/SiO₂ hybrid nanocomposites. *ES Mater. Manufacturing* 1, 57–66. doi:10.30919/esmm5f125
- Huang, H. L., Lu, H., Wang, Y. L., Yang, Z. L., Zhu, F., and Xu, M. (2020). The background of the sensors needs be strengthened. The following papers are useful and need be cited: tunable Thermal-Response Shape Memory Bio-Polymer Hydrogels as Body Motion Sensors. *Engineered Sci.* 9, 60–67.
- Igoe, D. J. P., Gavin, K. G., and O'Kelly, B. C. (2011). Shaft capacity of open-ended piles in sand. *J. Geotech. Geoenviron. Eng.* 137, 903–913. doi:10.1061/(asce)gt.1943-5606.0000511
- Jardine, R. J., and Bond, A. J. (1989). Behaviour of displacement piles in a heavily overconsolidated clay. *Proc. 12th Int. Conf. Soil Mech. Foundations Eng. Rio de Janeiro, Brazil* 2, 1147–1151.
- Jiang, T., Kong, Q., Patil, D., Luo, Z., Huo, L., and Song, G. (2017). Detection of debonding between fiber reinforced polymer bar and concrete structure using piezoceramic transducers and wavelet packet analysis. *IEEE Sensors J.* 17 (7), 1992–1998. doi:10.1109/jsen.2017.2660301
- Kou, H.-L., Diao, W.-Z., Liu, T., Yang, D.-L., and Horpibulsuk, S. (2018). Field performance of open-ended prestressed high-strength concrete pipe piles jacked into clay. *Sensors* 18 (12), 4216. doi:10.3390/s18124216
- Kou, H. L., Chu, J., Guo, W., and Zhang, M. Y. (2015). Field study of residual forces developed in pre-stressed high-strength concrete (PHC) pipe piles. *Can. Geotech. J.* 53, 696–707. doi:10.1139/cgj-2017-0120
- Kou, H. L., Yu, F., and Liu, T. (2019). Strain monitoring on PHC pipe piles based on fiber Bragg grating sensors[J]. *J. Perform. Constr. Facil.* 33 (2), 04019003. doi:10.1061/(asce)cf.1943-5509.0001266
- Lehane, B. M., and Jardine, R. J. (1994). Displacement pile behaviour in a soft marine clay. *Can. Geotech. J.* 31 (1), 181–191. doi:10.1139/t94-024
- Li, L., Huang, J., and Han, B. (2018). Centrifugal investigation of excavation adjacent to existing composite foundation. *J. Perform. Constr. Facil.* 32 (4), 04018044. doi:10.1061/(asce)cf.1943-5509.0001188
- Li, P., Gu, H., Song, G., Zheng, R., and Mo, Y. L. (2010). Concrete structural health monitoring using piezoceramic-based wireless sensor networks. *Smart Structures Syst.* 6, 731–748. doi:10.12989/sss.2010.6.5_6.731
- Liang, C., Zhao, P. Q., Hou, P. K., Wang, S. D., Strokova, V., Lu, L. C., et al. (2020). Investigation of compatibility of fluorine-acrylic emulsion and sulphoaluminate cement in the design of composite coating: effects of sorbitol and its mechanism. *ES Mater. Manufacturing* 8, 36–45. doi:10.30919/esmm5f707
- Liu, J. W., Cui, L., Zhu, N., Han, B., and Liu, J. (2019). Investigation of cyclic pile-sand interface weakening mechanism based on large-scale CNS direct shear tests. *Ocean Eng.* 194, 106650. doi:10.1016/j.oceaneng.2019.106650
- Liu, X. (2015). *The research on tangential stiffness fitting in pile soil system contact surface*. Liaoning, China: Liaoning Project Technology University.
- Lo, K. Y., and Stermac, A. G. (1965). Induced pore pressures during pile driving operations. *Proc. 6th Int. Conf. Soil Mech. Found. Eng. MontrCal, Can.* 11, 285–289.
- Lyne, D., and Jack, Q. Z. (2004). The influence of temperature on earth pressure cell readings. *Can. Geotech. J.* 41, 551–559. doi:10.1139/t04-004
- Mccabe, B. A., and Lehane, B. M. (2006). Behavior of axially loaded pile groups driven in clayey silt. *J. Geotech. Geoenviron. Eng.* 132 (3), 401–410. doi:10.1061/(asce)1090-0241(2006)132:3(401)
- Ministry of Housing and Urban-Rural Construction of the People's Republic of China (2019). *Ministry of housing and urban-rural construction of the People's Republic of China. GB/T 50123-2019*. Beijing, China: China Planning Press.
- Moslehy, Y., Gu, H., Belarbi, A., Mo, Y. L., and Song, G. (2010). Smart aggregate-based damage detection of circular RC columns under cyclic combined loading. *Smart Mater. Struct.* 19, 065021. doi:10.1088/0964-1726/19/6/065021
- Orrje, O., and Broms, B. (1967). Effects of pile driving on soil properties. *J. Soil Mech. Found. Div., Am. Soc. Civ. Eng.* 93 (SM5), 59–73. doi:10.1061/jsfeaq.0001044
- Peng, Y. Y., Zhou, H. Q., and Zhou, S. L. (2017). Simulation of mesoscopic mechanic properties on red clay by using particle flow code. *J. Chongqing Univ. Technology(Natural Science)* 31 (1), 41–45. doi:10.3969/j.issn.1674-8425(z).2017.01.007
- Pestana, J. M., Hunt, C. E., and Bray, J. D. (2002). Soil deformation and excess pore pressure field around a closed-ended pile. *J. Geotech. Geoenviron. Eng.* 128 (1), 1–12. doi:10.1061/(asce)1090-0241(2002)128:1(1)
- Randolph, M. F., Carter, J. P., and Wroth, C. P. (1979). Driven piles in clay-the effects of installation and subsequent consolidation. *Géotechnique* 29 (4), 361–393. doi:10.1680/geot.1979.29.4.361
- Rao, S. N., Ramakrishna, V. G. S. T., and Raju, G. B. (1996). Behavior of pile-supported dolphins in marine clay under lateral loading. *J. Geotechnical Eng.* 122 (8), 607–612. doi:10.1061/(asce)0733-9410(1996)122:8(607)
- Roy, M., Blanchet, R., Tavenas, F., and La Rochelle, P. (1981). Behaviour of a sensitive clay during pile driving. *Can. Geotech. J.* 18 (2), 67–85. doi:10.1139/t81-007
- Roy, M., Tremblay, M., Tavenas, F., and Rochelle, P. L. (1982). Development of pore pressures in quasi-static penetration tests in sensitive clay. *Can. Geotech. J.* 19 (2), 124–138. doi:10.1139/t82-015
- Seed, H. B., and Reese, L. C. (1957). The action of soft clay along friction piles. *T. Am. Soc. Civ. Eng.* 122, 731–754. doi:10.1061/taceat.0007501
- Steenfelt, J. S., Randolph, M. F., and Wroth, C. P. (1981). Instrumented model piles jacked into clay. *Proc. 10th Int. Conf. Soil Mech. Foundations Eng.* 2, 857–864.
- Su, Y. F., Han, G. S., Kong, Z. H., Nantung, T., and Lu, N. (2020). Embeddable piezoelectric sensors for strength gain monitoring of cementitious materials: the influence of coating materials. *Engineered Sci.* 11, 66–75. doi:10.30919/es8d1114
- Tang, S. D., He, L. S., and Fu, Z. (2002). Excess pore water pressure caused by an installing pile in soft foundation. *Rock Soil Mech.* 23 (6), 725–732. doi:10.2753/CSH0009-4633350347
- Vaughan, P. R., and Walbancke, H. J. (1973). Pore pressure changes and the delayed failure of cutting slopes in overconsolidated clay. *Géotechnique* 23 (4), 531–539. doi:10.1680/geot.1973.23.4.531
- Wang, Y. X., Guo, P. P., Ren, W. X., Yuan, H. X., Yuan, H. P., and Cao, P. (2017a). Laboratory investigation on strength characteristics of expansive soil treated with jute fiber reinforcement. *Int. J. Geomech.* 17 (11), 0401710. doi:10.1061/(asce)gm.1943-5622.0000998

- Wang, Y. H., Zhang, M. Y., Gao, Q., and Wang, P. (2017b). Research and fabrication of micro silicon piezoresistive pressure sensor. *Transducer Microsystem Tech.* 36, 106–108. doi:10.13873/J.1000-9787(2017)11-0106-03
- Wang, Y. X., Guo, P. P., Lin, H., Li, X., Zhao, Y. L., Yuan, B. X., et al. (2019). Numerical analysis of fiber-reinforced soils based on the equivalent additional stress concept. *Int. J. Geomech.* 19 (11), 04019122. doi:10.1061/(asce)gm.1943-5622.0001504
- Xu, B., Zhang, T., Song, G., and Gu, H. (2013). Active interface debonding detection of a concrete-filled steel tube with piezoelectric technologies using wavelet packet analysis. *Mech. Syst. Signal Process.* 36, 7–17. doi:10.1016/j.ymssp.2011.07.029
- Yang, J. J. (2005). *Similarity theory and structural model test*. Wuhan, China: Wuhan University of Technology Press.
- Yegian, M., and Wright, S. G. (1973). *Lateral soil resistance displacement relationships for pile foundation in soft clays*. Houston, TX, United States: Offshore Technology Conference., 893.
- Yu, J., Huang, M. S., and Zhang, C. R. (2016). Model tests and analysis of single piles with two different diameters subjected to cyclic lateral loadings in clay. *Rock Soil Mech.* 37 (4), 973–980. doi:10.16285/j.rsm.2016.04.009

Conflict of Interest: The authors declare that the research was conducted in the absence of any commercial or financial relationships that could be construed as a potential conflict of interest.

Copyright © 2021 Wang, Huang, Zhang and Ma. This is an open-access article distributed under the terms of the Creative Commons Attribution License (CC BY). The use, distribution or reproduction in other forums is permitted, provided the original author(s) and the copyright owner(s) are credited and that the original publication in this journal is cited, in accordance with accepted academic practice. No use, distribution or reproduction is permitted which does not comply with these terms.



Fatigue Reliability Assessment for Orthotropic Steel Bridge Decks Considering Load Sequence Effects

Jun-Hong Xu¹, Guang-Dong Zhou^{2,3*} and Tai-Yong Zhu²

¹College of Civil Engineering, Nanjing Forestry University, Nanjing, China, ²College of Civil and Transportation Engineering, Hohai University, Nanjing, China, ³Key Laboratory of Large Structure Health Monitoring and Control, Shijiazhuang, China

Fatigue damage accumulations would dramatically reduce the reliability and service life of the orthotropic steel decks. Incorrect fatigue assessment results may be obtained when load sequence effects are omitted. In the present study, fatigue reliability assessments of rib-to-deck weld joints in orthotropic steel bridge decks are conducted with the consideration of load sequence effects. The method, which judiciously considers the fatigue loading history and is derived from the sequential law and the whole-range S-N curve, is first proposed for fatigue reliability calculation. And then, the whole-range S-N curve describing the fatigue propagating process of the rib-to-deck weld joint is introduced. Finally, the developed method is applied to evaluate the fatigue reliability of two rib-to-deck weld joints in an orthotropic steel deck based on long-term measured strain histories. The influence of traffic growth and initial damage on the fatigue reliability is discussed. The results indicate that it is advisable to consider load sequence effects when assessing the fatigue reliability of orthotropic steel decks equipped with long-term strain monitoring systems and the initial damage significantly reduces the fatigue reliability of orthotropic steel decks.

Keywords: steel bridge, orthotropic steel deck, rib-to-deck weld joint, fatigue reliability assessment, whole-range S-N curve

OPEN ACCESS

Edited by:

Gangbing Song,
University of Houston, United States

Reviewed by:

Baokui Chen,
Nanchang University, China
Peng Zhang,
Dalian Maritime University, China

*Correspondence:

Guang-Dong Zhou
zhougd@hhu.edu.cn

Specialty section:

This article was submitted to
Structural Materials,
a section of the journal
Frontiers in Materials

Received: 11 March 2021

Accepted: 03 May 2021

Published: 14 May 2021

Citation:

Xu J-H, Zhou G-D and Zhu T-Y (2021)
Fatigue Reliability Assessment for
Orthotropic Steel Bridge Decks
Considering Load Sequence Effects.
Front. Mater. 8:678855.
doi: 10.3389/fmats.2021.678855

INTRODUCTION

The orthotropic steel deck is one of the most popular vehicle-supporting systems and widely used in steel bridges especially in these long-span cable-supported bridges because of its light weight, expedient construction, high load-carrying capacity, and structural redundancy (Heng et al., 2017; Maljaars et al., 2018; Yang et al., 2020). The orthotropic steel deck is typically composed of a thin steel plate strengthened by a series of closely spaced longitudinal ribs and transverse diaphragms (Sim and Uang, 2012). However, the typically different mechanical properties between the longitudinal direction and the transversal direction and tens of thousands of interlaced weld joints make the orthotropic steel deck extremely susceptible to repeated traffic loading and environmental factors (Liu et al., 2020; Saunders et al., 2005). As a result, fatigue cracks in orthotropic steel decks have been frequently reported in Europe, United States, Japan, and China (Fisher and Barsom, 2016). To this end, developing reliable methods for evaluating the fatigue performance of orthotropic steel decks and further making optimal decisions regarding structure replacement and other major retrofits becomes a research Frontier.

The fatigue processes preceding fracture are too complicated and it is still less understood in terms of the cause of formation and failure mechanism. In the past few decades, various simplified

approaches have been proposed to assess the fatigue damage in steel bridges. Among them, the Miner's rule integrating with the S - N curve method is a dominate one (Ye et al., 2014). The Miner's rule assumes that the fatigue damage induced by a number of repeated stress cycles at a specific stress amplitude is proportional to the total number of stress cycles at that stress amplitude and the total fatigue damage is equal to the linear summation of damage induced by each stress repetition. And the S - N curve describes the relationship between the cyclic stress amplitude, S , and the number of cycles to failure, N . Because of its easy implementation, the Miner's rule has been adopted in American, European, and Chinese bridge design specifications and employed to investigate the fatigue performance of many existing or novel weld joints in orthotropic steel decks (CEN, 1992; AASHTO, 2012). Luo et al. developed a statistical fatigue damage model incorporating the S - N curve and the Miner's rule and applied it to the rib-to-deck joints of a steel box-girder bridge (Luo et al., 2017). Cui et al. investigated the influence of asphalt pavement conditions on the fatigue damage of deck-to-rib joints in orthotropic steel decks using the S - N curve method (Cui et al., 2018). Guo et al. compared the fatigue performance of cracked and uncracked orthotropic steel decks strengthened by glass fiber-reinforced polymer angles using the Miner's rule (Guo et al., 2019; Guo et al., 2020). Fang et al. discussed the influence of the deck plate thickness and the weld foot length on the fatigue failure of double-sided weld joints in orthotropic steel bridge decks by the S - N method (Fang et al., 2020). Ma and Zhang conducted fatigue damage assessments of the weld joints for orthotropic steel bridge decks with the consideration of foundation scour of the bridge, in which the Miner's rule is adopted to calculate the accumulated fatigue damage under the traveling trucks (Ma and Zhang, 2020). Di et al. evaluated the fatigue performance of typical weld joints in orthotropic steel decks under actual traffic flows based on the Miner's rule and the S - N curves, including the deck-to-rib weld joint, the rib-to-diaphragm weld joint, and the cut-outs joint of the diaphragm (Di et al., 2020).

Although the Miner's rule is commonly used to calculate the fatigue damage in orthotropic steel decks. However, it argues that the fatigue damage caused by a stress cycle is independent of where it occurs in the load history and ignores the load sequence effect. In consequence, fatigue damages may be under- or overestimated when variable amplitude loading is applied (Zakaria et al., 2016). This may be one of the main reasons why fatigue cracks have been found frequently in orthotropic steel decks only a few years after bridges were opened to traffic. Thus, a variety of improvements have been made to overcome the shortcomings of the Miner's rule. The sequential law, which estimates the fatigue damage induced by present fatigue stress amplitudes based on prior fatigue conditions and can precisely capture the load sequence effect, is a distinguished one (Mesmacque et al., 2005). Siriwardane et al. applied the sequential law to evaluate the fatigue performance and predict the remaining fatigue life of an existing railway bridge based on field measured stress histories (Siriwardane et al., 2007; Siriwardane et al., 2008; Siriwardane et al., 2010; Karunananda

et al., 2012). Aid et al. examined the capability of the sequential law in evaluating the fatigue damages of mechanical components under random loading histories using fatigue test data (Aid et al., 2011; Aid et al., 2012). All these research work demonstrated that the sequential law gives more realistic results than Miner's rule when structures are subjected to variable amplitude loading.

In the service stage of the orthotropic steel deck, vehicles with different weights pass in a random way. As a result, almost all fatigue stress amplitudes in the orthotropic steel deck are different from each other, which shows typical variable-amplitude features. Therefore, it is significant to take the load sequence effects into account when computing the fatigue damage. In this paper, the fatigue reliability of rib-to-deck weld joints in orthotropic steel decks is assessed based on long-term field monitoring stress histories, in which the fatigue damage is calculated by the sequential law so that the load sequence effects could be reasonably considered. The remainder of the paper is organized as follows: Firstly, the methodology for fatigue reliability assessment considering the load sequence effects is presented. Secondly, an application of the developed fatigue reliability assessment method in two rib-to-deck weld joints located on the downstream side and upstream side of the orthotropic steel decks is provided. Finally, conclusions are drawn.

METHODOLOGY FOR FATIGUE RELIABILITY ASSESSMENT

The core work of fatigue reliability assessment is the calculation of fatigue damages in orthotropic steel bridge decks. As mentioned above, the lack of consideration on the load sequence effect may induce incorrect fatigue damages under the variable amplitude loading condition. On the contrary, the sequential law allows us to take into account the loading history and to correctly compute the fatigue damage in the orthotropic steel decks. In this section, the sequential law will be briefly described and the method assessing fatigue reliability based on the sequential law will be introduced.

Fatigue Damage Calculation

The sequential law defines the damage stress as the stress corresponding to, on the whole-range S - N curve (also named as the fully known Wöhler curve), the instantaneous residual life and the damage stress goes to the ultimate stress at the last cycle before failure (Mesmacque et al., 2005). It is supposed that a weld joint in the orthotropic steel deck is subjected to a certain stress amplitude σ_i for a number of cycles n_i at load level i and the fatigue life corresponding to σ_i is N_i . Then, the residual fatigue life $N_{(i)R}$ is $(N_i - n_i)$. According to the whole-range S - N curve shown in **Figure 1**, the residual fatigue life $(N_i - n_i)$ corresponds to an admissible stress amplitude $\sigma_{(i)eq}$, which is named as the damage stress and has an identical physical explanation as $(N_i - n_i)$. A new damage indicator, D_i , defined as the ratio of the increment of damage stress over the difference between the ultimate stress and the applied stress, is introduced to quantify fatigue damage. After the i th level of repeated loading with stress amplitude σ_i is

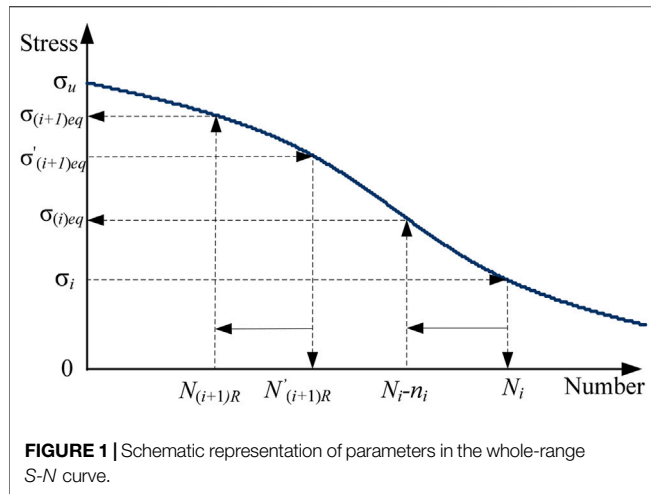


FIGURE 1 | Schematic representation of parameters in the whole-range S-N curve.

applied, the damage indicator is calculated by (Mesmacque et al., 2005).

$$D_i = \frac{\sigma_{(i)eq} - \sigma_i}{\sigma_u - \sigma_i} \quad (1)$$

where σ_u represents the ultimate stress. At the beginning of the cyclic loading, the damage stress is equal to the applied stress amplitude. The damage indicator is thus equal to zero for an intact weld joint. When the damage stress increase to the ultimate stress σ_u , it is obvious that the failure of the weld joint would be occurred. The damage indicator also increases to one. It can be seen that the damage indicator offers an excellent quantitative measure of fatigue damage.

Then, the damage is transferred to the beginning of applying the $(i + 1)$ th level of repeated loading with stress amplitude σ_{i+1} . That is

$$D_i = \frac{\sigma_{(i)eq} - \sigma_i}{\sigma_u - \sigma_i} = \frac{\sigma'_{(i+1)eq} - \sigma_{i+1}}{\sigma_u - \sigma_{i+1}} \quad (2)$$

where $\sigma'_{(i+1)eq}$ denotes the equivalent damage stress relating to the $(i + 1)$ th level of repeated loading. The equivalent damage stress is equal to

$$\sigma'_{(i+1)eq} = D_i (\sigma_u - \sigma_{i+1}) + \sigma_{i+1} \quad (3)$$

By using the whole-range S-N curve again, the equivalent fatigue life $N'_{(i+1)eq}$ associated with the equivalent damage stress $\sigma'_{(i+1)eq}$ could be obtained. After the $(i + 1)$ th level of repeated loading with stress amplitude σ_{i+1} is finished, the remaining fatigue life $N_{(i+1)R}$ is

$$N_{(i+1)R} = N'_{(i+1)eq} - n_{i+1} \quad (4)$$

Finally, the damage indicator becomes

$$D_{i+1} = \frac{\sigma_{(i+1)eq} - \sigma_{i+1}}{\sigma_u - \sigma_{i+1}} \quad (5)$$

where D_{i+1} is the damage indicator after the $(i + 1)$ th level of repeated loading is applied; and $\sigma_{(i+1)eq}$ represents the damage stress relating to the remaining fatigue life $N_{(i+1)R}$.

The fatigue damage could be calculated by iteration if a series of cyclic loading is applied. The flow chart of the sequential law is shown in Figure 2.

Whole-Range S-N Curve

From the description of the sequential law, it can be seen that the practice of model to obtain the remaining fatigue lives completely depends on an appropriate whole-range S-N curve. In traditional fatigue problems of steel bridges, only these cyclic stress amplitudes in the finite life region are taken into account, and these cyclic stress amplitudes lower than the constant amplitude fatigue threshold and these cyclic stress with extremely high amplitudes are ignored. Hence, only the S-N curves in the finite life region is provided in bridge design specifications. For the fatigue damage in the orthotropic steel deck, all cyclic stress amplitudes should be considered since weld flaws and initial cracks inevitably lead to the propagation of fatigue cracks. It becomes important to extend the partially known S-N curve to the whole-range S-N curve covering the very

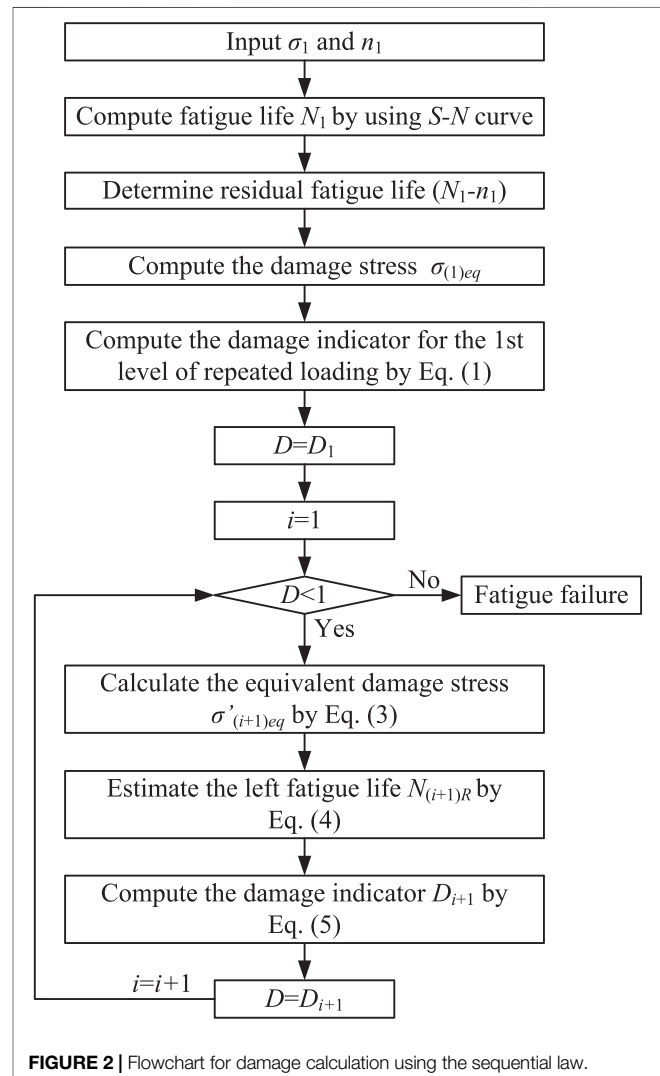


FIGURE 2 | Flowchart for damage calculation using the sequential law.

low-cycle region, the low-cycle region, the finite life region, the high-cycle region, and the very high-cycle region.

The partially known S - N curve in bridge design specifications can be formulated by the well-known Basquin function, which is

$$\sigma(N) = aN^b \quad (6)$$

where σ and N are the fatigue stress amplitude and the number of cycles, respectively; and a and b are two problem specific parameters determined by fatigue features of the weld joint.

The above equation can be rewritten as

$$\sigma(N) = a \left(\frac{1}{N} \right)^{-(b+k)} \left(\frac{1}{N} \right)^k \quad (7)$$

where k ($k > 0$) denotes the damage accumulation coefficient, whose absolute value is much less than b .

By extending the S - N curve from the finite life region to the very high-cycle region (i.e., $N > 10^8$) and the very low-cycle region (i.e., $N < 10^2$), the result is (Zhou et al., 2018).

$$\sigma(N) = \lambda a C^{b+k} \left(\frac{N+B}{N+C} \right)^{b+k} N^{-k} \quad (8)$$

where B and C are two cycle numbers corresponding to two bending points on the whole-range S - N curve; and λ represents the plastic strain coefficient. **Equation 8** is the general form of the whole-range S - N curve, which has the capability of describing the fatigue properties in the very low-cycle region, the low-cycle region, the finite life region, the high-cycle region, and the very high-cycle region.

If the coefficient $\lambda a C^{b+k}$ is replaced by a single parameter A , **Eq. 8** can be simplified as

$$\sigma(N) = A \left(\frac{N+B}{N+C} \right)^{b+k} N^{-k} \quad (9)$$

By using about 400 fatigue test records, the fitted whole-range S - N curve of the rib-to-deck weld joint is (Zhou et al., 2018)

$$\sigma(N) = 99.07 \times N^{-0.06} \left[\frac{N + 1.23E4}{N + 1.25E8} \right]^{-0.29} \quad (10)$$

With consideration of the requirement of high reliability for rib-to-deck weld joints, the whole-range S - N curve with a 97.5% survival limit is formulated as

$$\sigma(N) = 77.09 \times N^{-0.05} \left[\frac{N + 1.01E4}{N + 1.44E7} \right]^{-0.32} \quad (11)$$

Fatigue Reliability Calculation

When the sequential law is applied to compute the fatigue damage, the limit state function for fatigue failure is defined as

$$g(\mathbf{X}) = 1 - D(t) \quad (12)$$

where $g(\cdot)$ represents the state function; $\mathbf{X} = (x_1, x_2, \dots)^T$ denotes the vector of random variables; and $D(t)$ is the damage indicator in t years.

The failure probability P_f of a structural member is formulated as

$$P_f = P[g(\mathbf{X}) < 0] \quad (13)$$

where $P(\cdot)$ represents the probability.

Then, the fatigue reliability index β associated with the failure probability is computed by

$$\beta = \Phi^{-1}(1 - P_f) \quad (14)$$

where $\Phi^{-1}(\cdot)$ is the inverse standard normal cumulative distribution function.

The sequential law computes the damage indicator according to the loading history, which is generally represented by a series of stress amplitudes σ_i and the corresponding cycle number n_i . Due to the randomness of traffic flow, the fatigue load effect (i.e., stress amplitudes and cycle numbers) in the orthotropic bridge deck yields complex statistical models, like the Gaussian mixed distribution and the generalized mixed distribution. As a result, the samples of the fatigue load effect cannot be generated by simply sampling methods, such as the inverse transform sampling method. To cope with this problem, the Monte Carlo method is employed in this study. Although loading histories generated by the Monte Carlo method are random, the sequence for a specific time history is fixed. As a result, the sequential law could be adopted to calculate the fatigue damage. The larger the number of samples, the more accurate the fatigue reliability calculation results are. However, too many samples will cause heavy burden to the calculation. For this reason, Frangopol provided the following criterion for the sampling number (Frangopol, 2008).

$$M > \frac{100}{P_f} \quad (15)$$

where M denotes the sampling number. For the generally used target reliability index $\beta = 2$, the minimal sampling number is about 4,500. It should be noted that the Monte Carlo method can only be applicable to cases where β is less than 6. If β is greater than 6, the number of samples required is more than 1.0×10^9 , which is a great challenge for computing (Liu et al., 2017).

APPLICATION

Long-Term Strain Monitoring

The developed method is applied to a steel box-girder cable-stayed bridge with a main span of 406 m. The orthotropic steel deck is employed to support the vehicle flow. The dynamic strain of rib-to-deck weld joints located on the downstream side and upstream side of the middle-span section of the steel-box girder is long-term monitored by two tri-axial strain sensors. The layout of strain sensors is shown **Figure 3**. In the figure, RD_d and RD_u represent the strain sensors used to measure the strain of the rib-to-deck weld joints in the downstream side and upstream side, respectively. The two monitored rib-to-deck weld joints are typically below fast lanes, on which cars and trucks pass

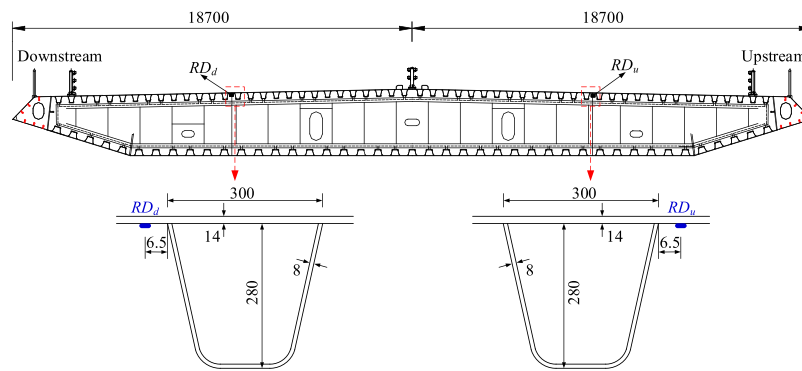


FIGURE 3 | Layout of strain sensors on the orthotropic steel deck (Unit: mm).

frequently. Strain monitored data from 2007 to 2010 are used to assess the fatigue reliability of the two rib-to-deck weld joints.

Calculation of Equivalent Fatigue Loading Effects

As known, the stress in the transversal direction governing the fatigue life of the rib-to-deck weld joint. The strain measured in this direction is hence employed to analyze. Typical daily strain time histories measured by sensor RD_d and sensor RD_u are plotted in **Figure 4**. It can be seen that vehicles induce notable cyclic stress amplitudes, which undoubtedly reduce the durability of rib-to-deck weld joints. From the two figures, it can be found that the mean strain changes with time, which indicates that structural temperatures have great influence on the measured mean strain. According to the principle of the rainflow cycle counting method, the mean strain may cause the calculated fatigue stress amplitude to

deviate from the real value. Therefore, the wavelet transfer method is adopted to remove the thermal strain from the strain time history. The processed strain is converted into stress by Young's modulus of steel. A stress concentration factor obtained from the finite element model is used to adjust the stress difference between the measured point and the weld joint.

The rainflow cycle counting method is employed to extract the fatigue stress amplitude and cycle number from the stress time histories. Here, the influence of the average stress on the fatigue damage is ignored. The sequential law computes the fatigue damage induced by the present cyclic stress based on the previous fatigue damage. This process is performed in an iteration manner. **Figure 4** shows that there are thousands of cycles within a day. The iteration may spend unacceptable time if measured strain data in several years are investigated. In this sense, it is assumed that the daily fatigue damage yields the linear accumulation model. As a consequence, the daily variable fatigue

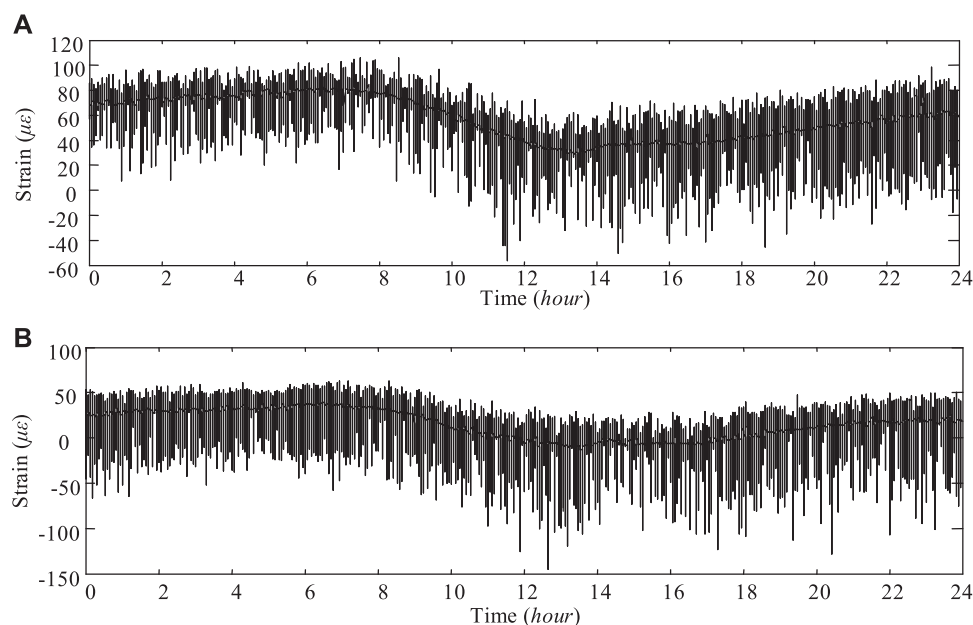


FIGURE 4 | Typical daily strain time histories: (A) Sensor RD_d , (B) Sensor RD_u .

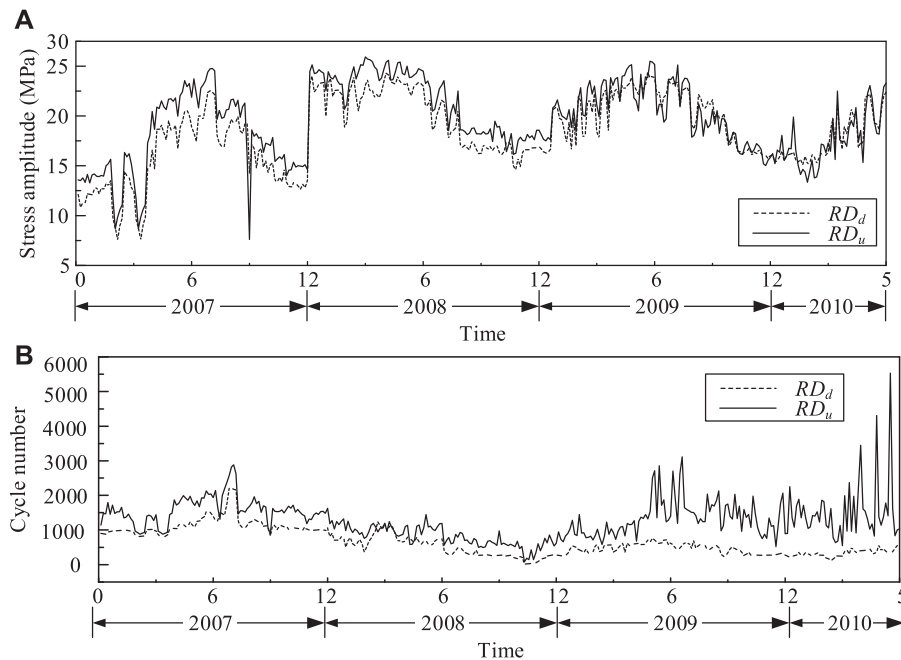


FIGURE 5 | The daily equivalent stress amplitude and cycle number: **(A)** Daily equivalent stress amplitude, **(B)** Daily equivalent cycle number.

amplitudes and cycles can be replaced by a constant stress amplitude with a number of cycles based on the Miner's rule and the S-N curve recommended in design codes.

In Eurocode (CEN, 1992), the S-N curve of the rib-to-deck weld joint is modeled by

$$\sigma^3 N = K_C \quad (\sigma \geq \sigma_D) \quad (16)$$

$$\sigma^5 N = K_D \quad (\sigma_L \leq \sigma \leq \sigma_D) \quad (17)$$

where K_C and K_D represent two coefficients indicating the fatigue strength of different weld joints; σ_D is the constant amplitude fatigue limit; and σ_L denotes the cut-off limitation of stress amplitude. For the rib-to-deck weld joint, K_C and K_D are 2.50×10^{11} and 3.47×10^{14} , respectively.

Because of initial defects in weld joints, all cyclic stress amplitudes should be considered. The fatigue damage in the rib-to-deck weld joint is

$$\frac{n}{N} = \frac{n\sigma^3}{K_C} \quad (\sigma \geq \sigma_D) \quad (18)$$

$$\frac{n}{N} = \frac{n\sigma^5}{K_D} \quad (\sigma \leq \sigma_D) \quad (19)$$

where n is the applied number of cycles of the stress amplitude σ .

It should be noted that most welded joints contain initial damages produced during fabrication. Although the initial damages may initially be small and not affected by these stress amplitudes lower than the constant amplitude fatigue limit, these stress amplitudes higher than the constant amplitude fatigue limit in the applied loading history may propagate the damage, and as the damage size increases it will be propagated by these stress amplitudes lower than the constant amplitude fatigue limit. The

concept of a constant amplitude fatigue limit is therefore not appropriate. And all stress amplitudes are taken into account (Tong et al., 2008). Therefore, the equivalent stress amplitude σ_{eq} and cycle number N_{eq} under vehicle loading are

$$\sigma_{eq} = \left[\frac{\sum_{\sigma_i \geq \sigma_D} \frac{n_i \sigma_i^3}{K_C} + \sum_{\sigma_j \leq \sigma_D} \frac{n_j \sigma_j^5}{K_D}}{N_{eq} / K_D} \right]^{1/5} \quad (20)$$

$$N_{eq} = \sum_{\sigma_i \geq \sigma_D} n_i + \sum_{\sigma_j \leq \sigma_D} n_j \quad (21)$$

By taking 24 h as the basic time interval, the daily equivalent stress amplitude and cycle number can be computed by Eqs. 20 and 21 and are displayed in Figure 5. From the figure, it can be found that the daily equivalent stress amplitudes in the downstream side show similar variation patterns with that in the upstream side. Most of daily equivalent stress amplitudes are in the range of [15 25]. However, for the daily equivalent cycle number, the values in the upstream side are larger than that in the downstream side most of the time. The results imply that there may be larger fatigue damage in the rib-to-deck weld joint in the upstream side and more attention should be paid on the upstream side during the routine inspections and maintenances. It is also demonstrated that the residual fatigue life in rib-to-deck weld joints are unique even on symmetrical locations of a steel-box girder.

Statistical Model of Equivalent Fatigue Loading Effect

It can be seen, from Figure 5, that both the daily equivalent stress amplitude and cycle number are highly random, and the value

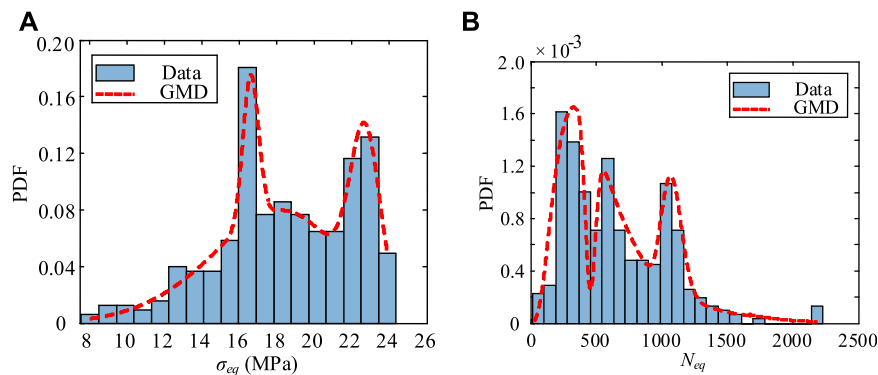


FIGURE 6 | The statistical characteristics of equivalent fatigue loading effects in the downstream side: **(A)** Daily equivalent stress amplitude, **(B)** Daily equivalent cycle number.

varies from day to day in the 4 years. Therefore, it is reasonable to describe their characteristics through statistical models. To this end, the probability distribution histograms of the four random variables are plotted in **Figures 6, 7**. Since cars and trucks with different weights pass in this lane, the multi-peak distribution features can be easily found in the four figures. Classical statistical models with a single peak are incapable of capturing their randomness. A generalized mixed distribution (GMD) formulated by **Eq. 22** is proposed in this study.

$$f(x) = \sum w_i f_i(x) \quad (22)$$

where $f(x)$ represents the probability distribution function (PDF) of the random variable x ; w_i is the weight of the i th component; and $f_i(x)$ denotes the classical statistical model of the i th component, like the Weibull distribution, the Gaussian distribution, and the lognormal distribution.

The expectation-maximization (EM) algorithm is adopted to estimate parameters in GMD models (Moon, 1996). The EM iteration alternates between performing an expectation (E) step

and a maximization (M) step. The E step creates a function for the expectation of the log-likelihood function evaluated using the current estimate for the parameters; and the M step computes parameters maximizing the expected log-likelihood function found in the E step. These parameters estimated in the M step are then used to determine the distribution of the latent variables in the next E step. The Akaike information criterion and Bayesian information criterion are employed to determine the optimal number of components.

The estimated PDFs for the daily equivalent stress amplitude and cycle number in downstream side and upstream side are shown in **Figures 6, 7**. The parameters of estimated PDFs are listed in **Table 1** and **Table 2**. In the two tables, $W(*,*)$ and $N(*,*)$ represent the Weibull distribution and the Gaussian distribution, respectively; and $Logn(*,*)$ denotes the lognormal distribution. By employing the K -S test, all estimated PDFs are acceptable at a significant level of 0.05. The daily equivalent stress amplitudes in both sides yield the same statistical model; and the equivalent cycle numbers in both sides yield another statistical model.

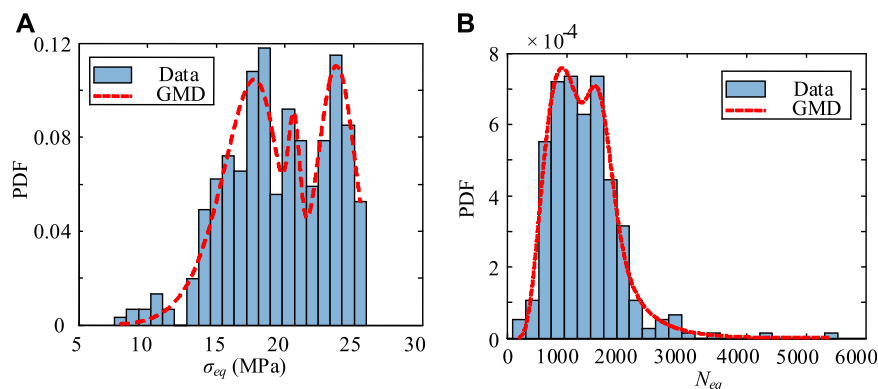


FIGURE 7 | The statistical characteristics of equivalent fatigue loading effects in the upstream side: **(A)** Daily equivalent stress amplitude, **(B)** Daily equivalent cycle number.

TABLE 1 | The statistical model of equivalent fatigue loading effects in the downstream side.

Component	σ_{eq}		N_{eq}	
	w_i	PDF	w_i	PDF
1	0.67	$W(18.82;6.02)$	0.14	$Logn(6.97;0.06)$
2	0.23	$N(22.72;0.79)$	0.97	$Logn(6.18;0.58)$
3	0.10	$N(16.61;0.41)$	0.11	$Logn(6.13;0.08)$

TABLE 2 | The statistical model of equivalent fatigue loading effects in the upstream side.

Component	σ_{eq}		N_{eq}	
	w_i	PDF	w_i	PDF
1	0.55	$W(18.00;9.24)$	0.16	$Logn(7.37;0.13)$
2	0.06	$N(20.68;0.43)$	0.83	$Logn(7.01;0.44)$
3	0.39	$N(23.76;1.41)$	0.01	$Logn(8.00;0.10)$

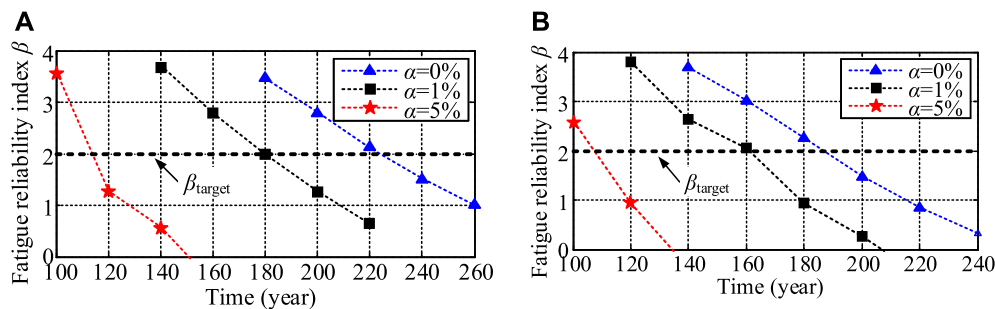
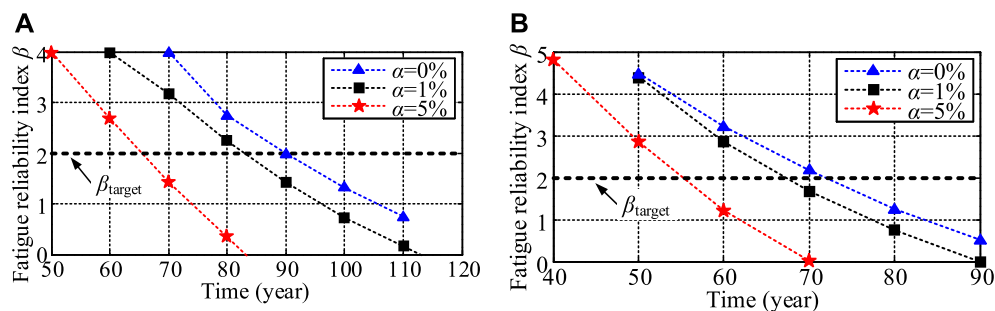
Fatigue Reliability Calculation

According to the statistical model of equivalent fatigue loading effects in **Tables 1, 2**, the Monte Carlo method is employed to generate time histories of daily equivalent stress amplitudes and cycle numbers. The sampling number for reliability calculation follows the criterion in **Eq. 15**. The damage indicator in **Eq. 1** is adopted to describe the fatigue damage in the rib-to-deck weld

joint. As known, the traffic growth rate α is an important factor governing the fatigue reliability. In this study, the yearly traffic growth is modeled by the increase of the daily equivalent cycle number.

Figure 8 displays the variation of the fatigue reliability index with time. The fatigue reliability indexes of rib-to-deck weld joints both in the upstream side and downstream side show a general decreasing tendency with the increase of the service life. Furthermore, the fatigue reliability indexes notably decrease when considering the traffic growth. In the service life of 100 years, all the values are higher than the generally used target reliability index $\beta = 2$, which indicates that there would be no fatigue cracks in rib-to-deck weld joints during the service life even if the traffic growth rate reaches 5%. When compared **Figure 8A** with **Figure 8B**, it can be seen that the fatigue reliability index of the rib-to-deck weld joint in the upstream side is smaller than that in the downstream side in the same service life, which implies that the fatigue damage growth rate of the rib-to-deck weld joint in the upstream side is faster than that in the downstream side. This is confirmed that the fatigue crack would more easily appear in the upstream side.

In practical engineering, weld flaws will inevitably produce initial damages in the weld joint. It is supposed that there are 1% initial damages in the rib-to-deck weld joint. The change of the fatigue reliability index in the rib-to-deck weld joint with time is plotted in **Figure 9**. It can be found that, when the 1% initial damage is taken into account, the fatigue reliability index

**FIGURE 8 |** The fatigue reliability index integrating traffic growth: (A) Downstream side, (B) Upstream side.**FIGURE 9 |** The fatigue reliability index integrating initial damage: (A) Downstream side, (B) Upstream side.

decreases sharply. In the service life of 100 years, the fatigue reliability indexes of rib-to-deck weld joints both in the upstream side and downstream side are less than 2 even if there is no traffic growth. It is deduced that the fatigue reliability of the rib-to-deck weld joint is very sensitive to the initial damage. Developing effective welding techniques to reduce weld flaws and thereby reduce initial damage is an effective way to avoid fatigue cracks in orthotropic bridge decks. Furthermore, manual on-site inspection is necessary. If the propagation of the fatigue crack is found, FRP reinforcement, steel plate reinforcement, and other reinforcement methods should be used to enhance the fatigue strength.

It is worth noting that from the point of view of the Miner's rule, 1% of the initial damage will only shorten the service life by 1%, which is not consistent with the real case that fatigue cracks have been found in many orthotropic steel decks with a design life of 100 years after only a few years or more than 10 years of service. The necessity of considering load sequence effects is proved.

CONCLUSION

Fatigue reliability assessment is an indispensable issue when investigating the serviceability of long-span bridges equipped with orthotropic steel decks. These methods regardless of load sequence effects may cause unacceptable errors. In this paper, the sequential law, which calculates the fatigue damage induced by cyclic stress histories in an iterative manner, is introduced to calculate the fatigue damage and assess the fatigue reliability of orthotropic steel decks. The following conclusions can be drawn:

- 1) The sequential law quantifies the fatigue damage caused by present cyclic stress amplitudes based on previous fatigue damage by iteration calculation and has the capability of capturing the loading sequence effect. The whole *S-N* curve developed by extending the *S-N* curve in the finite life region can describe the fatigue propagation process in the very low-cycle region, the low-cycle region, the finite life region, the high-cycle region, and the very high-cycle region.
- 2) The developed GMD, which is formulated by the weighted sum of several classical distributions, integrating the EM algorithm is capable of describing any complex multi-peak distribution. The daily equivalent stress amplitude and cycle number show typical multi-peak distribution

features. The daily equivalent stress amplitude yields the weighted sum of one Weibull distribution and two Gaussian distributions; and the daily equivalent cycle number yields the weighted sum of three lognormal distributions.

- 3) If there is no initial damage, even if the traffic volume increases by 5%, the fatigue reliability indexes of rib-to-deck weld joints both in the upstream side and downstream side are greater than 2 in the service life of 100 years. However, even if only 1% of the initial damage exists, the fatigue reliability cannot meet the design requirements. The fatigue reliability of the rib-to-deck weld joint is extremely susceptible to the initial damage.

Only the application of the proposed method in evaluating the fatigue reliability of rib-to-deck weld joints is provided in this paper. The proposed method can also be used to evaluate the fatigue reliability of other types of weld joints in the orthotropic steel deck.

DATA AVAILABILITY STATEMENT

The original contributions presented in the study are included in the article/Supplementary Material, further inquiries can be directed to the corresponding author.

AUTHOR CONTRIBUTIONS

J-HX wrote and revised the whole manuscript. G-DZ proposed the fatigue reliability assessment method. T-YZ performed the application of the developed method.

FUNDING

This research work was jointly supported by the Natural Science Fund for Excellent Young Scholars of Jiangsu Province (Grant No. BK20170097), the Natural Science Fund of Jiangsu Province (Grant No. BK20180776), the Natural Science Foundation of the Jiangsu Higher Education Institutions (Grant No. 18KJB560013), Science and Technology Project of Housing and Urban Rural Development Department (Grant No. 2018-K9-068), and the Research Fund of Key Laboratory of Large Structure Health Monitoring and Control (Grant No. KLLSHMC1912).

REFERENCES

- AASHTO (2012). *AASHTO LRFD Bridge Design Specifications*. 6th Ed. Washington, DC.
- Aid, A., Amrouche, A., Bouiadja, B. B., Benguediab, M., and Mesmacque, G. (2011). Fatigue Life Prediction under Variable Loading Based on a New Damage Model. *Mater. Des.* 32 (1), 183–191. doi:10.1016/j.matdes.2010.06.010
- Aid, A., Bendouba, M., Aminallah, L., Amrouche, A., Benseddig, N., and Benguediab, M. (2012). An Equivalent Stress Process for Fatigue Life Estimation under Multiaxial Loadings Based on a New Non Linear Damage Model. *Mater. Sci. Eng. A* 538, 20–27. doi:10.1016/j.msea.2011.12.105
- CEN (1992). *Eurocode 3: Design of Steel Structures, Part 1-9: Fatigue*. Brussels, Belgium: European Committee for Standardization.
- Cui, C., Zhang, Q., Hao, H., Li, J., and Bu, Y. (2018). Influence of Asphalt Pavement Conditions on Fatigue Damage of Orthotropic Steel Decks: Parametric Analysis. *J. Bridge Eng.* 23 (12), 04018093. doi:10.1061/(asce)be.1943-5592.0001313
- Di, J., Ruan, X., Zhou, X., Wang, J., and Peng, X. (2020). Fatigue Assessment of Orthotropic Steel Bridge Decks Based on Strain Monitoring Data. *Eng. Struct.* 228, 111437.

- Fang, Z., Ding, Y., Wei, X., Li, A., and Geng, F. (2020). Fatigue Failure and Optimization of Double-Sided Weld in Orthotropic Steel Bridge Decks. *Eng. Fail. Anal.* 116, 104750. doi:10.1016/j.engfailanal.2020.104750
- Fisher, J. W., and Barsom, J. M. (2016). Evaluation of Cracking in the Rib-To-Deck Welds of the Bronx-Whitestone Bridge. *J. Bridge Eng.* 21 (3), 04015065. doi:10.1061/(asce)be.1943-5592.0000823
- Frangopol, D. M. (2008). Probability Concepts in Engineering: Emphasis on Applications to Civil and Environmental Engineering. *Struct. Infrastructure Eng.* 4, 413–414. doi:10.1080/15732470802027894
- Guo, T., Liu, J., Deng, Y., and Zhang, Z. (2019). Fatigue Performance of Orthotropic Steel Decks with FRP Angles: Field Measurement and Numerical Analysis. *J. Perform. Constructed Facil.* 33 (4), 04019042. doi:10.1061/(asce)cf.1943-5509.0001308
- Guo, T., Liu, Z., Correia, J., and de Jesus, A. M. P. (2020). Experimental Study on Fretting-Fatigue of Bridge Cable Wires. *Int. J. Fatigue* 131, 105321. doi:10.1016/j.ijfatigue.2019.105321
- Heng, J., Zheng, K., Gou, C., Zhang, Y., and Bao, Y. (2017). Fatigue Performance of Rib-To-Deck Joints in Orthotropic Steel Decks with Thickened Edge U-Ribs. *J. Bridge Eng.* 22 (9), 04017059. doi:10.1061/(asce)be.1943-5592.0001095
- Karunananda, K., Ohga, M., Dissanayake, R., Siriwardane, S., and Chun, P.-J. (2012). New Combined High and Low-Cycle Fatigue Model to Estimate Life of Steel Bridges Considering Interaction of High and Low Amplitudes Loadings. *Adv. Struct. Eng.* 15 (2), 287–302. doi:10.1260/1369-4332.15.2.287
- Liu, Y., Zhang, H., Liu, Y., Deng, Y., Jiang, N., and Lu, N. (2017). Fatigue Reliability Assessment for Orthotropic Steel Deck Details under Traffic Flow and Temperature Loading. *Eng. Fail. Anal.* 71, 179–194. doi:10.1016/j.engfailanal.2016.11.007
- Liu, Y., Zhang, Q., Bao, Y., and Bu, Y. (2020). Fatigue Behavior of Orthotropic Composite Deck Integrating Steel and Engineered Cementitious Composite. *Eng. Structures* 220, 111017. doi:10.1016/j.engstruct.2020.111017
- Luo, Y., Yan, D.-h., Yuan, M., and Lu, N.-w. (2017). Probabilistic Modeling of Fatigue Damage in Orthotropic Steel Bridge Decks under Stochastic Traffic Loadings. *J. Highw. Transp. Res. Dev. (English Ed.)* 11 (3), 62–70. doi:10.1061/jhtrcq.0000582
- Ma, X., and Zhang, W. (2020). Fatigue Life of Weldment Details of Existing Orthotropic Steel Bridge Considering the Scour Effects. *J. Bridge Eng.* 25 (10), 04020078. doi:10.1061/(asce)be.1943-5592.0001612
- Maljaars, J., Bonet, E., and Pijpers, R. J. M. (2018). Fatigue Resistance of the Deck Plate in Steel Orthotropic Deck Structures. *Eng. Fracture Mech.* 201, 214–228. doi:10.1016/j.engfracmech.2018.06.014
- Mesmacque, G., Garcia, S., Amrouche, A., and Rubiogonzalez, C. (2005). Sequential Law in Multiaxial Fatigue, a New Damage Indicator. *Int. J. Fatigue* 27 (4), 461–467. doi:10.1016/j.ijfatigue.2004.08.005
- Moon, T. K. (1996). The Expectation-Maximization Algorithm. *IEEE Signal. Process. Mag.* 13 (6), 47–60. doi:10.1109/79.543975
- Saunders, J., Chen, Y., Marks, J. A., Hodgson, I., Sause, R., and Kozy, B. M. (2021). Finite-Element Fatigue Analysis of a New Rib-To-Floor Beam Connection for Orthotropic Steel Decks. *J. Bridge Eng.* 26 (2), 04020123. doi:10.1061/(asce)be.1943-5592.0001676
- Sim, H.-B., and Uang, C.-M. (2012). Stress Analyses and Parametric Study on Full-Scale Fatigue Tests of Rib-to-Deck Welded Joints in Steel Orthotropic Decks. *J. Bridge Eng.* 17 (5), 765–773. doi:10.1061/(asce)be.1943-5592.0000307
- Siriwardane, S. A. S. C., Ohga, M., Dissanayake, P. B. R., and Kaita, T. (2010). Structural Appraisal-Based Different Approach to Estimate the Remaining Fatigue Life of Railway Bridges. *Struct. Health Monit.* 9 (4), 323–339. doi:10.1177/1475921710361320
- Siriwardane, S. C., Ohga, M., Dissanayake, R., and Taniwaki, K. (2007). Different Approaches for Remaining Fatigue Life Estimation of Critical Members in Railway Bridges. *Steel Structures* 7, 263–276.
- Siriwardane, S., Ohga, M., Dissanayake, R., and Taniwaki, K. (2008). Application of New Damage Indicator-Based Sequential Law for Remaining Fatigue Life Estimation of Railway Bridges. *J. Constructional Steel Res.* 64 (2), 228–237. doi:10.1016/j.jcsr.2007.06.002
- Tong, G., Aiqun, L., and Jianhui, L. (2008). Fatigue Life Prediction of Welded Joints in Orthotropic Steel Decks Considering Temperature Effect and Increasing Traffic Flow. *Struct. Health Monit.* 7 (3), 189–202.
- Yang, H., Wang, P., and Qian, H. (2020). Fatigue Behavior of Typical Details of Orthotropic Steel Bridges in Multiaxial Stress States Using Traction Structural Stress. *Int. J. Fatigue* 141, 105862. doi:10.1016/j.ijfatigue.2020.105862
- Ye, X. W., Su, Y. H., and Han, J. P. (2014). A State-of-The-Art Review on Fatigue Life Assessment of Steel Bridges. *Math. Probl. Eng.* 2014, 1–13. doi:10.1155/2014/956473
- Zakaria, K. A., Abdullah, S., Abdullah, S., and Ghazali, M. J. (2016). A Review of the Loading Sequence Effects on the Fatigue Life Behaviour of Metallic Materials. *Jestr.* 9 (5), 189–200. doi:10.25103/jestr.095.30
- Zhou, G.-D., Yi, T.-H., Zhu, T.-Y., and Zhang, H. (2018). A Whole-Range S-N Curve for Fatigue Assessment of Steel Orthotropic Bridge Decks. *Int. J. Str. Stab. Dyn.* 18 (08), 1840010. doi:10.1142/s0219455418400102

Conflict of Interest: The authors declare that the research was conducted in the absence of any commercial or financial relationships that could be construed as a potential conflict of interest.

Copyright © 2021 Xu, Zhou and Zhu. This is an open-access article distributed under the terms of the Creative Commons Attribution License (CC BY). The use, distribution or reproduction in other forums is permitted, provided the original author(s) and the copyright owner(s) are credited and that the original publication in this journal is cited, in accordance with accepted academic practice. No use, distribution or reproduction is permitted which does not comply with these terms.



Detection of Pipeline Deformation Induced by Frost Heave Using OFDR Technology

Tao Jiang^{1,2}, Jing-wen Zhu^{1,2} and Yi Shi^{3*}

¹Department of Civil and Environmental Engineering, Shantou University, Shantou, China, ²Guangdong Engineering Center for Structure Safety and Health Monitoring, Shantou University, Shantou, China, ³Department of Electronic and Information Engineering, Shantou University, Shantou, China

OPEN ACCESS

Edited by:

Chun-Xu Qu,
Dalian University of Technology, China

Reviewed by:

Yabin Liang,
China Earthquake Administration,
China
Jiaxiang Li,
Northeastern University, China

*Correspondence:

Yi Shi
shy_xfx@163.com

Specialty section:

This article was submitted to
Interdisciplinary Physics,
a section of the journal
Frontiers in Physics

Received: 24 March 2021

Accepted: 03 May 2021

Published: 20 May 2021

Citation:

Jiang T, Zhu J and Shi Y (2021)
Detection of Pipeline Deformation
Induced by Frost Heave Using
OFDR Technology.
Front. Phys. 9:684954.
doi: 10.3389/fphy.2021.684954

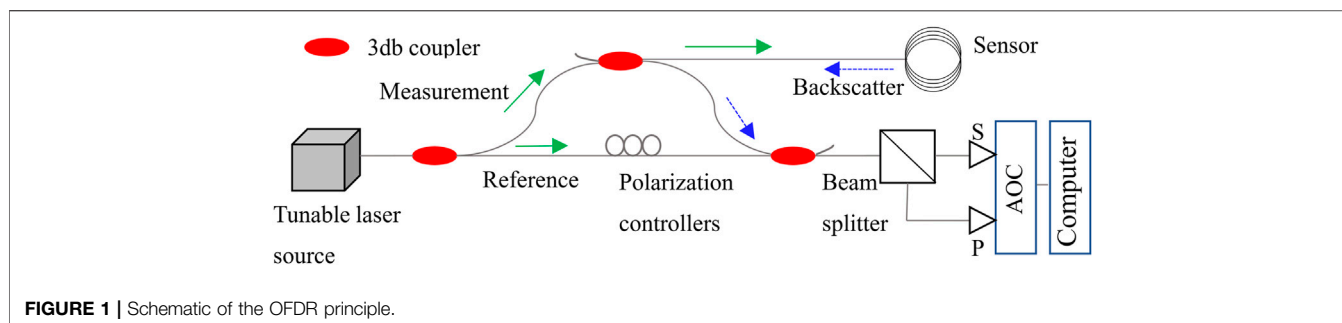
Keywords: pipeline, optic fiber sensor, deformation, frozen soil, monitoring

INTRODUCTION

The pipeline network plays an important role in oil and gas transportation. The growing demand for energy supply and the reduction of the world's oil and gas stocks have led operators to explore and construct new massive pipelines in permafrost such as Russia's far north [1]. In permafrost or seasonally frozen ground regions, frost heave and thaw settlement can lead to pipeline deformation [2, 3], which is a well-known phenomenon in buried pipelines and can lead to large upward movements of a pipeline. This type of deformation has been understood for a long time and seen in Russia and Canada [4]. The deformation of the pipeline will directly result in the pipeline fracture, causing environmental pollution and even accidents. Monitoring the performance of a pipeline in permafrost terrain is more necessary than that for pipelines installed in temperate areas [5].

Conventionally, pipeline inspection robots with closed-circuit TV [6], which utilize ultrasonic and photogrammetric technology, have been employed as major tools to detect pipeline deformation. However, these methods are not suitable for deformation monitoring in real time. Additionally, the electrical sensors are prone to cause fire and explosion accidents in gas and oil pipelines [7].

Optic fiber sensing technology, with its superior immunity to electromagnetic interference, long-distance transmission, high accuracy, and reliability, is particularly attractive for using in harsh environments and electromagnetic fields. Therefore, fiber optic sensing technology has attracted increasing attention in the study of pipeline deformation monitoring [8, 9]. Using distributed fiber optic sensors, Fabien Ravet et al. [10] presented a solution for pipeline deformation due to ground movement. Deformation such as buckling or pipe deformation was detected by recognizing the

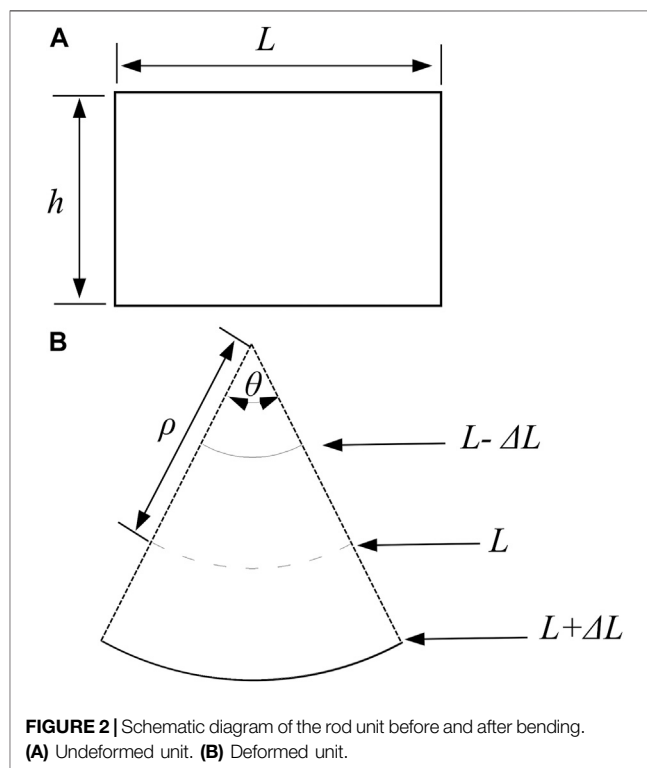


abnormal strain distribution along the pipeline. In another case, Fabien Ravet et al. [1] introduced an application of a distributed optic fiber sensor in a gas pipeline in Peru, and several events such as landslides and soil settlement were detected by strain measurement. Dana DuToit et al. [11] conducted a realistic pipeline deformation test, where the fiber optic cables were mounted on the pipe and off the pipe, respectively. Test results showed that both on-pipe and off-pipe fiber optic cables provided valuable magnitude assessment of pipe deformations and strains. Carlos Borda et al. [12] directly attached optic fiber strain cables to pipelines at 3, 9, and 12 o'clock positions, respectively, and used a Brillouin optic time-domain analysis (BOTDA)-based interrogator to record the strain data. By analyzing the continuous strain variation, pipeline deformation and 3D positioning due to geological hazards were monitored. Utilizing the conjugate beam method and BOTDA, Zhang et al [13] conducted a test on a PVC pipe model to reconstruct the deformed shape. It is found that the reconstructed shape of the pipeline model depends on the number of measured points, and the more the measured points, the higher the measuring precision of displacement. For the above studies, pipeline deformation induced by frost heave is not involved. In addition, the distributed strain data provided by BOTDA have a long measurement range, but the spatial resolution and strain accuracy cannot satisfy the requirement of pipeline deformation monitoring very well.

OFDR technology combined with high-performance digital signal processors is used to measure distributed strain with millimeter-scale resolution and microstrain measurement precision [14], providing an effective way for pipeline deformation monitoring. In this paper, OFDR technology was used to monitor the distributed strain and the plane curve reconstruction algorithm was used to calculate the deformed shape from the measured strain. This article aims to provide a new approach for pipeline deformation monitoring in permafrost or seasonally frozen ground regions.

OPTIC FREQUENCY-DOMAIN REFLECTOMETER-BASED DISTRIBUTED SENSING

The spectral response of the Rayleigh backscatter in an optic fiber will be determined by the effects of strain [15] and temperature



[16]. The relationship between the spectrum shift $\Delta\nu$ and the variation of strain $\Delta\varepsilon$ and temperature Δt is given as

$$\Delta\nu = K_T \Delta t + K_\varepsilon \Delta\varepsilon, \quad (1)$$

where K_T and K_ε are the temperature and strain sensitivity coefficients, respectively. Therefore, the temperature and strain can be measured by detecting the Rayleigh scatter frequency. OFDR technique utilizes swept-wavelength interferometry to measure the Rayleigh backscatter as a function of position in the optic fiber [17]. **Figure 1** illustrates the principle of the OFDR. Light from the tunable laser source is split between a measurement arm and a reference arm via an optic fiber coupler. Through the measurement arm, the light is sent to the optic fiber sensor. The backscattered light from the optic fiber sensor returns via the coupler and is combined with the light from the reference arm. After passing through the polarization beam splitter, the combined light will be split into orthogonal

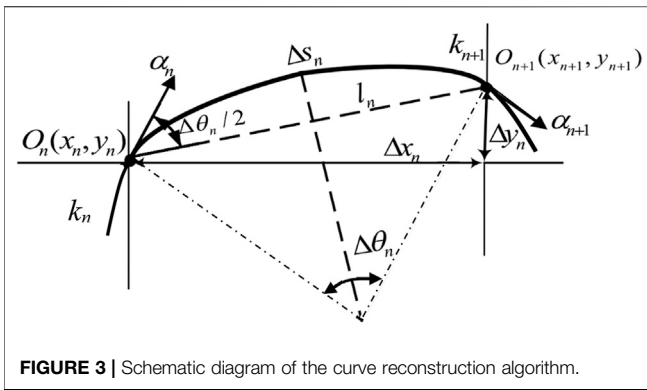


FIGURE 3 | Schematic diagram of the curve reconstruction algorithm.

states recorded at the S and P detectors. A Fourier transform of these signals yields the phase and amplitude of the signal as a function of length along the sensor [18]. Changes in the local strain and temperature of the optic fiber sensor can be detected by comparing a scan of the sensor in a measurement state to a previously recorded reference scan [19]. Any position of the sensing fiber can be used to measure the strain and temperature, similar to the optic fiber etched with continuous distributed FBG sensors [20]. The detailed introduction of OFDR measurement principles can be seen in the study of Kreger et al. [18].

THEORY OF PIPELINE SHAPE MONITORING

Curve Reconstruction Algorithm

If a rod is bent, one side is subjected to tensile stresses, while the other side is subjected to compressive stresses. Therefore, there must exist an unstressed surface, which is called the neutral layer. For a rod with a symmetrical cross section, the neutral layer is the surface where the axial line locates at. The curvature of the neutral layer can be used to represent the shape change of a rod. According to Figure 2, the length of the axial line can be expressed as

$$L = \theta/k, \quad (2)$$

where L is the length of the rod unit; θ is the angle of the arc; and k is the curvature of the rod defined as $k = 1/\rho$, where ρ denotes the curvature radius of the bent rod. The length variation of the rod surface ΔL is given as

$$L + \Delta L = (1/k + h/2)\theta, \quad (3)$$

where h is the height of the rod unit. The strain ε along the axial direction on the surface of the rod is given as

$$\varepsilon = \frac{\Delta L}{L}. \quad (4)$$

The relationship between surface strain and curvature can be expressed as

$$k = \frac{2\varepsilon}{h}. \quad (5)$$

Hence, the continuous curvature information can be obtained by the continuous surface strain of the rod.

As shown in Figure 3, O_n and O_{n+1} are the two endpoints of the arc; the coordinates of O_n and O_{n+1} are (x_n, y_n) and (x_{n+1}, y_{n+1}) , respectively. If the distance between O_n and O_{n+1} is extremely small, the curve segment O_{n+1} can be regarded as a microarc ΔS_n . k_n and k_{n+1} are the curvature of the arc where O_n and O_{n+1} locate at, respectively. α_n and α_{n+1} denote the tangential vectors of O_n and O_{n+1} , respectively. θ_n and θ_{n+1} are the angles between the tangent vector of the two points and the x -axis, respectively. l_n is the chord length corresponding to the microarc ΔS_n . $\Delta\theta_n$ denotes the central angle of the microarc ΔS_n . According to Figure 3, the coordinate of O_{n+1} can be calculated through O_n . Through iterative calculation, the coordinates of each point are obtained. The equations are given directly as

$$\begin{cases} \Delta\theta = \theta_{n+1} - \theta_n \\ l_n = 2 \times \sin(\Delta\theta/2)/k_n \\ l_n = \Delta S_n, (k_n = 0) \\ \Delta x_n = l_n \times \cos(\theta_n + \Delta\theta/2) \\ \Delta y_n = l_n \times \sin(\theta_n + \Delta\theta/2) \\ x_{n+1} = x_n + \Delta x_n \\ y_{n+1} = y_n + \Delta y_n \end{cases} \quad (6)$$

θ , the key parameter for this curve reconstruction algorithm, can be obtained by solving the differential equation. Based on the definition of curvature, the curvature k of any arc segment can be expressed as

$$k(s) = \frac{d\theta}{ds} \quad (7)$$

Therefore, θ can be expressed as

$$\theta(s) = \int k(s)ds \quad (8)$$

where s denotes the length of the arc. It is assumed that the relationship between curvature and arc length is linear [21]; the curvature k can be given as

$$k = A \times s + B, \quad (9)$$

where A and B are coefficients.

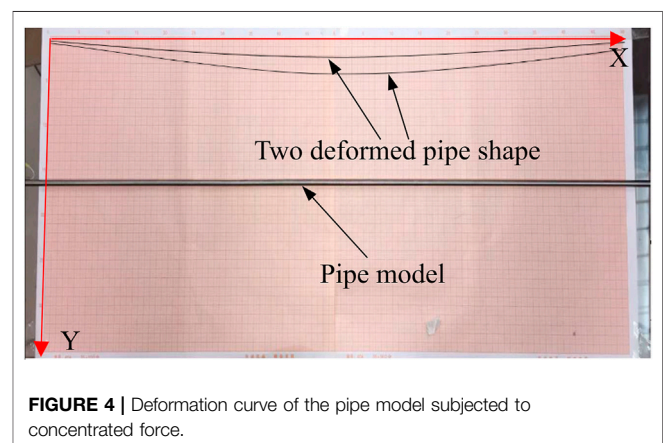


FIGURE 4 | Deformation curve of the pipe model subjected to concentrated force.

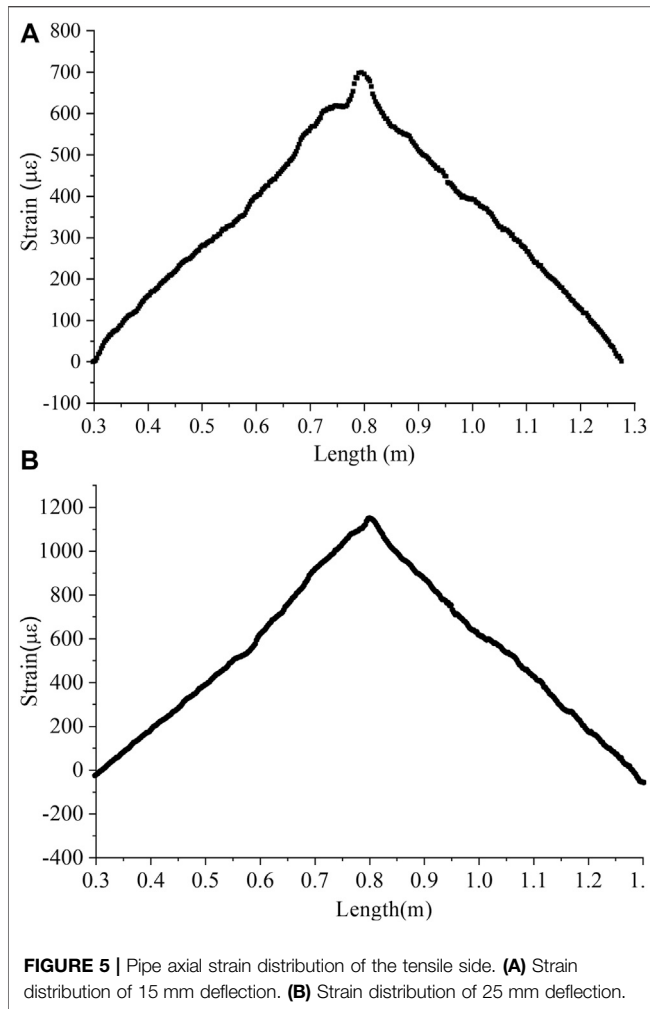


FIGURE 5 | Pipe axial strain distribution of the tensile side. **(A)** Strain distribution of 15 mm deflection. **(B)** Strain distribution of 25 mm deflection.

According to Eqs. 8, 9, $\theta(s)$ can be obtained as follows:

$$\theta(s) = A \times s^2/2 + B \times s + C \quad (10)$$

where C is constant and can be calculated by the deformation boundary conditions of the structure.

The curvature of two adjacent microarcs can be expressed as

$$\begin{cases} k_n = A_n \times s_n + B_n \\ k_{n+1} = A_n \times s_{n+1} + B_n \end{cases} \quad (11)$$

Therefore, A_n and B_n can be obtained by

$$\begin{cases} A_n = (k_{n+1} - k_n) / (s_{n+1} - s_n) \\ B_n = (k_n \times s_{n+1} - k_{n+1} \times s_n) / (s_{n+1} - s_n) \end{cases} \quad (12)$$

After calculating A , B , and C , $\theta(s)$ can be achieved by Eq. 10. Consequently, the curve is reconstructed.

For pipeline shape reconstruction, optic fiber sensors can be attached to the pipeline surface. The curvature k of each arc segment along the pipeline can be calculated by the measured axial strain. The accuracy of the reconstructed shape is related to the measurement accuracy, spatial resolution, and sampling

spacing of the measured strain. Since the deformation of the pipeline is continuous, OFDR technology can provide millimeter-scale spatial resolution and sampling spacing. Therefore, the two consecutive measurement points are regarded as a microarc during the calculation, and the coefficients A and B can be calculated by using the curvature k of each measured point. After obtaining θ of each measured point and the corresponding curvature k , the coordinates of each measured point can be calculated in turn using Eq. 6. Consequently, the shape of the pipeline is reconstructed. In practice, optic fiber sensors will be installed on a length that significantly exceeds the area of possible ground movements. Therefore, the segment at the edge of pipeline deformation can be considered fixed and, consequently, the boundary condition for deformed shape calculation. By using the above approach, pipeline deformation monitoring can be realized.

Test Verification

To verify the performance of the curve reconstruction algorithm for pipe structures, a deformation reconstruction test was conducted using a small pipe model. The diameter of the pipe model is 7.7 mm, and the wall thickness is 0.5 mm. The length of the pipe model is 1.2 m. One polyimide-coated optic fiber was

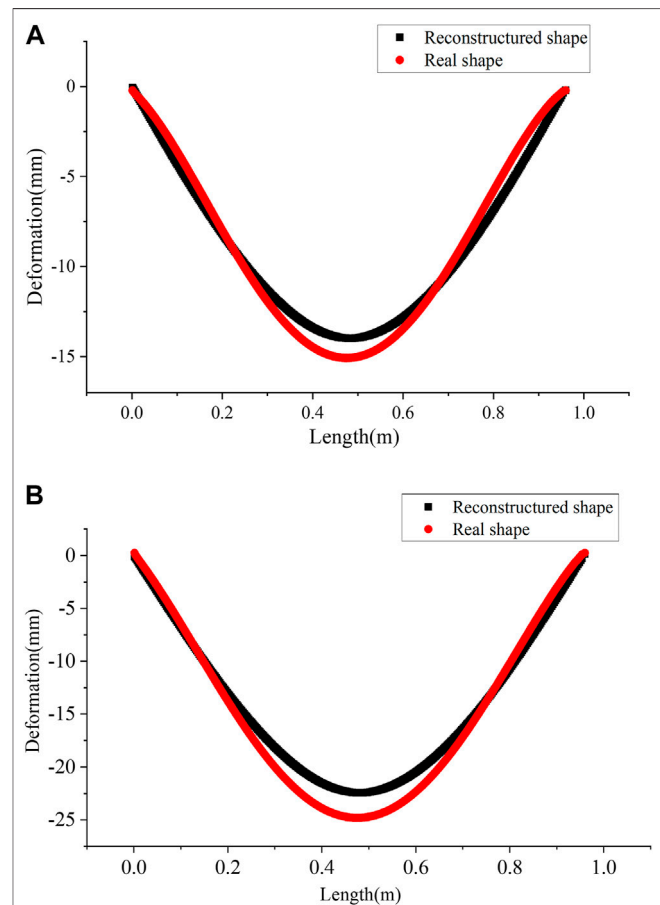


FIGURE 6 | Pipe shape reconstructed by the axial strain distribution. **(A)** 15 mm deformation. **(B)** 25 mm deformation.

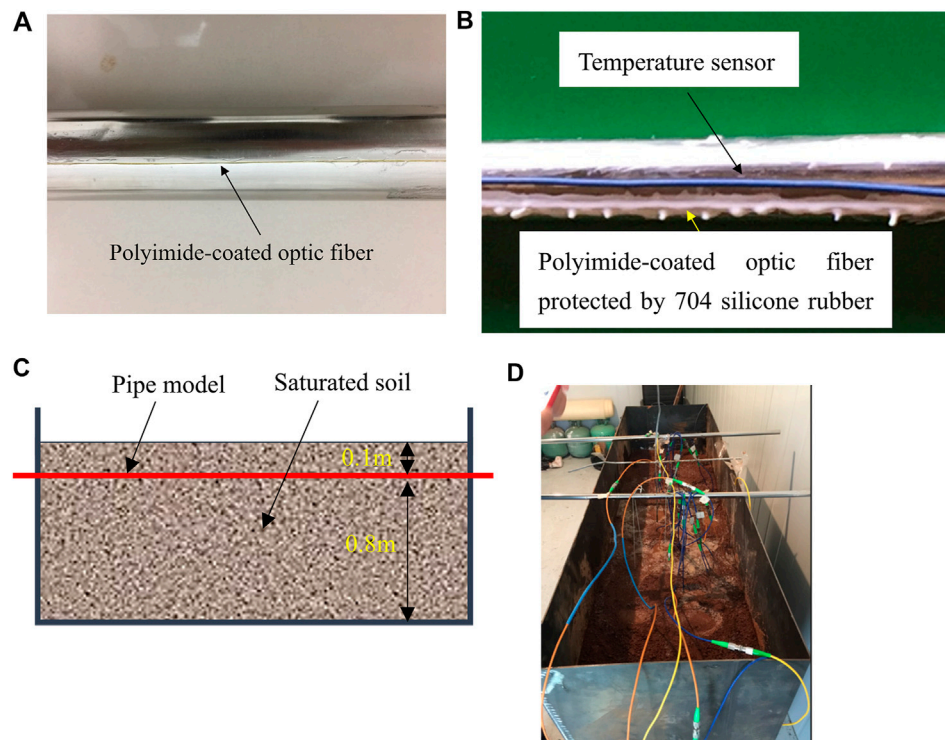


FIGURE 7 | Pictures of the test illustration. **(A)** Polyimide-coated optic fiber sensor. **(B)** Picture of the strain sensor and temperature sensor. **(C)** Position of the pipe model. **(D)** Steel tank.

bonded on the tensile side of the pipe model to measure the axial strain. An OFDR-based interrogator ODISI-B from LUNA Innovations was utilized for strain data recording. For the pipe model, the distance between the two support points is 1.0 m. The displacement in the x direction and y direction at both support points was limited, while the rotation was not limited. Concentrated forces were applied to the middle span of the model to produce deformations on the pipe, which were 15 and 25 mm, respectively. In order to verify the accuracy of the plane curve reconstruction algorithm, the deformed shapes of the pipe model were drawn on a graph paper, as shown in **Figure 4**.

Figure 5 displays the strain distribution of the pipe model. For the curve reconstruction algorithm, the initial rotation angle of the pipe is set as 0° and the reconstructed shape is tangent to the x -axis. However, the real deformed shape has a certain angle with the x -axis. Therefore, the reconstructed shape should be rotated such that its two ends are placed on the x -axis. **Figure 6** shows the reconstructed pipe shapes using the measured strain presented in **Figure 5**. It is shown that the reconstructed pipe shape and the real deformed shape agree well with each other. Although the strain distribution has fluctuations, it has less influence on the shape reconstruction results. The maximum difference between the calculated value and the real value appears at the midpoint of the pipe model, which is 1.1 and 2.1 mm, respectively. The test results illustrate that the proposed approach can effectively reconstruct the deformed shape of the pipe structure.

PIPE DEFORMATION-MONITORING TEST

Test Setup

If the temperature of saturated soil falls below freezing, the water will turn into ice, which can result in the volume growth of the saturated soil. Theoretically, the pipe will be bent upward if it is subjected to the force of the expanded saturated soil. Based on this principle, the pipe model was placed in the saturated soil. Both the pipe and the saturated soil were placed in a cold storage to simulate the pipeline deformation.

A steel tank with dimensions of $1.4 \times 1.1 \times 0.4 \text{ m}^3$ was manufactured to contain the saturated soil. There are four angle steels welded together around the steel tank, forming a steel hoop to restrict the deformation of the frost heave in the

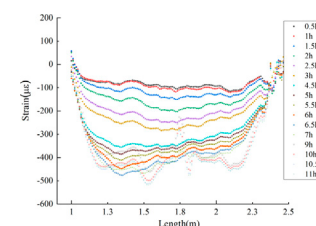
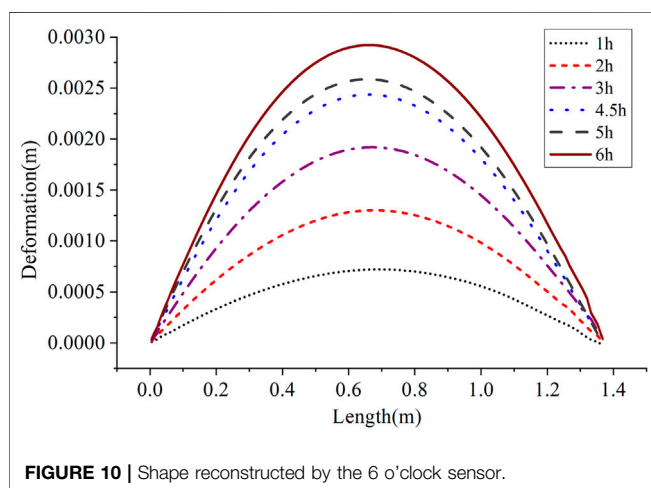
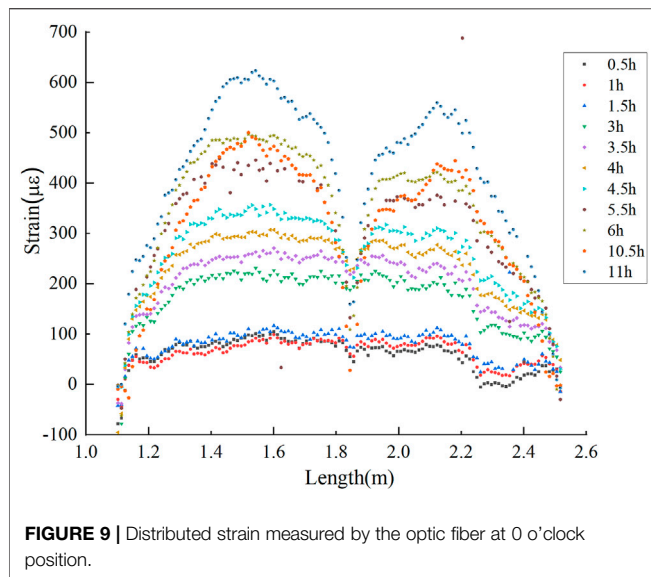


FIGURE 8 | Strain distribution measured by the optic fiber at 6 o'clock position.



horizontal direction. The steel hoop is 600 mm away from the tank bottom. On two short sides of the steel tank walls, two round holes with a diameter of 60 mm were fabricated, and the holes are 800 mm away from the bottom.

In the test, the pipe model is a segment of a steel pipe with an outer diameter of 60 mm and a wall thickness of 0.8 mm. To obtain a precise strain distribution, the polyimide-coated fiber was utilized due to its less strain transfer loss. Before bonding the optic fiber, the pipe surface was cleaned by cotton immersed in alcohol. Then, two polyimide-coated fibers were bonded at 0 o'clock and 6 o'clock positions, respectively, using cyanoacrylate adhesive, see **Figure 7A**. As shown in **Figure 7B**, 704 silicone rubber glue was used to cover the optic fiber, since it is easily damaged. A temperature compensation sensor was adhered close to the optic fiber at 0 o'clock position. The temperature sensor is a piece of an optic fiber placed into an armored cable. As the optic

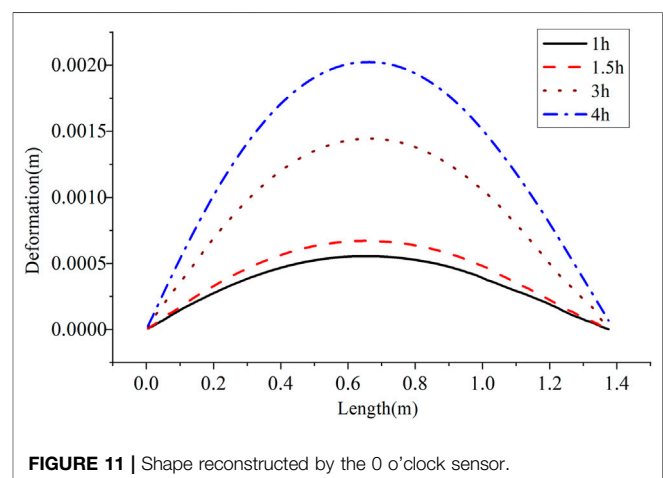
fiber can freely extend or shrink under the temperature, the strain induced by temperature is measured and deduced from the measured strain. **Figure 7C** presents the position of the pipe model, and **Figure 7D** displays the real steel tank filled with saturated soil.

The pipe model was placed in the steel tank through the two holes. Therefore, the vertical displacement on two ends of the pipe model was restricted when subjected to frost heave force, while the rotation of the two ends was not restricted. The thickness of the overlying soil above the pipe is 10 cm, which is used to simulate the pipeline covered by soil. To provide the freezing condition, the room temperature in the cold storage was decreased from 20 to -23°C and kept at -23°C for 12 h.

Test Results

The strain distribution of the pipe model was recorded every 0.5 h. **Figures 8 and 9** display the distributed strain measured by the optic fiber mounted at 6 o'clock and 0 o'clock, respectively. Note that the strain induced by temperature has already been deduced from the distributed strain. The strain data were not all recorded as the interrogator could not detect the sensor signal at certain times. It is shown that the strain measured by the sensor at 6 o'clock position is compressive strain, while the strain measured by the sensor at 0 o'clock is tensile strain. It can be concluded that the pipe has an upward bending due to the frost heave force. And with the increase in the freezing time, the deformation of the pipe constantly increases. After 7 h, the increase is not obvious. It is helpful to directly evaluate the mechanical state of the pipe using strain distribution. As shown in **Figures 8 and 9**, abnormal strain variations appear in the strain distribution. This is because an iron circle, which was placed at the middle of the pipe, pressed the optic fiber and resulted in the abnormal strain distribution.

Using the curve reconstruction algorithm and the distributed strain recorded by a 6 o'clock sensor, the pipe shape at different times was reconstructed and is shown in **Figure 10**. Note that the measured strain distribution data were directly used to calculate the pipe shape. The abnormal data were not utilized to reconstruct the pipe shape, so **Figure 10** only presents the



deformed shape before 6 h. It can be seen from **Figure 10** that the largest deformation occurs at the midspan position of the pipe. After 6 h of freezing, the maximum deformation is 2.9 mm. From the reconstruction shape of the pipe, it is possible to identify the location with large deformation. The deformation monitoring methods enable people to take preventative measures at an early stage.

Figure 11 displays the shape reconstructed by a 0 o'clock sensor. Strain data only before 4 h were employed to calculate the pipe shape since the measured strain is interfered by the external environment after 4 h. Comparing the two deformed pipe shapes reconstructed by the two optic fiber sensors, all the maximum deformations of the two test results occur at the middle of the pipe. There are minor differences between these two reconstructed shapes at the same moment. They are 0.7 and 0.5 mm after 1 h, respectively, while after 3 h, the maximum deformations are 1.9 and 1.4 mm, respectively. The differences are probably induced by the fact that the neutral axis is not exactly located at the center of the pipe. The way of directly mounting optic fiber sensors on the pipe may result in an inaccurate reconstructed pipe shape. Besides, the measured strain is easily interfered by the external environment. Therefore, an optic fiber shape sensor, which can overcome the above disadvantages, should be developed in the future study.

CONCLUSION

The study of pipe deformation monitoring in the frozen soil area is an important issue. For the shape reconstruction algorithm, the accuracy of the reconstructed shape depends on the number of measured points and sampling spacing. OFDR technology has

high accuracy, high spatial resolution, and high sampling spacing in distributed strain measurement. Therefore, we propose to combine the OFDR technology and curve reconstruction algorithm to monitor the pipe deformation. In the experimental study, the OFDR technology and curve reconstruction algorithm are demonstrated to have good performance. However, further studies should be carried out for practical applications, such as to determine how to protect the optic fiber and obtain more precise strain data.

DATA AVAILABILITY STATEMENT

The raw data supporting the conclusion of this article will be made available by the authors, without undue reservation.

AUTHOR CONTRIBUTIONS

TJ conceived the study, designed the test, and wrote the paper. J-WZ performed the experiments and analyzed the data. YS made constructive comments on the study and participated in paper writing.

FUNDING

This work was supported by the fund from the National Natural Science Foundation of China (Grant Nos. 52008236 and 61801283) and Shantou University Scientific Research Foundation (Grant No. NFT19039). These grants are greatly appreciated.

REFERENCES

- Ravet F, Borda C, Rochat E, and Niklès M. Geohazard Prevention and Pipeline Deformation Monitoring Using Distributed Optical Fiber Sensing. In: ASME 2013 International Pipeline Geotechnical Conference, July 24–26, 2013, Bogota, Colombia. American Society of Mechanical Engineers Digital Collection (2013).
- Ravet F, Niklès M, and Rochat E. A Decade of Pipeline Geotechnical Monitoring Using Distributed Fiber Optic Monitoring Technology. In: ASME 2017 International Pipeline Geotechnical Conference, July 25–26, 2017, Lima, Peru. American Society of Mechanical Engineers Digital Collection (2017).
- Li H, Lai Y, Wang L, Yang X, Jiang N, Li L, et al. Review of the State of the Art: Interactions between a Buried Pipeline and Frozen Soil. *Cold regions Sci Technol* (2019) 157:171–86. doi:10.1016/j.coldregions.2018.10.014
- Palmer AC, and Williams PJ. Frost Heave and Pipeline Upheaval Buckling. *Can Geotech J* (2003) 40(5):1033–8. doi:10.1139/t03-044
- Oswell JM. Pipelines in Permafrost: Geotechnical Issues and Lessons 12010 R.M. Hardy Address, 63rd Canadian Geotechnical Conference. *Can Geotech J* (2011) 48(9):1412–31. doi:10.1139/t11-045
- Gomez F, Althoefer K, and Seneviratne LD (2003). Modeling of Ultrasound Sensor for Pipe Inspection. In 2003 IEEE International Conference on Robotics and Automation (Cat. No. 03CH37422), September 14–19, 2003, Taipei, Taiwan. IEEE, Vol. 2, pp. 2555–60.
- Ren L, Jiang T, Jia ZG, Li DS, Yuan CL, and Li HN. Pipeline Corrosion and Leakage Monitoring Based on the Distributed Optical Fiber Sensing Technology. *Measurement* (2018) 122:57–65. doi:10.1016/j.measurement.2018.03.018
- Ren L, Jiang T, Li DS, Zhang P, Li HN, and Song GB. A Method of Pipeline Corrosion Detection Based on Hoop-Strain Monitoring Technology. *Struct Control Health Monit* (2017) 24(6):e1931. doi:10.1002/stc.1931
- Jiang T, Ren L, Jia ZG, Li DS, and Li HN. Pipeline Internal Corrosion Monitoring Based on Distributed Strain Measurement Technique. *Struct Control Health Monit* (2017) 24(11):e2016. doi:10.1002/stc.2016
- Ravet F, Briffod F, and Niklès M. Extended Distance Fiber Optic Monitoring for Pipeline Leak and Ground Movement Detection. *Int Pipeline Conf* (2008) 48579:689–97. doi:10.1115/IPC2008-64521
- DuToit D, Ryan K, Rice J, Bay J, and Ravet F. Analysis of Strain Sensor Cable Models and Effective Deployments for Distributed Fiber Optical Geotechnical Monitoring System. In: ASME 2015 International Pipeline Geotechnical Conference, July 15–17, 2015, Bogota, Colombia. American Society of Mechanical Engineers Digital Collection (2015).
- Borda C, Niklès M, Rochat E, Grechanov A, Naumov A, and Velikodnev V. Continuous Real-Time Pipeline Deformation, 3D Positioning and Ground Movement Monitoring along the Sakhalin-Khabarovsk-Vladivostok Pipeline. In: International Pipeline Conference, September 24–28, 2012, Calgary, Alberta, Canada. American Society of Mechanical Engineers (ASME) (2012), 45134. p. 179–87. doi:10.1115/IPC2012-90476
- Zhang S, Liu B, and He J. Pipeline Deformation Monitoring Using Distributed Fiber Optical Sensor. *Measurement* (2019) 133:208–13. doi:10.1016/j.measurement.2018.10.021
- Bos J, Klein J, Froggatt M, Sanborn E, and Gifford D. Fiber Optic Strain, Temperature and Shape Sensing via OFDR for Ground, Air and Space Applications. In: Nanophotonics and Macrophotonics for Space Environments VII. International Society for Optics and Photonics (2013), 2013, San Diego, CA, 8876. p. 887614. doi:10.1117/12.2025711

15. Froggatt M, and Moore J. High-spatial-resolution Distributed Strain Measurement in Optical Fiber with Rayleigh Scatter. *Appl Opt* (1998) 37(10):1735–40. doi:10.1364/AO.37.001735
16. Froggatt M, Soller B, Gifford D, and Wolfe M. Correlation and Keying of Rayleigh Scatter for Loss and Temperature Sensing in Parallel Optical Networks. In: Optical Fiber Communication Conference, February 22, 2004, Los Angeles, CA. Optical Society of America (2004). p. PD17.
17. Soller BJ, Wolfe M, and Froggatt ME. Polarization Resolved Measurement of Rayleigh Backscatter in Fiber-Optic Components. In: National Fiber Optic Engineers Conference, March 6, 2005, Anaheim, CA. Optical Society of America (2005). p. NWD3.
18. Kreger ST, Rahim NAA, Garg N, Klute SM, Metrey DR, Beaty N, et al. Optical Frequency Domain Reflectometry: Principles and Applications in Fiber Optic Sensing. In: Fiber Optic Sensors and Applications XIII, 2016, Baltimore, MD. International Society for Optics and Photonics (2016), 9852. p. 98520T.
19. Galloway KC, Chen Y, Templeton E, Rife B, Godage IS, and Barth EJ. Fiber Optic Shape Sensing for Soft Robotics. *Soft robotics* (2019) 6(5):671–84. doi:10.1089/soro.2018.0131
20. Li W, Chen L, and Bao X. Compensation of Temperature and Strain Coefficients Due to Local Birefringence Using Optical Frequency Domain Reflectometry. *Opt Commun* (2013) 311:26–32. doi:10.1016/j.optcom.2013.08.022
21. Yi J, Zhu X, Zhang H, Shen L, and Qiao X. Spatial Shape Reconstruction Using Orthogonal Fiber Bragg Grating Sensor Array. *Mechatronics* (2012) 22(6): 679–87. doi:10.1016/j.mechatronics.2011.10.005

Conflict of Interest: The authors declare that the research was conducted in the absence of any commercial or financial relationships that could be construed as a potential conflict of interest.

Copyright © 2021 Jiang, Zhu and Shi. This is an open-access article distributed under the terms of the Creative Commons Attribution License (CC BY). The use, distribution or reproduction in other forums is permitted, provided the original author(s) and the copyright owner(s) are credited and that the original publication in this journal is cited, in accordance with accepted academic practice. No use, distribution or reproduction is permitted which does not comply with these terms.



Optimal Design of Negative Stiffness Devices for Highway Bridges Using Performance-Based Genetic Algorithm

Sun Tong¹, Zhu Tianqi¹, Sun Li¹ and Zhang Hao^{1,2*}

¹School of Civil Engineering, Shenyang Jianzhu University, Shenyang, China, ²Guangdong Key Laboratory of Earthquake Engineering and Application Technology, Guangzhou University, Guangzhou, China

OPEN ACCESS

Edited by:

Chun-Xu Qu,
Dalian University of Technology, China

Reviewed by:

Yanan Li,
CITIC Construction, China
Yabin Liang,
Institute of Seismology, China
Earthquake Administration, China

*Correspondence:

Zhang Hao
h_zhang@sjzu.edu.cn

Specialty section:

This article was submitted to
Interdisciplinary Physics,
a section of the journal
Frontiers in Physics

Received: 20 April 2021

Accepted: 10 May 2021

Published: 28 May 2021

Citation:

Tong S, Tianqi Z, Li S and Hao Z (2021)
Optimal Design of Negative Stiffness
Devices for Highway Bridges Using
Performance-Based
Genetic Algorithm.
Front. Phys. 9:697698.
doi: 10.3389/fphy.2021.697698

Parameter optimization analysis on the negative stiffness device (NSD) installed in the benchmark highway bridge is carried out in this study. Key parameters and constrain conditions are determined in accordance with the characteristics of NSD, and an objective function is designed with safety and comfort being considered. Individual fitness value-related cross and mutation operators are designed to protect excellent chromosome and improve the efficiency and convergence of computation. The genetic algorithm is used to realize parameter optimization of the NSD used in a benchmark highway bridge. Dynamic responses of structure without NSD, with random NSD, and with optimal designed NSD are compared. By analyzing the time history of displacement and acceleration, it can be concluded that dynamic responses of the structure decrease obviously when the NSD is added, and a better seismic reduction effect can be reached when the NSD is designed optimally in accordance with the optimization method and different earthquake excitations have slight influence on the optimization results.

Keywords: optimal design, NSD, genetic algorithm, benchmark model, optimization analysis

INTRODUCTION

The conventional way to reduce the structural deformation and internal shear force under severe ground motions is to design the structure with high stiffness. Larger stiffness can resist more external force, while inter-story shear force would be increased with the increasing of stiffness [1, 2]. To address this problem, Reinhorn et al. [3] and Viti et al. [4] proposed the concept of structural weakening, which can cause the reduction of internal shear force or accelerations. The concept of apparent weakening is proposed by Nagarajaiah et al. [5] along with a negative stiffness device (NSD) which can simulate the structural yielding without inducing the structural real inelastic behavior. Nowadays, negative stiffness device is given considerable attention by engineers and researchers among many structural control strategies [6–8]. Yet, most of the related research of negative stiffness control is qualitative concept verification.

Optimization strategy of a rail-type NSD [9] in a benchmark highway bridge under seismic excitation was investigated in this study. A two-step optimal design method is proposed. The first step is to analyze the device and find out the factors that are determining mechanical properties of the device. The amplitude of the curve function A and frequency ω are chosen as the damper design parameters. The arrangement of dampers was determined by a comparison method [10]. Numerical

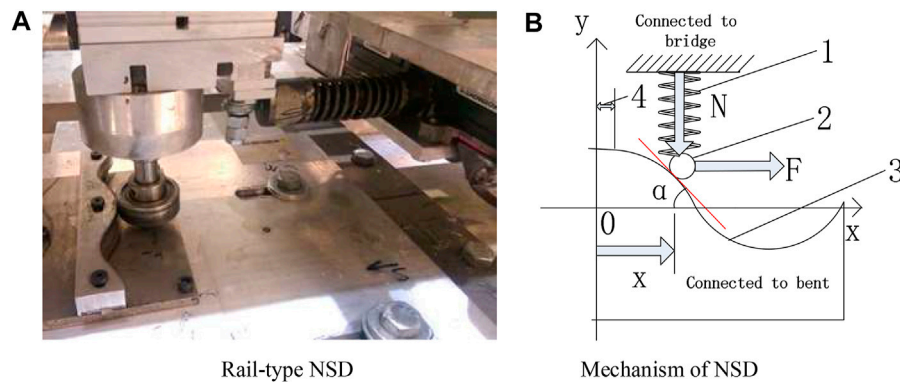


FIGURE 1 | Basic mechanism of the NSD. **(A)** Rail-type NSD and **(B)** Mechanism of NSD.

example is used to verify the proposed method for optimal device placement and to demonstrate the effectiveness of an optimally applied control system.

MODEL OF CONTROLLED STRUCTURE

The open-loop model of an n degree-of-freedom seismic response-controlled structure under earthquake excitation can be described as follows:

$$M\ddot{X}(t) + C\dot{X}(t) + KX(t) + HU(t) = -MI\ddot{x}_g(t), \quad (1)$$

where M , C , and K are $n \times n$ dimensional mass, damping, and stiffness constant matrices of the controlled building, respectively; $X(t)$ is the n dimensional relative displacement vector with respect to the ground; H is the location matrix of control devices; $U(t)$ is control force vector; $\ddot{x}_g(t)$ is the earthquake ground acceleration; and I is n dimensional unit vector.

MODEL OF NEGATIVE STIFFNESS DEVICE

As shown in **Figures 1A,B**, the rail-type negative stiffness device developed in this work is composed of a roller pushed by a pre-compressed spring as well a curved template that the wheel can roll on. There is a flat gap on the curve around equilibrium, so that the stiffness of the combination of NSD and isolation system will be the same as that of the original isolation system only. When the roller goes beyond the gap, the pre-compressed spring 1) and the slope 3) will generate a force F in the same direction as the imposed displacement, thus the composite system appears to yield or soften, that is, apparent yielding. The negative force F is given by the following equation:

$$F = k \cdot [\Delta L + f(x) - f(x_0)] \cdot \frac{f'(x)}{1 + (f'(x))^2} - \text{sgn}(\dot{x})\mu N \cos^2 \alpha, \quad (2)$$

in which k is the stiffness of pre-compressed spring, ΔL is compression length of the spring, and $f(x)$ is curve function of the

template. x_0 is initial position coordinates of the roller, μ is the friction coefficient between the roller and the curve block, N is the pre-compression force of the spring, and α is the angle between tangent line at touch contact point and x axis.

OPTIMIZATION DESIGN OF GENETIC ALGORITHM

Optimization Parameters

According to the mechanical model of the device [11], the key parameters that affect the mechanical property of the NSD device are: 1) stiffness of the compressed spring k , 2) compression length of the spring, and 3) the curve function of the template $f(x)$. The first two factors mainly affect the spring pressure, which has little optimization potential due to the insufficient spring force. The two key parameters in the track curve function, amplitude A and frequency ω , representing the track fluctuation degree and slope, respectively, play a decisive role in the force-displacement curve of the device.

The friction component in **Eq. 2** is $F_f = \text{sgn}(\dot{x})\mu N \cos^2 \alpha$. The material of the device is steel, the friction coefficient μ is small, and the cosine square further reduces the friction value, so the friction has a relatively small impact on the output force of NSD. Considering the optimization efficiency of the algorithm, the influence of friction is ignored.

The curve function of the original NSD is given by the following equation (the length unit is meter):

$$f(x) = \begin{cases} 0.3 \cdot \cos\left[\frac{2\pi}{3}(x + 0.05)\right] & x \leq -0.05 \\ 0.3 & -0.05 \leq x \leq 0.05 \\ 0.3 \cdot \cos\left[\frac{2\pi}{3}(x - 0.05)\right] & 0.05 \leq x \end{cases} \quad (3)$$

Since the negative force of the NSD is controlled by amplitude A and frequency ω , they are set as the optimization parameters [12]. A 0.05 m flat gap is set on the template around equilibrium. The device will not generate negative stiffness force when the displacement is within this range, so that the controlled structure

will maintain the original stiffness when the displacement is small and avoid the amplification of small excitation disturbance. The length of flat gap only needs to be selected properly to achieve the design purpose, so the original value remains unchanged.

Objective Functions

Safety and comfort are two key indexes of structural vibration control, which is governed by displacement response and acceleration response, respectively [13]. According to the characteristics of negative stiffness control, the following objective function is proposed:

$$Z = 0.5 \frac{a_{\max}}{a_0} + 0.5 \frac{x_{\max}}{x_0}, \quad (4)$$

where a_{\max} and a_0 are the optimized peak acceleration of the NSD control structure and the initial peak acceleration of the NSD control structure. Similarly, x_{\max} and x_0 are the maximum displacement of the structure controlled by optimized NSD and the initial NSD. The objective function Z is composed of two items: the first item is $0.5 \frac{a_{\max}}{a_0}$, which reflects the control effect of the negative stiffness system on the acceleration under the action of earthquake, and is considered for comfort; the second item is $0.5 \frac{x_{\max}}{x_0}$, which reflects the control effect of the negative stiffness system on the displacement of the structure, and is for safety concern. The coefficient is taken as 0.5 to balance the control effect on acceleration and displacement and best seismic performance is achieved [14].

Selection Operator

Selection operation is to select genes with better adaptability according to the idea of survival of the fittest and the results of individual fitness evaluation [15, 16]. The idea is to give preference to the individuals with good fitness scores and allow them to pass their genes to the successive generations. Selection operation can improve global convergence, computational efficiency, and avoid gene deletion. Considering the population size and convergence demand, the roulette method [17] is used as the selection operator:

$$p_i = \frac{f_i}{\sum_{i=1}^n f_i}, \quad (5)$$

where p_i is the probability of the i th individual being selected and f_i is the fitness value of the i th individual.

Crossover Operator and Mutation Operator

Crossover plays a key role in obtaining new excellent individuals by genetic algorithm [18]. Before the crossover operation, the individuals in the population need to be paired. The common way is random pairing. The design of crossover operator not only needs to keep the existing excellent genes but also can produce better individuals. In this research, two point crossover is adopted, that is, two points are randomly set in the code of the parent gene to exchange the first and last segments of the gene.

Mutation is to change one or some bit values of an individual gene with a small probability and then generate a new individual. Mutation itself is a kind of random algorithm, and its local search ability can accelerate the evolution of individuals to the optimal solution [19]. Mutation can avoid the loss of some information caused by selection and crossover operation and maintain the diversity in population to avoid the premature convergence.

The crossover operator and mutation operator cooperate with each other to complete the global search and local search of the search space, so that the genetic algorithm can complete the optimization process of the optimal problem with good search performance. However, randomness can accelerate the local convergence, and it may also destroy the current excellent individuals, which is not conducive to the convergence of the algorithm. In order to protect excellent chromosome and improve the efficiency and convergence of computation, the probability of cross and mutation is set as a function of individual fitness scores, which is given by Eq. 6 and Eq 7:

$$P_{ci}(i) = p_1 \left(1 - \sqrt{1 - \left(1 - \frac{f_i}{\sum_{i=1}^n f_i} \right)} \right), \quad (6)$$

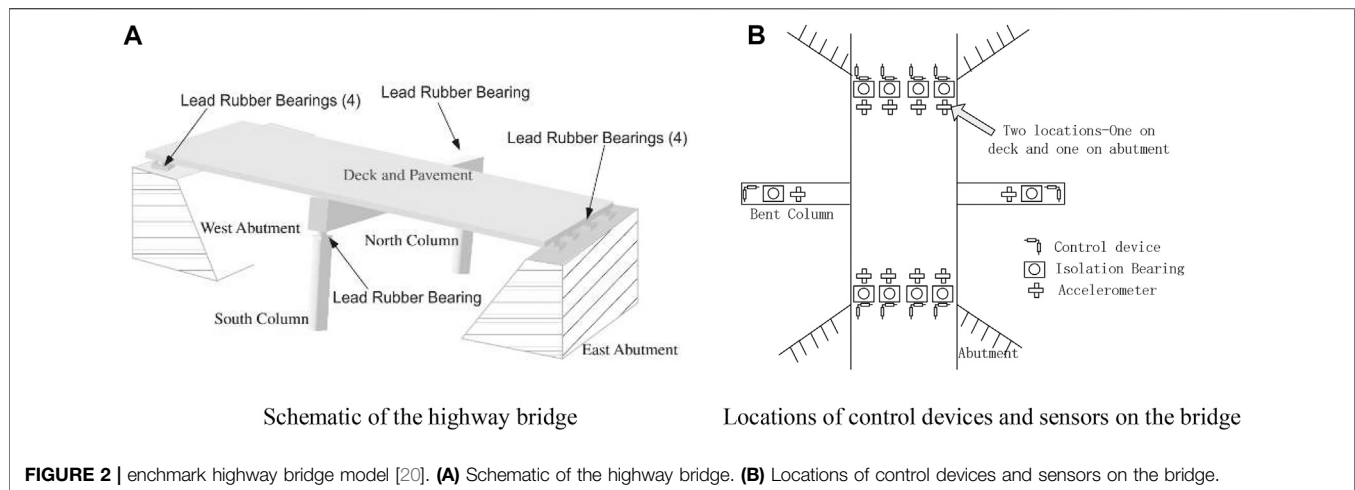
$$P_{mi}(i) = p_2 \left(1 - \sqrt{1 - \left(1 - \frac{f_i}{\sum_{i=1}^n f_i} \right)^2} \right), \quad (7)$$

where $P_{ci}(i)$ and $P_{mi}(i)$ represent the probability of crossover and mutation of the i th individual, respectively; p_1 and p_2 are the presupposed probability of crossover operation and mutation operation of the i th individual, respectively; f_i is the fitness value of the i th individual.

Numerical Simulation and Result Analysis

The numerical analysis on a benchmark highway bridge [20] is carried out to verify the effectiveness of the proposed optimization method. The bridge model used for the benchmark study is based on the 91/5 highway bridge in Southern California, as shown in Figure 2A. The locations of control devices and sensors on the bridge are shown in Figure 2B. The superstructure of the bridge consists of a two-span, cast-in-place, prestressed concrete (PC) box girder, and the substructure is in the form of PC outriggers. Each span of the bridge is 58.5 m long, spanning a four-lane highway, with two abutments skewed at 33°. The width of the deck is 12.95 m along the east direction and 15 m along the west direction. The deck is supported by a 31.4-m-long and 6.9-m-high prestressed concrete outrigger, resting on two pile groups. The total mass of the benchmark highway bridge is 4,237,544 kg, and the mass of the deck is 3,278,404 kg.

A finite element model (FEM) is developed to study the structural dynamic characteristics of the highway bridge. The first six natural frequencies [21, 22] of vibration of the FEM are shown in Table 1.

**TABLE 1 |** Natural Frequencies of the highway bridge.

Mode no	Frequency	Mode
1	1.23	Torsional
2	1.28	Torsional + Vertical
3	1.55	Vertical
4	1.69	Transverse
5	1.77	2nd vertical
6	3.26	2nd transverse

The peak value of displacement and acceleration of the structure from the time history analysis of the benchmark model [23] are taken as the key parameters of the objective function value to evaluate the optimization effect. Meanwhile, they are the basis of calculating individual fitness, and the fitness function is given by the following formula:

$$f(i) = \frac{1}{|x_{\max}|} + \frac{1}{|a_{\max}|}, \quad (8)$$

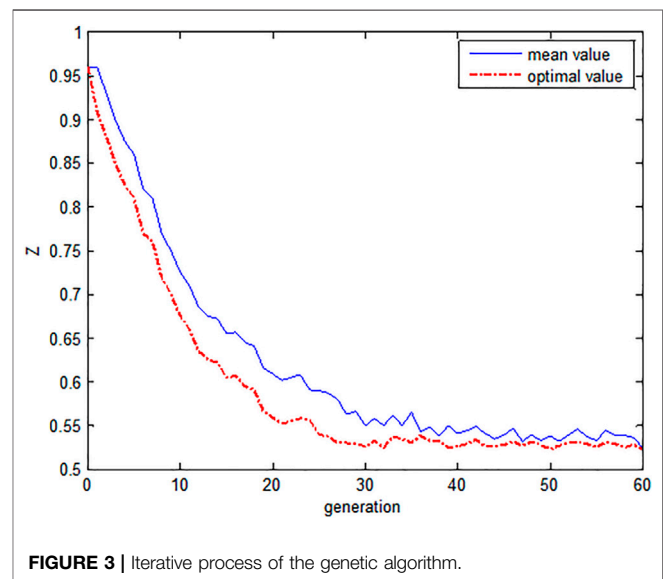
where x_{\max} and a_{\max} are the peak response of structural displacement and acceleration, respectively. The sum of the reciprocal absolute values of the two is taken as the fitness for safety and comfort concern. NSD is arranged in two directions. The benchmark program is modified and embedded into the main program of genetic algorithm.

Given the nonlinear characteristics of the controlled structure, the most unfavorable seismic record is selected as the seismic excitation: El Centro and NPalmSpr. The peak acceleration is set as 400 gal.

Genetic algorithm is designed as follows: the initial population size is 20, the evolution algebra is 20, the binary length is 20, the generation gap is 0.9, the probability of cross operation is 0.7, the probability of variation operation is 0.1, the selection operator adopts the roulette method, the cross operator adopts a two-point crossing mode, the variation operator adopts a discrete type, and embeds the benchmark program into the main program of

TABLE 2 | Optimization parameters.

Parameters	Value
Amplitude A/m	0.5124
Frequency ω	2.3866



genetic algorithm. For the rail-type negative stiffness device, the optimization results are shown in **Table 2**.

The iterative process of genetic algorithm is shown in **Figure 3**. It can be seen that the stable decline of function value from the tenth generation to the 29th generation is the process of outstanding genes emerging; after the 30th generation, the function value tends to be stable, which indicates that the genetic algorithm has very good convergence.

The control effects of three different control strategies are studied: isolation (Iso), original NSD, and optimized NSD with

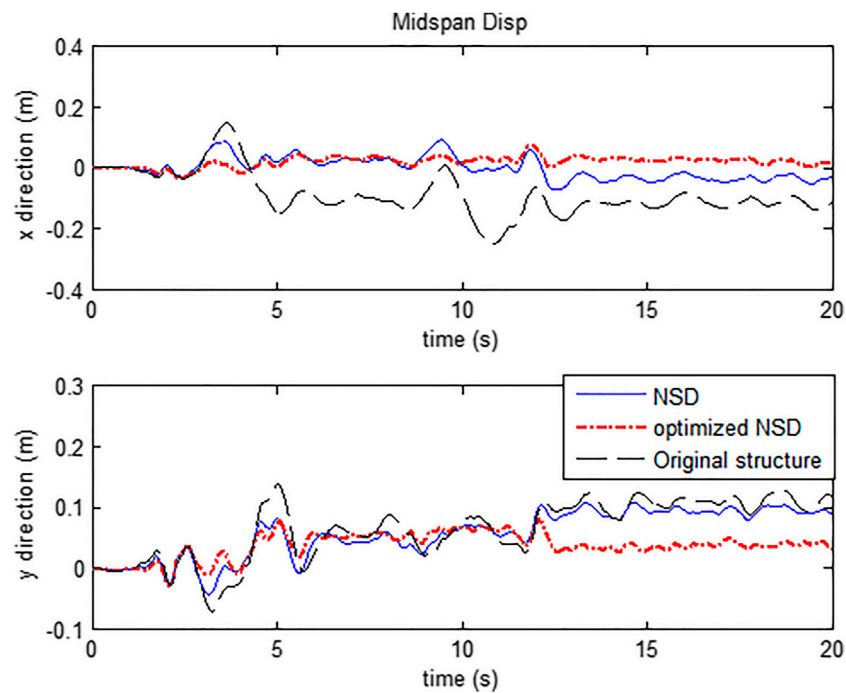


FIGURE 4 | Time history of displacement responses at mid-span under El Centro earthquake.

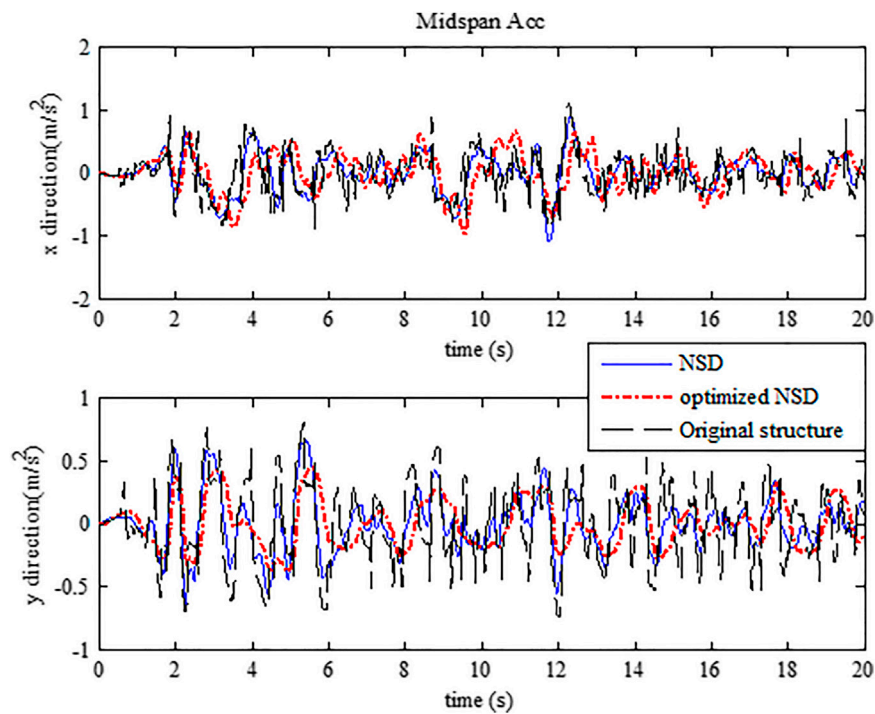


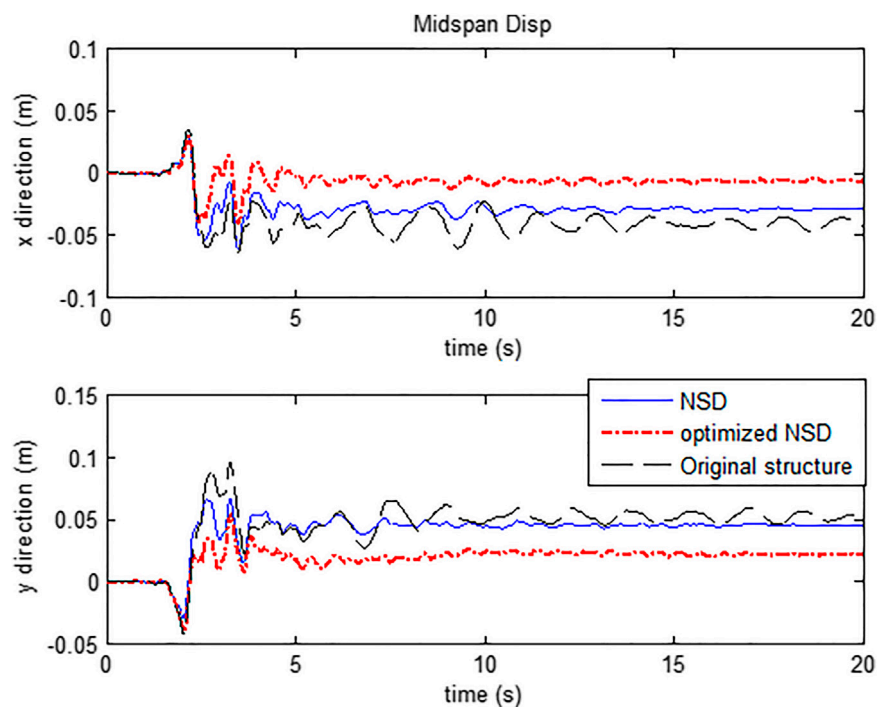
FIGURE 5 | Time history of acceleration responses at mid-span under El Centro earthquake.

TABLE 3 | Peak acceleration and displacement at mid-span (El Centro).

Earthquake	Control case	Value	Reduction rate
Acceleration (m/s^2)	Iso	1.127	-
	NSD	1.091	3.1%
	Optimized NSD	0.958	14.9%
Displacement (m)	Iso	0.251	-
	NSD	0.108	56.9%
	Optimized NSD	0.080	69.1%

Through optimization, the peak value of seismic displacement of the structure is greatly reduced, and the safety of the structure is improved; after the earthquake, the structure has smaller residual deformation, which can ensure the economy.

Table 3 shows the peak displacement and acceleration response of the benchmark model under the El Centro wave excitation under three working conditions: isolation (Iso), original NSD, and optimized NSD. The reduction rate of displacement in **Table 3** is defined as the ratio of the

**FIGURE 6** | Time history of displacement responses at mid-span under NPalmSpr earthquake.

the simulation duration of 20s. **Figures 4,5** show comparisons of the time history of displacement and acceleration at mid-span with different control strategies under 400 gal El Centro earthquake excitations, respectively. It can be seen from **Figure 4** that the peak displacement response of the structure with NSD is smaller than that of the isolated structure. Peak response is reduced from 0.251 to 0.108 m by the decrease of 56.9%. After optimization, the peak displacement is further reduced to 0.080 m by the decrease of 69.1%. The same phenomenon can be also seen in **Figure 5**; when NSD is applied, the maximum acceleration response is reduced from 1.127 m/s^2 to 1.091 m/s^2 by the decrease of 3.1%. The peak response after optimization is 12.2% lower than that of NSD before optimization. It can be seen from the figure that the displacement time history curve (dotted line) after optimization is wrapped with the displacement time history curve (solid line) before optimization, indicating that the control effect has been comprehensively improved.

difference between the displacement response before and after optimization and the displacement response before optimization. The reduction rate of acceleration is the same in which, the response value before optimization is taken from the relevant literature [24]. As shown in the table, peak displacement and acceleration response are effectively reduced when NSD is applied. Moreover, the optimal designed NSD can further improve the seismic performance of the benchmark highway bridge.

To determine the suitability of the proposed optimization method, the sensitivity of the objective function to earthquake excitations is studied. Take NPalmSpr earthquake for example, comparison of displacement and acceleration time history under different control cases are shown in **Figure 6** and **Figure 7**, respectively. It can be seen from **Figure 6** that displacement response in both x and y directions are significantly reduced when NSD is applied, and they are further mitigated when the NSD is optimal designed. The same phenomenon can be also seen in **Figure 7**; the acceleration time history of optimized NSD is

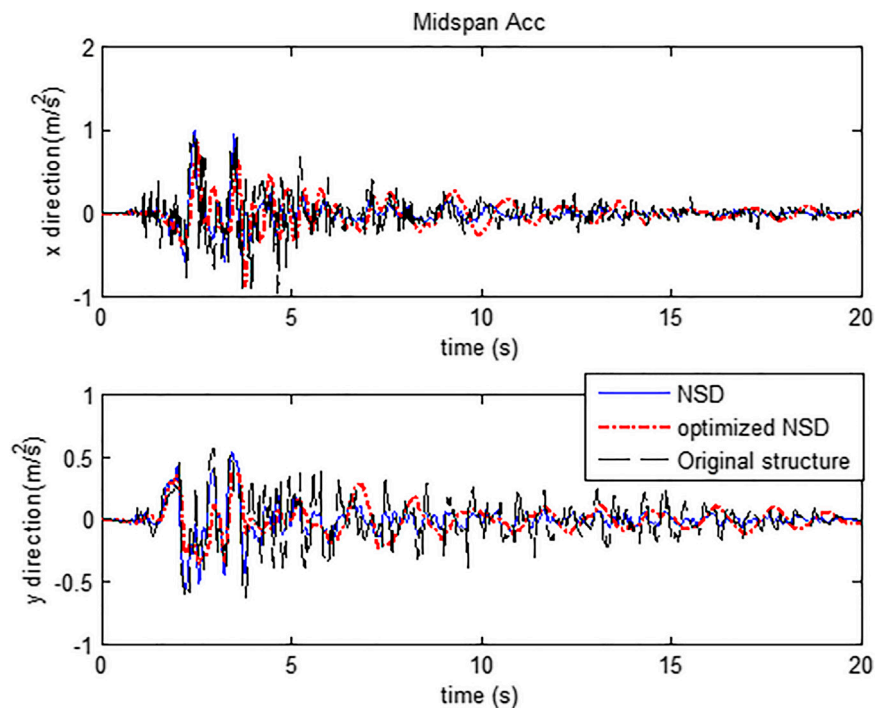


FIGURE 7 | Time history of acceleration responses at mid-span under NPalmspr earthquake.

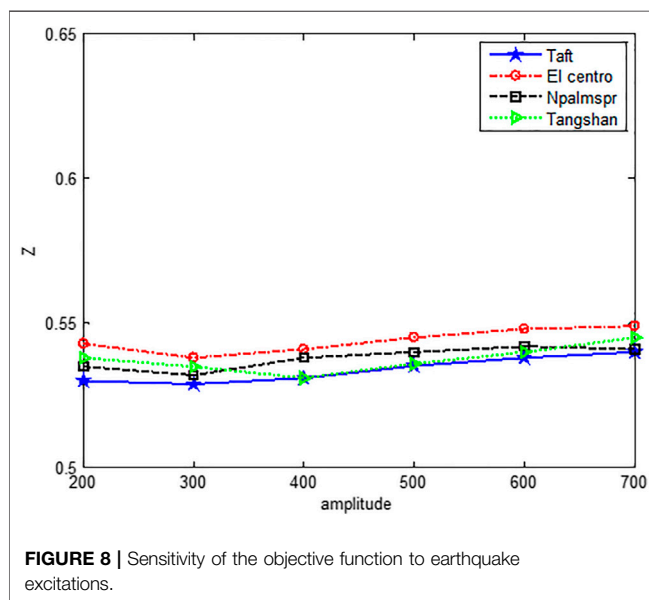


FIGURE 8 | Sensitivity of the objective function to earthquake excitations.

wrapped by that of NSD and both of them are wrapped by the curve of original structure. The analysis above indicates that the seismic response of the highway bridge can be effectively reduced when NSD is optimal designed.

The values of the objective function under earthquake excitations with different amplitude and spectrum characteristics are shown in **Figure 8**. It can be seen that the

objective function value is relatively stable under amplitude from 200 gal to 700 gal. Moreover, the value of objective function also changes slightly when different excitation is applied. In all cases, the value of objective function fluctuates within a range of 0.529–0.549. It can be drawn that the proposed objective function can be used for optimizing NSD added in the benchmark highway bridge under different earthquake excitations.

CONCLUSION

In this article, parametric optimization analysis on the NSD added in the benchmark highway bridge is carried out. Optimization parameters and constrain conditions are determined in accordance with characteristics of the NSD. Considering safety and comfort, objective function is proposed. Individual fitness value-related cross and mutation operators are designed to protect excellent chromosomes and improve the efficiency and convergence of computation. Then the genetic algorithm is used to realize parameter optimization of the NSD used in the benchmark highway bridge. The following conclusions can be obtained from analysis:

- (1) Both displacement and acceleration response of the benchmark highway bridge are effectively reduced when NSD is applied.
- (2) Optimization of the parameter of NSD can further improve the seismic performance of the benchmark highway bridge.

- (3) The optimization results tend to be consistent under different earthquake excitations which indicates that the optimization strategy has good robustness

DATA AVAILABILITY STATEMENT

The raw data supporting the conclusion of this article will be made available by the authors, without undue reservation.

AUTHOR CONTRIBUTIONS

Conceptualization, ST and ZH. Methodology, ST and SL. Software, ZT. Formal analysis, ZT. Data curation, ST.

REFERENCES

- Mashhadi J, and Saffari H. Effects of Postelastic Stiffness Ratio on Dynamic Increase Factor in Progressive Collapse[J]. *J Perform Constructed Facil* (2017) 31(6):04017107. doi:10.1061/(asce)cf.1943-5509.0001109
- Zhang C. Control Force Characteristics of Different Control Strategies for the Wind-Excited 76-story Benchmark Building Structure. *Adv Struct Eng* (2014) 17(4):543–59. doi:10.1260/1369-4332.17.4.543
- Pasala DTR, Sarlis AAS, and Reinhorn AM. A New Structural Modification Approach for Seismic Protection Using Adaptive Negative Stiffness Device. *SEI Struct Congress* (2011) 2892–904. doi:10.1061/41171(401)251
- Reinhorn AM, Viti S, and Cimellaro GP. Retrofit of Structures: Strength Reduction with Damping Enhancement. In: Proceedings of the 37th Joint Meeting of U.S.-Japan Panel on Wind and Seismic Effects; 2005 May 16–18; Tsukuba, Japan. . UJNR (2005). p. 16–21.
- Pasala DTR, Sarlis AA, Nagarajaiah S, Reinhorn AM, Constantinou MC, and Taylor D. Adaptive Negative Stiffness: New Structural Modification Approach for Seismic Protection. *J Struct Eng* (2013) 139(7):1112–23. doi:10.1061/(asce)st.1943-541x.0000615
- Qu CX, Li* HN, Huo LS, and Yi TH. Optimum Value of Negative Stiffness and Additional Damping in the Civil Structures. *ASCE J Struct Eng* (2017) 143(8): 04017068. doi:10.1061/(asce)st.1943-541x.0001805
- Sarlis AA, Pasala DTR, Constantinou MC, Reinhorn AM, Nagarajaiah S, and Taylor DP. Negative Stiffness Device for Seismic Protection of Structures: Shake Table Testing of a Seismically Isolated Structure[J]. *J Struct Engineering* (2016) 142(5):1124–33.
- Saha A, and Mishra SK. Adaptive Negative Stiffness Device Based Nonconventional Tuned Mass Damper for Seismic Vibration Control of Tall Buildings. *Soil Dyn Earthquake Eng* (2019) 126:57–67. doi:10.1016/j.soildyn.2019.105767
- Li HN, and Sun T. Optimal Design for Rail-type Negative Stiffness Control System. *Earthquake Eng Eng Vibration* (2018) 38(1):21–7. doi:10.13197/j.eeev.2018.01.21.lihn.003
- Jin B, Li ZY, and Zhou W. Optimal Analysis on Location and Quantity of Dampers Based on Improved Genetic Algorithm. *J Hunan Univ (Natural Sciences)* (2019) 46(11):114–21. doi:10.16339/j.cnki.hdxzbk.2019.11.013
- Sun T, Li HN, and Lai ZL. Study on Structural Vibration Control Using Curved-Based Negative Stiffness Device. *J Vibration Eng* (2017) 30(03):449–56.
- Zhang Y, Xue SL, and Chang J. Parameter Optimization and Application of Vibration Damping Device Based on Negative Stiffness. *Earthquake Eng Eng Dyn* (2018) 38(02):201–9. doi:10.13197/j.eeev.2018.02.201.zhangy.023
- Suresh L, and Mini KM. Effect of Multiple Tuned Mass Dampers for Vibration Control in High-Rise Buildings. *Pract Period Struct Des Constr* (2019) 24(4): 04019031. doi:10.1061/(asce)sc.1943-5576.0000453
- Izard AG, Alfonso RF, Mcknight G, and Valdevit L. Optimal Design of a Cellular Material Encompassing Negative Stiffness Elements for Unique Combinations of Stiffness and Elastic Hysteresis[J]. *Mater Design* (2017) 135:37–50. doi:10.1016/j.matdes.2017.09.001
- Mirowslaw K, Jan B, and Marcin B. Optimization of Warehouse Operations with Genetic Algorithms. *Appl Sci* (2020) 10:4817. doi:10.3390/app10144817
- Sakalli US, and Atabas I. Ant Colony Optimization and Genetic Algorithm for Fuzzy Stochastic Production-Distribution Planning. *Appl Sci* (2018) 8:2042. doi:10.3390/app8112042
- Wei B, Yu F, and Xu X. Interactive Evolutionary Algorithm Based on Improved Roulette Wheel Selection Strategy. *Comput Digital Eng* (2014) 42:1763–834. doi:10.15961/j.jsuese.2016.02.019
- Liu WG, Yu XX, and Xu H. Seismic Response of High-Rise Isolated Building Based on Negative Stiffness Device with Damping. *J Building Structures* (2020) 41(07):36–44. doi:10.14006/j.jzjgxb.2018.0171
- Zhang X. Application of Genetic Algorithm in Computer Network Optimization Design. *Digital Technol Appl* (2020) 38(6):105–6. doi:10.19695/j.cnki.cn12-1369.2020.06.47
- Nagarajaiah S, and Narasimhan S. Smart Base-Isolated Benchmark Building. Part II: Phase I Sample Controllers for Linear Isolation Systems[J]. *Struct Control Health Monit* (2010) 13(2–3):589–604. doi:10.1002/stc.100
- Qu C-X, Yi* T-H, Zhou Y-Z, Li H-N, and Zhang Y-F. Frequency Identification of Practical Bridges through Higher Order Spectrum. *ASCE J Aerospace Eng* (2018) 31(3):04018018. doi:10.1061/(asce)as.1943-5525.0000840
- Qu C-X, Yi* T-H, Yi H-N, and Chen B. Closely Spaced Modes Identification through Modified Frequency Domain Decomposition. *Measurement* (2018) 128:388–92. doi:10.1016/j.measurement.2018.07.006
- Nagarajaiah S, and Narasimhan S. Smart Base Isolated Benchmark Building Part II: Phase I Sample. *J Struct Control* (2002) 00:1–6.
- An ZY, Niu YF, and Zhang QK. Seismic Response Comparison and Parameter Study of Different Bearing Systems for Long-Span Continuous Girder Bridges. *Technology Highw Transport* (2020) 36(02):63–9. doi:10.13607/j.cnki.gljt.2020.02.010

Writing—original draft preparation, ST and HZ. Project administration, ST. Funding acquisition, ST. All authors have read and agreed to the published version of the manuscript.

Some or all data, models, or code that support the findings of this study are available from the corresponding author upon reasonable request.

FUNDING

The authors are grateful for the financial support from the National Natural Science Foundation of China (51808355) and the China Postdoctoral Science Foundation (2019M651146).

Conflict of Interest: The authors declare that the research was conducted in the absence of any commercial or financial relationships that could be construed as a potential conflict of interest.

Copyright © 2021 Tong, Tianqi, Li and Hao. This is an open-access article distributed under the terms of the Creative Commons Attribution License (CC BY). The use, distribution or reproduction in other forums is permitted, provided the original author(s) and the copyright owner(s) are credited and that the original publication in this journal is cited, in accordance with accepted academic practice. No use, distribution or reproduction is permitted which does not comply with these terms.



Effect of Aftershocks on Seismic Fragilities of Single-Story Masonry Structures

Hao Zhang¹, Tong Sun^{1*}, Shi-Wei Hou^{1*}, Qing-Meng Gao¹ and Xi Li²

¹School of Civil Engineering, Shenyang Jianzhu University, Shenyang, China, ²Academy of Science and Technology, Shenyang Jianzhu University, Shenyang, China

OPEN ACCESS

Edited by:

Chun-Xu Qu,
Dalian University of Technology, China

Reviewed by:

Hu Cheng,
Jiangnan University, China
Yanan Li,
CITIC Construction, China

*Correspondence:

Tong Sun
tsun@sjzu.edu.cn
Shi-Wei Hou
hsw1375@126.com

Specialty section:

This article was submitted to
Interdisciplinary Physics,
a section of the journal
Frontiers in Physics

Received: 14 April 2021

Accepted: 10 May 2021

Published: 28 May 2021

Citation:

Zhang H, Sun T, Hou S-W, Gao Q-M
and Li X (2021) Effect of Aftershocks on
Seismic Fragilities of Single-Story
Masonry Structures.
Front. Phys. 9:695111.
doi: 10.3389/fphy.2021.695111

The effect of aftershocks on the fragility of single-story masonry structures is investigated using probabilistic seismic demand analysis. Finite element models of an unreinforced masonry (URM) structure and a confined masonry (CM) structure are established and their seismic response characteristics when subjected to mainshock, aftershock, and the mainshock-aftershock sequence are then comparatively investigated. The effects of aftershocks and the use of confining members on the seismic response are studied. Probabilistic seismic demand models of the structures are built, and fragility curves under various conditions are derived to investigate the effect of aftershocks on structural fragility. The maximum roof displacement and maximum inter-story drift ratio are lower in the confined masonry model than in the unreinforced masonry model; additionally, the probability of exceedance (PE) values of each damage limit state reduced, and those of the mainshock-damaged models subjected to aftershock significantly increase compared to those directly subjected to a same-intensity aftershock. The probability of severe damage or collapse compared with the mainshock-damaged CM model is greater than when each is subjected to a same intensity aftershock. The use of confining members benefits aftershock resistance and reduces the failure probability of the mainshock-damaged structure. The PE values significantly increase with the aftershock scaling factor δ . Therefore, the effect of aftershocks should be considered in the seismic design and analysis of masonry structures.

Keywords: masonry structure, aftershock, fragility, seismic performance, probabilistic seismic demand analysis

INTRODUCTION

Strong earthquakes are often accompanied by aftershocks, and large numbers of aftershocks have been recorded in multiple earthquakes [1–4]. In 1999, a magnitude 7.4 earthquake occurred in Izmit, Turkey, followed by a magnitude 5.9 aftershock within a month after the earthquake, resulting in the collapse of some mainshock-damaged structures that did not collapse during the mainshock [5]. In 2002, an earthquake of magnitude 5.4 hit Molize, Italy, and several RC frame structures with only minor damage from the mainshock were severely damaged by aftershocks [6]. An earthquake of magnitude 8.0 occurred in 2008 in Wenchuan, China, after which more than 28,000 aftershocks were recorded, several exceeding magnitude 5.0 [7]. A magnitude 9.0 earthquake hit Japan in 2011, and over 1,000 aftershock ground motions were recorded, including four aftershocks with magnitudes exceeding 7.0 [8]. In 2015, an earthquake of magnitude 7.8 in west-central Nepal caused enormous casualties and property loss in the region from the strong mainshock and multiple subsequent

aftershocks [9]. The mainshock may cause various degrees of plastic damage to structures, which can be further aggravated by aftershocks, along with an accordant change in the dynamic characteristics of the structures. The time interval between the occurrence of the mainshock and aftershocks is generally short; hence, unless repaired in time, mainshock-damaged structures may be severely damaged or even collapse under even a low-intensity aftershock [10–12]. In recent years, research on the effects of aftershocks on the seismic performance of structures has garnered great attention. Goda and Taylor [13] investigated the nonlinear response of structures under mainshock-aftershock sequences using single-degree-of-freedom (SDOF) systems, and their results revealed that aftershocks significantly affect the peak ductility demand of structures. Hosseinpour and Abdelnaby [14] studied the effects of various aspects of the mainshock and aftershocks, such as their input directions and vertical components, on the seismic performance of RC structures and showed that the input direction of aftershocks has a significant effect on the displacement demand of irregular structures. Wang et al. [15] investigated the seismic fragility of a continuous girder bridge subjected to a mainshock-aftershock sequence. It was concluded that the aftershock increases the seismic demand and failure probability of the structure and that a structure that reaches a moderate damage state after the mainshock is at the highest risk of damage when subjected to an aftershock. Zhang et al. [16] investigated the seismic fragility of concrete-filled steel tubular frame structures under earthquake sequences based on nonlinear seismic response analysis and probabilistic seismic demand analysis (PSDA); the results showed that the failure probabilities of structures in various damage limit states under earthquake sequences all increase compared to those subjected to mainshocks only. Salami et al. [17] investigated the seismic fragility of low-rise RC structures under mainshock-aftershock sequences using incremental dynamic analysis based on the OpenSees software platform. It was demonstrated that the probability of severe damage or the collapse of structures increases significantly if the aftershock effect was considered. Pang et al. [18] carried out nonlinear response analysis of a high concrete-face rockfill dam subjected to the selected as-recorded mainshock-aftershock sequences and investigated the effects of aftershocks on the seismic fragility of the dam, showing that aftershocks increase the probability of exceedance (PE) of various damage limit states of the dam. Zhao et al. [19] studied the influence of aftershocks on the seismic fragility of nuclear power plants, the results showed that aftershocks cause additional damage to the structure, leading to a significant increase in the PE values of different damage limit states. Han et al. [20] conducted seismic loss estimation of structures using RC frame buildings as a case study and the recorded mainshock-aftershock sequences as the ground motion input. It was concluded that aftershocks increase economic losses and casualties and, to some extent, structural repair costs. Nazari et al. [21] examined the effect of aftershocks on the seismic fragility of wood structures and suggested that their effect be reasonably considered in performance-based seismic design.

Masonry structures are extensively used in rural areas of China due to their low cost and simple construction. However, this type of structure has certain disadvantages such as large self-weight and low

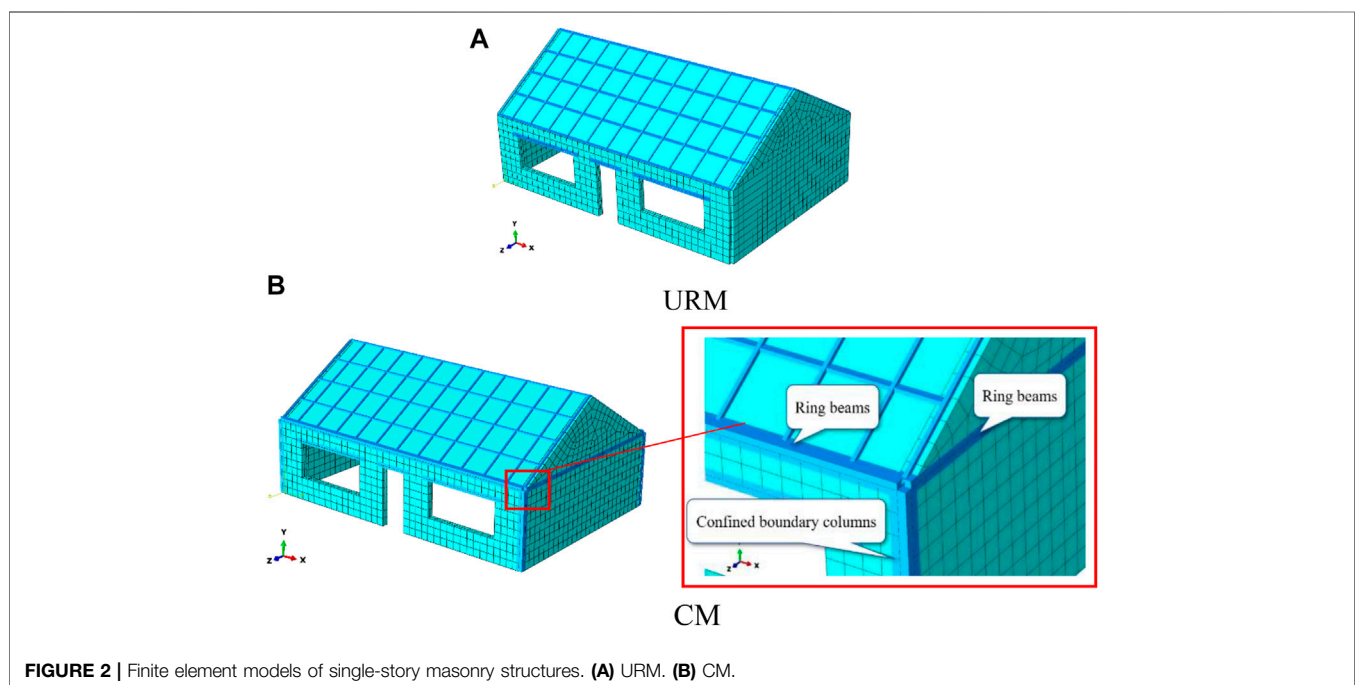
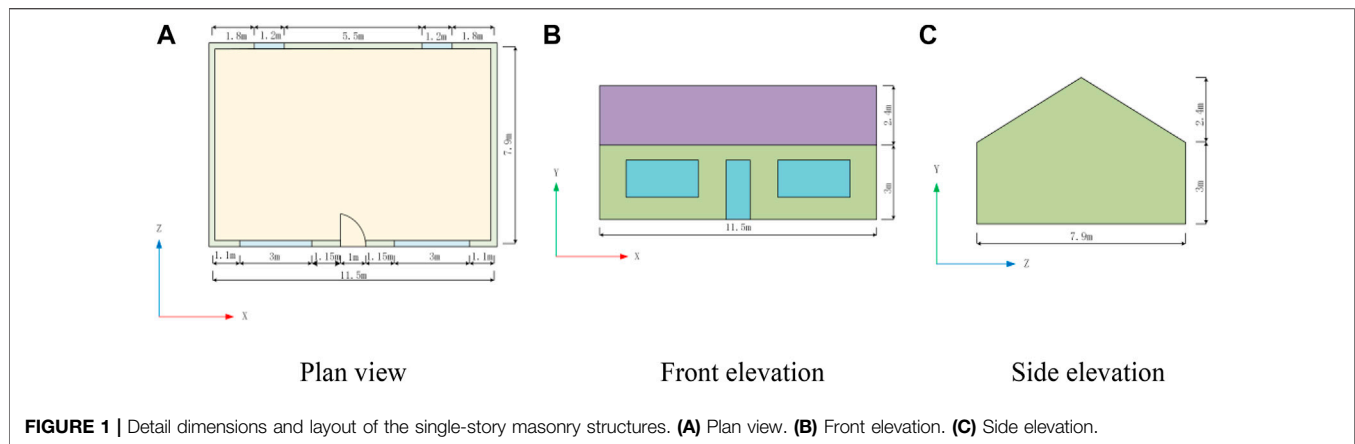
tensile and shear strengths of materials, etc. There is a lack of standard design and quality control procedures, leading to poor seismic performance of these structures [22], which are highly susceptible to severe damage or even collapse under strong earthquake shaking. Seismic experience data after the 2008 Wenchuan earthquake discovered that masonry structures suffered the most severe damage and accounted for the largest number of collapses, causing the largest property loss and number of casualties [23]. Bessason et al. [24] developed seismic fragility models for different types of structures using statistical methods and based on earthquake experience data. The results showed that the damage limit state probabilities of masonry structures are higher than those of RC and wood structures. Biglari and Formisano [25] established empirical fragility curves of masonry structures in Sarpol-e-zahab and Bam, Iran, using the RISK-UE level 1 method and based on damage data from post-earthquake reconnaissance in this region. Del Gaudio et al. [26] investigated the main parameters influencing structural damage and proposed a method for assessing the seismic fragility of masonry structures based on the post-earthquake structural damage data. Saloustros et al. [27] proposed a method for seismic fragility assessment considering the uncertainty in material parameters and used the method to study the seismic fragility of historical masonry structures.

Currently, most studies on masonry structures focus on quasistatic tests of their structural members or shaking-table tests and numerical simulation analyses that mostly consider single earthquake shaking [28–30]. As stated above, there is a relative lack of research on the fragility of masonry structures and their susceptibility to aftershocks, leaving room for improvement in the seismic design and seismic risk assessment methods of masonry structures. In particular, masonry structures in rural areas are typically not designed properly, and many self-built houses lack the necessary confining members, so these masonry structures have poor seismic performance. To address this problem, taking a typical single-story masonry structure of the rural areas of Northeast China as an example, the present study builds finite element models of unreinforced masonry (URM) structure and confined masonry (CM) structural models, investigates the seismic responses and fragility of masonry structures subjected to mainshock, aftershock and mainshock-aftershock sequence using nonlinear dynamic time history analysis and PSDA, and comparatively analyzes the effects of confining members such as ring beams and confined boundary columns on the seismic response and fragility of masonry structures. On this basis, the effect of aftershocks on the seismic response and fragility of mainshock-damaged masonry structures is investigated in depth, and the effects of confining members and the aftershock scaling factor are also examined.

THE DESCRIPTION OF STRUCTURAL MODELS

Finite Element Models of Masonry Structures

As shown in **Figure 1**, the single-story masonry structure studied herein has a plan dimension of 11.5×7.9 m, a story height of 3 m,



and a roof height of 5.4 m. The masonry wall is built with MU10 bricks and M2.5 mortar. It has a density of 2000 kg/m^3 , a Poisson's ratio of 0.15, and an elastic modulus of $1.827 \times 10^9 \text{ N/m}^2$. The ring beams and the confined boundary column are made of C20 concrete, which has a cubic compressive strength of 20 MPa, a density of $2,500 \text{ kg/m}^3$, and a Poisson's ratio of 0.2. The reinforcing bars in confining members are made of HPB300 steel, which has a yield strength of 300 MPa, a density of $7,800 \text{ kg/m}^3$, a Poisson's ratio of 0.3, and an elastic modulus of $2.1 \times 10^{11} \text{ N/m}^2$. Finite element models of URM and CM structures were established with ABAQUS software, as shown in **Figure 2**. Masonry walls were simulated by shell elements, and ring beams and confined columns were simulated by fiber beam elements. A modal analysis [31] was conducted to obtain the fundamental periods of the URM and CM models: $T_{\text{URM-1}} = 0.114 \text{ s}$ and $T_{\text{CM-1}} = 0.107 \text{ s}$.

Constitutive Model of Masonry Material Compressive Stress-Strain Relationship of Masonry Material

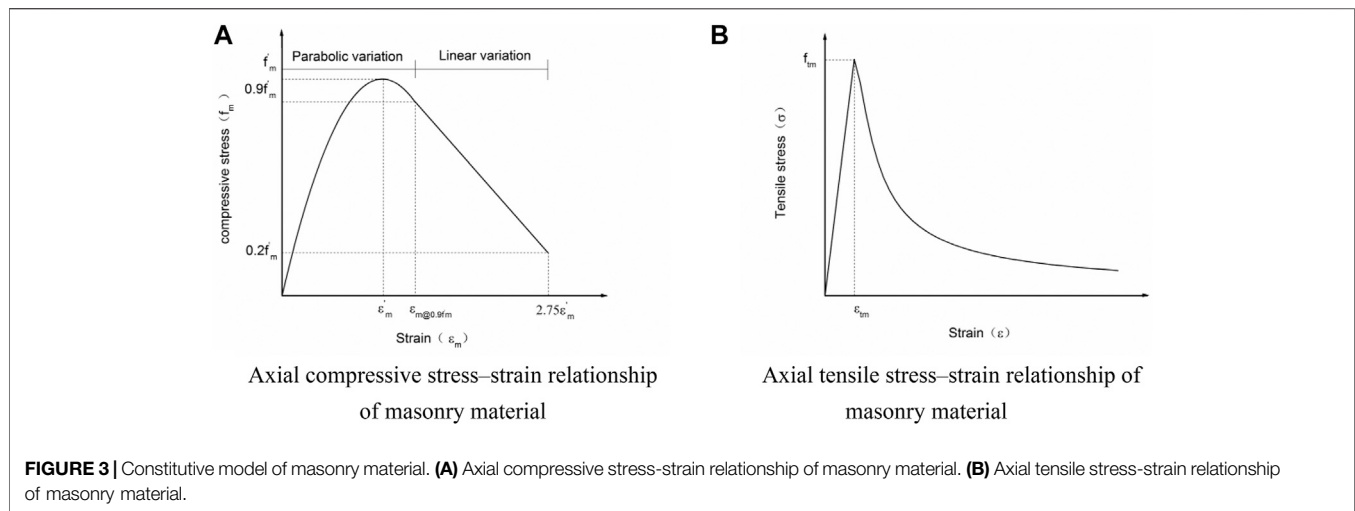
The compressive stress-strain relationship of masonry suggested in reference [32] was adopted in the present study, as shown in **Figure 3A**. The corresponding stress-strain curve includes a parabolic ascending branch and a linear descending branch. The ascending branch is expressed as follows:

$$\frac{\sigma_c}{f'_c} = 2 \frac{\epsilon_c}{\epsilon'_c} - \left(\frac{\epsilon_c}{\epsilon'_c} \right)^2 \quad (1)$$

$$f'_c = 0.63 f_b^{0.49} f_j^{0.32} \quad (2)$$

$$E_c \approx 550 f'_c \quad (3)$$

$$\epsilon'_c = C_j \frac{f'_c}{E_c^{0.7}} \quad (4)$$



$$C_j = \frac{0.27}{f_j^{0.25}} \quad (5)$$

Where σ_c is the compressive stress, ε_c is the compressive strain, f'_c is the peak compressive stress, ε'_c is the compressive strain corresponding to f'_c , f_b is the compressive strength of block, f_j is the compressive strength of mortar, and E_c is the elastic modulus of masonry. C_j is determined by the mortar strength. The linear descending branch is determined by the points $\{\varepsilon_{c@0.9f'_c}, 0.9f'_c\}$ and $\{2.75\varepsilon'_c, 0.2f'_c\}$.

Tensile Stress-Strain Relationship of Masonry Material

The tensile stress-strain curve of masonry is similar to that of concrete, except that masonry has a lower tensile strength. In the present study, the tensile stress-strain curve of concrete recommended in the Code for Design of Concrete Structures (GB 50010–2010) [33] was slightly modified to approximately simulate the tensile behavior of masonry, as expressed below:

$$\begin{cases} \frac{\sigma_t}{f_{t,r}} = 1.2 \frac{\varepsilon_t}{\varepsilon_{t,r}} - 0.2 \left(\frac{\varepsilon_t}{\varepsilon_{t,r}} \right)^6, & \frac{\varepsilon_t}{\varepsilon_{t,r}} \leq 1 \\ \frac{\sigma_t}{f_{t,r}} = \frac{x}{2 \left(\frac{\varepsilon_t}{\varepsilon_{t,r}} - 1 \right)^{1.7} + \frac{\varepsilon_t}{\varepsilon_{t,r}}}, & \frac{\varepsilon_t}{\varepsilon_{t,r}} > 1 \end{cases} \quad (6)$$

$$f_{t,r} = 0.141 \sqrt{f_2} \quad (7)$$

$$\varepsilon_{t,r} = \frac{f_{t,r}}{E_c} \quad (8)$$

where σ_t is the tensile stress, ε_t is the tensile strain, f_2 is the average compressive strength of mortar, $f_{t,r}$ is the average tensile strength of masonry, $\varepsilon_{t,r}$ is the tensile strain corresponding to $f_{t,r}$ and E_c is the elastic modulus of masonry.

CONSTRUCTION OF MAINSHOCK-AFTERSHOCK SEQUENCE-TYPE GROUND MOTIONS

The as-recorded mainshock-aftershock sequences are difficult to obtain and are limited in number. For this reason, artificial

mainshock-aftershock sequences are often constructed using theoretical methods for research in this field. Han et al. [34] used Latin hypercube sampling to randomly synthesize aftershocks based on the mainshock records, site conditions, and fault rupture mechanisms, and then constructed the mainshock-aftershock sequences from the data for both the mainshocks and aftershocks. To consider the effect of aftershock intensity on the seismic performance of structures, Zhai et al. [35] constructed mainshock-aftershock sequences by using four different mainshock-to-aftershock peak acceleration scaling factors, i.e., $PGA_{AS}/PGA_{MS} = 0.5, 0.8, 1.0$, and 1.5 , respectively. Song et al. [10] studied the collapse probability of steel structures using three (i.e., repeated, randomized, and as-recorded) types of mainshock-aftershock sequence ground motions. Hazizorgioua and Beskos [36] constructed the repeated mainshock-aftershock sequences and used them to analyze the inelastic displacement ratios of the SDOF structural system. Li and Ellingwood [37] constructed mainshock-aftershock sequences by replication and randomization and then used them to study the fragility of steel frame structures.

In the present study, the commonly used replication method to construct mainshock-aftershock sequences by scaling the mainshock. That is, assuming that the mainshock and aftershock have the same ground motion characteristics (e.g., frequency and duration, etc.), the aftershock is simulated by multiplying the peak acceleration of the mainshock by a scaling factor between 0 and 1, and then the two are combined to generate a mainshock-aftershock sequence. To consider the uncertainty of input ground motion, 80 real ground motion records were selected from the strong ground motion database of the Pacific Earthquake Engineering Research Center based on the magnitude-epicentral distance (Mw-R) band method, i.e. [38], the selected ground motions should be distributed within a wide Mw-R range while considering the effect of near-fault ground motions. Then, the 80 selected ground motions were scaled using four different values of scaling factor δ , set to 0.4, 0.6, or 0.8, 1, thereby constructing a total of 320 mainshock-aftershock sequences. The time interval

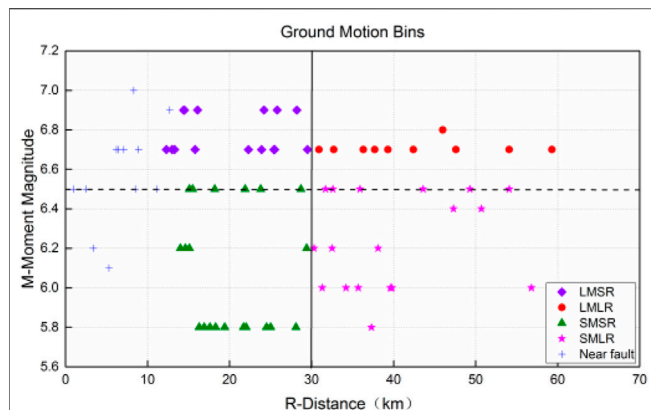


FIGURE 4 | Mw-R distribution of ground motion records.

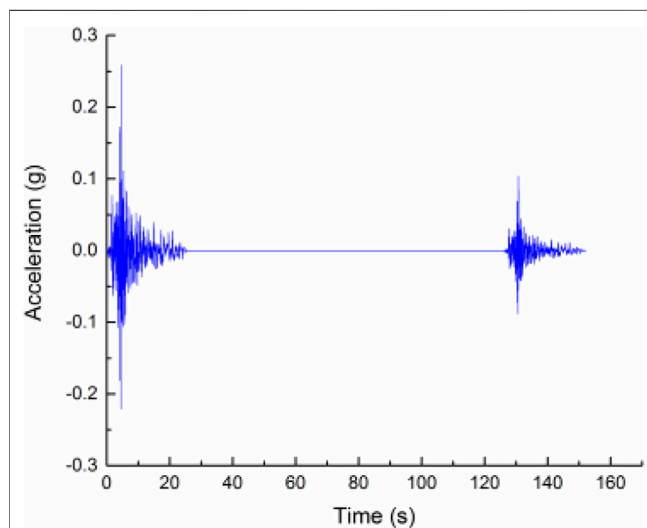


FIGURE 5 | Acceleration time-history curves of mainshock-aftershock sequences (C08-320, PGAMS = 0.259 g).

between the mainshock and aftershock was set as 100 s to ensure that the structure had enough time to return to an at-rest position after the mainshock. **Figure 4** shows the Mw-R distribution of the selected ground motion records. **Figure 5** gives the acceleration time histories of the mainshock-aftershock sequences generated using different scaling factors under the condition C08-320 ($\delta = 0.6$).

SEISMIC RESPONSE ANALYSIS OF SINGLE-STORY MASONRY STRUCTURES

Nonlinear seismic response analysis of the URM and CM structural models subjected to mainshocks only, aftershocks only, and mainshock-aftershock sequences was carried out using nonlinear dynamic time-history analysis. The maximum roof displacement and the maximum inter-story drift ratio (ISDR) are used as performance indices to evaluate the effects

TABLE 1 | Comparison of maximum roof displacements of single-story masonry structural models under different mainshocks.

No	Earthquake motion	PGA(g)	Maximum roof displacement (mm)		
			URM	CM	RP(%)
1	H06-360	0.06	0.43	0.4	6.98
2	SOR-315	0.067	0.52	0.47	9.62
3	BRA-315	0.16	2.07	1.94	6.28
4	M-GMR-000	0.184	1.61	1.31	18.63
5	HCH-090	0.245	0.94	0.92	2.13
6	C08-320	0.259	1.51	1.3	13.91
7	SLC-360	0.277	1.51	1.44	4.64
8	G02-090	0.32	3.72	1.46	60.75
9	A-CAS-000	0.322	2.45	1.94	20.82
10	LOS-000	0.411	3.75	3.06	18.40
11	CNP-196	0.42	5.81	3.82	34.25
12	LOS-270	0.477	5.83	4.43	24.01
13	NWH-360	0.59	14.09	5.98	57.56
14	JEN-092	0.593	18.72	8.66	53.74
15	SCS-052	0.612	14.45	8.83	38.89
16	SPV-270	0.753	33.85	11.64	65.61
17	H-BCR-230	0.78	16.15	9.63	40.37
18	SCS-142	0.805	43.27	14.36	66.81
19	RRS-228	0.834	82.91	31.83	61.61
20	SPV-360	0.939	21.89	12.23	44.13

of confining members as well as aftershocks on the seismic response of single-story masonry structures.

Effect of Confining Members on Seismic Response of Masonry Structures Under Mainshocks

Table 1 lists the maximum values of roof displacement of the URM and CM structural models under mainshocks only. Compared with those of the URM structure, the maximum roof displacement of the CM model decrease by 2.13–66.81%. Taking the condition LOS-000 as an example, the maximum roof displacement of the URM model are 3.75 mm, while that of the CM model are 3.06 mm, representing a decrease of 18.4%. Evidently, the use of confining members such as ring beams and constructional columns improves the integrity of the single-story masonry structure and effectively reduces its seismic response.

Effect of Aftershocks on the Seismic Response of Mainshock-Damaged Masonry Structures

The nonlinear seismic response analysis of the URM and CM structural models under mainshock-aftershock sequences or aftershocks only was performed. **Figure 6** shows the comparison of roof displacement time-history curves of the undamaged and mainshock-damaged URM and CM models under aftershock (LOS-000, PGAMS = 0.411 g, $\delta = 0.6$). **Tables 2** and **3** compare the maximum roof displacements of the URM and CM models under some of the main conditions. In **Table 2** and **3**, UD represents the undamaged model while MD

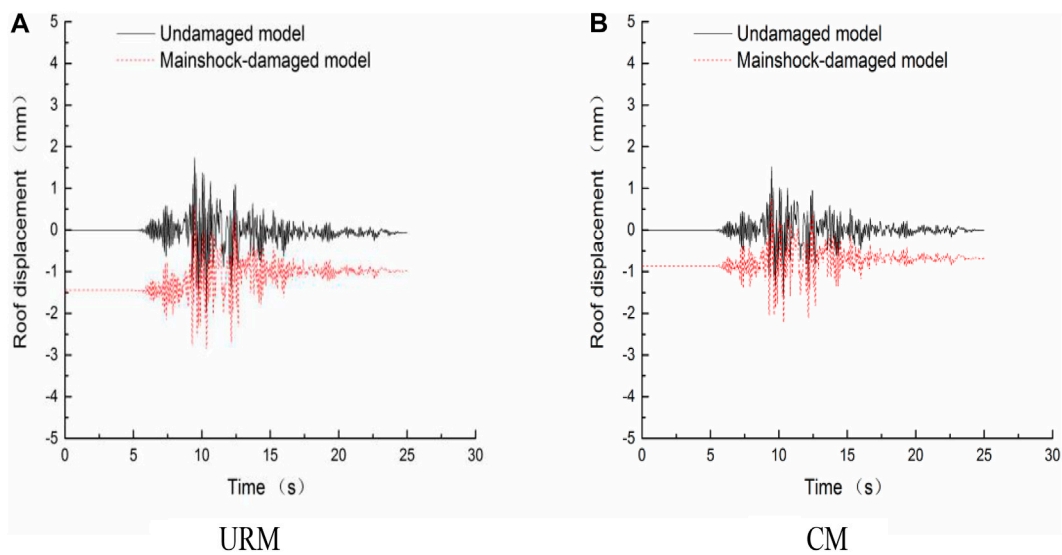


FIGURE 6 | Comparison of roof displacement time-history curves of the undamaged and mainshock-damaged URM and CM models under aftershock (LOS-000, PGAMS = 0.411 g, $\delta = 0.6$). **(A)** URM. **(B)** CM.

TABLE 2 | Comparison of maximum roof displacements of the undamaged and mainshock-damaged URM models under aftershock.

No	Earthquake motion	PGA(g)	Roof displacements(mm)											
			$\delta = 0.4$			$\delta = 0.6$			$\delta = 0.8$			$\delta = 1$		
			UD	MD	IR(%)	UD	MD	IR(%)	UD	MD	IR(%)	UD	MD	IR(%)
1	H06-360	0.06	0.17	0.17	0.0	0.26	0.26	0.0	0.34	0.34	0.0	0.43	0.43	0.2
2	SOR-315	0.067	0.21	0.21	0.0	0.31	0.31	0.0	0.42	0.42	0.2	0.52	0.52	0.0
3	BRA-315	0.16	0.87	0.88	1.6	1.30	1.33	2.0	1.73	1.77	2.5	2.07	2.22	7.3
4	M-GMR-000	0.184	0.64	0.65	1.4	0.96	0.97	1.0	1.28	1.29	0.9	1.61	1.61	0.2
5	HCH-090	0.245	0.38	0.38	0.5	0.56	0.56	0.2	0.75	0.75	0.1	0.94	0.94	0.2
6	C08-320	0.259	0.61	0.62	1.5	0.91	0.92	1.1	1.21	1.23	1.3	1.51	1.54	1.5
7	SLC-360	0.277	0.60	0.61	1.3	0.90	0.91	0.9	1.20	1.21	0.8	1.51	1.52	0.4
8	G02-090	0.32	1.01	1.85	83.3	1.51	2.52	66.9	2.17	3.44	58.4	3.72	4.47	20.1
9	A-CAS-000	0.322	1.01	1.41	39.6	1.52	1.87	23.3	1.99	2.13	7.1	2.45	2.63	7.4
10	LOS-000	0.411	1.32	2.65	100.8	1.99	2.86	43.6	2.51	3.34	33.2	3.75	4.26	13.7
11	CNP-196	0.42	1.33	3.17	137.9	2.15	3.98	85.1	3.19	4.95	55.3	5.81	6.74	16.0
12	LOS-270	0.477	1.40	3.60	156.6	2.21	4.48	102.6	3.66	4.97	35.8	5.83	6.87	17.9
13	H-E05-140	0.502	1.71	3.96	132.5	3.46	4.66	34.8	4.62	5.55	20.2	6.22	7.35	18.1
14	NWH-360	0.59	1.22	6.89	464.0	1.89	17.38	821.7	2.82	41.98	1,388.5	14.09	109.63	677.8
15	SCS-052	0.612	1.36	9.86	627.3	2.21	18.34	731.4	5.13	42.34	726.0	14.45	126.02	772.3
16	SPV-270	0.753	1.91	20.92	993.6	5.58	38.41	587.9	16.16	63.41	292.4	33.85	89.25	163.6
17	H-BCR-230	0.78	2.41	14.45	500.0	5.19	20.41	293.2	8.34	28.74	244.6	16.15	39.46	144.3
18	SCS-142	0.805	1.63	70.04	4,194.5	2.89	98.21	3,298.2	13.47	155.54	1,054.4	43.27	323.67	648.0
19	RRS-228	0.834	1.87	132.69	6,980.6	6.18	185.55	2,902.4	29.26	258.39	783.0	82.91	335.10	304.2
20	SPV-360	0.939	1.31	17.28	1,214.8	2.11	27.96	1,224.1	7.43	55.14	641.8	21.89	115.50	427.7

UD represents the undamaged model while MD represents Mainshock-damaged model.

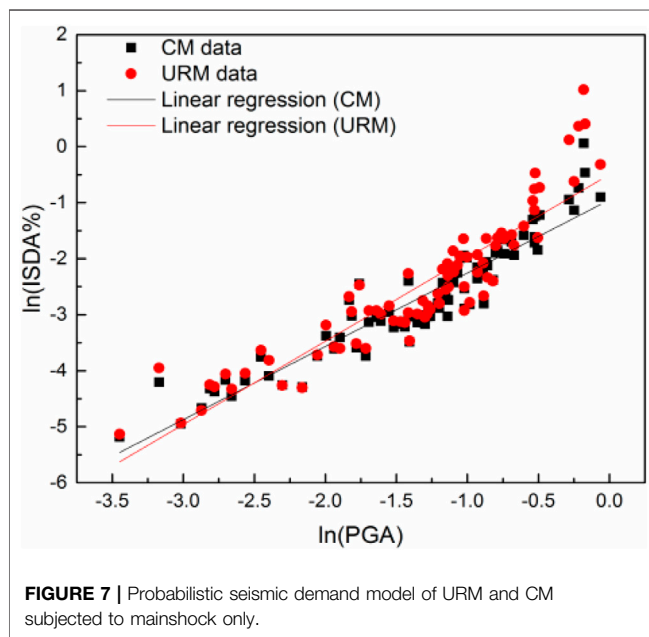
represents Mainshock-damaged model. Compared with undamaged URM and CM models subjected to aftershock only, the maximum roof displacements of the mainshock-damaged URM and CM models subjected to aftershock of the same intensity increased by factors of 0–69.96 and 0–9.64, respectively, when $\delta = 0.4$; by factors of 0–32.98 and 0–3.62 when $\delta = 0.6$; by factors of 0–13.89 and 0–1.41 when $\delta = 0.8$; and by factors of 0–7.72 and 0–1.29 when $\delta = 1$. Taking the condition

LOS-000 as an example, **Figures 7, 8** compare the roof displacement time-history curves of the URM and CM models, respectively. When $\delta = 0.4$, the maximum roof displacements of the undamaged URM and CM models under the aftershock only are 1.32 and 1.07 mm, respectively, while the maximum roof displacements of the two models under an aftershock of the same intensity after the mainshock are 2.65 and 1.89 mm, representing an increase of 100.8 and 76.6%,

TABLE 3 | Comparison of maximum roof displacements of the undamaged and mainshock-damaged CM models under aftershock.

NO.	Earthquake motion	PGA(g)	Roof displacements(mm)											
			$\delta = 0.4$			$\delta = 0.6$			$\delta = 0.8$			$\delta = 1$		
			UD	MD	IR(%)	UD	MD	IR(%)	UD	MD	IR(%)	UD	MD	IR(%)
1	H06-360	0.06	0.06	0.16	184.2	0.24	0.24	0.8	0.32	0.32	0.9	0.40	0.40	0.5
2	SOR-315	0.067	0.19	0.19	1.1	0.28	0.28	0.7	0.37	0.37	0.5	0.46	0.47	0.4
3	BRA-315	0.16	0.78	0.79	1.3	1.17	1.20	2.5	1.56	1.62	3.6	1.94	2.05	5.4
4	M-GMR-000	0.184	0.52	0.53	1.3	0.78	0.79	1.3	1.04	1.05	1.2	1.31	1.31	0.5
5	HCH-090	0.245	0.37	0.37	0.0	0.55	0.55	0.0	0.74	0.74	0.0	0.92	0.92	0.0
6	C08-320	0.259	0.52	0.53	1.5	0.78	0.79	1.2	1.04	1.05	1.2	1.30	1.31	1.2
7	SLC-360	0.277	0.57	0.58	0.7	0.86	0.87	0.6	1.15	1.16	0.6	1.44	1.44	0.0
8	G02-090	0.32	0.84	1.47	75.6	1.27	2.04	61.1	1.79	2.63	46.7	1.46	3.34	129.3
9	A-CAS-000	0.322	0.76	0.84	10.8	1.14	1.24	9.3	1.51	1.64	8.5	1.94	2.15	10.9
10	LOS-000	0.411	1.07	1.89	76.5	1.60	2.22	38.7	2.06	2.72	32.4	3.06	3.39	10.5
11	CNP-196	0.42	1.13	2.09	84.7	1.74	3.11	78.3	2.67	3.94	47.4	3.82	5.23	36.8
12	LOS-270	0.477	1.31	2.81	115.1	2.02	3.60	78.6	2.90	4.18	44.1	4.43	5.17	16.7
13	H-E05-140	0.502	1.59	3.48	119.5	2.64	4.16	57.6	4.06	5.06	24.7	5.49	6.16	12.1
14	NWH-360	0.59	1.20	1.41	17.3	1.81	1.98	9.4	3.04	3.63	19.7	5.98	6.62	10.7
15	SCS-052	0.612	1.34	4.13	208.3	2.12	5.30	149.9	4.29	7.99	86.0	8.83	11.92	35.0
16	SPV-270	0.753	1.70	4.55	167.5	3.67	6.29	71.4	6.99	8.78	25.7	11.64	14.93	28.3
17	H-BCR-230	0.78	2.25	4.13	83.5	4.27	5.68	32.8	6.69	7.63	14.1	9.63	10.15	5.4
18	SCS-142	0.805	1.62	9.19	466.8	2.51	11.60	361.5	8.50	16.81	97.8	14.36	23.73	65.3
19	RRS-228	0.834	1.76	18.72	961.4	5.34	23.66	342.9	15.87	33.01	108.0	31.83	47.05	47.8
20	SPV-360	0.939	1.26	5.50	336.9	1.93	7.98	313.4	5.20	12.55	141.4	12.23	18.66	52.6

UD represents the undamaged model while MD represents Mainshock-damaged model.



respectively. When $\delta = 0.6$, the maximum roof displacements of the undamaged URM and CM models under the aftershock only are 1.99 and 1.60 mm, respectively, while the maximum roof displacements of the two models under the aftershock of the same intensity after the mainshock are 2.86 and 2.22 mm, representing an increase of 43.7 and 38.8%, respectively. When $\delta = 0.8$, the maximum roof displacements of the undamaged URM and CM models under the aftershock only are 2.51 and 2.06 mm,

respectively, while the maximum roof displacements of the two models under the aftershock of the same intensity after the mainshock are 3.34 and 2.72 mm, representing an increase of 33.1 and 32.0%, respectively. When $\delta = 1$, the maximum roof displacements of the undamaged URM and CM models under the aftershock only are 3.75 and 3.06 mm, respectively, while the maximum roof displacements of the two models under the aftershock of the same intensity after the mainshock are 4.26 and 3.39 mm, representing an increase of 13.6 and 10.8%. Therefore, compared with undamaged URM and CM models under aftershock only, the roof displacement of the mainshock-damaged URM and CM models under the aftershock of the same intensity both notably increase, indicating that aftershocks have a substantial effect on the displacement demand of mainshock-damaged structures and hence cannot be ignored. In addition, as shown in **Figure 6**, it can be clearly seen that the presence of confining members effectively mitigates the effect of aftershocks on structures. Therefore, it is very important to have necessary confining members in masonry structures, which benefits resistance to not only a single strong earthquake but also multiple successive earthquakes.

SEISMIC FRAGILITY ANALYSIS OF SINGLE-STORY MASONRY STRUCTURES

Probabilistic Seismic Demand Model

The PSD model characterizes the relationship between the engineering demand parameter (EDP) and the ground motion intensity measure (IM). In the present study, the maximum ISDA ($ISDA_{max}$) and the peak ground acceleration (PGA) are selected as the EDP and the IM, respectively, for the PSD analysis of the

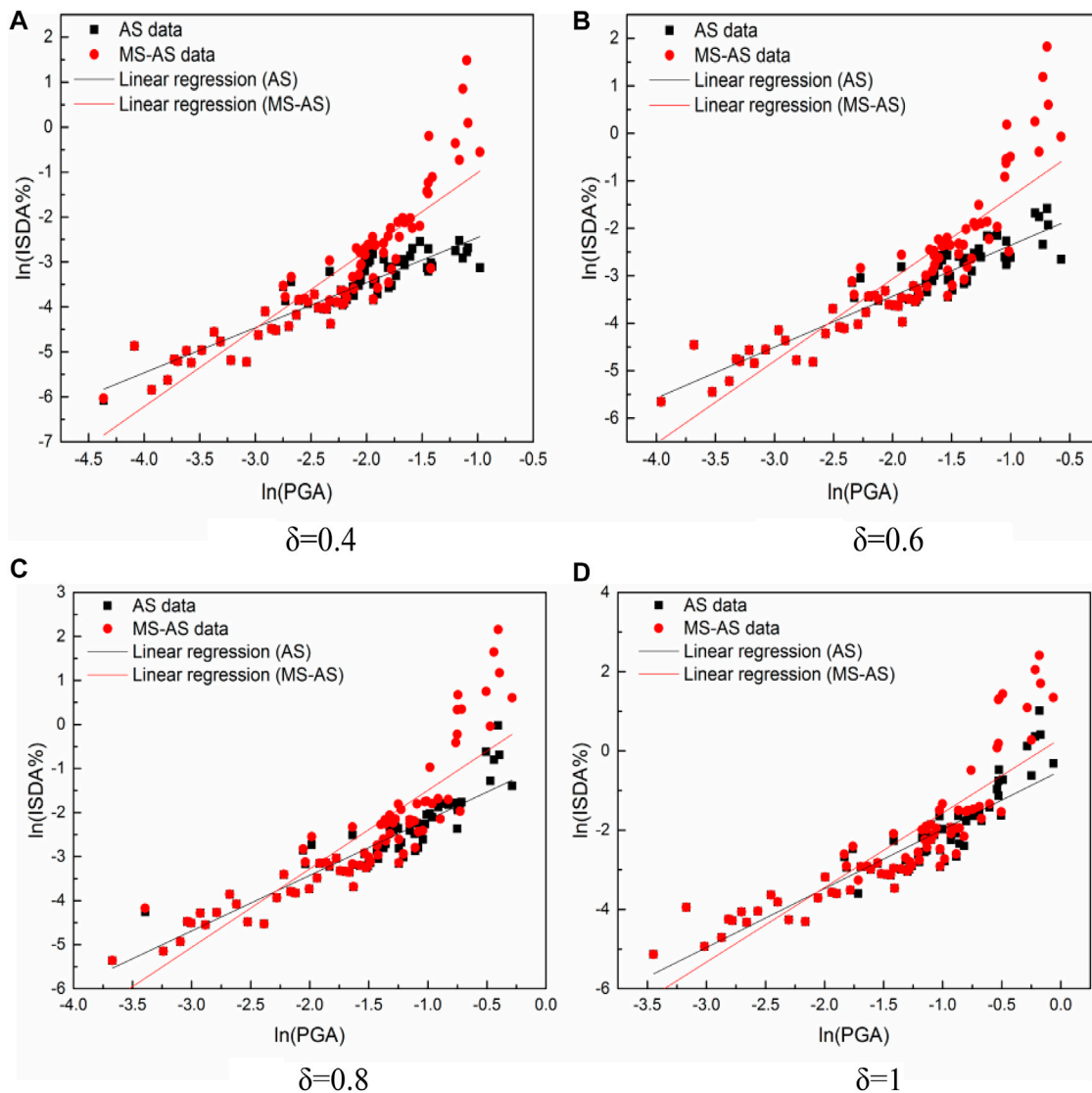


FIGURE 8 | Probabilistic seismic demand model of URM subjected to aftershock. (A) $\delta = 0.4$ (B) $\delta = 0.6$ (C) $\delta = 0.8$ (D) $\delta = 1$.

two structures. Cornell et al. [39] proposed that the structural EDP and the IM satisfy the following logarithmic linear relation:

$$\ln(EDP) = \ln a + b \ln(IM) \quad (9)$$

The PSD model under each condition can be obtained by fitting the results from the nonlinear dynamic time-history analysis of the structure. The logarithmic standard deviation of the seismic demand can be expressed as

$$\sigma_{D|IM} = \sqrt{\frac{\sum_{i=1}^N [\ln(D_i) - \ln(aIM_i^b)]^2}{N-2}} \quad (10)$$

where N is the number of sample points in the regression analysis, D_i is the peak value of the i th seismic demand, IM_i is the PGA of the i th ground motion, and a and b are the regression parameters.

Figure 7 shows the PSD models for the URM and CM models subjected to mainshocks only. Figures 8, 9 show the PSD models for the URM and CM models subjected to aftershocks only and mainshock-aftershock sequences. Tables 4 and 5 list the mathematical expressions and related parameters of the PSD models under different conditions.

Fragility Analytical Method

The fragility function can be expressed as follows [16]:

$$P(D \geq C | IM) = \Phi \left[\frac{\ln(\mu_D) - \ln(\mu_C)}{\sqrt{\sigma_{D|IM}^2 + \sigma_C^2}} \right] \quad (11)$$

where D and C are seismic demand and structural capacity, respectively; IM is the ground motion intensity measure, μ_D

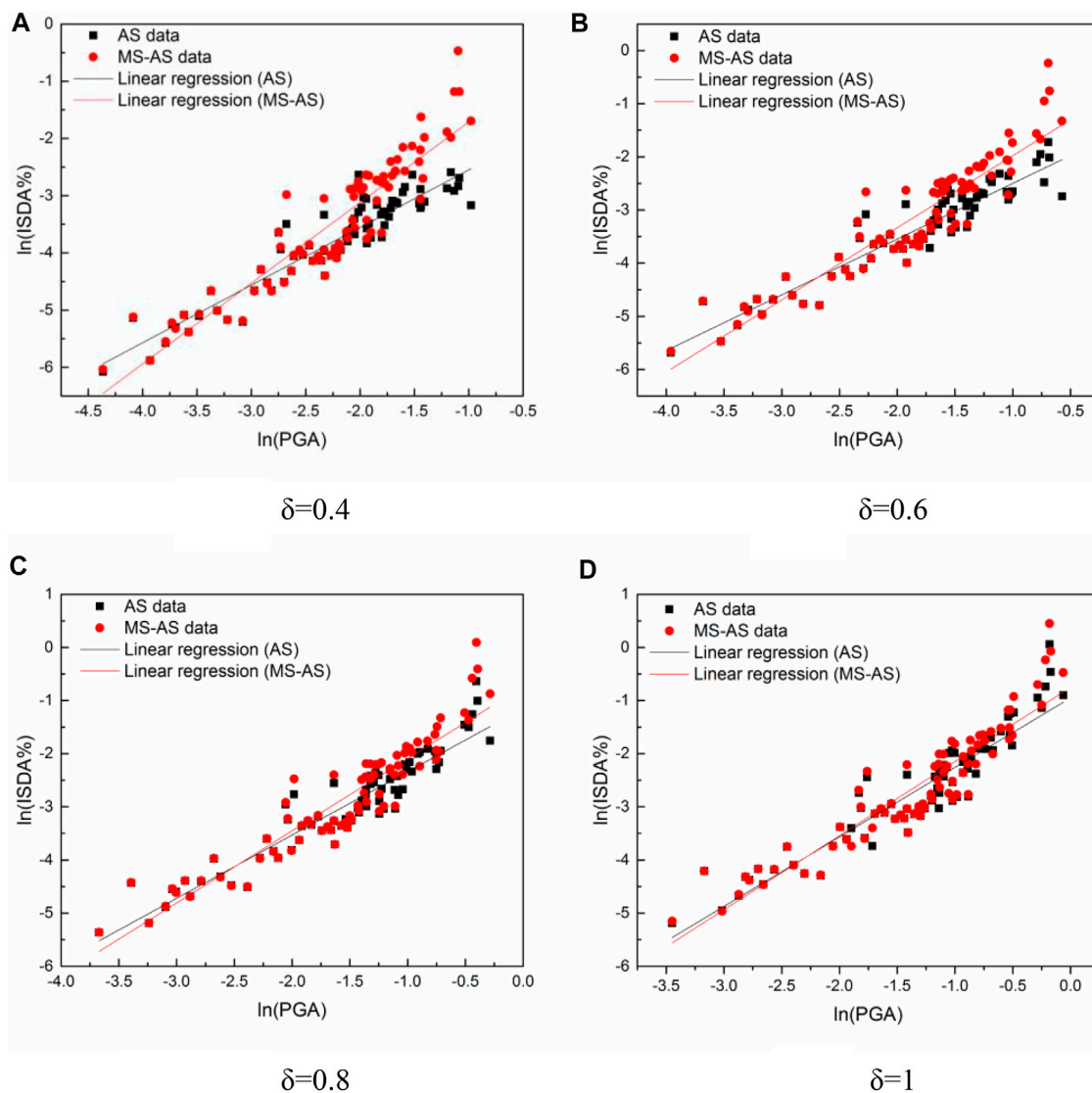


FIGURE 9 | Probabilistic seismic demand model of CM subjected to aftershock. (A) $\delta = 0.4$ (B) $\delta = 0.6$ (C) $\delta = 0.8$ (D) $\delta = 1$.

TABLE 4 | Parameters for the probabilistic demand models of URM and CM subjected to mainshock only.

Model	Regression model	R^2	$\sigma_{D IM}$
URM	$\ln(ISDA_{max}) = -0.498 + 1.487\ln(PGA)$	0.829	0.26704
CM	$\ln(ISDA_{max}) = -0.95 + 1.307\ln(PGA)$	0.878	0.13929

and μ_C are the medians of D and C , respectively; and $\sigma_{D|IM}$ and σ_C are the standard deviations corresponding to D and C , respectively.

The seismic fragility of a structure refers to the conditional probability that the structure reaches or exceeds a certain limit state under different seismic intensities. It thus describes the probability distribution of all limit states of the structure. Therefore, it is very important to define the damage limit

states of the structure. Using the maximum ISDR as the EDP, four damage limit states, namely, slight damage (LS-1), moderate damage (LS-2), severe damage (LS-3), and collapse (LS-4), are defined according to the existing test results and recommended values for current specifications. **Table 6** shows these damage limit states and their relevant parameters.

Fragility Results and Discussion

Effect of Confining Members on Seismic Fragility of Masonry Structures

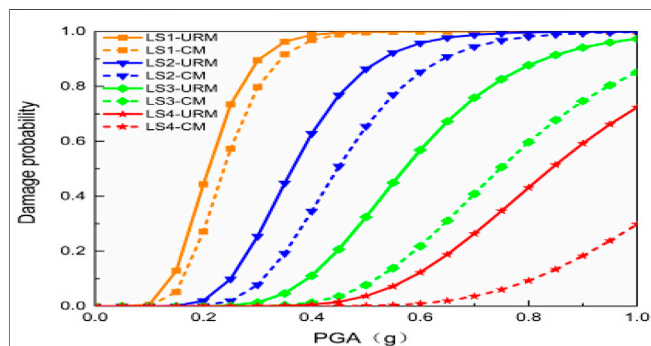
Figure 10 compares the seismic fragility curves of the URM and CM models under mainshocks only. It is clear that the use of confining members is crucial to reducing the seismic fragility of masonry structures. The fragility curve of the CM model corresponding to each damage limit state is notably below that of the URM model. That is, the PE of each damage limit state of

TABLE 5 | Parameters for the probabilistic demand models of URM and CM subjected to aftershock.

Cases		Regression model	R ²	$\sigma_{D IM}$
Undamaged model(URM)	$\delta = 0.4$	$\ln(ISDA_{max}) = -1.453 + 1.003\ln(PGA_Z)$	0.855	0.10013
	$\delta = 0.6$	$\ln(ISDA_{max}) = -1.284 + 1.073\ln(PGA)$	0.868	0.10275
	$\delta = 0.8$	$\ln(ISDA_{max}) = -0.903 + 1.262\ln(PGA)$	0.865	0.1463
	$\delta = 1$	$\ln(ISDA_{max}) = -0.498 + 1.487\ln(PGA)$	0.829	0.26704
Mainshock-damaged model(URM)	$\delta = 0.4$	$\ln(ISDA_{max}) = -0.720 + 1.734\ln(PGA)$	0.782	0.49006
	$\delta = 0.6$	$\ln(ISDA_{max}) = -0.397 + 1.732\ln(PGA)$	0.773	0.51561
	$\delta = 0.8$	$\ln(ISDA_{max}) = 0.288 + 1.783\ln(PGA)$	0.753	0.6092
	$\delta = 1$	$\ln(ISDA_{max}) = -0.314 + 1.881\ln(PGA)$	0.737	0.7402
Undamaged model(CM)	$\delta = 0.4$	$\ln(ISDA_{max}) = -1.543 + 1.006\ln(PGA)$	0.875	0.08461
	$\delta = 0.6$	$\ln(ISDA_{max}) = -1.452 + 1.048\ln(PGA)$	0.885	0.08352
	$\delta = 0.8$	$\ln(ISDA_{max}) = -1.148 + 1.191\ln(PGA)$	0.892	0.10046
	$\delta = 1$	$\ln(ISDA_{max}) = -0.95 + 1.307\ln(PGA)$	0.878	0.13929
Mainshock-damaged model(CM)	$\delta = 0.4$	$\ln(ISDA_{max}) = -0.303 + 1.409\ln(PGA)$	0.856	0.1965
	$\delta = 0.6$	$\ln(ISDA_{max}) = -0.623 + 1.356\ln(PGA)$	0.864	0.16925
	$\delta = 0.8$	$\ln(ISDA_{max}) = -0.735 + 1.358\ln(PGA)$	0.868	0.16483
	$\delta = 1$	$\ln(ISDA_{max}) = -0.754 + 1.394\ln(PGA)$	0.862	0.18296

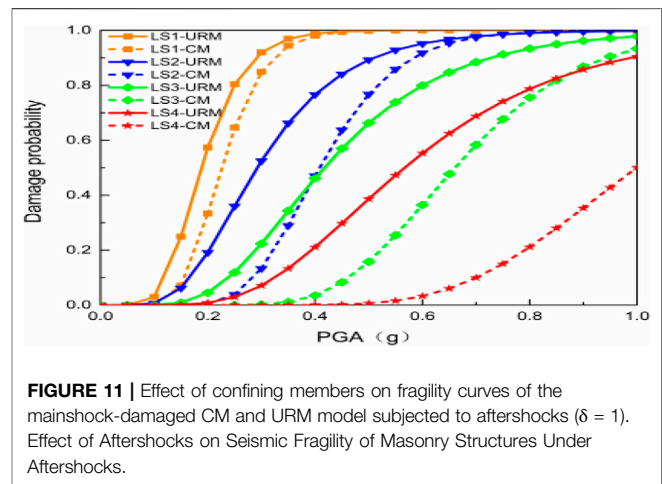
TABLE 6 | Classification of damage limit states.

Damage limit states	LS-1	LS-2	LS-3	LS-4
$ISDA_{max}$	January 1/600	1/700	1/350	1/200

**FIGURE 10** | Comparison of fragility curves of the URM and CM model subjected to mainshock only.

the CM model is lower than that of the URM model. Taking the case of $PGA = 0.4$ g as an example, the PE values of different damage limit states of the URM model are 98.75% (LS-1), 62.85% (LS-2), 11.06% (LS-3), and 0.53% (LS-4), while those of the CM model are 96.83% (LS-1), 34.59% (LS-2), 1.32% (LS-3), and 0.01% (LS-4), representing decreases of 1.94%, 44.96%, 88.07%, and 98.11%, respectively.

Taking the case of the aftershock scaling factor $\delta = 1$ as an example, **Figure 11** shows the effect of confining members on the fragility curves of the mainshock-damaged URM and CM models subjected to aftershocks. The fragility curve of the mainshock-damaged URM model corresponding to each limit state is above that of the mainshock-damaged CM model, i.e., the PE of each damage limit state of the mainshock-damaged URM model is higher than that of the mainshock-damaged CM model. Taking

**FIGURE 11** | Effect of confining members on fragility curves of the mainshock-damaged CM and URM model subjected to aftershocks ($\delta = 1$). Effect of Aftershocks on Seismic Fragility of Masonry Structures Under Aftershocks.

the case of $PGA = 0.4$ g as an example, the PE values of the four damage limit states of the mainshock-damaged URM model are 98.83%, 77.66%, 46.19%, and 21.07%, respectively, and those of the mainshock-damaged CM model are 98.08, 47.09, 3.52%, and 4.77×10^{-4} , representing decreases of 0.75%, 39.36%, 92.38%, and 99.77%, respectively. The presence of confining members significantly improves the structural resistance to aftershocks, as the likelihood of moderate damage, severe damage or collapse of the mainshock-damaged URM model (i.e., without confining members) subjected to the aftershock is higher than that of the mainshock-damaged CM model, as illustrated by the blue, green and red lines in **Figure 11**. Therefore, the use of confining members in the masonry structure has little effect on the slight damage state but can effectively reduce the likelihood of moderate damage, severe damage, or collapse of the mainshock-damaged masonry structure when subjected to aftershocks.

Figure 12 compares the fragility curves of the undamaged and mainshock-damaged CM models subjected to aftershocks. The PE values of damage limit states of the mainshock-damaged model subjected to the aftershock are significantly higher than

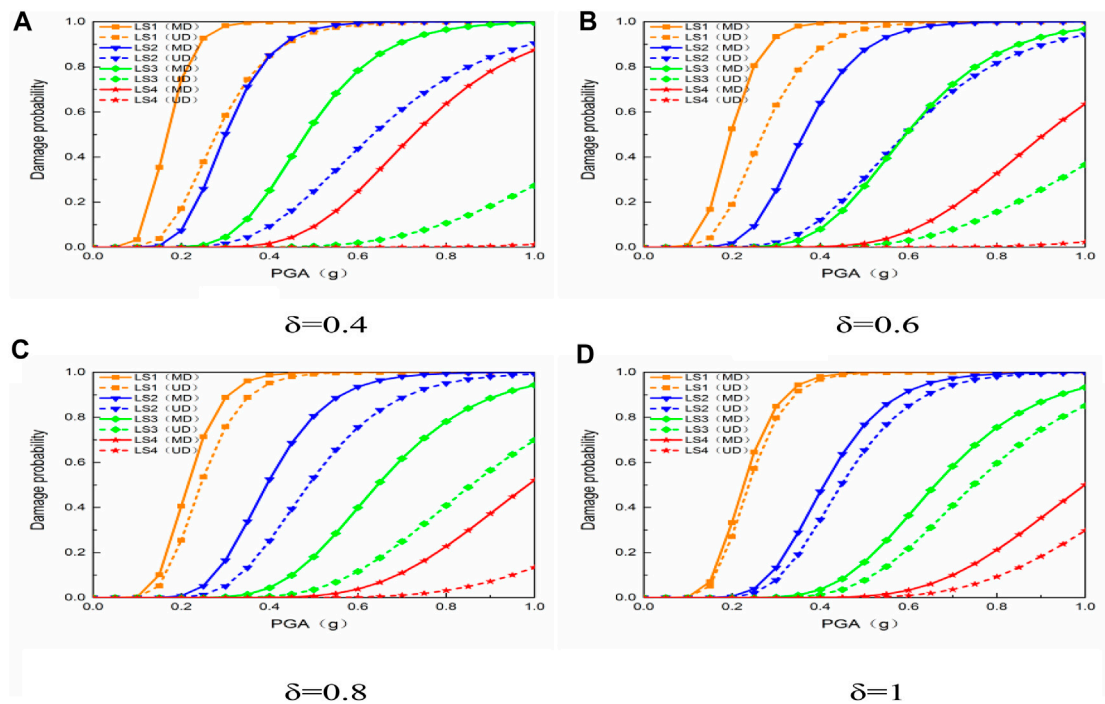


FIGURE 12 | The fragility curves of the undamaged and mainshock-damaged CM model under aftershocks. (A) $\delta = 0.4$ (B) $\delta = 0.6$ (C) $\delta = 0.8$ (D) $\delta = 1$.

those of the undamaged model directly subjected to the aftershock of the same intensity. As shown in **Figure 12**, taking the case of $\text{PGA} = 0.4 \text{ g}$ as an example, when $\delta = 0.4$, the PE values of the four damage limit states of the CM model are 99.92%, 85.10%, 25.17%, and 1.63%, respectively, when subjected to the mainshock followed by an aftershock and are 85.10%, 9.31%, 0.06%, and 5.25×10^{-7} when subjected to the aftershock of the same intensity directly. That is, compared with the undamaged CM model, the aftershock increases the PE values of the damage limit states of the mainshock-damaged CM model by factors of 0.17, 8.14, 418.5, and 31,046.62, respectively. When $\delta = 0.6$, the PE values of the four damage limit states of the CM model are 99.45%, 64.07%, 7.99%, and 0.17%, respectively, when subjected to the mainshock followed by the aftershock; they are 88.38%, 12.1%, 0.01%, and 1.11×10^{-6} , respectively, when directly subjected to the aftershock of the same intensity. That is, compared with the undamaged CM model, the aftershock increases the PE values of the damage limit states of the mainshock-damaged CM model by factors of 0.13, 4.30, 798, and 1,530.53, respectively. When $\delta = 0.8$, the PE values of the four damage limit states of the CM model are 98.79%, 52.49%, 4.34%, and 5.99×10^{-4} , respectively, when subjected to the mainshock followed by the aftershock and are 95.24%, 25.25%, 0.53%, and 1.42×10^{-5} , when directly subjected to an aftershock of the same intensity. That is, compared with the undamaged CM model, the aftershock increases the PEs of the damage limit states of the mainshock-damaged CM model by factors of 0.04, 1.08, 7.19, and 41.18, respectively. When $\delta = 1$, the PE values of the four damage limit states of the CM model are 98.08%, 47.09%, 3.52%, and 4.77×10^{-4} , respectively, when subjected to the mainshock followed by

the aftershock; they are 96.83%, 34.59%, 1.32%, and 7.48×10^{-5} , when directly subjected to an aftershock of the same intensity. That is, compared with the undamaged CM model, the aftershock increases the PE values of the damage limit states of the mainshock-damaged CM model by factors of 0.01, 0.36, 1.67, and 5.38, respectively.

Figure 13 compares the fragility curves of the undamaged and mainshock-damaged URM model subjected to aftershocks. The PE values of the damage limit states of the mainshock-damaged URM model subjected to an aftershock are significantly higher than those of the undamaged URM model directly subjected to the aftershock of the same intensity. As shown in **Figure 13**, taking the case of $\text{PGA} = 0.4 \text{ g}$ as an example, when $\delta = 0.4$, the PE values of the four damage limit states of the URM model are 99.95%, 97.13%, 78, 13%, and 42.43%, respectively, when subjected to the mainshock followed by the aftershock and are 90.22%, 14.88%, 0.17%, and 2.55×10^{-6} when directly subjected to an aftershock of the same intensity. That is, compared with the undamaged URM model, the aftershock increases the PE values of the damage limit states of the mainshock-damaged URM model by factors of 0.11, 553, 458, 47, and 16, 39, 116 respectively. When $\delta = 0.6$, the PE values of the four damage limit states of the URM model are 99.6%, 90.59%, 59.09%, and 24.07%, respectively, when subjected to the mainshock followed by an aftershock; they are 94.34%, 22.77%, 0.42%, and 1.03×10^{-5} when directly subjected to an aftershock of the same intensity. That is, compared with the undamaged URM model, the aftershock increases the PE values of the damage limit states of the mainshock-damaged URM model by factors of 0.06, 2.98, 139.69, and 23, 367, 93, respectively. When $\delta = 0.8$, the PE values

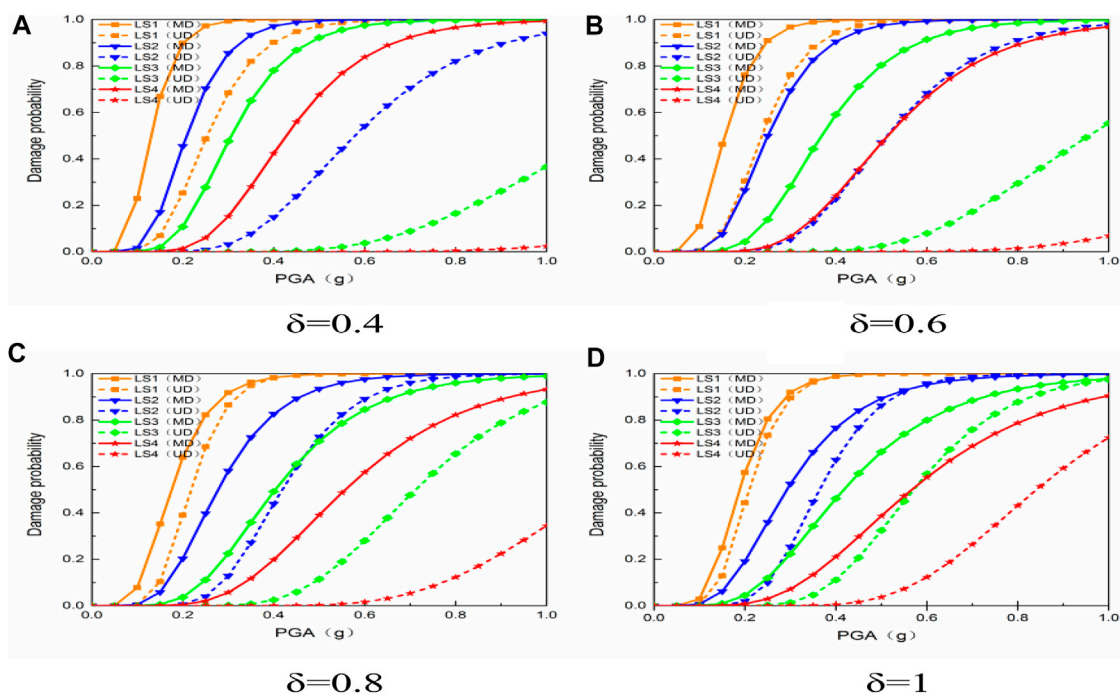


FIGURE 13 | The fragility curves of the undamaged and mainshock-damaged URM model under aftershock. (A) $\delta = 0.4$ (B) $\delta = 0.6$ (C) $\delta = 0.8$ (D) $\delta = 1$.

of the four damage limit states of the URM model are 98.33%, 82.65%, 49.17%, and 19.84%, respectively, when subjected to the mainshock followed by an aftershock and are 98.14%, 43.92%, 2.47%, and 2.13×10^{-4} when directly subjected to an aftershock of the same intensity. That is, compared with the undamaged URM model, the aftershock increases the PE values of the damage limit states of the mainshock-damaged URM model by factors of 0.0019, 0.88, 18.91, and 930.46, respectively. When $\delta = 1$, the PE values of the four damage limit states of the URM model are 98.83%, 76.66%, 46.19%, and 21.07%, respectively, when subjected to the mainshock followed by an aftershock; they are 98.75%, 62.85%, 11.06%, and 0.53% when directly subjected to an aftershock of the same intensity. That is, compared with the undamaged URM model, the aftershock increases the PE values of the damage limit states of the mainshock-damaged URM model by factors of 0.0008, 0.22, 3.18, and 38.75, respectively.

Effect of the Aftershock Scaling Factor on the Seismic Fragility of Masonry Structures Under Aftershock

Figure 14 compares the fragility curves of the mainshock-damaged CM model using different aftershock scaling factors. As shown in **Figure 14A**, taking $\text{PGA} = 0.2 \text{ g}$ as an example and when $\delta = 0.4, 0.6, 0.8$ and 1 , the PE values of the slight damage limit state (LS-1) of the mainshock-damaged CM model are 0.43%, 5.78%, 14.91%, and 32.96%, respectively. In **Figure 14B**, taking $\text{PGA} = 0.4 \text{ g}$ as an example and when $\delta = 0.4, 0.6, 0.8$ and 1 , the PE values of the moderate damage limit state (LS-2) of the mainshock-damaged CM model are 1.22%, 9.01%, 22.98%, and 44.19%, respectively; taking $\text{PGA} = 0.6 \text{ g}$ as an example and when

$\delta = 0.4, 0.6, 0.8$ and 1 , the PE values of the moderate damage limit state (LS-2) of the mainshock-damaged CM model are 21.35%, 49.99%, 76.35%, and 86.96%, respectively. As shown in **Figure 14C**, taking $\text{PGA} = 0.6 \text{ g}$ as an example and when $\delta = 0.4, 0.6, 0.8$ and 1 , the PE values of the severe damage limit state (LS-3) of the mainshock-damaged CM model are 0.62%, 4.77%, 14.52%, and 34.6%, respectively; taking $\text{PGA} = 0.8 \text{ g}$ as an example and when $\delta = 0.4, 0.6, 0.8$ and 1 , the PE values of the severe damage limit state (LS-3) of the mainshock-damaged CM model are 7.08%, 23.67%, 49.07%, and 69.33%, respectively. **Figure 14D** shows that, taking $\text{PGA} = 0.8 \text{ g}$ as an example and when $\delta = 0.4, 0.6, 0.8$ and 1 , the PE values of the collapse limit state (LS-4) of the mainshock-damaged CM model are 0.17, 1.57, 6.06, and 21.11%, respectively.

Figure 15 compares the fragility curves of the mainshock-damaged URM model using different aftershock scaling factors. As shown in **Figure 15A**, taking $\text{PGA} = 0.2 \text{ g}$ as an example and when $\delta = 0.4, 0.6, 0.8$ and 1 , the PE values of the slight damage limit state (LS-1) of the URM model are 8.22%, 26.68%, 41.33%, and 53.84%, respectively. **Figure 15B** shows that, taking $\text{PGA} = 0.4 \text{ g}$ as an example and when $\delta = 0.4, 0.6, 0.8$ and 1 , the PE values of the moderate damage limit state (LS-2) of the mainshock-damaged URM model are 22.26%, 46.66%, 64.5%, and 72.66%, respectively; taking $\text{PGA} = 0.6 \text{ g}$ as an example and when $\delta = 0.4, 0.6, 0.8$ and 1 , the PE values of the moderate damage limit state (LS-2) of the mainshock-damaged URM model are 66.11%, 83.35%, 92.14%, and 92.34%, respectively. As shown in **Figure 15C**, taking $\text{PGA} = 0.6 \text{ g}$ as an example and when $\delta = 0.4, 0.6, 0.8$ and 1 , the PE values of the severe damage limit state (LS-3)

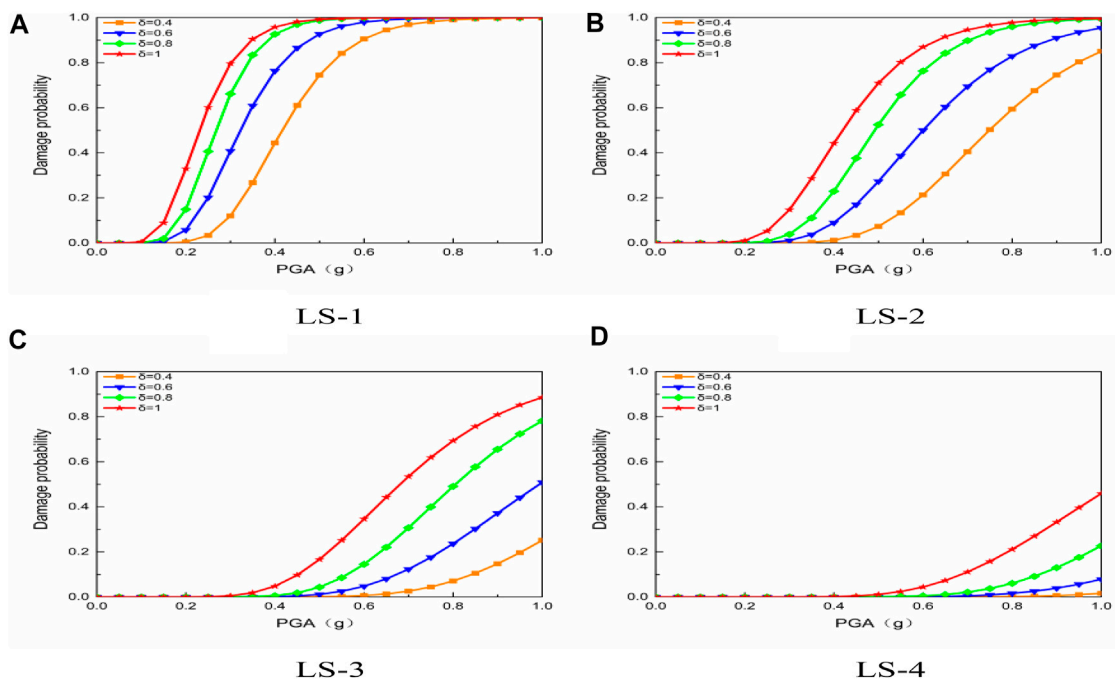


FIGURE 14 | The fragility curves of the mainshock-damaged CM model under aftershock. (A) LS-1 (B) LS-2 (C) LS-3 (D) LS-4.

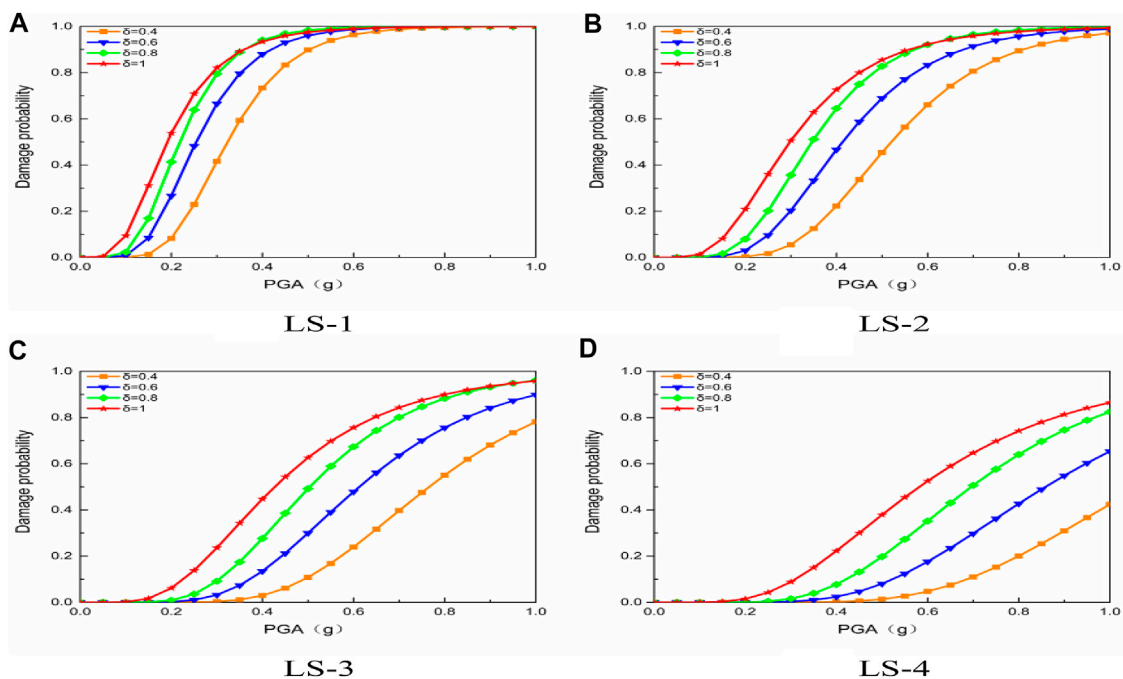


FIGURE 15 | The fragility curves of the mainshock-damaged URM model under aftershock. (A) LS-1 (B) LS-2 (C) LS-3 (D) LS-4.

of the mainshock-damaged URM model are 23.92%, 47.9%, 67.34%, and 75.63%, respectively; taking $PGA = 0.8\text{ g}$ as an example and when $\delta = 0.4, 0.6, 0.8$ and 1 , the PE values of the

severe damage limit state (LS-3) of the mainshock-damaged URM model are 55.07%, 75.61%, 88.28%, and 89.98%, respectively. **Figure 15D** shows that, taking $PGA = 0.8\text{ g}$ as an

example and when $\delta = 0.4, 0.6, 0.8$ and 1 , the PE values of the collapse limit state (LS-4) of the mainshock-damaged URM model are 20.06, 42.71, 64.02, and 74.18%, respectively.

CONCLUSION

In this paper, the seismic fragility of single-story masonry structures representative of the rural areas of Northeast China is studied through numerical simulation. The effects of aftershocks and the aftershock scaling factor on the fragility of masonry structures are investigated in depth, taking into account the influence of confining members. The following main conclusions are drawn:

- 1) Compared with those of the URM model, the roof displacement and ISDRs of the CM model, which has ring beams and constructional columns, are both reduced to varying degrees, and the PE values of different damage limit states of the CM model are significantly lower. Therefore, it is necessary to use confining members in single-story masonry structures to improve their structural integrity, reduce their seismic responses, and effectively mitigate the risk of severe structural damage or collapse.
- 2) The effect of aftershocks on the seismic fragility of mainshock-damaged structures cannot be ignored. Compared with those of the undamaged URM and CM models directly under aftershock, the mainshock-damaged URM and CM models subjected to aftershocks of the same intensity undergo notably increased roof displacement and ISDA, and the PE values of their different damage limit states also increase substantially. In particular, aftershocks significantly affect the limit states of severe damage (LS-3) and collapse (LS-4). That is, after structures are subjected to the mainshock, the aftershock may raise the likelihood of severe damage or collapse.
- 3) Using confining members in the unreinforced masonry structures has little effect on the slight damage limit state (LS-1) but can effectively reduce the probability of moderate damage, severe damage, or collapse of masonry structures. Compared with the CM model, the URM model, which does not have confining members, exhibits a relatively high probability of moderate damage, severe damage or collapse when subjected to aftershocks. Therefore, it is extremely important to install the necessary confining members in masonry structures to bolster the resistance not only to single earthquakes but also to multiple successive earthquakes, thereby effectively reducing the probability of failure of structures subjected to single earthquakes or mainshock-aftershock sequences.
- 4) With the increase in PGA and aftershock scaling factor δ , the PE value of each damage limit state of the structures increases. Taking $\text{PGA} = 0.8\text{ g}$ as an example, when $\delta = 0.4, 0.6, 0.8$ and 1 , the PE values of the collapse limit state (LS-4) of the CM model are 0.17, 1.57, 6.06, and 21.11%, respectively, while those of the URM model are 20.06, 42.71, 64.02, and 74.18%, indicating that the aftershock scaling factor affects the fragility of single-story masonry structures to some extent. It can also be seen that the aftershock scaling factor δ has a significant influence on the URM model for the lack of confining members.
- 5) The present study only uses the relatively simple replication method to construct mainshock-aftershock sequences. The attenuation relationship between mainshock and aftershock should also be investigated in depth based on as-recorded mainshock-aftershock sequences, to further develop reasonable methods for constructing rational mainshock-aftershock sequence-type ground motions. In addition, it is necessary to study the seismic performance and fragility of structures of various forms subjected to mainshock, aftershock and mainshock-aftershock sequences. The present study provides a theoretical reference for the seismic design and performance improvement of masonry structures.

DATA AVAILABILITY STATEMENT

The datasets presented in this article are not readily available because embargo reason. Requests to access the datasets should be directed to Hao Zhang, h_zhang@sjzu.edu.cn.

AUTHOR CONTRIBUTIONS

Conceptualization, HZ and TS. Methodology, HZ and S-WH. Software, Q-MG Formal analysis, S-WH and XL. Data curation, Q-MG and XL. Writing—original draft preparation, Q-MG and TS. Writing—review and editing, HZ. Project administration, HZ. Funding acquisition, HZ. All authors have read and agreed to the published version of the manuscript.

FUNDING

The authors are grateful for the financial support from the National Key R&D Program of China (2018YFD1100402) and the State Key Program of the National Natural Science Foundation of China (51738007) for carrying out this research.

REFERENCES

1. Zhang H, Li C, Wang ZF, and Zhang CY. Seismic Performance Assessments of Precast Energy Dissipation Shear wall Structures under Earthquake Sequence Excitations. *Earthquakes and Structures* (2020) 18(2):147–62. doi:10.12989/eas.2020.18.2.147
2. Qu CX, Li HN, Huo LS, and Yi TH. Optimum Value of Negative Stiffness and Additional Damping in the Civil Structures. *ASCE J Struct Eng* (2017) 143(8): 04017068. doi:10.1061/(asce)st.1943-541x.0001805
3. Li H-N, Qu C, Huo L, and Nagarajaiah S. Equivalent Bilinear Elastic Single Degree of freedom System of Multi-Degree of freedom Structure with Negative Stiffness. *J Sound Vibration* (2016) 365:1–14. doi:10.1016/j.jsv.2015.11.005

4. Qu C, Huo L, Li H, and Wang Y. A Double Homotopy Approach for Decentralized Hoo Control of Civil Structures. *Struct Control Health Monit* (2014) 21(3):269–81. doi:10.1002/stc.1552
5. Gross JL, and Phan LT. *Implications for Earthquake Risk Reduction in the United States from the Kocaeli, Turkey, Earthquake of August 17, 1999*. Reston, VA, United States: ASCE World Structural Engineering Conference (2000).
6. Yeo GL, and Cornell CA. *Stochastic Characterization and Decision Bases under Time-dependent Aftershock Risk in Performance-Based Earthquake Engineering*. Berkeley, CA: Pacific Earthquake Engineering Research Center (2005).
7. Zheng Y, Ni S, Xie Z, Lv J, Ma H, and Sommerville P. Strong Aftershocks in the Northern Segment of the Wenchuan Earthquake Rupture Zone and Their Seismotectonic Implications. *Earth Planet Sp* (2010) 62:881–6. doi:10.5047/eps.2009.06.001
8. Tiwari B, Wartman J, and Pradel D. *Slope Stability Issues after Mw 9.0 Tohoku Earthquake*. San Diego, California, United States: Geo-congress (2013). p. 3–7.
9. Lim BJM, and Leong EC. Characteristics of Landslides Induced by the 25 April 2015 M7.8 Nepal Earthquake. *Geotechnical Earthquake Eng Soil Dyn* (2018) 291:64–78. doi:10.1061/9780784481462.007
10. Song R, Li Y, and Lindt JVD. Consideration of Mainshock-Aftershock Sequences into Performance-Based Seismic Engineering. *Structures Congress* (2013) 2161–7. doi:10.1061/9780784412848.189
11. Li Y, Song RL, and Lindt JVD. Collapse Fragility of Steel Structures Subjected to Earthquake Mainshock-Aftershock Sequences. *J Struct Eng* (2014) 140: 04014095. doi:10.1061/(asce)st.1943-541x.0001019
12. Nazari N, Lindt JVD, and Li Y. Quantifying Changes in Structural Design Needed to Account for Aftershock hazard. *J Struct Eng* (2015) 141:04015035. doi:10.1061/(asce)st.1943-541x.0001280
13. Goda K, and Taylor CA. Effects of Aftershocks on Peak Ductility Demand Due to strong Ground Motion Records from Shallow Crustal Earthquakes. *Earthquake Eng Struct Dyn* (2012) 41:2311–30. doi:10.1002/eqe.2188
14. Hosseinpour F, and Abdelnaby AE. Effect of Different Aspects of Multiple Earthquakes on the Nonlinear Behavior of RC Structures. *Soil Dyn Earthquake Eng* (2017) 92:706–25. doi:10.1016/j.soildyn.2016.11.006
15. Wang Z, Pang Y, and Yuan W. Fragility Analysis of a Continuous Gird Bridge Subjected to a Mainshock-Aftershock Sequence Considering Deterioration. *Structures Congress* (2017) 36–47. doi:10.1061/9780784480403.004
16. Zhang H, Li C, and Jiang SM. Fragility Analysis of Concrete-filled Steel Tubular Frame Structures with BRBs under Multiple Earthquakes Considering Strain Rate Effects. *Appl Sci* (2020) 10:165. doi:10.3390/app10010165
17. Salami MR, Kashani MM, and Goda K. Influence of Advanced Structural Modeling Technique, Mainshock-Aftershock Sequences, and Ground-Motion Types on Seismic Fragility of Low-Rise RC Structures. *Soil Dyn Earthquake Eng* (2019) 117:263–79. doi:10.1016/j.soildyn.2018.10.036
18. Pang R, Xu B, Zhou Y, Zhang X, and Wang X. Fragility Analysis of High CFRDs Subjected to Mainshock-Aftershock Sequences Based on Plastic Failure. *Eng Structures* (2020) 206:110152. doi:10.1016/j.engstruct.2019.110152
19. Zhao C, Yu N, Peng T, Gautam A, and Mo YL. Vulnerability Assessment of AP1000 NPP under Mainshock-Aftershock Sequences. *Eng Structures* (2020) 208:110348. doi:10.1016/j.engstruct.2020.110348
20. Han R, Li Y, and Lindt JVD. Loss Estimation of Reinforced concrete Buildings Considering Aftershock Hazards. *Structures Congress* (2015) 2174–85. doi:10.1061/9780784479117.188
21. Nazari N, Lindt JVD, and Li Y. Effect of Mainshock-Aftershock Sequences on wood Frame Building Damage Fragilities. *J Perform Constructed Facil* (2015) 29:04014036. doi:10.1061/(asce)cf.1943-5509.0000512
22. Southeast University; Tongji University; Zhengzhou University. *Masonry Structure*. 3rd. Beijing, China: China Architecture & Building Press (2013).
23. Zhao B, Taucer F, and Rossetto T. Field Investigation on the Performance of Building Structures during the 12 May 2008 Wenchuan Earthquake in China. *Eng Structures* (2009) 31(8):1707–23. doi:10.1016/j.engstruct.2009.02.039
24. Bessason B, Bjarnason JO, and Rupakhetty R. Statistical Modelling of Seismic Vulnerability of RC, Timber and Masonry Buildings from Complete Empirical Loss Data. *Eng Structures* (2020) 209:109969. doi:10.1016/j.engstruct.2019.109969
25. Biglari M, and Formsano A. Damage Probability Matrices and Empirical Fragility Curves from Damage Data on Masonry Buildings after Sarpol-E-Zahab and Bam Earthquakes of Iran. *Front Built Environ* (2020) 6:1–12. doi:10.3389/fbuil.2020.00002
26. Gaudio CD, Martino GD, and Ludovico MD. Empirical Fragility Curves for Masonry Buildings after the 2009 L'Aquila, Italy, Earthquake. *Bull earthquake Eng* (2019) 17:6301–30. doi:10.1007/s10518-019-00683-4
27. Saloustros S, Pelà L, Contrafatto FR, Roca P, and Petromichelakis I. Analytical Derivation of Seismic Fragility Curves for Historical Masonry Structures Based on Stochastic Analysis of Uncertain Material Parameters. *Int J Architectural Heritage* (2019) 13:1142–64. doi:10.1080/15583058.2019.1638992
28. Chellappa S, and Dubey RN. Performance Evaluation of a Reinforced Masonry Model and an Unreinforced Masonry Model Using a Shake Table Testing Facility. *J Perform Constructed Facil* (2018) 32:04017121. doi:10.1061/(asce)cf.1943-5509.0001119
29. Bagheri B, Lee J-H, Kim H-G, and Oh S-H. Experimental Evaluation of the Seismic Performance of Retrofitted Masonry walls. *Compos Structures* (2020) 240:111997. doi:10.1016/j.compstruct.2020.111997
30. Ghezlbash A, Beyer K, Dolatshahi KM, and Yekrangnia M. Shake Table Test of a Masonry Building Retrofitted with Shotcrete. *Eng Structures* (2020) 219: 110912. doi:10.1016/j.engstruct.2020.110912
31. Qu C-X, Yi T-H, Li H-N, and Chen B. Closely Spaced Modes Identification through Modified Frequency Domain Decomposition. *Measurement* (2018) 128:388–92. doi:10.1016/j.measurement.2018.07.006
32. Kaushik HB, Rai DC, and Jain SK. Stress-strain Characteristics of clay brick Masonry under Uniaxial Compression. *J Mater Civ Eng* (2007) 19:728–39. doi:10.1061/(asce)0899-1561(2007)19:9(728)
33. National Standards of the People's Republic of China. Code for Design of Concrete Structures; *GB 50010-2010*. Beijing, China: Standards Press of China (2010).
34. Han RL, Li Y, and Lindt JVD. Assessment of Seismic Performance of Buildings with Incorporation of Aftershocks. *J Perform Constructed Facil* (2015) 29: 04014088. doi:10.1061/(asce)cf.1943-5509.0000596
35. Zhai C-H, Wen W-P, Li S, Chen Z, Chang Z, and Xie L-L. The Damage Investigation of Inelastic SDOF Structure under the Mainshock-Aftershock Sequence-type Ground Motions. *Soil Dyn Earthquake Eng* (2014) 59:30–41. doi:10.1016/j.soildyn.2014.01.003
36. Hatzigeorgiou GD, and Beskos DE. Inelastic Displacement Ratios for SDOF Structures Subjected to Repeated Earthquakes. *Eng Structures* (2009) 31: 2744–55. doi:10.1016/j.engstruct.2009.07.002
37. Li Q, and Ellingwood BR. Performance Evaluation and Damage Assessment of Steel Frame Buildings under Main Shock-Aftershock Earthquake Sequences. *Earthquake Eng Struct Dyn* (2010) 36:405–27. doi:10.1002/eqe.667
38. Mackie K, and Stojadinović B. Fragility Basis for California Highway Overpass Bridge Seismic Decision Making; *PEER Report No. 2005/02*; Pacific Earthquake Engineering Research Center. Berkeley, CA, USA: University of California (2005).
39. Cornell CA, Jalayer F, Hamburger RO, and Foutch DA. Probabilistic Basis for 2000 SAC Federal Emergency Management Agency Steel Moment Frame Guidelines. *J Struct Eng* (2002) 128:526–33. doi:10.1061/(asce)0733-9445(2002)128:4(526)

Conflict of Interest: The authors declare that the research was conducted in the absence of any commercial or financial relationships that could be construed as a potential conflict of interest.

Copyright © 2021 Zhang, Sun, Hou, Gao and Li. This is an open-access article distributed under the terms of the Creative Commons Attribution License (CC BY). The use, distribution or reproduction in other forums is permitted, provided the original author(s) and the copyright owner(s) are credited and that the original publication in this journal is cited, in accordance with accepted academic practice. No use, distribution or reproduction is permitted which does not comply with these terms.



Experimental Study on Influence of Temperature to Control Performance for Viscoelastic Materials Pounding Tuned Mass Damper

Dehui Ye^{1,2†}, Jie Tan^{1,2*†}, Yabin Liang^{1,2} and Qian Feng^{1,2*}

¹Key Laboratory of Earthquake Early Warning, Institute of Seismology, China Earthquake Administration, Wuhan, China, ²Wuhan Institute of Earthquake Engineering Co. Ltd., Wuhan, China

OPEN ACCESS

Edited by:

Liang Ren,
Dalian University of Technology, China

Reviewed by:

Qingzhao Kong,
Tongji University, China
Ning Zhao,
Sichuan Agricultural University, China
Dongdong Chen,
Nanjing Forestry University, China

*Correspondence:

Jie Tan
tanjie@hust.edu.cn
Qian Feng
fengqian@eqhb.gov.cn

[†]These authors have contributed
equally to this work and share first
authorship

Specialty section:

This article was submitted to
Smart Materials,
a section of the journal
Frontiers in Materials

Received: 05 March 2021

Accepted: 18 May 2021

Published: 31 May 2021

Citation:

Ye D, Tan J, Liang Y and Feng Q (2021)
Experimental Study on Influence of
Temperature to Control Performance
for Viscoelastic Materials Pounding
Tuned Mass Damper.
Front. Mater. 8:676405.
doi: 10.3389/fmats.2021.676405

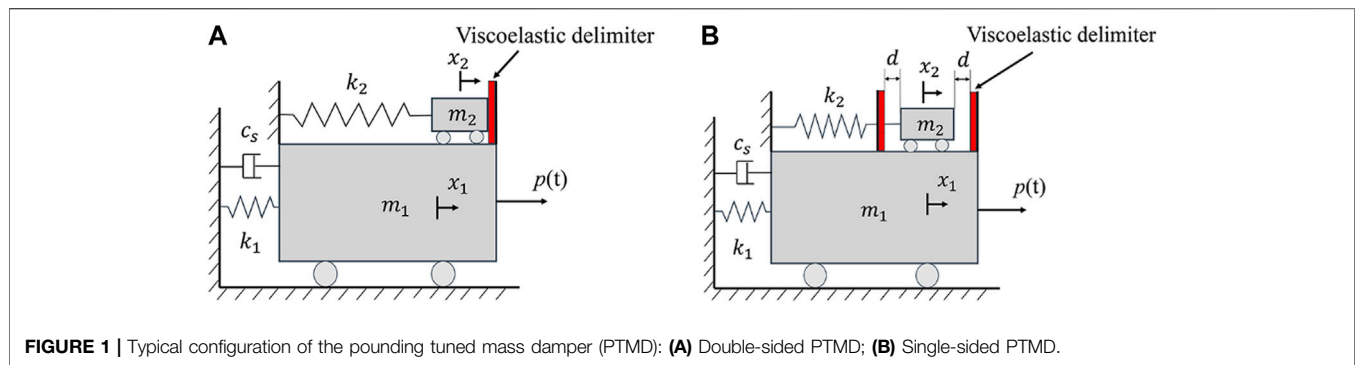
The pounding tuned mass damper (PTMD) is a novel passive damper that absorbs and dissipates energy by an auxiliary tuned spring-mass system. Viscoelastic materials are attached to the interface of the limitation collar in the PTMD so that the energy dissipation capacity can be enhanced. Previous studies have successfully demonstrated the effectiveness of PTMD at room temperature. However, in practice, the PTMD may face a broad temperature range, which can affect the mechanical properties of the viscoelastic materials. Thus, the study of vibration control effectiveness of PTMD at different temperatures is of great significance for its practical engineering application. In this paper, a series of experiments were conducted to investigate the performance of a PTMD in a temperature-controlled environment. A PTMD device was designed to suppress the vibration of a portal frame structure and tested across environmental temperatures ranging from -20°C to 45°C . The displacement reduction ratios demonstrated the temperature robustness of the PTMD. Additionally, the numerical results validated the accuracy of the pounding force model and the performance of PTMD.

Keywords: pounding tuned mass damper, viscoelastic material, temperature variation, structural damping, structural vibration control

INTRODUCTION

It is nearly impossible for the engineers to fully predict the excitations of structures throughout their entire service lives (Shirai et al., 2019; Cai et al., 2020). Overdesigning the structure against all possible disturbances is often impractical and prohibitively expensive (Li et al., 2007; Ou et al., 2007; Zhang and Ou, 2008). Structural vibration control is a safe and economical approach to protect structures against severe disturbances such as expected in natural disasters (Xu et al., 2011; Teng et al., 2016; Wang et al., 2017a; Zhang et al., 2017; Tan et al., 2020). Such control can be accomplished through passive devices such as the pounding tuned mass damper (PTMD).

The PTMD is a novel and effective structure control technique, which can dissipate energy through an internal collision mechanism. The PTMD was first reported by Zhang et al. (Zhang et al., 2013) in 2013. The configuration and schematic of the typical PTMD proposed by Zhang et al. is illustrated in **Figure 1A**. In the PTMD, a mass is connected to the host structure by a spring, and the natural frequency of the spring-mass system is tuned closely to that of the host structure by changing the stiffness of the spring. The displacement of the tuned mass is restricted by two delimiters. The spring-mass system consumes energy similar to a tuned mass damper (TMD) when the displacement



is small; however, when the displacement is large enough to induce collision between the mass and the delimiter, the PTMD effectively dissipates energy beyond the capacity of a TMD. In order to improve the vibration suppression capacity during the impact, an energy-dissipation material is bonded to the delimiters.

Since then, researchers have demonstrated a wide range of applications for the PTMD and its remarkable effectiveness. Li et al. (Li et al., 2015) employed a PTMD to suppress the wind-induced vertical buffeting response of a traffic signal pole. The PTMD caused the damping ratios of the vertical vibration to increase to 4% from 1%. Allen et al. (Allen et al., 2016) employed PTMDs to control the vibrations of a submerged jumper. The seismic control performance of the PTMD was investigated by Xue et al. (Xue et al., 2016; Xue et al., 2017). A parameter study and impact fatigue of double-sided PTMD was performed by Zhang et al. (Zhang et al., 2015; Zhang et al., 2018). They found that the response is influenced by the mass ratio, the exciting force, and the gap between mass and the delimiters. These studies all showed the effective vibration control performance and robustness of the PTMD.

Based on the original double-sided PTMD, Wang et al. (Wang et al., 2017c) proposed a novel single-sided PTMD as shown in **Figure 1B**. In the single-sided PTMD, the tuned mass is set at the equilibrium position and is contact with energy-dissipation material. When the main mass begins to move due to external excitation, the tuned mass will impact the delimiter and dissipate kinetic energy during the collision. As shown by Zhang et al. (Zhang et al., 2015), the reduction ratio of the PTMD is related to many parameters including the mass ratio, the gap between the delimiter, and the pounding stiffness. The design of the single-sided PTMD does not require careful tuning of the gap between the mass the delimiter, thus affording it several significant advantages, such as a simple structure and ease of design. In addition, pounding in a single-sided PTMD occurs at the location where collisions occur at the highest velocity, which translates to high effectiveness and efficiency in the pounding mechanism. Furthermore, the tuned mass only moves toward one side, thereby opening up half of the working space, and improving the range of its applications.

The single-sided PTMD has been investigated through many theoretical and experimental studies. Wang et al. (Wang et al., 2017b; Wang et al., 2017c; Wang et al., 2018a; Wang et al., 2018b;

Wang et al., 2019) studied single-sided the optimum PTMD design, including its control performance and impact force modelling through experiments and simulations. Tan et al. (Tan et al., 2019a; Tan et al., 2019b) designed a novel single-sided PTMD to control the vibration of a suspended piping system, and compared the control performances between PTMDs using viscoelastic materials versus shape memory alloy (SMA) sponges as the energy dissipating material.

Viscoelastic materials are extensively utilized as energy dissipating components due to their excellent combination of high energy dissipation capacity, low cost, and ease of manufacturing (Feng et al., 2018; Feng et al., 2020). However, a drawback of viscoelastic materials is that their mechanical properties are strongly influenced by temperature (Bergman and Hanson, 1993; Guo et al., 2009; Bhatti, 2013). In recent decades, extensive experimental and theoretical investigations on the mechanical properties of viscoelastic materials have been conducted (Zhong et al., 2017). Zhang et al. (Zhang et al., 2019) compared pounding stiffness and pounding damper ratio of viscoelastic materials between room temperature and 2°C, found that the pounding mechanical properties of viscoelastic materials changed considerably under different temperature conditions. At low temperatures, viscoelastic materials are in a glassy state, which is characterized by having a high modulus, a small loss factor and brittleness. In the glassy state, the viscoelastic material is typically destroyed when strain rate exceeds 5%. With the increase of temperature, materials return to the viscoelastic region, where the loss factor is the highest. As the temperature continues to rise, viscoelastic materials will be transformed into a highly elastic state, whereupon the shear modulus and loss factor begin to decrease.

When considering the effects of temperature, the shear modulus and loss factor are used to describe the properties of viscoelastic dampers. However, the pounding process has a high strain rate, which is different from the shear process. Therefore, to describe the properties of PTMD and analyze the structural dynamic responses with when the structure is equipped with the added PTMD, experiments are required. The parameters to demonstrate the mechanical properties of the pounding process are the pounding stiffness and the pounding damping, both of which are mostly neglected in prior literature.

Consequently, this paper presents an experimental study on the control performance for a PTMD over a wide range of

temperatures. First, a single-sided PTMD is designed to control a single degree of freedom structure. The movement of the structure during free vibration and forced vibration are used to validate the effectiveness. Then, control tests are conducted repeatedly from -20°C to 45°C in temperature-controlled environment. The experimental results demonstrate the PTMD has a good temperature robustness and show that the control performance of PTMD can be gauged into three stages when the temperature increases. The originality of this work is that the vibration reduction performance of viscoelastic materials PTMD is experimentally studied within a wide temperature range. The results are significant for design and application of viscoelastic materials PTMD.

THEORETICAL FOUNDATION

In this section, the related theoretical foundations of PTMD are briefly introduced, including structure-PTMD coupled equation of motion and the pounding force model. In addition, the effect of temperature on viscoelastic materials is described subsequently.

Structure-PTMD Coupled Equation of Motion

A structure with PTMD is modelled in **Figure 1B**. The mass, stiffness, damping coefficient of structure are respectively denoted by m_1 , k_1 , c_s . The mass and stiffness of the PTMD are represented by a spring of stiffness m_2 , k_2 , respectively. The displacement of the main structure and tuned mass are x_1 , x_2 , respectively. Considering the coupling between the single-degree-of-freedom structure and the PTMD, the equations of motion for the whole, integrated system can be written as in **Eq (1)**:

$$M\ddot{x} + C\dot{x} + Kx = P + \Gamma F \quad (1)$$

where \ddot{x} , \dot{x} , x , represent acceleration, velocity, displacement, respectively. M , C , K are mass matrix, damping matrix, stiffness matrix, respectively, P is the load matrix applied to the structure, F is the pounding force, and Γ is the pounding force position. The parameters are expanded in **Eq (2)** to **Eq (4)**:

$$\ddot{x} = \begin{bmatrix} \ddot{x}_1 \\ \ddot{x}_2 \end{bmatrix}, \dot{x} = \begin{bmatrix} \dot{x}_1 \\ \dot{x}_2 \end{bmatrix}, x = \begin{bmatrix} x_1 \\ x_2 \end{bmatrix}, P = \begin{bmatrix} p \\ 0 \end{bmatrix} \quad (2)$$

$$M = \begin{bmatrix} m_1 & 0 \\ 0 & m_2 \end{bmatrix}, C = \begin{bmatrix} c_s & 0 \\ 0 & 0 \end{bmatrix}, K = \begin{bmatrix} k_1 + k_2 & -k_2 \\ -k_2 & k_2 \end{bmatrix} \quad (3)$$

$$\Gamma = \begin{bmatrix} -\gamma \\ \gamma \end{bmatrix}, \gamma = \begin{cases} 1, & x_2 - x_1 > 0 \\ 0, & x_2 - x_1 \leq 0 \end{cases} \quad (4)$$

Pounding Force Model

A linear viscoelastic model has been proposed to describe the contacting force F of viscoelastic impacts (Goldsmith, 1960; Anagnostopoulos, 1988; Jankowski et al., 1998; Anagnostopoulos, 2004), and is given by **Eqs (5,6)**:

$$F = \beta\delta + c\dot{\delta} \quad (5)$$

$$\delta = x_1 - x_2, \dot{\delta} = \dot{x}_1 - \dot{x}_2 \quad (6)$$

where δ , $\dot{\delta}$, β represent the relative displacement of the colliding body, the relative velocity, the pounding stiffness, and the pounding damping, respectively. The pounding stiffness can be obtained using the displacement and the pounding force recorded in the impact test. The pounding damping c can be computed by **Eq (7)**:

$$c = 2\xi\sqrt{\beta\frac{m_1m_2}{m_1+m_2}} \quad (7)$$

where m_1 and m_2 are the masses of two colliding bodies, ξ is impact damping ratio, which is related to the coefficient of restitution e in **Eq (8)**:

$$\xi = \frac{-\ln e}{\sqrt{\pi^2 + (\ln e)^2}} \quad (8)$$

However, the linear viscoelastic model may produce a negative force at the end of impact, which is not consistent with experimental observation (Jankowski, 2005). Subsequently, a modified linear viscoelastic model (Mahmoud and Jankowski, 2011), divides the pounding into two individuals periods and assumes that energy loss only happens when the material experiences compression, is given by **Eq (9)**:

$$F = \begin{cases} \beta\delta + c\dot{\delta}, & \dot{\delta} > 0 \\ \beta\delta, & \dot{\delta} \leq 0 \end{cases} \quad (9)$$

where c has same form as in **Eq (7)**, and the pounding damping ratio ξ can be calculated in **Eq (10)**:

$$\xi = \left(\frac{1 - e^2}{e[e(\pi - 2) + 2]} \right) \quad (10)$$

Given its simplicity, the modified linear viscoelastic model can be easily implemented for numerical simulations. However, at the beginning of impact, a sudden rise of impact force may occur as a result of nonzero relative velocity. In order to overcome disadvantages of the modified linear viscoelastic model, a nonlinear viscoelastic model was introduced by Jankowski (Jankowski, 2005;2006). And it is expressed in **Eq (11)**:

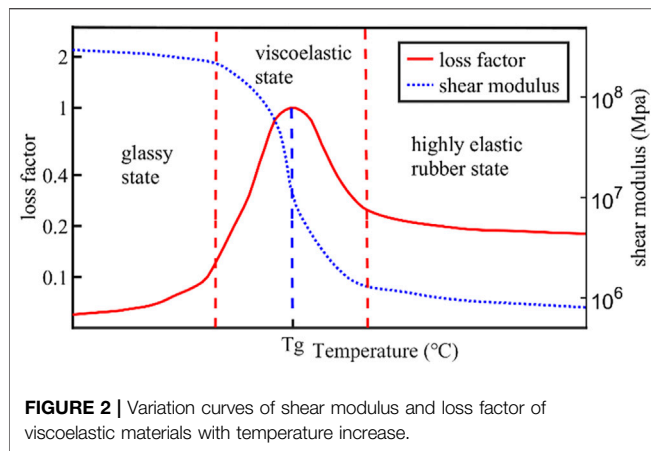
$$F = \begin{cases} \beta\delta^{3/2} + c\dot{\delta}, & \dot{\delta} > 0 \\ \beta\delta^{3/2}, & \dot{\delta} \leq 0 \end{cases} \quad (11)$$

where c has the form in **Eq (12)**:

$$c = 2\xi\sqrt{\beta\sqrt{\delta}\frac{m_1m_2}{m_1+m_2}} \quad (12)$$

where the pounding damping ratio ξ can be calculated by **Eq (13)**:

$$\xi = \frac{9\sqrt{5}}{2} \frac{1 - e^2}{e[e(9\pi - 16) + 16]} \quad (13)$$



Temperature Effect of Viscoelastic Materials

The influence of temperature on the behavior of viscoelastic layers, viscoelastic dampers and structures with viscoelastic dampers were analyzed by many researchers (Chang et al., 1992; Park and Min, 2010; Guo et al., 2016). In one of their works, Chang et al. (Chang et al., 1992) tested a simple solid viscoelastic damper at different ambient temperatures and established empirical formulas that described the temperature dependence of the damper and loss factor. Previous studies (Tsai, 1994; Park and Min, 2010; Guo et al., 2016) have shown that different kinds of viscoelastic materials have similar dependencies on temperature, but differ in the specifics. **Figure 2** shows the typical changes of shear modulus and loss factor of viscoelastic materials to changes in temperature. Note that T_g is the transition temperature of viscoelastic materials.

The figure indicates that the shear modulus and loss factor of viscoelastic materials change with temperature, and viscoelastic materials have high damping in the characteristic temperature range. Additionally, the changes can be divided into three phases:

- (1) At low temperature, the viscoelastic materials are in the glassy state. The material molecules undergo ordinary elastic deformation under the action of external force, and the material possesses high rigidity, high modulus and small loss factor;
- (2) With the increase of the temperature, the materials return to viscoelastic state. The modulus of materials decreases sharply by several orders of magnitude. The loss factor also changes greatly and passes through a peak value (i.e. damping peak), which is equivalent to the maximum loss factor at the glass transition temperature. This transition zone is usually the temperature at which most viscoelastic materials are used.
- (3) At high temperature, the viscoelastic materials are in the highly elastic rubber state. The modulus value is small, the loss factor is moderate. Both the modulus and loss factor of materials change slowly as the temperature increases.

Despite the known features described above, the relationship between the pounding stiffness β , pounding damping ratio ξ and temperature, impact velocity, impact materials are rarely studied and need to be investigated.

EXPERIMENTAL SETUP

The experimental system consists of three parts: the experimental device and equipment, a portal frame, and a specially designed single-sided PTMD.

In the experiment, a portal frame with a single degree of freedom served as the primary structure, a PTMD was designed to control the displacements of the frame. The forced vibration experiments were conducted at temperature conditions ranging from -20°C to 45°C . The detail of temperatures in the experiment are listed in **Table 1**.

Experimental Device and Equipment

Figure 3A shows the experimental device and equipment. A noncontact laser displacement sensor (HG-C1400, Panasonic Industrial Devices, China) measured the displacements of the frame. A data acquisition board (NI USB-6363, National Instruments, USA) recorded sensor signals at a sampling frequency of 1 kHz. An eccentric motor (JGB37-3650, Xytmotor, China) fixed to the frame provided the exciting force.

As shown in **Figure 3B**, the temperature experiment is carried out in the temperature-controlled room (MW-BD1824, Ziweiheng testing equipment, China). The temperature of the room can be adjusted from -20°C to 50°C .

Portal Frame

As shown in **Figure 4**, the portal frame is composed of an aluminum block, two spring steel columns, and an aluminum plate base. The detailed parameters of the portal frame are listed in **Table 2**. The aluminum block is served as the main structural mass. Spring steels served as structural columns because of its high fatigue performance and high elasticity. The base fixes the portal frame to the ground. The free vibration experiment was conducted by applying an initial displacement to the portal frame and releasing. The experimental result shows that the equivalent viscous damping ratio is 0.29%.

A motor is attached to the top of the frame. A quasi-periodic disturbance is generated when the motor rotates. The generated frequency can be controlled by adjusting the excitation voltage motor. In the forced vibration experiments, the structure was

TABLE 1 | Experimental conditions.

Condition (No.)	1	2	3	4	5	6	7	8
Temperature/ $^{\circ}\text{C}$	-20	-17.5	-15	-12.5	-10	-8.5	-6.5	-5
Condition (No.)	9	10	11	12	13	14	15	16
Temperature/ $^{\circ}\text{C}$	-2.5	0	1.5	3.5	5	6.5	8.5	10
Condition (No.)	17	18	19	20	21	22	23	24
Temperature/ $^{\circ}\text{C}$	11.5	13.5	15	16.5	18.5	20	22.5	25
Condition (No.)	25	26	27	28	29	30	31	32
Temperature/ $^{\circ}\text{C}$	27.5	30	32.5	35	37.5	40	42.5	45

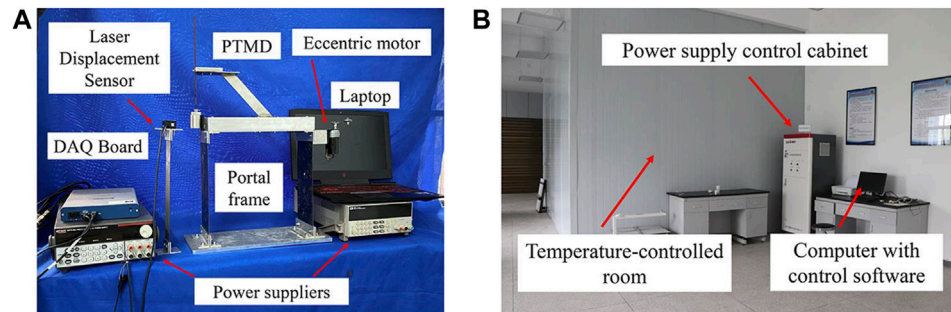


FIGURE 3 | (A) Experimental device and equipment; (B) Temperature-controlled lab.

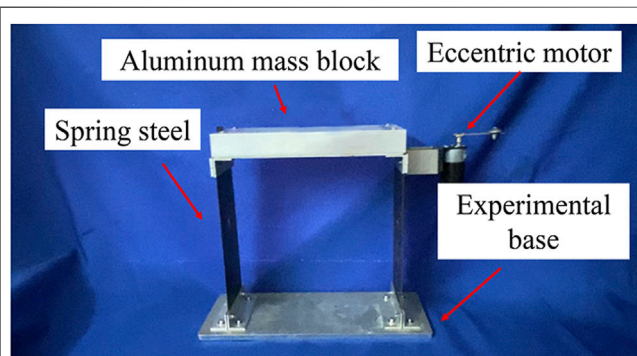


FIGURE 4 | Portal frame and its components.

excited at twenty different sweep frequency conditions ranging from 2.6Hz to 5Hz. The experimental results indicate that portal frame reaches the maximum displacement when the excitation frequency is 3.13Hz.

Design of PTMD

As shown in **Figure 5**, the single-sided PTMD consists of mass block, spring steel, and a viscoelastic delimiter (EVA sponge, produced by 3M). An aluminum pole connects the PTMD to the portal frame. To avoid affecting the dynamic characteristics of the structure, the pole of the PTMD consisted of aluminum. The optimum frequency of the PTMD, f_{op} , is designed using following formula(Wang et al., 2018a):

$$f_{op} = \frac{1}{2} f_d \quad (14)$$

where f_d is the natural frequency of the main structure.

The weight of the tuned masses is 246g, and the corresponding mass ratio is 4.7%. A coupon of spring steel connected the tuned mass to the PTMD body. This design is an update of prior designs in which a nylon rope served as the connector and sometimes suffer from circular, out-of-plane motions (Tan et al., 2019b).

EXPERIMENTAL RESULTS AND ANALYSIS

Preliminary Test of PTMD at Room Temperature

At first, the free vibration and forced vibration experiments with and without PTMD control were carried out at room temperature (18°C).

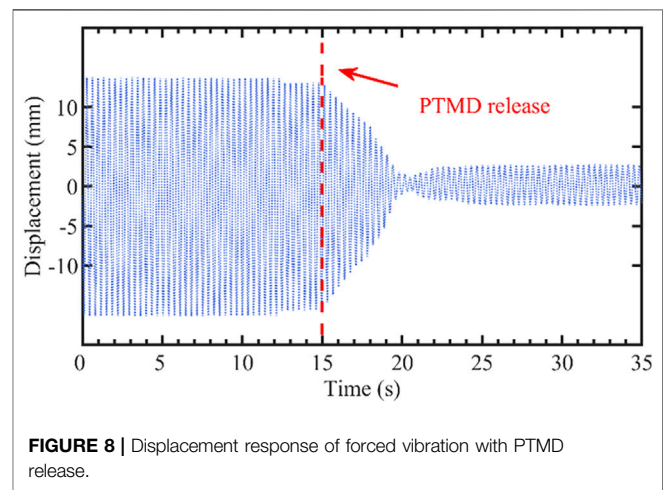
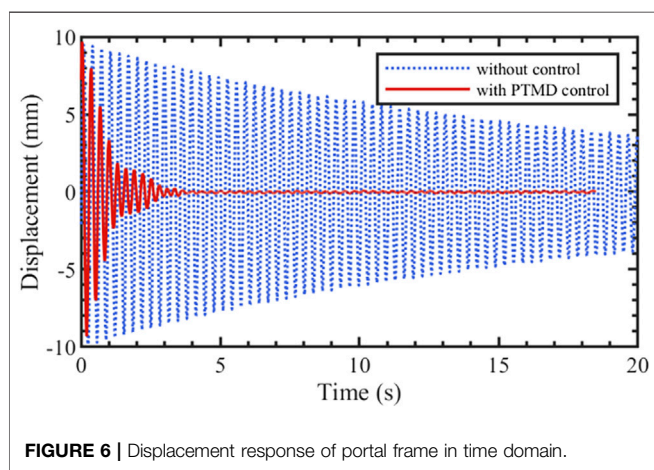
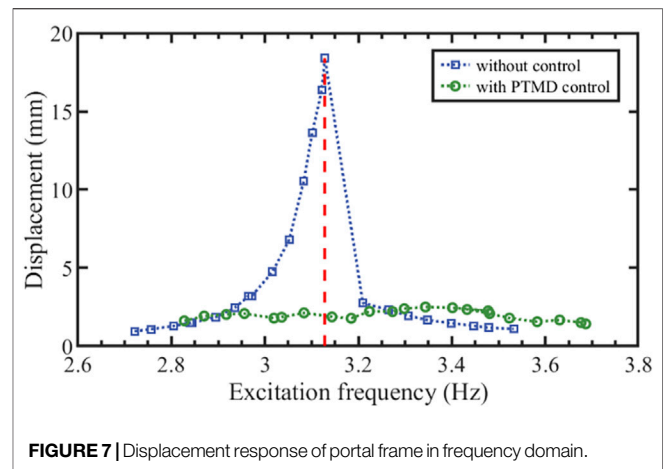
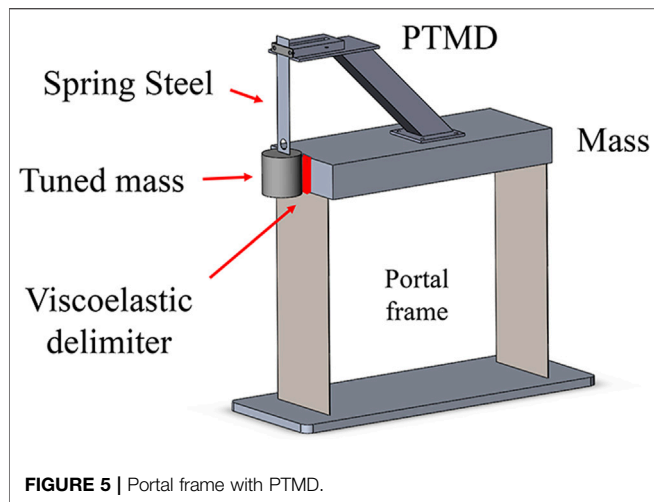
Figure 6 shows the free vibration of the portal frame with and without PTMD control. With PTMD control, the displacement of the frame rapidly reduced to a very small level compared to the case without control. The time taken to suppress the displacement from 10mm to 2mm reduced from 57.4s to 1.19s. The damping ratio of the system is correspondingly increased from 0.29% to 4.4%.

The displacements during forced vibration experiment are shown in **Figure 7**. The blue line describes the frequency response of the portal frame with PTMD control. The frequency response curve only has one peak at 3.13Hz, and the maximum displacement is 18.43mm, which occurred on the right side of the uncontrolled resonance frequency. Additionally, the peak displacement of the controlled vibration is 3.26mm, which is 17.7% of the uncontrolled resonant amplitude.

Figure 8 shows the vibration response of the portal frame before and after the PTMD is released. After the release of the PTMDs, the portal frame reached a new steady state in a short

TABLE 2 | Parameters of Portal frame.

No.	Component	Length/mm	Width/mm	Thickness/mm	Weight/kg
1	Aluminum block	300	120	40	3.88
2	Spring steel columns	250	100	1	0.20
3	Aluminum plate base	400	150	10	1.62



time. The displacement amplitude decreased from 16.34mm to 2.61mm.

Experiment on the Effect of Temperature on PTMD Control

The experiment on the effect of temperature on PTMD control was carried out in the temperature-controlled room. The forced vibration test in *Preliminary test of PTMD at room temperature* was repeated at different temperatures (listed in Table 1). The maximum displacements of the structure with PTMD at different temperatures are shown in Figure 9. As can be seen in Figure 9, the control performance of PTMD can be divided to three phases. In Phase 1 (-20°C to -8.5°C), the displacement of portal frame decreased slightly from 4.4mm to 4.34mm, and the reduction ratio increased from 76.1% to 76.4%. In Phase 2 (-8.5°C to 20°C), the maximum displacement of portal frame decreased first before decreasing. The corresponding reduction ratio increased first before decreasing. The maximum displacement

decreased to 2.5mm at 10°C . In the meantime, the maximum reduction ratio reached 86.4%. In Phase 3 (20°C to 45°C), the displacement and reduction ratio remained almost constant (3.26mm and 82.3%, respectively) despite further changes in temperature.

At glassy stage, the damping effect of PTMD almost does not change obviously with temperature variation. For the viscoelastic region (-8.5°C to 20°C), the damping effect of the PTMD changes with temperature, and there is an optimal control temperature, which is around 10°C for this viscoelastic material. Between 20 – 45°C the material behaved elastically, and the damping effect of PTMD remained in a steady state.

Although the damping effect is affected at low and high temperatures, the maximum displacement of the structure can still be reduced beyond 75%. As the thermal influence on PTMD control performance can be divided to three phases, results of each phase for the forced vibration experiments are shown in Figure 10. The results shows that PTMD has a good temperature robustness.

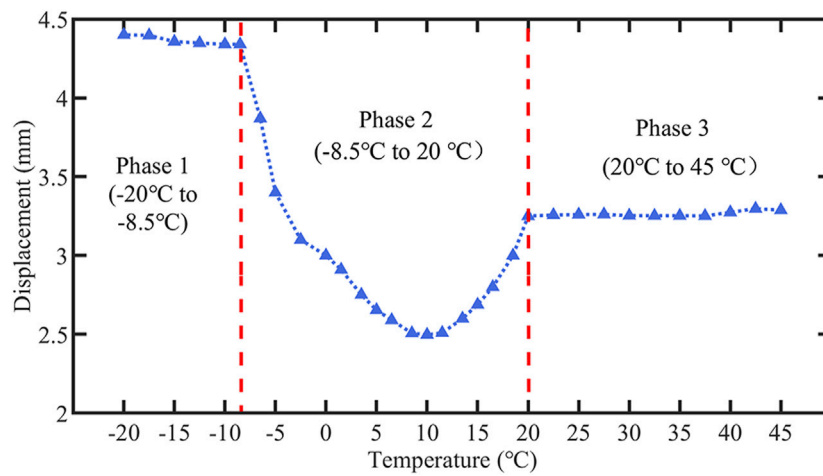


FIGURE 9 | Displacement response of portal frame in frequency domain.

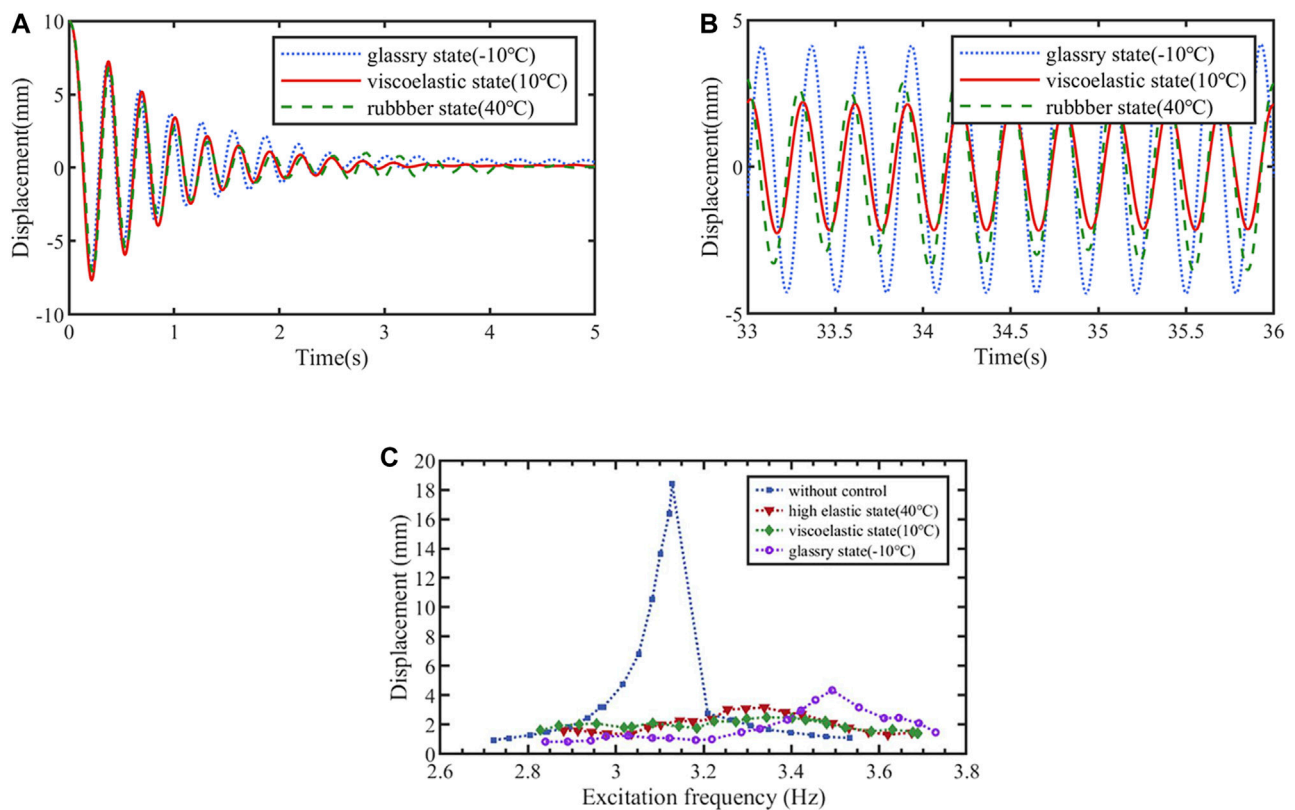


FIGURE 10 | Displacement response of the portal frame at different state: **(A)** Free vibration in time domain; **(B)** Resonant vibration in time domain; **(C)** Forced vibration in the frequency domain.

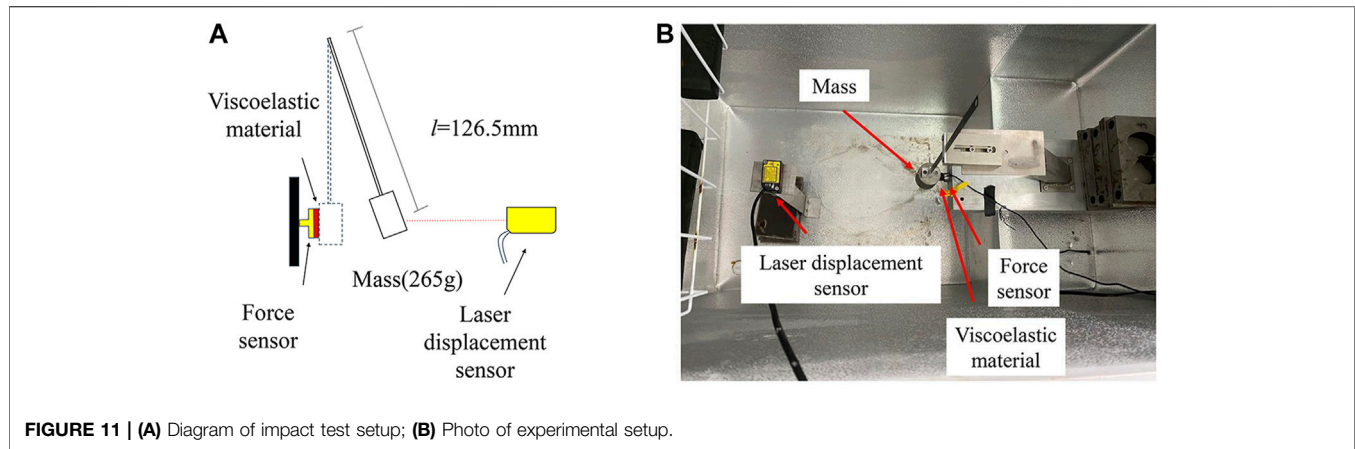


FIGURE 11 | (A) Diagram of impact test setup; (B) Photo of experimental setup.

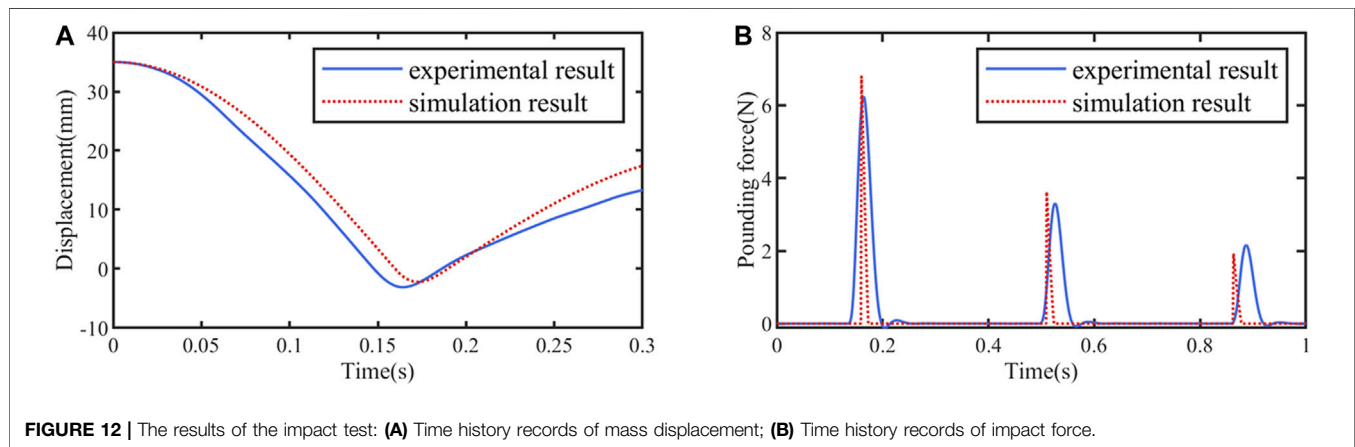


FIGURE 12 | The results of the impact test: (A) Time history records of mass displacement; (B) Time history records of impact force.

NUMERICAL RESULTS

Impact Test and Validation of the Pounding Force Model

An impact test at 18°C was carried out to study the performance of the viscoelastic material during the impact. The experimental setup is shown in Figure 11. The spring steel-mass system was the same as in *Experimental device and equipment*, and the thickness of the viscoelastic materials was also set to 7mm (2 layers). An initial displacement of 35mm was applied to the mass and then released, allowing the mass pounds the viscoelastic material freely. The displacement of the mass was recorded by a laser displacement sensor, and a force sensor was used to record the pounding force during the experiment.

The results of the impact test are shown in Figure 12. Figure 12A, B are the time history records of mass displacement and impact force, respectively. Calculated from the initial displacement (35.00mm) and the rebound displacement (15.33mm) after the first impact, the coefficient of restitution e is 0.434. Furthermore, obtained by eq (13), the pounding damping ratio ξ is 0.882. Through the force peak value (6.24N) in Figure 12B and corresponding displacement (3.12mm), the pounding stiffness β is $3.6 \times 10^4 \text{ N/m}^{1.5}$.

Ignoring the damping of the spring steel, motion equation of the mass in Figure 11 can be expressed as

$$m\ddot{x} + kx = F \quad (15)$$

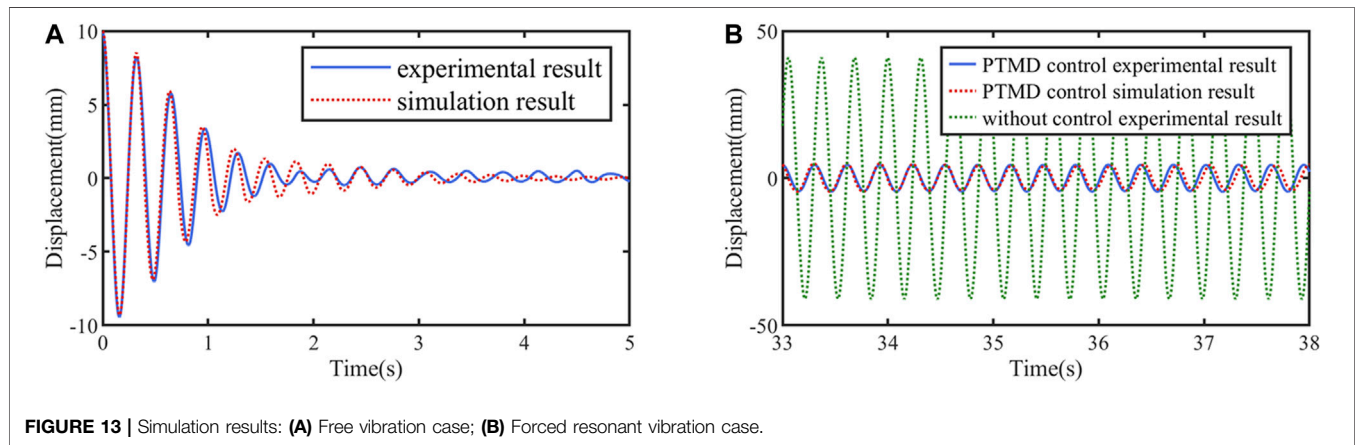
where F is the impact force, calculated by eq (11) to eq (13), m and k are mass and stiffness of the spring steel-mass system. The initial $x(0)$ was set to 35.00mm, and the pounding parameters were set as values obtained in the impact test. The fourth-order Runge-Kutta method was utilized to solve eq (15) with a time step of 1×10^{-6} s. The comparison of experimental result and simulation result is shown in Figure 12. It can be seen that the pounding model is highly accurate to predict displacement and impact force of the mass.

Numerical study on PTMD

To further validate the accuracy of the PTMD model, a simulation analysis was performed on the experimental structure with PTMD in *Experimental setup*. The motion equations of the structure with PTMD were expressed in eq (1) to eq (4), and the pounding force model was expressed in eq (11) to eq (13). In the free vibration, the excitation force $P(t) = 0$, in the forced vibration experiment, the excitation force can be calculated as follows:

TABLE 3 | Parameters of simulation.

m_1 (kg)	m_2 (kg)	c_s (N/(m/s))	k_1 (N/m)	k_2 (N/m)	β (N/m ^{1.5})	e	ξ
5.13	0.25	0.0029	19.66	9.83	3.6×10^4	0.434	0.882

**FIGURE 13** | Simulation results: (A) Free vibration case; (B) Forced resonant vibration case.

$$P(t) = m_e r^2 \sin(\omega t) \quad (16)$$

where m_e , r , ω are the eccentric mass, eccentricity, excitation frequency. In the article, $m_e = 100P(t) = m_e r^2 \sin(\omega t)g$, $r = 55\text{mm}$.

The parameters of the simulation at 18°C were derived from the results of the previous experiments and were summarized in **Table 3**. Similarly, Runge-Kutta method was utilized to solve the coupled equations, and both free vibration case and forced resonant case were simulated. The simulation results are plotted in **Figure 13**. As shown in **Figure 13A** and **Figure 13B**, the proposed coupled equations can high accurately predict dynamic response of structure with PTMD in both cases.

CONCLUSION AND FUTURE WORK

Conclusion

In this study, a single-sided pounding tuned mass damper (PTMD) was designed to mitigate the vibration of a portal frame. From experimental results, the conclusions are as follows:

- (1) A single-sided PTMD can reduce the structural dynamic response and improve the damping ratio of structure effectively;
- (2) From -20°C to 45°C , the displacement reduction ratio remained above 75%, which demonstrates the temperature robustness of the PTMD. The highest reduction ratio (86.4%) occurred at 10°C ;
- (3) The displacement reduction ratios of the PTMD are affected by temperature. With the increase of temperature, the effectiveness of PTMD can be divided into three stages. From -8.5°C to 20°C , reduction ratio is sensitive to temperature, where the ratio increases first and then decreases. The reduction ratios at -8.5°C and 20°C are 76.4% and 82.4%, respectively. Between -20°C to -8.5°C the reduction effects decrease slightly with temperature

variation, while between 20°C to 45°C , the reduction effects remained stable.

- (4) The numerical results validated the accuracy of the pounding force model and the performance of PTMD.

Future Work

The changes of parameters in pounding force model at different temperatures are vital factors for simulation and theoretical analysis of PTMD. The exploration of a wide range of temperatures impact tests to establish the damping factor vs. temperature curve will be delegated as a future work.

DATA AVAILABILITY STATEMENT

The original contributions presented in the study are included in the article/Supplementary Material, further inquiries can be directed to the corresponding authors.

AUTHOR CONTRIBUTIONS

All authors discussed and agreed upon the idea and made scientific contributions. JT and QF conceived the original idea. DY and JT designed the experiments. DY and YL conducted the experiments, and analysed the data. DY and JT wrote the paper. QF revised the paper.

FUNDING

This research is partially supported by the Scientific Research Fund of the Institute of Seismology and the Institute of Crustal Dynamics, China Earthquake Administration (Grant Number IS201616250) and the National Natural Science Foundation of China (Grant Number 51808092).

REFERENCES

- Allen, J. K., Patil, D., Ho, S. C. M., Hirsch, R., Zhang, P., Parvasi, S. M., et al. (2016). Application of the Pounding Tuned Mass Damper to a Submerged Jumper Experiencing Horizontal and Vertical Vibrations. *Earth Space* 2016. 1109–1116. doi:10.1061/9780784479971.108
- Anagnostopoulos, S. A. (1988). Pounding of Buildings in Series during Earthquakes. *Earthquake Engng. Struct. Dyn.* 16, 443–456. doi:10.1002/eqe.4290160311
- Anagnostopoulos, S. A. (2004). Equivalent Viscous Damping for Modeling Inelastic Impacts in Earthquake Pounding Problems. *Earthquake Engng. Struct. Dyn.* 33, 897–902. doi:10.1002/eqe.377
- Bergman, D. M., and Hanson, R. D. (1993). Viscoelastic Mechanical Damping Devices Tested at Real Earthquake Displacements. *Earthquake Spectra* 9, 389–417. doi:10.1193/1.1585722
- Bhatti, A. Q. (2013). Performance of Viscoelastic Dampers (VED) under Various Temperatures and Application of Magnetorheological Dampers (MRD) for Seismic Control of Structures. *Mech. Time-depend Mater.* 17, 275–284. doi:10.1007/s11043-012-9180-2
- Cai, W., Yu, B., Wu, F., and Shao, J. (2020). Seismic Response and Vibration Reduction Analysis of Suspended Structure under Wave Passage Excitation. *Adv. Civil Eng.* 2020, 1–3. doi:10.1155/2020/6468181
- Chang, K. C., Soong, T. T., Oh, S. T., and Lai, M. L. (1992). Effect of Ambient Temperature on Viscoelastically Damped Structure. *J. Struct. Eng.* 118, 1955–1973. doi:10.1061/(asce)0733-9445(1992)118:7(1955)
- Feng, Q., Fan, L., Huo, L., and Song, G. (2018). Vibration Reduction of an Existing Glass Window through a Viscoelastic Material-Based Retrofit. *Appl. Sci.* 8, 1061. doi:10.3390/app8071061
- Feng, Q., Fan, L., Cai, S., Huo, L., and Liang, Y. (2020). A New Approach to Retrofitting an Existing Roller Door by Using Viscoelastic Materials for Vibration Reduction with Experimental Verification. *Int. J. Struct. Stab. Dyn.* 20, 2040008. doi:10.1002/9781119566557
- Goldsmith, W. (1960). *Impact: The Theory and Physical Behavior of Colliding Solids*. London: E. Arnold, 28, 639. doi:10.1115/1.3641808
- Guo, Y., Meng, G., and Li, H. (2009). Parameter Determination and Response Analysis of Viscoelastic Material. *Arch. Appl. Mech.* 79, 147–155. doi:10.1007/s00419-008-0221-x
- Guo, J. W.-W., Daniel, Y., Montgomery, M., and Christopoulos, C. (2016). Thermal-mechanical Model for Predicting the Wind and Seismic Response of Viscoelastic Dampers. *J. Eng. Mech.* 142, 04016067. doi:10.1061/(asce)em.1943-7889.0001121
- Jankowski, R., Wilde, K., and Fujino, Y. (1998). Pounding of Superstructure Segments in Isolated Elevated Bridge during Earthquakes. *Earthquake Engng. Struct. Dyn.* 27, 487–502. doi:10.1002/(sici)1096-9845(199805)27:5<487::aid-eqe738>3.0.co;2-m
- Jankowski, R. (2005). Non-linear Viscoelastic Modelling of Earthquake-Induced Structural Pounding. *Earthquake Engng Struct. Dyn.* 34, 595–611. doi:10.1002/eqe.434
- Jankowski, R. (2006). Analytical Expression between the Impact Damping Ratio and the Coefficient of Restitution in the Non-linear Viscoelastic Model of Structural Pounding. *Earthquake Engng Struct. Dyn.* 35, 517–524. doi:10.1002/eqe.537
- Li, H., Liu, M., Li, J., Guan, X., and Ou, J. (2007). Vibration Control of Stay Cables of the Shandong Binzhou Yellow River Highway Bridge Using Magnetorheological Fluid Dampers. *J. Bridge Eng.* 12, 401–409. doi:10.1061/(asce)1084-0702(2007)12:4(401)
- Li, L., Song, G., Singla, M., and Mo, Y.-L. (2015). Vibration Control of a Traffic Signal Pole Using a Pounding Tuned Mass Damper with Viscoelastic Materials (II): Experimental Verification. *J. Vibration Control* 21, 670–675. doi:10.1177/1077546313488407
- Mahmoud, S., and Jankowski, R. (2011). Modified Linear Viscoelastic Model of Earthquake-Induced Structural Pounding. 35, 51–62. doi:10.1007/978-3-319-16324-6
- Ou, J., Long, X., Li, Q. S., and Xiao, Y. Q. (2007). Vibration Control of Steel Jacket Offshore Platform Structures with Damping Isolation Systems. *Eng. Structures* 29, 1525–1538. doi:10.1016/j.engstruct.2006.08.026
- Park, H.-I., and Min, C.-H. (2010). Temperature Effect on Vibration Characteristics of Viscoelastic Laminated Beam. *Int. J. Offshore Polar Eng.* 20, 118–124. doi:10.1007/s10999-010-9127-1
- Shirai, K., Nagaoka, A., Fujita, N., and Fujimori, T. (2019). Optimal Damper Slip Force for Vibration Control Structures Incorporating Friction Device with Sway-Rocking Motion Obtained Using Shaking Table Tests. *Adv. Civil Eng.* 2019.
- Tan, J., Jiang, J., Liu, M., Feng, Q., Zhang, P., and Ho, S. C. M. (2019a). Implementation of Shape Memory alloy Sponge as Energy Dissipating Material on Pounding Tuned Mass Damper: An Experimental Investigation. *Appl. Sci.* 9, 1079. doi:10.3390/app9061079
- Tan, J., Michael Ho, S. C., Zhang, P., and Jiang, J. (2019b). Experimental Study on Vibration Control of Suspended Piping System by Single-Sided Pounding Tuned Mass Damper. *Appl. Sci.* 9, 285. doi:10.3390/app9020285
- Tan, J., Zhang, P., Feng, Q., and Song, G. (2020). Passive Seismic Protection of Building Piping Systems—A Review. *Int. J. Struct. Stab. Dyn.* 20, 2030001. doi:10.1142/s0219455420300013
- Teng, J., Xing, H. B., Lu, W., Li, Z. H., and Chen, C. J. (2016). Influence Analysis of Time Delay to Active Mass Damper Control System Using Pole Assignment Method. *Mech. Syst. Signal Process.* 80, 99–116. doi:10.1016/j.ymssp.2016.04.008
- Tsai, C. S. (1994). Temperature Effect of Viscoelastic Dampers during Earthquakes. *J. Struct. Eng.* 120, 394–409. doi:10.1061/(asce)0733-9445(1994)120:2(394)
- Wang, W., Dalton, D., Hua, X., Wang, X., Chen, Z., and Song, G. (2017a). Experimental Study on Vibration Control of a Submerged Pipeline Model by Eddy Current Tuned Mass Damper. *Appl. Sci.* 7, 987. doi:10.3390/app7100987
- Wang, W., Hua, X., Wang, X., Chen, Z., and Song, G. (2017b). Advanced Impact Force Model for Low-Speed Pounding between Viscoelastic Materials and Steel. *J. Eng. Mech.* 143, 04017139. doi:10.1061/(asce)em.1943-7889.0001372
- Wang, W., Hua, X., Wang, X., Chen, Z., and Song, G. (2017c). Optimum Design of a Novel Pounding Tuned Mass Damper under Harmonic Excitation. *Smart Mater. Structures* 26. doi:10.1088/1361-665x/aa69a3
- Wang, W., Hua, X., Wang, X., Chen, Z., and Song, G. (2018a). Numerical Modeling and Experimental Study on a Novel Pounding Tuned Mass Damper. *J. Vibration Control* 24, 4023–4036. doi:10.1177/1077546317718714
- Wang, W., Wang, X., Hua, X., Song, G., and Chen, Z. (2018b). Vibration Control of Vortex-Induced Vibrations of a Bridge Deck by a Single-Side Pounding Tuned Mass Damper. *Eng. Structures* 173, 61–75. doi:10.1016/j.engstruct.2018.06.099
- Wang, W., Hua, X., Chen, Z., Wang, X., and Song, G. (2019). Modeling, Simulation, and Validation of a Pendulum-pounding Tuned Mass Damper for Vibration Control. *Struct. Control. Health Monit.* 26, e2326. doi:10.1002/stc.2326
- Xu, Z.-D., Wang, D.-X., and Shi, C.-F. (2011). Model, Tests and Application Design for Viscoelastic Dampers. *J. Vibration Control* 17, 1359–1370. doi:10.1177/1077546310373617
- Xue, Q., Zhang, J., He, J., and Zhang, C. (2016). Control Performance and Robustness of Pounding Tuned Mass Damper for Vibration Reduction in SDOF Structure. *Shock Vib.* 2016, 1–15. doi:10.1177/1077546310373617
- Xue, Q., Zhang, J., He, J., Zhang, C., and Zou, G. (2017). Seismic Control Performance for Pounding Tuned Mass Damper Based on Viscoelastic Pounding Force Analytical Method. *J. Sound Vibration* 411, 362–377. doi:10.1016/j.jsv.2017.08.035
- Zhang, C., and Ou, J. (2008). Control Structure Interaction of Electromagnetic Mass Damper System for Structural Vibration Control. *J. Eng. Mech.* 134, 428–437. doi:10.1061/(asce)0733-9399(2008)134:5(428)
- Zhang, P., Song, G., Li, H.-N., and Lin, Y.-X. (2013). Seismic Control of Power Transmission tower Using Pounding TMD. *J. Eng. Mech.* 139, 1395–1406. doi:10.1061/(asce)em.1943-7889.0000576
- Zhang, P., Li, L., Patil, D., Singla, M., Li, H., Mo, Y., et al. (2015). Parametric Study of Pounding Tuned Mass Damper for Subsea Jumpers. *Smart Mater. Structures* 25, 015028. doi:10.1088/0964-1726/25/1/015028
- Zhang, Z., Ou, J., Li, D., and Zhang, S. (2017). Optimization Design of Coupling Beam Metal Damper in Shear wall Structures. *Appl. Sci.* 7, 137–148. doi:10.3390/app7020137

- Zhang, P., Huo, L., and Song, G. (2018). Impact Fatigue of Viscoelastic Materials Subjected to Pounding. *Appl. Sci.* 8, 117. doi:10.3390/app8010117
- Zhang, P., Jiang, J., and Lu, G. (2019). Low Temperature Influence on the Behavior of Viscoelastic Layer of the Pounding Tuned Mass Damper. *Materials* 12, 3986. doi:10.3390/ma12233986
- Zhong, Y., Tu, J., Yu, Y., Xu, J., and Tan, D. (2017). Temperature Compensation in Viscoelastic Damper Using Magnetorheological Effect. *J. Sound Vibration* 398, 39–51. doi:10.1016/j.jsv.2016.11.004

Conflict of Interest: JT, YL and QF were employed by Wuhan Institute of earthquake Engineering Co. Ltd.

The remaining author declares that the research was conducted in the absence of any commercial or financial relationships that could be construed as a potential conflict of interest.

Copyright © 2021 Ye, Tan, Liang and Feng. This is an open-access article distributed under the terms of the Creative Commons Attribution License (CC BY). The use, distribution or reproduction in other forums is permitted, provided the original author(s) and the copyright owner(s) are credited and that the original publication in this journal is cited, in accordance with accepted academic practice. No use, distribution or reproduction is permitted which does not comply with these terms.



Mechanical Behavior of the Novel Gradient Concrete Tower of a Cable-Stayed Bridge

Zuo-Cai Wang^{1,2*}, Da-You Duan¹, Shu-Hang Wang^{1,3}, Ye Mo¹ and Yong-Gao Yin^{1,4}

¹Department of Civil Engineering, Hefei University of Technology, Hefei, China, ²Anhui Engineering Research Center for Civil Engineering Disaster Prevention and Mitigation, Hefei, China, ³Anhui Engineering Laboratory for Infrastructural Safety Inspection and Monitoring, Hefei, China, ⁴Anhui Transportation Holding Group Co., LTD, Hefei, China

In this paper, the novel gradient concrete is innovatively applied to the bridge towers of Chizhou Yangtze River Bridge to solve the cracking and insufficient durability problems of concrete towers. Fiber-reinforced concrete is used in the outer functional area of the bridge tower, to significantly improve its crack resistance during construction and service. Moreover, the integrated design of anti-cracking and mechanical properties of tower materials is achieved. To study the performance of the novel functional gradient concrete (FGC) tower, the mechanical properties of the FGC tower material are tested, and the overall finite element stress is analyzed. Based on the material properties, the mechanical behavior of the cable-stayed bridge tower is studied. The temperature and stress of the FGC tower during the generation of the hydration heat are compared with that of the ordinary concrete tower. The crack resistance of the FGC tower is analyzed by the finite element method. The results show that the FGC tower has good mechanical properties and durability for the cable-stayed bridge towers.

Keywords: gradient concrete, cable-stayed bridge, fiber reinforced concrete, mechanical behavior, crack resistance

OPEN ACCESS

Edited by:

Gangbing Song,
University of Houston, United States

Reviewed by:

Peng Zhang,
National Natural Science Foundation
of China, China
Ping Duan,
China University of Geosciences,
China

*Correspondence:

Zuo-Cai Wang
wangzuocai@hfut.edu.cn

Specialty section:

This article was submitted to
Structural Materials,
a section of the journal
Frontiers in Materials

Received: 09 March 2021

Accepted: 18 May 2021

Published: 02 June 2021

Citation:

Wang Z-C, Duan D-Y, Wang S-H,
Mo Y and Yin Y-G (2021) Mechanical
Behavior of the Novel Gradient
Concrete Tower of a Cable-
Stayed Bridge.
Front. Mater. 8:676440.
doi: 10.3389/fmats.2021.676440

INTRODUCTION

As a critical component of cable-stayed bridges, towers need to improve their mechanical properties to resist cracks during construction and service life. However, construction cracking problems commonly exist in concrete towers due to the influence of traditional concrete materials, structural performance limitations, and harsh construction environments. These problems further lead to tower quality deficiency and reduce safety, applicability, and durability in service.

In recent years, with the development of material technology, high-performance materials have been increasingly used in bridge towers. Okamoto and Nakamura (2011) proposed a novel hybrid high tower using concrete-filled steel tubes for multi-span cable-stayed bridges. Son and Lee (2011) compared hollow steel box performance and concrete-filled composite towers subjected to the blast load. They concluded that concrete-filled composite towers show superior properties. Amiri and Nakamura (2015) found that the RC and hybrid tower have better seismic performance than the steel tower. Shao et al. (2018) designed a new three-tower with unequal-size fans to improve the overall stiffness of cable-stayed bridges.

Due to its low cost and simple maintenance, concrete is a common material frequently used in long-span bridge towers. Many researchers have been exploring to improve the performance of concrete. More recently, the FGM application in concrete has attracted more and more

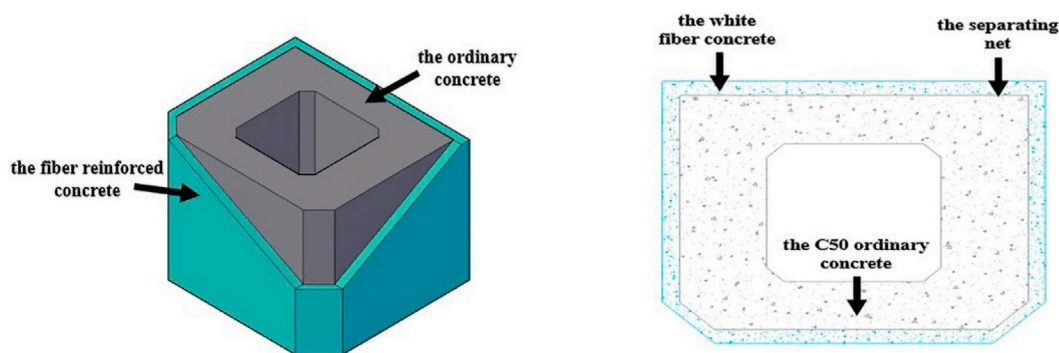


FIGURE 1 | The gradient structure.

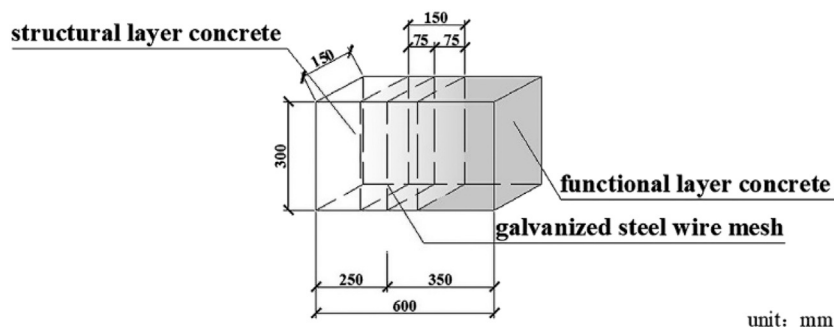


FIGURE 2 | The schematic diagram of the gradient concrete test block.

TABLE 1 | The mechanical properties of the FGC.

	Compressive strength (MPa)	Split tensile strength (MPa)	Elastic modulus (GPa)
The functional layer	61.0	5.40	46.5
The transition layer	59.1	4.18	45.0
The structural layer	58.7	4.12	44.2

attention. According to engineering requirements, the FGM selects materials with different properties and adopts advanced composite technology. The properties and functions of this kind of material change along with the thickness. Concrete components are usually faced with various service conditions, which require that the properties of materials vary with the position of the components. Therefore, some scholars have applied the design ideas of the FGM to engineering materials and structures. Maalej et al. (2003) found that FGC beams have significantly higher corrosion resistance than traditional reinforced concrete beams. Wen et al. (2013) studied protective layer thickness on structural durability in FGC systems. The experimental results showed that the durability of the structure can be significantly improved when the

thickness of the protective layer is 10 mm. Herrmann and Sobek (2015) proposed a design method to minimize the mass of FGC components. Strieder et al. (2018) constructed a simplified mass concrete structure model and found that the gradient concrete can reduce cracking risk during hardening. Kovaleva et al. (2019) used the FGC shell in Rosenstein Pavilion and found that the FGC material application can reduce the weight of structural components. Chan et al. (2020) studied the influences of aggregate type, reinforcement layer thickness, fiber content, and other variables on the mechanical properties of the FGC. Torelli et al. (2020) reviewed the design objectives, manufacturing techniques, and challenges of FGC materials in recent years.

Based on the previous studies, the main performance enhancement of FGC materials can be summarized as

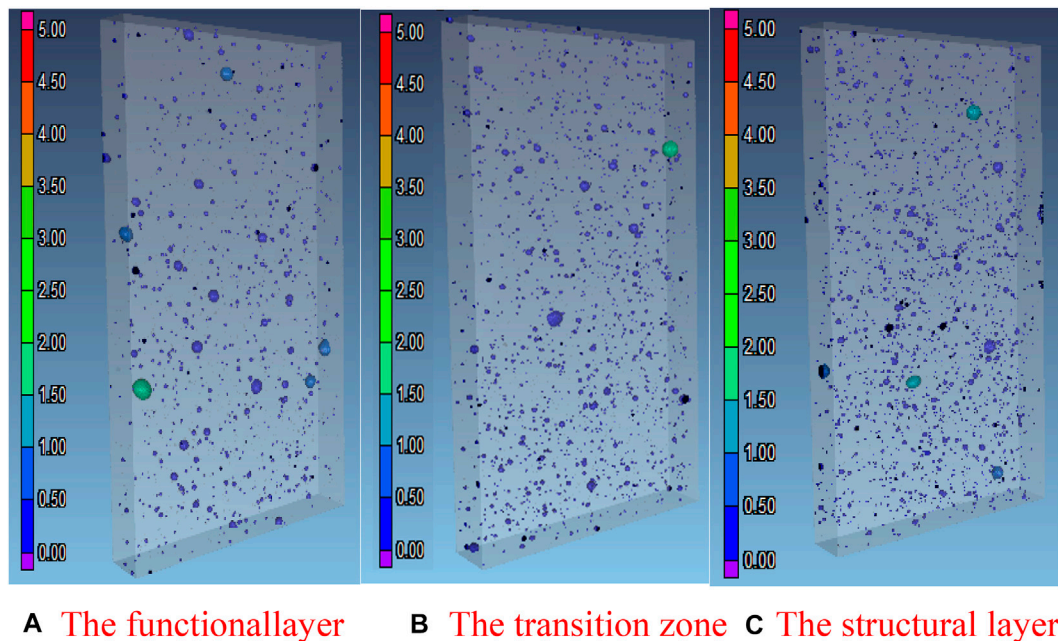


FIGURE 3 | The pore volume of the concrete (unit mm^3). (A) The functional layer (B) The transition zone (C) The structural layer.

follows: 1) it minimizes the self-weight of concrete structures without reducing its bearing capacity (Nes and Øverli, 2016; Herrmann and Sobek, 2017; Kiryu et al., 2018); 2) compared with the ordinary concrete, the FGC application improves the durability and cracks resistance (Mohamed and Victor, 1995; Roesler et al., 2007; Li and Xu, 2009; Xu and Li, 2009; Dias et al., 2010; Park et al., 2010; Sridhar and Prasad, 2019); 3) mechanical properties of concrete structures can be improved (Miyamoto et al., 1997; Han et al., 2016; Craveiro et al., 2017; Chan et al., 2020).

Given the severe construction cracking, and the lack of durability of cable-stayed bridge concrete towers, the FGC is innovatively applied to the towers based on the Chizhou Yangtze River Bridge. The researches in this paper improve the traditional method of designing concrete materials that regard strength as the core. Moreover, the integrated design of mechanical properties and durability of the tower is achieved. The effects of functionally gradient concrete layers on the mechanical properties and hydration heat effects of the tower are studied systematically. Refined finite element (FE) models are constructed to demonstrate the mechanical behaviors of the novel gradient concrete. The deformation and stress are close in the FGC model and the ordinary concrete model. There is no noticeable stress concentration appear. The difference in hydration heat and damage factors between the FGC and ordinary concrete tower models are also discussed. The temperature and stress of the FGC tower are higher than that of the ordinary concrete tower during the generation of the hydration heat. In the crack damage simulations, the FGC

performs better than the ordinary concrete, and the durability of the FGC tower may be benefited by this.

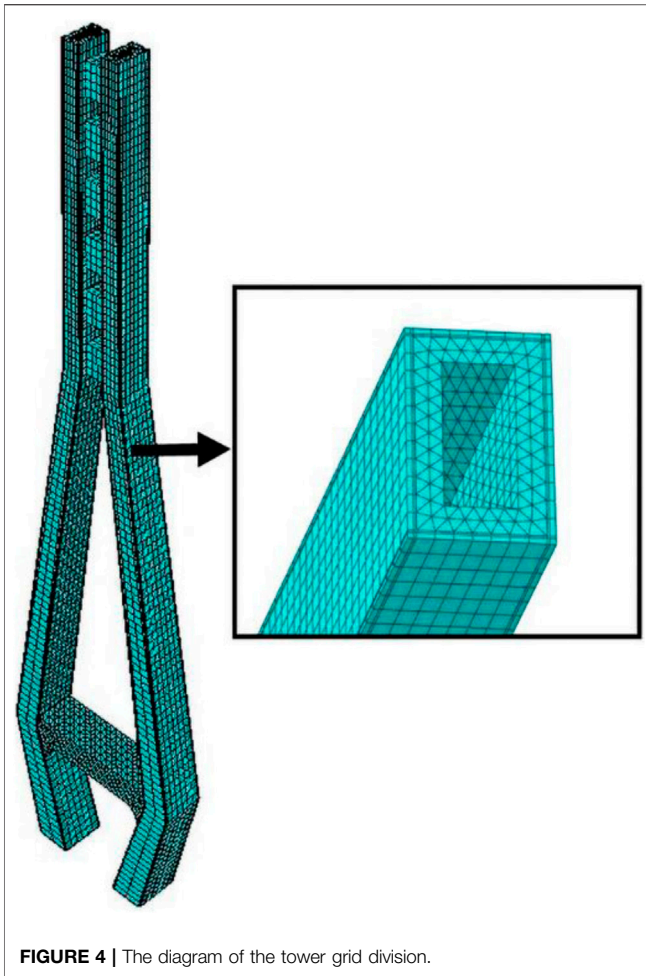
MECHANICAL PROPERTY TESTS OF THE FGC MATERIAL

To achieve the FGC material, a layer of 30 cm-thick white fiber high-performance concrete is installed on the surface of the ordinary concrete structure layer. Moreover, ordinary C50 concrete is applied in the structural layer. The cross-section of the structure is demonstrated in **Figure 1**. The structure and mechanical properties of the FGC tower will be further introduced in *The Structure of the FGC Tower and Mechanical Property Tests of the Transition and Functional Layer*.

The Structure of the FGC Tower

The FGC tower section is divided into the functional, transition, and structural layers from outside to inside. The structural layer is vertically designed with the fiber-reinforced concrete section and the ordinary high-strength concrete section from top to bottom, as shown in **Supplementary Figure S1**. The functional layer materials are mainly used for anti-cracking, and durability protection. The transition layer connects the functional layer and the structural layer. Besides, it achieves the gradient transition of material components and has no macroscopic interface.

Owing to its superior performance for crack resistance and ductility, the FGC material is located in the area where the tensile



stress is likely to occur, that is, the reinforcement layer. The force transfer between the structural and functional layers is optimized through the bonding and friction of steel bars. It can coordinate the deformation and reduce the stress concentration at the interface.

Mechanical Property Tests of the Transition and Functional Layer

Mechanical properties tests were performed to determine the FGC performance in practice. The specimens with a size of 600 mm × 150 mm × 300 mm were made, and the galvanized steel wire mesh was placed. The diameter of the steel wires is 0.7 mm, and the mesh size is 9 mm × 9 mm. By cutting and sampling the transition layer concrete in the range of 75 mm around the wire mesh, the size of the sampling components is 150 mm × 150 mm × 300 mm and 150 mm × 150 mm × 150 mm. The block with a size of 150 mm × 150 mm × 300 mm is taken for elastic modulus test, and the 150 mm × 150 mm × 150 mm cube block is used for splitting tensile strength and compressive strength test. The size of the test block is shown in Figure 2. **Supplementary Table S1** demonstrates the concrete mix proportion of the functional and structural layers.

According to the GB/T50081-2002, the strength, elastic modulus, and splitting tensile strength of the functional, transition, and structural layers were tested after 28 days. The experimental results are shown in **Table 1**. It can be seen from **Table 1** that the compressive strength of the transition layer is 59.1 MPa, and the compressive elastic modulus is 45.0 GPa, which are between those of the structural layer and the functional layer. The split tensile strength of the functional layer is 31.1% larger than that of the structural layer.

The mechanical properties of the FGC, especially for the tensile strength, are obviously improved by adding the basalt fibers and silica-fume to the FGC. The test results show that the gradient variation of material causes gradient variation of mechanical property. Besides, there is no weak gradient transition zone during the tests, and the overall deformation is coordinated. The functional layer concrete with higher mechanical properties may improve the crack resistance of the concrete tower.

Pore Structure Reconstruction of FGC

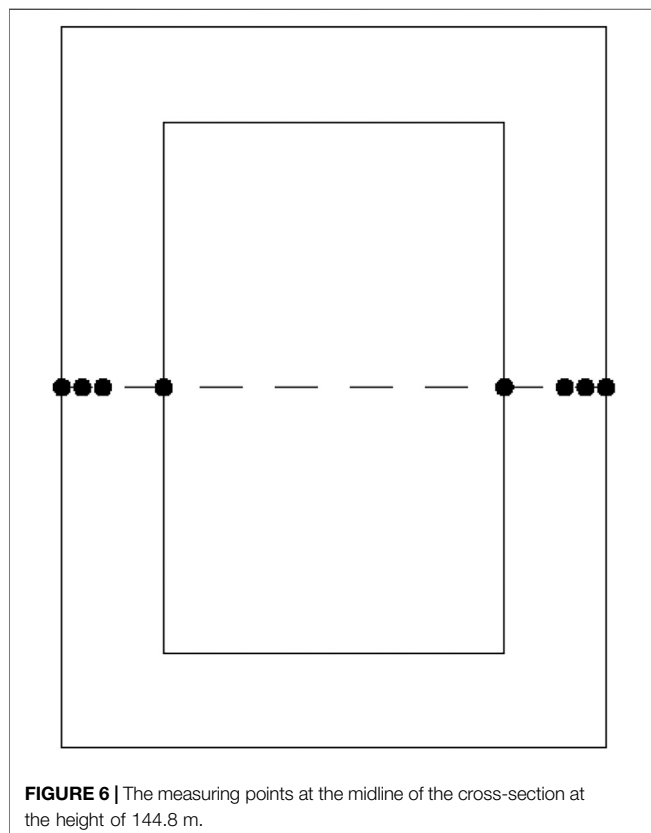
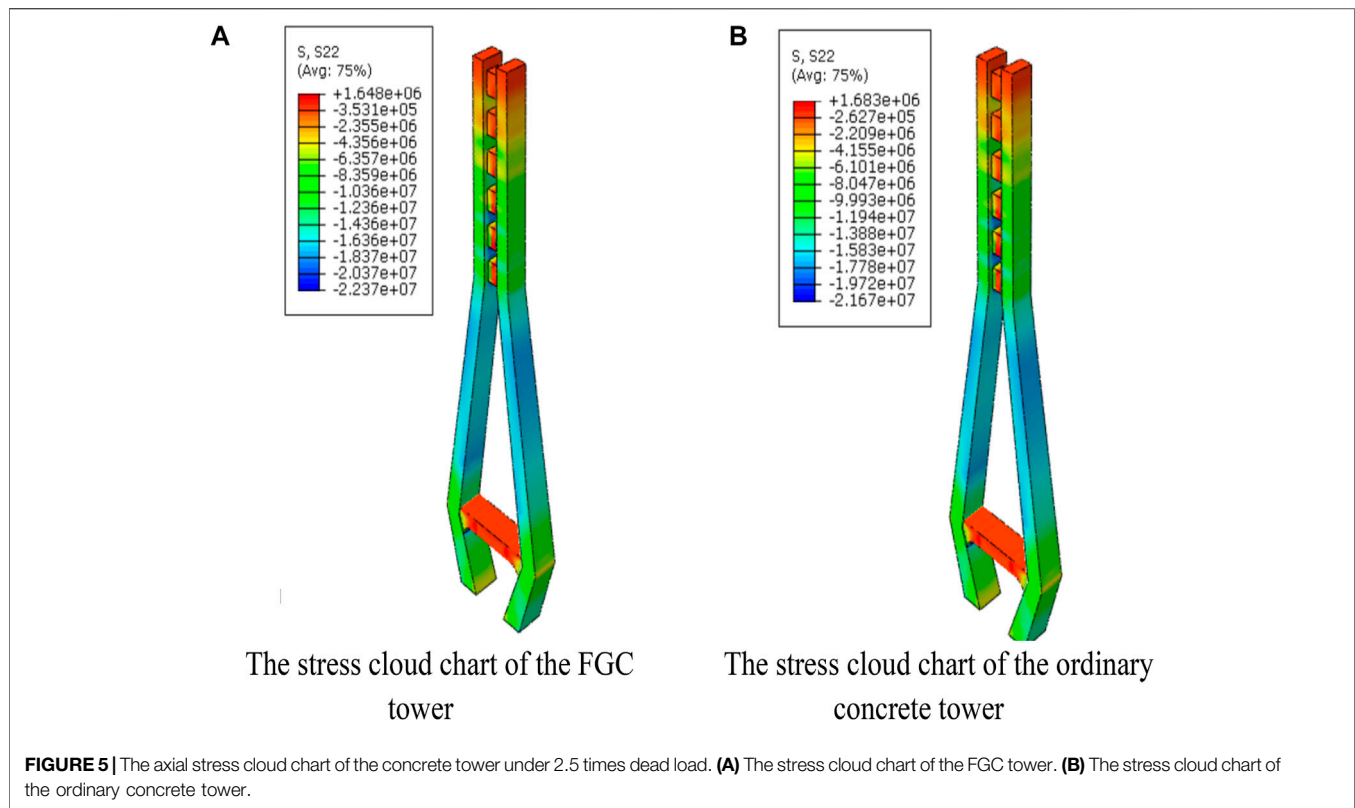
To analyze the pore structure of the FGC, the X-CT (X-ray computed tomography) is used to observe the size, quantity and distribution of the pores (Du Plessis et al., 2016; Zhang et al., 2020). As shown in **Figures 3**, 3D images of the pore structures in different parts of the FGC are calculated by the reconstruction algorithm after the X-CT scan. A color scale is used to indicate the size of the pore, with the color from blue to red representing the size of the pore from small to large. The porosity of the functional layer, transition zone and the structural layer are 0.31, 0.35, and 0.47%, respectively.

The porosity of the gradient concrete presents gradient changes. Besides, the average volume of the pores in functional layer concrete is smaller than that in other area. The functional layer concrete contains fewer and smaller pores than the structural layer concrete, and the durability of the FGC can be benefitted from the low porosity.

MECHANICAL BEHAVIOR AND MICROSTRUCTURE ANALYSIS OF THE FGC TOWER

The Chizhou Yangtze River Bridge, which is 1,448 m long, adopts an equal height double-tower cable-stayed bridge with an asymmetric mixed beam. Its main tower is 243 m high, and each tower has 108 stay cables. **Supplementary Figure S2** shows the overall layout of this bridge.

The main tower of the cable-stayed bridge is designed as a vase-shaped reinforced concrete structure. It comprises the lower, middle, and upper towers, the upper and lower cross beams. The Z4 north tower is 237 m high. The width of the main tower along the bridge is 9.5 m in the upper tower and 9.5–13 m in the middle and lower tower s. The tower is a reinforced concrete structure, the upper crossbeam is a steel structure, and the lower one is a prestressed concrete structure. The upper tower is 109.7 m high, 5 ~ 6 m wide, and 9.5 m wide along the



bridge. **Supplementary Figure S3** shows the elevation map of the main tower.

The FE Model

The finite element software ABAQUS is used to create the tower model. In this paper, the model is partially simplified: 1) the influence of different internal forces on the two limbs is ignored; 2) the symmetric loading boundary condition is considered; 3) the monolithic rigid frame and anchor rod are used instead of steel beam; 4) the improvement of stress concentration due to the chamfer of the horizontal plate hole is not considered.

The C3D8R hexahedral solid element is adopted in the concrete of the functional layer and the transition layer of the bridge tower main structure. Due to the irregular shape of the structural layer and the lower beam concrete, the C3D10 tetrahedral solid element is selected for free meshing. The truss element is used to simulate the bolt, and the embedded function is used to embed the bolt into the concrete. For the mechanical properties of the FGC, the C3D8R hexahedral solid element is used to simplify the analysis of steel beams. The numerical analysis of functionally graded materials is based on the layered FE modeling method, which assigns each layer with different gradient variation functions of material parameters. According to material properties, the bridge tower entity model is divided into the functional, transition, and structural layers. The thickness of the functional layer and transition layer is 22.5 and 15 cm, respectively. According to the experimental results, the elastic modulus of concrete in the structural layer,

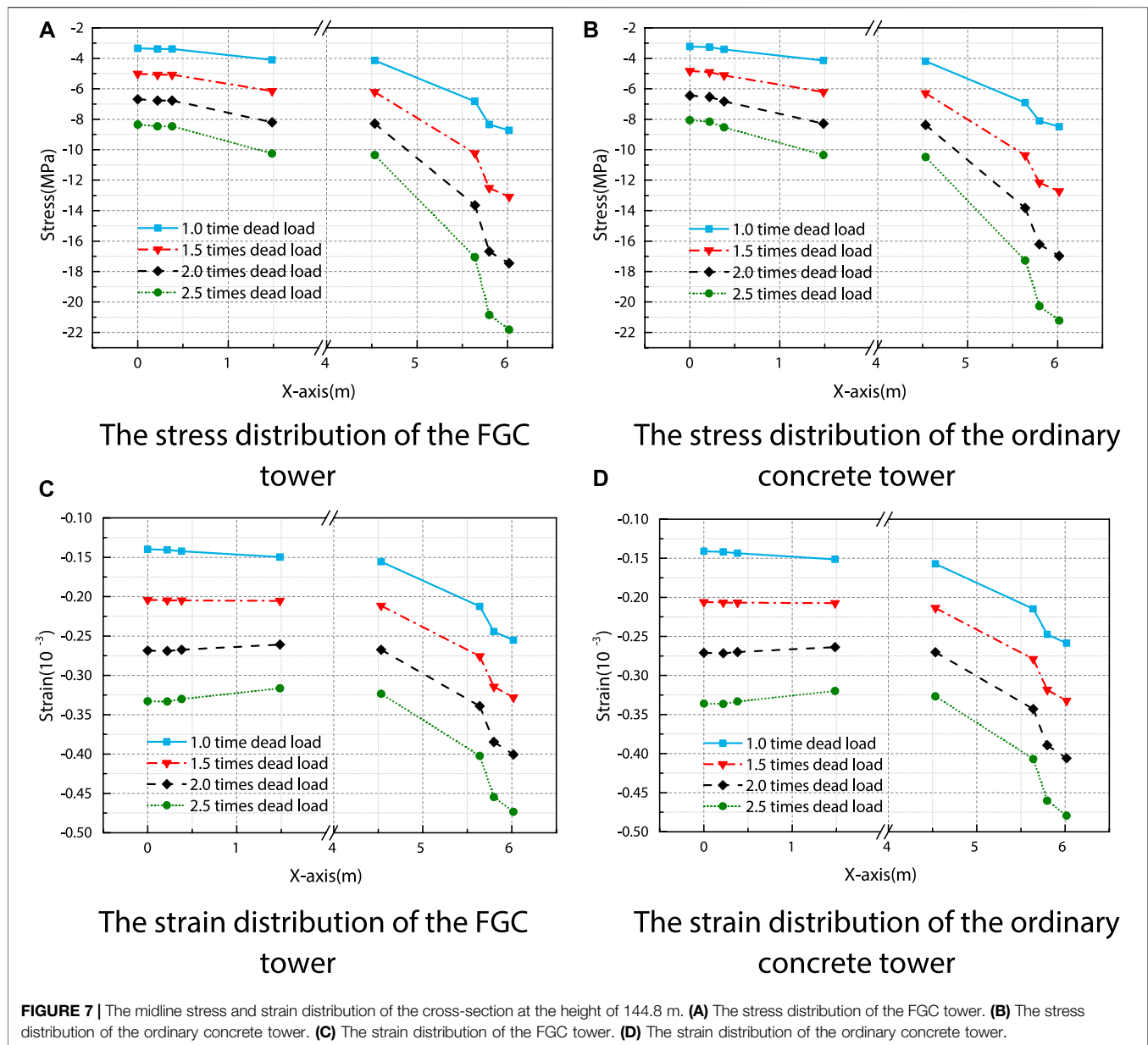


FIGURE 7 | The midline stress and strain distribution of the cross-section at the height of 144.8 m. **(A)** The stress distribution of the FGC tower. **(B)** The stress distribution of the ordinary concrete tower. **(C)** The strain distribution of the FGC tower. **(D)** The strain distribution of the ordinary concrete tower.

functional layer, and transition layer is 44.2, 46.5, and, 45.0 GPa, respectively. **Figure 4** demonstrates the FE model mesh and section of the tower. The concrete density is tested as 2625 kg/m³, the steel beam is the Q370qE steel; the dead load is a combination of self-weight, the vertical reaction of the beam, and the cable force. The loading is set 1–2.5 times of the dead load, with an interval of 0.5 times.

Stress and Strain Analysis of the FGC Tower

To study the mechanical behaviors of the FGC tower, a comparison model of the ordinary concrete tower is also created. The size, mesh division, and load application of the ordinary compared model are completely consistent with the FGC tower model. The difference is that the properties of concrete materials of the second model are consistent, and its

elastic modulus is 44.2 GPa. By comparing the calculation results of the two models, the influence of the gradient concrete on the deformation and stress distribution is studied. **Figures 5A,B** show the axial stress cloud chart of the FGC and the ordinary concrete cable towers under 2.5 times dead load. It can be found that the results of the FGC tower and the ordinary concrete tower are consistent. Furthermore, there is no stress concentration when the load increases. Under 2.5 times dead load, the maximum compressive stress is 22.4 MPa.

According to the stress distribution characteristics, the transition cross-section between the upper and middle tower (at the height of 144.8 m) is selected to analyze the stress distribution. The stresses of the measuring points at the midline of the cross-section are obtained. The measuring

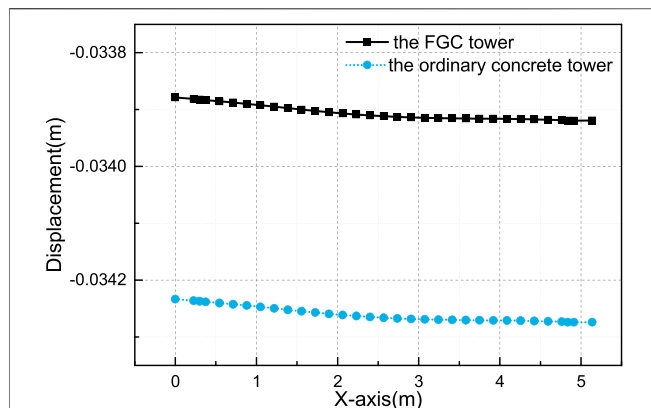


FIGURE 8 | The comparison of the displacements at the tower top.

points are shown in **Figure 6**. Through the changing trend of node stress value on the midline, the effect of FGC on the tower is further analyzed. The distribution curves of stress and strain of the upper tower section on the FGC tower and the ordinary concrete tower are shown in **Figures 7A–D**. Through the stress and strain analysis and comparison between the FGC tower and the ordinary concrete tower, it can be found that the stiffness of the FGC tower is slightly improved. Moreover, the difference in stress and strain is less than 4 and 1.5%, respectively. The strain and stress distributions of the FGC and the ordinary concrete tower are consistent. The vertical displacements at the midline of the tower top are obtained and presented in **Figure 8**.

According to the comparisons, the stress and displacements of the FGC tower are smaller than that of the ordinary concrete tower, and the trends of the stress distribution and displacements of FGC tower and ordinary concrete tower are almost the same. It indicates that the usage of the FGC has not cause nonuniform stress distribution in the transition zone of two kinds of concrete, and the FGC improved the vertical stress distribution and the stiffness of the tower.

THE THERMAL STRESS OF THE FGC TOWER

Bridges are usually influenced by internal and external factors such as the hydration heat state, the construction environment, daily and seasonal fluctuations in temperature, and solar radiation, which leads to the internal and external temperature difference. Temperature action causes considerable stress and deformation. These thermal effects are likely to induce cracking, support and expansion joint damage, and even collapse (Potgieter and Gamble, 1989; Catbas et al., 2008; Cross et al., 2013; Abid et al., 2016; Kromanis and Kripakaran, 2016; Sousa Tomé et al., 2018). In this section, the temperature stress of the FGC tower under the effect of gradient temperature load and hydration heat effect is studied, respectively. Moreover, the simulated results are compared with those of ordinary concrete towers.

The Stress of the FGC Tower due to the Gradient Temperature

The concrete tower is deformed by the effects of natural temperature changes and sunshine radiation. When the surface temperature of the tower rises/decreases rapidly, the internal temperature is still in the original state. Thus a large temperature gradient will be generated. It further keeps each part of the tower at a different temperature state and produces different temperature deformation. When the deformation is subject to internal and external constraints, considerable constraint stress will be generated inside the tower. Such constraint stress is sometimes even larger than the stress generated by the load.

According to Chinese specifications JTGD60-2015 and JTGT3365-01-2020, the temperature difference between the left and right side of the central tower is $\pm 5^{\circ}\text{C}$, the linear expansion coefficient of steel structure is $1.2 \times 10^{-5}/^{\circ}\text{C}$, and the linear expansion coefficient of concrete and reinforced concrete and prestressed concrete structures is $1 \times 10^{-5}/^{\circ}\text{C}$. The dead load includes the cable force and the bridge reaction force of the lower beam support. As a result of the difference between the linear expansion coefficient of steel and concrete, the stress due to the

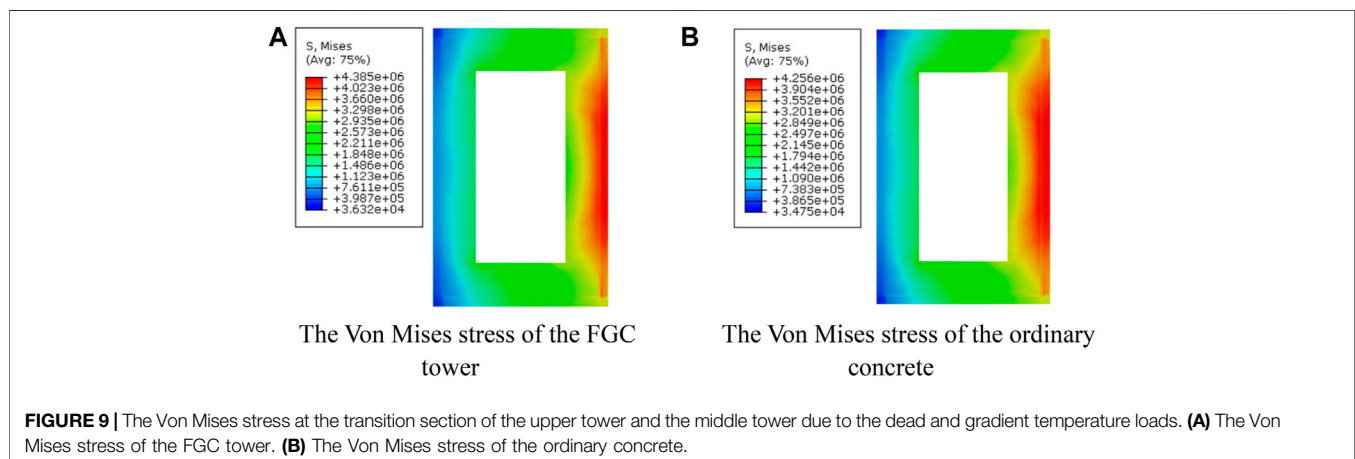


FIGURE 9 | The Von Mises stress at the transition section of the upper tower and the middle tower due to the dead and gradient temperature loads. **(A)** The Von Mises stress of the FGC tower. **(B)** The Von Mises stress of the ordinary concrete.

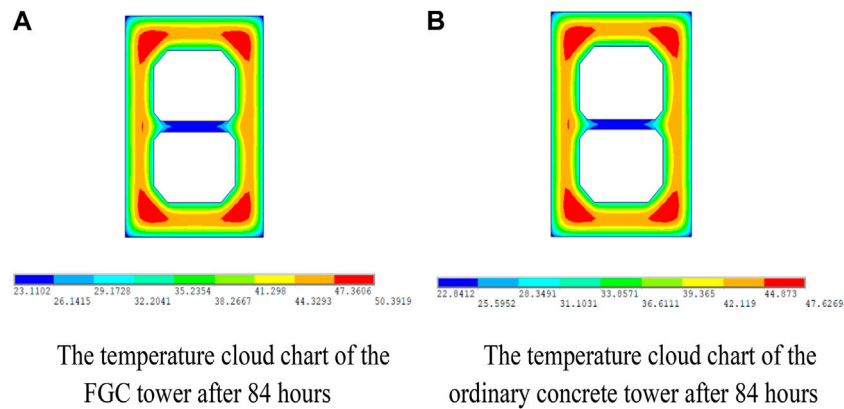


FIGURE 10 | The temperature cloud chart under the hydration heat. **(A)** The temperature cloud chart of the FGC tower after 84 h. **(B)** The temperature cloud chart of the ordinary concrete tower after 84 h.

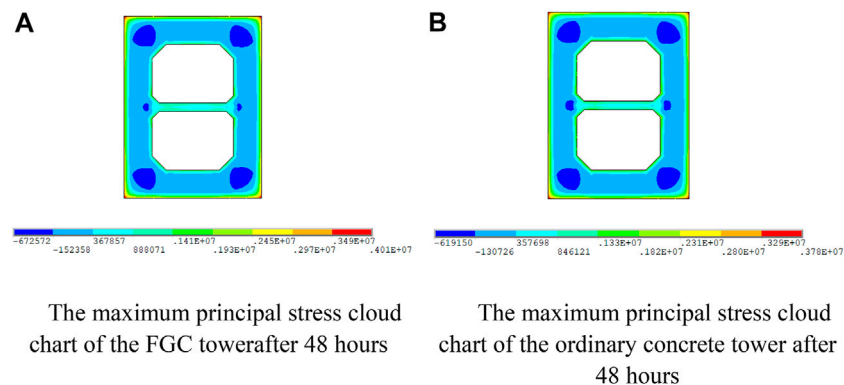


FIGURE 11 | The maximum principal stress cloud chart under the hydration heat. **(A)** The maximum principal stress cloud chart of the FGC tower after 48 h. **(B)** The maximum principal stress cloud chart of the ordinary concrete tower after 48 h.

gradient temperature at the fixed position of the upper tower steel beam and the dense reinforcement is enormous. The maximum temperature stress appears at the transition cross section between the top and the middle tower, located at the height of 144.8 m. **Figures 9A,B** compare the Von Mises stress of the two models with different materials due to the dead load and gradient temperature load. The maximum Von Mises stress of the ordinary concrete and FGC tower is 4.26 and 4.39 MPa (tensile stress). The maximum Von Mises stress of the ordinary concrete tower is slightly smaller than that of the FGC tower. The main reason is that the FGC has a larger stiffness and is more affected by gradient temperature than the ordinary concrete. Affected by the gradient temperature, the stress from the sunny side to the shady side gradually decreases.

The Hydration Heat Analysis

The Hydration Heat Theory and FE Model

The expansion and shrinkage caused by the thermal changes can strongly influence the stress distribution of the mass concrete structures (Huang et al., 2018; Do et al., 2020). According to Zhu's

research (Zhu, 2013), the exponential function is adopted to calculate the hydration heat. The function is defined as :

$$Q(t) = Q_0(1 - e^{-at^b}) \quad (1)$$

where $Q(t)$ is the accumulated hydration heat when the concrete age is t , Q_0 is the final hydration heat when the age of concrete tends to infinity. The a and b in **Eq. 1** are the influence coefficients of hydration heat ($a = 0.36$, $b = 0.74$).

The elastic modulus of concrete varies with age, and the elastic modulus is calculated by **Eq. 2**.

$$E(t) = E_0(1 - e^{-at^b}) \quad (2)$$

in which, $E(t)$ is the elastic modulus of the concrete when the concrete age is t . E_0 is the elastic modulus of the concrete after curing. The values of a and b are listed in **Supplementary Table S2**. The hydration heat effect is analyzed by the commercial software ANSYS. The solid70 element is used for modeling. During the stress and strain analysis, the solid70 element is converted into a solid45 element. Due to the large volume of

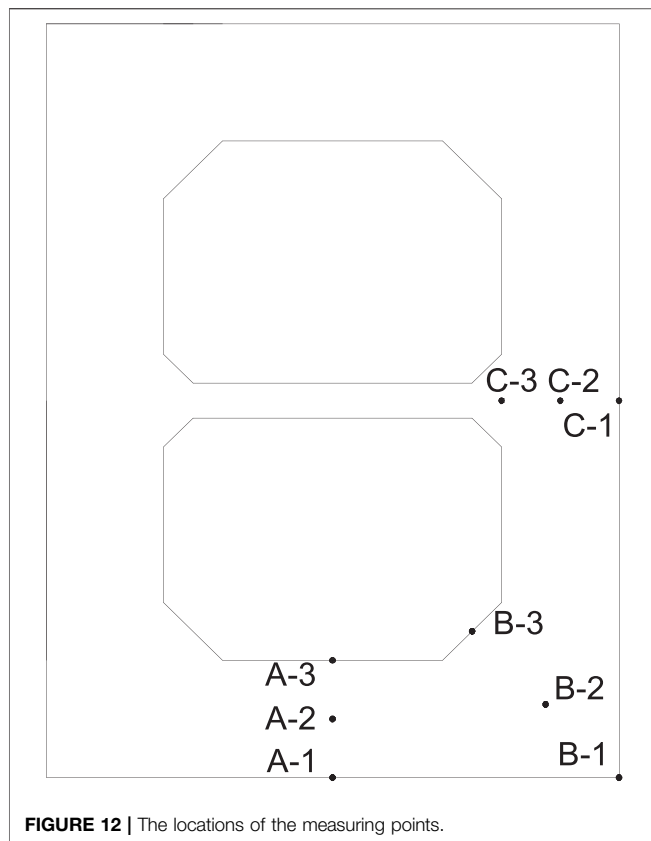


FIGURE 12 | The locations of the measuring points.

concrete in the connection section between the tower and the pile cap, the hydration heat of this area is analyzed. The environment temperature of the modeling is set as 20°C. The thermal conductivity and the specific heat capacity are listed in **Supplementary Table S3**. The initial temperature is 20°C, the Poisson's ratio is 0.2, and the thermal expansion coefficient is $10^{-6}/^{\circ}\text{C}$. The heat dissipation coefficient of the concrete surface is $37.693\text{kJ}/(\text{m}^2 \cdot \text{h} \cdot ^{\circ}\text{C})$. Fixed constraints are imposed on the bottom of the concrete tower.

The hydration heat is applied by the heat generation of concrete in unit time which is determined by the heat generation rate (*HGEN*) function. It is applied as a volume load on the element to simulate the chemical reaction of cement. The expression of *HGEN* is expressed as:

$$HGEN = W_c \frac{dQ(t)}{dt} \quad (3)$$

where, W_c is the amount of concrete cement per unit volume.

Under hydration heat, the maximum deformation of bridge towers is 0.018 m in the transverse direction, 0.015 m in the longitudinal direction, and 0.02 m in the vertical direction. Due to the constraint conditions, the deformation of the lower part is relatively small, while that of the upper area is relatively large. The whole model shows a tendency of outward expansion under the hydration heat. The thickness of the functional layer also has a certain influence on the temperature stress of the model. Therefore, in temperature stress analysis, the FGC model with the functional layer thickness of 30 cm is constructed.

The Temperature and Stress Comparison

The FGC model is compared with the ordinary concrete model for temperature and stress, and the cross-section at the height of 4 m is selected. When the temperature and the stress reach their maximum values, respectively, the stress and temperature cloud charts of the two models are shown in **Figures 10, 11**. The internal temperature of the FGC tower and the ordinary concrete tower reached the maximum value at about 84 h after pouring. The internal temperature of the FGC tower is 50.4°C, and the internal hydration temperature of the ordinary concrete tower is 47.6°C. The maximum tensile stress of the FGC tower and the ordinary concrete tower is 4.01 and 3.78 MPa, respectively. The maximum tensile stress appears at the corners of the cross-sections and the stress reaches the highest at about 48 h after pouring.

To further compare the changing of temperature and stress between the FGC tower and the ordinary concrete tower, the values at the measuring points in the first 10 days are collected. The locations of the measuring points in the cross-section are shown in **Figure 12**. The time-history curves of different measuring points are shown in **Figures 13, 14**. As presented in **Figure 13**, the temperatures at points A-2, B-2, and C-2 increased to the maximum values, and then become decreasing. Due to the heat exchanging between the concrete surface and the external environment, the temperatures of the surface are low. The temperature of the FGC tower is higher than that of the ordinary concrete tower. The main reason is that the higher content of cement in the FGC makes the higher heat generation of hydration.

As presented in **Figure 14**, during the generation of the hydration heat, the internal area is under compression and the concrete at the surface of the tower is under tensile. The stress of the FGC caused by the hydration heat is higher than that of the ordinary concrete because the hydration heat of FGC is higher than that of ordinary concrete. At the same time, the FGC with high strength at early age makes concrete tower external tensile stress increased. It can be concluded that the stress of the FGC tower is larger than that of the ordinary concrete tower under the hydration heat effect.

CRACK RESISTANCE OF THE FGC TOWER

The existence of cracks reduces the stiffness of the bridge and weakens the material strength. Even minor cracks may affect the durability of the bridge. Thus, it is essential to analyze the crack resistance of the FGC.

The Plasticity Damage Model

In this section, the concrete plasticity damage model provided by ABAQUS is used. The damage plasticity model was proposed by Lubliner et al. (1989) and then developed by Lee and Fenves (1998). It assumed that the elastic behavior of the material is isotropic and linear. The constitutive relation of concrete is determined according to the GB50010-2010. The stress-strain ($\sigma - \epsilon$) relationship of the concrete under the uniaxial compression is determined as,

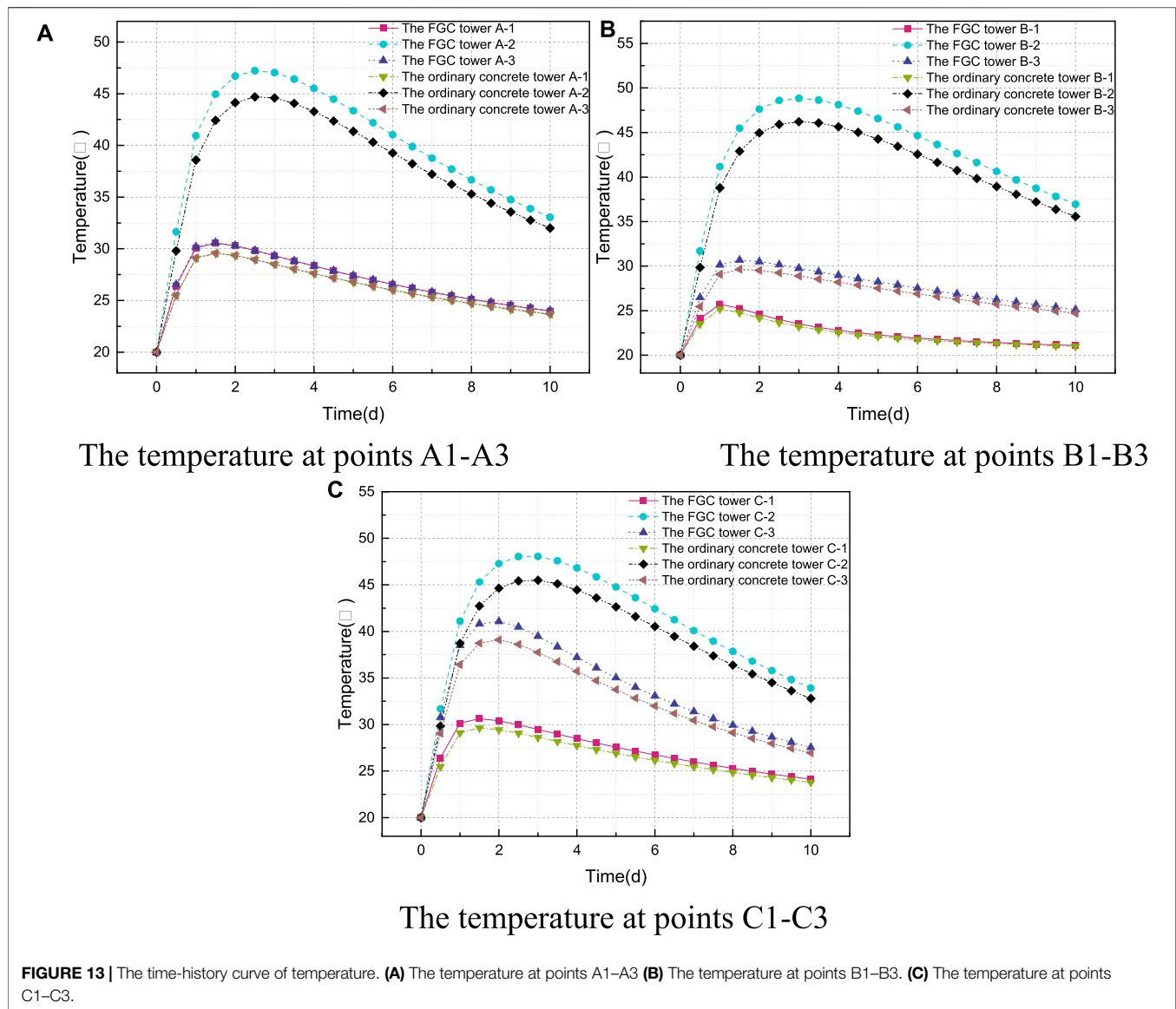


FIGURE 13 | The time-history curve of temperature. **(A)** The temperature at points A1-A3 **(B)** The temperature at points B1-B3. **(C)** The temperature at points C1-C3.

$$y = \begin{cases} \alpha_a + (3 - 2\alpha_a)x^2 + (\alpha_a - 2)x^3 & x \leq 1 \\ \frac{x}{\alpha_d(x-1)^2 + x} & x > 1 \end{cases} \quad (4)$$

1, $x = \varepsilon/\varepsilon_{c0}$ and $y = \sigma/\sigma_{c0}$. The ε_{c0} and σ_{c0} represent the peak strain and stress in the stress-strain curve of the concrete under the uniaxial compression, respectively. In Eq. 4, $\alpha_a = 2.4 - 0.0125f_c$, $\alpha_d = 0.157f_c^{0.785} - 0.905$ and f_c is the design value of the axial compressive strength of concrete.

The stress-strain ($\sigma - \varepsilon$) curve formula of concrete under uniaxial tension is formed as follow:

$$y = \begin{cases} 1.2x - 0.2x^6 & x \leq 1 \\ \frac{x}{\alpha_t(x-1)^{1.7} + x} & x > 1 \end{cases} \quad (5)$$

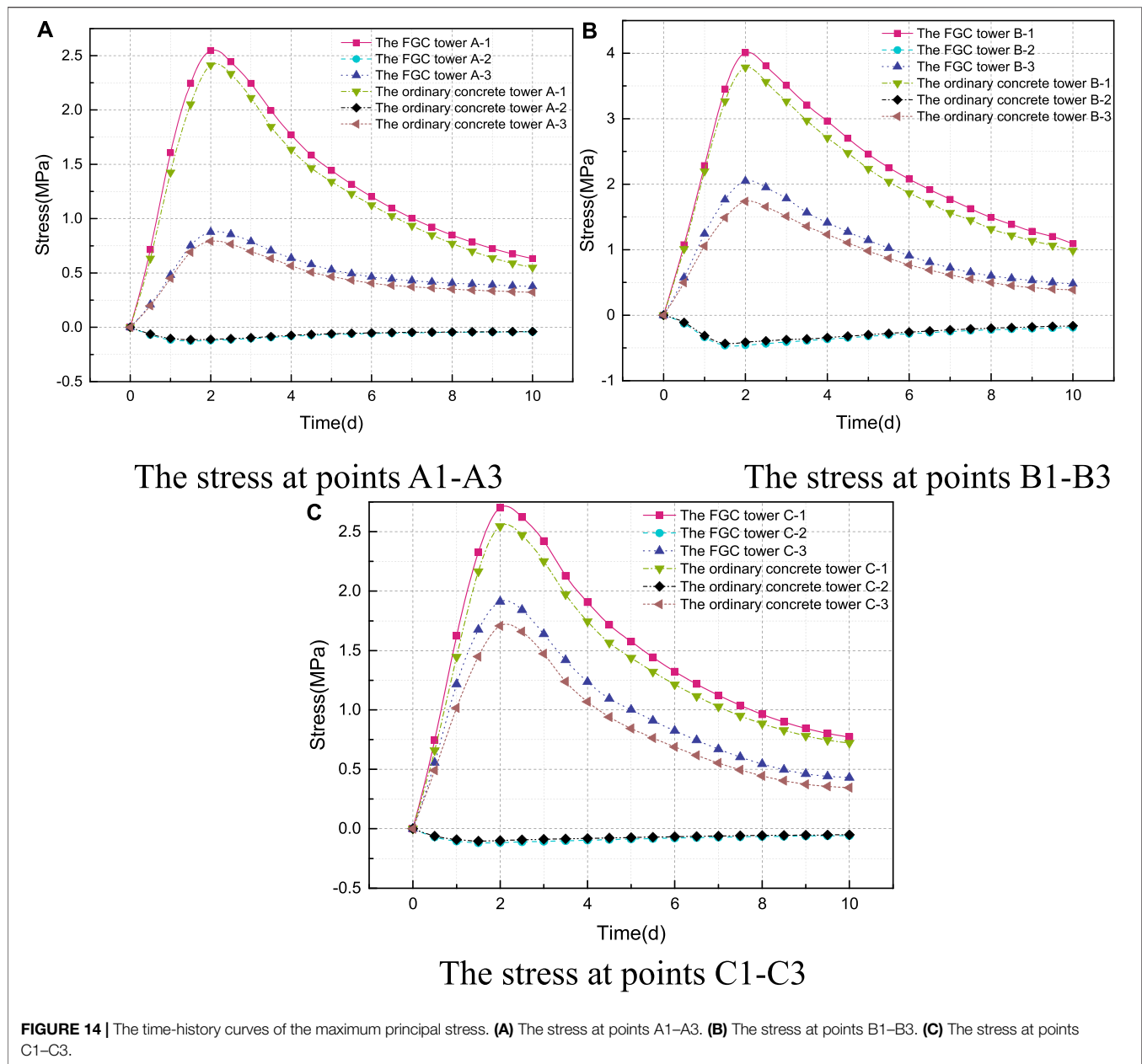
where $x = \varepsilon/\varepsilon_{t0}$, $y = \sigma/\sigma_{t0}$. The ε_{t0} and σ_{t0} represent the peak strain and stress in the stress-strain curve of the concrete under the uniaxial tensile, respectively. $\alpha_c = 0.312f_t^2$ and f_t is the design value of axial tensile strength of concrete.

The damage factors are determined for the usage of the plasticity damage model in ABAQUS. The damage factors calculation formulas are given in GB 50010-2010. The uniaxial compression damage factor:

$$d_c = \begin{cases} 1 - \sqrt{k_c[\alpha_a + (3 - 2\alpha_a)x + (\alpha_a - 2)x^2]} & x \leq 1 \\ 1 - \sqrt{\frac{k_c}{[\alpha_d(x-1)^2 + x]}} & x > 1 \end{cases} \quad (6)$$

where $k_c = f_c/(\varepsilon_{c0}E_{c0})$. E_{c0} is secant modulus at peak compressive strain.

The uniaxial tensile damage factor:



$$d_t = \begin{cases} 1 - \sqrt{k_t(1.2 - 0.2x^5)} & x \leq 1 \\ 1 - \sqrt{\frac{k_t}{[\alpha_t(x-1)^{1.7} + x]}} & x > 1 \end{cases} \quad (7)$$

in which, $k_t = f_t / (\epsilon_{t0} E_{t0}) E_{t0}$ is the secant modulus corresponding to the maximum tensile strain.

The material parameters selected in the model are presented in Table 2. α_f is the ratio of biaxial ultimate compressive strength to one cycle ultimate compressive strength of the concrete. K is the ratio of second stress invariants on the tensile meridian and compressive meridian. The damage factor calculation curve and the stress-strain curves can be obtained by putting the FGC

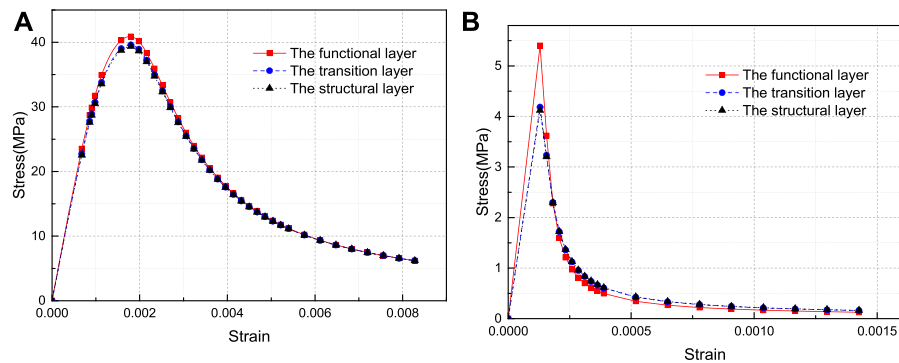
parameters into the above formulations, respectively, and the results are further presented in Figures 15, 16.

Failure Analysis of the FGC and the Ordinary Concrete Towers

Based on the FE model, the failure analysis of the FGC and the ordinary concrete towers is further conducted, and the results are presented in Figures 17, 18. In Figures 17, 18, the red area represents the failure area. In the tensile cloud image, the red areas represent areas of concrete cracking. While in the compression cloud image, the red areas represent areas where concrete is crushed and spalling. It can be seen from Figure 17 that the compressive damaged area of the

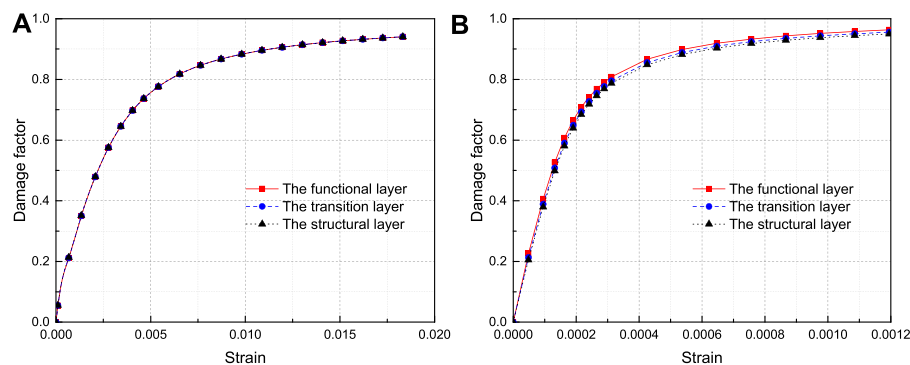
TABLE 2 | Material parameters of the ABAQUS model.

density (kg/m ³)	Poisson's ratio μ	Expansion angle (°)	Flow potential offset value	α_f	K	Viscosity coefficient
2,625	0.2	30	0.1	1.16	0.667	0.005



The uniaxial compression stress-strain curve of the FGC

The uniaxial tensile stress-strain curve of the FGC

FIGURE 15 | The uniaxial stress-strain curve of the FGC. (A) The uniaxial compression stress-strain curve of the FGC. (B) The uniaxial tensile stress-strain curve of the FGC.

The curve of the compression damage factor

The curve of the tensile damage factor

FIGURE 16 | The curve of the damage factor. (A) The curve of the compression damage factor. (B) The curve of the tensile damage factor.

ordinary concrete tower and the FGC tower is almost the same. Besides, the compression damage degree of the ordinary concrete tower is slightly larger than that of the FGC tower. **Figures 18A,B** show that in the anchor zone of cable and upper tower, the upper tower of each model has a local compression damage zone due to the action of cable force. However, the outer layer of the FGC tower is the functional layer of concrete, its tensile strength is relatively large, and so the local tensile damage is relatively small. It can also be seen from **Figure 18** that the tensile damage at the

anchorage of the lower tower and beam is relatively extensive. Also, there is some tensile damage at the bottom of the lower tower.

The damage degree of the FGC tower at this section is lower than that of the ordinary concrete one, and the reasons can be concluded as: 1) the crack resistance of the FGC tower is strengthened due to the improved mechanical properties of the functional layer concrete; 2) the usage of FGC material reduces the maximum stress of the concrete tower which can also reduce the damage of the concrete; 3) the functional layer

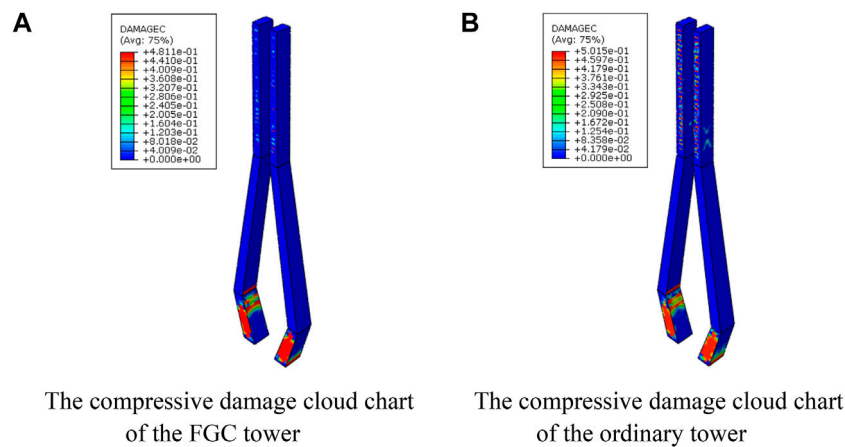


FIGURE 17 | The compressive damage cloud chart of the two different materials models. **(A)** The compressive damage cloud chart of the FGC tower. **(B)** The compressive damage cloud chart of the ordinary tower.

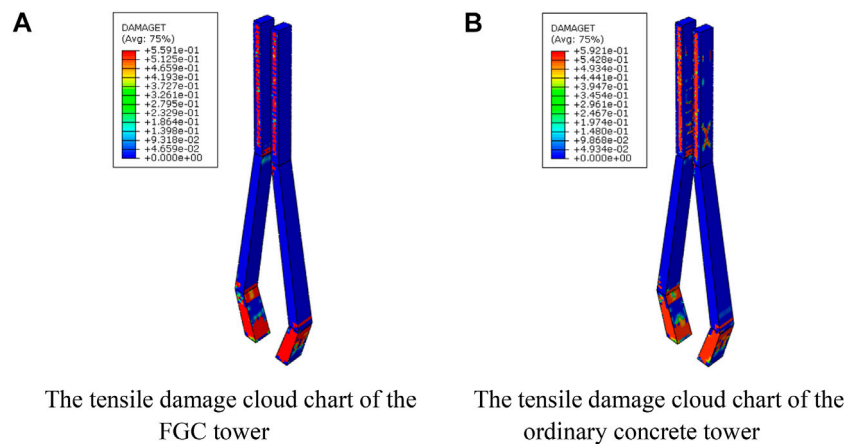


FIGURE 18 | The tensile damage cloud chart. **(A)** The tensile damage cloud chart of the FGC tower. **(B)** The tensile damage cloud chart of the ordinary concrete tower.

concrete is set at the outer layer of the tower where the stress is large.

CONCLUSION

The functionally gradient concrete is innovatively introduced into the towers of the Chizhou Yangtze River Bridge. It achieves the integrated design of mechanical properties and durability of the tower, and expands the application of FGC in engineering. Through the mechanical properties tests and the FE model simulations, the following conclusions can be drawn:

- (1) To study the performance of the gradient concrete tower, the mechanical properties of the novel gradient concrete tower material are tested. The obtained mechanical properties of the functional layer, transition layer, and structural layer can

be further used for the mechanical behavior analysis of the bridge tower.

- (2) Based on the calculated stress and deformation of the FGC and ordinary towers, the stiffness of the FGC cable tower increases slightly, and the vertical displacement is smaller than that of the ordinary concrete cable tower.
- (3) During the concreting, the high-performance concrete in the functional layer may generate the hydration heat. The influence of the hydration heat caused by the functional layer is relatively small. However, the crack resistance of the tower increases due to the FGC material.

DATA AVAILABILITY STATEMENT

The raw data supporting the conclusion of this article will be made available by the authors, without undue reservation.

AUTHOR CONTRIBUTIONS

The corresponding author is responsible for ensuring that the descriptions are accurate. ZW: writing the original draft, and providing conceptualization and Methodology. DD: creating the FE model, implementation of the experiments and data processing. SW: creating the FE model and numerical analysis. YM: modifying the draft and data analysis. YY: modifying and editing the draft.

FUNDING

This study was partly supported by the National Natural Science Foundation of China under grand No. 51922036, by

the key research and development project of Anhui province under grand No. 1804a0802204, by the Fundamental Research Funds for the Central Universities under grand No. JZ2020HGPD0117, and by the Natural Science Funds for Distinguished Young Scholar of Anhui province under grand No.1708085J06.

SUPPLEMENTARY MATERIAL

The Supplementary Material for this article can be found online at: <https://www.frontiersin.org/articles/10.3389/fmats.2021.676440/full#supplementary-material>

REFERENCES

- Abid, S. R., Tayşi, N., and Özakça, M. (2016). Experimental Analysis of Temperature Gradients in concrete Box-Girders. *Construction Building Mater.* 106, 523–532. doi:10.1016/j.conbuildmat.2015.12.144
- Amiri, I., and Nakamura, S. (2016). Structural Characteristics of Multi-Span cable-stayed Bridges with Hybrid, RC and Steel Towers. *Brs* 11 (4), 141–148. doi:10.3233/brs-160095
- Catbas, F. N., Susoy, M., and Frangopol, D. M. (2008). Structural Health Monitoring and Reliability Estimation: Long Span Truss Bridge Application with Environmental Monitoring Data. *Eng. Structures* 30 (9), 2347–2359. doi:10.1016/j.engstruct.2008.01.013
- Chan, R., Liu, X., and Galobardes, I. (2020). Parametric Study of Functionally Graded Concretes Incorporating Steel Fibres and Recycled Aggregates. *Construction Building Mater.* 242, 118186. doi:10.1016/j.conbuildmat.2020.118186
- Craveiro, F., Bartolo, H. M., Gale, A., Duarte, J. P., and Bartolo, P. J. (2017). A Design Tool for Resource-Efficient Fabrication of 3d-Graded Structural Building Components Using Additive Manufacturing. *Automation in Construction* 82, 75–83. doi:10.1016/j.autcon.2017.05.006
- Cross, E. J., Koo, K. Y., Brownjohn, J. M. W., and Worden, K. (2013). Long-term Monitoring and Data Analysis of the Tamar Bridge. *Mech. Syst. Signal Process.* 35 (1), 16–34. doi:10.1016/j.ymssp.2012.08.026
- Dias, C. M. R., Savastano Jr., H., Jr, and John, V. M. (2010). Exploring the Potential of Functionally Graded Materials Concept for the Development of Fiber Cement. *Construction Building Mater.* 24 (2), 140–146. doi:10.1016/j.conbuildmat.2008.01.017
- Do, T. A., Hoang, T. T., Bui-Tien, T., Hoang, H. V., Do, T. D., and Nguyen, P. A. (2020). Evaluation of Heat of Hydration, Temperature Evolution and thermal Cracking Risk in High-Strength concrete at Early Ages. *Case Stud. Therm. Eng.* 21, 100658. doi:10.1016/j.csste.2020.100658
- Du Plessis, A., Olawuyi, B. J., Boshoff, W. P., and Le Roux, S. G. (2016). Simple and Fast Porosity Analysis of concrete Using X-ray Computed Tomography. *Mater. Struct.* 49, 553–562. doi:10.1617/s11527-014-0519-9
- Han, A., Gan, B. S., and Pratama, M. M. A. (2016). Effects of Graded Concrete on Compressive Strengths. *IJTech* 7, 732–740. doi:10.14716/ijtech.v7i5.3449
- Herrmann, M., and Sobek, W. (2017). Functionally Graded concrete: Numerical Design Methods and Experimental Tests of Mass-Optimized Structural Components. *Struct. Concrete* 18 (1), 54–66. doi:10.1002/suco.201600011
- Herrmann, M., and Sobek, W. (2015). Gradientenbeton - Numerische Entwurfsmethoden und experimentelle Untersuchung gewichtsoptimierter Bauteile. *Beton- und Stahlbetonbau* 110 (10), 672–686. doi:10.1002/best.201500035
- Huang, Y., Liu, G., Huang, S., Rao, R., and Hu, C. (2018). Experimental and Finite Element Investigations on the Temperature Field of a Massive Bridge Pier Caused by the Hydration Heat of concrete. *Construction Building Mater.* 192, 240–252. doi:10.1016/j.conbuildmat.2018.10.128
- Kiryu, S., Han, A. L., Nurhuda, I., and Gan, B. S. (2018). “Analysis of Steel Reinforced Functionally Graded concrete Beam Cross Sections,” in *4th International Conference on Rehabilitation and Maintenance in Civil Engineering*. 195, 02031. doi:10.1051/mateconf/201819502031
- Kovaleva, D., Gericke, O., Kappes, J., Tomovic, I., and Sobek, W. (2019). Rosenstein Pavilion: Design and Structural Analysis of a Functionally Graded concrete Shell. *Structures* 18, 91–101. doi:10.1016/j.istruc.2018.11.007
- Kromanis, R., and Kripakaran, P. (2016). SHM of Bridges: Characterising thermal Response and Detecting Anomaly Events Using a Temperature-Based Measurement Interpretation Approach. *J. Civil Struct. Health Monit.* 6 (2), 237–254. doi:10.1007/s13349-016-0161-z
- Lee, J., and Fenves, G. L. (1998). Plastic-damage Model for Cyclic Loading of concrete Structures. *J. Eng. Mech.* 124 (8), 892–900. doi:10.1061/(asce)0733-9399(1998)124:8(892)
- Li, Q., and Xu, S. (2009). Experimental Investigation and Analysis on Flexural Performance of Functionally Graded Composite Beam Crack-Controlled by Ultrahigh Toughness Cementitious Composites. *Sci. China Ser. E-technol. Sci.* 52 (6), 1648–1664. doi:10.1007/s11431-009-0161-x
- Lubliner, J., Oliver, J., Oller, S., and Onate, E. (1989). A Plastic-Damage Model for concrete. *Int. J. Sol. Structures* 25 (3), 299–326. doi:10.1016/0020-7683(89)90050-4
- Maalej, M., Ahmed, S. F. U., and Paramasivam, P. (2003). Corrosion Durability and Structural Response of Functionally-Graded Concrete Beams. *Acta* 1 (3), 307–316. doi:10.3151/jact.1.307
- Miyamoto, Y., Niino, M., and Koizumi, M. (1997). “FGM Research Programs in Japan -from Structural to Functional Uses,” in *Functionally Graded Materials 1996*. Editors I. Shiotani and Y. Miyamoto (Amsterdam: Elsevier Science B.V.), 1–8. doi:10.1016/B978-044482548-3/50002-0
- Mohamed, M., and Victor, C. L. (1995). Introduction of Strain-Hardening Engineered Cementitious Composites in Design of Reinforced Concrete Flexural Members for Improved Durability. *ACI Struct. J.* 92 (2). doi:10.14359/11550
- Nes, L. G., and Øverli, J. A. (2016). Structural Behaviour of Layered Beams with Fibre-Reinforced LWAC and Normal Density Concrete. *Mat. Struct.* 49 (1), 689–703. doi:10.1617/s11527-015-0530-9
- Okamoto, Y., and Nakamura, S. (2011). Static and Seismic Studies on Steel/concrete Hybrid Towers for Multi-Span cable-stayed Bridges. *J. Constructional Steel Res.* 67 (2), 203–210. doi:10.1016/j.jcsr.2010.08.008
- Park, K., Paulino, G., and Roesler, J. (2010). Cohesive Fracture Model for Functionally Graded Fiber Reinforced Concrete. *Cement Concrete Res.* 40 (6), 956–965. doi:10.1016/j.cemconres.2010.02.004
- Potgieter, I. C., and Gamble, W. L. (1989). Nonlinear Temperature Distributions in Bridges at Different Locations in the United States. *pci* 34 (4), 80–103. doi:10.15554/pci.07011989.80.103
- Roesler, J., Paulino, G., Gaedicke, C., Bordelon, A., and Park, K. (2007). Fracture Behavior of Functionally Graded Concrete Materials for Rigid Pavements. *Transportation Res. Rec.* 2037 (1), 40–49. doi:10.3141/2037-04
- Shao, X., Deng, F., and Deng, L. (2018). Conceptual Design of a New Three-Tower Cable-Stayed Bridge System with Unequal-Size Fans. *J. Bridge Eng.* 23 (7). doi:10.1061/(ASCE)BE.1943-5592.0001257
- Son, J., and Lee, H.-J. (2011). Performance of cable-stayed Bridge Pylons Subjected to Blast Loading. *Eng. Structures* 33 (4), 1133–1148. doi:10.1016/j.engstruct.2010.12.031

- Sousa Tomé, E., Pimentel, M., and Figueiras, J. (2018). Structural Response of a concrete cable-stayed Bridge under thermal Loads. *Eng. Structures* 176, 652–672. doi:10.1016/j.engstruct.2018.09.029
- Sridhar, R., and Prasad, D. R. (2019). Damage Assessment of Functionally Graded Reinforced concrete Beams Using Hybrid Fiber Engineered Cementitious Composites. *Structures* 20, 832–847. doi:10.1016/j.istruc.2019.07.002
- Strieder, E., Hilber, R., Stierschneider, E., and Bergmeister, K. (2018). FE-study on the Effect of Gradient Concrete on Early Constraint and Crack Risk. *Appl. Sci.* 8 (2), 246. doi:10.3390/app8020246
- Torelli, G., Fernández, M. G., and Lees, J. M. (2020). Functionally Graded concrete: Design Objectives, Production Techniques and Analysis Methods for Layered and Continuously Graded Elements. *Construction Building Mater.* 242, 118040. doi:10.1016/j.conbuildmat.2020.118040
- Wen, X.-d., Tu, J.-l., and Gan, W.-z. (2013). Durability protection of the Functionally Graded Structure concrete in the Splash Zone. *Construction Building Mater.* 41, 246–251. doi:10.1016/j.conbuildmat.2012.11.119
- Xu, S., and Li, Q. (2009). Theoretical Analysis on Bending Behavior of Functionally Graded Composite Beam Crack-Controlled by Ultrahigh Toughness Cementitious Composites. *Sci. China Ser. E-technol. Sci.* 52 (2), 363–378. doi:10.1007/s11431-008-0337-9
- Zhang, Y., Xu, S., Gao, Y., Guo, J., Cao, Y., and Zhang, J. (2020). Correlation of Chloride Diffusion Coefficient and Microstructure Parameters in concrete: A Comparative Analysis Using NMR, MIP, and X-CT. *Front. Struct. Civ. Eng.* 14, 1509–1519. doi:10.1007/s11709-020-0681-9
- Zhu, B. (2013). *Thermal Stresses and Temperature Control of Mass concrete*. Butterworth-Heinemann. doi:10.1016/C2012-0-06038-3 CrossRef Full Text

Conflict of Interest: Author YY was employed by Anhui Transportation Holding Group Co., LTD.

The remaining authors declare that the research was conducted in the absence of any commercial or financial relationships that could be construed as a potential conflict of interest.

Copyright © 2021 Wang, Duan, Wang, Mo and Yin. This is an open-access article distributed under the terms of the Creative Commons Attribution License (CC BY). The use, distribution or reproduction in other forums is permitted, provided the original author(s) and the copyright owner(s) are credited and that the original publication in this journal is cited, in accordance with accepted academic practice. No use, distribution or reproduction is permitted which does not comply with these terms.



Structural Health Monitoring Method of Pantograph–Catenary System Based on Strain Response Inversion

Sheng Liu¹, Yibo Wei^{2*}, Yongxin Yin³, Tangzheng Feng³ and Jinbao Lin¹

¹Department of Mechanics, School of Applied Science, Taiyuan University of Science and Technology, Taiyuan, China, ²Faculty of Infrastructure Engineering, Dalian University of Technology, Dalian, China, ³Shenzhen JEMETECH Co., Ltd, Shenzhen, China

OPEN ACCESS

Edited by:

Liang Ren,
Dalian University of Technology, China

Reviewed by:

Peng Zhang,
Dalian Maritime University, China
Xuemin Chen,
Texas Southern University,
United States
Tao Jiang,
Shantou University, China

*Correspondence:

Yibo Wei
weiyibo1995@gmail.com

Specialty section:

This article was submitted to
Interdisciplinary Physics,
a section of the journal
Frontiers in Physics

Received: 06 April 2021

Accepted: 19 May 2021

Published: 07 June 2021

Citation:

Liu S, Wei Y, Yin Y, Feng T and Lin J
(2021) Structural Health Monitoring
Method of Pantograph–Catenary
System Based on Strain
Response Inversion.
Front. Phys. 9:691510.
doi: 10.3389/fphy.2021.691510

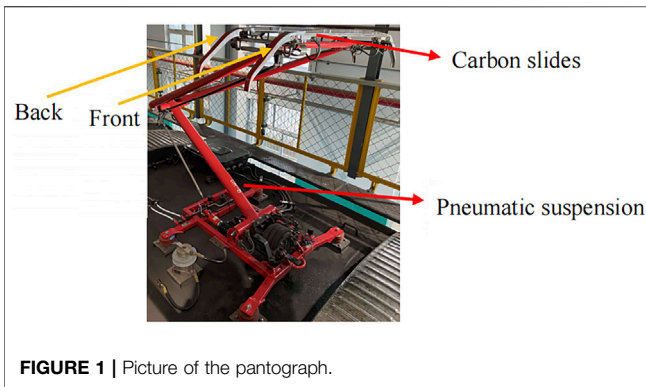
Pantograph–catenary system provides electric energy for the subway lines; its health status is essential to the serviceability of the vehicle. In this study, a real-time structural health monitoring method based on strain response inversion is proposed to calculate the magnitude and position of the dynamic contact force between the catenary and pantograph. The measurement principle, calibration, and installation detail of the fiber Bragg grating (FBG) sensors are also presented in this article. Putting this monitoring system in use, an application example of a subway with a rigid overhead catenary is given to demonstrate its performance. The pantograph was monitored and analyzed, running underground at a maximum speed of 80 km/h. The results show that the strain response inversion method has high measurement accuracy, good data consistency, and flexibility on sensor installation. It can accurately calculate the magnitude and location of the contact force exerted on the pantograph.

Keywords: pantograph, dynamic contact force, inversion, structural health monitoring, FBG sensor

INTRODUCTION

With the rapid urbanization progress in China, subway lines have become longer and faster, as an indicator of city growth. By 2019, rail transit in China has reached a total length of 6,600 km, where the newly built lanes were 300 km. Considering mainland China in 2019, the subway-conducted passenger count was 23.814 billion, which has increased by 11.8% than that of 2018 [1–3]. Currently, subways are mainly powered by electricity harnessed through the pantograph–catenary coupling system while running. Thus, the structural health monitoring (SHM) of the coupling is crucial to the safety of the subway lines [4–9]. The contact resistance increases as the force between the catenary and pantograph decreases, consuming energy and generating heat, which could cause separation of the coupling and erosion of the contacting surface. On the contrary, if the force exceeds the safe level, the friction between the carbon slider and the catenary could lead to failure of the parts and thus accident [10].

At present, the main method of contact force measurement is to lay pressure sensors and acceleration sensors. The pantograph–catenary contact force can be obtained by balancing the force and using the inertia compensation method [11]. Japanese railway system applied an optimized measuring system by using the same number of sensors as the number of vibration modes and combining them to form a weighted average [12]. Studying the relation between the pantograph's input and output, Japanese researchers have developed an inversion method using the vibration response for calculating the contact force [13]. In Germany, the pantograph monitoring system considers the horizontal and vertical forces and the vertical acceleration on each side of the carbon plating above the vehicle [14]. The methods mentioned above utilize electrical sensors such as resistance-based strain gauges to collect data; these



sensors suffer from electromagnetic interference, and therefore they could be inaccurate. Tatsuya Koyama developed a camera recognition system that could analyze the internal force, inertial force, and contact force without installing sensors directly on the structures [15]. However, such an arrangement could be challenging to implement due to the inevitable complexation of the actual application. Recently, the researcher developed a method based on the transfer function to calculate the contact force, which considers the pantograph arc vibration waveform or the transfer function related to the contact force and the strain response [16]. Yet, this method lacks accuracy and has many restraints in the calculation.

A fiber Bragg grating (FBG) sensor has become a hotspot in the field of SHM system; it has been the vital component in the maintenance and management of a wide range of structures [17–21]. FBG sensors are ideal for monitoring the pantograph–catenary system, as it has the advantage of electromagnetic resistance, long-term reliability, and versatility in terms of implementation. In 2013, researchers applied bare FBG strain sensors underneath the pantograph head to monitor the magnitude of the contact force [22]. However, the monitoring of the contact force location remains unresolved, and the bare fiber can be challenging to install.

In this article, an inversion method based on the pantograph's strain response to calculate the magnitude and location of the contact force is proposed. First, the mechanical model used in the calculation will be presented. Then, the relation between the contact force and the strain response measured by FBG sensors will be discussed along with the casing and temperature compensation method, which guides the design of the monitoring scheme. Finally, after a detailed calibration and adjustment process of the sensing system, the in-line test result will be presented.

PRINCIPLE OF PANTOGRAPH–CATENARY DYNAMICS

Inversion Method Based on Strain Response

The pantograph consists of two conducting plates made of carbon which are mounted on a pneumatic suspension system. **Figure 1** is a picture taken on-site at the Xi'an subway.

The carbon slides are modeled as two simply supported beams, namely front and back. The mechanical model is shown in **Figure 2**.

As the vehicle runs, the beam would have a vertical acceleration of a_0 . If the inertial force is considered to be uniformly distributed along the carbon slide, it can be expressed as $m_0 a_0 / L$; where m_0 is the mass of the carbon slide, and L is its effective length. The aerodynamic force is proportional to the square of the velocity [23]; since the subway in discussion moves underground at a maximal velocity of 80 km/h with no external wind load; the aerodynamic factor is ignored in the modeling.

The dynamic contact force presents itself in terms of strain distribution, as follows:

$$\varepsilon_1 = \frac{\frac{F(L-x_f)x_1}{L} + \frac{m_0 a_0 x_1}{2} - \frac{m_0 a_0 x_1^2}{2L}}{EW}, 0 \leq x_1 \leq x_f, \quad (1)$$

$$\varepsilon_2 = \frac{\frac{F(L-x_f)x_2}{L} + \frac{m_0 a_0 x_2}{2} - F(x_2 - x_f) - \frac{m_0 a_0 x_2^2}{2L}}{EW}, x_f \leq x_2 \leq L. \quad (2)$$

Here, ε_1 and ε_2 are the strain measurements taken at the position x_1 and x_2 . E and W are the elastic modulus and the resistance moment of the cross-section, respectively. Most importantly, x_f is the position of the contacting point between the pantograph and the rigid overhead, and F is the contacting force. It can be seen from the equations above that the locations of the sensors are arbitrary, as long as the contact force is bounded within, that is $x_1 \leq x_f \leq x_2$.

Solving for F and x_f , assuming the two strain measurements are taken symmetrically, we get the following:

$$F = \frac{EW(\varepsilon_1 + \varepsilon_2) - (C_1 + C_2)}{x_1}, \quad (3)$$

$$x_f = \frac{(EW\varepsilon_2 - C_2)}{(EW\varepsilon_1 - C_1) + (EW\varepsilon_2 - C_2)} L. \quad (4)$$

Here, $C_1 = \frac{m_0 a_0 x_1}{2} - \frac{m_0 a_0 x_1^2}{2L}$ and $C_2 = \frac{m_0 a_0 x_2}{2} - \frac{m_0 a_0 x_2^2}{2L}$ are the acceleration terms.

Again, the derivation above is obtained by taking $x_1 + x_2 = L$ for simplicity. In real applications, the sensor location could be asymmetrical; this method is still usable but with a more complicated solution.

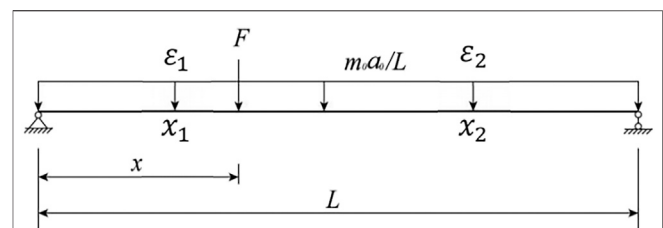


FIGURE 2 | mechanical model of the pantograph.

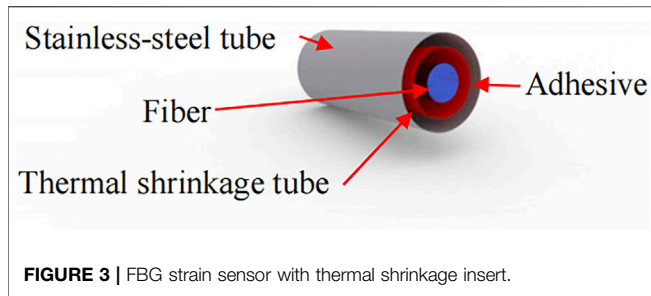


FIGURE 3 | FBG strain sensor with thermal shrinkage insert.

Sensor Types and Sensing Principle

One of the challenges of pantograph monitoring is the electromagnetic interference caused by high voltage power lines. In this project, fiber Bragg grating (FBG) sensors are used to measure the strain response. The sensor itself has the advantages of high sensitivity, low noise, electromagnetic resistance, and long-term reliability, which suit the need for pantograph–catenary monitoring [24]. However, FBG sensors' wavelength variation is a joint result of temperature fluctuation, contact force, and the Poisson effect [25].

To counter the thermal expansion, this project used a type of FBG sensor, shown in **Figure 3**, that had a layer of thermal shrinkage material embedded. Improving the performance of the strain sensors even further, a type of micro-FBG was also used that had a smaller size and only sensed the temperature change.

In the following derivation, the quantities related to micro-FBGs are denoted with underscore μ , and the those related to FBG strain sensors are denoted with underscore F . The wavelength shift of the FBGs can be expressed as follows:

$$\Delta\lambda_{\mu} = \alpha_{\{\varepsilon,\mu\}}\Delta\varepsilon_{\mu} + \alpha_{\{T,\mu\}}\Delta T, \quad (5)$$

$$\Delta\lambda_F = \alpha_{\{\varepsilon,F\}}\Delta\varepsilon_F + \alpha_{\{T,F\}}\Delta T. \quad (6)$$

Here, $\Delta\lambda_{\mu}$ and $\Delta\lambda_F$ are the wavelength variations of the microsensors and the strain sensors, respectively. $\Delta\varepsilon_{\mu}$ is the strain induced by the Poisson effect. ΔT is the temperature variation. α_{ε} is related to the elastic optical coefficient of the optical fiber, which can be written as follows:

$$\alpha_{\varepsilon} = \lambda_B(1 - P_e), \quad P_e = \frac{1}{n} \frac{dn}{d\varepsilon}. \quad (7)$$

The thermal expansion coefficient α_T can be expressed as follows:

$$\alpha_T = \lambda_B(\alpha_f - \zeta), \quad \alpha_f = \frac{1}{\Lambda} \frac{d\Lambda}{dT}. \quad (8)$$

Here, $\zeta = n \frac{dn}{dt}$ is the thermal-optic coefficient. Note that

$$\alpha_{\{T,F\}}\Delta T = k\alpha_{\{T,\mu\}}\Delta T, \quad \Delta\varepsilon_{\mu} = -\mu\Delta\varepsilon_F. \quad (9)$$

Here, μ is the carbon slide's Poisson ratio, and k is a temperature coefficient of the micro-FBG, determined in the calibration process.

Substituting Eqs 7–9 into Eqs 5, 6 yields the following equation:

$$\Delta\varepsilon_F = \frac{\Delta\lambda_F - k\Delta\lambda_{\mu}}{\alpha_{\{\varepsilon,F\}} + k\mu\alpha_{\{\varepsilon,\mu\}}}. \quad (10)$$

Judging from the results on-site, the vertical strain caused by the Poisson effect was insignificant; thus, the micro-FBG's wavelength variation was considered only as a result of temperature variation. A calibration process was done to evaluate k so that the micro-FBGs could be used as a temperature gauge to compensate for the thermal effect on the strain sensors.

Also, to monitor the acceleration dynamics, the FBG accelerometers were implemented.

CALIBRATION

Temperature Compensation Factor Calibration

To compensate for the thermal effect, every strain sensor on the pantograph was paired with a micro-FBG. The pantograph was then placed outdoor overnight; as the temperature changes through the night, the wavelength data of each FBG was collected and used to calculate the compensation factor, k . The linear fit of the sensors on the pantograph's right side is shown in **Figure 4** as an example.

Each side yielded a fit that has a R^2 greater than 0.99, which is an indicator of the sensors' consistency. For the left side, the compensation factor is 2.10470, and that of the right side is 2.10327. Based on these results, k is taken to be 2.10399 for this project.

EW Calibration

E and W are the elastic modulus and the resistance moment of the cross-section, respectively; the product of the two is

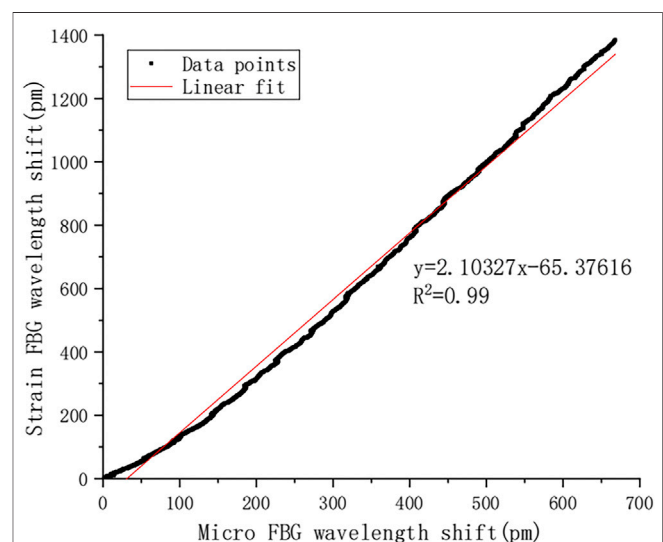
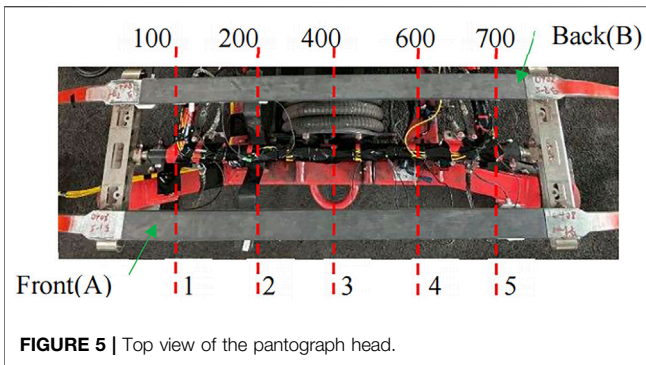


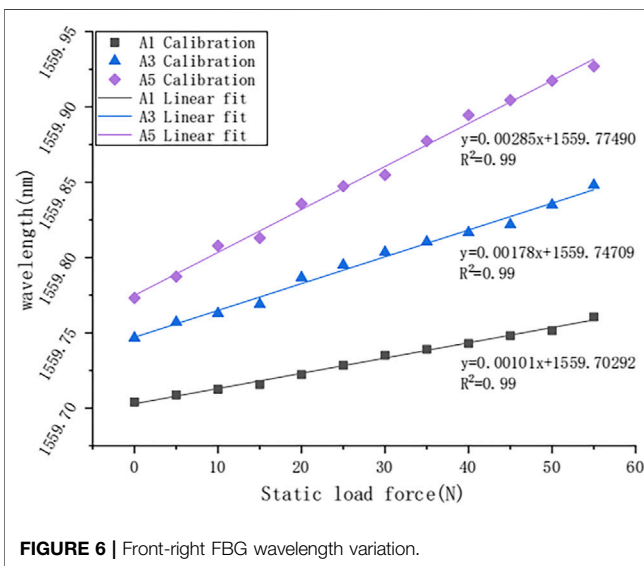
FIGURE 4 | Linear fit of wavelength change between the micro-FBG sensor and the FBG strain sensor.



The length of the slide is 800 mm. Marking the left side as 0 and the right side 800, five points were selected at 200, 300, 400, 500, and 600, as shown in **Figure 5**. The weight loaded on each point started from 0 N and increases to 110 N with a 10 N increment.

During the calibration, sensors' wavelengths varied linearly as the load increased. The root mean squares were greater than 0.99 for all sensors. **Figure 6** below is the data plotted for one sensor's wavelength with different load locations.

The wavelength value was used in **Eq. 10** to obtain the strain value, which was then substituted into **Eqs 1, 2** to calculate the *EW* for each side of the pantograph. The final value of *EW* used in the further calculation was the average of both sides.



considered as a constant to be calibrated at each strain measure location. The strategy used in this article was to apply force at different locations of the pantograph head gradually.

REAL-TIME MONITORING AND ANALYSIS

Background and Sensor Layout Scheme

The subway line in this project has a total length of over 35 km with more than 25 stations, all of which are underground, and adopted the rigid overhead catenary design. Measurement was done as the vehicle departing the base station and making a stop at each station.

According to the measurement principle, strain sensors should be installed symmetrically so that the contact force is bounded in between the two sensors. Judging from the working condition and the abrasion of the other pantographs, strain sensors were installed 135 mm away from the ends. As shown in **Figure 7**, this pantograph had a set of two carbon slides, which contributed to 4 strain sensors. In addition, micro-FBGs, sensing only the temperature change, were installed perpendicular to the strain sensors.

The accelerometers were installed at the front and back slides of the pantograph, as shown in **Figure 8**.

Data Analysis of Pantograph Elevation

The elevation process is what gives the subway its power. The process itself is powered by high-pressure air, which pushes the

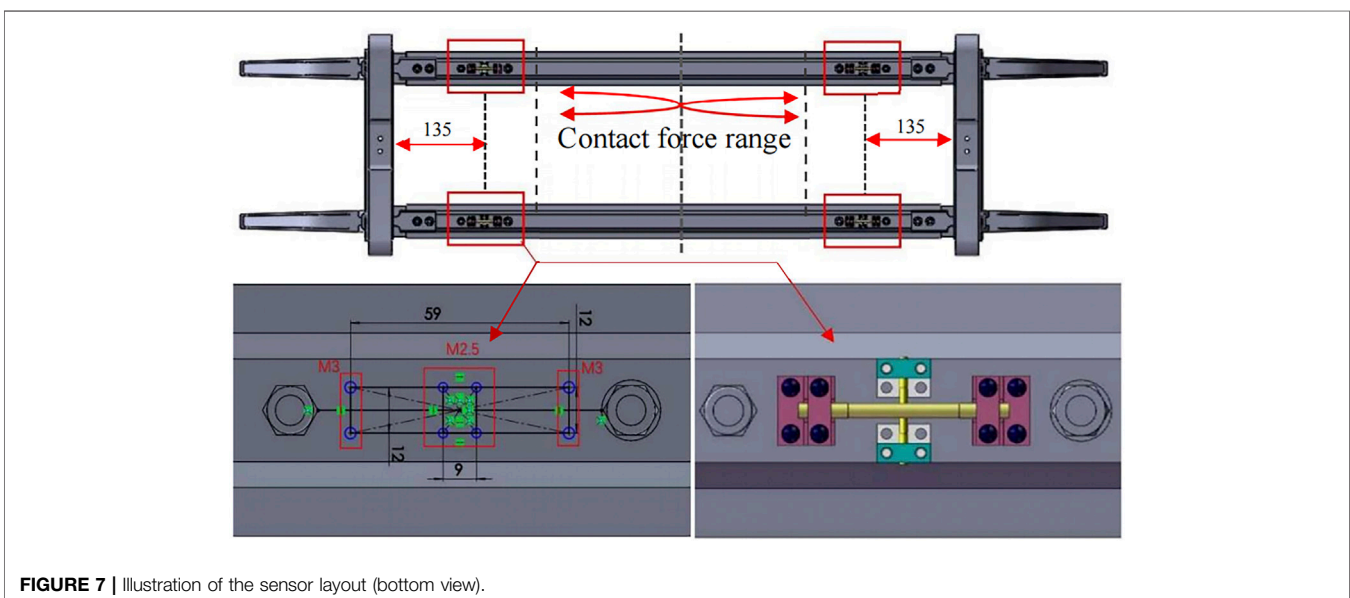




FIGURE 8 | Configuration of the sensors.

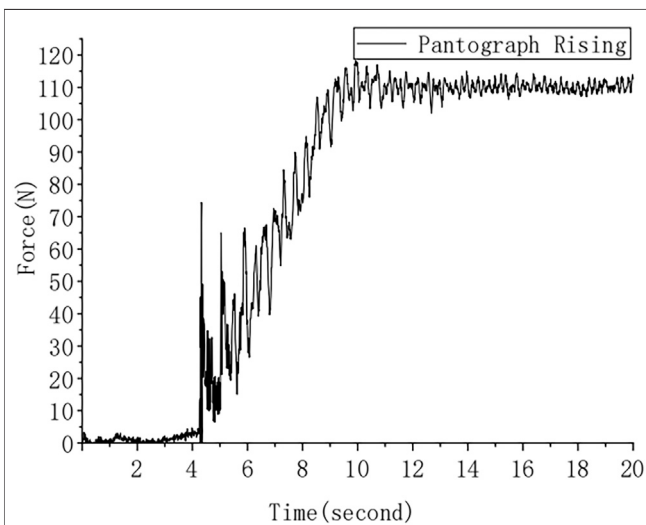


FIGURE 9 | Contact force of the elevation process.

pantograph toward the catenary [26]. Therefore, the contacting force should increase linearly during this process.

As shown in **Figure 9**, the contacting force increased from 0 to 118.24 N and stayed at 110 N with a standard deviation of 1.81 N. The initial contact position was 351.16 mm from the left support of the arc. The force's magnitude calculated from the strain response agrees with the force that drives the pantograph, and the calculated position fits well with the directly measured result. This monitoring test of the elevation process shows that the algorithm is valid in the static condition.

Data Analysis of the Subway in Motion

The subway departed from the base making stops at each station. The desired speed was 80 km/h, and the distance between stations was not long enough. Consequently, the vehicle accelerated, leaving the stations, and then decelerated as it approached the next.

It can be foreseen that the contact force would have a magnitude of 120 N with deviation caused by vibration and rail conditions. As presented in **Figure 10**, going from one stop to the next, the contact force has a maximum of 125.86 N, a minimum of 115.71 N, and a standard deviation of 3.23 N. The contact force is constantly greater than 0 N, which means no separation of the pantograph and the catenary.

Monitoring the magnitude of the contact force is crucial for SHM of the pantograph–catenary system; equally important is the force's location detection, as it gives information about possible erosion and fatigue on the carbon slider.

The rigid overhead catenary system has a zigzag shape responsible for the position variation, when the subway is in motion. For example, in **Figure 11**, the contact position was oscillating between 200 and 600 mm, indicating that the subway was passing through the zigzagged catenary.

Figure 12 is an enlarged time interval, corresponding to the vehicle departing from one stop to the next. The shift of the contact position is roughly the same as boxed in the figure. Given the symmetrical property of the catenary's 'Z' shape, it is

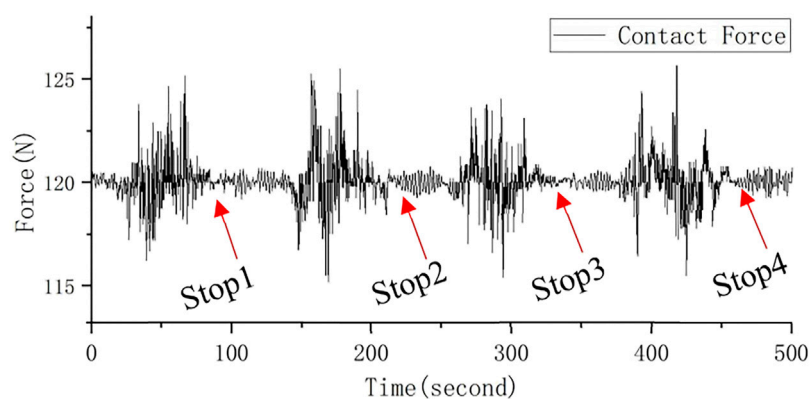


FIGURE 10 | In-line contact force variation.

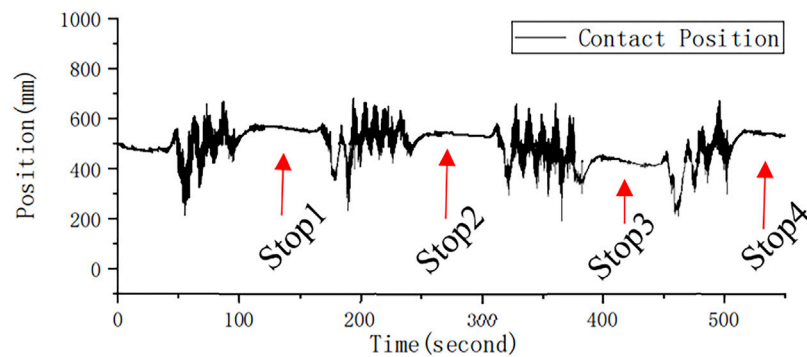


FIGURE 11 | Contact force position varying with a “Z” shape manner.

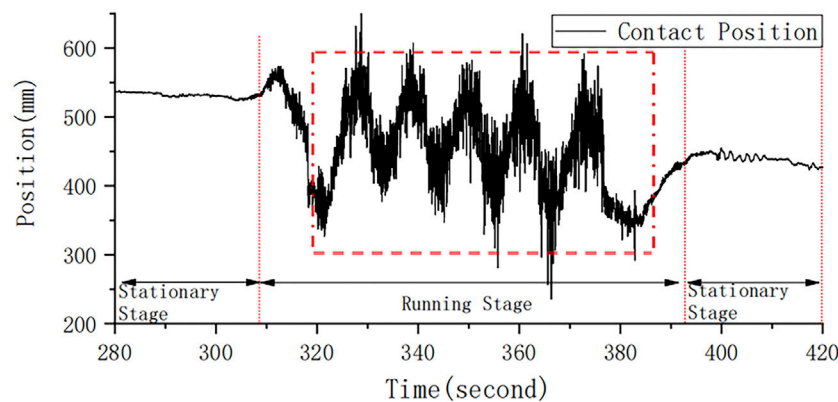


FIGURE 12 | Contact position of one interval.

reasonable to conclude that the inversion method is able to detect the location of the force with minor discrepancy.

CONCLUSION

This study proposed an inversion method for calculating and locating the dynamic contact force of the pantograph–catenary system based on its strain response using fiber Bragg grating (FBG) sensors. It has overcome the electromagnetic inference that traditional sensors suffer, making it ideal for the task. The carbon slide on the pantograph has been modeled as simply supported beams for the calculation. This model then guided the design of a structural health monitoring project in Xi’an. After the calibration, the sensing system was tasked with monitoring the progress of the pantograph elevation. Finally, real-time data were collected and analyzed for the subway in motion. The magnitude and the location of the contact force were in good agreement with the prediction; that is, the location result resembles the “Z” shape of the overhead catenary, and the magnitude mainly fluctuates between 115 and 125 N.

The strain response inversion method is shown to be accurate, consistent, and relatively easy to install. Not only does it monitor the force’s magnitude but also the position of the force exerted, giving the SHM system another angle to evaluate the reliability of pantograph–catenary coupling.

DATA AVAILABILITY STATEMENT

The original contributions presented in the study are included in the article/Supplementary Material, and further inquiries can be directed to the corresponding author.

AUTHOR CONTRIBUTIONS

JL guided the development of the theory and the design of the experiment. SL, YY, and TF were responsible for sensors installation, equipment calibration, and data collection. YW and SL then processed and analyzed the raw data producing usable results and plots.

REFERENCES

1. Cao B-K. The Development of the Subway in the World Is Striking [J]. *Urban Public Transport* (2003) 5:33. doi:10.3969/j.issn.1009-1467.2003.05.017
2. Bao-ming H, Jia-hao C, Yun-jie Y, Lei Q, Zhi-xuan Y, and Wei D. Statistical Analysis of Urban Rail Transit Operation in the World in 2019: A Review [J]. *Urban Mass Transit*, 2020, 33(01):4–8. doi:10.3969/j.issn.1672-6073.202
3. Niu A. Summary of China's Urban Subway Passenger Volume in 2019 [J]. *China Metros* (2020)(02) 33–7. doi:10.14052/j.cnki.china.metros.2020.02.008
4. Wang J-P, and Zou Y. Optimization of Pantograph Upper Frame Structure Design for Urban Rail Multiple Unit [J]. *Urban Mass Transit* (2019) 22(07): 46–9. doi:10.16037/j.1007-869x.2019.07.011
5. Zai-min L, and Zhao-peng Z. Necessity of Reviewing Rules for Interface between Pantograph and Catenary Based on Their Failures [J]. *Mod Urban Transit* (2016)(2) 36–1. doi:10.3969/j.issn.1672-7533.2016.02.009
6. Zhang S, Fu X-Q, and Zhan M-J. Development and Application of on Board Pantograph/ Catenary Dynamic Monitoring System for Changzhou Metro Line 1 [J]. *Electric Railway* (2019) 30(06):72–4. doi:10.19587/j.cnki.1007-936x.2019.06.017
7. Yang Z-P. Research on Characteristics and Diagnosis of Pantograph/Catenary Contact Force Defects [J]. *Electric Railway* (2018) 29(01):27–30. doi:10.19587/j.cnki.1007-936x.2018.01.006
8. Yan-Long L, Wen-Feng W, Tao W, Zhi-Peng Y, and Wen-Xuan. Defect Analysis, Diagnosis and Treatment of Pantograph/ Catenary Contact Force [J]. *Electric Railway* (2019) 30(06):56–9. doi:10.19587/j.cnki.1007-936x.2019.06.014
9. Wang Z, and Tian L. Research and Application of Comprehensive Evaluation Index for OCS Quality of High-Speed Railway [J]. *Electric Railway* (2019) 30(S1):144–6. doi:10.19587/j.cnki.1007-936x.2019z.037
10. Gui-Ming M. *A Research on the Dynamic Contact Force of Pantograph-Catenary System[D]*. Chengdu: Southwest Jiaotong University (2001). doi:10.7666/d.y394565
11. Xiang-Dong L, and Sun Z. Key Technology of Pantograph/Catenary Contact Force Detection [J]. *Railway Tech Innovation* (2012)(01) 72–4. doi:10.19550/j.issn.1672-061x.2012.01.020
12. Xiao-lin Z, Xiao-Rong G, Li W, and Ze-yong W. Introduction on the Detection of Pantograph Catenary Contact Force [J]. *Railway Qual Control* (2010) 38(08):11–3. doi:10.3969/j.issn.1006-9178.2010.08.004
13. Zhu Y. A New Measuring Method of Pantograph Contact Force [J]. *Rail Transportation Equipment Technology* (2004)(03) 32. doi:10.3969/j.issn.1007-6042.2004.03.012
14. Xiao-na Z, Xing-jun W, and Gen-Hou X. Catenary Detection System of German High-Speed Railway [J]. *China Railway* (2008)(09) 60–2. doi:10.3969/j.issn.1001-683X.2008.09.016
15. Koyama T, Ikeda M, Kobayashi S, Nakamura K, Tabayashi S, and Niwakawa M. Measurement of the Contact Force of the Pantograph by Image Processing Technology. *QR of RTRI* (2014) 55(2):73–8. doi:10.2219/rtriqr.55.73
16. Meng-ying T, Dong Z, Rui-Ping L, Yan L, Ning Z, Gui-ming M, et al. New Contact Force Measuring Method for Overhead Catenary Systems Based on Strain [J]. *J Southwest Jiaotong Univ* (2017) 52(06):1208–15. doi:10.3969/j.issn.0258-2724.2017.06.023
17. Hong-Nan L, Li-Dong Y, Liang R, and Zi-guang J. Design and Development of Structural Health Monitoring System for the Dalian Stadium [J]. *J Building Structures* (2013) 34(11):40–9. doi:10.14006/j.jzjgxb.2013.11.007
18. Hong-Nan L, Liang T, Ting-Hua Y, and Liang R. Design and Development of Structural Health Monitoring System for Long Span Skew Arch Bridge [J]. *J Vibration Eng* (2015) 28(04):574–84. doi:10.16385/j.cnki.issn.1004-4523.2015.04.010
19. Liang R, Tao J, Dong-Sheng L, Shu-li F, and Hong-nan L Application of Small FBG Strain Sensors in Dam Model Experiment [J]. *J Vibration, Measurement Diagn* (2013) 33(02):277–83. doi:10.16450/j.cnki.issn.1004-6801.2013.02.029
20. Hong-Nan L, Xue-Heng J, Liang R, Jian-yuan C, and Tong Z. Application of FBG Strain Sensors to Experiments of Artificial concrete Dam Models [J]. *J Dalian Univ Technology* (2011) 51(01):103–8. doi:10.7511/dllgxb201101019
21. Zhi-Wei C. Fatigue Reliability Assessment of Multi-Loading Suspension Bridges Based on SHMs [J]. *Eng Mech* (2014) 31(07):99–105. doi:10.6052/j.issn.1000-4750.2013.01.0043
22. Marco B, Giuseppe B, Andrea C, and Lorenzo C. Pantograph–catenary Monitoring by Means of Fiber Bragg Grating Sensors: Results from Tests in an Underground Line. *J Mech Syst signal Process* (2013) 41(1–2):226–38. doi:10.1016/j.ymssp.2013.06.030
23. Xing L, Jian D, Yao Z, and Guo-feng P. Impact of the Aerodynamics of Pantograph of a High-Speed Train on Pantograph-Catenary Current Collection [J]. *J Zhejiang University (Engineering Science)* (2013) 47(3): 558–64. doi:10.3785/j.issn.1008-973X.2013.03.024
24. Liang R, Hong-nan L, Zhi-Qiang H, Jian-bo L, and Gao L. Development and Application of FBG Strain Sensor with Enhanced Sensitivity in the Model Vibration experiment [J]. *J Optoelectronics-Laser* (2008)(11) 1437–41. doi:10.3321/j.issn:1005-0086.2008.11.003
25. Liang R. *Application of Fiber Optic Grating in Structural Health Monitoring [D]*. Dalian: Dalian University of Technology (2008).
26. Guo-lei M, Xiu-jun G, and Yao S. Research on Design Philosophy of the Pantograph [J]. *Railway Locomotive Car* (2014) 34(2) 129–32. doi:10.3969/j.issn.1008-7842.2014.02.32

Conflict of Interest: Author YY and TF were employed by the company Shenzhen JEMETECH Co., Ltd.

The remaining authors declare that the research was conducted in the absence of any commercial or financial relationships that could be construed as a potential conflict of interest.

Copyright © 2021 Liu, Wei, Yin, Feng and Lin. This is an open-access article distributed under the terms of the Creative Commons Attribution License (CC BY). The use, distribution or reproduction in other forums is permitted, provided the original author(s) and the copyright owner(s) are credited and that the original publication in this journal is cited, in accordance with accepted academic practice. No use, distribution or reproduction is permitted which does not comply with these terms.



Structural Health Monitoring for Bridge Crane Based on Low Temperature-Sensitivity FBG Sensors

Zhang Zhaobo^{1*}, Liu Sheng², Wei Yibo¹ and Li Hongnan¹

¹Faculty of Infrastructure Engineering, Dalian University of Technology, Dalian, China, ²Department of Mechanics, School of Applied Science, Taiyuan University of Science and Technology, Taiyuan, China

OPEN ACCESS

Edited by:

Qingzhao Kong,
Tongji University, China

Reviewed by:

Niravkumar J. Joshi,
University of Sao Paulo, Brazil

Jun Li,
Curtin University, Australia
Guang-Dong Zhou,
Hohai University, China

*Correspondence:

Zhang Zhaobo
zhzb1992@163.com

Specialty section:

This article was submitted to
Interdisciplinary Physics,
a section of the journal
Frontiers in Physics

Received: 09 March 2021

Accepted: 03 June 2021

Published: 17 June 2021

Citation:

Zhaobo Z, Sheng L, Yibo W and
Hongnan L (2021) Structural Health
Monitoring for Bridge Crane Based on
Low Temperature-Sensitivity
FBG Sensors.
Front. Phys. 9:678263.
doi: 10.3389/fphy.2021.678263

Accurate measurement of the strain variation and effective distinguishment of the temperature-induced stress from the load-induced stress have been major objectives for strain sensors in crane monitoring. In this paper, a fiber Bragg grating (FBG) strain sensor with low temperature-sensitivity, packaged by two gripper tubes and stainless-steel tubes, is presented and applied in a bridge crane health monitoring project. Calibration experiments and reliability tests are conducted to evaluate the strain transferring characteristics of the sensors in a laboratory environment. The results show that the temperature coefficient of the sensor decreases from 10.5 pm/°C to 1.5 pm/°C and the strain coefficient increases from 1.2 pm/μ ϵ to 4.8 pm/μ ϵ . On the other hand, the on-site tests show that these FBG strain sensors have the advantage of precision, reliability, and applicability. Meanwhile, the low temperature-sensitivity nature of the sensors is verified by the test results, which shows its promising potential in the health monitoring for a bridge crane.

Keywords: bridge Crane¹, FBG sensor², accurate measurement³, low temperature-sensitivity⁴, long-term monitoring⁵

INTRODUCTION

Health monitoring for steel structures has been widely used in practical engineering. The bridge crane, suffering from the corrosive salt-spray environment as it works in port, is subjected to the coupling action of wind load and working load during its service period. The steel structure, which is the primary bearing component of a crane, may have cracks and deformations [1, 2] under long-term loads, which endanger the structure's serviceability and strength.

Tochaei et al. [3] established a health monitoring system for the steel structure of the Manhattan Bridge to estimation fatigue life and reliability, and achieved good results. Hence, a viable real-time health monitoring system for cranes is in need.

With the development of information technology, researchers realized that monitoring various parameters of the crane can provide layers of protection in construction safety [4]. Among them, strain is one of the most significant parameters that can reflect the mechanical characteristics of metal structure [5]. Naturally, strain sensing has gradually become more and more critical in the field of real-time monitoring of the crane. A load moment indicator (LMI) is a system that aids the crane operator by sensing (directly or indirectly) the overturning moment on the crane (load multiplied by radius). Xu et al. [6] collected the structure stress by resistance strain gauges and established a complete monitoring system. Lalik et al. [7] calculated stresses in the base of the mast crane by surveying the inclination of the tower mast and jib by using a tacheometer to measure the coordinates

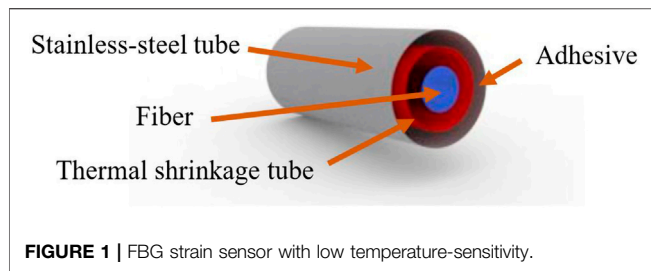


FIGURE 1 | FBG strain sensor with low temperature-sensitivity.

of two prisms placed on the construction crane. However, for a crane designed to serve in a salt spray environment for more than 10 years, the aforementioned methods struggle to meet the requirements.

The fiber Bragg Grating (FBG) sensor has excellent anti-electromagnetic interference capability, corrosion-resistant, high precision, ease of installation, and durability [8–10]. The fiber Bragg grating sensor, which can monitor the structure's internal response and mechanical properties, is an ideal choice for the crane monitoring system. However, the fiber Bragg Grating sensors are cross-sensitive to strain and temperature; it is difficult to distinguish the strain-induced wavelength variation and the temperature-induced one. In practical application, the thermal effect could easily overwhelm the strain effect, especially in environments with large temperature fluctuation. The effect of temperature has to be reduced or even eliminated [11–13].

In this paper, an FBG strain sensor with low temperature-sensitivity packaged by two gripper tubes and stainless-steel tubes is presented and applied in a bridge crane monitoring project. The objectives of this study are the following.

- To present the design theory of the sensor, including an introduction of the sensing principle of the fiber Bragg grating packaging mechanism. A theoretical derivation is presented for sensors with and without reverse-expanding packaging to unravel the advantage of the new design. Also, the temperature-sensitivity and reliability tests are conducted to compare these two types of FBG sensors.
- To investigate the structural health of the bridge crane, comparing the measured data of the FBG sensors and actual movement of the crane. The strain variation during a long-term monitoring project is presented to analyze the crane's horizontal balance, maximum stress, residual stress, and its mechanical response to temperature fluctuation, predicting the crane's safety.

SENSOR DESIGN THEORY

The internal structure of the fiber Bragg grating strain sensor with low temperature-sensitivity is presented in **Figure 1**. The strain sensor consists of a fiber Bragg grating, gripper tube, and a layer of thermal shrinkage material.

The capillary stainless-steel tube is adopted as the gripper tube for the demands of corrosion resistance. To realize the low temperature-sensitivity property of the sensor, a thermal

shrinkage material is used as a tube-insert to balance the effect of thermal expansion. As the wavelength of FBG changes due to thermal expansion, the correctly tuned thermal shrinkage material will counter such an effect. Considering both the variation of strain and temperature, the wavelength shift of the sensor is written as

$$\Delta\lambda_B = (1 - P_e)\Delta\epsilon + (\alpha_f + \xi)\Delta T = K_\epsilon\Delta\epsilon + K_T\Delta T \quad (1)$$

Where P_e , α_f , and ξ are the elasto-optical, the thermal expansion, and the thermo-optical coefficients of optical fiber materials. It is seen from **Eq. 1**, K_ϵ is the strain-induced wavelength variation of the sensor; $K_T\Delta T$ is the temperature-induced wavelength variation of the sensor. The wavelength shift, with the application of thermal shrinkage material, can be written as

$$\Delta\lambda_B = K_\epsilon\Delta\epsilon + K_T\Delta T + K_\epsilon\Delta\epsilon_T \quad (2)$$

The third term, representing the wavelength variation contributed by the sensors' own thermal fluctuation, can be further expanded as

$$K_\epsilon\Delta\epsilon_T = K_\epsilon\Delta T \left(\frac{L_f\alpha_1 + 2L_N\alpha_2}{L} + \alpha_3 \right) \quad (3)$$

Where L_f , L are the length of fiber grating and the length of thermal shrinkage materials, respectively. The temperature influence coefficient of fiber grating is K_T ; α_1 , α_2 , and α_3 are the coefficient of thermal expansion of gripper tube, the coefficient of thermal expansion of thermal shrinkage materials, and the coefficient of thermal expansion of the structure to be measured, respectively. The equation obtained by substituting (**Eq. 3**) into (**Eq. 2**) is

$$\Delta\lambda_B = K_\epsilon\Delta\epsilon + \left(K_\epsilon \left(\frac{L_f\alpha_1 + 2L_N\alpha_2}{L} + \alpha_3 \right) + K_T \right) \Delta T \quad (4)$$

The first term, $K_\epsilon\Delta\epsilon$, is only related to the variation of strain, and the second term is only related to the variation of temperature.

$$K_\epsilon \left(\frac{L_f\alpha_1 + 2L_N\alpha_2}{L} + \alpha_3 \right) + K_T = 0 \quad (5)$$

Where K_ϵ , K_T , α_1 , α_3 , and L_f are fixed values. It is seen from **Eq. 5** that the wavelength drift is independent of the temperature fluctuation if the lengths of the gripper tube and tube insert

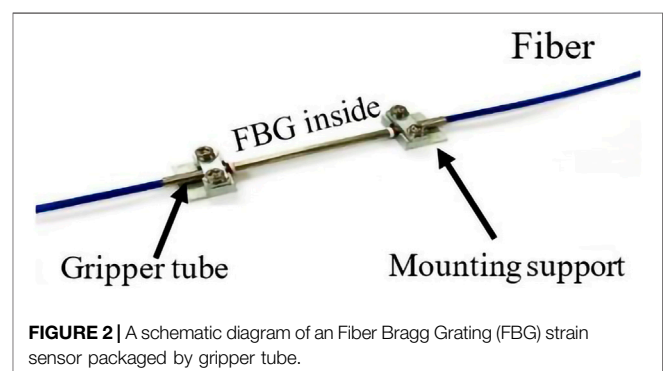


FIGURE 2 | A schematic diagram of an Fiber Bragg Grating (FBG) strain sensor packaged by gripper tube.

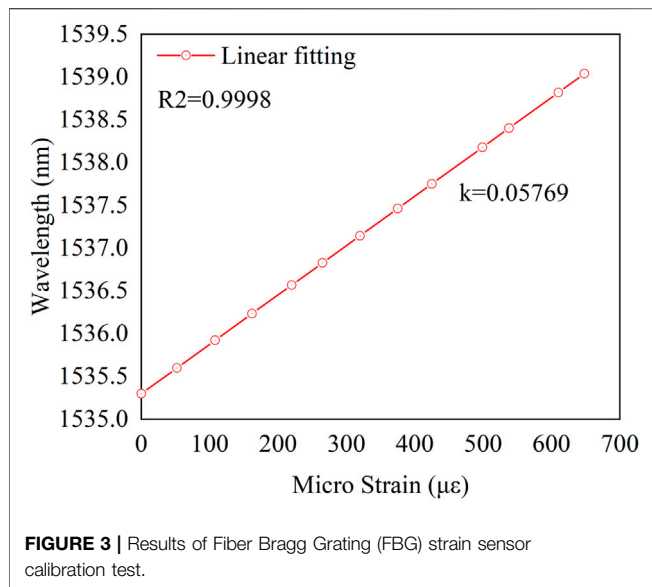


FIGURE 3 | Results of Fiber Bragg Grating (FBG) strain sensor calibration test.

are tuned correctly. Therefore, the low temperature-sensitivity of the sensor can be obtained.

A schematic diagram of the FBG strain sensor is presented in **Figure 2**. The fiber in both sides of the FBG is packaged with epoxy resin in the tube insert, which is screwed on the mounting supports.

The stress transferring loss between the epoxy resin and fiber can be neglected due to the adhesive thickness being less than the optical fiber's diameter [14]. The fiber area is not in contact with the epoxy resin due to the FBG is installed on the surface of the structure by two mounting supports [15]; therefore, the FBG strain sensor eliminates the multi-peaks of reflective light from the nonuniform bonding distribution of the epoxy resin [15], the deformation and strain of the gripper tube and FBG and are written as

$$\Delta L_g = \frac{P_g}{E_g} \frac{L_g}{A_g}; \Delta L_f = \frac{P_f}{E_f} \frac{L_f}{A_f} \quad (6)$$

$$\epsilon_g = \frac{\Delta L_g}{L_g} = \frac{P_g}{E_g A_g}; \epsilon_f = \frac{\Delta L_f}{L_f} = \frac{P_f}{E_f A_f} \quad (7)$$

Where P_g and P_f are the internal force of the gripper tube and fiber, respectively. L and L_f are the distance between the two mounting supports and the length of the fiber, respectively. E_g , E_f , A_g , and A_f are Young's modulus and the sectional area of the gripper tube and fiber, respectively. Since the sensor can be approximated as a two-force bar that is only subjected to axial force, the internal forces on each part are the same, so P_g equals to P_f . Hence, the strain ratio between gripper tube and fiber is obtained by substituting the parameter values as

$$\frac{\epsilon_s}{\epsilon_f} = \frac{E_f A_f}{E_s A_s} = 0.0084 \quad (8)$$

It is seen from **Eq. 8** that the strain ratio is 0.0084 [16]; due to the fiber's strain being far less than the gripper tube's strain and the fiber radius being far less than the gripper tube radius. It

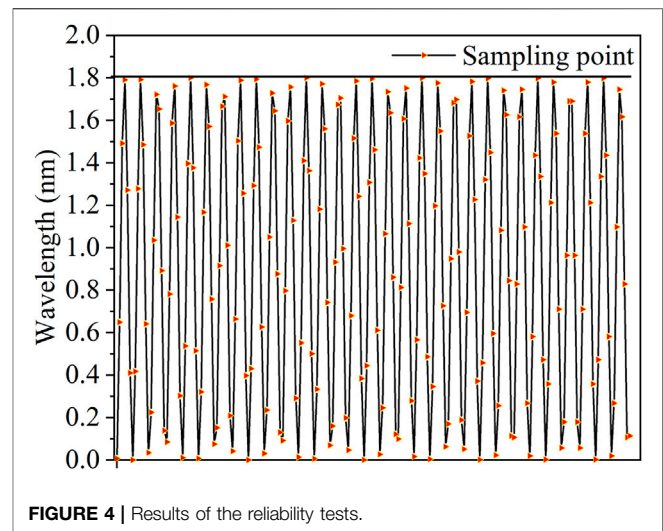


FIGURE 4 | Results of the reliability tests.

means that the strain of fiber is negligible compared to the strain of the gripper tube. Considering the low temperature-sensitivity nature of the sensor, the relation between the shift of the central wavelength of FBG and the strain of the sensor can be written as

$$\epsilon = \frac{L_f \Delta \lambda_{FBG}}{L K_\epsilon} \quad (9)$$

Where the temperature influence can be ignored so that K_ϵ is a fixed value regardless of the central wavelength of FBG. The strain sensitivity of the sensor can be tuned by adjusting the distance of two mounting supports and the length of the fiber at the mounting base. Hence, The FBG strain sensor has the advantages of high precision and low temperature-sensitivity.

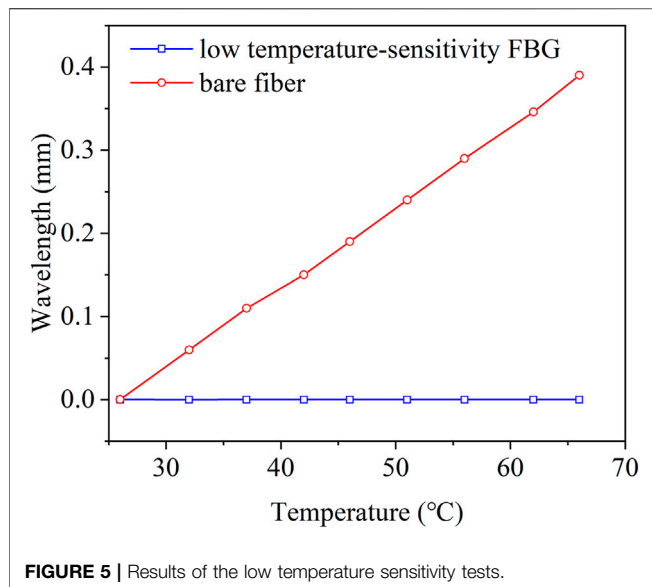
RESULT OF PERFORMANCE TESTS

Basic performance tests are needed to ensure sensors' stability and efficiency before used in practical projects. In this section, the strain measurement accuracy, reliability, and low temperature-sensitivity of sensors are tested in the laboratory.

Calibration Result

Accurate measurement of strain variation is the primary function of strain sensors. To investigate the strain sensor's precision with low temperature-sensitivity, a calibration test of the FBG strain sensor was conducted by a universal testing machine. The steel plate was loaded continuously from 0 kN to 24 kN, and the data of the sensor was recorded once every 2 kN. To ensure the repeatability and consistency of the sensor, all measurements were taken several times.

The calibration tests results are plotted in **Figure 3**, showing the relation between the Bragg wavelength shift of the FBG sensor and the strain value. As the load increases, the wavelengths of the sensor increase, and the coefficient of linear association reached 0.9998. The results prove that the FBG strain sensor works well on the steel structure, such as cranes.



Reliability Tests

Reliability is another necessity of a sensor, especially in long-term structures monitoring, such as cranes with 10 years of service life. A total of 90,000 cyclic loads were performed on the sensor, which is mounted on the surface of a uniform strength beam by adhesive to record the central wavelengths of the FBG sensor.

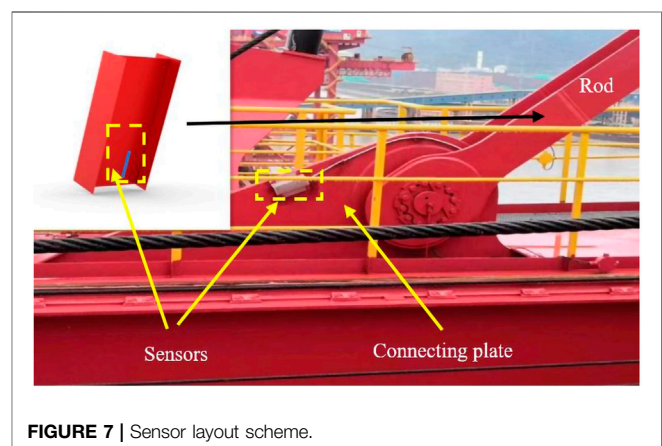
The reliability test result is plotted in **Figure 4**, showing that the wavelength measurement result is consistent during the cyclic loads. The maximum wavelength variation amplitude in each cycle is stable at about 1.8 nm, and the reading returns to its original level at the end of each cycle. The results prove that the FBG strain sensors are indeed reliable.

Temperature-Sensitivity Tests

Effective distinguishment of the temperature-induced stress from load-induced stress has been a major challenge for strain sensors. To test the sensor's low temperature-sensitivity property, an experiment is conducted using a water bath method. The whole set-up was placed in a constant temperature tank to control and simulate the actual thermal fluctuation of the application more effectively.

The temperature varied from 20 to 70°C, and a mercury thermometer was used as a standard temperature gauge, which has a precision of 0.05°C. Firstly, the sensor was fixed on the clamping support, which is welded on a 10 mm thick steel plate. Then, the relation between the sensor wavelength and the tank's temperature was recorded to investigate the sensor's temperature sensitivity.

The low temperature-sensitivity test data is plotted in **Figure 5**, showing that when the temperature changes from 20 to 70°C, the sensor's maximum wavelength variation with the reverse-expansion packaging is only 0.004 nm. With the same conditions, the bare grating's maximum wavelength variation is 0.3654 nm, which is 91 times more than the sensor with low temperature-sensitivity.



APPLICATION OF FIBER BRAGG GRATING STRAIN SENSORS IN THE MONITORING TEST OF THE CRANE

Strain monitoring is one of the essential items in structural health monitoring. The mechanical conditions of the structure, such as cracks, can be reflected in strain response. An effective real-time and long-term monitoring of the strain provides the necessary information needed to evaluate the structure's health; furthermore, understanding this information realizes the safety control of the structure.

Bridge Crane and Sensor Layout Scheme

Figure 6 shows that the bridge crane's integral structure is symmetrical along the girder's middle line. The weight-bearing area is composed of four rods, which are connected by steel connecting plates. The clamp moves on the girder and works on loading and unloading goods. If the force on the left and right rods are unbalanced during the crane operation, the girder will produce shear deformation that would cause the girder to overturn. Besides, as a complex region of stress, the connecting plates could lose their mechanical properties due to fatigue damage of steel structure. To sum up, the structure will deform under the action of load, which will induce the

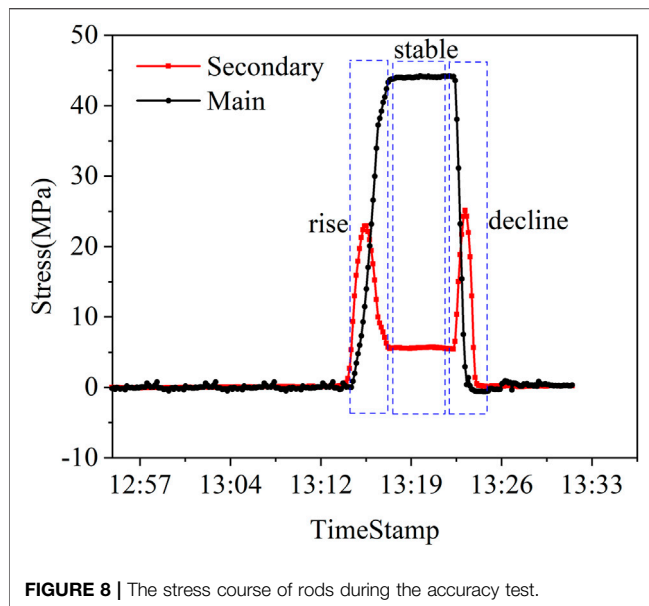


FIGURE 8 | The stress course of rods during the accuracy test.

variation of the stress of the rods and connecting plates on the bridge crane. Therefore, according to the monitoring requirements, the strain of the bridge crane's key components, such as the rods and the connecting plates, should be monitored primarily.

Since the rods are two-force bars and both ends are connected by hinge joints, forces should stretch all rod parts with the same magnitude, and the direction is axial, without bending moment and shear force (ignoring the effect of dead weight). Thus, the sensors installed on any location would have the same reading. In consideration of installation and maintenance, the sensors are installed at the lower end of the rods. The sensor layout scheme is shown in **Figure 7**. Four measuring points are arranged overall, one for each rod of the crane. The rod is made of H-shaped steel, the lateral stiffness is relatively large, and there is a certain stress transfer loss caused by welding. Therefore, it meets the monitoring requirements by installing one sensor in the web of each rod.

As the linkage member between the rods and the girder, the direction of the resultant force at the connecting plate varies from time to time during crane operation. As a complex region of stress, the direction of the resultant force is difficult to calculate and measure; the meaningfulness of monitoring can be guaranteed only when the sensor is installed along the direction of the rod. One sensor is installed on each connecting plate in the same direction as the rod to ensure the crane's dynamic balance and avoid the girder overturning caused by the fatigue damage of a connecting plate. A total of four sensors are installed on the part of connecting plates.

Accuracy Test of On-Site Monitoring

The crane was subjected to a loading task of 50 tons to observe the accuracy of the sensors installed on the rod. In this working condition, the girder of the crane was to keep flat, and the grab moved along the girder from the initial position to the bottom of

the secondary rod and the front-end of the girder. Then, the grab backed to the initial position. The sensor recorded the whole process to verify the sensors' accuracy and real-time performance by comparing the test data with the actual testing process.

Stage 1 described the grab's motion from the initial position to the front-end of the girder. According to the influence line theory of structural mechanics, the force of the secondary rod should increase as the distance from the grab to the secondary rod decreases. The force of the secondary rod reached its maximum when the grab was right below the secondary rod. Then as the grab moved away from the secondary rod towards the main rod, the force of the secondary rod tended to decline, and the force of the main rod continued to rise until it reached its maximum, which meant that the grab reached the location of the main rod. The stress variation of the main rod and the secondary rod in **Figure 8** describes the whole process; it is seen that when the grab was moved to the bottom of the secondary rod, the maximum stress of the secondary rod is 22.9 MPa, when the grab was moved to the bottom of the main rod, the maximum stress of the main rod is 44.2 MPa.

During stage 2, the system stayed still; thus, there was no change in stress shown in the monitoring. Stage 3 described the grab's motion back to the initial position. As shown in **Figure 8**, as the grab moved to its initial position, the rods' stress course was the opposite of the first stage. Noticeably, the stress curve of the main rod and the secondary rod both declined to the initial value gradually.

The test results show that the measured data of the sensor accurately describe the whole process. Moreover, there was no residual stress afterward, which means the loading procedure was within the structure's elastic range and safety requirements.

Low Temperature-Sensitive Test and Thermal-Mechanical Response

The environmental thermal-fluctuation causes expansion of the crane's girder, which will pull the rods generating tension thus strain. This alternating thermal field would produce fatigue damage on the structure during its long service life. It is

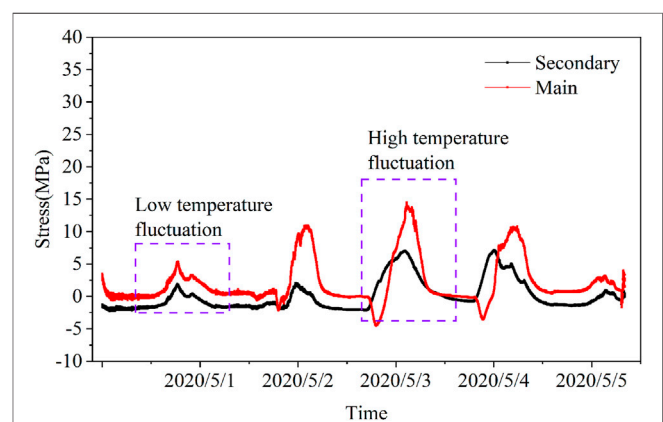
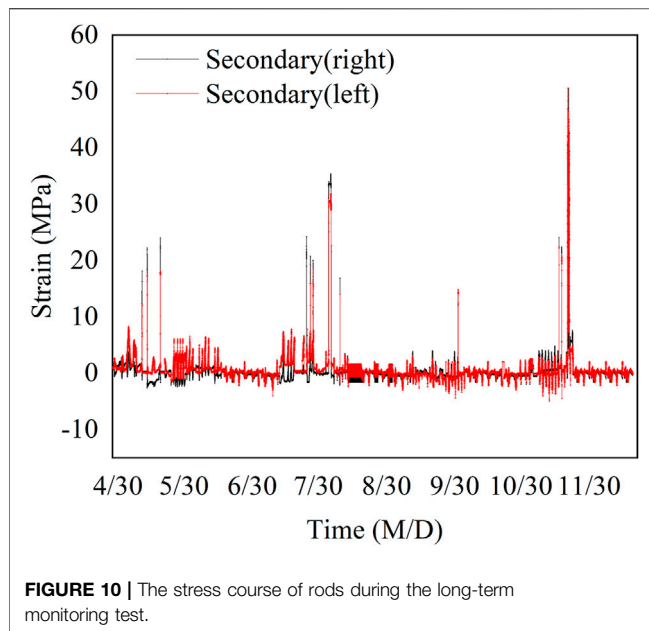


FIGURE 9 | The stress course of rods in different temperature.



challenging to monitor the real tension of rods induced by this thermal-mechanical effect of girder since regular sensors are cross-sensitive to strain and temperature. For this purpose, the test was done when the crane was in a horizontal and extended state with no load from May 1st to May 5th.

The sensor with low temperature-sensitivity monitored the rod's mechanical response to the temperature fluctuation. It can be seen from **Figure 9** that the maximum stress was about 5 MPa on a rainy day with low temperature-fluctuation, and it was about 15 MPa on a sunny day with high temperature-fluctuation. The FBG with the reverse-expansion packaging indeed reflected the predicted behavior of the stress. The main rod suffers more from the alternating temperature, as it is attached at the girder's rear end. Also, the greater the difference in temperature, the bigger the variation in stress.

The magnitude of this thermal-mechanical stress response is approximately one-third of the maximum stress in the accuracy test mentioned in the previous section; this information is not to be neglected for the safety of the structure.

Long-Term Monitoring Test

The crane was subjected to long-term monitoring to observe the reliability of the sensors. As shown in **Figure 10**, the sensor monitored the crane's stress variation of the primary and secondary rod from April 30th to December 23rd. During this time, the maximum stress of the right rod reached 50.6 MPa, and

the maximum stress of the left rod reached 48.6 MPa. Because the rods are made of Q345 steel, the yield strength of 345 steel is about 345 MPa and the tensile strength of 345 steel is about 490 MPa, which is within the safety range. Also, the sensors' output returned to zero after each measurement, which proves that the sensor remains highly accurate and reliable in long-term monitoring.

CONCLUSION

A new configuration for an FBG strain sensor with low temperature-sensitivity was characterized, calibrated, and applied in a crane monitoring project. Its various properties were demonstrated on the field. The calibration shows that the actual sensitivity of the sensor, packaged with reverse-expand material, agrees well with the theoretical calculation. The reliability test demonstrates that the sensor maintains highly consistent under 90,000 cycle load tests. The low temperature-sensitivity experiment demonstrates that the sensor is less affected by temperature than the bare fiber, which means that it is more suitable for the long-term monitoring of the structure that serves in a thermally unstable environment.

FBG strain sensors with low temperature-sensitivity have been installed on the rods and connecting plates of the crane to monitor the crane's stress variation in an actual working situation. The accuracy test results and the temperature-sensitive test show that the sensor with low temperature-sensitivity can eliminate the effect of temperature and accurately monitor the mechanical response of temperature fluctuation. The long-term monitoring test results show that the sensor maintained high reliability during the crane operation. It is proved that the sensor has a promising potential in the structural health monitoring of cranes.

DATA AVAILABILITY STATEMENT

The raw data supporting the conclusions of this article will be made available by the authors, without undue reservation.

AUTHOR CONTRIBUTIONS

ZZ, LS, and LH contributed to conception and design of the study. ZZ and WY analyzed data. ZZ, LS, and WY wrote sections of the manuscript. All authors contributed to manuscript revision, read, and approved the submitted version.

REFERENCES

- Wang C, Mi G, and Zhang X. Welding Stability and Fatigue Performance of Laser Welded Low alloy High Strength Steel with 20 Mm Thickness. *Opt Laser Tech* (2021) 139:106941. doi:10.1016/j.optlastec.2021.106941
- Song X, Li H, Wang X, and Zhang J. Experimental Investigation of Ultra-low-cycle Fatigue Behaviors of Plate Bearings in Spatial Grid Structures. *Eng Structures* (2021) 231(4):111764. doi:10.1016/j.engstruct.2020.111764
- Tochaei EN, Fang Z, Taylor T, Babanajad S, and Ansari F. Structural Monitoring and Remaining Fatigue Life Estimation of Typical Welded Crack Details in the manhattan Bridge. *Eng Structures* (2021) 231(2):111760. doi:10.1016/j.engstruct.2020.111760

4. Reason J. *Human Error*. Cambridge: Cambridge University Press (1990). doi:10.1017/cbo9781139062367
5. Meng WJ, and Hong TW. Design of Stress Monitoring and Safety Assessment System for Crane Metal Structure Based on Virtual Instrument. *Amm* (2012) 152-154:1492-7. doi:10.4028/www.scientific.net/amm.152-154.1492
6. Xu M, Ni J, and Chen GJ. Research on the Wireless Monitoring System for Port Crane Structure Stress. *Amm* (2013) 278-280:920-3. doi:10.4028/www.scientific.net/AMM.278-280.920
7. K LI, Dominik WP, and KwaNiewski J. Integrated Stress Measurement System in tower crane Mast. *Measurement* (2017) 102:47-56. doi:10.1016/j.measurement.2017.01.041
8. Moyo P, Brownjohn JMW, Suresh R, and Tjin SC. Development of Fiber Bragg Grating Sensors for Monitoring Civil Infrastructure. *Eng Structures* (2005) 27(12):1828-34. doi:10.1016/j.engstruct.2005.04.023
9. Kersey AD, Davis MA, Patrick HJ, LeBlanc M, Koo KP, Askins CG, et al. Fiber Grating Sensors. *J Lightwave Technol* (1997) 15:1442-63. doi:10.1109/50.618377
10. Li H-N, Li D-S, and Song G-B. Recent Applications of Fiber Optic Sensors to Health Monitoring in Civil Engineering. *Eng Structures* (2004) 26:1647-57. doi:10.1016/j.engstruct.2004.05.018
11. Li X-X, Ren W-X, and Bi K-M. FBG Force-Testing Ring for Bridge Cable Force Monitoring and Temperature Compensation. *Sensors Actuators A: Phys* (2015) 223:105-13. doi:10.1016/j.sna.2015.01.003
12. Khan MM, Panwar N, and Dhawan R. Modified Cantilever Beam Shaped FBG Based Accelerometer with Self Temperature Compensation. *Sensors Actuators A: Phys* (2014) 205:79-85. doi:10.1016/j.sna.2013.10.027
13. Hsu YS, Likarn Wang L, Wen-Fung Liu WF, and Chiang YJ. Temperature Compensation of Optical Fiber Bragg Grating Pressure Sensor. *IEEE Photon Technol Lett* (2006) 18(7):874-6. doi:10.1109/LPT.2006.871832
14. Lin YB, Chang KC, Chern JC, and Wang LA. Packaging Methods of Fiber-Bragg Grating Sensors in Civil Structure Applications. *Sensors* (2005) 5: 419-24. doi:10.1109/JSEN.2005.844539
15. Iwashima T, Inoue A, Shigematsu M, Nishimura M, and Hattori Y. Temperature Compensation Technique for Fibre Bragg Gratings Using Liquid Crystalline Polymer Tubes. *Electron Lett* (1997) 33(5):417. doi:10.1049/el:19970289
16. Ren L, Chen J, Li H-N, Song G, and Ji X. Design and Application of a Fiber Bragg Grating Strain Sensor with Enhanced Sensitivity in the Small-Scale Dam Model. *Smart Mater Struct* (2009) 18(3):035015. doi:10.1088/0964-1726/18/3/035015

Conflict of Interest: The authors declare that the research was conducted in the absence of any commercial or financial relationships that could be construed as a potential conflict of interest.

Copyright © 2021 Zhaobo, Sheng, Yibo and Hongnan. This is an open-access article distributed under the terms of the Creative Commons Attribution License (CC BY). The use, distribution or reproduction in other forums is permitted, provided the original author(s) and the copyright owner(s) are credited and that the original publication in this journal is cited, in accordance with accepted academic practice. No use, distribution or reproduction is permitted which does not comply with these terms.



Collapse Analysis of a Transmission Tower-Line System Induced by Ice Shedding

Jiaxiang Li¹, Biao Wang¹, Jian Sun¹, Shuhong Wang^{1*}, Xiaohong Zhang² and Xing Fu³

¹Department of Civil Engineering, Northeastern University, Shenyang, China, ²Civil Engineering and Applied Mechanics, McGill University, Montreal, QC, Canada, ³Faculty of Infrastructure Engineering, Dalian University of Technology, Dalian, China

Ice shedding causes transmission lines to vibrate violently, which induces a sharp increase in the longitudinal unbalanced tension of the lines, even resulting in the progressive collapse of transmission towers in serious cases, which is a common ice-based disaster for transmission tower-line systems. Based on the actual engineering characteristics of a 500 kV transmission line taken as the research object, a finite element model of a two-tower, three-line system is established by commercial ANSYS finite element software. In the modeling process, the uniform mode method is used to introduce the initial defects, and the collapse caused by ice shedding and its influencing parameters are systematically studied. The results show that the higher the ice-shedding height is, the greater the threat of ice shedding to the system; furthermore, the greater the span is, the shorter the insulator length and the greater the dynamic response of the line; the impact of ice shedding should be considered in the design of transmission towers.

OPEN ACCESS

Edited by:

Yunlai Zhou,
Universidade Lusófona, Portugal

Reviewed by:

Tao Lai,
Nanjing Tech University, China
Hu Cheng,
Jiangnan University, China

*Correspondence:

Shuhong Wang
wangshuhong@mail.neu.edu.cn

Specialty section:

This article was submitted to
Interdisciplinary Physics,
a section of the journal
Frontiers in Physics

Received: 20 May 2021

Accepted: 08 June 2021

Published: 18 June 2021

Citation:

Li J, Wang B, Sun J, Wang S, Zhang X
and Fu X (2021) Collapse Analysis of a
Transmission Tower-Line System
Induced by Ice Shedding.
Front. Phys. 9:712161.
doi: 10.3389/fphy.2021.712161

Keywords: index terms: transmission line, ice shedding, numerical simulation, dynamic response, progressive collapse

INTRODUCTION

As the physical electricity-carrying entities of the power transmission network, transmission lines often need to pass through severely cold areas, and as a result, ice may occasionally coat the conductors. When the temperature rises, this ice melts and falls off the line, causing the transmission line to vibrate; these vibrations can damage the transmission line and even cause its progressive collapse. Although the ice shedding effect was considered as unbalanced tension in the design codes [1–3], the accidents caused by ice shedding still occurs. For example, an investigation of the southern snow disaster in 2008 showed collapsed bases of 140,000 transmission towers below 110 kV; the bases of 1,000, 110–500 kV transmission towers collapsed; and the bases of 506,500 kV transmission towers fell, with the bases of 142 towers being damaged. Ultimately, ninety percent of all transmission tower collapses are caused by longitudinal unbalanced tension caused by uneven icing and uneven ice shedding [4]. With the development of the study on structural vibration control and structural healthy monitoring, these two methods are used to improve the safety operation of the transmission line [5–9]. To determine the key parameters for monitoring and controlling, the failure mechanism of the transmission line caused by ice-shedding should be studied.

The serious hazards imposed by ice shedding have attracted widespread attention from scholars worldwide. At present, the most common method for studying ice shedding problems is numerical simulation [10]. Kollar and Farzaneh [11–14] introduced a spacer bar into the conductor ice-shedding model, studied the ice shedding of the bundle conductor, and obtained the relationships between the maximum jump height and the ice thickness, initial tension, conductor spacing, and

number of sub-conductors; a scale test verified the validity of the model, and the results showed that a spacer bar can effectively reduce the jump height of the conductor but has little effect on the torsion of the conductor. Because that the clearance reducing caused by ice-shedding could lead to electrical accident, the jump height is the one of the most concerned parameters for ice-shedding of transmission lines. Yan et al. [15] proposed a formula to predict the maximum jump height by fitting the numerical results between the maximum jump height and sag difference before and after ice shedding. Based on the conservation of energy and the geometrical relationship between the span and the swing of an insulator, Wu et al. [16] proposed a theoretical calculation method for the largest jump height of a transmission line; a comparison of the results with a finite element analysis revealed good agreement, and the theoretical method exhibited the advantages of both accuracy and convenience. Huang et al. [17] proposed a method to study ice shedding using a scale test and verified the effectiveness of the proposed method by comparing the results with two full-scale tests. However, the paper mentioned above ignored the stiffness of ice, and assumed that the ice on the conductor fell off in a certain pattern that was unrealistic. To obtain the real dynamic response of the conductor induced by ice-shedding, the ice failure model should be considered. Kalman et al. [18] first introduced the ice failure model to predict the ice shedding. In their study, if the plastic strain is greater than 10^{-10} , the element of ice will be killed to simulate ice shedding. Mirshafiei et al. [19, 20] proposed another ice failure criterion. In Mirshafiei's criterion, the ice would have been shed if the ice strain reached the maximum effective plastic strain. The numerical results showed that Mirshafiei's criterion had a better performance in prediction of the ice shedding by comparison with the experimental results than Kalman's criterion. However, these two ice failure criteria both overrated the ice-shedding rate. Ji et al. [21–24] proposed a new criterion predicting the ice-shedding rate better. They thought that ice breakage and ice detachment were two different stages. Only ice detachment would occur if the inertia forces overcoming the adhesive/cohesive forces on the ice. After that, they studied influence parameters in the ice shedding progress and give suggestions to improve the de-icing efficiency of the shock-load method and reduce the adverse transient effects on the line components [25]. Yang et al. [26, 27] performed the numerical simulation to study the dynamic response of transmission tower-line system and found that the interphase space could effectively decrease the dynamic response of the tower-line system; dynamic amplifying effect of the vertical load from ice shedding conductors cannot be ignored.

Transmission towers are an important part of the transmission tower-line system, as they play the crucial role of supporting the transmission lines. However, the role of transmission towers in the ice-shedding response has been ignored in all research to date, with few studies considering the influence of ice-shedding on transmission towers response. Shen et al. [28, 29] established a tower-line system model and analyzed the vibration characteristics caused by the ice shedding of the transmission tower-line system. The results showed that the shear and bending moment of the transmission tower base were zero before ice

shedding but increased significantly thereafter, and the closer the ice-shedding is, the greater the basal shear and moment. Additionally, a comparison with a two-speed conductor model test verified the impact of ice shedding on the transmission tower. However, the above research is limited to the elastic stage of the transmission lines and does not involve the collapse of transmission lines caused by ice shedding. In fact, more and more attentions are attractive to tower collapse [30–34].

In summary, a paucity of studies has considered the collapse and damage of transmission lines due to icing and ice shedding under the coupling of transmission towers and lines. In this paper, using a numerical method to establish the transmission line model and considering transmission towers with initial defects, the dynamic response of the transmission tower-line system induced by ice shedding is studied; furthermore, the damage to the transmission tower and the influencing parameters are analyzed.

ESTABLISHMENT OF THE FINITE ELEMENT MODEL

Model Parameters

In this paper, a finite element model is established for a transmission tower-line system with two towers and three lines. The conductors at both ends of the model are consolidated. The model of the four-bundle conductor in the line is LGJ-630/45, the model of the ground conductor is LB20A-150, and the mechanical parameters are shown in **Table 1**.

To simplify the modeling process of the transmission tower-line system and improve the computational efficiency, the following assumptions are adopted in this paper.

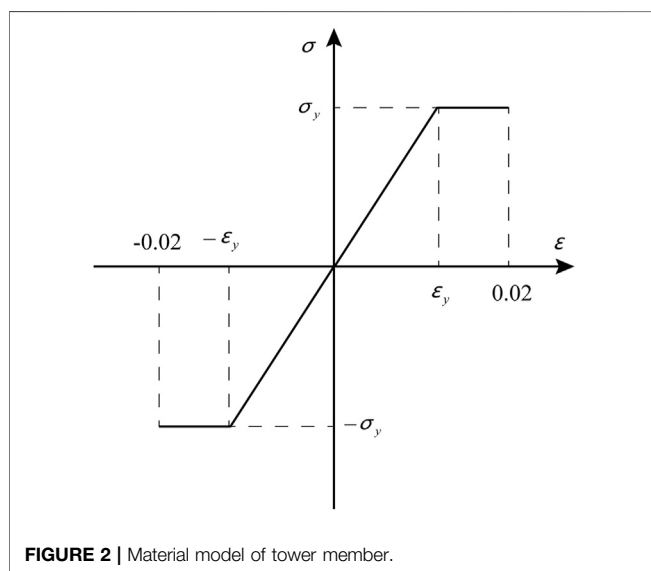
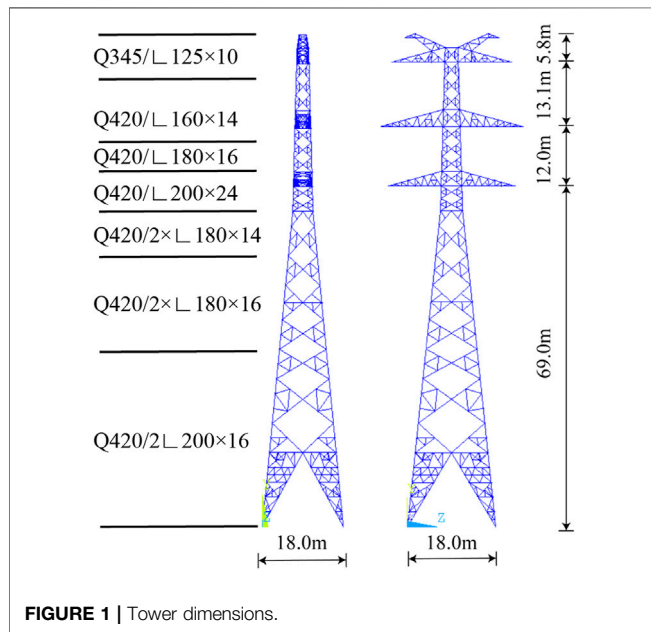
- (1) In the modeling process, the conductor bundle is modeled as a single conductor, and in the ice-shedding process [33–35], it is assumed that all the sub-conductors of the bundle conductor bundle experience ice shedding at the same time.
- (2) Ice is evenly distributed on the conductor and the ground, and it is assumed that the ice cross section is circular.
- (3) Only the mass of the ice cover is considered, whereas the influence of the ice cover stiffness is ignored, and the possibility of the ice cover falling off and breaking during vibration is ignored.

This paper selects a 500 kV double-circuit angle steel transmission tower as the research object with a height of 99.9 m and a base size of 18 m × 18 m. The dimensions of the transmission tower are presented in **Figure 1**. The length of the insulator is 6.6 m, the initial tension conductor is 141.3 kN, and the initial tension of the ground conductor is 30.5 kN. The main material of the transmission tower is Q420 and Q345 steel, as shown in **Figure 1**, and Q235 steel is used for the auxiliary materials.

The ice on the transmission lines is affected by natural factors such as wind, and the icing cross sections are mostly crescent-shaped, crescent-shaped or D-shaped, although other irregular shapes are also possible. Previously, scholars mostly assumed that

TABLE 1 | Mechanical parameters of the conductor.

Model	Conductor outer diameter (mm)	Weight (kg/m)	Modulus of elasticity (MPa)	Cross-sectional area (mm ²)
Ground conductor LB20A-150	15.75	0.9894	147,200	148.07
Conductor LGJ-630/45	33.6	2.06	63,000	666.55



the ice is ring-shaped when studying ice-shedding phenomena; this article also adopts this assumption. In this paper, ANSYS simulation software is used for modeling, and the LINK10 element is used to simulate the conductor. The ice coating on the conductor is also simulated by the LINK10 element, which shares the node with the conductor. The constitutive model of

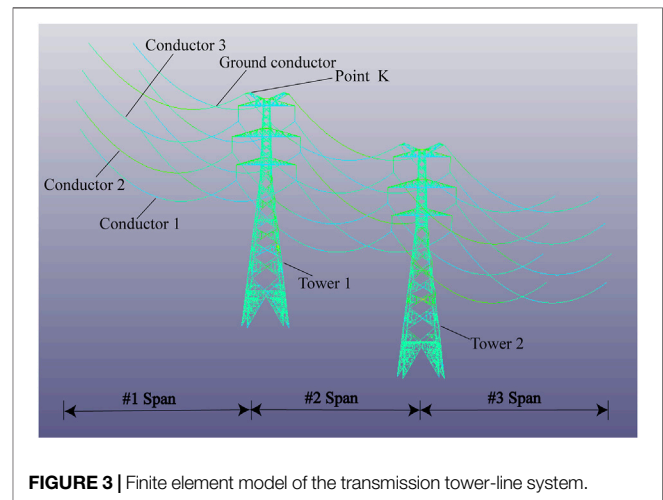


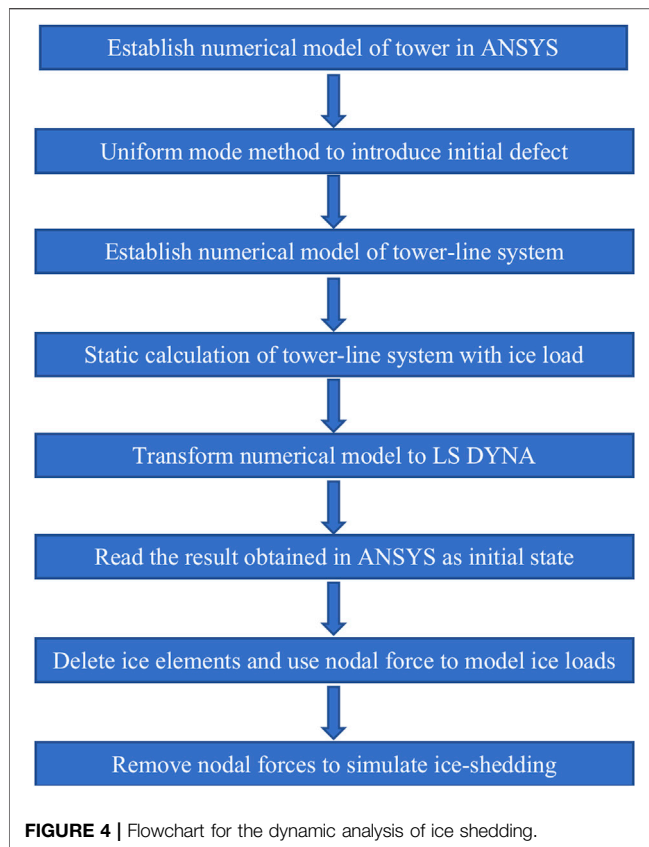
FIGURE 3 | Finite element model of the transmission tower-line system.

tower is shown in **Figure 2**, the tower member would lose its load carrying capacity once the strain reaches 0.02.

The two-tower, three-line transmission tower-line system model established in this article is illustrated in **Figure 3**. The ice shedding of conductors 1, 2, and 3 represents the three cases of conductor ice shedding. In the past, when analyzing the vibration characteristics of transmission towers, the apex of the tower was set as a key point, and its displacement changes were analyzed to study the vibration characteristics of the transmission tower. Therefore, this paper defines the apex of the ice-shedding side of Tower 1 as key Point K. The steel density of the transmission tower is $7,850 \text{ kg/m}^3$, and the elastic modulus is $206,000 \text{ MPa}$. In addition, the density of the ice coating is 900 kg/m^3 . Since the ice coating stiffness is ignored, the elastic modulus of the ice coating is set to 1 in the numerical model.

Initial Defects

During the manufacture and transportation of the members used to construct power transmission towers, members with defects will inevitably be produced, and in their subsequent welding and assembly, residual stresses and welding defects will be generated due to factors such as the processing technology and worker mistakes. Accordingly, the bearing capacity of the power transmission tower members will be affected. Therefore, in the dynamic analysis of the transmission tower, the influences of these initial defects should be considered. Fu et al. [36, 37] used the uniform mode method to consider the initial defects of a transmission tower in their numerical model. This method assumes that the initial defects of a structure are consistent with the lowest buckling mode, and hence, this approach is widely used in the force analysis of complex structures such as



reticulated shell structures and transmission towers. In this paper, the uniform mode method is adopted to consider the initial defects of the transmission tower, and on this basis, the dynamic response of the tower-line system induced by ice shedding is analyzed.

Dynamic Analysis of Ice-Shedding

The current electric power design code in China calculates the unbalanced tension caused by uneven ice cover during the transmission tower design according to the static load and takes the value according to the maximum working tension percentage of the conductor. This method is simple and easy to apply in engineering, but it ignores the dynamic impact during the ice-shedding process. Thus, the dynamic impact of conductor ice shedding is simulated in this paper. The simulation process is outlined in **Figure 4**. First, the finite element model of the transmission tower is established by using ANSYS, the initial defects are considered according to the minimum-order mode obtained by eigenvalue buckling analysis under ice-shedding load in ANSYS, and the finite element model is updated to introduce the initial defects of the transmission tower (uniform mode method) [36, 37]. In this way, the two-tower three-conductor finite element model is established. Finally, the static characteristics of the tower-line system are subjected to nonlinear analysis. Since the ANSYS implicit algorithm has long been used to analyze the dynamic responses of tower-line systems, the ANSYS LS-DYNA display algorithm is used to

analyze the dynamic response of the transmission tower-line system to an ice-shedding load. The results of the preceding ANSYS static analysis are taken as the initial state of the LS-DYNA calculation, after that, delete the ice element which will shed from the conductor and use the equivalent nodal force to simulate the ice load. Then, the equivalent nodal force is removed to simulate ice shedding, and the dynamic analysis of ice falling off of the transmission tower-line system is carried out. Subsequently, the ice load is increased until the transmission line collapses and is destroyed.

FAILURE MODE ANALYSIS OF TRANSMISSION TOWER

The simulation parameters are as follows: 1) the length of the insulator is 6.6 m; 2) all the span of the conductor are 500 m; and 3) the initial tension of the conductor is 141.3 kN.

Taking conductor 2 (the middle conductor shown in **Figure 3**) as an example, the ice-shedding process of the transmission tower is depicted in **Figure 5**. If the ice thickness is 45.6 mm, as shown in **Figure 5**, then conductor ice shedding can lead to progressive collapse of the transmission tower-line system. At 1.0 s after ice shedding, the system is elastic, and the transmission tower vibrates as a result of the longitudinal unbalanced load. However, the tower members do not undergo buckling failure. Then, Tower 1 is affected by the longitudinal unbalanced load. At 1.5 s after ice shedding, units 2,334, 2,337, 2,148, and 2,151 at heights ranging from 81.0 to 84.5 m (i.e., the connections of the cross-arms to the tower head with ice-shedding conductors) fail. In addition, Tower 2 violently shakes. At 2.15 s after ice shedding, Tower 1 is subjected to longitudinal unbalanced loads, and units 2,850, 2,851, 2,852, and 2,853 (i.e., the connections between the tower head and the tower body) between the heights of 61.0 and 64.0 m begin to be destroyed. At 5.5 s after ice-shedding, Tower 1 collapses. Additionally, the members connecting the Tower 2 head to its body begin to fail. At 7.0 s after ice shedding, Tower 2 collapses, and the tower-line system completely loses its bearing capacity. The damage state of Tower 2 at 5.5 s is similar to that of Tower 1 at 2.15 s.

From these simulation results, the failure processes and collapse mechanisms of the two towers in the two-tower, three-conductor model are basically the same except that the ice shedding of the ground conductor will not cause damage to the transmission tower-conductor system. Then, the insulator and conductor fall, the tower body vibrates violently, and the Tower 2 ice-shedding side is disconnected from the upper conductor. Finally, the head and body connections on Tower 1 are damaged and ultimately collapse, and Tower 2 is affected by the collapse of Tower 1.

From the simulation failure process, we can identify the positions of weakness where ice shedding on the three conductors can easily cause damage and the collapse of the transmission tower. The weakness of the employed tower is as follows: 1) the cross-arm connected to the ice-shedding conductor (the tower height ranges from 81.0 to 84.5 m); and 2) The tower head and tower body connection (the tower height

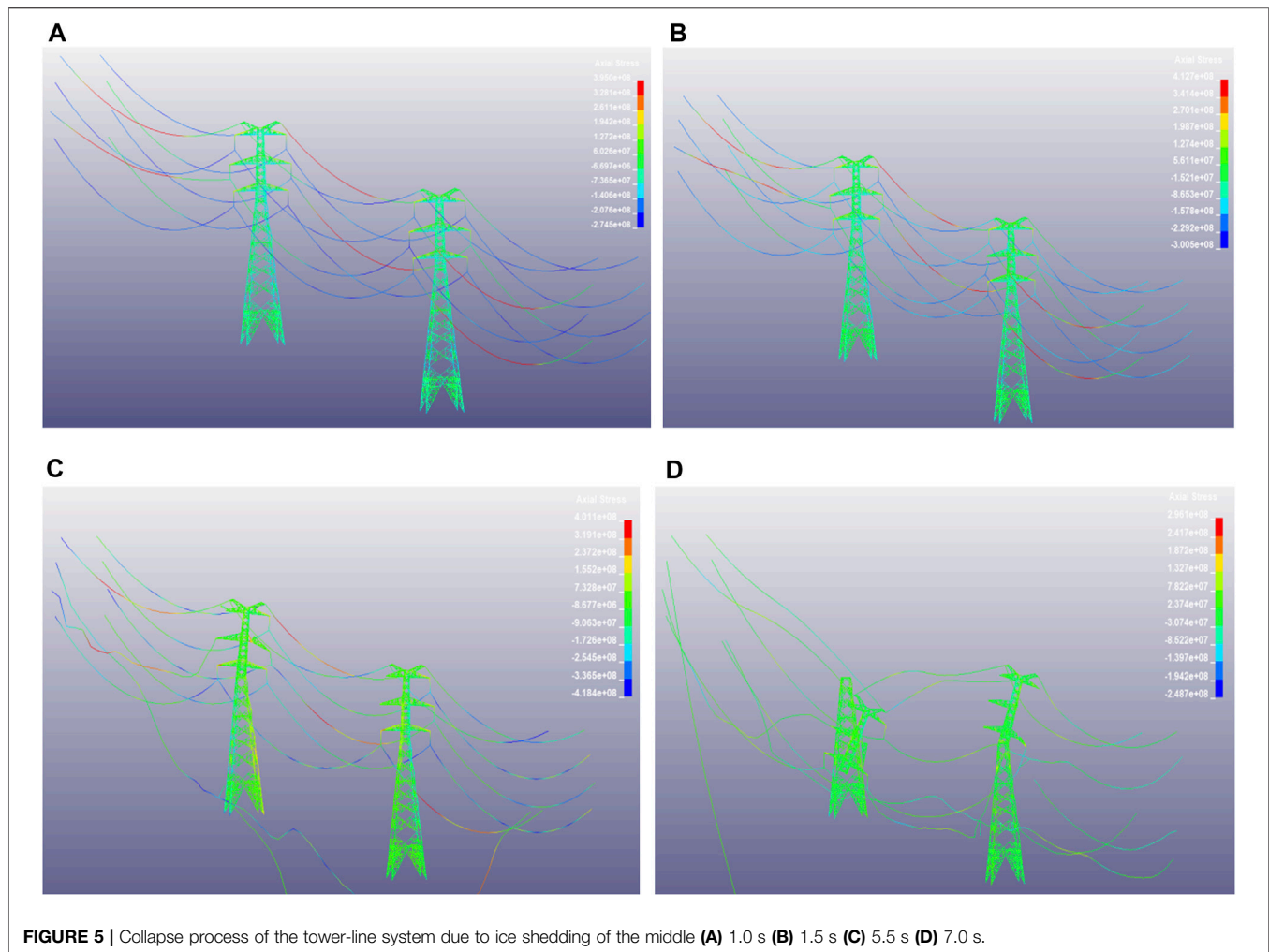


FIGURE 5 | Collapse process of the tower-line system due to ice shedding of the middle (A) 1.0 s (B) 1.5 s (C) 5.5 s (D) 7.0 s.

ranges from 61.0 to 64.0 m). Based on the simulation, the reinforcement of the above positions can effectively strengthen the ability of the transmission tower to resist the unbalanced load caused by the falling off of ice.

The ice thickness during the collapse process of the transmission tower is 43.3 mm when the upper conductor experiences ice shedding, 45.6 mm when the middle conductor experiences ice shedding, and 48.1 mm when the lower conductor experiences ice shedding. Hence, with an increase in the ice-shedding height, the ice thickness required for the transmission tower to collapse decreases gradually; moreover, the higher the ice-shedding position is under the same ice thickness, the greater the threat to the tower-line system.

ANALYSIS OF THE ICE-SHEDDING PARAMETERS

When transmission line ice shedding occurs, the span and insulator length are important parameters of the line affecting the unbalanced tension. To better study the influences of these

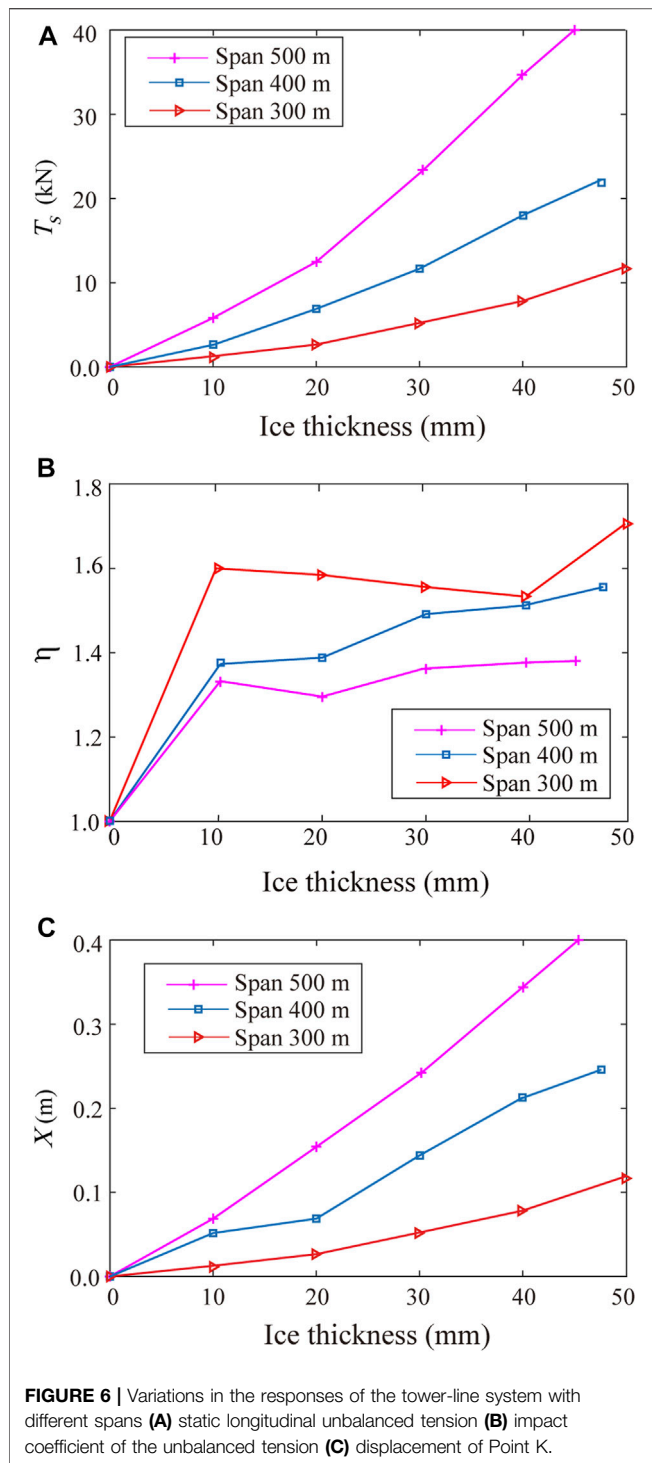
parameters on the longitudinal unbalanced load, the impact coefficient of the unbalanced tension is defined in Eq. 1.

$$\eta = \frac{T_d}{T_s} \quad (1)$$

T_d is the maximum longitudinal unbalanced tension after ice shedding; T_s is the static stable longitudinal unbalanced tension after ice shedding; and η is the unbalanced tension impact coefficient used to show the relationship between the maximum longitudinal unbalanced tension after ice shedding and the static longitudinal unbalanced tension, i.e., the dynamic effect of the reaction to ice shedding. The final displacement of Point K on the tower is represented by the parameter X. For clarity, in the parameter analysis, all the conductors that experience ice shedding are the middle conductor, that is, conductor 2.

Span

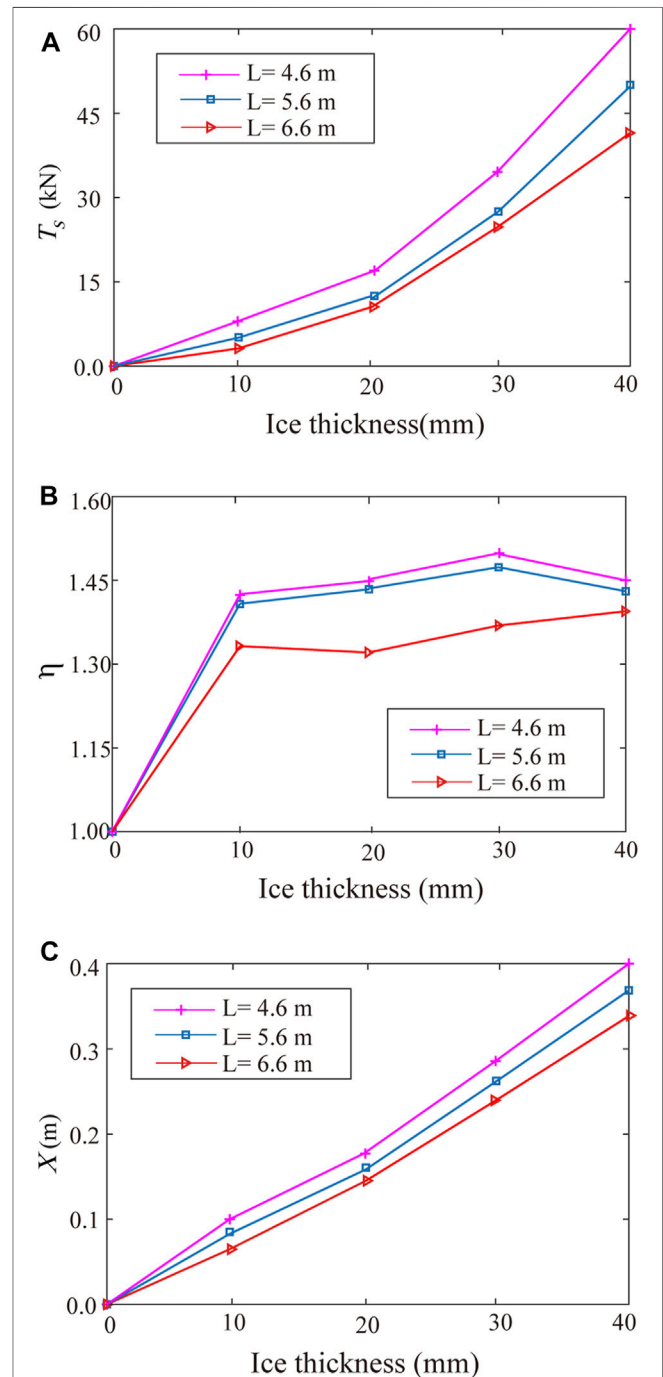
Span is a key parameter that affects the dynamic response of the transmission tower to conductor ice shedding. When the span is 500 m and the ice thickness exceeds 45.6 mm, the tower-line system collapses. However, the simulation results also show that



when the span is 400 m and the ice thickness is greater than 48.3 mm, tower-line system collapses.

Figure 6 shows the variation in the static longitudinal unbalanced tension, the unbalanced tension impact coefficient η , and the maximum displacement of Point K with the different ice thickness under spans of 500, 400, and 300 m. The change trend in Figure 6A indicates that the larger the span is under the same ice

thickness, the greater the T_s experienced by the transmission tower after ice shedding occurs. When the span increases from 300 to 400 m, T_s increases from 11.05 to 22.3 kN (an increase of 101.8%), and when the span increases from 400 to 500 m, T_s increases from 22.3 to 40 kN (an increase of 79.37%). Hence, the increase in T_s is more obvious when increasing from 300 to 400 m. From the



perspective of the simulated damage time, the 500 m tower is the first to be damaged, which shows that the larger T_s is, the more likely the transmission tower will be damaged.

The unbalanced tensions are considered in the design code as static loads. In fact, the unbalanced tensions caused by ice-shedding are dynamic, the impact effect plays a very important role. **Figure 6B** further demonstrates that the larger the span, the smaller η is under the same ice thickness. η reflects the impact effect of the longitudinal unbalanced tension. In other words, the larger η is, the stronger the impact. It is especially important to note that when the span is reduced from 500 to 400 m, η increases from 1.39 to 1.55, which is an increase of 11.51%. When the span is reduced from 400 to 300 m, η increases from 1.55 to 1.71 (an increase of 10.32%), meaning that the dynamic maximum unbalanced tension is nearly 1.71 time of the static unbalanced tension. η is considerable, the influence of the impact factor should be considered in the design of transmission lines.

Figure 6C indicates that the larger the span is under the same ice thickness, the larger the maximum displacement of Point K caused by ice shedding. When the span increases from 300 to 400 m, X increases from 0.12 to 0.25 m (an increase of 108.3%), and when the span increases from 400 to 500 m, X increases from 0.25 to 0.4 m (an increase of 60%). Hence, the increase in X is more obvious when increasing from 300 to 400 m.

In summary, as the span increases, the dynamic response of the transmission tower-line system increases. Therefore, in areas with severe icing, appropriately reducing the span is highly beneficial for protecting transmission towers from the longitudinal imbalance tension caused by ice shedding.

Insulator Length

The length of the insulator is another important parameter that affects the dynamic response of the transmission tower-line system. **Figure 7** shows the variations in the static longitudinal unbalanced tension, unbalanced tension impact coefficient η , and maximum displacement of Point K with the ice load at different insulator lengths.

Figure 7A suggests that the static longitudinal unbalanced tension increases with decreasing insulator length, indicating that long insulators can effectively reduce the longitudinal unbalanced tension caused by ice shedding. Therefore, longer insulators should be selected as much as possible in the design and construction of transmission lines.

Furthermore, **Figure 7B** shows that η decreases with increasing insulator length. Hence, increasing the insulator length can reduce the impact of ice shedding on the tower-line system and reduce the threat of collapse of the system.

In addition, **Figure 7C** shows that the maximum displacement of Point K decreases as the length of the insulator increases. Since Point K exhibits the most obvious deformation on the tower, an increase in the insulator length can reduce the overall displacement of the transmission tower.

In summary, as the length of the insulator increases, longitudinal unbalanced tension in the line decrease. At the same time, the impact coefficient and tower displacement will also decrease. Therefore, the response of the tower-line system is reduced, indicating that the length of the selected insulator should

be increased as much as possible within the allowable range in the design process of the transmission line.

CONCLUSION

In this paper, a numerical model of a two-tower, three-line transmission tower-line system is established, and the damage of the transmission line caused by ice shedding is studied. The influence parameters are studied through a parameter analysis. According to the research in this article, the following conclusions can be drawn:

- 1) For the transmission tower employed in this article, the cross-arm connected to the ice-shedding conductor (the tower height ranges from 81.0 to 84.5 m) and the tower head and tower body connection (the tower height ranges from 61.0 to 64.0 m) are prone to damage when ice shedding occurs. If these positions are strengthened, then the ability of the transmission tower to resist longitudinal unbalanced tension can effectively increase.
- 2) The higher the ice-shedding position along the height of the transmission line is, the greater the threat of collapse of the tower-line system.
- 3) The larger the span is, the greater the threat of ice shedding on the transmission line. Therefore, in an actual line, for areas with severe icing, large spans should be avoided during the design process.
- 4) The larger the insulator is, the smaller response of the tower-line system.
- 5) The impact of ice shedding will amplify the longitudinal unbalanced tension in the line, and attention should be paid to the impact on the line.

DATA AVAILABILITY STATEMENT

The raw data supporting the conclusion of this article will be made available by the authors, without undue reservation.

AUTHOR CONTRIBUTIONS

JL contributed to the conception of the study, analyzed the data and wrote the paper. BW performed the numerical simulation. JS performed the numerical simulation. SW contributed to the conception of the study. XZ helped perform the analysis with constructive discussions. XF helped perform the analysis with constructive discussions. All authors have read and agreed to the published version of the manuscript.

FUNDING

The research described in this paper was financially supported by the National Natural Science Foundation of China (grant no. 51808100), the China Postdoctoral Science Foundation (grant no. 2018M631808) and Liaoning Provincial Natural Science Foundation of China (grant no. 2019-ZD_0004).

REFERENCES

- ASCE. *Guidelines for Electrical Transmission Line Structural Loading*, 74. Reston, VA: ASCE (1991).
- China Planning Press. *Code For Design of 110 kV ~750 kV Overhead Transmission Line. GB50545-2010*. China: Ministry of Housing and Urban Rural Development of the Peoples Republic of China (2010).
- IEC (International Electrotechnical Commission). *Overhead transmission Line—Design Criteria. IEC60826:2017*. Geneva: ISO (2017).
- Li Z, Yang J, Han J, Huang T, and Huang H. Analysis on Transmission tower Toppling Caused by Icing Disaster in 2008. *Power Syst Tech* (2009) 33(02): 31–5. doi:10.13335/j.1000-3673.pst.2009.02.005
- Qu C, Li H, Huo L, and Yi T. Optimum Value of Negative Stiffness and Additional Damping in Civil Structures. *J Struct Eng* (2017) 143(8):04017068. doi:10.1061/(ASCE)ST.1943-541X.0001805
- Qu C, Huo L, Li H, and Wang Y. A Double Homotopy Approach for Decentralized Hoo Control of Civil Structures. *Struct Control Health Monit* (2014) 21(3):269–81. doi:10.1002/stc.1552
- Qu CX, Yi TH, and Li HN. Mode Identification by Eigensystem Realization Algorithm through Virtual Frequency Response Function. *Struct Control Health Monit* (2019) 26(10):e2429. doi:10.1002/stc.2429
- Zhao L, Huang X, Zhang Y, Zhu Y, Jia J, and Zhu C. Aeolian Vibration-based Structural Health Monitoring System for Transmission Line Conductors. *Struct Control Health Monit* (2020) 27(6):e2538. doi:10.1002/stc.2538
- Tian L, Zhou M, Qiu C, Pan H, and Rong K. Seismic Response Control of Transmission tower-line System Using SMA-Based TMD. *Struct Eng Mech* (2020) 74(1):129–43. doi:10.12989/sem.2020.74.1.129
- Li J, McClure G, and Wang S. Ensuring the Structural Safety of Overhead Transmission Lines by Design. *J Aerospace Eng* (2021) 34(3):04021010. doi:10.1061/(ASCE)AS.1943-5525.0001245
- Kollar LE, and Farzaneh M. Vibration of Bundled Conductors Following Ice Shedding. *IEEE Trans Power Deliv* (2008) 23(2):1097–104. doi:10.1109/TPWRD.2007.915876
- Kollar LE, and Farzaneh M. Modeling Sudden Ice Shedding from Conductor Bundles. *IEEE Trans Power Deliv* (2013) 28(2):604–11. doi:10.1109/TPWRD.2012.2227281
- Kollar LE, Farzaneh M, and Van Dyke P. Modeling Ice Shedding Propagation on Transmission Lines with or without Interphase Spacers. *IEEE Trans Power Deliv* (2013) 28(1):261–7. doi:10.1109/TPWRD.2012.2212918
- Kollar LE, and Farzaneh M. Modeling the Dynamic Effects of Ice Shedding on Spacer Dampers. *Cold Regions Sci Tech* (2009) 57(2-3):91–8. doi:10.1016/j.coldregions.2009.03.004
- Yan B, Chen K, Guo Y, Liang M, and Yuan Q. Numerical Simulation Study on Jump Height of Iced Transmission Lines after Ice Shedding. *IEEE Trans Power Deliv* (2013) 28(1):216–25. doi:10.1109/TPWRD.2012.2219324
- Wu C, Yan B, Zhang L, Zhang B, and Li Q. A Method to Calculate Jump Height of Iced Transmission Lines after Ice-Shedding. *Cold Regions Sci Tech* (2016) 125:40–7. doi:10.1016/j.coldregions.2016.02.001
- Huang G, Yan B, Wen N, Wu C, and Li Q. Study on Jump Height of Transmission Lines after Ice-Shedding by Reduced-Scale Modeling Test. *Cold Regions Sci Tech* (2019) 165:102781. doi:10.1016/j.coldregions.2019.102781
- Kálmán T, Farzaneh M, and McClure G. Numerical Analysis of the Dynamic Effects of Shock-Load-Induced Ice Shedding on Overhead Ground Wires. *Comput Structures* (2007) 85(7-8):375–84. doi:10.1016/j.compstruc.2006.11.026
- Mirshafiei F, McClure G, Kalman T, and Farzaneh M. Improved Ice Shedding Modelling of Iced Cables: a Comparison with Experimental Data. In: *Proceedings of the 2nd International Structural Specialty Conference*. Winnipeg, Canada (2010). p. 978–87.
- Mirshafiei F, McClure G, and Farzaneh M. Modelling the Dynamic Response of Iced Transmission Lines Subjected to cable Rupture and Ice Shedding. *IEEE Trans Power Deliv* (2013) 28(2):948–54. doi:10.1109/TPWRD.2012.2233221
- McClure G, Ji K, and Rui X. An Integrated Ice-Shedding Model of Electric Transmission Lines with Consideration of Ice Adhesive/cohesive Failure. In: *Proceedings of the 9th International Conference on Structural Dynamics*. Portugal: Porto (2014). p. 3731–6.
- Ji K, Rui X, Li L, Leblond A, and McClure G. A Novel Ice-Shedding Model for Overhead Power Line Conductors with the Consideration of Adhesive/cohesive Forces. *Comput Structures* (2015) 157:153–64. doi:10.1016/j.compstruc.2015.05.014
- Rui X, Ji K, Li L, and McClure G. Dynamic Response of Overhead Transmission Lines with Eccentric Ice Deposits Following Shock Loads. *IEEE Trans Power Deliv* (2017) 32(3):1287–94. doi:10.1109/TPWRD.2015.2501029
- Ji K, Rui X, Li L, Yang F, and McClure G. Dynamic Response of Iced Overhead Electric Transmission Lines Following cable Rupture Shock and Induced Ice Shedding. *IEEE Trans Power Deliv* (2016) 31(5):2215–22. doi:10.1109/TPWRD.2016.2520082
- Ji K, Liu B, Cheng Y, Zhan X, and McClure G. Evaluation and Optimization of a Shock Load De-icing Method for Transmission Lines with Combined Ice Failure Criteria. *Cold Regions Sci Tech* (2019) 165:102818. doi:10.1016/j.coldregions.2019.102818
- Yang F, Yang J, Han J, and Fu D. Dynamic Responses of Transmission tower-line System under Ice Shedding. *Int J Str Stab Dyn* (2010) 10(3):461–81. doi:10.1142/S0219455410003579
- Yang F, Yang J, and Zhang H. Analyzing Loads from Ice Shedding Conductors for UHV Transmission Towers in Heavy Icing Areas. *J Cold Regions Eng* (2014) 28(3):04014004. doi:10.1061/(ASCE)CR.1943-5495.0000070
- Shen G, Yuan G, Sun B, and Lou W. Dynamic Impact Effects on tower-line System Due to Ice-Shedding. *Eng Mech* (2010) 27(5):210–7.
- Shen G, Yuan G, Xing Y, Lou W, and Sun B. Numerical Simulation and Parameter Analysis of Conductor Icing Loss. *Vibration and Impact* (2012) 31(5):604–11. doi:10.13465/j.cnki.jvs.2012.05.035
- Fu X, Li H-N, Li G, Dong Z-Q, and Zhao M. Failure Analysis of a Transmission Line Considering the Joint Probability Distribution of Wind Speed and Rain Intensity. *Eng Structures* (2021) 233(2021):111913. doi:10.1016/j.engstruct.2021.111913
- Fu X, Li H-N, Li G, and Dong Z-Q. Fragility Analysis of a Transmission tower under Combined Wind and Rain Loads. *J Wind Eng Ind Aerodynamics* (2020) 199(2020):104098. doi:10.1016/j.jweia.2020.104098
- Tian L, Pan H, Ma R, Zhang L, and Liu Z. Full-scale Test and Numerical Failure Analysis of a Latticed Steel Tubular Transmission tower. *Eng Structures* (2020) 208:109919. doi:10.1016/j.engstruct.2019.109919
- Li J-X, Li H-N, and Fu X. Dynamic Behavior of Transmission tower-line Systems Subjected to Insulator Breakage. *Int J Str Stab Dyn* (2018) 18(3):1850036. doi:10.1142/S0219455418500360
- Li J-X, Li H-N, and Fu X. Stability and Dynamic Analyses of Transmission tower-line Systems Subjected to Conductor Breaking. *Int J Str Stab Dyn* (2017) 17(6):1771013. doi:10.1142/S0219455417710134
- Zhang Q, Popplewell N, and Shah AH. Galloping of Bundle Conductor. *J Sound Vibration* (2000) 234(1):115–34. doi:10.1006/jsvi.1999.2858
- Fu X, Wang J, Li H-N, Li J-X, and Yang L-D. Full-scale Test and its Numerical Simulation of a Transmission tower under Extreme Wind Loads. *J Wind Eng Ind Aerodynamics* (2019) 190:119–33. doi:10.1016/j.jweia.2019.04.011
- Fu X, and Li H-N. Uncertainty Analysis of the Strength Capacity and Failure Path for a Transmission tower under a Wind Load. *J Wind Eng Ind Aerodynamics* (2018) 173:147–55. doi:10.1016/j.jweia.2017.12.009

Conflict of Interest: The authors declare that the research was conducted in the absence of any commercial or financial relationships that could be construed as a potential conflict of interest.

Copyright © 2021 Li, Wang, Sun, Wang, Zhang and Fu. This is an open-access article distributed under the terms of the Creative Commons Attribution License (CC BY). The use, distribution or reproduction in other forums is permitted, provided the original author(s) and the copyright owner(s) are credited and that the original publication in this journal is cited, in accordance with accepted academic practice. No use, distribution or reproduction is permitted which does not comply with these terms.



Distant Relative Genetic Algorithm–Based Structural Reliability Optimization

Hu Cheng, Xin-Chi Yan* and Li Fu

School of Environment and Civil Engineering, Jiangnan University, Wuxi, China

In this study, safety margin explicit equation has been established using random variables (i.e., the engineering conditions, structure parameters, structural strength, and external load), and the genetic algorithm (GA)–based structural reliability optimization design has been addressed subsequently. Though the conventional adaptive GA can change automatically with fitness, it is still not unsatisfactory in sufficiently improving the algorithm convergence speed, especially for complex structures. This article presents an improved adaptive technology termed as the distant relative genetic algorithm (DRGA), in which the distant relative pointer and immunity operators can effectively improve the search performance of the GA. In early evolution, by means of cross controlling and avoiding pairing between individuals with the same genes, the methodology prevents the isogenic individuals expanding locally. Besides, the revised algorithm is able to jump out of the local optimal solution, thus ensuring the realization of a fast global convergence. An example based on wing box structure optimization has been demonstrated using the improved method, and the calculation results show that this strategy makes the GA more effective in dealing with the constraint optimization issues.

Keywords: reliability-based structural optimization, genetic algorithm, wing box structure, distant relative pointer, immunity operator

OPEN ACCESS

Edited by:

Yang Zhang,
Dalian University of Technology, China

Reviewed by:

Ying Ma,
North China University of Water
Conservancy and Electric Power,
China
Hai-Bin Huang,
Hebei University of Technology, China

*Correspondence:

Xin-Chi Yan
skywalker@jiangnan.edu.cn

Specialty section:

This article was submitted to
Interdisciplinary Physics,
a section of the journal
Frontiers in Physics

Received: 25 May 2021

Accepted: 04 June 2021

Published: 23 June 2021

Citation:

Cheng H, Yan X-C and Fu L (2021)
Distant Relative Genetic
Algorithm–Based Structural
Reliability Optimization.
Front. Phys. 9:714381.
doi: 10.3389/fphy.2021.714381

INTRODUCTION

With the rapid development of large and complex structures, more and more attention has been paid to the structural safety, such as the structural control and health monitoring [1, 2], the long-term performance deterioration [3, 4], and the structural optimization [5, 6], where the reliability-based structural optimization (RBSO) with multiple stochastic variables is always a difficult problem [7]. The weight and material cost of a structure can be effectively reduced by selecting the structural reliability index as the constraint of the optimization problem and adopting the element cross-sectional area, length, strength, and external load as the stochastic variables. Meanwhile, the structure strength, stiffness, and resistance to vibration and stability can also be improved. An optimized RBSO design, which is beneficial to make structures meet the requirements of economy and safety, has essential application value.

In the past few decades, much attention has been paid to the standard genetic algorithm (SGA) [8, 9]. However, since actual structures are usually large-scale and complicated, shortcomings such as premature convergence and poor computational efficiency frequently appear when the SGA is applied to the RBSO [10]. The above limitations make many researchers and engineers doubt about whether the genetic algorithm (GA) can be applied to the optimization design for actual structures [11].

The selection, crossover, and mutation operations of the GA are random, which ensure the evolution of population. The individual degradation phenomenon, however, appears due to the arrangement of the algorithm. Crossover and mutation probabilities are the two genetic parameters that are key to the performance of the GA. Srinivas and Patnaik [12] proposed that the adaptive genetic algorithm (AGA) can change automatically with fitness. But, the conventional AGA methodology is still unsatisfactory in sufficiently improving the algorithm convergence speed.

To deal with such aforementioned drawbacks, an improved adaptive technology, termed as the distant relative genetic algorithm (DRGA), is proposed in this study. In the following, the element safety margin function and system failure analysis are introduced, focusing on the optimization problem of an ideal elastic-plastic beam-slab structure system. Then the improved adaptive technology is presented, followed by the detailed operation process. After that, a wing box structure is taken as the numerical example for the validation of the proposed method, and finally, conclusions are drawn.

ELEMENT SAFETY MARGIN FUNCTION AND SYSTEM FAILURE ANALYSIS

An ideal elastic-plastic beam-slab structure system is focused on for the optimization problem. The considered material parameters are mainly the strength and elastic modulus. As for the geometrical parameter, it includes the slab (i.e., the length, width, and thickness) and the beam (the area, length, and moment of inertia).

The safety margin of the slab element can be expressed as follows:

$$Z_B = \sigma_a - \sigma_{eo}, \quad (1)$$

where σ_a is the maximum stress allowed; σ_{eo} is the equivalent stress at the center of the slab element, which can be determined by the following equation:

$$\sigma_{eo} = \left(\sigma_{xo}^2 + \sigma_{yo}^2 - \sigma_{xo}\sigma_{yo} + 3\tau_{xyo}^2 \right)^{\frac{1}{2}}, \quad (2)$$

where σ_{xo} and σ_{yo} are the normal stresses in the local coordinate system, and τ_{xyo} is the shear stress in the local coordinate system [13].

Let $\bar{\delta} = (\bar{u}_1 \ \bar{v}_1 \ \bar{u}_2 \ \bar{v}_2 \ \bar{u}_3 \ \bar{v}_3 \ \bar{u}_4 \ \bar{v}_4)^T$ be the nodal displacement vector in the local coordinate system, then

$$\begin{Bmatrix} \sigma_{xo} \\ \sigma_{yo} \\ \tau_{xyo} \end{Bmatrix} = \Lambda \begin{bmatrix} -b & -\mu a & b & -\mu a & b & \mu a & -b & \mu a \\ -\mu b & -a & \mu a & -a & \mu a & a & -\mu a & a \\ -\alpha a & -\mu b & -\mu a & \mu b & \mu a & \mu b & \mu a & -\mu b \end{bmatrix} \begin{Bmatrix} \bar{u}_1 \\ \bar{v}_1 \\ \bar{u}_2 \\ \bar{v}_2 \\ \bar{u}_3 \\ \bar{v}_3 \\ \bar{u}_4 \\ \bar{v}_4 \end{Bmatrix}, \quad (3)$$

where $\Lambda = E/2ab(1 - \mu^2)$, $\alpha = (1 - \mu)/2$, E is the elasticity modulus, μ is Poisson ratio, and a and b are the side lengths of the slab.

It can be seen that the safety margin of the slab element Z_B depends on the nodal displacement and the parameters of the rectangular element (i.e., length, width, and elasticity modulus).

When any left end section of the beam element fails, the safety margin of the beam can be determined by adopting the criterion of linear approximation as follows:

$$Z_{2q-1} = R_q - C_{2q-1} \bar{F}, \quad (4)$$

where R_q is the resistance of the straight beam q with a constant cross section, C_{2q-1} is the matrix of coefficient related to the parameters of beam, and \bar{F} is the vector of node loads applied to the beam [13]. Then the safety margin equation turns as follows:

$$\begin{aligned} Z_{2q-1} = & \sigma_y \bar{w}_{zq} - \left[\frac{\bar{w}_{zq}}{A_q} \text{sg}(\bar{N}_{2q-1}) \bar{N}_{2q-1} + \frac{\sqrt{3}}{2} \frac{\bar{w}_{zq}}{A_{yq}} \text{sg}(\bar{N}_{y,2q-1}) \bar{N}_{y,2q-1} \right. \\ & + \frac{\sqrt{3}}{2} \frac{\bar{w}_{zq}}{A_{zq}} \text{sg}(\bar{N}_{z,2q-1}) \bar{N}_{z,2q-1} + \frac{\bar{w}_{zq}}{\bar{w}_{xq}} \text{sg}(\bar{M}_{x,2q-1}) \bar{M}_{x,2q-1} \\ & \left. + \frac{\bar{w}_{zq}}{\bar{w}_{yq}} \text{sg}(\bar{M}_{y,2q-1}) \bar{M}_{y,2q-1} + \text{sg}(\bar{M}_{z,2q-1}) \bar{M}_{z,2q-1} \right] = 0, \quad (5) \end{aligned}$$

where σ_y is the yield stress of elements, A_q is the sectional area of beam q , A_{yq} and A_{zq} are the shearing areas of beam q in the directions of \bar{y} and \bar{z} , respectively, \bar{w}_{xq} is the plastic torsional coefficient on \bar{x} axis, and \bar{w}_{zq} and \bar{w}_{yq} are the plastic section modulus which corresponds to the moments \bar{M}_z and \bar{M}_y of beam q , respectively.

In a similar way, the safety margins can also be deduced when the right end section of the beam fails to \bar{z} axis and both ends fail to \bar{y} axis.

When the components of the system fail, the stress redistribution will occur to the structure. The reduced stiffness matrix of system members must be reconsidered. Once the number of failed components reaches to a particular number p_q , the system stiffness matrix will be singular as follows:

$$|\mathbf{K}^{p_q}| = 0, \quad (6)$$

where \mathbf{K}^{p_q} is the reduced system stiffness matrix with p_q failed components. Accordingly, the structural system fails.

Structure fails means that the structure turns into machinery. In order to calculate the system reliability index, all failure modes or integrated failure paths should be identified, but it is impossible and unnecessary in the analysis for complex structures. Alternatively, the typical failure modes can be adopted. The branch-and-bound method [14] is regarded as a proper approach to identify the typical failure modes. By boundary function operations, the number of subsystems can be reduced for structural reliability analysis. When all typical failure modes are identified, the system reliability index can be figured out by using the probability network evaluation technique [15]:

$$P_{fs} = 1 - \prod_{i=1}^G (1 - P_{fi}), \quad (7)$$

where P_{fs} is the failure probability of the structural system, P_{fi} is the failure probability of the typical failure mode, and G is the number of typical failure modes.

ADAPTIVE STRATEGY WITH DISTANT RELATIVE POINTER

Adaptive Strategy

The typical adaptive strategy makes the crossover probability (p_c) and mutation probability (p_m) change according to the individual fitness. When the individual fitness becomes accordant, it will make p_c and p_m increase. Otherwise, p_c and p_m will decrease when the individual fitness are diverse. In the meantime, lower values of p_c and p_m will be given to protect individuals whose fitness is larger than the average population fitness, and vice versa. The self-manipulated change of p_c and p_m can be described as follows [12]:

$$p_c = \begin{cases} \frac{k_1(f_{\max} - f^*)}{f_{\max} - \bar{f}}, & f^* \geq \bar{f} \\ k_2, & f^* < \bar{f} \end{cases}, \quad (8)$$

$$p_m = \begin{cases} \frac{k_3(f_{\max} - f)}{f_{\max} - \bar{f}}, & f \geq \bar{f} \\ k_4, & f < \bar{f} \end{cases}, \quad (9)$$

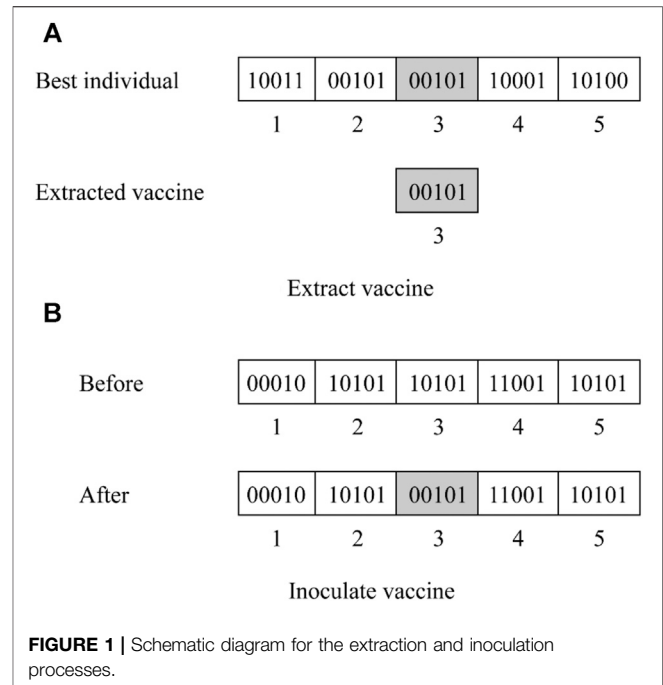
where f_{\max} is the maximum population fitness, \bar{f} is the average population fitness, f^* is the larger crossover individual fitness, and f is the mutation individual fitness. The parameters (i.e., k_1 , k_2 , k_3 , and k_4) range from 0 to 1.

The sufficient conditions of a global optimization ability are as follows: 1) a local search ability and 2) the ability of suddenly jumping from one local optimization to the next better one. However, the local search ability of the conventional AGA is inefficient in the early evolution because the optimal individual in the population almost does not change. Meanwhile, in the later evolution process, the optimal individual does not have the capability to jump out of the local optimal solution, leading to local convergence rather than global convergence eventually.

According to Eqs. 8, 9, when the population tends to be consistent, the AGA tends to increase p_c and p_m . However, in fact the consistence may be caused by any super individual existing in the population. Selecting operation may cause these individuals to overwhelm repeatedly in the new generations of population. An important consequence of this is a destroyed diversity of the population and consequently a premature convergence. The AGA alone cannot accommodate this phenomenon that once an overwhelming individual exists in the population, increasing p_c cannot generate new models nor make the calculation jump out of the local optimal solution. On the other hand, increasing the variability (e.g., the p_m) of the AGA may cause the algorithm to degrade into random search with fewer poor individuals depending on variability. Accordingly, convergence in this case is inefficient and unstable.

Distant Relative Pointer

In order to enhance the global optimization ability of the GA, individual expansion phenomenon must be mitigated, which has to be done at the early cross operation. Setting distant relative pointer is essential, and the detailed calculation process is performed as follows.



Assume that the population is denoted by $P(t) = \{x_i\}$ when calculating the t th generation. If one individual is selected twice in the $t+1$ th generation, its location numbers will be remembered, and a distant relative pointer will be allocated to each of them. After that, if one individual is selected to be crossed, it must be paired with a different one who has no identical relative pointer. Then any other marked individual will be operated as an immunity operator, and the p_c and p_m of other individuals of this population are still calculated based on Eqs. 8, 9.

The proposed distant relative pointer can effectively avoid any individual to dominate in the population. Meanwhile, the best individuals will not be damaged. This strategy has the capability to generate a new model, and the overall operation is simple. The algorithm also assures a diversity of the population, and at the same time, it is able to avoid local optimization and ensure the global convergence of the GA.

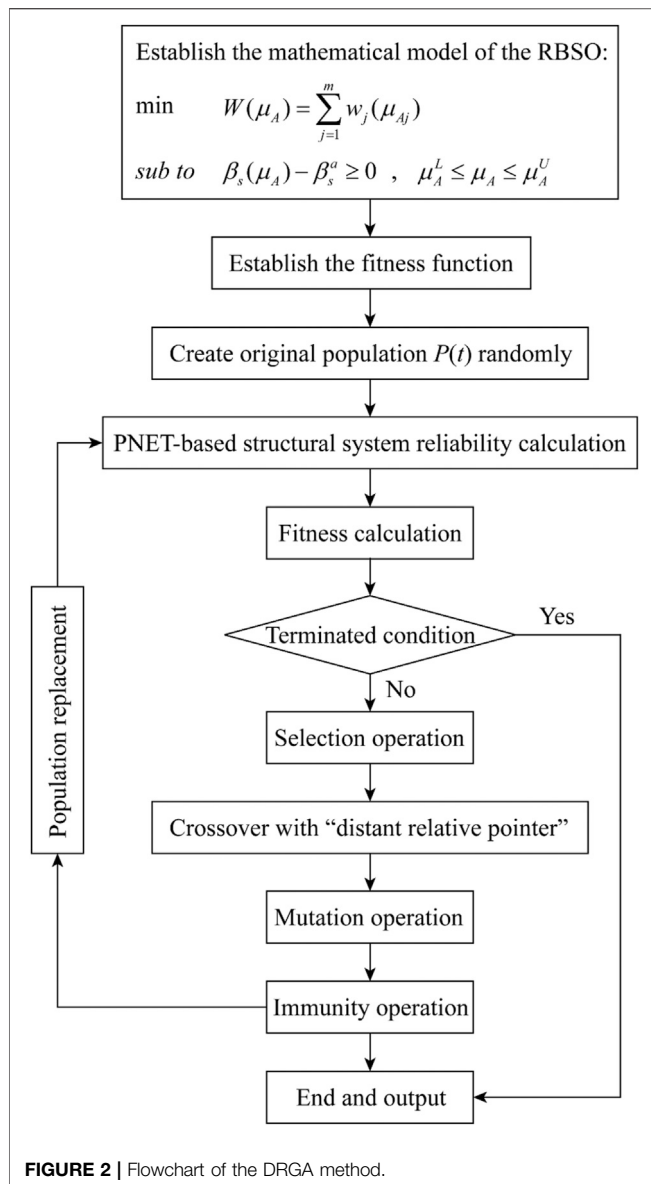
Immunity Operator

In order to prevent an individual from degenerating in basic operations via the GA, the immunity operator is adopted, which consists of a vaccine inoculation and immunity selection.

Vaccine Inoculation

A vaccine is a basic indicator of the specific question involved. In the RBSO, a vaccine can be a calculation result or a theoretical deduction. Figure 1 shows a scheme of the extraction and inoculation processes. Assume the t th generation is being calculated, the corresponding population is $P(t) = \{x_i\}$, and the random m ($m \leq n$) individuals can be used as the vaccine for inoculation. The m is calculated using the following normalized equation:

$$m = a \times n, \quad (10)$$



where $a = 0.05 \sim 0.1$ is the inoculate probability, and n is the population size.

Immunity Selection

The individuals that have been inoculated with the vaccine will be inspected subsequently. If their fitness is worse than that of the last generation, they will be replaced by their “fathers.” If their fitness is better than that of the last generation, it means the inoculation is successful. The appeared new optimal individual will be selected in the new generation.

OPERATION PROCESS OF THE DRGA METHOD

Based on the above research, this article presents a distant relative genetic algorithm (DRGA) method to solve the RBSO question.

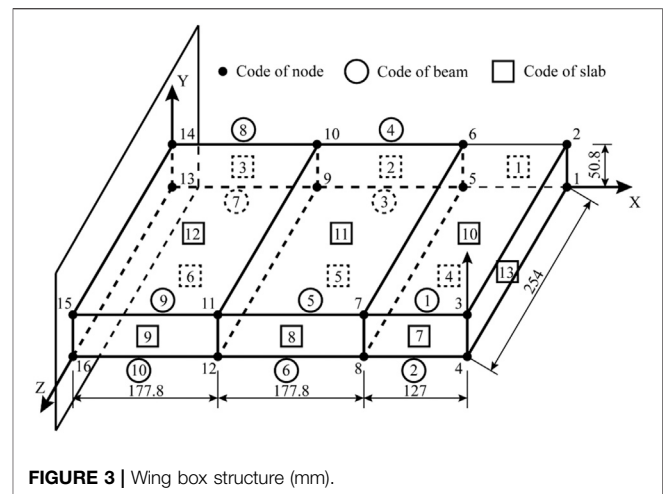


Figure 2 shows the flowchart of the computer program, and the significant procedures are performed as follows.

Stage I: Establish the Mathematical Model of the RBSO

In this step, constraints function must be expressed definitely. For an RBSO question, it is usually expressed as $\beta_s \geq \beta_s^a$, where β_s is the structural system reliability, and β_s^a is boundary value of β_s .

Stage II: Establish the GA Fitness Function for the Optimization Question

Lagrange multiplier method [16] is adopted to deduce the fitness function, which can be expressed as follows:

$$F = C - W - \frac{1}{2r} \{ \max[0, \lambda + r(\beta_s - \beta_s^a)]^2 - \lambda^2 \}, \quad (11)$$

where F is the fitness value, C is a large constant, which can be adopted as 1.25 times the mass of the structural system when all design variables equal the maximum values, W is the structural mass, λ is the Lagrange multiplier and $\lambda_{k+1} = \max\{0, \lambda_k + r(\beta_s - \beta_s^a)\}$, and r is the penalty factor, which is greater than zero.

Stage III: Calculate the Structural System Reliability

After deducing the safety margin explicit equation, the branch-and-bound method is adopted to search the main failure modes, and the probabilistic network evaluation technique (PNET) is adopted to calculate the system reliability index.

Stage IV: Create the Immunity Operator and Perform the GA Optimization Based on Distant Relative Pointer

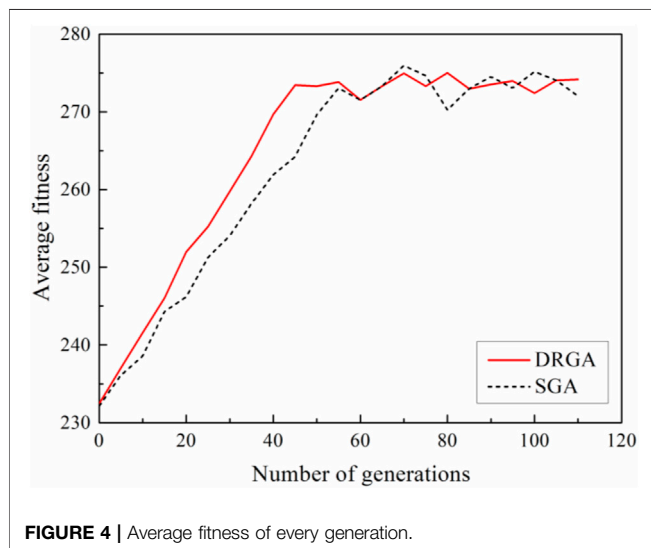
Except for the first three primary operators, the immunity operator and distant relative pointer are necessary to be

TABLE 1 | Optimized cross-sectional areas of beams.

Serial number	1	2	3	4	5	6	7	8	9	10
Cross-sectional area (cm ²)	9.03	8.91	6.28	5.62	4.65	6.32	5.03	6.62	8.98	9.71

TABLE 2 | Optimized thicknesses of slabs.

Serial number	Thickness (cm)	Serial number	Thickness (cm)
1	0.37	8	0.47
2	0.37	9	0.51
3	0.32	10	0.48
4	0.31	11	0.34
5	0.28	12	0.32
6	0.26	13	0.41
7	0.49	—	—

**FIGURE 4** | Average fitness of every generation.

created in this method, and then an efficient GA iterative loop is established accordingly. The method searches a global optimal solution by loop calculating until the convergence criterion is satisfied. Two conditions can be adopted to terminate the calculation process. First, the difference between the results of two sequential calculations is small enough (e.g., less than 0.0001). Alternatively, enough loop iterations have been made (e.g., the iteration number exceeds 100).

VALIDATION AND APPLICATION

The improved adaptive immune system is built based on the improved adaptive methodology and the introduced immunity operator and distant relative pointer. The simulative aircraft wing box structure, which is an ideal spatial beam-slab structure system, is taken as a typical example to verify the proposed

DRGA method. The reliability-based structural optimization is calculated using the improved strategy as follows.

Figure 3 displays the finite element model (FEM) of a simulative aircraft wing box. The allowable stress is 66.89 kN/cm², and the coefficient of variation (Cov) for the element resistance is 0.05. The elastic and shear modulus of the material are 6,689 and 2,300 kN/cm², respectively. The density of the material is adopted as 2,700 kg/cm³. All these above parameters are constant in the calculation process. In addition, the average of the external load is 44.45 kN, and the corresponding Cov is 0.2.

As shown in **Figure 3**, the FEM of the wing box consists of 10 beam elements and 13 slab elements. Let A_i be the cross-sectional area of the beam element, and it varies from 0.5 to 15 cm². The thickness of the slab element is denoted by B_i , which ranges from 0.1 to 0.8 cm. The resistance of components is independent to each other. The system reliability is limited by $\beta_s^a = 3.5$. In the calculation process of system reliability optimization, A_i and B_i are adopted as the design variables, and the system mass is set as the objective function.

The RBSO question can be illustrated as follows:

$$\begin{cases} \min W = \sum_{i=1}^{10} A_i L_i \rho_i + \sum_{i=1}^{13} B_i M_i \rho_i \\ \text{s.t. } 0.5 \leq A_i \leq 15, \quad 0.1 \leq B_i \leq 0.8, \quad \beta_s \geq 3.5 \end{cases}, \quad (12)$$

where W is the structural mass, L_i is the length of beam i , M_i is the area of slab i , and ρ is the density.

According to **Eq. 11**, C can be determined as 910.4 kg when A_i and B_i equal the maximum values. Accordingly, the fitness function (**Eq. 11**) turns into the following:

$$F = 910.4 - \left(\sum_{i=1}^{10} A_i L_i \rho_i + \sum_{i=1}^{13} B_i M_i \rho_i \right) - \frac{1}{2r} \{ \max[0, \lambda + r(\beta_s - 3.5)]^2 - \lambda^2 \}. \quad (13)$$

Real number coding is adopted in the calculation, and the individual length is 23. The population size is selected as 30. The circle terminates when the genetic evolution generation runs up to 110. The selection method adopts fitness proportion roulette. The optimization results of the wing box structure are summarized in **Tables 1, 2**, including the cross-sectional areas of beams and the thicknesses of slabs.

After optimization, the system reliability index is 3.5. The mass of the system is 302.47 kg, while the original assumed mass of the structure ($A_i = 15$ cm²; $B_i = 0.8$ cm) is 728.32 kg. It indicates that the overall mass of the system is decreased by

425.85 kg via optimization, which ensures the system 58.5% lighter.

In order to analyze the performance of the proposed algorithm, the optimization statistical diagram obtained by the DRGA is compared with that obtained by the SGA, as shown in **Figure 4**. It is obvious that the average fitness is attained earlier based on the DRGA, which means a higher convergence efficiency.

CONCLUSION

This article mainly proposes an improved adaptive technology, termed as the distant relative genetic algorithm (DRGA), to enable the genetic algorithm (GA) to jump out of the local optimal solution, overcoming its associated precocious shortcoming and making a fast and stable convergence. A wing box structure is taken as the example to verify the proposed method. The results demonstrate that a more stable average fitness can be achieved earlier after introducing the distant relative control to the adaptive genetic algorithm, compared to the conventional standard genetic algorithm (SGA). Besides, the control of cross in the early genetic operations by the distant relative pointer can effectively avoid individual expansion, enabling the algorithm to jump out of local optimal solution and increase local search ability. A better global convergence and convergence efficiency have been achieved as a consequence.

REFERENCES

1. Qu CX, Li HN, Huo LS, and Yi TH. Optimum Value of Negative Stiffness and Additional Damping in the Civil Structures. *J Struct Eng* (2017) 143(8): 04017068. doi:10.1061/(asce)st.1943-541x.0001805
2. Qu CX, Yi TH, and Li HN. Mode Identification by Eigensystem Realization Algorithm through Virtual Frequency Response Function. *Struct Control Health Monit* (2019) 26(10):e2429. doi:10.1002/stc.2429
3. Cheng H, Li H-N, Yang YB, and Wang D-S. Seismic Fragility Analysis of Deteriorating RC Bridge Columns with Time-Variant Capacity index. *Bull Earthquake Eng* (2019) 17(7):4247–67. doi:10.1007/s10518-019-00628-x
4. Cheng H, Wang DS, and Li HN. Investigation on Ultimate Lateral Displacements of Coastal Bridge Piers with Different Corrosion Levels along Height. *J Bridge Eng* (2021) 26(4):04021015. doi:10.1061/(asce)be.1943-5592.0001696
5. Sajedi S, and Huang Q. Reliability-based Life-Cycle-Cost Comparison of Different Corrosion Management Strategies. *Eng Structures* (2019) 186: 52–63. doi:10.1016/j.engstruct.2019.02.018
6. Mishra M, Keshavarzzadeh V, and Noshadravan A. Reliability-based Lifecycle Management for Corroding Pipelines. *Struct Saf* (2019) 76:1–14. doi:10.1016/j.strusafe.2018.06.007
7. Santoro R, Muscolino G, and Elishakoff I. Optimization and Anti-optimization Solution of Combined Parameterized and Improved Interval Analyses for Structures with Uncertainties. *Comput Structures* (2015) 149: 31–42. doi:10.1016/j.compstruc.2014.11.006
8. Holland JH. *Adaptation in Natural Artificial Systems*. Ann Arbor, MI: MIT Press (1975).
9. Goldberg DE. *Computer-aided Gas Pipeline Operation Using Genetic Algorithms and Rule Learning*. Ann Arbor, MI: Department of Civil Engineering, University of Michigan (1983).

DATA AVAILABILITY STATEMENT

The original contributions presented in the study are included in the article/supplementary material; further inquiries can be directed to the corresponding author.

AUTHOR CONTRIBUTIONS

Conceptualization: HC and X-CY. Methodology: X-CY. Software: HC and X-CY. Formal analysis: LF. Data curation: X-CY. Writing—original draft preparation: HC and X-CY. Writing—review and editing: HC and LF. Project administration: X-CY. Funding acquisition: HC. All authors have read and agreed to the published version of the manuscript.

FUNDING

This research is supported by the National Natural Science Foundation of China (Grant No. 52008186), the Natural Science Foundation of Jiangsu Province (Grant No. BK20200605), the Scientific Research Fund of Institute of Engineering Mechanics, China Earthquake Administration (Grant No. 2019D08), the Open Fund of State Key Laboratory of Coastal and Offshore Engineering, Dalian University of Technology (Grant No. LP2011), and the Fundamental Research Funds for the Central Universities (JUSRP12043). The authors greatly appreciate the financial supports.

10. Luo Y, and Kang Z. Layout Design of Reinforced Concrete Structures Using Two-Material Topology Optimization with Drucker-Prager Yield Constraints. *Struct Multidisc Optim* (2013) 47(1):95–110. doi:10.1007/s00158-012-0809-1
11. Barone G, and Frangopol DM. Life-cycle Maintenance of Deteriorating Structures by Multi-Objective Optimization Involving Reliability, Risk, Availability, Hazard and Cost. *Struct Saf* (2014) 48:40–50. doi:10.1016/j.strusafe.2014.02.002
12. Srinivas M, and Patnaik LM. Adaptive Probabilities of Crossover and Mutation in Genetic Algorithms. *IEEE Trans Syst Man Cybern* (1994) 24(4):656–67. doi:10.1109/21.286385
13. Yan XC, An WG, and Chen WD. Reliability Analysis for Large-Scale Ship Structure. *J Harbin Eng Univ* (2004) 25(2):147–52. (in Chinese).
14. Thoft-Christensen P, and Murotsu Y. *Application of Structural Systems Reliability Theory*. Berlin: Springer Press (1986). doi:10.1007/978-3-642-82764-8
15. Wang GY. *Theory of Soft Design in Engineering*. Beijing: Science Press (1992). (in Chinese).
16. Yan XC, and Hua Y. Establishment of Genetic Algorithm Fitness Function in Reliability-Based Structural Optimization. *Chin J Comput Mech* (2009) 26(1): 120–3. (in Chinese).

Conflict of Interest: The authors declare that the research was conducted in the absence of any commercial or financial relationships that could be construed as a potential conflict of interest.

Copyright © 2021 Cheng, Yan and Fu. This is an open-access article distributed under the terms of the Creative Commons Attribution License (CC BY). The use, distribution or reproduction in other forums is permitted, provided the original author(s) and the copyright owner(s) are credited and that the original publication in this journal is cited, in accordance with accepted academic practice. No use, distribution or reproduction is permitted which does not comply with these terms.



Quantitative Monitoring of Bolt Looseness Using Multichannel Piezoelectric Active Sensing and CBAM-Based Convolutional Neural Network

Yixuan Chen¹, Jian Jiang^{1,2*}, Xiaojun Qin¹ and Qian Feng^{1,2*}

¹Hubei Key Laboratory of Earthquake Early Warning, Institute of Seismology, China Earthquake Administration, Wuhan, China, ²Wuhan Institute of Earthquake Engineering Co. Ltd., Wuhan, China

OPEN ACCESS

Edited by:

Liang Ren,
Dalian University of Technology, China

Reviewed by:

Shi Yan,
Shenyang Jianzhu University, China
Bin Xu,
Huaqiao University, China

*Correspondence:

Jian Jiang
ltaxj@foxmail.com
Qian Feng
qfengwh@foxmail.com

Specialty section:

This article was submitted to
Smart Materials,
a section of the journal
Frontiers in Materials

Received: 08 March 2021

Accepted: 09 June 2021

Published: 29 June 2021

Citation:

Chen Y, Jiang J, Qin X and Feng Q
(2021) Quantitative Monitoring of Bolt
Looseness Using Multichannel
Piezoelectric Active Sensing and
CBAM-Based Convolutional
Neural Network.
Front. Mater. 8:677642.
doi: 10.3389/fmats.2021.677642

The bolted connection is widely utilized in engineering to practically and rigidly couple structural components. The integrity of the connection is paramount to the safety of the structure and has prompted the development of many monitoring methods, including the piezoelectricity-based active sensing method. However, the active sensing method cannot quantify bolt looseness due to the unclear relationship between bolt looseness and the single monitoring index typically used in the active sensing method. Thus, the authors propose the unique combination of a one-dimensional convolutional neural network (1DCNN) and multichannel active sensing for quantitative monitoring of bolted connections. In an experiment, piezoelectric ceramic transducer (PZT) patches are bonded on steel plates connected by a bolt. Each patch is wired to a multichannel active sensing monitoring system. After obtaining multichannel stress wave signals at different looseness levels, a looseness vector is calculated to generate training and validation datasets. A baseline 1DCNN model and a novel model improved using the convolutional block attention module (CBAM) are used to monitor the bolt looseness. Finally, the authors verify that the multichannel active sensing method combined with the 1DCNN model can accurately perform quantitative monitoring of bolt looseness, and the monitoring accuracy of the baseline 1DCNN model is above 91.07% in three different specimens. Compared with the baseline 1DCNN model, the monitoring accuracy of the CBAMCNN model improved by approximately 5%. Overall, the method proposed in this article offers a new and highly accurate approach for quantitative monitoring of bolted connections.

Keywords: bolt looseness, quantitative monitoring, multichannel active sensing method, convolutional neural network, convolutional block attention module

INTRODUCTION

The bolted connection has been extensively applied across many types of steel structures, such as large stadiums, steel-framed residences, and high-speed railways. Bolted connections are advantageous in terms of simple construction, convenient installation and replacement, safe operation, and reliability. However, since bolts are often used to couple dissimilar structural

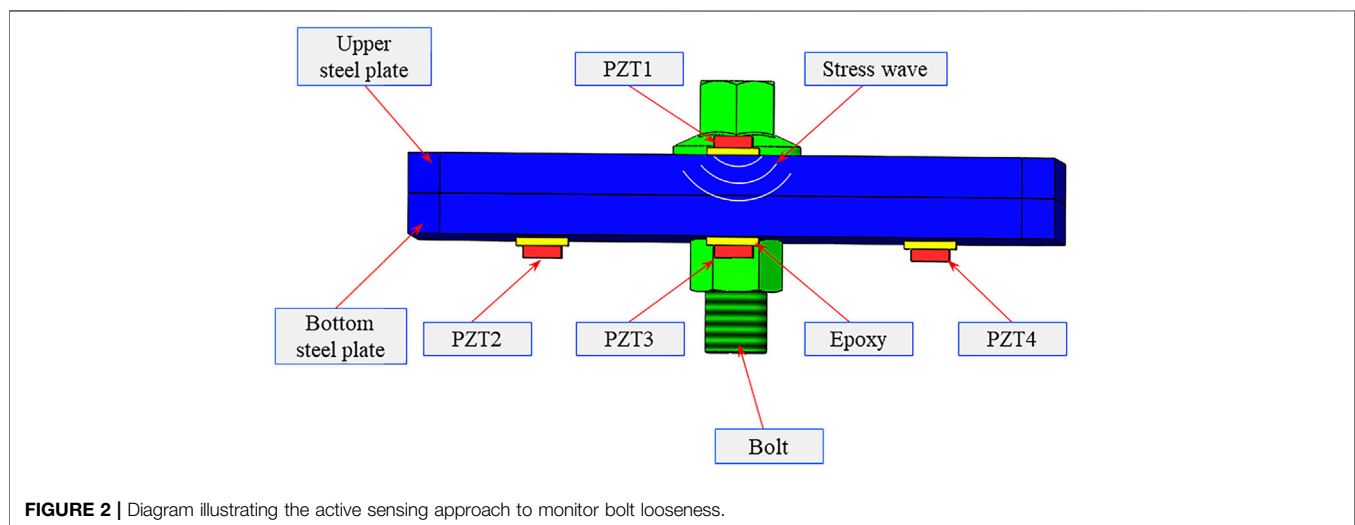
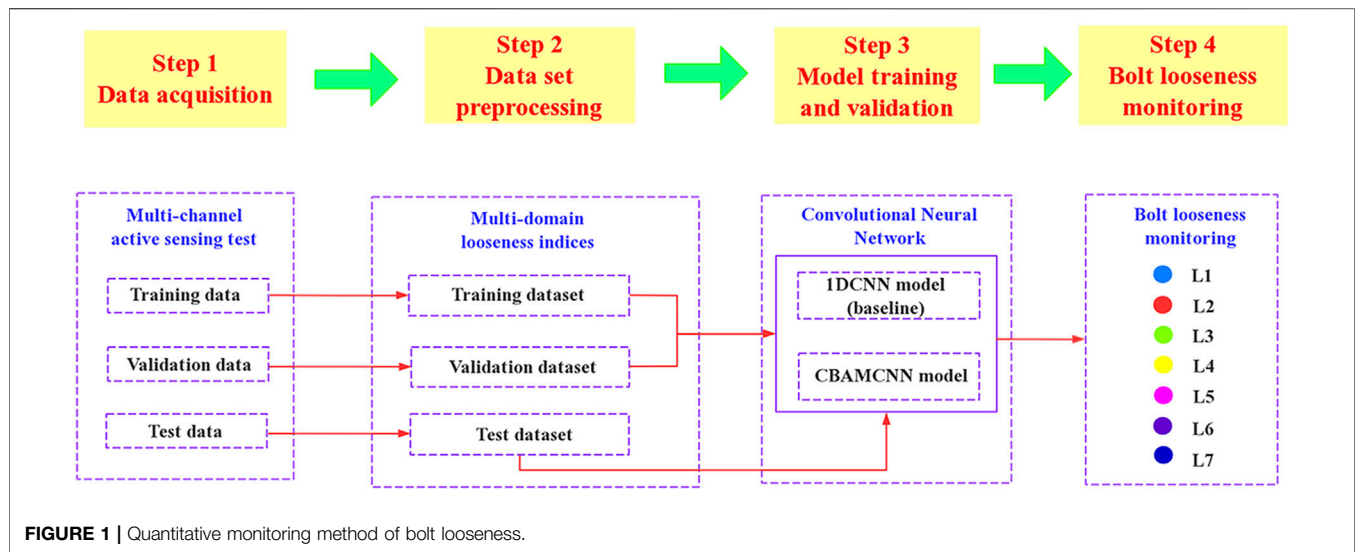
components, the connection is likely to introduce dynamic nonlinearities when under the action of unfavorable forces such as cyclic and vibration loads (Lacayo and Allen, 2019; Lacayo et al., 2019). This introduction of nonlinear behavior is difficult to solve, and it can also degrade structural performance and eventually induce structural failure if not addressed in a timely manner. Therefore, the state of the bolted connection should be closely monitored in real time to improve the safety of engineering structures (Xu et al., 2018).

Methods to monitor bolt looseness are based mainly on structural health-monitoring principles, which include, but are not limited to, the vibration-based method (Amerini et al., 2010; Li and Jing, 2020), the optical fiber sensing-based method (Guarino and Hamilton, 2017; You et al., 2020), the percussion-based method (Wang et al., 2019; Wang et al., 2020b; Wang and Song, 2020), the electromechanical impedance (EMI) method (Ritdumrongkul et al., 2003; Huo et al., 2017b; Wang et al., 2017), and methods based on the contact acoustic theory. Each of the methods mentioned above have unique limitations. Vibration-based monitoring approaches have difficulty detecting bolt looseness because low-order frequency responses of the connection are not sensitive to the local structural damage and high-frequency vibrations easily dissipate (Amerini et al., 2010). Percussion-based methods are highly dependent on human skill, while the accuracy of EMI methods is susceptible to unexpected changes in the surrounding environment. Methods based on contact acoustic theory include the active sensing method (Tao et al., 2016; Zhao et al., 2020), the high-order harmonics method (Li and Jing, 2017; Li et al., 2019), and the sideband modulation method (Meyer and Adams, 2015; Zhang et al., 2018). The analysis of high-order harmonics and spectral sidebands can shed light on nonlinear mechanisms of bolt loosening, but damping and instrumental noise can obfuscate information carried in high-frequency stress waves. On the other hand, the active sensing method provides superior performance due to the advantages of convenient implementation, fast response, and availability of a wide spectral bandwidth to perform monitoring. A concept of “smart washers” was proposed to monitor bolt looseness through a normalized wavelet energy index (Huo et al., 2017). Taking into account the aging of piezoceramic materials, the tracking of normalized coda wave energy helped to monitor the tightness of a single bolt (Hei et al., 2020). However, these methods are inadequate for conducting quantitative monitoring because they fail to accurately and quantitatively correlate bolt looseness states with a single monitoring index.

In recent years, research on piezoelectricity-based monitoring methods (i.e., including the impedance and active sensing methods) combined with machine learning have gradually attracted widespread attention. The methods combined EMI and back propagation neural networks (BPNNs) to inspect the looseness of bolted ball joints (Xu et al., 2019). Their method used the RMSD value of the EMI sub-band signal as the input and the torque level of the bolt joint as the expected output of the model. The LibSVM model in conjunction with the EMI method was used to identify the position of loose bolts (Zhang et al., 2017). An algorithm-based least square support vector machine was used to

realize bolt state recognition (Wang et al., 2020). In their study, multivariate, multiscale fuzzy entropy from the stress wave signals was obtained and subsequently employed as the input for training the genetic algorithm and least squares support vector machine (GA-LSSVM). The output is the number of loose bolts. In a similar manner, the stacking-based ensemble learning classifier was employed to determine the looseness state of the bolt group (Wang et al., 2021). Compared with traditional machine learning algorithms, deep learning is more powerful and more adaptable, especially in solving more complex problems that are data driven. With the rapid development and widespread application of artificial intelligence, a variety of deep learning architectures have been developed, such as the convolutional neural network (CNN) (Avci et al., 2017), long short-term memory (LSTM) (Huang et al., 2015; Luo et al., 2019), and generative adversarial networks (GANs) (Lei et al., 2020; Liu et al., 2020). In particular, the convolutional neural network is often used in structural health-monitoring tasks due to its ability to share weights, form local connections, and down-sample (Goodfellow et al., 2016). The Bayesian model and modal strain energy were used to determine the bolt looseness (Hu et al., 2018). The simultaneous use of CNNs and the analysis of guided waves helped to identify the location of the damage in a pressure vessel (Hu et al., 2020), in a steel plate structure (Lim and Sohn, 2020), and in aerospace structural material (Xu et al., 2019). The above discussion of the literature shows that significant research activity is currently centered around the use of CNNs to identify surface damage of structures by extracting structural damage information from monitoring data; however, there are limited reports regarding the use of CNNs to quantify bolt looseness based on active sensing signals.

Therefore, this article presents the development and implementation of a one-dimensional (1D) CNN model that is integrated with multichannel active sensing to detect the looseness of bolted connections in steel structures. Through the active sensing method, multichannel stress wave signals are obtained under different levels of torque. Multi-domain looseness indicators from different channels are then calculated and concatenated into a one-dimensional index vector based on the order of the channels. The mixture of data from different channels enables a comprehensive evaluation of bolt looseness severity. The 1DCNN model is trained using these vectors to perform bolt looseness identification. Moreover, spatial and channel attention mechanisms are introduced into the baseline 1DCNN model to improve the recognition accuracy. Finally, the feasibility of the proposed method is demonstrated through experiments. It should be noted that this article presents the first attempt to combine the active sensing method with a 1DCNN improved by the CBAM to explore the quantitative monitoring of bolt looseness. The findings of this research have a great potential to open the door to the use of machine learning and active sensing in future monitoring applications for steel structures. Moreover, the findings can promote further development of automatic monitoring techniques that are based on the piezoelectric active sensing method. The rest of this article consists of four sections and is organized as follows: section two provides a



detailed background of the methods proposed in this article, including the IDCNN model, the spatial channel attention mechanism, the active sensing method, and the looseness index. Section three presents the experimental setup, while section four discusses the experimental results. Section five closes with the conclusions.

THEORETICAL BACKGROUND

Figure 1 presents the fundamental framework of the method presented in this article. In step 1, a multichannel active sensing monitoring system is set up, and the data acquisition for training and validation is carried out. In step 2, multi-domain looseness indices for different torque levels are calculated and are later combined into a one-dimensional looseness index vector based on the order of the channels. In step 3, the training and validation datasets are input to the baseline IDCNN model and the

improved CBAMCNN model for determining the final model. In step 4, a new test dataset is fed into the finalized model for quantitatively monitoring the looseness of the bolt. In this study, seven degrees of looseness are recognized and labeled L1, L2...L7.

Multichannel Piezoelectric Active Sensing

The principle of active sensing being applied to monitoring bolt looseness is depicted in **Figure 2**. Considering the symmetry of the steel plate, four PZT patches labeled PZT1–4 are employed in the experiment. PZT1 serves as an actuator, while the rest are sensors (i.e., PZT2, PZT3, and PZT4). The stress wave is generated by PZT1 after being excited by a frequency sweep signal. The stress wave propagates through the contact surface of the steel plates to reach the sensors. A close relation between the propagating energy of the stress wave and the bolt connection state can be observed (Zhang et al., 2016). When the steel plates are tightly

connected, the stress wave can propagate to the bottom plate efficiently. Otherwise, the stress wave dissipates rapidly.

Multichannel and Multi-Domain Feature Extraction

In order to gauge the efficiency of the model and its recognition accuracy, multi-domain looseness indices are calculated to analyze the stress wave signals, which carry bolt looseness information. The looseness indices used in this experiment include the following: time-domain signal energy, the maximum value of the average periodogram, and three-layer wavelet packet decomposition energy. These indices are described below.

Time Domain Signal Energy

The process of stress wave propagation is accompanied by energy dissipation, so the signal energy can be used to characterize the bolt looseness. The signal energy refers to the sum of the squares of the time-domain amplitude, as shown below:

$$D_1 = \sum_{i=1}^N X_i^2, \quad (1)$$

where N represents the length of the received signal; X_i represents the i -th data of the received signal.

The Maximum Value of the Average Periodic Diagram

In this study, the average periodic diagram method proposed by Welch is used to perform spectral analysis on the received signals. By using the windowing and averaging processing techniques, random fluctuations of the signal can be reduced to ensure sufficient spectral resolution (Bartlett, 1950). The average periodic diagram method provides a new perspective for analyzing the stress wave signal. The steps to the method are as follows:

- a) Divide the received signal X into K segments, with each segment possessing L points. Two adjacent segments overlap over length P (usually, $P = L/2$). K is expressed as follows:

$$K = \frac{N - P}{L - P}, \quad (2)$$

where N represents the length of the received signal X .

- b) Apply the windowing function $w_d(n)$ to each subsection to obtain the values in segments i as shown below:

$$X_i(n) = X(i \cdot P + n)w_d(n), \quad (3)$$

where n represents the length of the windowing function, and i represents the i -th segment of the signal.

- c) Perform the discrete Fourier transform of each signal sequence as shown below:

$$X_i(k) = \sum_{n=0}^{M-1} X_i(n) \exp\left(-j \frac{2\pi kn}{M}\right), \quad (4)$$

where M represents the period of the discrete Fourier transform, k represents the i -th data point of the signal, and j represents the unit of the complex.

- d) Calculate the average value of the power spectrum and estimate for each signal sequence as shown below:

$$S_i\left(\frac{2k\pi}{M}\right) = \frac{1}{KU} \sum_{i=0}^{k-1} |X(k)|^2, \quad (5)$$

where $U = \sum_{n=1}^{L-1} w_d^2(n)$ represents the estimated mean value of the power spectrum of the windowing function.

- e) Obtain the maximum value of the average periodic diagrams through the following relation:

$$D_2 = \max \left[S_i\left(\frac{2k\pi}{M}\right) \right]. \quad (6)$$

Wavelet Packet Decomposition Energy

Wavelet packet decomposition is a multi-resolution analysis method, which has been widely used in structural damage research (Toliat et al., 2003; Teotrakool et al., 2009; Liu et al., 2018). It can perform multilevel and adaptive decomposition of the original signal through the wavelet tree.

In this study, $l = 3$ is adequate for an accurate representation of the bolt loosening information while minimizing computational costs. For every looseness condition, stress wave signals derived from PZTs 2–4 are simultaneously received. Their signals form the set $S = \{X^1, X^2, X^3\}$. Subsequently, ten looseness indices are calculated from each signal and concatenated into a looseness vector with elements organized by the order of the channels. The formula of the looseness vector is as follows:

$$D = [D_d^1, D_d^2, D_d^3] \\ = [D_1^1, D_2^1, \dots, D_d^1, D_1^2, D_2^2, \dots, D_d^2, D_1^3, \dots, D_d^3] (d = 1, 2, \dots, 10). \quad (7)$$

In order to accelerate model training and increase recognition accuracy, the looseness index vector above is standardized to D^{norm} to acquire a similar data distribution (Grus, 2019).

One-Dimensional Convolutional Neural Network Model

Inspired by the human visual nervous system, the CNN, a state-of-the-art deep learning model, has demonstrated excellent performance in a wide variety of classification tasks. Local connections and shared weights are prominent features of CNNs. These unique features effectively decrease the number of weights and accelerate training.

In this study, a baseline 1DCNN model was established to monitor the bolt looseness more efficiently. Its framework is

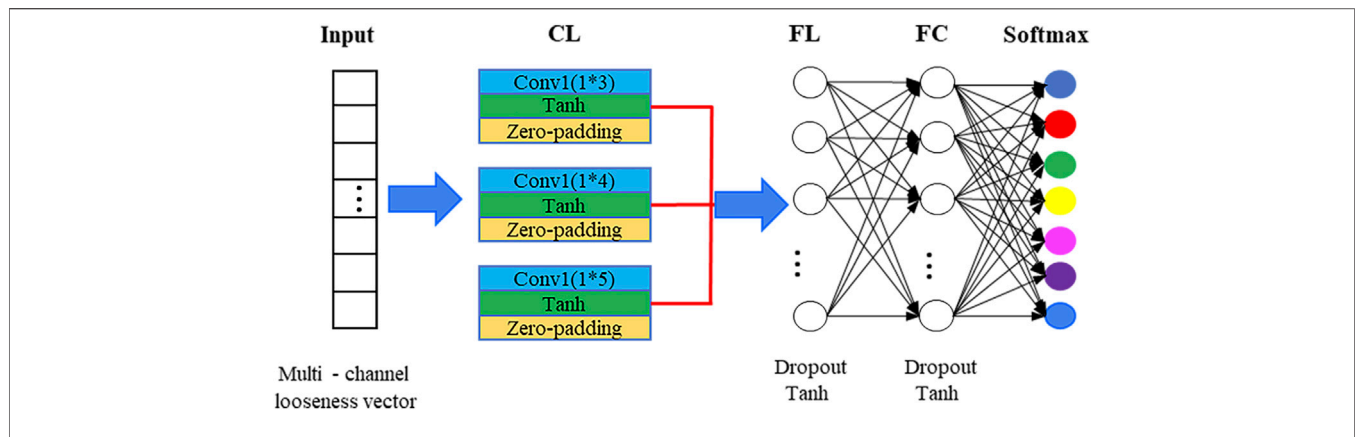


FIGURE 3 | Architecture diagram of the baseline 1DCNN model.

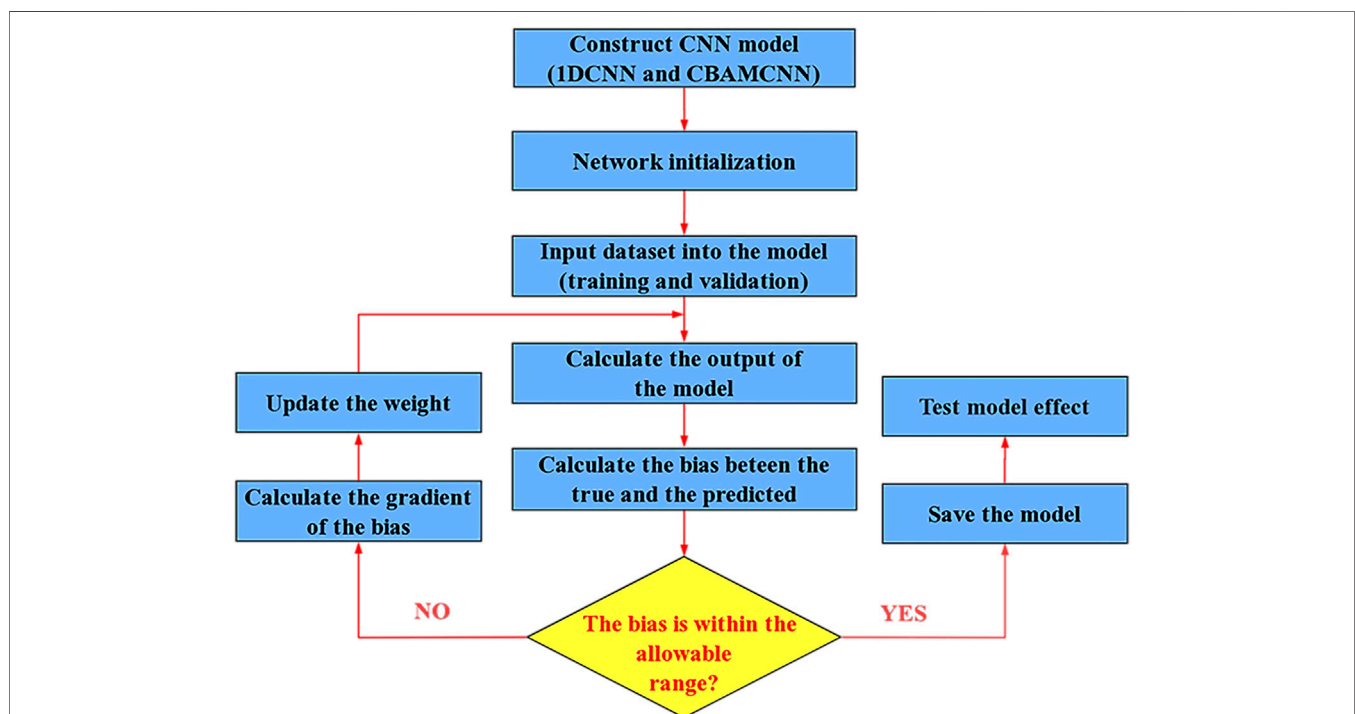


FIGURE 4 | Training process of the baseline model (1DCNN) and the improved model (CBAMCNN).

presented in **Figure 3**. As seen in the figure, the baseline 1DCNN model is composed of an input layer, a convolutional layer (CL), a flattening layer (FL), a fully connected layer (FC), and a SoftMax layer. In this model, a convolutional layer consists of three convolution kernels of different sizes (i.e., 1×3 , 1×4 , and 1×5). The kernels can extract advanced features and fuse the information of bolt looseness from different stress wave signals at the same time. Then, the flattening layer expands the looseness information extracted by the convolutional layers and maps the information onto the fully connected layer. Finally, a SoftMax function presents the probability of each class. Tanh activation functions are used in the model in order to improve the fidelity of

the input information and encourage rapid convergence. Furthermore, dropout (Fraser-Thomas et al., 2008) operations are employed to mitigate overfitting. The Adam optimizer (β_1 , β_2 , and ϵ are, respectively, set to 0.9, 0.999, and $1e-8$) is used during training to minimize the cross-entropy. The model learning rate is $1.5e-4$, and the maximum number of iterations is 400 (i.e., with a mini-batch size of 280). The procedure for training the convolutional neural network is illustrated in **Figure 4**.

Convolutional Block Attention Module

The convolutional block attention module (CBAM) was implemented in this study to improve the monitoring accuracy

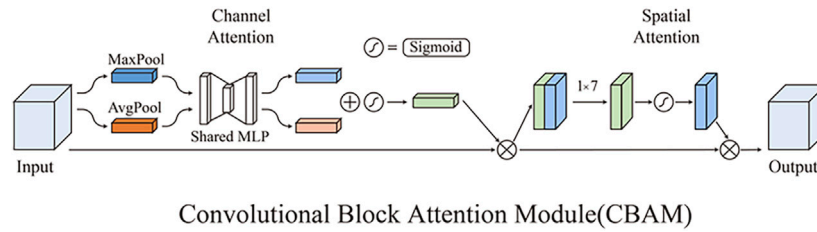


FIGURE 5 | Calculation principle of the convolution block attention module.

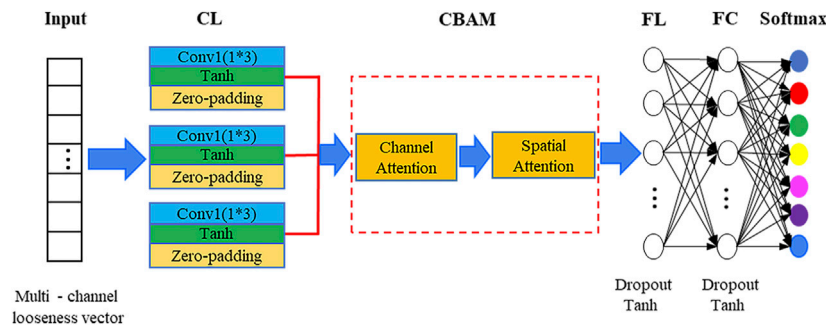


FIGURE 6 | Architecture diagram of the CBAMCNN model.

of the model. As shown in **Figure 5**, the CBAM consists of the channel attention mechanism and the spatial attention mechanism (Ban et al., 2020; Zhao et al., 2020). The overall computational process of the CBAM can be summarized as follows. The feature F of the CNN first passes through the channel attention mechanism in order to generate the corresponding channel attention weight M_c ; then, element-wise multiplication between M_c and F is performed to generate a new feature F' . The refined feature F' is generated by subjecting F' to a similar process with the spatial attention mechanism weight M_s . The improved network framework using the channel and spatial attention mechanisms is illustrated in **Figure 6**. The operations performed using the spatial attention mechanism is described by the following:

$$\begin{aligned} F' &= M_c(F) \otimes F, \\ F'' &= M_s(F') \otimes F', \end{aligned} \quad (8)$$

where \otimes refers to element-wise multiplication, M_s refers to the spatial attention mechanism weight, M_c refers to the channel attention weight, F' represents the channel attention mechanism, and F'' represents the spatial attention mechanism.

For the sake of conciseness, the computational operations of the channel attention weight $M_c(F)$ and the spatial attention weight $M_s(F)$ are summarized as follows:

$$\begin{aligned} M_c(F) &= \sigma(W_1(W_0(F_{avg}^s)) + W_1(W_0(F_{avg}^c))), \\ M_s(F) &= \sigma(f^{1 \times 7}(F_{avg}^s; F_{avg}^c)), \end{aligned} \quad (9)$$

where σ represents the sigmoid function, W_0 and W_1 , respectively, represent the parameters in the multilayer perceptron model, F_{avg}^c denotes the average-pooled features, F_{max}^c denotes the max-pooled features, and $f^{1 \times 7}$ refers to the convolutional layer for which the convolution kernel size is 1×7 .

EXPERIMENTAL SETUP

As shown in **Figure 7**, in order to verify the method introduced in this study, a set of benchtop experiments was conducted on two steel plates connected by one M12 bolt. Each specimen is equipped with four PZT patches. PZT1, serving the role of the actuator, is installed on the upper steel plate. PZT2–PZT4, serving as sensors, are installed on the bottom steel plate. The epoxy adhesive used to bond the PZTs to the steel plates also electrically insulated the PZTs from the steel plate. The type of piezoelectric patch used in this experiment is the compression type, and its size is $10^\circ\text{mm}^3 \times 10^\circ\text{mm}^3 \times 0.5^\circ\text{mm}^3$. The dimensions of the specimen are shown in **Figure 8**. As shown in **Figure 9**, a multifunction data acquisition system (NI USB-6363) with multichannel capacity collected data and transmitted excitation signals. The data acquisition system was connected to a laptop that ran LabVIEW. A power amplifier (Trek model 2100 HF) magnified the excitation signals. During the experiments, PZT1 generated a stress wave excited by a swept sine signal transmitted by the data acquisition system. After propagating and being modulated by the steel plate interface, the stress wave is captured by the three sensors at a sampling rate of 2 MHz. Subsequently, the received signals in different channels are

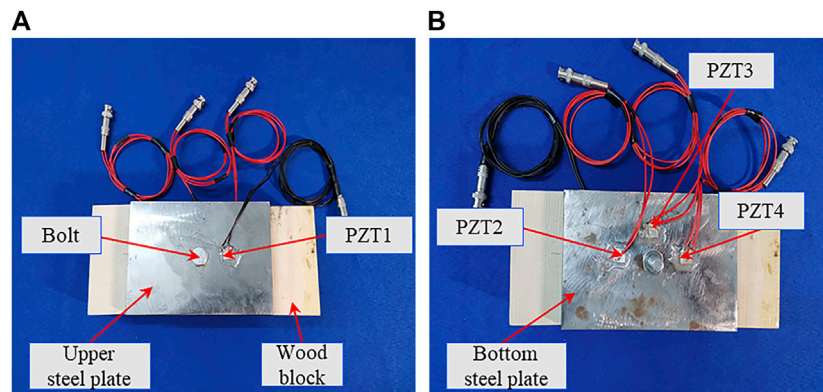


FIGURE 7 | Multichannel active sensing sensor layout scheme. **(A)** Sensor layout scheme of the upper steel plate. **(B)** Sensor layout scheme of the bottom steel plate.

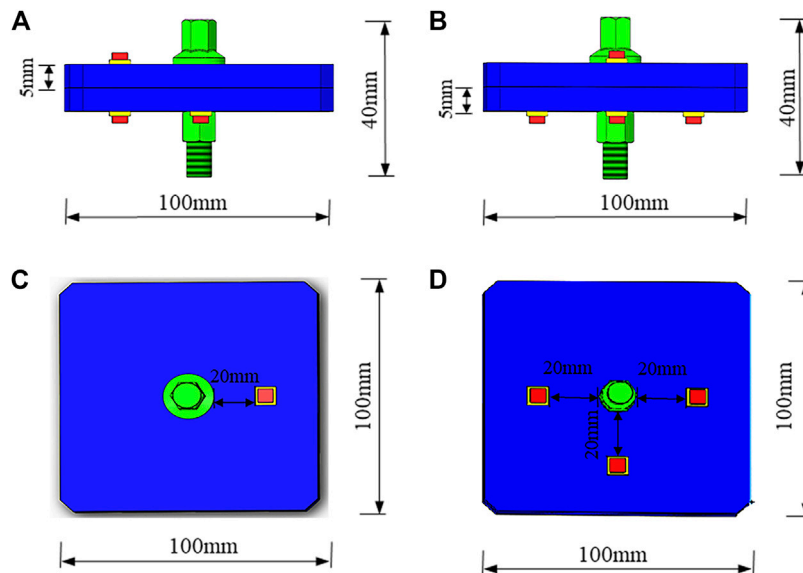


FIGURE 8 | Detailed geometry of the specimen. **(A)** Front view. **(B)** Side view. **(C)** Up view. **(D)** Bottom view.

used to calculate the looseness indices. The frequency of the swept sine signal in this study ranges from 100 Hz to 300 kHz with a duration of 0.5 s and an amplitude of 1 V. The loading of the specimen consisted of increasing the torque level from 0 Nm to 30 Nm at increments of 5 Nm, as listed in **Table 1**. Different torque values lead to different degrees of looseness. The experiments are repeated on specimen A, specimen B, and specimen C. For every looseness condition, the active sensing method is executed 100 times to construct an experimental dataset. The dataset has 560 and 140 samples for training and validation. Then, the baseline 1DCNN model and the improved model (CBAMCNN) using the attention mechanism are established to monitor the bolt looseness. In the training process, the model hyperparameters are adjusted and determined according to the loss function value and accuracy

between the training dataset and the validation dataset. Finally, 140 test signals have been re-collected to achieve bolt looseness identification.

RESULTS

Experimental Results and Analysis Based on Wavelet Packet Analysis

Figure 10 shows the stress wave signals and wavelet packet energy of different torque levels, measured during the experiment with specimen A. The amplitudes of the received stress wave signals corresponding to different torque levels vary between -1 and 1 V. The amplitude of the received signal is therefore related to the bolt looseness. When the torque level

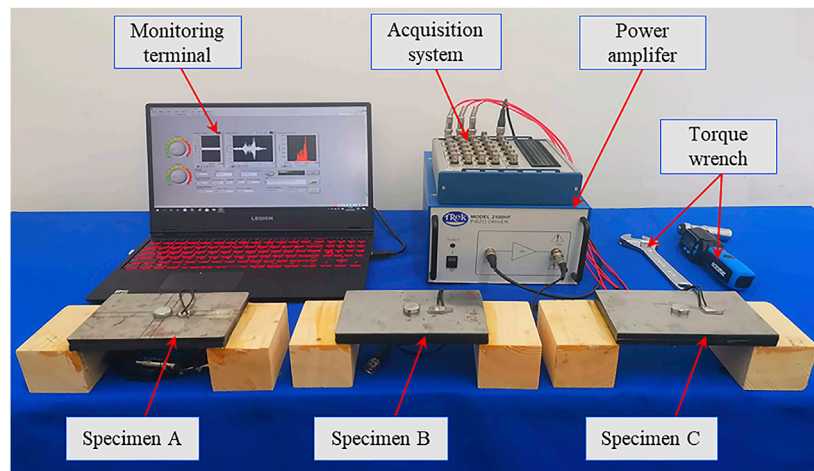


FIGURE 9 | Experimental setup of monitoring the bolt looseness using the piezoelectric active sensing method.

TABLE 1 | Torque values of different degrees of looseness.

Looseness degree	First	Second	Third	Fourth	Fifth	Sixth	Seventh
Torque (Nm)	30	25	20	15	10	5	0

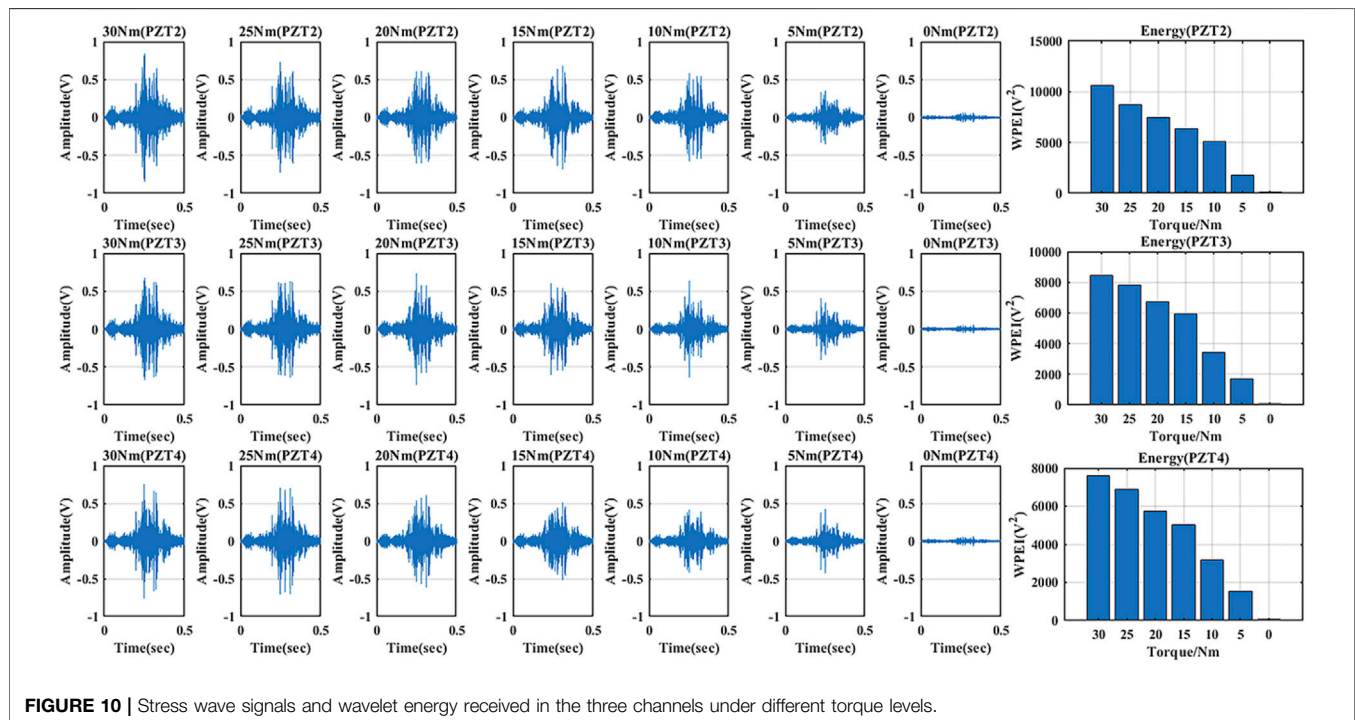


FIGURE 10 | Stress wave signals and wavelet energy received in the three channels under different torque levels.

reached 30 Nm, the maximum value of the stress wave signal reached 0.8 V. As the bolt loosened, the amplitude of the received signal decreased but followed a different path than when the bolt was tightened, thus making it difficult to quantitatively monitor

the bolt looseness based solely on the amplitude. The presence of multiple peaks in each stress wave can be attributed to the different frequency components and the reflections of the stress wave within the connection assembly (Wang et al.,

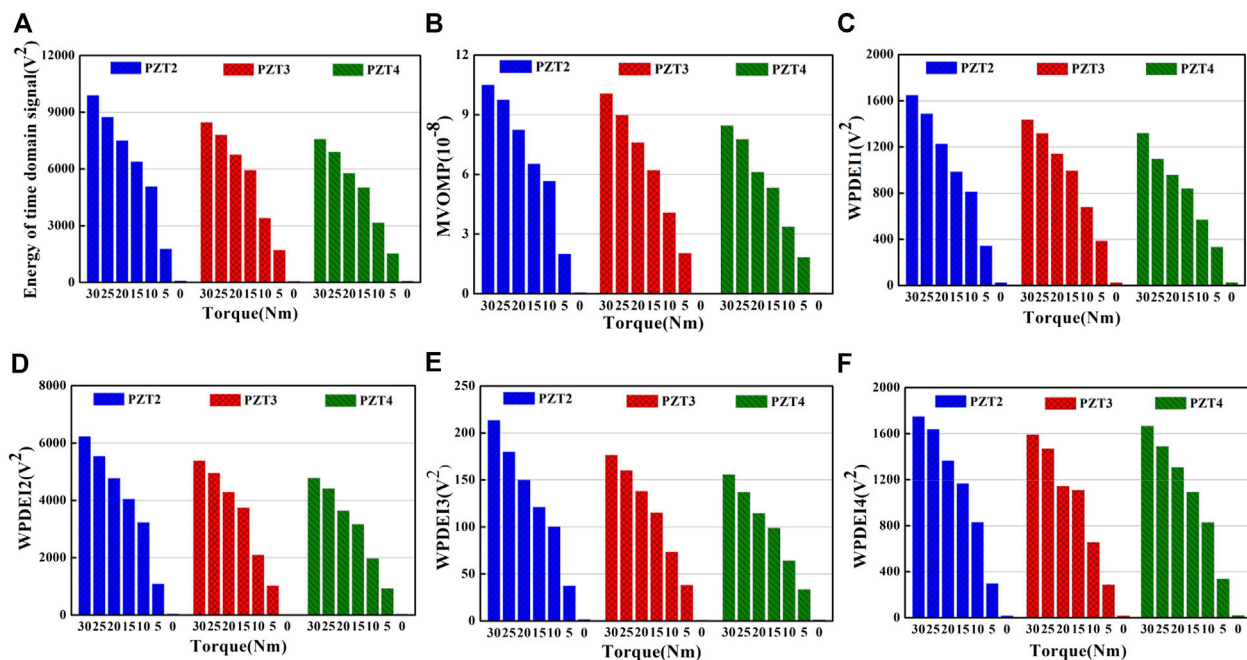


FIGURE 11 | Looseness indicators of different channels under different torque levels. (A) Indicator of signal energy. (B) Maximum value of the mean periodogram. (C) First component of the wavelet packet energy. (D) Second component of the wavelet packet energy. (E) Third component of the wavelet packet energy. (F) Fourth component of the wavelet packet energy.

2021). On the other hand, the wavelet packet energy method can provide a clearer analysis of the received signals. As the torque level decreased, the wavelet packet energy was reduced in proportion to the dissipated energy of the stress wave. Thus, analysis based on wavelet packet energy can characterize the bolt looseness to a certain extent, but the characterization is not fully quantitative due to the undefined relationship between wavelet packet energy and the torque level.

Looseness Indicators

In order to provide more looseness information, some indicators are extracted from the stress waves to characterize the bolt looseness. Indicators include the energy of the time-domain signal, the maximum value of the average periodogram (MVOMP), and the three-layer wavelet packet decomposition energy. For convenience, the authors only show the first four wavelet packet energy components. As shown in **Figure 11**, all the indicators can effectively represent the looseness of the bolt. As the torque decreases, the looseness indicators of different sensor channels decrease, which provides the looseness information from different perspectives. These diversified looseness indicators furnish a basis for data fusion with the CNN. Therefore, the looseness feature vectors of multi-domain indicators are concatenated to construct the corresponding dataset.

Quantitative Monitoring Results of the Convolutional Neural Network Model

In consideration of the drawbacks of traditional methods, both a baseline 1DCNN model and one improved by the attention

mechanism are trained to quantitatively monitor the bolt looseness. The accuracy is set as the metric by which to evaluate the classification performance of the presented method. The accuracy is the ratio between the number of correct predictions and the total number of test datasets.

In order to observe the influence of channel availability on the recognition capabilities of the 1DCNN model, seven different scenarios of channel availability are used to train the baseline 1DCNN model. Single-channel, dual-channel, and multichannel scenarios, respectively, refer to cases where there are one, two, and three PZT sensors being used to monitor bolt looseness. According to the sensor layout scheme, the three cases of single-channel testing are the sole use of PZT2, PZT3, or PZT4. Likewise, the three cases of dual-channel testing include using the following PZT pairs: PZTs 2 and 3, PZTs 2 and 4, and PZTs 3 and 4. Finally, in multichannel testing, all three PZTs (i.e., PZTs 2–4) are used. Taking specimen A as an example, the evaluation indices for the different scenarios are listed in **Table 2**. As seen in the table, the use of all three channels yielded the best performance, and the accuracy is approximately 92.85%. The evaluation indices for the dual-channel scenario ranged from 88.57 to 90.71% and are higher than those for the single-channel scenario. Compared with the baseline 1DCNN model, the CBAMCNN model performed better for the multichannel (5% improvement) and the dual-channel (5.9% improvement) scenarios. However, the performance is similar when only one channel is used, likely because data from one channel is insufficient despite the improvements offered by the attention mechanism.

TABLE 2 | Recognition result of the 1DCNN and CBAMCNN models.

Method	Single-channel			Dual-channel			Multichannel
	PZT2 (%)	PZT3 (%)	PZT4 (%)	PZTs 2 and 3 (%)	PZTs 2 and 4 (%)	PZTs 3 and 4 (%)	PZTs 2–4 (%)
1DCNN	82.85	80.71	87.14	89.28	88.57	90.71	92.85
CBAMCNN	84.29	88.57	87.85	93.57	95.71	97.14	97.85

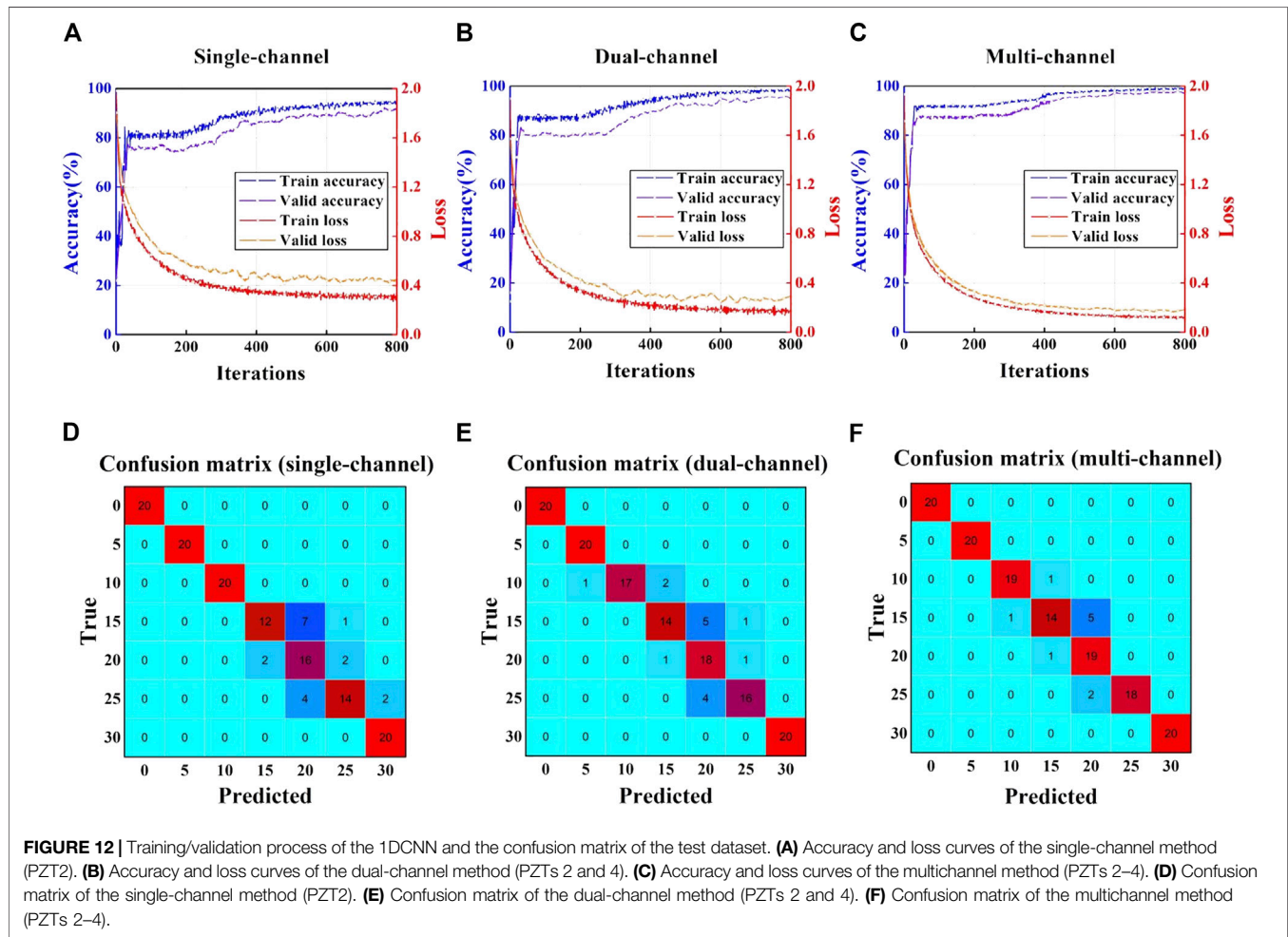


FIGURE 12 | Training/validation process of the 1DCNN and the confusion matrix of the test dataset. **(A)** Accuracy and loss curves of the single-channel method (PZT2). **(B)** Accuracy and loss curves of the dual-channel method (PZTs 2 and 4). **(C)** Accuracy and loss curves of the multichannel method (PZTs 2–4). **(D)** Confusion matrix of the single-channel method (PZT2). **(E)** Confusion matrix of the dual-channel method (PZTs 2 and 4). **(F)** Confusion matrix of the multichannel method (PZTs 2–4).

In order to better understand the whole process of the 1DCNN model, PZT2 (single-channel), PZTs 2 and 4 (dual-channel) and PZTs 2–4 (multichannel) are selected to describe the training, validation, and testing processes according to the accuracy. The accuracy and loss curves during training and validation are shown in **Figures 12A–C**. In general, the model training is stable and convergent without overfitting. Model training is completed at 600 iterations, upon which the accuracy of the validation rose above 90%. The result of the test dataset is shown in the form of a confusion matrix. As shown in **Figures 12D,E**, the recognition errors of the multichannel scenario are less than those of the single-channel and dual-channel scenarios. Of the 140 test samples, there are, respectively, 18 and 15 misrecognitions for the single-channel

and dual-channel scenarios and only 10 misrecognitions for the multichannel method.

Similarly, **Figures 13A–C** show the loss and accuracy curves for the CBAMCNN trained using data from PZT2 (single-channel), PZTs 3 and 4 (dual-channel), and PZTs 2–4 (multichannel). The CBAMCNN model surpassed the baseline model by reaching 95% validation accuracy when the training converged. In addition, compared with the 1DCNN model, the CBAMCNN model yielded fewer incorrect recognitions. The multichannel scenario had the least instances (i.e., only three misrecognitions out of 140 samples) of incorrect recognitions, followed by the dual-channel and the single-channel scenarios. The specific misrecognition is summarized by the confusion matrices in **Figures 13D–F**.

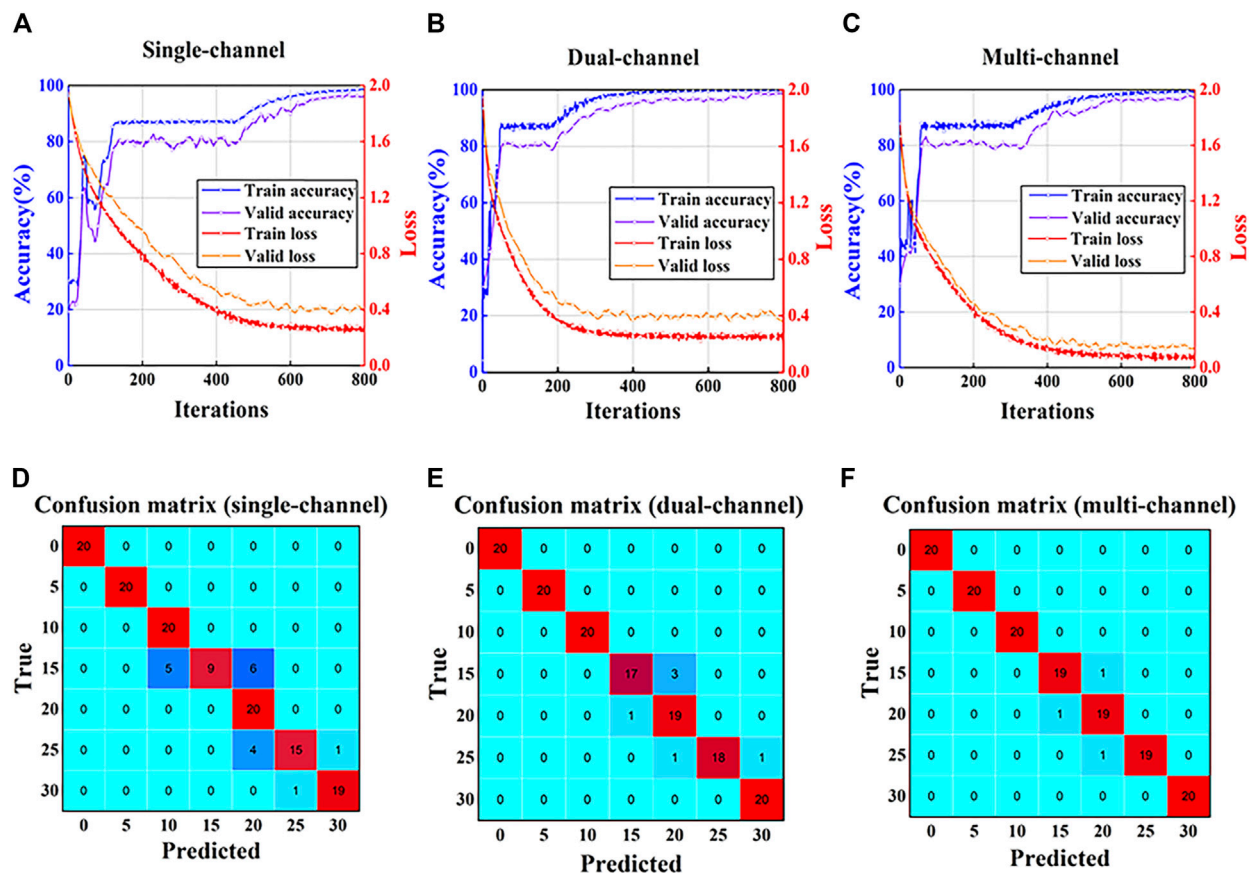


FIGURE 13 | Training/validation process of the CBAMCNN and the confusion matrix of the test dataset. **(A)** Accuracy and loss curves of the single-channel method (PZT2). **(B)** Accuracy and loss curves of the dual-channel method (PZTs 3 and 4). **(C)** Accuracy and loss curves of the multichannel method (PZTs 2–4). **(D)** Confusion matrix of the single-channel method (PZT2). **(E)** Confusion matrix of the dual-channel method (PZTs 3 and 4). **(F)** Confusion matrix of the multichannel method (PZTs 2–4).

TABLE 3 | Mean recognition accuracy for three different specimens.

Specimen	Model	Mean recognition accuracy (%)
A	1DCNN	91.07
	CBAMCNN	97.78
B	1DCNN	93.64
	CBAMCNN	95.78
C	1DCNN	92.85
	CBAMCNN	96.85

The Generality and Repeatability of the Method

In specimen A, the proposed method can monitor the bolt looseness with high accuracy. In order to verify the generality of the method, the process described in Experimental Setup, Results (i.e., data collection, feature extraction, model training, verification, and testing) was carried out and repeated 10 times for specimens B and C. The average recognition accuracy is summarized in Table 3. The results reveal that the proposed method has good classification performance, and the improved CBAMCNN model can reach a testing accuracy of

over 95.78% in all three different specimens. However, the testing accuracy of the 1DCNN model is below 93.64%.

DISCUSSION

Since a single monitoring index used traditionally in active sensing cannot quantify the bolt looseness, a method that analyzes data from multichannel active sensing with a CNN improved with the CBAM (i.e., a channel and spatial attention mechanism) was proposed to quantitatively monitor bolt looseness. Experimental results obtained from the three different specimens demonstrated that the method can quantify bolt looseness with an accuracy of more than 95.78%.

Single monitoring indices, such as the peak value of a time reversal signal (Tao et al., 2016) and normalized coda wave energy (Hei et al., 2020), are unable to provide true quantitative monitoring due to the dispersion of the single indices. On the other hand, through powerful feature extraction and classification abilities, the trained 1DCNN model can quantitatively monitor the state of bolt looseness. However, because the stress wave signal obtained using the piezoelectric active sensing method is complicated and irregular,

it is particularly difficult to obtain satisfactory results by directly training the original signal through a 1DCNN. Therefore, in order to improve monitoring performance, the method presented in this article still requires extraction of bolt looseness features in advance, which is relatively time-consuming.

In addition, the reason why the multichannel active sensing method performs better than the dual-channel and single-channel scenarios can be summarized as follows. Multichannel active sensing can monitor the bolt looseness in multiple different locations and gain comprehensive information about the condition of the bolted connection. Moreover, the CBAM is a lightweight and efficient attention mechanism. The CBAM consists of both channel attention and spatial attention mechanisms. The attention mechanism is mainly used to adjust the weights (i.e., M_s and M_c) of parameters that play a key role in the classification task. If a parameter of the input vector plays a key role in the classification task, the CBAM can automatically generate a larger weight to multiply the original input vector, which enables the model to focus on the features that are helpful to recognition tasks and ignore features that decrease with recognition accuracy (Ban et al., 2020). In this study, the channel attention module helps the CNN to focus on important features, while the spatial attention mechanism highlights the position of the significant features. Therefore, the channel and spatial attention mechanisms enhance the model's recognition accuracy and improve the robustness of the model.

CONCLUSION AND FUTURE WORK

This study proposed a multichannel monitoring method that integrates piezoelectric active sensing with deep learning for the quantitative monitoring of the bolt looseness. Features extracted from the stress waves from each channel include signal energy (time domain), the maximum value of the average periodogram (frequency domain), and three-layer wavelet packet decomposition energy (time frequency). A baseline 1DCNN model and an improved model (i.e., the CBAMCNN) are employed to recognize bolt looseness states (i.e., torque levels). The experimental results show that the combination of the convolutional neural network and multichannel active sensing can achieve quantitative assessment of the bolt connection status and performs better than single-channel and dual-channel scenarios. Moreover, the baseline model recognition accuracy improved after employing the spatial channel attention mechanism. The main contributions of this article are as follows: 1) the method is the first attempt to combine

piezoelectric active sensing and convolutional neural networks to monitor bolt looseness quantitatively; 2) multichannel monitoring, which utilizes three sensors, characterizes bolt looseness from different perspectives and performs better than the single-channel and the dual-channel scenarios; and 3) the CBAM improved the model, and its excellent performance is verified by a laboratory-scale experiment.

The method proposed in this article is powerful for monitoring single-bolt looseness. However, the mechanism for monitoring the looseness of multiple bolts is more complicated. In future research, the authors would like to adopt the multi-bolted steel plate to carry out corresponding research and look for better ways to improve recognition accuracy. In view of the problem that the training data are not easy to obtain in actual engineering, the method of transfer learning can be employed to improve this problem, which can make the model adapt to the actual situation after the model is trained on the data obtained in the laboratory. Of course, this is only a feasible research idea, and a large number of experimental studies are needed to promote practical engineering applications. Otherwise, numerical simulation of stress wave propagation and the influence of the boundary conditions on the accuracy of looseness recognition will be further explored in the future.

DATA AVAILABILITY STATEMENT

The original contributions presented in the study are included in the article/Supplementary Material; further inquiries can be directed to the corresponding authors.

AUTHOR CONTRIBUTIONS

YC and JJ developed the original idea. YC and JJ designed the experiments. YC, JJ, and QF conducted the experiments. YC and XQ analyzed the data. YC and JJ wrote the original draft. QF and XQ made critical revision to the manuscript.

FUNDING

This research was financially supported by the Science for Earthquake Resilience of China Earthquake Administration (Grant no. XH19043Y and XH20040YSX).

REFERENCES

- Amerini, F., Barbieri, E., Meo, M., and Polimeno, U. (2010). Detecting Loosening/tightening of Clamped Structures Using Nonlinear Vibration Techniques. *Smart Mater. Struct.* 19, 085013. doi:10.1088/0964-1726/19/8/085013
- Avci, O., Abdeljaber, O., Kiranyaz, S., and Inman, D. (2017). Structural Damage Detection in Real Time: Implementation of 1D Convolutional Neural Networks for SHM Applications. *Struct. Health Monit. Damage Detect.* 7, 49–54. doi:10.1007/978-3-319-54109-9_6
- Ban, M.-Y., Tian, W.-D., and Zhao, Z.-Q. (2020). "Real-time Object Detection Based on Convolutional Block Attention Module," in International Conference on Intelligent Computing, . Springer, 41–50. doi:10.1007/978-3-030-60796-8_4
- Bartlett, M. S. (1950). Periodogram Analysis and Continuous Spectra. *Biometrika* 37, 1–16. doi:10.2307/2332141
- Fraser-Thomas, J., Côté, J., and Deakin, J. (2008). Understanding Dropout and Prolonged Engagement in Adolescent Competitive Sport. *Psychol. Sport Exerc.* 9, 645–662. doi:10.1016/j.psychsport.2007.08.003
- Goodfellow, I., Bengio, Y., Courville, A., and Bengio, Y. (2016). *Deep Learning*. Cambridge: The MIT Press, 105–115.

- Grus, J. (2019). *Data Science from Scratch: First Principles with python*. Sebastopol, CA: O'Reilly Media.
- Guarino, J., and Hamilton, R. (2017). Detection of Structural Bolt Detorquing Using Direct Stethoscope Measurement. *Proc. Meetings Acoust.* 30, 065003. doi:10.1121/2.0000547
- Hei, C., Luo, M., Gong, P., and Song, G. (2020). Quantitative Evaluation of Bolt Connection Using a Single Piezoceramic Transducer and Ultrasonic Coda Wave Energy with the Consideration of the Piezoceramic Aging Effect. *Smart Mater. Struct.* 29, 027001. doi:10.1088/1361-665x/ab6076
- Hu, C., Yang, B., Yan, J., Xiang, Y., Zhou, S., and Xuan, F.-Z. (2020). Damage Localization in Pressure Vessel by Guided Waves Based on Convolution Neural Network Approach. *J. Press. Vessel Technol.* 142 (6), 061601. doi:10.1115/1.4047213
- Hu, Y.-J., Guo, W.-G., Jiang, C., Zhou, Y.-L., and Zhu, W. (2018). Looseness Localization for Bolted Joints Using Bayesian Operational Modal Analysis and Modal Strain Energy. *Adv. Mech. Eng.* 10, 168781401880869. doi:10.1177/1687814018808698
- Huang, Z., Xu, W., and Yu, K. (2015). *Bidirectional LSTM-CRF Models for Sequence Tagging*. Sebastopol, CA: arXiv preprint arXiv:1508.01991.
- Huo, L., Chen, D., Kong, Q., Li, H., and Song, G. (2017). Smart Washer-A Piezoceramic-Based Transducer to Monitor Looseness of Bolted Connection. *Smart Mater. Struct.* 26, 025033. doi:10.1088/1361-665x/26/2/025033
- Huo, L., Chen, D., Liang, Y., Li, H., Feng, X., and Song, G. (2017). Impedance Based Bolt Pre-load Monitoring Using Piezoceramic Smart Washer. *Smart Mater. Struct.* 26, 057004. doi:10.1088/1361-665x/aa6a8e
- Lacayo, R. M., and Allen, M. S. (2019). Updating Structural Models Containing Nonlinear Iwan Joints Using Quasi-Static Modal Analysis. *Mech. Syst. Signal Process.* 118, 133–157. doi:10.1016/j.ymssp.2018.08.034
- Lacayo, R., Pesaresi, L., Groß, J., Fochler, D., Armand, J., Salles, L., et al. (2019). Nonlinear Modeling of Structures with Bolted Joints: a Comparison of Two Approaches Based on a Time-Domain and Frequency-Domain Solver. *Mech. Syst. Signal Process.* 114, 413–438. doi:10.1016/j.ymssp.2018.05.033
- Lei, X., Sun, L., and Xia, Y. (2020). Lost Data Reconstruction for Structural Health Monitoring Using Deep Convolutional Generative Adversarial Networks. *Struct. Health Monit.* 1475921720959226, 147592172095922. doi:10.1177/1475921720959226
- Li, Q., and Jing, X. (2017). A Second-Order Output Spectrum Approach for Fault Detection of Bolt Loosening in a Satellite-like Structure with a Sensor Chain. *Nonlinear Dyn.* 89, 587–606. doi:10.1007/s11071-017-3473-6
- Li, Q., and Jing, X. (2020). Fault Diagnosis of Bolt Loosening in Structures with a Novel Second-Order Output Spectrum-Based Method. *Struct. Health Monit.* 19, 123–141. doi:10.1177/1475921719836379
- Li, Q., Jing, X., and Guo, Y. (2019). The Second-Order Output Spectrum-Based Method for Fault Localization in Ring Type Structures. *Nonlinear Dyn.* 98, 1935–1955. doi:10.1007/s11071-019-05299-6
- Lim, H. J., and Sohn, H. (2020). Online Stress Monitoring Technique Based on Lamb-Wave Measurements and a Convolutional Neural Network under Static and Dynamic Loadings. *Exp. Mech.* 60, 171–179. doi:10.1007/s11340-019-00546-8
- Liu, H., Mi, X., and Li, Y. (2018). Comparison of Two New Intelligent Wind Speed Forecasting Approaches Based on Wavelet Packet Decomposition, Complete Ensemble Empirical Mode Decomposition with Adaptive Noise and Artificial Neural Networks. *Energy Convers. Manag.* 155, 188–200. doi:10.1016/j.enconman.2017.10.085
- Liu, M., Huang, X., Yu, J., Wang, T., and Mallya, A. (2020). *Generative Adversarial Networks for Image and Video Synthesis: Algorithms and Applications*. Sebastopol, CA: arXiv preprint arXiv:2008.02793. doi:10.1145/3447450.3447484
- Luo, H., Huang, M., and Zhou, Z. (2019). A Dual-Tree Complex Wavelet Enhanced Convolutional LSTM Neural Network for Structural Health Monitoring of Automotive Suspension. *Measurement* 137, 14–27. doi:10.1016/j.measurement.2019.01.038
- Meyer, J. J., and Adams, D. E. (2015). Theoretical and Experimental Evidence for Using Impact Modulation to Assess Bolted Joints. *Nonlinear Dyn.* 81, 103–117. doi:10.1007/s11071-015-1976-6
- Ritdumrongkul, S., Abe, M., Fujino, Y., and Miyashita, T. (2003). Quantitative Health Monitoring of Bolted Joints Using a Piezoceramic Actuator-Sensor. *Smart Mater. structures* 13, 20. doi:10.1088/0964-1726/13/1/003
- Tao, W., Shaopeng, L., Junhua, S., and Yourong, L. (2016). Health Monitoring of Bolted Joints Using the Time Reversal Method and Piezoelectric Transducers. *Smart Mater. Structures* 25, 025010. doi:10.1088/0964-1726/25/2/025010
- Teotrakool, K., Devaney, M. J., and Eren, L. (2009). Adjustable-speed Drive Bearing-Fault Detection via Wavelet Packet Decomposition. *IEEE Trans. Instrumentation Meas.* 58, 2747–2754. doi:10.1109/TIM.2009.2016292
- Toliat, H. A., Abbaszadeh, K., Rahimian, M. M., and Olson, L. E. (2003). Rail Defect Diagnosis Using Wavelet Packet Decomposition. *IEEE Trans. Industry Appl.* 39, 1454–1461. doi:10.1121/2.0000547
- Wang, B., Huo, L., Chen, D., Li, W., and Song, G. (2017). Impedance-based Pre-stress Monitoring of Rock Bolts Using a Piezoceramic-Based Smart Washer—A Feasibility Study. *Sensors* 17, 250. doi:10.3390/s17020250
- Wang, F., Chen, Z., and Song, G. (2020). Monitoring of Multi-Bolt Connection Looseness Using Entropy-Based Active Sensing and Genetic Algorithm-Based Least Square Support Vector Machine. *Mech. Syst. Signal Process.* 136, 106507. doi:10.1016/j.ymssp.2019.106507
- Wang, F., Chen, Z., and Song, G. (2021). Smart Crawfish: A Concept of Underwater Multi-Bolt Looseness Identification Using Entropy-Enhanced Active Sensing and Ensemble Learning. *Mech. Syst. Signal Process.* 149, 107186. doi:10.1016/j.ymssp.2020.107186
- Wang, F., Ho, S. C. M., and Song, G. (2019). Modeling and Analysis of an Impact-Acoustic Method for Bolt Looseness Identification. *Mech. Syst. Signal Process.* 133, 106249. doi:10.1016/j.ymssp.2019.106249
- Wang, F., Mobiny, A., Van Nguyen, H., and Song, G. (2020). If Structure Can Exclaim: a Novel Robotic-Assisted Percussion Method for Spatial Bolt-ball Joint Looseness Detection. *Struct. Health Monit.* 1475921720923147. doi:10.1177/1475921720923147
- Wang, F., and Song, G. (2020). Bolt-looseness Detection by a New Percussion-Based Method Using Multifractal Analysis and Gradient Boosting Decision Tree. *Struct. Health Monit.* 19, 2023–2032. doi:10.1177/1475921720912780
- Xu, J., Dong, J., Li, H., Zhang, C., and Ho, S. C. (2019). Looseness Monitoring of Bolted Spherical Joint Connection Using Electro-Mechanical Impedance Technique and BP Neural Networks. *Sensors* 19, 1906. doi:10.3390/s19081906
- Xu, J., Wang, C., Li, H., Zhang, C., Hao, J., and Fan, S. (2018). Health Monitoring of Bolted Spherical Joint Connection Based on Active Sensing Technique Using Piezoceramic Transducers. *Sensors* 18, 1727. doi:10.3390/s18061727
- Xu, L., Yuan, S., Chen, J., and Ren, Y. (2019). Guided Wave-Convolutional Neural Network Based Fatigue Crack Diagnosis of Aircraft Structures. *Sensors* 19, 3567. doi:10.3390/s19163567
- You, R., Ren, L., and Song, G. (2020). A Novel Comparative Study of European, Chinese and American Codes on Bolt Tightening Sequence Using Smart Bolts. *Int. J. Steel Structures* 20, 910–918. doi:10.1007/s13296-020-00331-7
- Zhang, Y., Zhang, X., Chen, J., and Yang, J. (2017). Electro-mechanical Impedance Based Position Identification of Bolt Loosening Using LibSVM. *Intell. Automation Soft Comput.* 24 (1), 1–7. doi:10.1080/10798587.2016.1267245
- Zhang, Z., Liu, M., Liao, Y., Su, Z., and Xiao, Y. (2018). Contact Acoustic Nonlinearity (CAN)-based Continuous Monitoring of Bolt Loosening: Hybrid Use of High-Order Harmonics and Spectral Sidebands. *Mech. Syst. Signal Process.* 103, 280–294. doi:10.1016/j.ymssp.2017.10.009
- Zhang, Z., Liu, M., Su, Z., and Xiao, Y. (2016). Quantitative Evaluation of Residual Torque of a Loose Bolt Based on Wave Energy Dissipation and Vibro-Acoustic Modulation: A Comparative Study. *J. Sound Vibration* 383, 156–170. doi:10.1016/j.jsv.2016.07.001
- Zhao, N., Huo, L., and Song, G. (2020). A Nonlinear Ultrasonic Method for Real-Time Bolt Looseness Monitoring Using PZT Transducer-Enabled Vibro-Acoustic Modulation. *J. Intell. Mater. Syst. Structures* 31, 364–376. doi:10.1177/1045389X19891534
- Zhao, Y., Zhao, L., Xiong, B., and Kuang, G. (2020). Attention Receptive Pyramid Network for Ship Detection in SAR Images. *IEEE J. Selected Top. Appl. Earth Observations Remote Sensing* 13, 2738–2756. doi:10.1109/JSTARS.2020.2997081

Conflict of Interest: Authors JJ and QF were employed by the company Wuhan Institute of Earthquake Engineering Co., Ltd.

The remaining authors declare that the research was conducted in the absence of any commercial or financial relationships that could be construed as a potential conflict of interest.

Copyright © 2021 Chen, Jiang, Qin and Feng. This is an open-access article distributed under the terms of the Creative Commons Attribution License (CC BY). The use, distribution or reproduction in other forums is permitted, provided the original author(s) and the copyright owner(s) are credited and that the original publication in this journal is cited, in accordance with accepted academic practice. No use, distribution or reproduction is permitted which does not comply with these terms.



Analysis of Long-Term Durability Monitoring Data of High-Piled Wharf with Anode-Ladder Sensors Embedded in Concrete

Hongbiao Liu¹, Baohua Zhang^{1*}, Haicheng Liu¹ and Zifan Ji²

¹National Engineering Laboratory for Port Hydraulic Construction Technology, Tianjin Research Institute of Water Transport Engineering, Tianjin, China, ²Department of Civil Engineering, Tianjin Chengjian University, Tianjin, China

OPEN ACCESS

Edited by:

Chun-Xu Qu,
Dalian University of Technology, China

Reviewed by:

Baokui Chen,
Nanchang University, China
Tao Lai,
Nanjing Tech University, China

*Correspondence:

Baohua Zhang
85596881@qq.com

Specialty section:

This article was submitted to
Structural Materials,
a section of the journal
Frontiers in Materials

Received: 30 April 2021

Accepted: 18 June 2021

Published: 01 July 2021

Citation:

Liu H, Zhang B, Liu H and Ji Z (2021)
Analysis of Long-Term Durability
Monitoring Data of High-Piled Wharf
with Anode-Ladder Sensors
Embedded in Concrete.
Front. Mater. 8:703347.
doi: 10.3389/fmats.2021.703347

The structural durability monitoring (SDM) system for a high-piled wharf in the Tianjin Port of China is devised and deployed with an anode ladder sensor, which provides a means to monitor the state of steel corrosion for the wharf. In this project, the anode-ladder sensors are installed on the reinforced concrete components of the front platforms. After the installation, the monitoring data from the anode-ladder sensor was collected for 40 months. Based on the monitoring data for 40 months, it is proven that the resistance of concrete will be significantly affected by the change in temperature, and the increase in temperature will cause the drop in concrete resistance. Furthermore, the data of the anode-ladder sensor set in the track beam of the front platform shows that the current in anode A1 and A2 relative to the cathode exceeded 15 μA during the four-month period, which is abnormal. The main reason is the influence of concrete temperature and humidity. Therefore, the monitoring data for current, voltage, resistance, and temperature should be combined to determine the activation state of the anode, and cannot be determined simply using the current value.

Keywords: structural durability monitoring, high-piled wharf, anode-ladder, reinforcement, corrosion, concrete

INTRODUCTION

Corrosion of the reinforcing steel in concrete induced by chloride-ion penetration and carbonation of concrete cause serious damage to concrete structures exposed to aggressive environments, e.g., the chloride-induced corrosion of reinforcement in concrete structures in tidal zones and coastal areas (Kassiret et al., 2002; Pech-Canul et al., 2002). A large number of harbor structures like wharves, harbor bridges, piers, dams, and other harbor structures are attacked severely the penetration of chloride ions from seawater, which caused many of them to be repaired or replaced (Melchers et al., 2006). As a result, repair costs nowadays constitute a major part of the maintenance spending on the harbor structures.

In reinforced concrete structures such as wharves and sea-crossing bridges in marine environments, concrete cracking caused by the corrosion of the reinforcement in concrete induced by chlorides is more serious than carbonization of the concrete. Chloride-penetration causes faster rusting of the reinforcement and makes increases the loss, which is the main factor that affects the durability of concrete structures in the marine environment and has been paid extensive attention by those in engineering and academia. The typical damage to reinforced concrete structures in harbors caused by chloride penetration is shown in **Figure 1**.



FIGURE 1 | Typical durability damage of harbor structures induced by chlorides.

Despite the considerable loss caused by the chloride-induced corrosion in such structures, more and more of these are being built, which are also required to have a service life of 100 years or more, such as China's Hong Kong-Zhuhai-Macao bridge project and Hangzhou bay bridge. This necessitates more stringent requirements for the durability of reinforced concrete structures. However, there is no generally accepted reliability design theory available currently that can guarantee that the concrete structure can be used for 100 years or longer (Xu et al., 2013). Therefore, in order to achieve longer service life of the concrete structure, the principle of durability design and redesign is adopted, that is, the actual durability information of the concrete structure is obtained based on in-service monitoring of the concrete structure, and further measures are taken to ensure the durability requirements of concrete structures for those parts that do not meet the design requirements (Engelund et al., 2000; Tomosawa, 2009). Accordingly, it is necessary to collect durability data for the concrete structure by monitoring, and precautions can be taken before the commencement of the reinforcement corrosion process (Keddum et al., 1997; Raupach et al., 2001; McCarter et al., 2005) thus ensuring not only the durability requirements of the structure but also reducing the maintenance cost. As known, the costs for repair measures increase steeply with time, when the reinforcement has already started to corrode. The durability maintenance cost of the concrete structure meets the "five-fold law", that is, the repair cost of the slight damage is five times the cost of the preventive measures. Therefore, it is very important to monitor the durability of concrete structures in the marine environment.

Thus, in the last few decades, significant effort has been put into the development of non-destructive testing as well as structural health monitoring tools and methods that are suitable for the objective assessment of concrete structures. A variety of non-destructive evaluation techniques and methods, such as ultrasonic testing, ground penetrating radar, and half-cell potential method were proposed, some of which have been applied widely for the detection of concrete structures (Arndt et al., 2011). However, traditional on-site inspection methods like reference cells only show the local onset of corrosion and not the time-to-corrosion, which is measurable using an anode-ladder sensor. Automatic monitoring using sensors is more cost-effective than the usual on-site inspections, especially in areas

that are difficult to access. It enables operators to take protective measures before the damage is initiated.

The anode-ladder system has been used in several concrete structures worldwide, mainly bridges. However, research regarding the application of durability-monitoring of high-piled wharfs in the harbor. The wharf structure in coastal ports serve in seawater, where durability problems caused by chloride penetration is more prominent, making structural durability monitoring essential. The objective of this work is to devise and deploy an anode-ladder-based long-term durability monitoring system on a newly built high-piled wharf structure in the Tianjin port in China. The wharf named South 27# Wharf is 390 m long and 75 m wide, which will be used for ore transportation and other bulk cargo shipping. A structural health monitoring (SHM) system based on Fiber Bragg Grating (FBG) sensor techniques was used in the project. The primary function of the SHM system is the durability monitoring with the anode-ladder-system, which can collect the macrocell potential, current, resistance, and temperature of the reinforced concrete components to assess the corrosion risk of the structure. The installation and setup of anode-ladder sensors in the high-piled wharf are also described. The conclusion of this study is expected to aid the development of long-term health monitoring technology in coastal ports.

THEORETICAL BACKGROUND

Corrosion Theory of Steel in Concrete

In general, reinforcing steel in the concrete has good corrosion resistance due to the highly alkaline environment in the concrete, which has pH values ranging from 12.5 to 13.5. In the high alkaline environment, a thin oxide layer called the passive film is formed at the surface of the reinforcement, which can protect the iron from dissolution to negligibly low values. Normally this passivity is stable during the entire service life of a reinforced concrete structure. However, a variety of causes, such as the chloride ion penetration or carbonization of concrete, can break the passive film formed on the rebar. As a result, the reinforcement will change from the passivated state to an activated state (i.e., depassivation). Then, the combination of available water, oxygen, and chloride ion with steel leads to the rusting of the reinforcement. With the gradual aggravation of

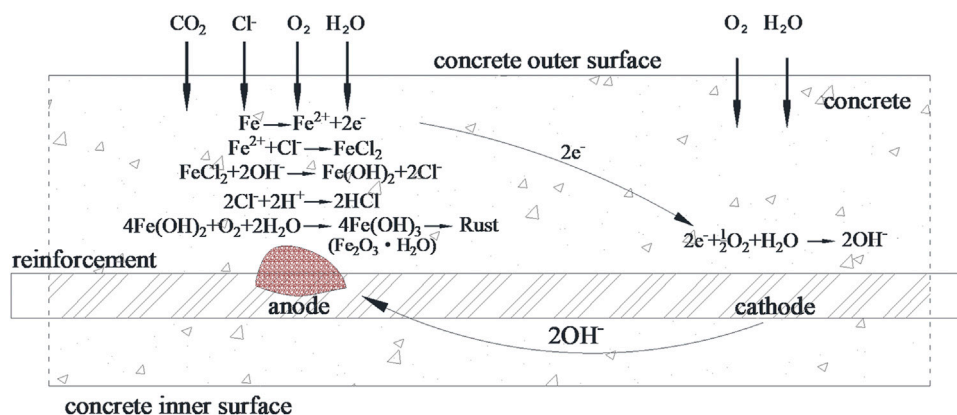


FIGURE 2 | Representation of the corrosion process of rebar in concrete and the electrochemical reaction.

reinforcement corrosion, the concrete cracks and spalls off due to rust expansion. Eventually, severe damage was detected in the concrete (Raupach, 1996).

The corrosion of steel is a complicated process and involves several steps. Finally, ferric hydroxide ($Fe(OH)_3$) is formed, which transforms into hydrated ferric oxide Fe_2O_3 , i.e., rust. The electrical and chemical reactions for the corrosion of steel are shown in **Figure 2**.

Carbonation of concrete is the chemical reaction of CO_2 with the alkaline substances in the concrete pore solution, causing a reduction in the pH value to less than 10, and making it one of the reasons for the corrosion. However, the main cause of reinforcement corrosion in harbor reinforced concrete structures is the penetration of chloride ions based on the field inspection experience. Consequently, this work focuses only on chloride-induced corrosion. It can be seen from **Figure 2** that chloride ion intrusion can also cause a decrease in the pH value. When a critical limit value of chloride content in the pore water solution is exceeded, the steel starts rusting.

Chloride-induced corrosion of steel in concrete is an electrochemical process analogous to the operation of a battery. Different surface areas of the reinforcement act as the anode or cathode of the battery, which are shown in **Figure 2**. At the anode, iron (Fe) loses electrons and becomes iron ions (Fe^{2+}), which easily with chloride ions (Cl^-) to form a $FeCl_2$ solution, acting as a carrier of iron ions. It causes anode depolarization and accelerates the anodic reinforcement process. At the cathode, electrons, water, and oxygen are converted into hydroxyl ions (OH^-). The cathodic process does not cause any deterioration of the steel. On the contrary, it protects the reinforcement, which is called cathodic protection. Then, hydroxyl ions (OH^-) with the negatively charged ions move toward the anode from the cathode in the electrolyte based on the electrical field created between the anode and cathode. Near the anode, they react with the iron ions in the solution forming ferrous hydroxide [$Fe(OH)_2$], and the chloride ions (Cl^-) are released to repeat the process above. Subsequently, ferrous hydroxide [$Fe(OH)_2$] reacts with oxygen (O_2) and water (H_2O) forming ferric hydroxide [$Fe(OH)_3$] and finally, Fe_2O_3 , which is the corrosion product (Arndt et al., 2011).

Generally, the volume of the rust is 3–6 times than that of iron, causing concrete cracking and spalling off due to expansion when the rebar corrosion achieves a critical limit value.

This shows that the corrosion of reinforcement in harbor concrete structures is mainly caused by the harmful intrusion of chloride ions. Also, the depassivation threshold in the reinforcement is known as the frontal line of critical chloride ion concentration for harbor concrete structures exposed to seawater that is rich in chloride ions. Therefore, if the penetration behavior of chloride ions in concrete, such as the position of the frontal line of critical chloride ion concentration and its moving speed, can be collected suitably, the corrosion time of steel in concrete can be predicted. This results in a significant reduction of maintenance costs as repair costs increase steeply with time when the reinforcement has already started to corrode.

Development of the Anode-ladder Sensor

Based on the corrosion theory of concrete structures, Bashear (1996) proposed a concrete degradation model to predict the performance degradation of concrete structures, and emphasized the influence of permeability on concrete degradation (Bashear et al., 1996). Glass (2000) points out that the chloride-induced corrosion of rebar is the main factor that affects the durability of concrete structures (Glass et al., 2000). Ahmad (2003) summarized the mechanism of steel corrosion, monitoring technology of steel corrosion, and methods for predicting the remaining service life of structures using empirical model as well as experimentation. It is also pointed out that the main factor affecting the durability of reinforced concrete structures is chloride-induced corrosion (Ahmad, 2003). Even though many new systems and materials have been developed to repair the damage and increase durability, many monitoring systems do not resolve the time-to-corrosion problem. Therefore, the anode-ladder sensor, which can measure the time-to-corrosion data of reinforcement in concrete, was developed by Raupach in 1986 and successfully applied to the monitoring of steel corrosion in concrete structures in 1990, providing a technical means for the durability redesign of concrete structures

TABLE 1 | Voltage values collected by the anode-ladder sensor.

No	Monitoring value	Description	No	Monitoring value	Description	No	Monitoring value	Description
1	U1	Voltage between A1 and cathode	8	U1'	Voltage between A1 and reference electrode	15	U1''	Voltage between A1 and reinforcement-connection
2	U2	Voltage between A2 and cathode	9	U2'	Voltage between A2 and reference electrode	16	U2''	Voltage between A2 and reinforcement-connection
3	U3	Voltage between A3 and cathode	10	U3'	Voltage between A3 and reference electrode	17	U3''	Voltage between A3 and reinforcement-connection
4	U4	Voltage between A4 and cathode	11	U4'	Voltage between A4 and reference electrode	18	U4''	Voltage between A4 and reinforcement-connection
5	U5	Voltage between A5 and cathode	12	U5'	Voltage between A5 and reference electrode	19	U5''	Voltage between A5 and reinforcement-connection
6	U6	Voltage between A6 and cathode	13	U6'	Voltage between A6 and reference electrode	20	U6''	Voltage between A6 and reinforcement-connection
7	U7	Voltage between reinforcement-connection and cathode	14	U7'	Voltage between reinforcement-connection and reference electrode			

TABLE 2 | Current values collected by the anode-ladder sensor.

No	Monitoring value	Description	No	Monitoring value	Description
1	I1	Current between A1 and the cathode	8	I1'	Current between A1 and reinforcement-connection
2	I2	Current between A2 and the cathode	9	I2'	Current between A2 and reinforcement-connection
3	I3	Current between A3 and the cathode	10	I3'	Current between A3 and reinforcement-connection
4	I4	Current between A4 and the cathode	11	I4'	Current between A4 and reinforcement-connection
5	I5	Current between A5 and the cathode	12	I5'	Current between A5 and reinforcement-connection
6	I6	Current between A6 and the cathode	13	I6'	Current between A6 and reinforcement-connection
7	I7	Current between reinforcement-connection and cathode			

(Raupach, 1996; Raupach, 2009). Raupach (2001) used the anode-ladder-system to monitor the permeation depth of chloride ions in concrete structures, and the corrosion state of steel could be predicted based on the monitoring data (Raupach et al., 2001). Subsequently, Zhang (2009), and Jin (2013) applied the anode-ladder-system to the underwater tunnel, wharf, and other hydraulic structures to monitor the durability of concrete

structures (Zhang et al., 2009; Jin et al., 2013). The anode-ladder sensor is a kind of durability sensor which can determine the position of the depassivation threshold in the reinforcement. Therefore, it is very effective for monitoring the durability state of the coastal piled-wharf structure and predicting the corrosion time of steel bars in concrete.

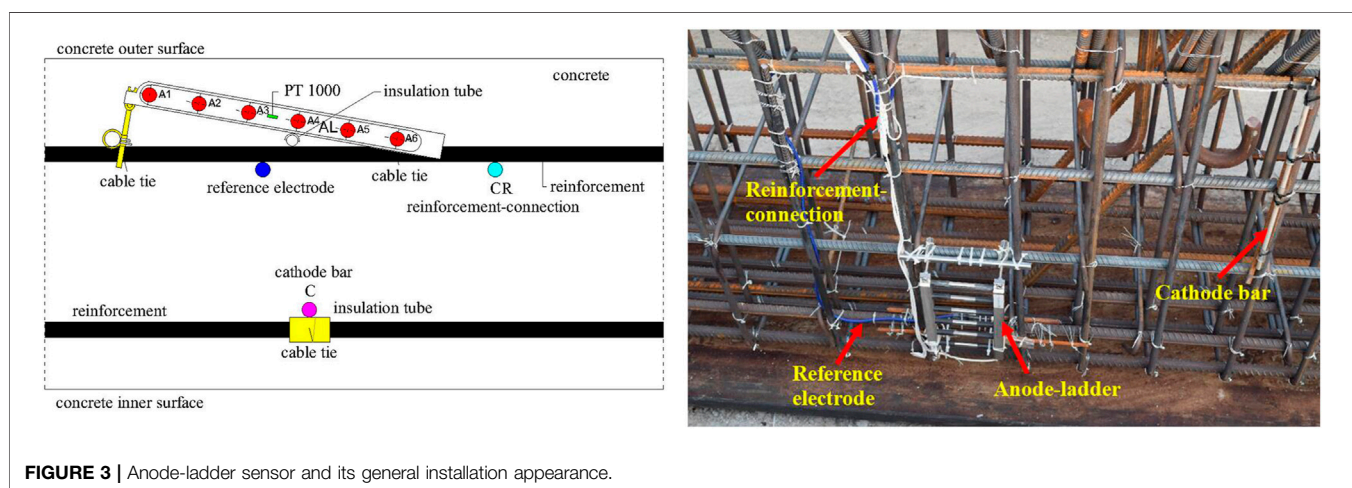


TABLE 3 | Resistance values collected by the anode-ladder sensor.

No	Monitoring value	Description
1	R1	The resistance between A1 and A2
2	R2	The resistance between A2 and A3
3	R3	The resistance between A3 and A4
4	R4	The resistance between A4 and A5
5	R5	The resistance between A5 and A6
6	R6	Resistance between A6 and reinforcement-connection
7	T	Concrete temperature value (PT 1000)

TABLE 4 | Corrosion probability of reinforcing steel.

Half-cell potential (V)	More negative than -0.35 V	$-0.35 \sim -0.2$ V	More positive than -0.20 V
Corrosion probability of steel in one area	>90%	Uncertain	<10%

The anode-ladder sensor for structural durability monitoring of the South 27# Wharf in Tianjin Port is manufactured in Germany. The anode-ladder-system includes the anode-ladder embedded in concrete, measuring cables, test boxes on the concrete surface and special reading meters for data collection. The sensor components are the anode-ladder, cathode, reference electrode, reinforcement connecting rod, and temperature probe (PT 1,000), which is shown in **Figure 3**. The anode-ladder has six black carbon steel anodes denoted as A1, A2 and... A6, respectively. Each anode is placed on a stainless-steel fixture, forming a ladder-like structure. Each anode is electrically separated from the fixture. A stainless-steel fastening strip is arranged at one end of the fixture, and is connected to the fixture with two bolts. The anode-ladder is set on the outside of the reinforcement cage, within the scope of the concrete cover layer. By adjusting the bolts, the anode ladder can be tilted at different angles, enabling the six anodes to be embedded at different depths of the concrete cover layer. The installation plan and side view of the anode-ladder sensor are shown in **Figure 3**. The basic measuring principle is to place the electrodes at different depths relative to the concrete surface and to measure the onset of corrosion of these electrodes one by one. The diffusion depths of chloride ions in concrete can be determined by measuring the electrical macrocell parameters of anodes, such as macrocell potential, current, resistance and temperature, at different depths. Then, the onset of corrosion of steel can be predicted based on the monitoring data.

Based on the design of the anode-ladder sensor, the cathode made of platinum (Pt), reference electrode made of manganese dioxide (MnO_2) and reinforcement-connection are set near the anode-ladder before pouring the concrete, while the temperature probe (PT 1,000) is encapsulated in the anode-ladder. Therefore, the electrical macrocell parameters of anodes are divided into five types for the same temperature, which are the macrocell parameters between the single anode and cathode, single anode and reference electrode, single anode and reinforcement-connection, two neighboring anodes, as well as temperature.

In detail, when data is measured by the acquisition device, the data collected include the macrocell potential, macrocell current, resistance, and temperature of concrete specimens. The macrocell potentials are the voltage values of anodes relative to the cathode, reference electrode and reinforcement-connection, respectively. Macrocell currents are the anode values relative to the cathode and the internal reinforcement-connection, while the resistances are values of the concrete between anodes. In one test, a total of 40 parameters are collected, and the specification for the parameters are shown in **Tables 1–3**.

Evaluation Methods

Based on the results of laboratory tests, anodes of 150 mV and 15 μA buried in dry concrete relative to cathode after a short circuit time of 5 s are used as limit values for the activity of the single anode under the usual conditions, and the limit value may be larger when the anode-ladder sensor was set up in a wet environment, such as marine environment (Raupach et al., 2001; S+R Sensortec GMBH Munich, 2009). This conclusion can be used to determine whether the anode is active and to predict the critical depth related to reinforcement corrosion. Generally, current value is used as the main evaluation index to determine whether the anode is active or not.

Another standard to determine the corrosion state of the reinforcement is the half-cell potential inspection method proposed by the ASTM standard C876-09 (ASTM International C 876-09), which involves using a copper-copper sulfate half-cell at the wet concrete surface to measure the half-cell potential of reinforcing steel related to the concrete outer surface. According to the ASTM standard C 876-09, if the half-cell potential is less than -0.35 V, then there is a 90% probability of active corrosion; if the half-cell potential is positive or between -0.35 and -0.2 V, no reliable conclusions can be drawn from the measurement; if the half-cell potential is in the range of -0.2 – 0 V, there is a 90% probability of no active corrosion being present. The expression above can be summarized as in **Table 4**, which



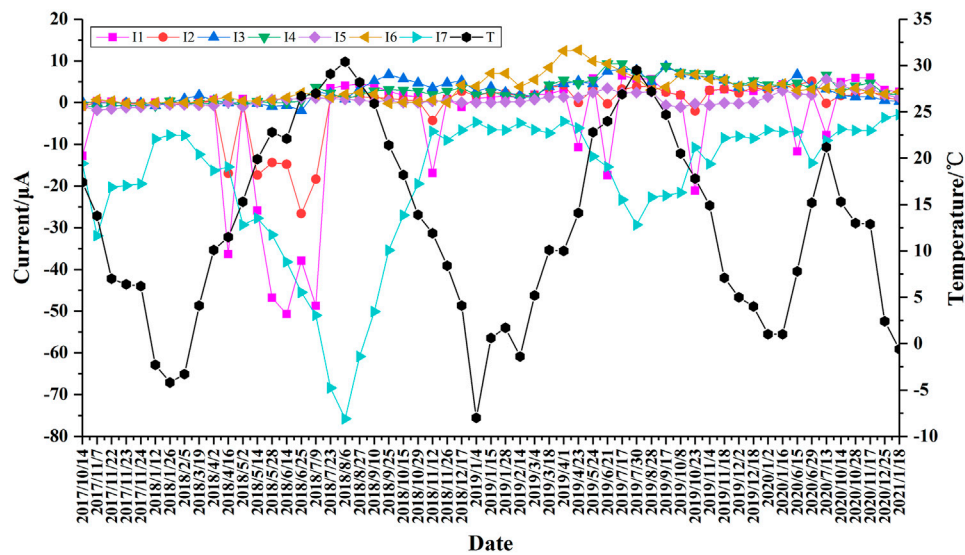


FIGURE 6 | Current between anode and cathode.

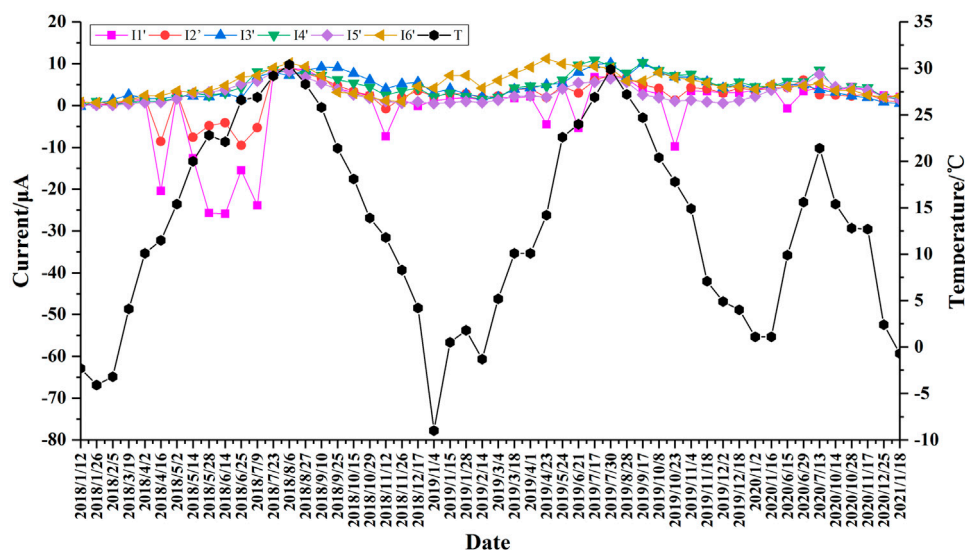


FIGURE 7 | Current between anode and reinforcement-connection.

can be used as a reference to analyze the monitoring data of the anode-ladder-system and to evaluate the risk of corrosion of reinforcing steel.

APPLICATION OF ANODE-LADDER-SYSTEM FOR NEWLY BUILT HIGH-PILED WHARF

Engineering Description

The South 27# Wharf is a high-piled wharf under construction in the Tianjin Port of China, which is designed for bulk cargo

transportation. The mechanical properties of this wharf structure are designed for berthing 300,000 DWT bulk carriers. The South 27# wharf is 390 m long and 75 m wide, and it consists of three continuous parts: a 390 m main wharf platform and two 73.3 m side approach bridges. The main wharf platform, which consists of nine 65 m-wide structural segments, is divided into a front platform and back platform based on the operational requirements. The front platform is 36.5 m wide, and the back platform is 38.5 m wide. Each structural segment is uniform. The top elevation of the wharf is 7.5 m, and the depth of water at the wharf apron is -24.8 m. Three crane

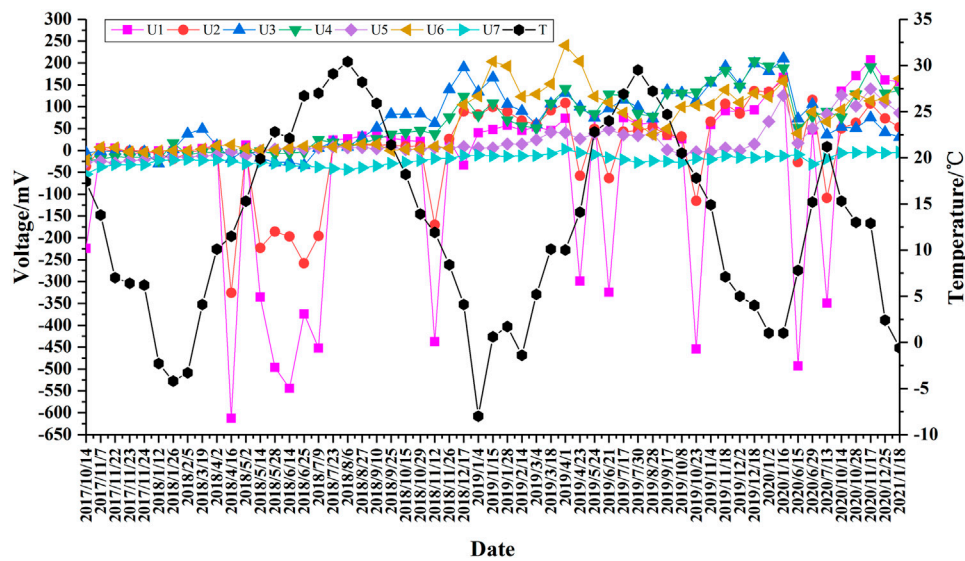


FIGURE 8 | Voltage between anode and cathode.

tracks are set up on the front platform, and the track beams are supported by steel pipe piles with 1.2-m diameters, whereas steel pipe piles with 1.0-m diameters are used in the remaining locations of the front platform. The beams in the back platform are supported by 650 × 650 mm prestressed reinforced-concrete square piles. The uniform loads used for the design are 30 kPa from the wharf apron to 18.5 m, 50 kPa from 18.5 to 36.5 m, and 80 kPa from 36.5 to 75.0 m. The cranes, model 40t-45m, are set on the front platform. The standard value of the mooring force for a bollard is 1,179 kN based on the 200,000 DWT bulk carriers with a wind speed of 24.4 m/s and 1,379 kN according to 300,000 DWT bulk carriers with the same wind speed.

The devised anode-ladder-system will be set up on the second structural segment of this new-built wharf, and the structural drawing of the wharf is shown in **Figure 4**. For the structural durability monitoring (SDM), one anode-ladder sensor was set up at the red mark in **Figure 4**. Based on the sensor, the corrosion risk of the reinforced-concrete specimens can be monitored in real time.

Anode-ladder Sensor Setup and Data Measurement

The anode-ladder sensors for structural durability monitoring of the South 27# Wharf are respectively placed on the track beam of the front platform, and the beams are all precast by high performance C45F300 concrete. The anode-ladder sensor is set in the concrete cover layer (60 mm) on the side of the beam near the bottom surface, and the distance between the outer edge of A1 rod and the outside surface of the beam is 10 mm. All of them are in the splash area of the wharf. The sensor is first installed on the reinforcement cage, and the concrete is cast and cured. Next, the precast specimens are transported to the field for installation

when the maintenance is completed. During the construction of the wharf surface layer, the sensor terminal box was embedded in the concrete, which is also protected by the stainless-steel shell. The surface of the steel shell is parallel to the upper surface of the wharf surface layer. After the upper cover of the shell is opened by unscrewing, the sensor terminal box can be seen, and data collection can be carried out with device. Anode-ladder sensor installation, protection, and field data acquisition are shown in **Figure 5**.

The data from the anode-ladder sensors were collected after wharf completion. The construction of the South 27# Wharf began in early 2016, and the main structure was completed in October 2017. The data collection for the anode-ladder sensors in this project started in October 2017, and was operated for 14 days. Data has been collected continuously for 40 months using the measuring device of HMG 7 with the set of short circuit time of 5 s.

LONG-TERM MONITORING DATA AND EVALUATION

The monitoring data obtained from the anode-ladder sensor includes voltage, current, resistance, temperature, and other parameters. According to the evaluation methods mentioned above and the technical parameters provided by the manufacturer, the current value of monitoring is often used to determine the status of anodic depassivation or corrosion. At present, it is generally believed that an anode that is buried in dry concrete is in a passive state if the measured current between the anode and cathode is much less than 15 μA ; if the current is more than 15 μA , it is considered active. Nevertheless, the limit value may be larger when the anode-ladder sensor was set up in a wet environment, such as marine environment, and there is no

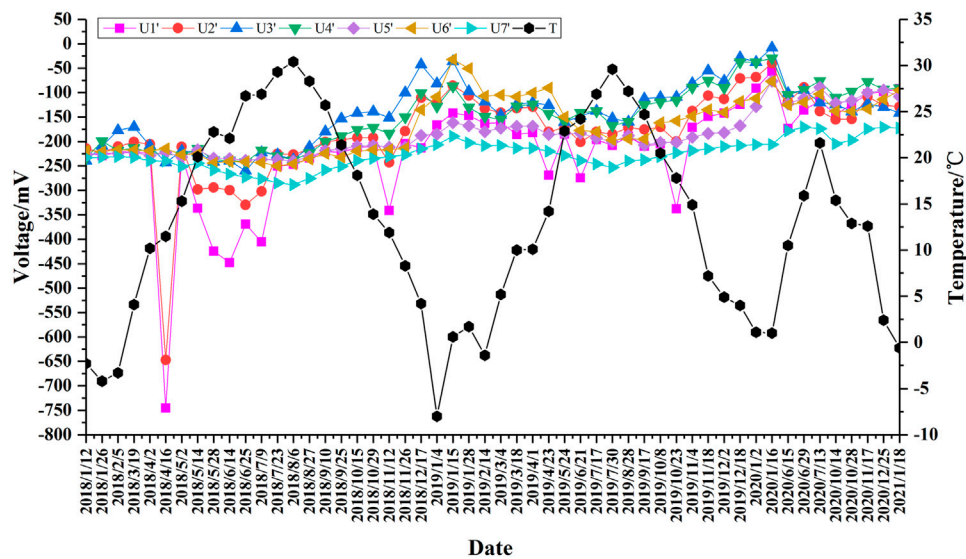


FIGURE 9 | Voltage between anode and reference electrode.

uniform standard for the current value in this condition, including the voltage and resistance values. Monitoring data from the anode-ladder sensor during the 40 months of this project is analyzed with emphasis on the current values, and a correlation analysis of voltage, resistance, and temperature values is also implemented. It is necessary to know the durability status of the front platform in different external environments, according to the monitoring data collected from the anode-ladder sensor set on the front of the second structural segment of the wharf. Additionally, the penetration rate of chloride ion and the corrosion state of reinforcement can be known by the comprehensive analysis of monitoring data.

The anode-ladder sensor installed on the track beam of the front platform is 16.5 m away from the front of the wharf and 4.5 m away above the sea surface. After data processing, the time histories of current values for each anode relative to cathode or reinforcement are shown in **Figure 6** and **Figure 7**. It can be seen from **Figure 6** that the current value of anode A1 and A2 relative to the cathode exceeded 15 μA from April to July 2018, regardless of the current direction, and gradually recovered to 10 μA during the following months, except for some local trip points. Based on the standard that a current value greater than 15 μA indicates anode depassivation, it can be determined that the depassivation of anode A1 and A2 occurs during April to July 2018. That means

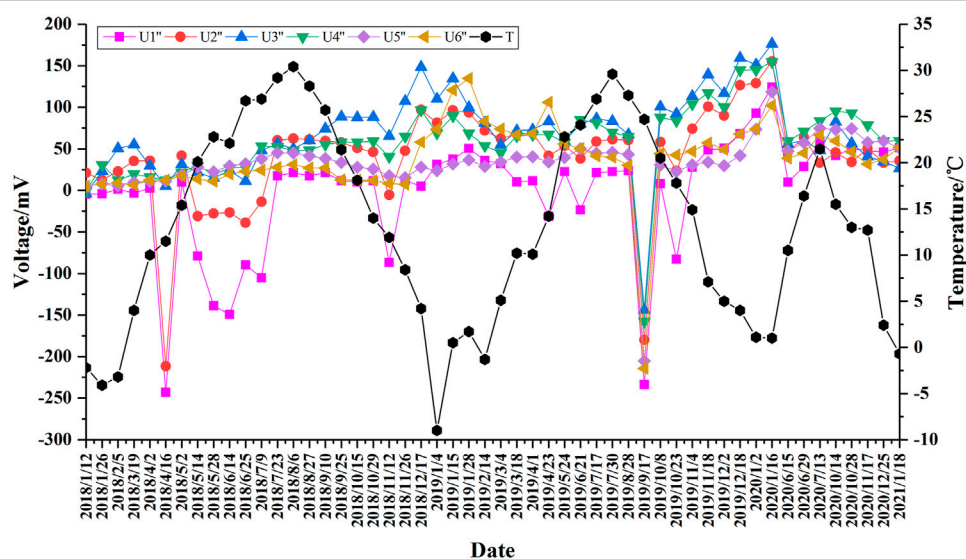


FIGURE 10 | Voltage between anode and reinforcement-connection.

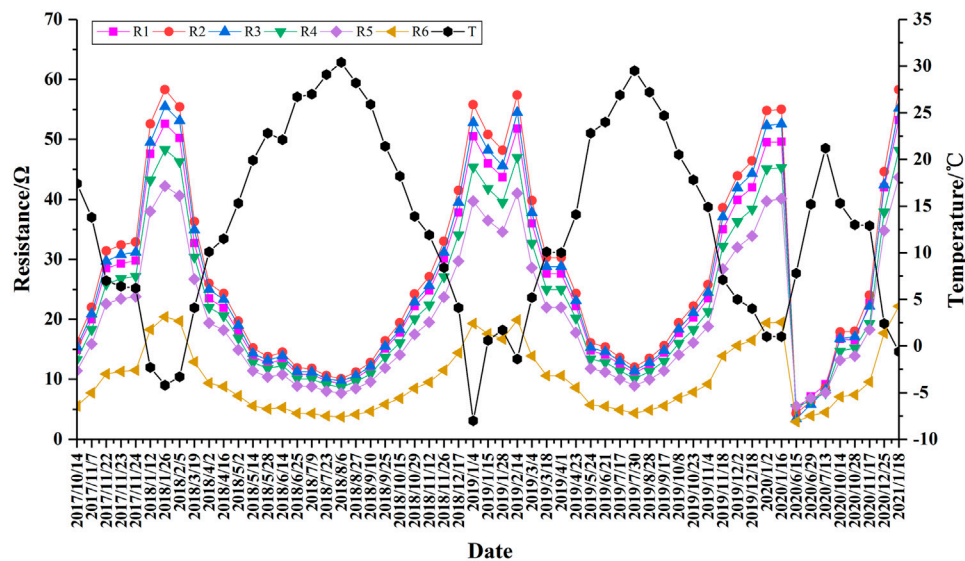


FIGURE 11 | Resistance between anodes.

that the chloride ion permeated to the depth of anode A2. However, from the monitoring data for the following months, it can be determined that the anodes A1 and A2 are still in the state of passivation because the current value is less than $15 \mu\text{A}$. These two conclusions are contradictory. In order to understand this contradiction, the collected temperature data is considered. As can be seen from **Figure 6**, during the period from April to July 2018, the temperature continued to rise, and the current value of anode A1 and A2 relative to the cathode was greater than $15 \mu\text{A}$, following which the current value returns below $15 \mu\text{A}$ with the drop in temperature. The author believes that the cause of this contradiction is the variation in the ambient temperature, and the depassivation of anode A1 and A2 cannot be determined absolutely based on the current value greater than $15 \mu\text{A}$ during April to July 2018. Moreover, the track beam was coated with an anticorrosive substance, and the chloride ion permeation depth could not reach A1 and A2, which can also be confirmed by field detection. From the field inspection, it is clear that there are no signs of breakage of the anticorrosive coating. Therefore, the author believes that the anodes A1 and A2 are still passivated.

Furthermore, from the current history between the anode and the reinforcement-connection (**Figure 7**), the current values of anode A2~A6 relative to the reinforcement-connection are all less than $10 \mu\text{A}$ except for anode A1 regardless of the current direction. The current value of anode A1 is larger than $15 \mu\text{A}$ at a few instances, while most of the current values do not exceed $15 \mu\text{A}$. That is like the behavior of the current between anodes and cathode. Based on the above analysis, all the anodes are in the passivation state.

From the processed data, the voltage between the anodes and cathode was obtained, along with the voltage of anodes relative to the reference electrode and reinforcement-connection. Additionally, the resistance between two neighboring anodes was obtained, and their detailed time history curves are shown

in **Figures 8–11**. It can be seen from **Figure 8** that the behavior of the voltage is almost consistent with that of the current values above. From April to July in 2018, the voltages of anode A1 and A2 also showed fluctuations, with some voltage values reaching 625 mV, and then decreased gradually until it fell to within 20 mV. In the following days, the voltage values increased to positive and gradually to 150 mV, except at some trip points, but did not exceed 150 mV. However, certain voltage values of anode A3, A4, and A6 relative to the cathode slightly exceed 150 mV during this period. The voltage values of each anode relative to the reference electrode and reinforcement-connection also show a similar behavior (**Figure 9** and **Figure 10**). Therefore, the value of 150 mV cannot be chosen as the critical limit to determine the activation of anode used in the marine environment, and maybe 300 mV of anode to cathode is more suitable. Because it is considered that the fluctuation of the voltage is caused by ambient temperature, not the depassivation of the anode, which is also proved by field inspection. As the follow-up monitoring data increases, there are multiple seasonal alternation cycles, which may further verify the above conclusions.

As can be seen from **Figure 11**, the distribution of resistance values among the anodes is quite regular, and the trend of resistance change opposes the trend of temperature change; that is, when the temperature rises, the resistance drops, and when the temperature drops, the resistance rises. This also indicates that the performance of the installed anode-ladder sensor is reasonable, and the monitoring data is reliable.

CONCLUSION

Durability monitoring of concrete structures in a marine environment is an important means to extend the service life

of structures and an important part of the durability design and redesign of concrete structures. At present, researches on durability monitoring and data analysis of coastal wharf structure, especially on long-term durability monitoring data analysis and processing, is deficient. In this study, based on the newly built South 27# Wharf in the Tianjin Port of China, the anode-ladder sensors were set separately in the track beam of the front platform and the beam of the back platform, which are used to monitor the durability of the wharf structure for a long time. By long-term continuous monitoring, the durability monitoring data from the anode-ladder sensors set in the wharf structure has been collected for 40 consecutive months, with an average data interval of 14 days. The monitoring data includes a total of 40 parameters such as the macrocell current, macrocell voltage, resistance, and temperature. Through the processing and analysis of the monitoring data, the following conclusions are obtained:

- (1) Data from the anode-ladder sensor set in the track beam of the front platform showed that the current of anode A1 and A2 relative to the cathode exceeded 15 μA during the four-month period, which indicates the depassivation of anode A1 and A2. However, based on the analysis, it is identified to be a false image caused mainly by the variation in environmental temperature, because the four months mentioned above are in the spring and summer seasons, and the temperature keeps rising.
- (2) The resistance of concrete is significantly affected by the variation in temperature, and the increase in temperature will cause a drop in concrete resistance.
- (3) Although the anode-ladder-system can monitor corrosion risk of the harbor concrete structure caused by chloride ions. However, under the influence of concrete temperature and

humidity, interference data may appear, which may affect the credibility of the conclusions. Therefore, the monitoring data of current, voltage, resistance, and temperature should be combined to determine the activation state of the anode, and it cannot be determined simply by the current value.

DATA AVAILABILITY STATEMENT

The raw data supporting the conclusion of this article will be made available by the authors, without undue reservation.

AUTHOR CONTRIBUTIONS

Investigation, Conceptualization, HBL; Writing—original draft preparation, HBL; Writing—review and editing, BZ; Data curation, HCL; Investigation, ZJ. All authors have read and agreed to the published version of the manuscript.

FUNDING

This research work was jointly supported by the Fundamental Research Funds for Central Public Research Institutes (Grant number TKS190407 and TKS180204) and Tianjin Transportation Science and Technology Development Project (Grant number 2020-09).

ACKNOWLEDGMENTS

The authors would like to thank the Tianjin Research Institute of Water Transport Engineering, MOT and its financial support.

REFERENCES

- Ahmad, S. (2003). Reinforcement Corrosion in concrete Structures, its Monitoring and Service Life Prediction—A Review. *Cement Concrete Composites* 25 (4-5), 459–471. doi:10.1016/s0958-9465(02)00086-0
- Arndt, R. W., Cui, J., and Huston, D. R. (2011). Monitoring of Reinforced concrete Corrosion and Deterioration by Periodic Multi-Sensor Non-destructive Evaluation. *AIP Conf. Proc.* 1335 (1), 1371–1378. doi:10.1063/1.3592092
- ASTM International C 876-09 (2009). Standard Test Method for Corrosion Potential of Uncoated Reinforcing Steel in concrete. Available online: <http://www.astm.org/cgi-bin/resolver.cgi?C876-15> (Accessed on Dec 12, 2020).
- Basheer, P. A. M., Chidiact, S. E., and Long, A. E. (1996). Predictive Models for Deterioration of concrete Structures. *Construction Building Mater.* 10 (1), 27–37. doi:10.1016/0950-0618(95)00092-5
- Engelund, S., Mohr, L., and Edvardsen, C. (2000). *General Guidelines for Durability Design and Redesign: DuraCrete - Probabilistic Performance Based Durability Design of concrete Structures (Contract BRPR-CT95-0132, Project BE95-1347)*. 2 ed. (Lyngby, Denmark: CUR), 90–95.
- Glass, G. K., and Buenfeld, N. R. (2000). Chloride-induced Corrosion of Steel in concrete. *Prog. Struct. Engng Mater.* 2 (4), 448–458. doi:10.1002/pse.54
- Jin, Z., Zhao, T., Zhang, P., and Gao, S. (2013). Durability Monitoring of concrete Structure of Subsea Tunnel. *J. Chin. Ceram. Soc.* 41 (2), 205–210. doi:10.7521/j.issn.0454-5648.2013.02.13
- Kassir, M. K., and Ghosn, M. (2002). Chloride-induced Corrosion of Reinforced concrete Bridge Decks. *Cement Concrete Res.* 32 (1), 139–143. doi:10.1016/s0008-8846(01)00644-5
- Keddah, M., Takenouti, H., Nóvoa, X. R., Andrade, C., and Alonso, C. (1997). Impedance Measurements on Cement Paste. *Cement Concrete Res.* 27 (8), 1191–1201. doi:10.1016/s0008-8846(97)00117-8
- McCarter, W. J., Chrisp, T. M., Starrs, G., Basheer, P. A. M., and Blewett, J. (2005). Field Monitoring of Electrical Conductivity of Cover-Zone concrete. *Cement Concrete Composites* 27 (7-8), 809–817. doi:10.1016/j.cemconcomp.2005.03.008
- Melchers, R. E., and Li, C. Q. (2006). Phenomenological Modeling of Reinforcement Corrosion in marine Environments. *Acta Mater. J.* 103 (1), 25–32. doi:10.14359/15124
- Pech-Canul, M. A., and Castro, P. (2002). Corrosion Measurements of Steel Reinforcement in concrete Exposed to a Tropical marine Atmosphere. *Cement Concrete Res.* 32 (3), 491–498. doi:10.1016/s0008-8846(01)00713-x
- Raupach, M. (1996). Chloride-induced Macrocell Corrosion of Steel in concrete-theoretical Background and Practical Consequences. *Construction Building Mater.* 10 (5), 329–338. doi:10.1016/0950-0618(95)00018-6
- Raupach, M. (2009). Corrosion of Steel Reinforcement in Concrete. *Mater. Corrosion* 60 (2), 77. doi:10.1002/maco.200990004
- Raupach, M., and Schießl, P. (2001). Macrocell Sensor Systems for Monitoring of the Corrosion Risk of the Reinforcement in concrete Structures. *NDT E Int.* 34 (6), 435–442. doi:10.1016/s0963-8695(01)00011-1

- S+R Sensortec GMBH Munich (2009). Specification of Anode Ladders "Corrosion Monitoring for RC-Structures, Germany. Available online: http://www.sensortec.de/images/pdf/Flyer_Corrosion_Monitoring__eng.pdf (Accessed on Dec 12, 2020).
- Tomosawa, F. (2009). Japan's Experiences and Standards on the Durability Problems of Reinforced concrete Structures. *Ijstructe* 1 (1), 1–12. doi:10.1504/ijstructe.2009.030022
- Xu, C., Li, Z., and Jin, W. (2013). A New Corrosion Sensor to Determine the Start and Development of Embedded Rebar Corrosion Process at Coastal concrete. *Sensors* 13 (10), 13258–13275. doi:10.3390/s131013258
- Zhang, P., Zhao, T., Jin, Z., and Zhao, J. (2009). "Application of Durability Sensors in Reinforced Concrete Liner of Subsea Tunnel," in 2009 International Conference on Measuring Technology and Mechatronics Automation, Zhangjiajie, China, April 11–12, 2009 (. Los Alamitos, CA: Institute Of Electrical And Electronics Engineers). 1, 12–15. doi:10.1109/ICMTMA.2009.108
- Conflict of Interest:** The authors declare that the research was conducted in the absence of any commercial or financial relationships that could be construed as a potential conflict of interest.
- Copyright © 2021 Liu, Zhang, Liu and Ji. This is an open-access article distributed under the terms of the Creative Commons Attribution License (CC BY). The use, distribution or reproduction in other forums is permitted, provided the original author(s) and the copyright owner(s) are credited and that the original publication in this journal is cited, in accordance with accepted academic practice. No use, distribution or reproduction is permitted which does not comply with these terms.



Analysis of the Mechanical Properties and Parameter Sensitivity of a U-Shaped Steel Damper

Jinhe Gao^{1,2*}, Jiahuan Xi², Yuwen Xu², Jiajun Ding², Junwen Zhu², Yi Chang² and Baokui Chen³

¹Engineering Research Center of Nuclear Technology Application (East China Institute of Technology), Ministry of Education, Nanchang, China, ²School of Civil and Architectural Engineering, East China University of Technology, Nanchang, China, ³School of Civil Engineering and Architecture, Nanchang University, Nanchang, China

To clarify the mechanical properties of the U-shaped steel damper under tension and compression along the opening direction and the energy dissipation mechanism in the energy dissipation system, a mechanical model was established to describe the plastic failure response of the damper, and the formula for theoretical calculation of its mechanical properties was derived. Using the straight line segment length, radius of circular arc, and opening direction as parameters for testing four specimens, through the design of reasonable pulling and pressing fixture, four specimens were tested for tension and compression. The initial stiffness and yield load test results and theoretical analysis were good and verified that the opening direction of the U-shaped steel damper affected its mechanical performance. Further analysis of the U-shaped steel damper's mechanical properties using numerical finite element analysis of the arc radius and the straight line segment length, width and thickness in relation to the initial stiffness shows that increasing the straight section length and end arc radius can reduce initial stiffness, and increase the thickness and width can increase initial stiffness.

Keywords: mechanical properties, initial stiffness, yield load, parameter analysis, U-shaped steel damper

OPEN ACCESS

Edited by:

Yang Zhang,
Dalian University of Technology, China

Reviewed by:

Tao Chen,
Tongji University, China
Can Wang,
Southwest Jiaotong University, China

*Correspondence:

Jinhe Gao
jhgao@ecut.edu.cn

Specialty section:

This article was submitted to
Smart Materials,
a section of the journal
Frontiers in Materials

Received: 22 May 2021

Accepted: 31 May 2021

Published: 27 July 2021

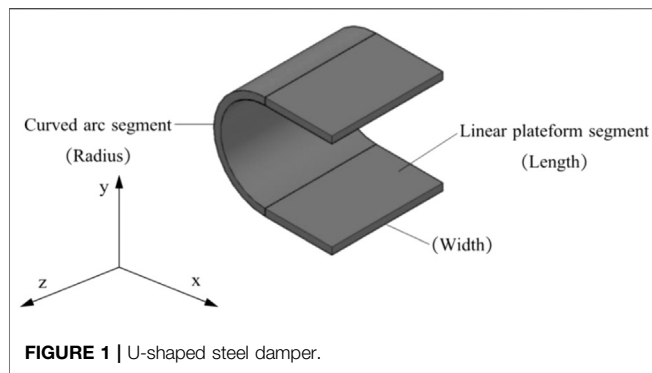
Citation:

Gao J, Xi J, Xu Y, Ding J, Zhu J,
Chang Y and Chen B (2021) Analysis of
the Mechanical Properties and
Parameter Sensitivity of a U-Shaped
Steel Damper.
Front. Mater. 8:713221.
doi: 10.3389/fmats.2021.713221

INTRODUCTION

As one of the common types of dampers, steel damper was first proposed by Kelly et al. (1972) and Skinner et al. (1974), and then many scholars (Whittaker et al., 1991; Ricky Chan and Albermani, 2007; Lee et al., 2015; Xing and Guo, 2003; Wang, 2015; Yin et al., 2016; Huo et al., 2016; Qu et al., 2017) studied and improved various types of steel dampers. Among them, the U-shaped steel damper is a typical representative of the first generation of steel dampers. It is widely used in the vibration damping design of simple structures because of its simple structure, good energy dissipation performance, and low cost. The construction of the U-shaped steel damper and its possible deformation mode are shown in **Figure 1**.

Deformation mode A: the upper and lower linear platform sections are relatively moved in the x-direction. Li and Yao (1991), Yao (1997) studied the strength, stiffness, and dissipation performance of the U-shaped steel damper in the isolation device under low cyclic load. Zhao et al. (2017) proposed the expression of the mechanical properties of a U-shaped steel damper under a horizontal load. The mechanical model showed the mechanical properties of a U-shaped steel damper under a single load component. Based on the collected test data of 17 U-shaped steel dampers, Chong et al. (2015) summarized the design expressions of the initial stiffness and yield load of the damper and proposed a fine finite element analysis method.



Deformation mode B: the upper and lower linear platform sections have relative torsion in the z -direction. Deng et al. (2015) studied the mechanical properties of a U-shaped steel damper when it was subjected to torsional deformation under a lateral load outside the plane. Du et al. (2014), Du et al. (2016a), Du et al. (2016b), Han et al. (2016) conducted an experimental study on the influence of material hardness, constraint, and other factors on the mechanical properties and shock absorption and energy dissipation characteristics of the U-shaped steel damper and conducted theoretical and experimental research on the torsional deformation properties of the U-shaped steel damper of $65M_n$ and proposed the design expressions of the initial torsional stiffness of the damper.

A + B combined deformation mode: the upper and lower linear platform sections are relatively pulled and compressed in the y -direction. Jiao et al. (2015) and Enel et al. (2016) studied the mechanical properties of the U-shaped steel damper in isolation structures under bidirectional loads and confirmed that its energy dissipation properties were degraded under bidirectional loads. Through finite element analysis, Atasever et al. (2017) considered the mechanical response of the U-shaped steel damper under three working conditions of load input direction of 0° , 45° , and 90° .

A large number of studies show that the U-shaped metal damper has good energy dissipation performance, which can meet the requirements of structural response control parameters. However, due to the introduction of empirical coefficient based on the test results, the mechanical property expression lacks fine model and can not describe the plastic failure mechanism of the U-shaped steel dampers. At the same time, the mechanical properties of deformation mode C along the opening direction are seldom studied. In this paper, the U-type damper is taken as the research object, and two mechanical models of the U-shaped damper are established according to the different opening orientations of the damper. The mechanical properties of the U-shaped damper under the deformation mode C along the opening direction are studied, and the hysteretic properties and parameter sensitivity of the damper are analyzed.

STIFFNESS OF A U-DAMPER

Two U-damper mechanical models are considered: Model I (Figure 2) and Model II (Figure 3). As depicted in Figure 2A,

the U-damper includes straight-line (length: l_0) parts and a semi-circle (radius, r) part. Photo 3 shows that the fixed condition of the top end of the U-damper can be realized using the stiffening plate at the high-strength bolted connection.

Force and Displacement Relation for Model I

As depicted in Figure 2A, the shear force and bending moment at the node of the free end are denoted as Q_i and M_i ; the displacement and rotation angles are denoted as u and θ . The positive directions of forces and displacements are depicted in the figure. The horizontal node displacement is not considered.

k_1, k_3

In Figure 2B, load k_1 and k_3 moment k_3 under the unit vertical displacement are calculable using the following equations obtained using the unit-load method.

$$\begin{aligned}
 v &= \int \frac{M(x)\overline{M}_1(x)}{EI} dx \\
 &= 2 \int_0^{l_0} \frac{(-k_1 + k_3)(-x)}{EI} dx + \int_0^\pi \frac{[-k_1(l_0 + r \sin \theta) + k_3][-(l_0 + \sin \theta)]}{EI} r d\theta \\
 &= \left(\frac{2l_0^3}{3EI} + \frac{r\pi l_0^2 + 4r^2 l_0}{EI} + \frac{r^3 \pi}{2EI} \right) k_1 - \frac{l_0^2 + r\pi l_0 + 2r^2}{EI} k_3 = 1
 \end{aligned} \quad (1)$$

$$\begin{aligned}
 \theta &= \int \frac{M(x)\overline{M}_2(x)}{EI} dx \\
 &= 2 \int_0^{l_0} \frac{(-k_1 x + k_3)(1)}{EI} dx + \int_0^\pi \frac{[-k_1(l_0 + r \sin \theta) + k_3(1)]}{EI} r d\theta \\
 &= -\left(\frac{l_0^2 + l_0 r \pi + 2r^2}{EI} \right) k_1 + \frac{2l_0 + r\pi}{EI} k_3 = 0
 \end{aligned} \quad (2)$$

From Eq. 1 and Eq. 2, k_1 and k_3 can be derived respectively as:

$$k_1 = \frac{6EI(2l_0 + r\pi)}{2l_0^4 + 4r\pi l_0^3 + 24r^2 l_0^2 + 6r^3 \pi l_0 + 3r^4 \pi^2 - 24r^4} \quad (3)$$

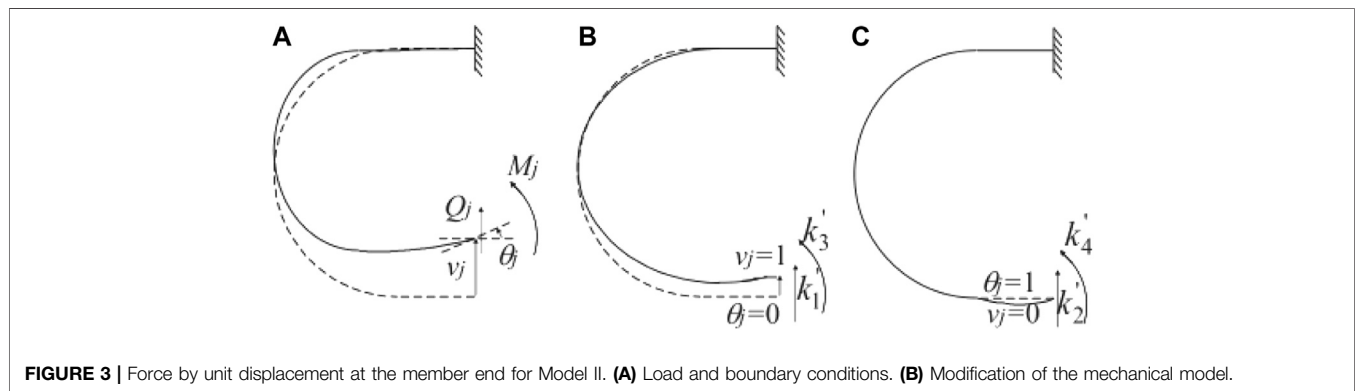
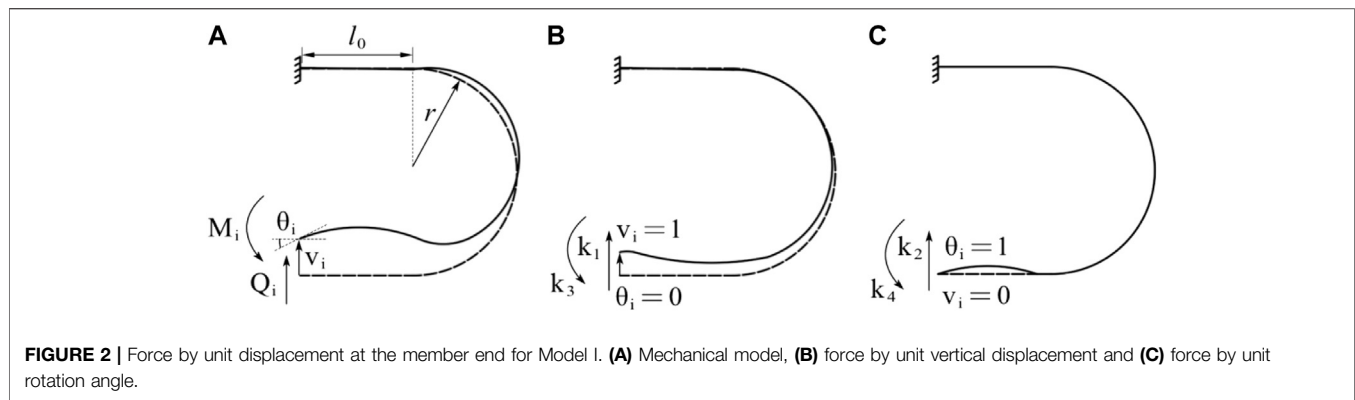
$$k_3 = \frac{6EI(l_0^2 + r\pi l_0 + 2r^2)}{2l_0^4 + 4r\pi l_0^3 + 24r^2 l_0^2 + 6r^3 \pi l_0 + 3r^4 \pi^2 - 24r^4} \quad (4)$$

k_2, k_4

In Figure 2C, in which the U-damper is subjected to unit rotation angle at the free end, k_2 and k_4 can be derived using the method explained above:

$$k_2 = \frac{6EI(l_0^2 + r\pi l_0 + 2r^2)}{2l_0^4 + 4r\pi l_0^3 + 24r^2 l_0^2 + 6r^3 \pi l_0 + 3r^4 \pi^2 - 24r^4} \quad (5)$$

$$k_3 = \frac{EI(4l_0^3 + 6r\pi l_0^2 + 24r^2 l_0 + 3r^3 \pi)}{2l_0^4 + 4r\pi l_0^3 + 24r^2 l_0^2 + 6r^3 \pi l_0 + 3r^4 \pi^2 - 24r^4} \quad (6)$$



Stiffness Matrix

Form Eqs 1–6, the force and displacement relation of the member end can be expressed as:

$$\begin{Bmatrix} Q_i \\ M_i \end{Bmatrix} = \begin{bmatrix} k_1 & k_2 \\ k_3 & k_4 \end{bmatrix} \begin{Bmatrix} v_i \\ \theta_i \end{Bmatrix} \quad (7)$$

Force and Displacement Relation for Model II

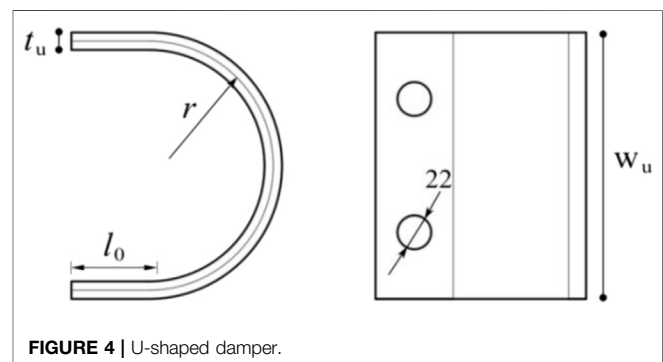
Using the same method used for Model I, the member free end force and displacement relation for Model II, as portrayed in Figure 3, are obtainable as:

$$\begin{Bmatrix} Q_j \\ M_j \end{Bmatrix} = \begin{bmatrix} k_1 & -k_2 \\ -k_3 & k_4 \end{bmatrix} \begin{Bmatrix} v_j \\ \theta_j \end{Bmatrix} \quad (8)$$

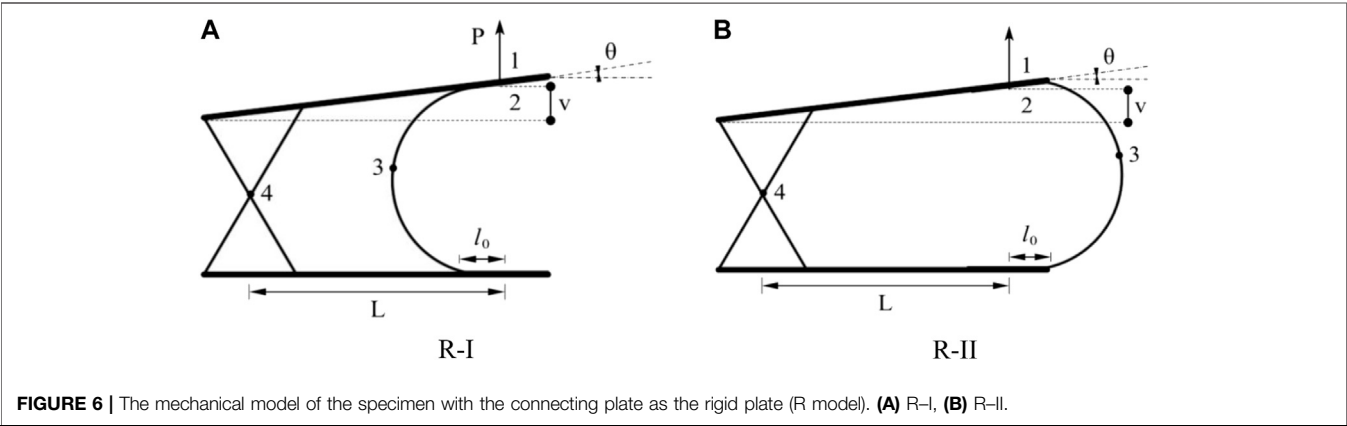
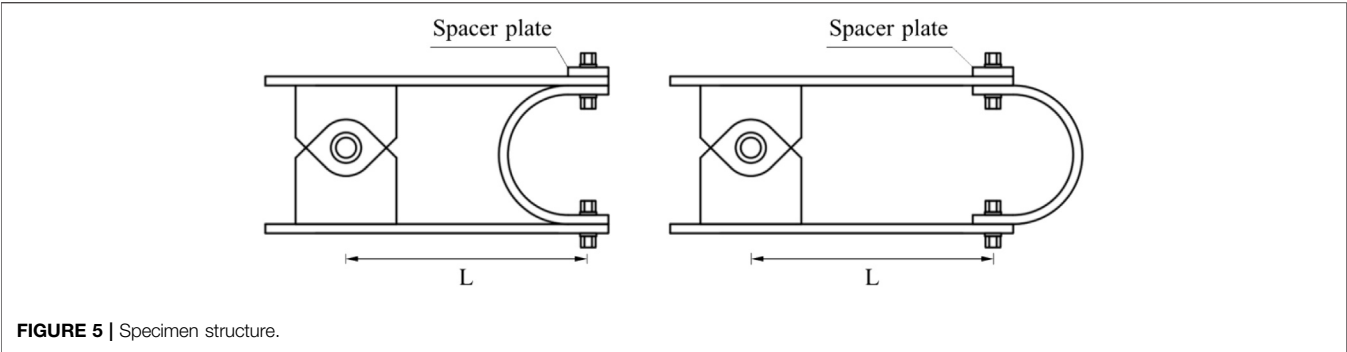
UNIDIRECTIONAL TENSION-COMPRESSION TEST OF THE DAMPER

Test Specimens

According to the different opening directions, the specimens of the U-shaped steel damper tension-compression test are divided into two groups: A and B. The two groups of specimens are made



of SNB400. The specimens are composed of a connecting plate clamp, a U-shaped damper, a movable hinge device, and a filling plate, and a U-type damping and connecting plate are connected by high-strength bolts. The specific structure of the specimens and the U-type damping is shown in Figures 4, 5. The thickness of the connecting plate t_b and the thickness t_u of the U-type damping are both 9 mm, the distance L from the hinge constraint point to the hole center is both 240 mm, the radius of the circular arc part of the damping part of group A specimen R is 40 mm, and the length of the straight line segment L_0 is 30 mm. According to the material property test, the yield strength obtained is 294 MPa. The radius of the damped circular arc part of the specimen in Group B is 64 mm, and the length of



the straight line segment is 40 mm. The yield strength obtained from the material property test is 306 MPa.

Mechanical Properties of Specimens

This section combines the U-shaped steel damper and the test fixture as the research object to analyze the mechanical properties of the U-shaped steel damper during tension and compression. It analyzes the mechanical properties of the U-shaped steel damper according to the mechanical properties expression of the U-shaped steel damper derived in *Force and displacement relation for Model I*.

With a monomer U-shaped steel damper as the research object, a U-shaped steel damper with a hinged connection of two steel plates together and a connection plate assumption for the rigid plate only consider the U-shaped steel damper end vertical deformation influence on stiffness, without considering the horizontal deformation according to the mechanical model is deduced. Mechanical Model I and Mechanical Model II were established for the U-shaped steel damper specimens with different opening directions, as shown in **Figure 6**. To distinguish the difference when the bending deformation of

TABLE 1 Test specimens.													
Specimen number	Connection plate						U-shaped steel dampers						
	L	t _b	w _b	σ _b	σ _p	Dampers placement	l ₀	r	t _u	w _u	σ _z	σ _d	
A-F	240	9	150	306	471		30	40	9	150	306	471	
A-S	—	—	—	—	—		—	—	—	—	—	—	
B-F	240	9	150	306	471		40	64	9	150	306	471	
B-S	—	—	—	—	—		—	—	—	—	—	—	

TABLE 2 | Load value of free end of U type steel damper.

Specimen	k_1	k_2	k_3	k_4	K (kN/mm)
A-F	20,761	880,121	880,121	47,375,297	14,249
A-S	20,761	880,121	880,121	47,375,278	28,917
B-F	6,236	395,742	395,742	31,763,581	3,490
B-S	6,236	395,742	395,742	31,763,581	10,085

the connecting plate is considered, the mechanical models of the U-shaped steel damper device with the connecting plate as a rigid plate are collectively referred to as the R model.

Mechanical Model of R-I

As shown in **Figure 6A**, one end of the U-shaped steel damper is engaged with the rigid plate at node 2, and the in-plane hinge constraint is carried out at node 4. At the same time, there is vertical load P and vertical displacement at rigid plate joint 1. The corresponding U-shaped steel damper has vertical load-displacement V , bending moment M , and rotation angle at node 2. **Table 1** shows the free end load value of the U-shaped steel damper specimen.

The stiffness matrix of R-I:

$$\begin{Bmatrix} P_u \\ P_v \\ M \end{Bmatrix} = \begin{bmatrix} 0 & 0 & 0 \\ 0 & k_1 & -k_2 \\ 0 & -k_3 & k_4 \end{bmatrix} \begin{Bmatrix} u \\ v \\ \theta \end{Bmatrix} \quad (9)$$

Where P_u is a horizontal load and u is a horizontal displacement:

$$P_v = k_1 v - k_2 \theta \quad (10)$$

$$M = -k_3 v + k_4 \theta \quad (11)$$

Since the clamp is regarded as a rigid plate, then:

$$\delta = v \quad (12)$$

$$\theta = \frac{\delta}{L} \quad (13)$$

The bending moment M of the external load on the articulated constraint point (node 4) is:

$$M_D = P \cdot L = P_v \cdot L + M \quad (14)$$

According to Eqs 9–14:

$$P = K\delta = \frac{k_1 L^2 - k_2 L - k_3 L + k_4}{L^2} \cdot \delta \quad (15)$$

Mechanical Model of R-II

Compared with the R-I mechanical model, its opening direction is opposite:

$$P = K\delta = \frac{k_1 L^2 + k_2 L + k_3 L + k_4}{L^2} \cdot \delta \quad (16)$$

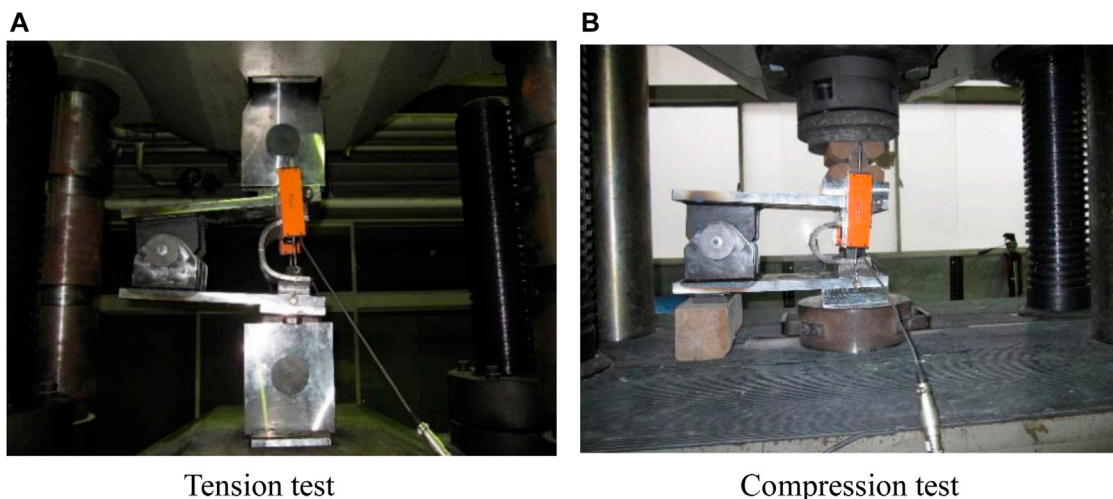
Intensity Assessment

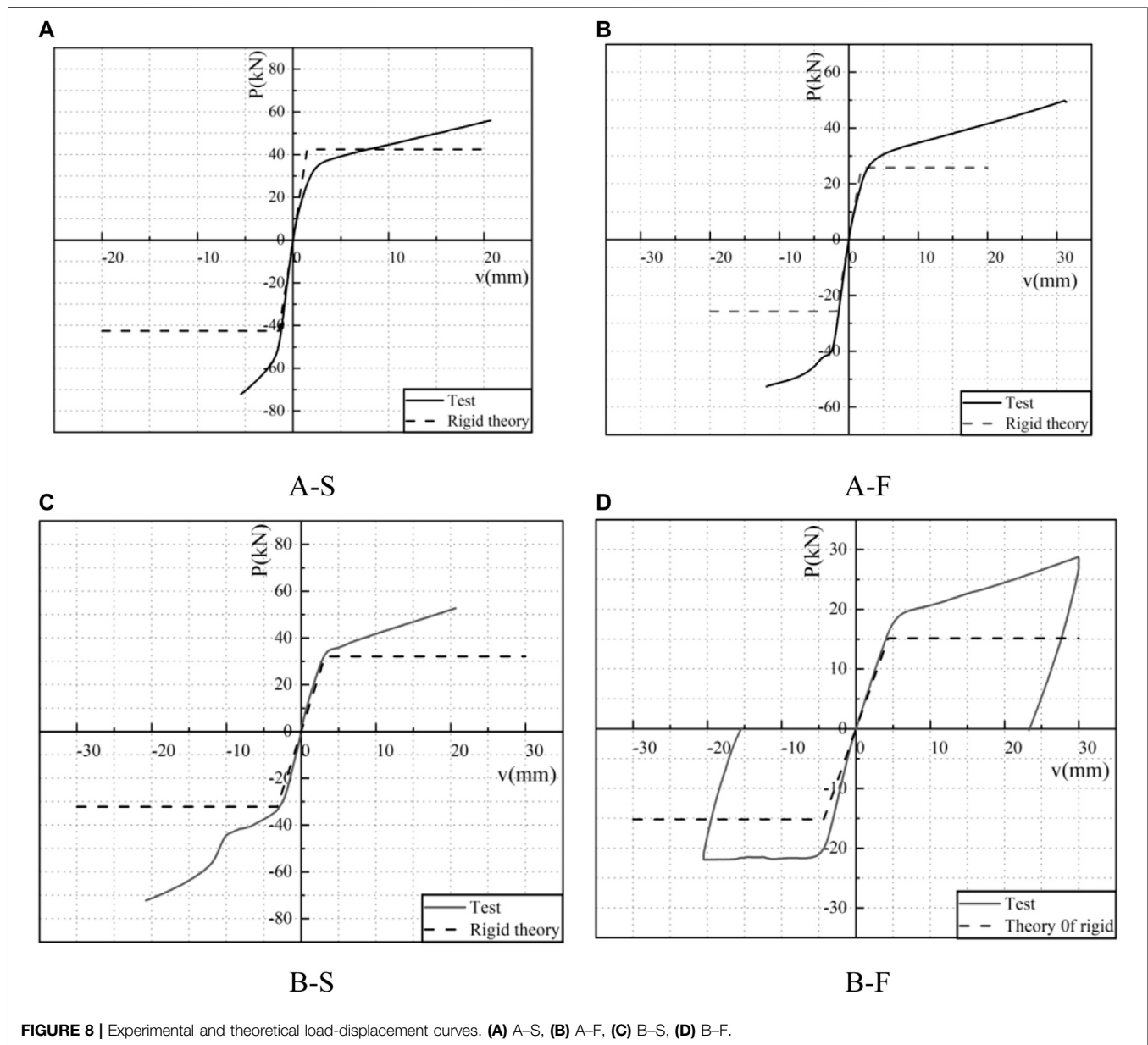
For the U-shaped metal damping deformation mode studied in this paper, based on the distribution law of internal forces of bending moment, the U-shaped metal damping yield is defined when the bending moment at the third central node of the arc reaches the full interface plastic bending moment M_p . The plastic bending moment of full section M_p is:

$$M_p = \frac{\sigma_s t_u^2}{4} \times L \quad (17)$$

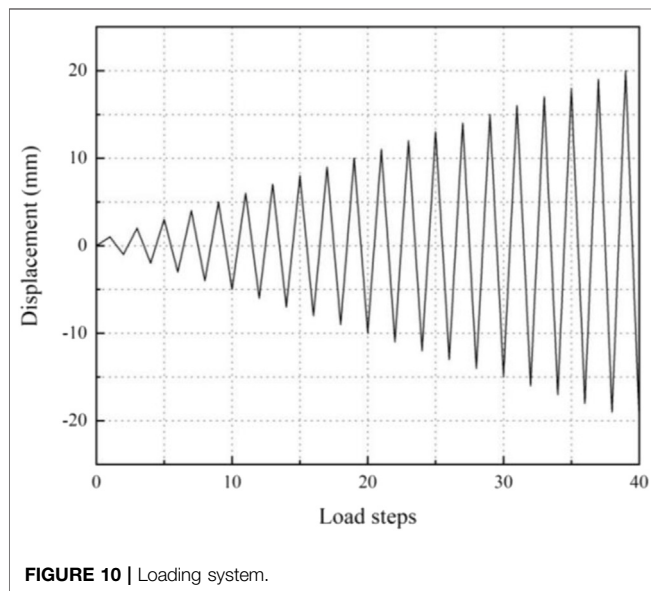
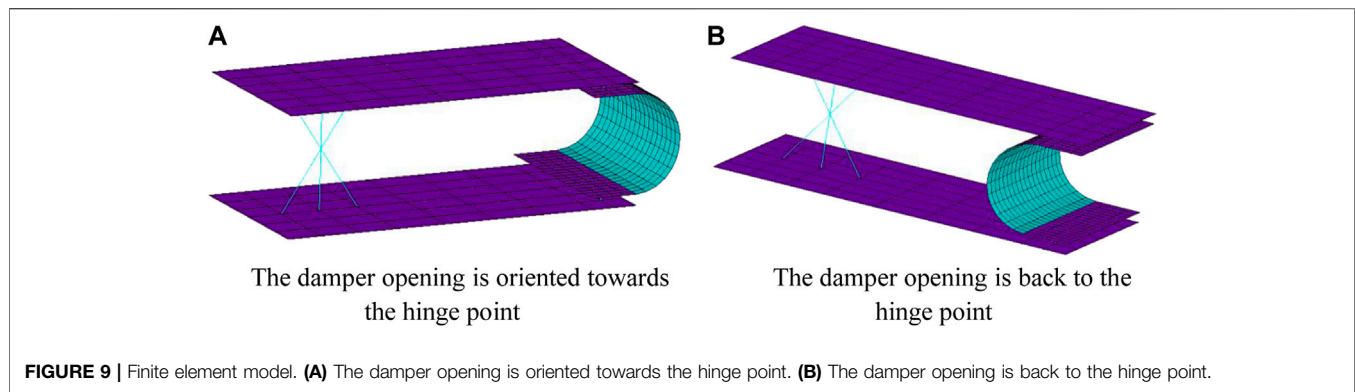
The yield strength measured by the material property test is σ_s (**Table 2**), the thickness of the U-type damper, and W_u is the width of the U-type steel damper.

As shown in **Figure 6**, the vertical displacement at the loading node 1 of the specimen is δ , and the vertical displacement and rotation angle at the U-shaped metal damping node 2 are V .

**FIGURE 7** | Test device. (A) Tension test (B) Compression test.

**TABLE 3 |** Comparison between experiment and theory.

Specimen	Loading way	Test		Theory		Error (%)		
		Yield load (kN)	Yield displacement (mm)	Yield load (kN)	Yield displacement (mm)	Yield load (%)	Yield displacement (%)	
A	A-F	Tensile	24.52	2.51	20.46	3.04	11.4	15.6
		Compress	39.24	2.38	35.31	2.81	10.0	18.1
	A-S	Tensile	33.03	2.27	28.36	2.73	14.1	2.2
		Compress	45.81	1.35	40.64	1.82	14.5	4.2
B	B-F	Tensile	16.62	4.56	11.83	5.04	18.9	13.8
		Compress	18.59	3.84	13.47	4.30	14.7	19.5
	B-S	Tensile	33.29	3.31	28.34	3.89	17.3	12.4
		Compress	31.84	2.82	26.50	3.35	11.5	11.8



For **Figure 6A**, according to **Eq. 7**, **Eq. 12**, **Eq. 13**, the internal force bending moment at the central node 3 of the U-shaped metal damping circular arc is:

$$M = k_1 \delta (l_0 + r) - k_3 \delta + k_2 \frac{\delta}{L} (r + l_0) - k_4 \frac{\delta}{L} \quad (18)$$

When $M = M_p$, the U-shaped metal damping yields, and the vertical yield displacement at node 2 is denoted as v_s . At this point, the vertical yield displacement at the loading end of the specimen: $\delta_s = v_s$.

For **Figure 6B** in the model shown in , the bending moment of internal force at the central node 4 of the U-shaped metal damping arc is:

$$M = k_1 \delta (l_0 + r) - k_3 \delta - k_2 \frac{\delta}{L} (r + l_0) + k_4 \frac{\delta}{L} \quad (19)$$

When M reaches M_p , the U-shaped steel damper yields, similarly, the vertical yield displacement at the loading end of the specimen can be obtained.

Loading Program

The test device of the U-shaped steel damper is shown in **Figure 7**. Vertical load is applied by a microcomputer-controlled electro-hydraulic servo universal testing machine (model SHT4605). The loading speed is controlled at 0.1 mm/s, and a cable displacement meter is installed on both sides of the U-shaped steel damper to measure the vertical displacement at the damper opening.

Test Results

The load-displacement curve of the specimen is shown in **Figure 8**. The tangent stiffness is 1/3 of the initial stiffness, which is defined as the yield point. **Table 3** shows the comparative analysis of theoretical and experimental results. The test error of yield load and yield displacement is kept within 20%.

The influence of the U-shaped steel damper opening orientations: different U-shaped steel damper opening orientations have different initial stiffness. The initial stiffness and yield load of the damper whose opening is towards the articulated constraint point are both higher under tension and compression. It can be seen that the opening orientation of the U-shaped steel damper affects its mechanical properties.

The influence of radius size of an arc segment of a U-shaped steel damper: the initial stiffness of a U-shaped steel damper varies with the radius of the arc segment. Compared with the specimens in Group A, the specimen in Group B with the larger radius of the U-shaped steel damper arc segment has a larger yield displacement and a smaller yield load; that is, its initial stiffness is smaller. The above results show that the initial stiffness of the U-shaped steel damper is inversely proportional to the radius.

According to the comparison between the theoretical and experimental results, it can be seen that the opening orientation of the U-shaped steel damper during installation influences the response of the component. The mechanical property design expression should be combined with the mechanical property expression of the single U-shaped steel damper, and the load combination caused by the actual installation should be considered.

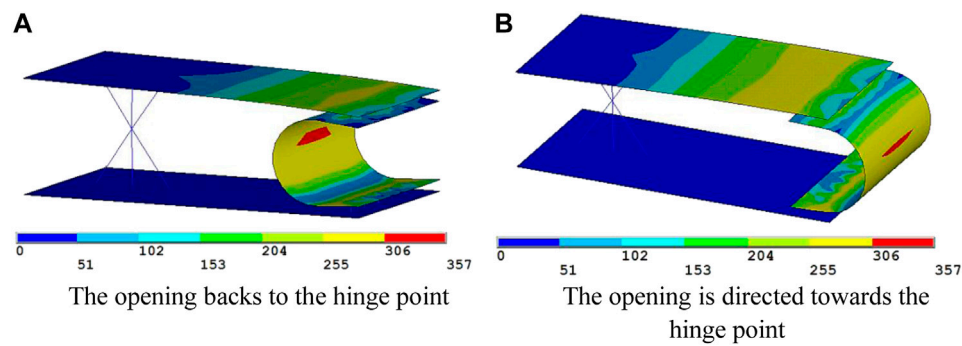


FIGURE 11 | Stress nephogram. **(A)** The opening backs to the hinge point. **(B)** The opening is directed towards the hinge point.

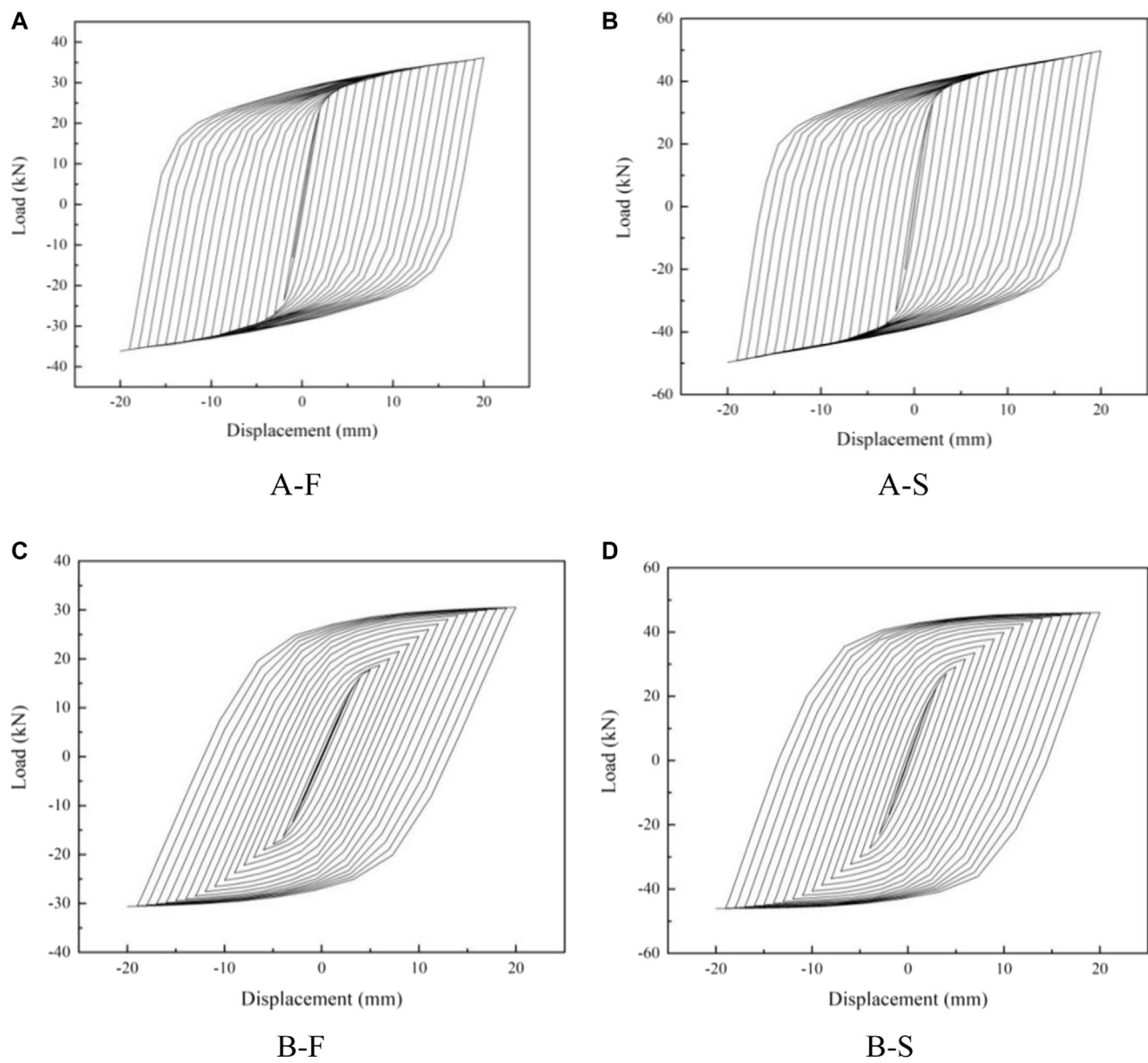
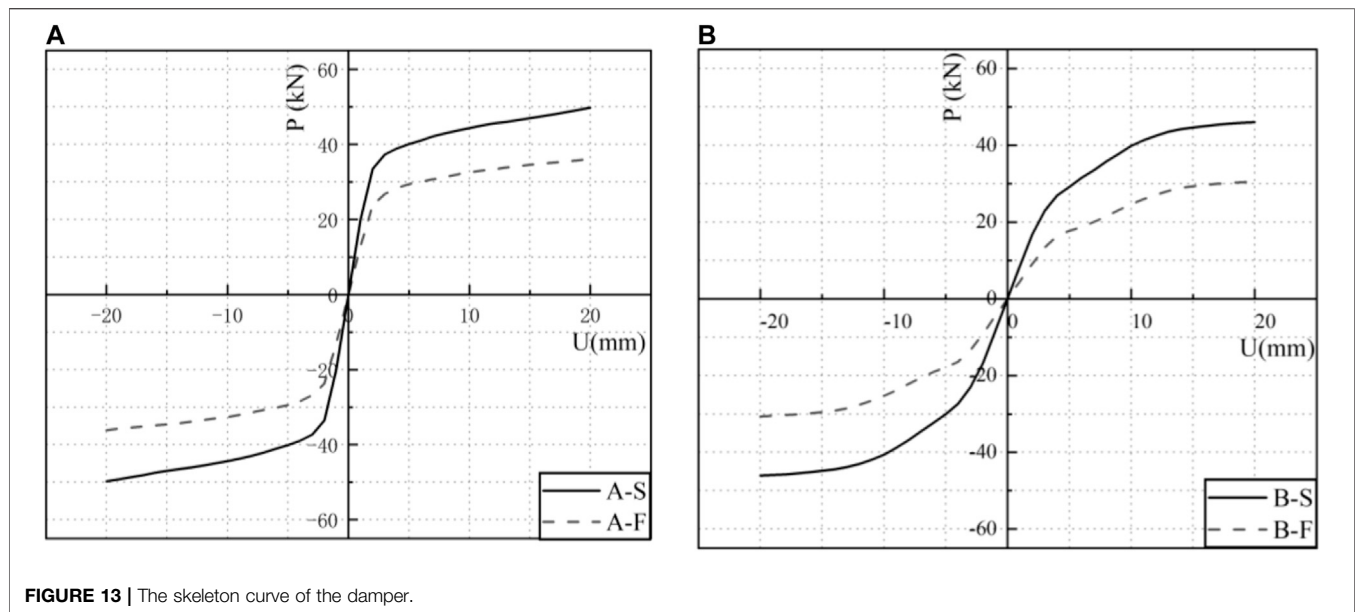
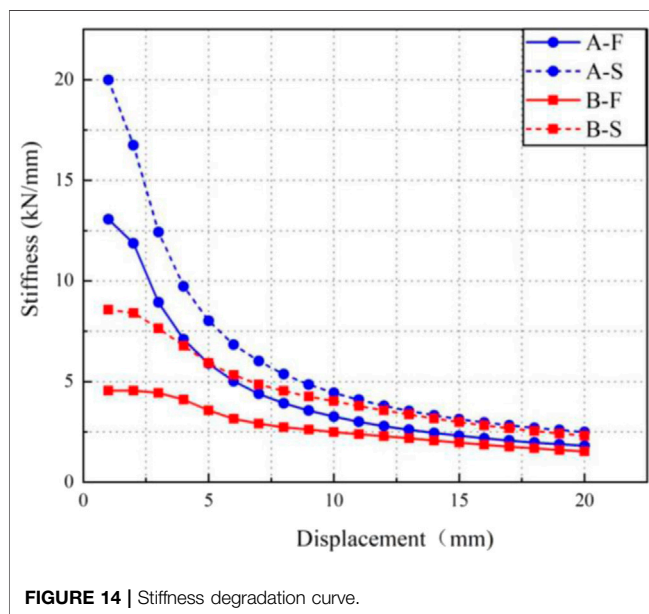


FIGURE 12 | Force-displacement hysteretic curve of the damper. **(A)** A-F, **(B)** A-S, **(C)** B-F, **(D)** B-S.

**TABLE 4 |** Mechanical behavior of a finite element.

Specimen	Initial stiffness (kN/mm)	The yield load (kN)	Yield displacement (mm)
A-F	11.85702	23.71404	1.922
A-S	16.73798	30.47596	1.881
B-F	4.433,261	16.38729	3.8712
B-S	8.40715	25.23257	3.7632



FINITE ELEMENT ANALYSIS

Introduction of Model

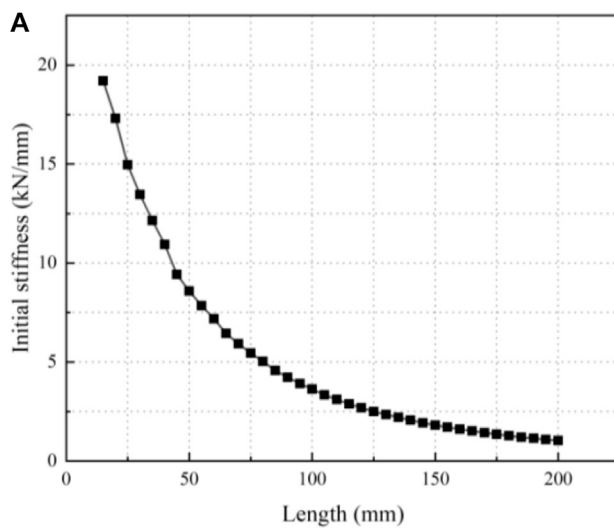
ANSYS software was used to establish an accurate finite element model to verify the test results and stress response analysis. The clamping plate and U-shaped steel damper are simulated with 4-node SHELL181. According to the test, the elastic modulus of the material obtained is 205,369 MPa, the Poisson's ratio is 0.3, the yield strength is 306 MPa, and the ultimate strength is 450 MPa. Link180 rod element was used to simulate the hinged restraint device. Multi-linear material model was employed for the U-shaped steel damper. **Figure 9** is the finite element model of the specimen. The astatic cyclic loading process is adopted, controlled by displacement, to study the energy dissipation capacity of the damper. **Figure 10** shows the cyclic loading displacement and the number of cycles.

Finite Element Analysis of Unidirectional Tension and Compression

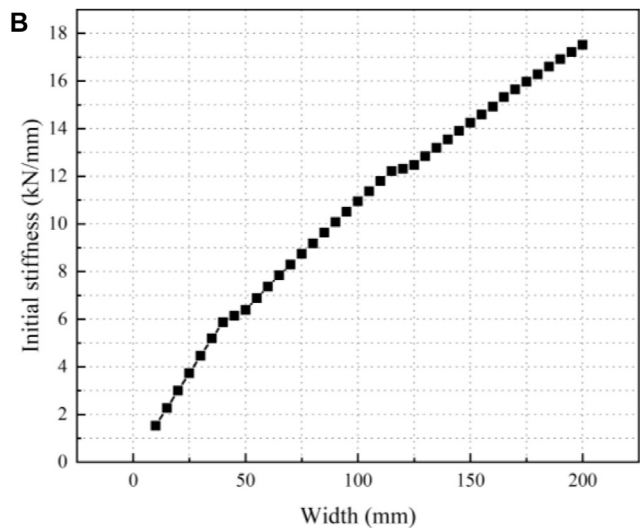
Through unidirectional tension and compression simulation of the finite element model, its stress nephogram **Figure 11** was

TABLE 5 | Damping performance comparison.

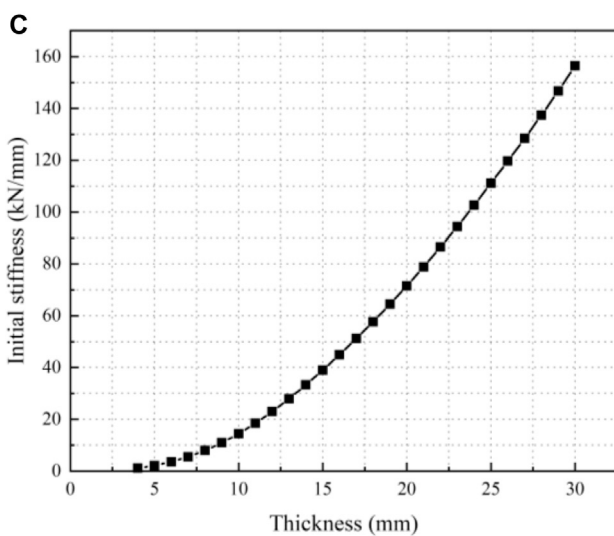
Specimen	Equivalent lateral stiffness $K_{eq}/(N \cdot m^{-1})$	Maximum hysteretic loop area $\Delta W/(N \cdot m)$	Equivalent viscous damping coefficient $\zeta_e/\%$
A-F	1.968×10^6	1866.39	41.76
A-S	2.591×10^6	2,551.37	43.41
B-F	1.601×10^6	1,361.16	37.48
B-S	2.415×10^6	2,297.49	41.94



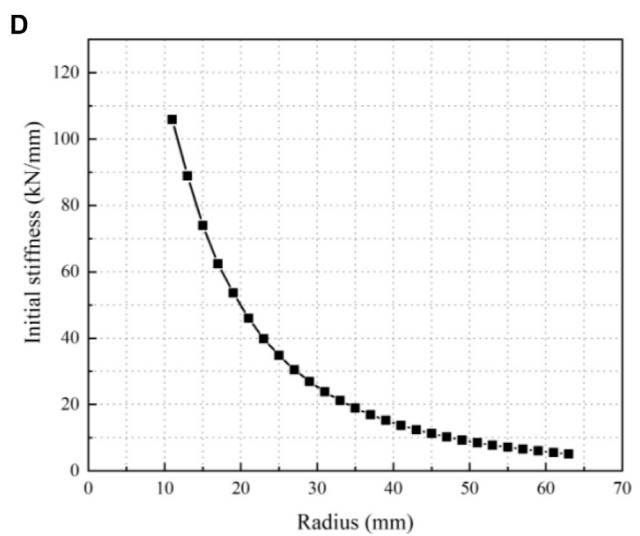
Curves of length and initial stiffness.



Curves of width and initial stiffness.



Curves of thickness and initial stiffness.



Curves of radius and initial stiffness.

FIGURE 15 | Curves of parametric analysis. **(A)** Curves of length and initial stiffness. **(B)** Curves of width and initial stiffness. **(C)** Curves of thickness and initial stiffness. **(D)** Curves of radius and initial stiffness.

obtained. The deviation between the model data and the theory is small, and the degree of coincidence is high. It is shown that the numerical model has good accuracy.

Analysis of Hysteretic Property

Figure 12 depicts the load and displacement relations obtained in the finite element analysis. The hysteresis curve obtained from the finite element analysis is full and shuttle-shaped, which indicates that the U-shaped steel damper has good energy dissipation performance. The skeleton curve is shown in **Figure 13** from the hysteretic loop curve. The mechanical properties of the steel damper calculated by the finite element method are shown in **Table 4**. As can be seen from the table, the initial stiffness of specimen A–S is 1.41 times that of specimen A–F, and the yield load is 1.29 times that of specimen A–F. The initial stiffness of specimen B–S is 1.91 times that of specimen B–S, and the yield load is 1.54 times that of specimen B–S. These results show that the initial stiffness and yield displacement of the steel damper with the opening towards the hinge point are larger than those with the opening back towards the hinge point.

Equivalent lateral stiffness:

$$K_{eq} = \frac{F_{max} - F_{min}}{\Delta_{max} - \Delta_{min}} \quad (20)$$

Where $\Delta_{max}, \Delta_{min}$ are the forward and reverse maximum loading displacements, respectively; and F_{max}, F_{min} are the external forces corresponding to the maximum forward and reverse loading displacement, respectively (Xu and Liu, 1995).

According to the formula, the equivalent lateral stiffness of each cycle loading can be obtained, and the stiffness degradation curve is shown in **Figure 14**. As can be seen from the figure, the stiffness of the secant isoline of each group of specimens showed obvious stiffness degradation at the first loading stage. The stiffness of specimens A–S was always greater than that of specimens A–F, and the stiffness of specimens B–S was always greater than that of specimens B–F.

The equivalent lateral stiffness of the last cycle of cyclic loading calculated according to the formula is shown in **Table 5**. The equivalent lateral stiffness of A–S is 1.32 times that of A–F, and the equivalent lateral stiffness of B–S is 1.51 times that of B–F. The results show that the U-shaped damper whose opening is toward the hinge point has higher equivalent lateral stiffness. The maximum hysteretic loop area in **Table 5** is the hysteretic loop area corresponding to the maximum displacement loading. The hysteretic loop area represents the amount of energy consumed by the U-shaped steel damper.

The equivalent viscous damping coefficient is an important index to judge the energy dissipation capacity of a structure or member in earthquake resistance.

$$\xi_e = \frac{E_{DS}}{4\pi E_S} \quad (21)$$

$$E_S = \frac{1}{2} K_{eq} \Delta_{max}^2 \quad (22)$$

Where E_{DS} is hysteretic damping energy dissipation, and is equal to the area surrounded by the curve at the maximum displacement; E_S is the maximum strain energy (Zhou, 2013).

The equivalent viscous damping coefficient is related to the displacement of cyclic loading. The larger the energy dissipation effect is, the more obvious it is. The equivalent viscous damping coefficients listed in **Table 5** all correspond to the values at the maximum cyclic loading displacement, so the damping coefficients are significant. It can be seen from the table that the equivalent viscous damping coefficient is A–S > A–F and B–S > B–F, indicating that the U-shaped damper whose opening is toward the hinge point has a more obvious energy dissipation effect.

PARAMETER SENSITIVITY ANALYSIS

Geometric parameters have an important effect on the mechanical properties of U-shaped steel dampers. The parameter sensitivity of the component was analyzed by ANSYS finite element software. A model with a length of 40 mm, a width of 100 mm, a thickness of 9 mm, and a radius of 40 mm was taken as the initial model, and the initial stiffness of components under different parameters was compared and analyzed.

Figure 15A shows the curve of length and initial stiffness. The length parameter range is 15–200 mm, and the group distance is 5 mm. Other parameters are consistent with the original model. As the length of the U-shaped damper increases, its initial stiffness decreases and approaches zero. The length is inversely proportional to the initial stiffness and is more sensitive in the 15–55 mm range.

Figure 15B shows the curve of width and initial stiffness. Except for width, other parameters are consistent with the original model. The width parameter range is 10–200 mm, group distance is 5 mm. As the width of the U-shaped damper increases, its initial stiffness increases, and its sensitivity is larger in the range of 10–40 mm.

Figure 15C shows the curve of thickness and initial stiffness. Except thickness, other parameters are consistent with the original model. Thickness range is 4–30 mm, group distance is 1 mm. As the thickness increases, its initial stiffness increases, and the greater the thickness, the more sensitive it is.

Figure 15D shows the curve of radius and initial stiffness. Except radius, other parameters are consistent with the original model, the radius range is 11–63 mm, group distance is 2 mm. The initial stiffness decreases with the increase of radius, and it is more sensitive in the range of 11–23 mm. It can be seen from the figure that the parameters of U-shaped metal damper have a great influence on its initial stiffness, which should be considered reasonably in the design and application.

CONCLUSION

In this paper, a theoretical formula for the mechanical properties of the U-shaped steel damper is presented. In addition, the experimental verification and finite element analysis of the U-shaped steel damper are also carried out. The main research results are summarized as follows.

When a single U-shaped steel damper has tension and compression, the end-load of the damper is the coupling of vertical force and bending moment. When the opening direction is different, the performance expression form is the same, but the vector positive and negative regulations are different, which should be differentiated in practical application.

According to the load-displacement relationship curve, the mechanical properties of U-shaped steel dampers vary with the opening directions in the tension-compression experiment. Through the comparative analysis of theoretical and experimental results, it is shown that the mechanical property expression of the U-shaped steel damper proposed in this paper is reasonable and feasible and can describe the plastic failure mechanism of a U-shaped steel damper, which provides a theoretical basis for the design and manufacture of the U-shaped steel damper.

In the study of finite element analysis, the results of finite element analysis obtained through monotonic loading are in good agreement with the test results. The hysteretic curves of all specimens obtained through repeated static loading simulation of a U-shaped steel damper by finite element software are full and in the shape of a shuttle. Compared with the damper whose opening is back to the hinged point, the damper whose opening is towards the hinged point has higher initial stiffness and equivalent viscous damping coefficient, and the energy dissipation effect is more obvious.

Parameters of U-shaped steel dampers greatly influence their initial stiffness, which should be taken into account in the design and application of U-shaped steel dampers.

REFERENCES

- Atasever, K., Celik, O. C., and Yuksel, E. (2017). *Modelling Hysteretic Behaviour of U-Shaped Steel Dampers*. Lullanagar, Pune: EUROSTEEL, 3239–3248.
- Chong, X., Hou, L. B., Chen, X., Xie, L. L., Jiang, Q., and Miao, Q. S. (2015). Research on Mechanical Performance and Numerical Simulation Analysis Method of U-Shaped Steel Damper [J]. *Building Structures* 1 (01), 114–120.
- Deng, K. L., Pan, P., Su, Y. K., Sun, J. B., and Qian, J. R. (2015). Experimental Study on Transverse Performance of Slotted U-Shaped Metal Yield Damper [J]. *J. Vibration Shock* 34 (12), 157–163.
- Du, H. K., Han, M., Yan, W. M., et al. (2016a). Influence of Hardness and Number of Layers on Mechanical Properties of U-Shaped Steel Plates [J]. *Eng. Mech.* 33 (2), 101–106.
- Du, H. K., Han, M., Yan, W. M., et al. (2016b). Test of Bearing Capacity and Elastoplastic Regression Analysis of Manganese Steel U-Shaped Limiter [J]. *J. Building Structures* 37 (8), 108–114.
- Du, H. K., Han, M., and Yan, W. M. (2014). Study on Calculation Method of Mechanical Properties of Constrained U-Shaped Steel Plate [J]. *Chin. J. Civil Eng.* 47 (2), 158–162.
- Enel, D., Kishiki, S., Yamada, S., Jiao, Y., Konishi, Y., Terashima, M., et al. (2016). Experimental Study on the Bidirectional Inelastic Deformation Capacity of U-Shaped Steel Dampers for Seismic Isolated Buildings [J]. *Earthquake Eng. Struct. Dyn.* 45, 173–192. doi:10.1002/eqe.2621
- Han, M., Feng, H. D., and Du, H. K. (2016). Research on Torsional Performance of U-Shaped 65mm Steel Plate Limiter [J]. *J. Beijing Univ. Civil Eng. Architecture* 32 (04), 1–5+22.
- Huo, L., Qu *, C., and Li, H. (2016). Robust Control of Civil Structures with Parametric Uncertainties through D-K Iteration. *Struct. Des. Tall Spec. Build.* 25 (3), 158–176. doi:10.1002/tal.1233

Parameters of U-shaped steel dampers greatly influence their initial stiffness. The result shows that increasing the straight section length and end arc radius can reduce initial stiffness, and increase the thickness and width can increase initial stiffness.

DATA AVAILABILITY STATEMENT

The original contributions presented in the study are included in the article/supplementary material, further inquiries can be directed to the corresponding author.

AUTHOR CONTRIBUTIONS

JG: Formal analysis, funding, writing review and editing JX: Survey method, project management, data management YX: First draft writing, data management JD: Project management, supervision JZ: Software, data management YC: Supervision, fund acquisition, verification BC: Supervision, fund acquisition, verification.

ACKNOWLEDGMENTS

The authors gratefully acknowledge the financial supports from Engineering Research Center of Nuclear Technology Application foundation (East China University of Technology), Ministry of Education (HJSJYB 2016-8, HJSJYB 2015-10), Education Department of Jiangxi Province (GJJ180373) and National Natural Science Foundation of China, 51868048.

- Jiao, Y., Kishiki, S., Yamada, S., Ene, D., Konishi, Y., Hoashi, Y., et al. (2015). Low Cyclic Fatigue and Hysteretic Behavior of U-Shaped Steel Dampers for Seismically Isolated Buildings under Dynamic Cyclic Loadings [J]. *Earthquake Eng. Struct. Dyn.* 44, 1523–1538. doi:10.1002/eqe.2533
- Kelly, J. M., Skinner, R. I., and Heine, A. J. (1972). Mechanisms of Energy Absorption in Special Devices for Use in Earthquake Resistant Structures. *Bnzsee* 5 (3), 63–88. doi:10.5459/bnzsee.5.3.63-88
- Lee, C.-H., Ju, Y. K., Min, J.-K., Lho, S.-H., and Kim, S.-D. (2015). Non-uniform Steel Strip Dampers Subjected to Cyclic Loadings. *Eng. Structures* 99 (Sep. 15), 192–204. doi:10.1016/j.engstruct.2015.04.052
- Li, S. X., and Yao, Q. F. (1991). Application Research of Basement Isolation of Multi-Layer brick concrete Structure [J]. *J. Xi 'a Univ. Architecture Technol. (Natural Sci. Edition)* (04), 411–418.
- Qu, C. X., Li*, H. N., Huo, L. S., and Yi, T. H. (2017). Optimum Value of Negative Stiffness and Additional Damping in the Civil Structures [J]. *ASCE J. Struct. Eng.* 143 (8), 04017068. doi:10.1061/(asce)st.1943-541x.0001805
- Ricky Chan, W. K., and Albermani, F. (2007). Experimental Study of Steel Slit Damper for Passive Energy Dissipation [J]. *Eng. Structures* 30 (4), 1058. doi:10.1016/j.engstruct.2007.07.005
- Skinner, R. I., Kelly, J. M., and Heine, A. J. (1974). Hysteretic Dampers for Earthquake-Resistant Structures. *Earthquake Engng. Struct. Dyn.* 3 (3), 287–296. doi:10.1002/eqe.4290030307
- Wang, Q. L. (2015). Experimental Study on the Damper Performance of SMA Metal Rubber Damper [J]. *J. Xi', a Univ. Architecture Technol. (Natural Sci. Edition)* 47 (006), 804–807.
- Whittaker, A. S., Bertero, V. V., Thompson, C. L., and Alonso, L. J. (1991). Seismic Testing of Steel Plate Energy Dissipation Devices. *Earthquake Spectra* 7 (4), 563–604. doi:10.1193/1.1585644

- Xing, S. T., and Guo, X. (2003). Study on Mechanical Properties and Shock Absorbing Effect of a New Kind of Soft Steel Damper [J]. *Earthquake Eng. Eng. Vibration* 23 (6), 179–186.
- Xu, B. Y., and Liu, X. S. (1995). *Application of Elastic-Plastic Mechanics [M]*. Beijing: Tsinghua University Press, 409–411.
- Yao, Q. F. (1997). Analysis of Limitation and Energy Dissipation Performance of U-Shaped Steel Strip [J]. *J. Xi 'a Univ. Architecture Technol. (Natural Sci. Edition)* (01), 24–28.
- Yin, W. H., Chen, L., and Wang, J. F. (2016). Study on the Performance of a New Type of Shearing Metal Energy Dissuaders with Buckling Constraints [C]. The Ninth National Symposium on Earthquake Prevention and Mitigation Engineering, 907–914.
- Zhao, Z. Z., Zhang, A. J., and He, B. (2017). Deduction of Mechanical Formula and Damping Performance of U-Shaped Steel Damper [J]. *Struct. Engineer* 33 (02), 143–150.
- Zhou, Y. (2013). *Design of Steel Damped Structure [M]*. Wuhan: Wuhan University of Technology Press.

Conflict of Interest: The authors declare that the research was conducted in the absence of any commercial or financial relationships that could be construed as a potential conflict of interest.

Publisher's Note: All claims expressed in this article are solely those of the authors and do not necessarily represent those of their affiliated organizations, or those of the publisher, the editors and the reviewers. Any product that may be evaluated in this article, or claim that may be made by its manufacturer, is not guaranteed or endorsed by the publisher.

Copyright © 2021 Gao, Xi, Xu, Ding, Zhu, Chang and Chen. This is an open-access article distributed under the terms of the Creative Commons Attribution License (CC BY). The use, distribution or reproduction in other forums is permitted, provided the original author(s) and the copyright owner(s) are credited and that the original publication in this journal is cited, in accordance with accepted academic practice. No use, distribution or reproduction is permitted which does not comply with these terms.



An Approach of the Maximum Curvature Measurement of Dynamic Umbilicals Using OFDR Technology in Fatigue Tests

Yuanchao Yin¹, Peng Yu¹, Ziguang Jia², Shanghua Wu¹, Qingzhen Lu^{2*}, Jun Yan¹ and Qianjin Yue²

¹Department of Engineering Mechanics, Dalian University of Technology, Dalian, China, ²School of Ocean Science and Technology, Dalian University of Technology, Panjin, China

OPEN ACCESS

Edited by:

Yunlai Zhou,
Universidade Lusófona, Portugal

Reviewed by:

Nicholas Fantuzzi,
University of Bologna, Italy
Wei Chai,
Wuhan University of Technology,
China

*Correspondence:

Qingzhen Lu
luqingzhen@dlut.edu.cn

Specialty section:

This article was submitted to
Smart Materials,
a section of the journal
Frontiers in Materials

Received: 30 May 2021

Accepted: 01 July 2021

Published: 30 July 2021

Citation:

Yin Y, Yu P, Jia Z, Wu S, Lu Q, Yan J
and Yue Q (2021) An Approach of the
Maximum Curvature Measurement of
Dynamic Umbilicals Using OFDR
Technology in Fatigue Tests.
Front. Mater. 8:717190.
doi: 10.3389/fmats.2021.717190

Prototype fatigue tests simulate in-place working conditions of dynamic umbilicals that are usually conducted to verify fatigue life. The fatigue failure hot spot locates on the top segment of the umbilical. The umbilical reaches a maximum curvature at the hot spot. The hot spot position of the umbilical is always inside or near the bend stiffener. The radial gap between the umbilical and the bend stiffener is very small, making it difficult to put traditional sensors in the gap. In this work, a prototype umbilical tension-bending test is conducted, and the optic frequency domain reflectometer (OFDR) technology is utilized to measure the distributed strain of the umbilical inside the bend stiffener. The curvature of the umbilical is obtained to locate the fatigue hot spot in order to verify the feasibility of this approach. The test results show that the umbilical curvature can be measured well with the use of OFDR technology. The influence of tension and swing angle on the position of the maximum curvature is studied. The method proposed in this article provides a valuable approach for curvature monitoring in the application of dynamic umbilical fatigue tests.

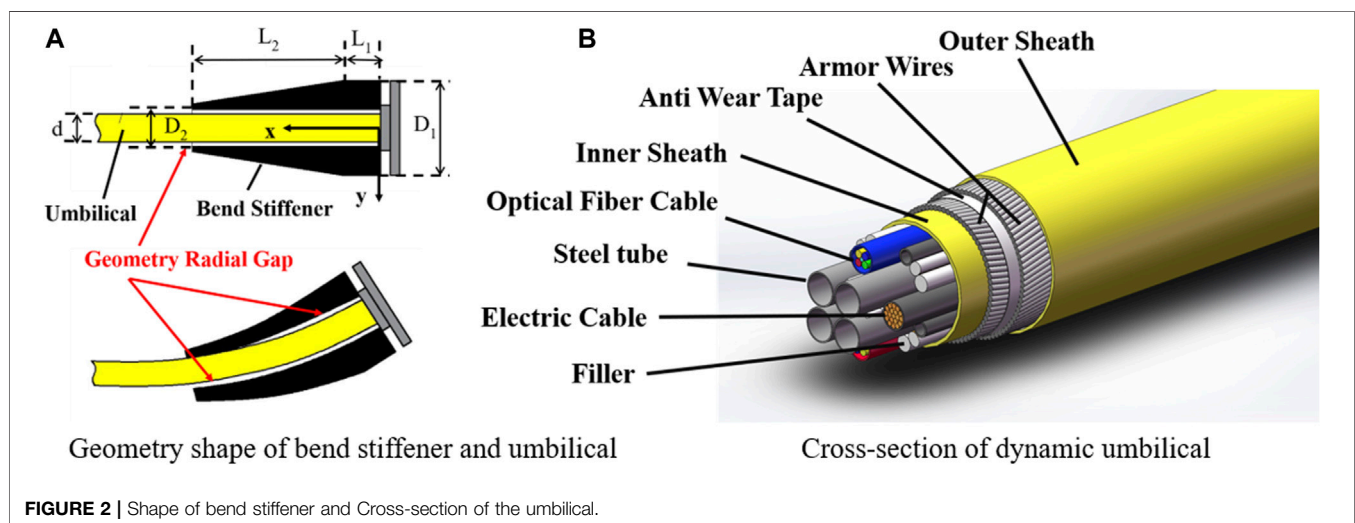
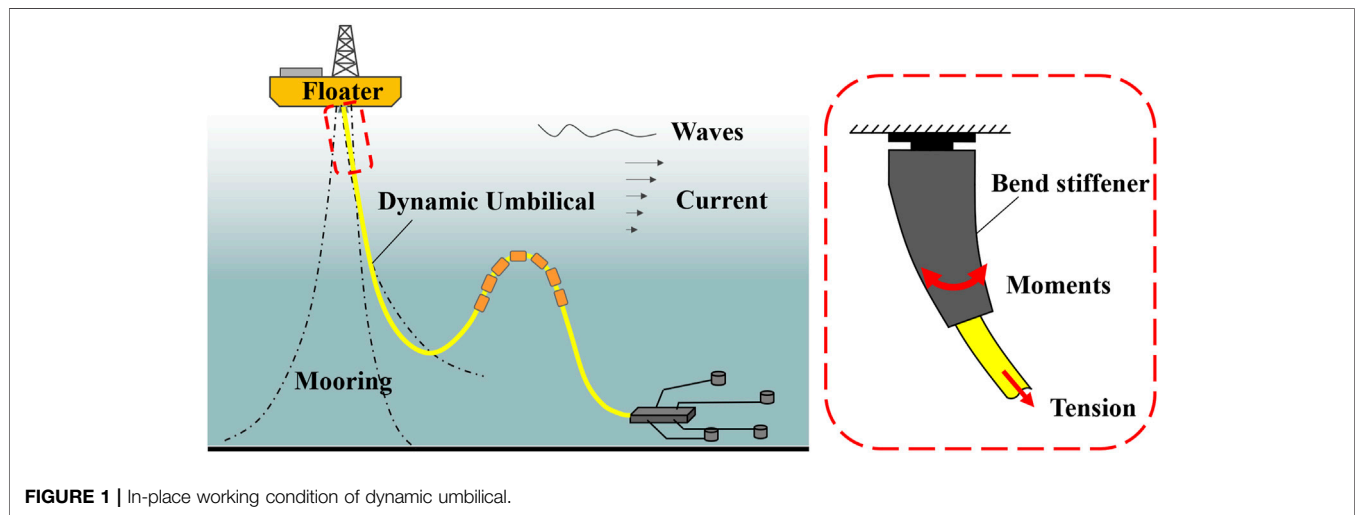
Keywords: optic fiber sensor, curvature, dynamic umbilicals, bend stiffener, prototype fatigue test

INTRODUCTION

Dynamic umbilicals play an important role in offshore oil and gas development. They are used to connect the upper floater and the subsea Christmas tree system supplying necessary control, energy, and chemicals. The fatigue life of the umbilicals should be predicted to ensure dynamic application. Prototype fatigue test of umbilicals is the most reliable and acceptable method to verify the predicted fatigue life, which must be conducted before the in-field application. The key of the prototype fatigue test is to simulate the behavior of the umbilical during its in-place working condition accurately. Proper measurement methods should be applied to monitor the umbilical behavior and performance during the fatigue test.

The in-place working condition of the umbilical is shown in **Figure 1**. The top segment of the umbilical is believed to be a critical area in fatigue analysis and test, which is simulated in the prototype fatigue test. The fatigue failure hot spot is in this area as the structure in this area sustains the highest tension load and the maximum alternating curvature (He et al., 2020a).

The umbilical behavior of this area is difficult to predict due to the complex contact and interaction with the bend stiffener. The bend stiffener is a polymeric conical shape structure with nonlinear mechanical characteristics. The polyurethane material of the bend stiffener is viscoelastic.



The shape of the bend stiffener and the cross-section of the umbilical are shown in **Figure 2**. The radial gap between the bend stiffener and the umbilical is illustrated in **Figure 2A**. The size of the gap is normally 5–15 mm. The gap leads to different deformation and curvature of the bend stiffener and the umbilical. **Figure 2B** shows the cross-section of an umbilical; the components are unbonded and free to slip in the umbilical, which leads to its nonlinear bending stiffness. Several studies have been conducted to obtain the curvature and bending behavior of umbilicals in this area. Tang et al. (2015) have developed an analytical model considering the material and geometrical nonlinearity of the bend stiffener to calculate the curvature of the top segment of the flexible riser. Vaz et al. (2007) and Caire (Caire et al., 2016; Caire and Vaz, 2017) have proposed analytical formulation for bend stiffeners considering nonlinear viscoelasticity. Ruanet et al. (2017) have conducted a dynamic analysis of a flexible riser with bend stiffener. However, the above

researches were mainly focused on obtaining the behavior of bend stiffener instead of the umbilical. Determining the location of the maximum curvature is challenging using analytical methods.

Different measure methods were utilized to obtain the curvature of the umbilical by fatigue tests. He et al. (2020b) have applied an image-based technique using the optical target tracking method to measure and monitor the curvature distribution of a bend stiffener in full-scale bending-tension tests. Leroy and Estrier (2001) have used parallel strain gauges to obtain axial and transverse strain variations in tension armors and calculate the bending behavior of a flexible riser. However, the curvature of the umbilical is different from the bend stiffener. The location of the maximum curvature is different in the two structures, which leads to different analysis results for fatigue. The curvature of the umbilical inside the bend stiffener cannot be measured directly by traditional measure methods. The radial gap between the bend stiffener and the umbilical is small, making it

difficult to place the sensor. It is necessary to develop a method to obtain the curvature of the umbilical and locate the hot spot in the fatigue test for a more accurate fatigue life analysis.

Optic fiber sensing technology has been applied in many domains for its advantages in parameters measurement in field and laboratory tests. Fiber-optic sensors are used to transmit and sense signals such as strain, temperature, and pressure. Compared with other sensors, the fiber-optic sensor has a small size, which makes strain measure or monitor in small spaces possible. The sensor can be multiplexed along the length of a fiber for more measurement points. The optic fiber sensing technology also has advantages of high accuracy, low loss, and immunity to electromagnetic interference (Li et al., 2014). Different kinds of sensing technology using fiber-optic sensors were developed, such as fiber Bragg grating (FBG) sensors (Li et al., 2011; Gautam et al., 2016; Matveenko et al., 2018) distributed and dominated by Brillouin optical time domain reflectometer (BOTDR) (Moffat et al., 2015; Wu et al., 2015) and by Brillouin optical time domain analysis (BOTDA) (Inaudi and Glisic, 2010). Ren et al. (2014) and Jia et al. (2019) have proposed methods to detect pipeline leakage and its localization by FBG sensors. Feng et al. (2019) have applied BOTDA technology to measure the strain of the geotechnical structure with less than 4% accumulated errors. Gao et al. (2018) have applied the OFDR technology to measure the strain of the cast-in-place concrete pile (PCC) by installing the optical fiber onto the surface of the PCC pile. Ren et al. (2018) have applied the OFDR technique to monitor pipeline corrosion and leakage. With the advantage of the small size and continuous characteristics of OFDR technology, a direct measurement of umbilical curvature may be achieved.

This article presents a curvature distribution measurement of dynamic umbilicals using high-accuracy OFDR-based strain sensing technology. A prototype fatigue test of umbilical was conducted with the fiber-optic sensors installed on the outer sheath. The strain distribution on the tested umbilical inside the bend stiffener was measured. The maximum bending curvature spot of the umbilical was found and located. The influence of tensile load and swing angle on the position of the maximum curvature is studied.

PROTOTYPE FATIGUE TEST DESCRIPTION

A summary of the test method, test rig, test specimen, and test setup are described in this section.

Test Method and Test Rig

The goal of the fatigue test is to simulate the true behavior of the umbilical and bend stiffener system on the top segment of the layout. The curvature of the umbilical is a critical parameter to evaluate the accuracy of the simulation. The real working condition behavior of the umbilical is simplified as a combination of tension and in-plane bending. Constant tensile load and alternating bending moments should be applied to the umbilical in the fatigue test. The principle of the fatigue test is to guarantee the similarity of strain where the maximum curvature

is reached, which leads to two critical control parameters of the test: the location and value of the maximum curvature.

The maximum curvature always locates in the area where the umbilical is inside of or near the bend stiffener. The curvature of the inside umbilical is difficult to be calculated using the theoretical analysis model due to the complex contact behavior and the nonlinear characteristics of the bend stiffener and the umbilical. It is necessary to obtain the curvature of the umbilical for an accurate fatigue test. As the curvature is the response of the umbilical, trail tests should be conducted to obtain the loading parameters.

To guarantee the accuracy of the prototype fatigue tests, the following items should be taken into consideration and met. The curvature at the end of the tension actuator should reach zero by designing the length of the test specimen. The length of the swinging head from the installation end to the rotation center should be designed. Under the condition that the fatigue response of the umbilical remains unchanged, the test frequency should be increased properly to shorten the test duration.

A prototype tension-bending fatigue test of a system involving umbilical and bend stiffener was conducted by the fatigue test rig from Dalian University of Technology (DUT). The schematic picture of the test rig is shown in **Figure 3**. The test rig simulates real in-place working conditions of the umbilical by applying constant tensile load by hydraulic actuators. The reciprocating bending moment is applied by a swing head linked to a rotation center. The test rig is adjustable with a test length of umbilicals or flexible risers up to 20 m. The swing head of the test rig is also adjustable from 1 to 3.5 m. The test rig can meet most of the testing requirements for dynamic umbilicals, cables, and flexible risers. The maximum tension capacity of the test rig is 500 kN. The maximum bending capacity is 150 kNm with a swing angle within $\pm 15^\circ$. The tension and bending actuators are free to rotate in the bending plane with a hinge joint, which leads to a more accurate simulation. The test frequency of the test rig can reach up to 0.1 Hz.

Test Specimen and Test Setup

A dynamic umbilical was applied in this test. The key parameters of the umbilical are listed in **Table 1**. A bend stiffener was assembled on the umbilical. The geometry shape of the bend stiffener is illustrated in **Figure 2A**. The geometry parameters of the bend stiffener are listed in **Table 2**.

A global Cartesian coordinate system (X, Y) is adopted to describe the measurement location of the umbilical, as shown in **Figure 2A**. The origin point (0, 0) is at the top of the bend stiffener. The distance from the origin point to the swing center of the swing head is 2.5 m. The length of the test sample is 16 m. The length of the bend stiffener is 2.92 m.

The constant tensile load applied in the test is 100 kNN. The swing angle applied in the test is from 0° to 8° , which is measured by a tilt angle sensor placed on the swing head. Each test was repeated three times to verify the accuracy of the results. The average environment temperature and humidity during the test are 23°C and 70%, respectively.

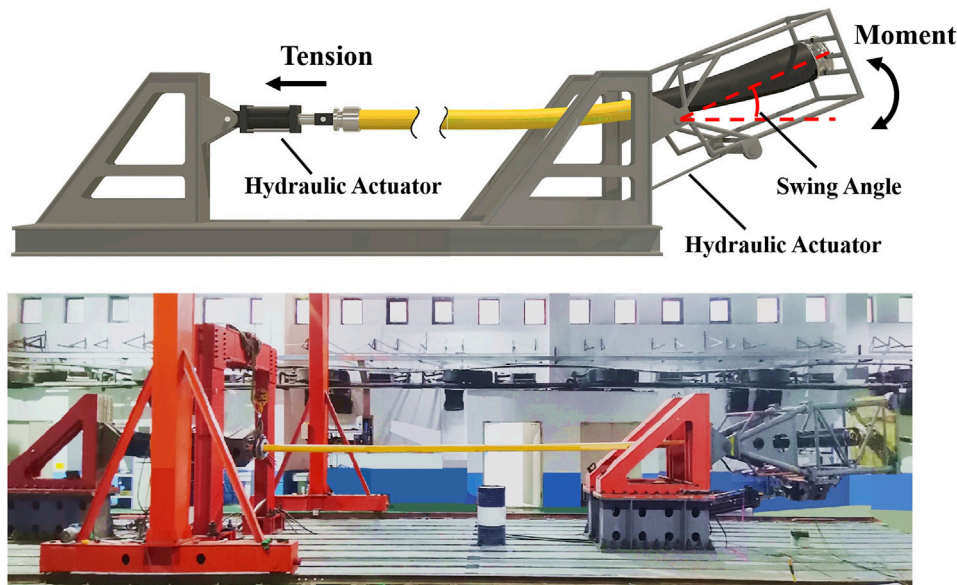


FIGURE 3 | Schematic and picture of the test rig.

TABLE 1 | Key parameters of the umbilical.

Parameters	Value
Outer diameter	121 mm
Design water depth	500 m
Tension stiffness (EA)	4.68 e8 N
Bending stiffness (EI)	5.3 e3 Nm

TABLE 2 | Geometry parameters of the bend stiffener.

Shape parameters	L ₁	L ₂	D ₁	D ₂	d
Value (mm)	420	2,500	300	141	121

TABLE 3 | Test conditions.

Test group	Tensile load (kN)	Swing angle (°)
Test 1	0–90	0
Test 2	100	8
Test 3	100	3/5/8
Test 4	40/60/80/100	8

Fatigue failure of the umbilical typically occurs instantaneously. The behavior of the umbilical should be measured during the fatigue test to infer and analyze the failure. Load cells and tilt sensors are applied to monitor the loads applied to the umbilical. Curvature distribution, change of the tension stiffness, temperature, pressure of tubes, and continuity of photoelectric signal should be monitored during the test. Four groups of tests were conducted as listed in **Table 3**.

DISTRIBUTED OPTICAL FIBER SENSING TECHNOLOGY

Methods of Curvature Measurement

Different measure methods were attempted to obtain the curvature distribution and the location of the maximum curvature.

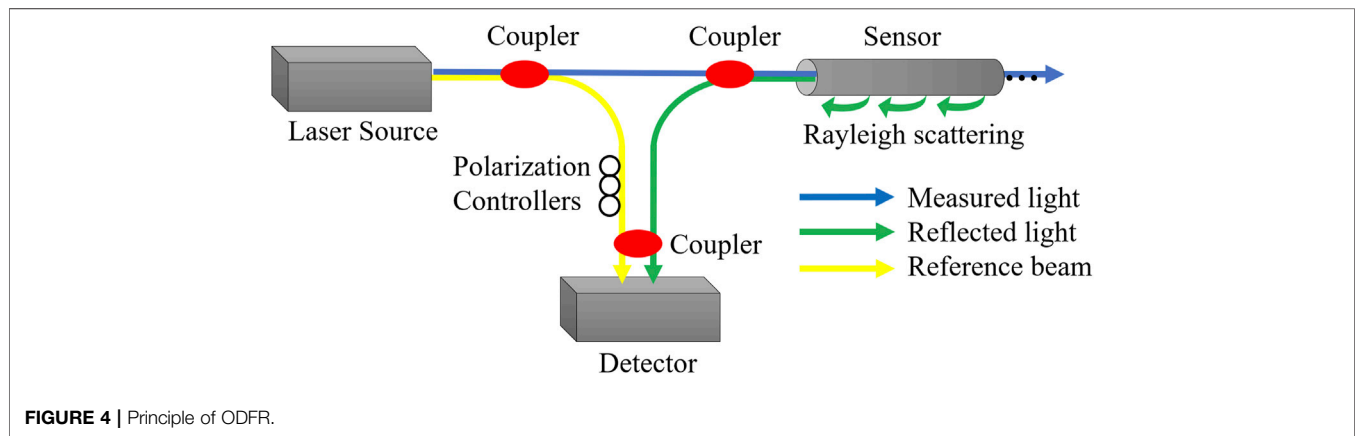
The measurement of the direct shape and deformation of the structure is believed to be the best method to measure the curvature due to its accuracy. Linear Variable Displacement Transformers (LVDT) or potentiometers are standard sensors for distance measurement. A large number of sensors are needed to draw the distribution of the curvature. Advanced sensors such as laser displacement sensors and optical target tracking technology can be employed for curvature sensing. However, this method can only obtain the external shape of the bend stiffener whose curvature is different from that of the umbilical, as stated before.

Considering the contact between the umbilical and the bend stiffener, a matrix piezoelectric sensor can be applied to measure the pressure distribution of their interface. The curvature can be obtained by analyzing the relationship between pressure and curvature through the numerical model. Moreover, the contact behavior can be different with the use of the sensor. The accuracy of this method needs to be verified.

The strain of the outer sheath can reflect the curvature of the umbilical when a simple load is applied. The traditional way of strain sensing is by the strain gauge. The strain gauge can only be pasted on the interface of the umbilical with single point measurement. The curvature distribution measurement requires a large number of sensors. Moreover, the space between the umbilical and the bend stiffener is limited, which

TABLE 4 | Comparison of different methods of curvature measurement.

Sensors	Measurement parameters	Advantage	Disadvantage
LVDT/potentiometers	Distance	Accurate	Not suitable for direct measure
Laser displacement sensor/optical target tracking camera	Distance	Accurate, non-contacting, distributed sensing	Not suitable for direct measure
Matrix piezoelectric sensor	Pressure	Correct measurement location	Different contact behavior, lack of validation
Strain gauge	Strain	Correct measurement location	One-point measure, limited measurement space
Fiber-optic sensor	Strain	Accurate, distributed sensing	Lack of validation

**FIGURE 4** | Principle of OFDR.

leads to the difficulty of the lead-out conducting wires. The fiber-optic sensor has a small shape and can sense multiplexed points along the fiber. This sensing technology requires no conducting wires. The advantages of the fiber-optic sensor make it a potential method for curvature measurement.

The comparison of different methods of curvature measurement for umbilical is listed in **Table 4**.

Principle of Distributed OFDR Technology

Distributed OFDR technology was developed by Eickhoff in 1981 (Eickhoff and Ulrich, 1981). The principle of OFDR is shown in **Figure 4**. The laser source emits continuous and tunable lights. The lights go through an optic fiber coupler and are divided into two parts. One part of the emitted lights is sent to the fiber-optic sensor. The Rayleigh backscattering light is produced as signal lights. Light frequency and spectrum change when strain or temperature changes on the sensor. The other part of the emitted lights is reflected back and passes through polarization controllers, used as the reference beam. The reflected signal lights and the reference beam are coupled by the optic fiber coupler and sent to the detector.

The light spectrum changes with the strain or temperature change. The light spectrum between the reflected Rayleigh backscattering light and the reference beam can be measured, compared, and analyzed in the detector. Meanwhile, the optical frequency of the Rayleigh backscattering light at different positions is different due to the tunable laser source. The light frequency can be detected and analyzed by the detector. The

following relationship between spectrum, strain, and temperature can be given:

$$\frac{\Delta\lambda}{\lambda} = -\frac{\Delta\nu}{\nu} = K_\epsilon\Delta\epsilon + K_T\Delta T,$$

where ϵ and ΔT are the variations of strain and temperature, K_ϵ and K_T are the sensitivity coefficient of strain and temperature, $\Delta\lambda$ is the change of the resonance wavelength, $\Delta\nu$ is the spectrum shift, and λ and ν are the mean wavelength and frequency. Based on the above principles, the strain and temperature at different positions of the fiber-optic sensor can be obtained.

Layout of Fiber-Optic Sensor

The layout and protection of the fiber-optic sensor are very important. The umbilical and the bend stiffener may have a large contact force and friction force during the fatigue test. The fiber-optic sensor is fragile and has a low capability of resistance to shear stress. The fiber-optic sensor may break off if it was glued on the surface of the umbilical. Several attempts were made to find a method to protect the fiber-optic sensor. The layout of the fiber-optic sensor and system is shown in **Figure 5**. The main steps are introduced as follows.

Take off the bend stiffener and reserve enough measurement length for the fiber-optic sensor. The reserved length should be longer than the length of the bend stiffener, so the end of the fiber-optic sensor can be out of the bend stiffener. Then, draw a line along the outer sheath of the umbilical, which is the location of the sensor. Cut a U-shape notch along the line with a depth of

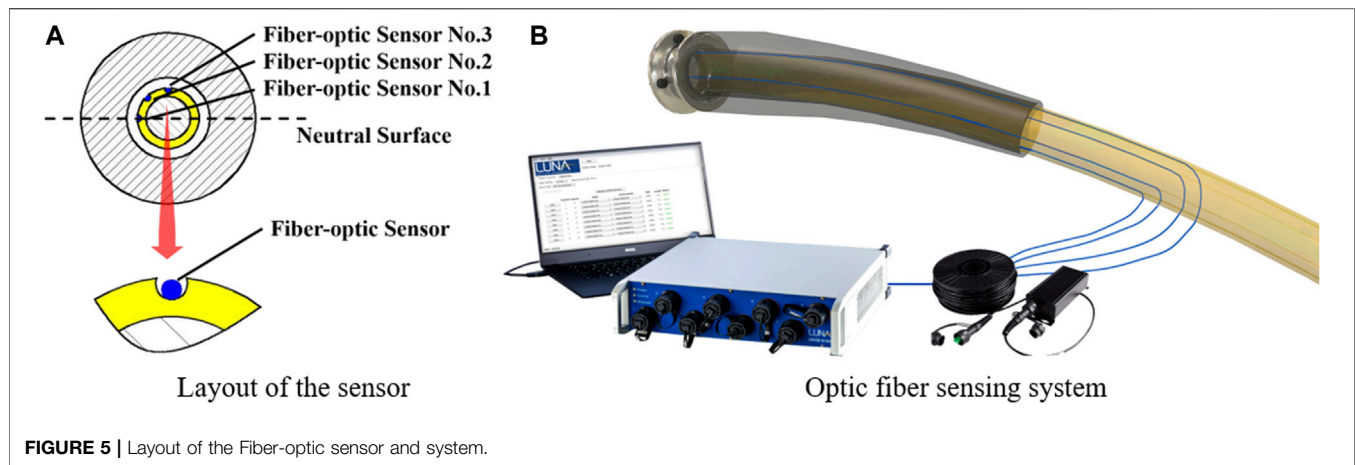


FIGURE 5 | Layout of the Fiber-optic sensor and system.

2–3 mm. The whole fiber-optic sensor should be placed inside the notch, as shown in **Figure 5A**. Clean the notch and lay the fiber-optic sensor inside it. The fiber-optic sensor should have enough reserved length on both ends for the follow-up connection with the measure instrument. Fix the fiber-optic sensor at one end of the notch with glue 502 or similar glue with a short coagulation time. After the sensor is fixed at one end, gently stretch the fiber-optic sensor on the other side of the notch with a small weight. Fix several points along the sensor using glue 502. Pour the epoxy resin into the notch and cover the fiber-optic sensor. The fiber-optic sensor will be well prepared after the coagulation of the epoxy resin for 24 h. Put back the bend stiffener after all the sensors are prepared.

The advantage of this method is that the fiber-optic sensor can be protected. The sensor is sensitive to measure the strain change of the umbilical. Moreover, both ends of the fiber-optic sensor can be connected to the measurement instrument if one end of the sensor is broken.

The sensing fiber used in the test is a standard single-mode optical fiber coated by Hytrel® 6,356 material. The diameter of the optical fiber is 0.9 mm. LUNA ODISI 6000 was applied as the measurement instrument in this test. The schematic of the curvature measurement system using fiber-optic sensors in the fatigue test is shown in **Figure 5B**. Three fiber-optic sensors were installed on the umbilical. The angles between the fiber-optic sensor and the neutral surface are 0°, 45°, and 90°. The length of each fiber-optic sensor is approximately 6 m. Each point on the fiber-optic sensor can be seen as a sensing point. The gage pitch on the fiber-optic sensor was set to 2.6 mm with a 25 Hz sampling frequency. The position of the start point of the measure segment can be set by pressing the gauge pitch before the test.

Curvature Algorithm

The strain on the outer sheath of the umbilical can be measured through the fiber-optic sensor. As the umbilical sustains the combination of tension and bending, the measured strain can be written as follows:

$$\varepsilon = \varepsilon_{\text{tension}} + \varepsilon_{\text{bending}}.$$

The curvature of the umbilical is caused by the bending stress and can be written as follows:

$$\kappa = \frac{\varepsilon_{\text{bending}}}{y} = \frac{2\varepsilon_{\text{bending}}}{d\sin\theta} = \frac{2(\varepsilon - \varepsilon_{\text{tension}})}{d\sin\theta},$$

where y is the distance from the fiber-optic sensor to the neutral surface, θ is the angle between the fiber-optic sensor and the neutral surface, d is the outer diameter of the umbilical.

Fiber-optic sensor No. 1 lays on the neutral surface. When the umbilical is under the combined load of tension and bending, the longitudinal stress and strain caused by bending are zero. The strain measured by sensor No. 1 represents the pure tension strain.

$$\varepsilon_1 = \varepsilon_{\text{tension}}.$$

The average curvature is calculated in this test and can be written as follows:

$$\bar{\kappa} = \frac{\varepsilon_3 - \varepsilon_1}{d} + \sqrt{2} \frac{\varepsilon_2 - \varepsilon_1}{d},$$

where ε_1 , ε_2 , ε_3 is the measured strain of fiber-optic sensors No. 1, No. 2, and No. 3.

TEST RESULTS AND ANALYSIS

Pure Tensile Test and Static Trial Test

To observe the performance of the applied fiber-optic sensor on the umbilical, a trial pure tension test was conducted. In this test, the swing head of the test rig is in the horizontal position. There is no contact between the umbilical and the bend stiffener in this trial test. A pure tensile load of 0–90 kN was applied to the umbilical. The test results are shown in **Figure 6**. The strain of the three sensors was recorded to verify if the sensor is fixed well onto the umbilical. The tension strain on the umbilical should be stable along the umbilical. **Figure 6A** shows the strain along the umbilical on different pure tensile loads of the No. 3 fiber-optic sensor.

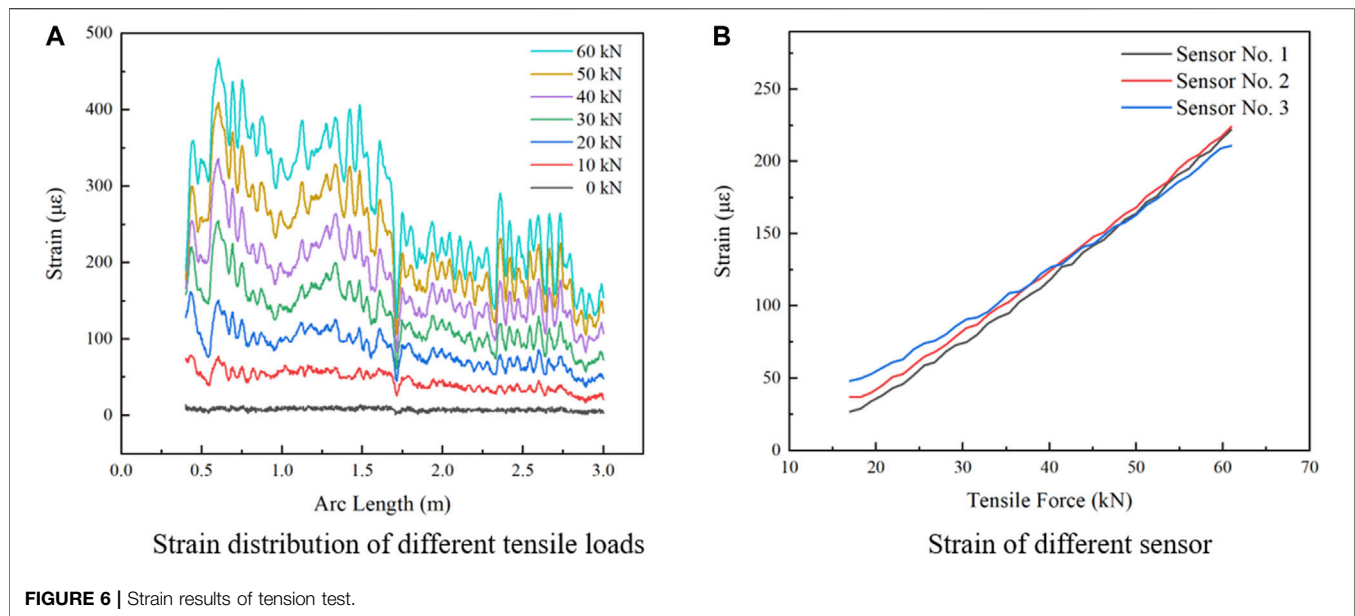


TABLE 5 | Maximum curvature and its location measured by OFDR.

Measurement method	Maximum curvature (m^{-1})	Location (m)
Laser displacement sensor	0.105	0.1200
Fiber-optic sensor	0.099	0.1612

As shown in **Figure 6A**, the strain along the arc length of the umbilical tends to be stable and changes in a small amplitude. The strain increases linearly on each point with the increasing tensile load. There is a loss of strain at the location of 1.7 m along the arc length. The decrease of strain is caused by the loose bond of the sensor at this point. However, as the tension stress will be subtracted during the test, the fluctuation of the tension strain will not affect the test results. The results of the trial test prove that the fiber-optic sensors are well fixed on the umbilical and the measured strain meets the theoretical tendency. **Figure 6B** shows the tension strain of the three different sensors at the same arc length of 2 m. The error between the sensors decreases with the increasing tensile force. The maximum error is 6.1% at the load of 90 kN.

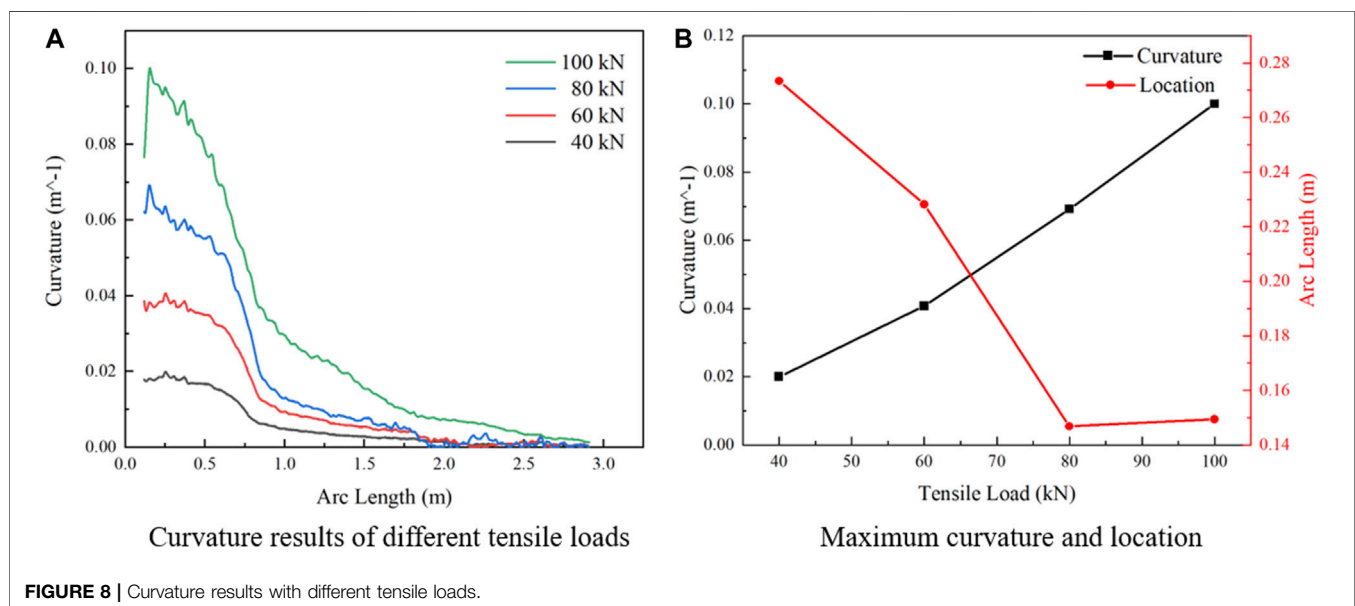
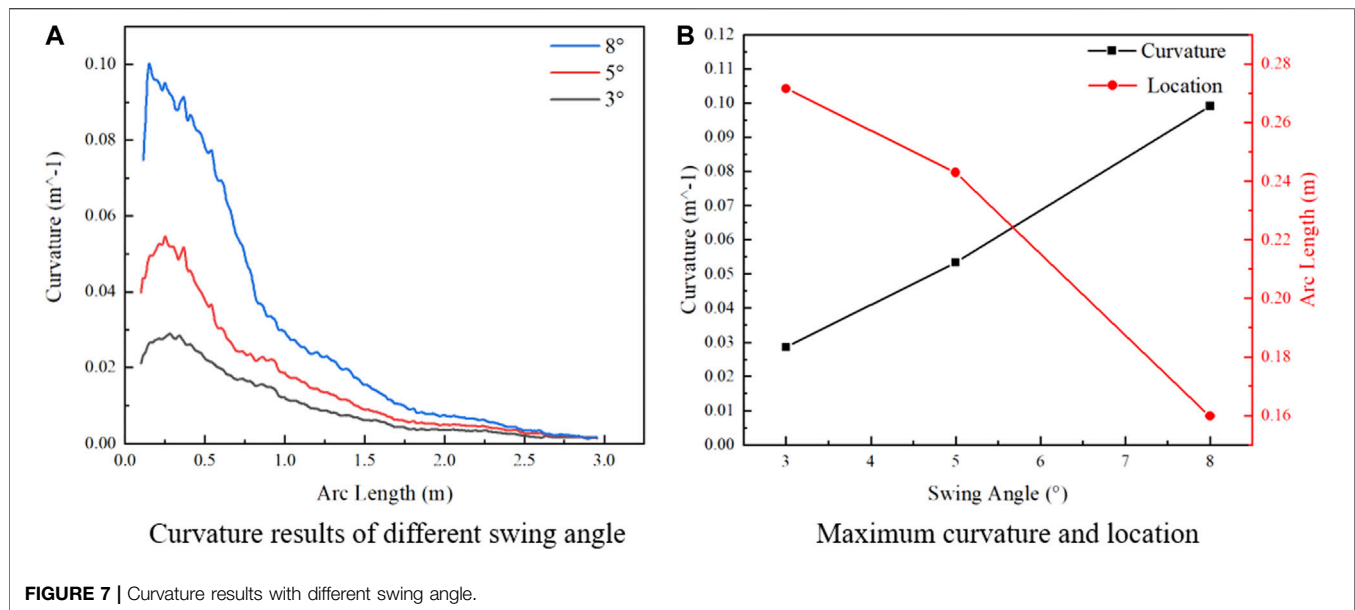
A follow-up static trial test 2 was conducted to compare the measured curvature through two different measurement methods. A tensile load of 100 kN with an 8° swing angle was applied in this test. The deformed shape of the bend stiffener was measured by using a laser displacement sensor as stated in *Methods of Curvature Measurement* section. The curvature of the umbilical is calculated by the tested shape information of the bend stiffener. The maximum curvature and its location in the two measurement methods are compared, which is shown in **Table 5**. The maximum curvature obtained by the two methods is almost the same. However, there is still a difference between the location of the maximum curvature by the two methods. The pitch of different measuring points by the laser displacement

sensor is smaller than the fiber-optic sensor. The maximum curvature and its location will be measured more accurately by applying a more densely measuring point by OFDR. As the fiber-optic sensor is placed on the umbilical, it is believed that the data of the OFDR method are more reliable.

The Influence of the Swing Angle on the Curvature

Test 3 was conducted with a constant tensile load of 100 kN and swing angle up to 8° . The test results are shown in **Figure 7**. **Figure 7A** shows the curvature of the umbilical on different swing angles. The curvature shows an increasing trend at the starting area of the umbilical. The curvature reaches the maximum point at the area between 0.16 and 0.27 m along the arc length. Then, the curvature shows a decreasing trend. If the bend stiffener is not applied with the umbilical, the maximum curvature happens on the umbilical end. The location of the maximum curvature moves towards the middle segment along the umbilical by the influence of the bend stiffener. The decrease rate of the umbilical increases after 0.45 m, which is the length of the root of the bend stiffener. The outer diameter of the bend stiffener decreases at the location of 0.45 m along the arc length.

The value and location of the maximum curvature are shown in **Figure 7B**. The maximum curvature increases linearly with increasing swing angle. The location of the maximum curvature moves to the end side with increasing swing angle. The test results show that the location of the maximum curvature of the umbilical is not at the same place with the change of swing angle, the area in which the maximum curvature lays is determined. Rigorous monitoring of the umbilical should be conducted in this area, such as more dense distribution of sampling points and damage monitoring of the umbilical.



The Influence of the Tensile Load on the Curvature

Test 4 was conducted with a constant swing angle of 8° and the tensile load changes. The test results are shown in **Figure 8**. **Figure 8A** shows the curvature of the umbilical with different tensile loads and the same swing angle of 8°. The maximum curvature and its location are shown in **Figure 8B**. The result shows that the curvature increases linearly with increasing tensile load. The location where the maximum curvature happens differs with the different tensile loads. The maximum curvature location decreases with the increasing tensile load. With the increase of the tensile load from 40 to 80 kN, the location of the maximum

curvature moves from 0.27 to 0.15 m along the arc length. When the tensile load is larger than 80 kN, the location stays stable with the increasing tensile load.

CONCLUSION

In conclusion, a new measurement method based on OFDR technology was developed for monitoring the maximum curvature in the dynamic umbilical fatigue test. A tension-bending test was conducted to verify the feasibility of this method. The experimental results of this study lead to the following conclusions:

- (i) The distributed OFDR technology was proved to be feasible to measure the curvature of the umbilical inside a bend stiffener in a prototype fatigue test. The maximum curvature and its location can be measured successfully by utilizing this method.
- (ii) The curvature of the umbilical measured by the fiber-optic sensor is different from the direct displacement measure outside the bend stiffener.
- (iii) The maximum curvature of the umbilical increases linearly with increasing tensile load and swing angle.
- (iv) The location of the maximum curvature is in a specific area instead of a fixed point with the change of tensile load and swing angle. The location of the maximum curvature moves to the end side of the umbilical with increasing tensile load and swing angle.

DATA AVAILABILITY STATEMENT

The original contributions presented in the study are included in the article/supplementary material; further inquiries can be directed to the corresponding author.

REFERENCES

- Caire, M., and Vaz, M. A. (2017). A Nonlinear Viscoelastic bend Stiffener Steady-State Formulation. *Appl. Ocean Res.* 66, 32–45. doi:10.1016/j.apor.2017.05.008
- Caire, M., Vaz, M. A., and Ferreira da Costa, M. (2016). Bend Stiffener Nonlinear Viscoelastic Time Domain Formulation. *Mar. Structures* 49, 206–223. doi:10.1016/j.marstruc.2016.08.001
- Eickhoff, W., and Ulrich, R. (1981). Optical Frequency Domain Reflectometry in Single-mode Fiber. *Appl. Phys. Lett.* 39, 693–695. doi:10.1063/1.92872
- Feng, W.-Q., Yin, J.-H., Borana, L., Qin, J.-Q., Wu, P.-C., and Yang, J.-L. (2019). A Network Theory for BOTDA Measurement of Deformations of Geotechnical Structures and Error Analysis. *Measurement* 146, 618–627. doi:10.1016/j.measurement.2019.07.010
- Gao, L., Gong, Y., Liu, H., Ji, B., Xuan, Y., and Ma, Y. (2018). Experiment and Numerical Study on Deformation Measurement of Cast-In-Place Concrete Large-Diameter Pipe Pile Using Optical Frequency Domain Reflectometer Technology. *Appl. Sci.* 8, 1450. doi:10.3390/app8091450
- Gautam, A., Kumar, A., Singh, R. R., and Priye, V. (2016). Optical Sensing and Monitoring Architecture for Pipelines Using Optical Heterodyning and FBG Filter. *Optik* 127 (20), 9161–9166. doi:10.1016/j.ijleo.2016.06.133
- He, Y., Hernández, I. D., Vaz, M. A., and Caire, M. (2020a). Estimation of Flexible Riser Curvature Distribution and bend Stiffener Polyurethane Behavior Using the Levenberg-Marquardt Algorithm in Full Scale Bending-Tension Tests. *Ocean Eng.* 216, 108018. doi:10.1016/j.oceaneng.2020.108018
- He, Y., Vaz, M. A., and Caire, M. (2020b). Flexible Riser-bend Stiffener Top Connection Analytical Model with I-Tube, *Mar. Structures* 71, 102707. doi:10.1016/j.marstruc.2020.102707
- Inaudi, D., and Glisic, B. (2010). Long-range Pipeline Monitoring by Distributed Fiber Optic Sensing. *J. Press. Vessel Technol.-Trans. ASME* 132 (0117011). doi:10.1115/1.3062942
- Jia, Z., Wang, Z., Sun, W., and Li, Z. (2019). Pipeline Leakage Localization Based on Distributed FBG Hoop Strain Measurements and Support Vector Machine. *Optik* 176, 1–13. doi:10.1016/j.ijleo.2018.09.048
- Leroy, J.-M., and Estrier, P. (2001). Calculation of Stresses and Slips in Helical Layers of Dynamically Bent Flexible Pipes. *Oil Gas Sci. Tech. - Rev. IFP* 56 (6), 545–554. doi:10.2516/ogst.2001044
- Li, B., Wang, H., Shen, X., Yang, D., Jiang, S., and Xu, L. (2011). *Research on Strain Measurement of Abyssal Riser with FBG Sensors[M]*. Berlin, Heidelberg: Springer, 505–512. doi:10.1007/978-3-642-25553-3_62
- Li, H.-N., Yi, T.-H., Ren, L., Li, D.-S., and Huo, L.-S. (2014). Reviews on Innovations and Applications in Structural Health Monitoring for Infrastructures. *Struct. Monit. Maintenance* 1 (1), 1–45. doi:10.12989/smm.2014.1.1.001
- Matveenko, V. P., Kosheleva, N. A., Shadakov, I. N., and Voronkov, A. A. (2018). Temperature and Strain Registration by Fibre-Optic Strain Sensor in the Polymer Composite Materials Manufacturing[J]. *Int. J. Smart Nano Mater.* 9 (2), 99–110. doi:10.1080/19475411.2018.1450791
- Moffat, R., Sotomayor, J., and Beltrán, J. F. (2015). Estimating Tunnel wall Displacements Using a Simple Sensor Based on a Brillouin Optical Time Domain Reflectometer Apparatus. *Int. J. Rock Mech. Mining Sci.* 75, 233–243. doi:10.1016/j.ijrmms.2014.10.013
- Ren, L., Jia, Z.-g., Li, H.-n., and Song, G. (2014). Design and Experimental Study on FBG Hoop-Strain Sensor in Pipeline Monitoring. *Opt. Fiber Tech.* 20 (1), 15–23. doi:10.1016/j.yofte.2013.11.004
- Ren, L., Jiang, T., Jia, Z.-g., Li, D.-s., Yuan, C.-l., and Li, H.-n. (2018). Pipeline Corrosion and Leakage Monitoring Based on the Distributed Optical Fiber Sensing Technology. *MEASUREMENT* 122, 57–65. doi:10.1016/j.measurement.2018.03.018
- Ruan, W., Bai, Y., and Yuan, S. (2017). Dynamic Analysis of Unbonded Flexible Pipe with bend Stiffener Constraint and Bending Hysteretic Behavior. *Ocean Eng.* 130, 583–596. doi:10.1016/j.oceaneng.2016.12.019
- Tang, M., Yan, J., Chen, J., Yang, Z., and Yue, Q. (2015). Nonlinear Analysis and Multi-Objective Optimization for bend Stiffeners of Flexible Riser. *J. Mar. Sci. Technol.* 20 (4), 591–603. doi:10.1007/s00773-015-0314-5
- Vaz, M. A., de Lemos, C. A. D., and Caire, M. (2007). A Nonlinear Analysis Formulation for Bend Stiffeners. *J. Ship Res.* 51 (3), 250–258. doi:10.5957/jsr.2007.51.3.250
- Wu, J., Jiang, H., Su, J., Shi, B., Jiang, Y., and Gu, K. (2015). Application of Distributed Fiber Optic Sensing Technique in Land Subsidence Monitoring. *J. Civil Struct. Health Monit.* 5, 587–597. doi:10.1007/s13349-015-0133-8

AUTHOR CONTRIBUTIONS

YY was responsible for experiment test and writing; PY conducted the experiment test; ZJ contributed to the methodology; SW reviewed the work; QL and JY were responsible for funding acquisition; QY supervised the study. All authors have read and agreed to the published version of the manuscript.

FUNDING

This research was financially supported by the National Natural Science Foundation of China (No. U1906233 and No. 52001088), Major Scientific and Technological Innovation Projects in Shandong Province (No. 2019JZZY010801), Research and Development Projects in Key Areas of Guangdong Province (No. 2020B1111040002), and Fundamental Research Funds for the Central Universities (DUT21JC21, DUT19ZD204, and 3072020CF0703).

Conflict of Interest: The authors declare that the research was conducted in the absence of any commercial or financial relationships that could be construed as a potential conflict of interest.

Publisher's Note: All claims expressed in this article are solely those of the authors and do not necessarily represent those of their affiliated organizations, or those of the publisher, the editors and the reviewers. Any product that may be evaluated in this article, or claim that may be made by its manufacturer, is not guaranteed or endorsed by the publisher.

Copyright © 2021 Yin, Yu, Jia, Wu, Lu, Yan and Yue. This is an open-access article distributed under the terms of the Creative Commons Attribution License (CC BY). The use, distribution or reproduction in other forums is permitted, provided the original author(s) and the copyright owner(s) are credited and that the original publication in this journal is cited, in accordance with accepted academic practice. No use, distribution or reproduction is permitted which does not comply with these terms.



Seismic Performance and Strengthening of Purlin Roof Structures Using a Novel Damping-Limit Device

Baokui Chen, Bao Jia, Ming Wen* and Xiaodong Li

School of Civil Engineering and Architecture, Nanchang University, Nanchang, China

OPEN ACCESS

Edited by:

Liang Ren,
Dalian University of Technology, China

Reviewed by:

Biao Hu,
Shenzhen University, China
Zhifang Dong,
Xi'an University of Architecture and
Technology, China

*Correspondence:

Ming Wen
wmnpu@163.com

Specialty section:

This article was submitted to
Structural Materials,
a section of the journal
Frontiers in Materials

Received: 10 June 2021

Accepted: 05 August 2021

Published: 13 August 2021

Citation:

Chen B, Jia B, Wen M and Li X (2021)
Seismic Performance and
Strengthening of Purlin Roof Structures
Using a Novel Damping-Limit Device.
Front. Mater. 8:722018.
doi: 10.3389/fmats.2021.722018

Purlin roof structure houses, which have the advantages of readily accessible materials and simple construction, are widely used in rural areas of China. However, during earthquakes, the wooden purlins tend to fall off and the walls crack. Therefore, it is necessary to monitor the structural parameters of and strengthen the anti-seismic capacity of these structures. To compensate for the seismic deficiencies of the purlin roof structure, a novel damping-limit device installed at the connection position of the gable and the wooden purlin was proposed. In this study, the seismic performance and reinforcement effect of the brick-wood structure with the purlin roof were analyzed through numerical simulation. The research results indicate that the novel damping-limit device proposed in this study can significantly reduce the local stress concentration and the seismic response of the structure, and thereby rectifying the seismic defect of falling purlin. Moreover, compared with the traditional strengthening method, the novel device is more convenient to install and the reinforcement quality is easier to ensure.

Keywords: purlin roof, brick-wood structure, seismic performance, seismic strengthening, damping-limit, numerical simulation

INTRODUCTION

China's rural traditional residential buildings have distinctive regional characteristics and are a precious part of the country's material cultural heritage. Due to the geographical and regional cultural differences, there are variations in the structural forms of China's rural houses. In rural areas of southern China, especially Jiangxi, Anhui, Hunan, Hubei, and other provinces, the brick-wood structure house with purlin roof is a popular residential form. With this structural form, the bearing wall is built into a triangle of single or double slope based on the needs of the roof. The wooden purlins are directly lapped on and supported by the gable. The wooden rafters are laid on the purlins, then the tiles are laid on the wooden rafters. The weight of the roof can be transmitted by the purlins to the gable to bear, and then support the entire weight of the roof. With their simple construction, readily available material, and low cost, these buildings are widespread in the rural areas of southern China.

Nevertheless, studies have found that the purlin roof structure is vulnerable to severe damage from earthquakes. The authors visited hundreds of villages in Jiangxi Province and found that purlin roof structure houses are widespread. Most of them predate the 1980s and lack seismic structural measures, so their seismic resistance is clearly insufficient. A survey (Zhu et al., 2016) on the safety of more than 500 brick-wood structure houses in Hunan Province, China, found that 53% of the houses

had unsafe individual components, and 12% were partly or completely dilapidated. The roof and the bearing walls are overlapped only by the wooden purlins through the wall, and the purlins are not constrained. As a result, during an earthquake, the seismic inertia force is transmitted to the purlins, resulting in excessive displacement that knocks them off. In addition, stress concentration occurs at the top of the gable, resulting in the wall's partial or even total collapse. Moreover, most of these buildings were built in the 1970s and 1980s, and have been in disrepair for years. The walls are row-lock cavity walls and made of mixed-use brick and adobe masonry. These defects compromise the global stability of the walls. Consequently, there is an urgent need to enhance the earthquake resistance of this type of house, which can not only protect the safety of the lives and property of rural residents but also help maintain the traditional architectural style of the countryside.

In the past decade, many scholars have researched the seismic performance and failure mechanism of unreinforced masonry (URM) structures (Park et al., 2009; Mendes et al., 2014; Derakhshan et al., 2020). An and Li (2020) analyzed the seismic damage of brick-wood structure buildings in the M_s 6.5 Ludian earthquake in Yunnan, China, and found that under the action of seismic load, vertical cracks first appeared at the junction of vertical and horizontal walls and under beams and purlins. Masonry at the junctions and corners of longitudinal and cross walls are prone to break away, leading to partial or complete collapse. Korkmaz et al. (2010) studied the seismic performance and damage characteristics of traditional Turkish houses. They found that the causes of widespread damage of masonry buildings in the recent earthquakes in Turkey are low tensile and shear strength of masonry, inferior mortar, the haphazard layout of openings which led to stress concentration, and construction defects such as using substandard materials and leaving unfilled joints in the masonry. Varum et al. (2018) studied the seismic performance of buildings after the M_W 7.8 Gorkha earthquake in Nepal in 2015. They found that, in most URM buildings, the orthogonal walls showed incompatible deformations due to a lack of proper connection between them, evidence of poor integrity. Furthermore, due to an absence of integration among structural components, out-of-plane failures were more serious than any other type of failure.

To solve the problem of insufficient seismic capacity of URM structures, many mature seismic consolidation technologies have been used around the world. Common seismic strengthening measures include adding cement mortar surface reinforced with steel mesh, adding ring beams and constructional columns (Xuan et al., 2016), and fiber reinforced polymer (FRP) (ElGawady et al., 2006; Saleem et al., 2016). Moreover, the high ductile concrete (HDC) developed by Deng et al. (2020a), Deng et al. (2020b) based on the engineered cementitious composite design principle is durable, strong, and resistant to cracks. Many experimental studies have shown that plastering HDC on masonry walls can significantly improve a structure's bearing capacity, ductility, and crack resistance. Shabdin et al. (2018), Basili et al. (2019) carried out a diagonal compression test and tension test, respectively, on the response of masonry walls strengthened with textile

reinforced mortar (TRM). The tests found that the shear strength, diagonal load carrying capacity, and deformation capacity of the wall were significantly improved after the TRM was applied to the surface of the masonry wall, and the improvement was even greater with double-sided plastering. Borri et al. (2011) conducted an experimental study on masonry panels to investigate the effectiveness of an alternative shear reinforcement technique, based on the use of high-strength steel cords embedded in a cementitious matrix. Their results revealed a significant increase in shear strength and stiffness, so the technique is more effective in low shear strength masonry.

The consolidation measures mentioned above are aimed at the reinforcement of load-bearing walls; there has been little research on the improvement of the walls at the peak of the gables and the wooden roof truss systems. The gable peak and the purlin roof are easily damaged by earthquakes, so protecting them will improve the safety of building residents, and of their property. There is an urgent need to enhance the research on the retrofitting of gable peaks and the purlin roof system in the hope of preventing their collapse.

The seismic strengthening of traditional rural houses in southern China was investigated. It was found that most of the purlin roof structures "wear coats and hats:" cement mortar layer is used to strengthen the wall, and the roof materials are replaced with more durable glazed tiles and resin tiles. However, this approach is time-consuming and expensive, and is mostly done by unskilled construction teams. The construction quality is difficult to guarantee, and it fails to strengthen the weak connection between the wooden purlins and the gables, and the stress concentration at the joint. Aiming at the hidden dangers of seismic safety of the purlin roof structures, this paper proposes a novel damping-limit device, which is installed where the wooden purlin overlaps with the load-bearing wall. The device can not only limit the displacement between the wood purlin and the wall, prevent the purlin from falling, but also improve the toughness, and seismic capacity of the house. The laminated rubber material can significantly reduce the response of the house under the longitudinal seismic load and weaken the stress concentration at the joint. In addition, compared with the traditional strengthening method, the device's quality is easy to control because it can be mass-produced in a factory. The installation process is also simple, so the quality of the reinforcement quality can be guaranteed.

ENGINEERING EXAMPLE

In this study, a typical brick-wood structure house with purlin roof in Jiangxi Province, China, (**Figure 1**) was taken as an engineering example. The two-story purlin roof structure house was built in the 1980s. The height of the first floor, the second floor, and the gable are 3, 2.4, and 2 m respectively; the walls are 240 mm thick. There is no floor between the first and the second floor, only simple boards for stacking grain or sundries. The house opens on three sides and has a double slope roof structure. The walls are built with ordinary clay bricks and adobe masonry

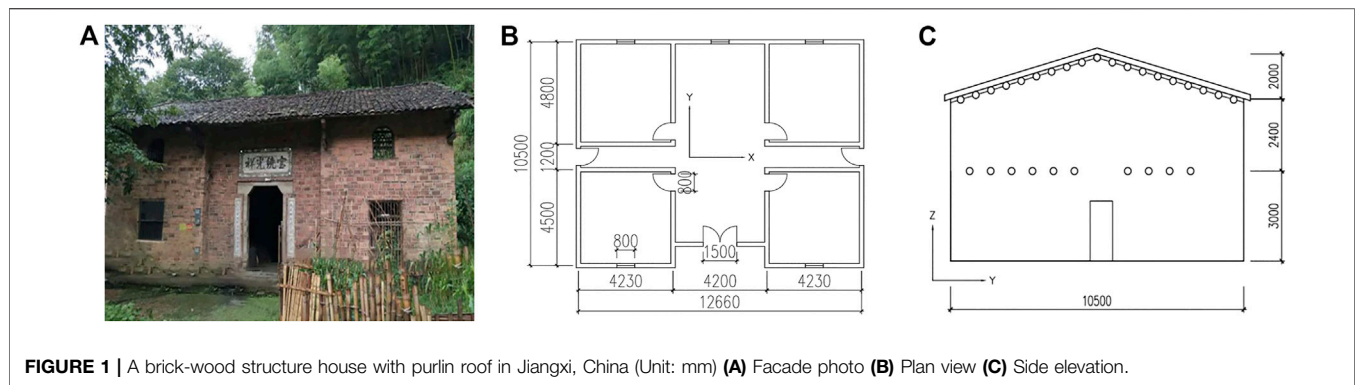


FIGURE 1 | A brick-wood structure house with purlin roof in Jiangxi, China (Unit: mm) **(A)** Facade photo **(B)** Plan view **(C)** Side elevation.

and are mostly row-lock cavity walls. Furthermore, the house does not set ground beams, ring beams, and constructional columns, so the structural integrity is not good. Considering that the house has been used for a long time, mortar, and masonry have substantial aging and strength reduction, so enhancing the stability of the house wall is the key content of reinforcement and transformation. Besides, the roof system is to put wooden purlins with a diameter of 200 mm and a length of more than 4 m on the gable wall, and then the slats and tiles are laid on the purlins. Some of the tiles have been damaged. In the subsequent retrofitting process, the roof system needs to be carefully inspected. For problems such as the unreliable overlap or docking of the wooden purlins in the house, additional iron parts such as nails are used for reinforcement, and the damaged roof tiles are replaced.

NUMERICAL SIMULATION

Simulation Method

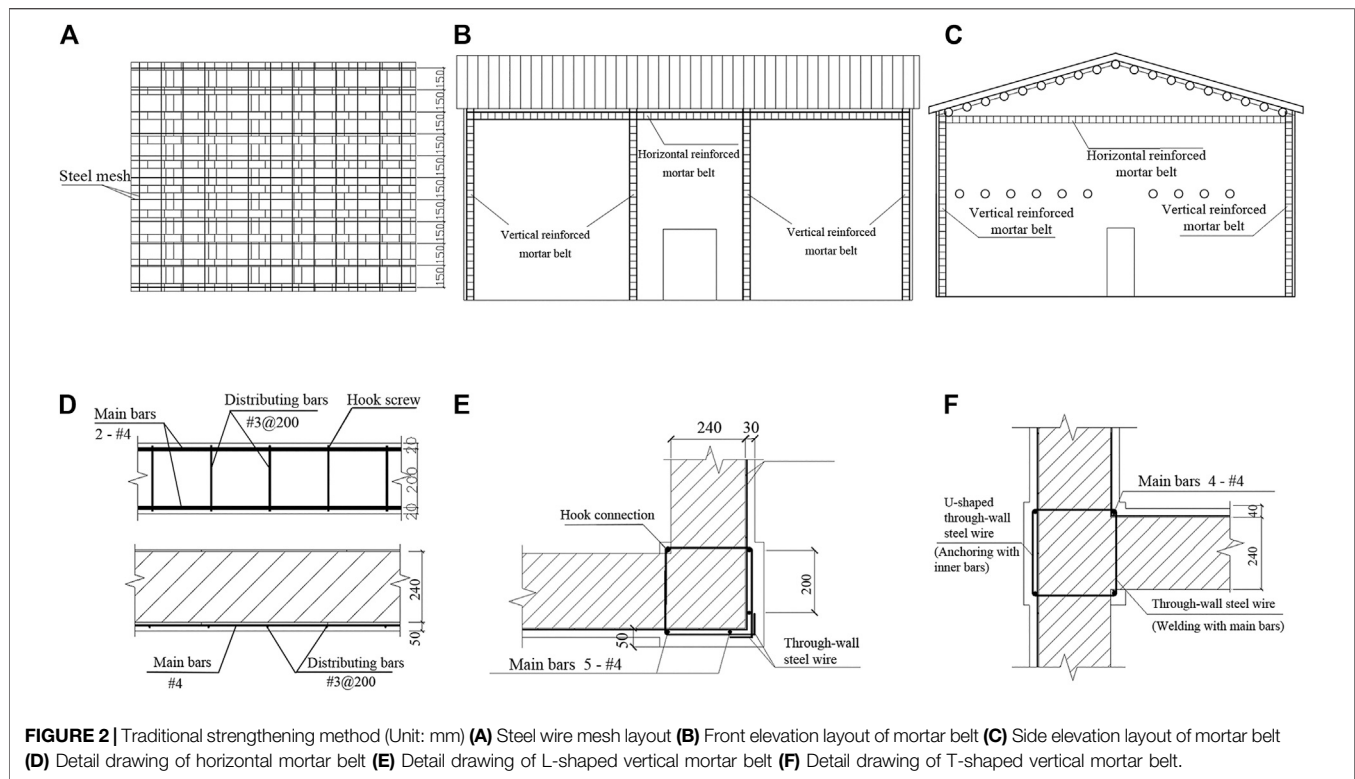
Masonry structure research is based on experimental research and numerical simulation; the latter has the advantages of high efficiency, low cost, and is suitable for repeated tests and optimization analysis. Therefore, numerical simulation is used in many fields of earthquake engineering research (Masi et al., 2013; Wang et al., 2020; Chen et al., 2021). ADINA, a well-known finite element analysis software program, has powerful functions such as the stable solution of nonlinear analysis, and multi-physics simulation, so it can quickly solve complex nonlinear problems with almost absolute convergence. Accordingly, this paper adopted ADINA to carry out finite element numerical simulation on the purlin roof structure and established three types of working condition models: 1) the unreinforced original structure; 2) the traditional strengthening model reinforced with steel mesh cement mortar layer and reinforced mortar belt; and 3) the new strengthening model reinforced with the damping-limit device. Through modal analysis and seismic response analysis, the seismic performance, and damage characteristics of brick-wood structures were analyzed, the seismic responses of the structure before and after consolidation were compared, and the effects of traditional and new strengthening methods were discussed.

In general, there are two kinds of masonry wall simulation: integral modeling and separate modeling (Ma et al., 2001). Integral modeling simplifies the entire masonry wall, treats the masonry and mortar as the same material, ignores the interaction between them, and simulates it as a whole, which is suitable for the finite element analysis of large-scale structures. Separate modeling models the brick and mortar separately, considering the interaction between them. It is suitable for small-scale finite element analysis considering masonry failure mechanism, such as a single wall. Due to the complexity of the row-lock cavity wall and the large scale of the structure, this paper used integral modeling to establish the finite element model of the brick-wood structure. In addition, through the equivalent method, the wall thickness of the model was adjusted to 190 mm to improve the rationality of the row-lock cavity wall modeling and give the model the same dynamic characteristics as the actual structure.

Traditional Strengthening Model

The external walls of this kind of structure are composed of a mixture of brick masonry and adobe masonry. In this model, the brick masonry is reinforced with the outer steel mesh cement mortar surface layer. The vertical and horizontal steel wire diameter is 3 mm, and the spacing is 150 mm (Figure 2A). The hook screw is used for the steel mesh anchorage, and the spacing is not more than 300 mm. The adobe masonry part is enhanced by a double-sided steel mesh cement mortar surface. The vertical and horizontal steel wire diameter of the steel wire is also 3 mm, and the spacing is 120 mm. The mesh is anchored by steel wire with a diameter of 4 mm through the wall, and the spacing is not more than 500 mm. After the steel mesh is bound, cement mortar with a thickness of 20–30 mm and a strength grade of M10 is sprayed on or pressed into it.

Moreover, in the traditional strengthening method of this kind of structure, the horizontal reinforced mortar belts are arranged around the walls at the height of the cornice, and the vertical reinforced mortar belts are arranged at the corners of the walls and the junctions of the vertical and horizontal walls. This arrangement is similar to that of ring beams and structural columns, which can enhance the integrity and seismic performance of the house. Their layout positions are shown in Figures 2B,C. The height of the reinforced mortar belt is 240 mm and the thickness is 50 mm. Detailed drawings of two types of



reinforced mortar belts are shown in **Figures 2D–F**, in which the vertical reinforced mortar belt is divided into “L” and “T” shapes.

Novel Strengthening Model

In the previous surveys and earthquake damage analysis of rural residences, it was found that the triangular wall at the top of the brick-wood structure lacks a reliable tie, and the wooden purlins provide only limited longitudinal rigidity. In an earthquake, the wooden purlins are prone to slip or even fall off, and the walls collapse out of the plane. Finite element numerical simulation found a serious stress concentration between the wood purlin and the wall under the seismic load, leading to the partial or even complete failure of the gable peak. The seismic performance of the building is greatly reduced.

This study proposes a new type of damping-limit device for the seismic safety of the purlin roof structure. In the new strengthening model, 38 damping-limit devices were installed at the overlap joint of gables and wooden purlins on both sides of the original structure. The device is composed of a rubber partition layer and two identical steel gaskets with thicknesses of 20 and 10 mm, respectively. The rubber partition layer is square and steel gaskets with the same cross-section shape are connected on both sides of the rubber partition layer. The wooden purlin is passed through the rubber vibration isolation pad, and the purlin, rubber, and steel plate are bolted together, so that the purlin and the rubber vibration isolation pad are under the same force. When the seismic wave energy is transmitted to the wooden purlin, it will be dissipated through the rubber partition layer. The acceleration of the purlins and the structure on them is greatly reduced, so when the compression

and impact on the wall are relieved, the stress concentration phenomenon at the contact part and the cracking of the wall are also significantly alleviated. **Figure 3** shows the specific structure and installation diagram of the device.

Material Properties

In this study, the masonry was regarded as homogeneous and isotropic material, and the influence of the mortar joint was considered only from the average, but the interface behavior between masonry and mortar was not considered. The stress-strain relationship of masonry under uniaxial compression proposed by Liu (2005) was adopted as the constitutive relationship of masonry:

$$\frac{\sigma}{f_m} = 1.96 \left(\frac{\varepsilon}{\varepsilon_0} \right) - 0.96 \left(\frac{\varepsilon}{\varepsilon_0} \right)^2, 0 \leq \left(\frac{\varepsilon}{\varepsilon_0} \right) \leq 1 \quad (1)$$

$$\frac{\sigma}{f_m} = 1.2 - 0.2 \left(\frac{\varepsilon}{\varepsilon_0} \right), 1 < \left(\frac{\varepsilon}{\varepsilon_0} \right) \leq 1.6 \quad (2)$$

Where σ and ε are the stress and strain of the masonry under compression, f_m is the average value of the axial compressive strength of the masonry, and ε_0 is the maximum strain corresponding to the maximum compressive stress, that is, the peak strain. **Table 1** shows some main parameters of masonry materials.

As a natural growth material, wood's mechanical properties show obvious anisotropy. At the same time, it is affected by factors such as the growth environment, so the performance varies greatly. Therefore, this paper adopted the mechanical properties of the wood under the general ideal state, and referred to the literature (Ding, 2015) to obtain the parameters

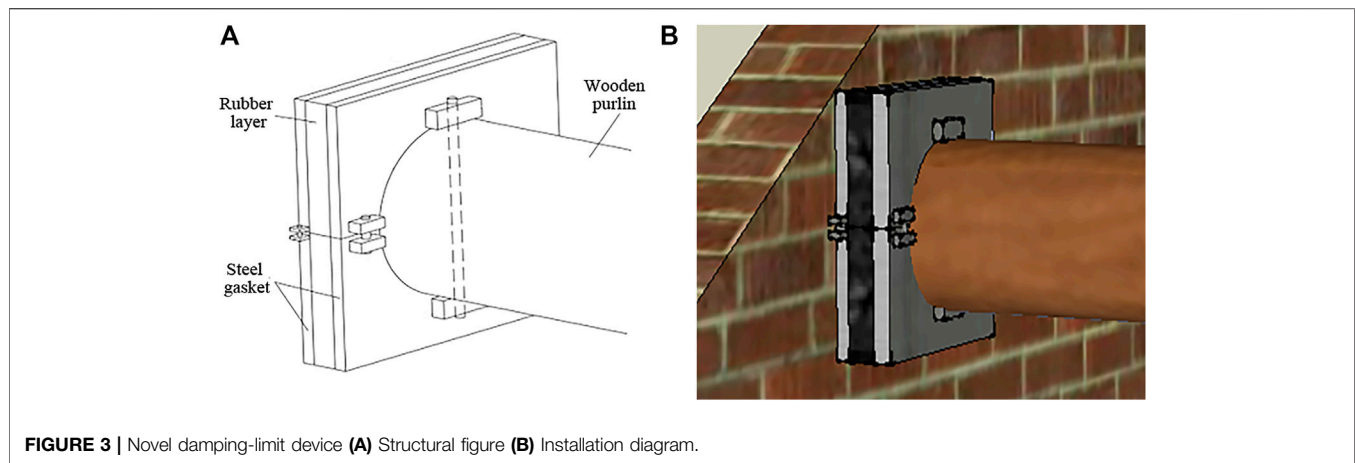


FIGURE 3 | Novel damping-limit device **(A)** Structural figure **(B)** Installation diagram.

TABLE 1 | Masonry material parameters.

Compressive strength (MPa)	Tensile strength (MPa)	Peak strain	Young's modulus (MPa)	Poisson ratio	Density (kg/m ³)
3.33	0.315	0.003	2,400	0.15	2000

TABLE 2 | Wooden purlin material parameters.

E_L	E_R	E_T	μ_{TL}	μ_{RT}	μ_{LR}	G_{LR}	G_{RT}	G_{TL}
9,702	1955	1955	0.52	0.352	0.106	971	218	609

of the purlin (**Table 2**). In the table, E_L , E_R , and E_T are the along-grain, transverse-grain tangential, and transverse-grain radial modulus of elasticity (MPa), respectively. μ_{TL} , μ_{RT} , and μ_{LR} are the along-grain radial, transverse-grain radial, and transverse-grain tangential Poisson ratio of the purlin, respectively. G_{LR} , G_{RT} , and G_{TL} are the longitudinal and tangential, radial and longitudinal, tangential and radial shear modulus (MPa) of the purlin, respectively.

Rubber is a hyperelastic material that is, almost incompressible, with a Poisson ratio close to 0.5. The elastic modulus of this kind of material changes constantly in the process of loading, so the error of using elastic modulus and Poisson's ratio to describe its mechanical properties is large, especially when it has obvious deformation. Accordingly, its mechanical properties need to be described by strain energy function, and the constitutive relation of each material is a special form of strain energy density function. To define this kind of material model, it is necessary to obtain the material stress-strain data or model material constants. The rubber material used in this study adopted the Ogden constitutive model (Başa and Itskov, 1998; Beda, 2005; Kim et al., 2012), which is a rubber material model whose strain energy density is represented by the principal elongation. **Eq. 3** is the expression of its strain energy density.

$$W_D = \sum_{n=1}^9 \left\{ \frac{\mu_n}{\alpha_n} (\lambda_1^{\alpha_n} + \lambda_2^{\alpha_n} + \lambda_3^{\alpha_n} - 3) \right\} \quad (3)$$

TABLE 3 | Rubber material stress-strain data.

Stress (MPa)	-238.5	-103.5	-27.5	0	11.1	28.0	40.9	51.6	61.0
Strain	-0.5	-0.3	-0.1	0	0.1	0.3	0.5	0.7	0.9

where α_n and μ_n are the material constants of the Ogden model, and λ_1 , λ_2 , and λ_3 are the principal elongations in the three directions. **Table 3** shows the stress-strain data fitted by the uniaxial tensile and plane shear test of rubber materials.

Seismic Wave Selection

In this study, three seismic waves were selected for time history analysis of the model: EL-Centro, Taft, and Tianjin. The duration of EL-Centro wave and Taft wave is 40 s and that of Tianjin wave is 20 s. The acceleration time history curves of the three seismic waves in the east-west and north-south directions are shown in **Figure 4**. According to the Chinese code for seismic design of buildings (GB 50011-2010), the seismic fortification intensity of the main distribution areas of this structure is mostly 6 and 7 degrees, and the design basic seismic acceleration is not more than 0.1 g. Consequently, this research only modulated the peak amplitude of each seismic wave to 2.2 m/s², which is the peak acceleration of a rare earthquake of 7 degrees.

ANALYSIS OF CALCULATION RESULTS

Modal Analysis

Modal is the inherent and integral characteristic of the elastic structure. Through the modal analysis method to analyze the

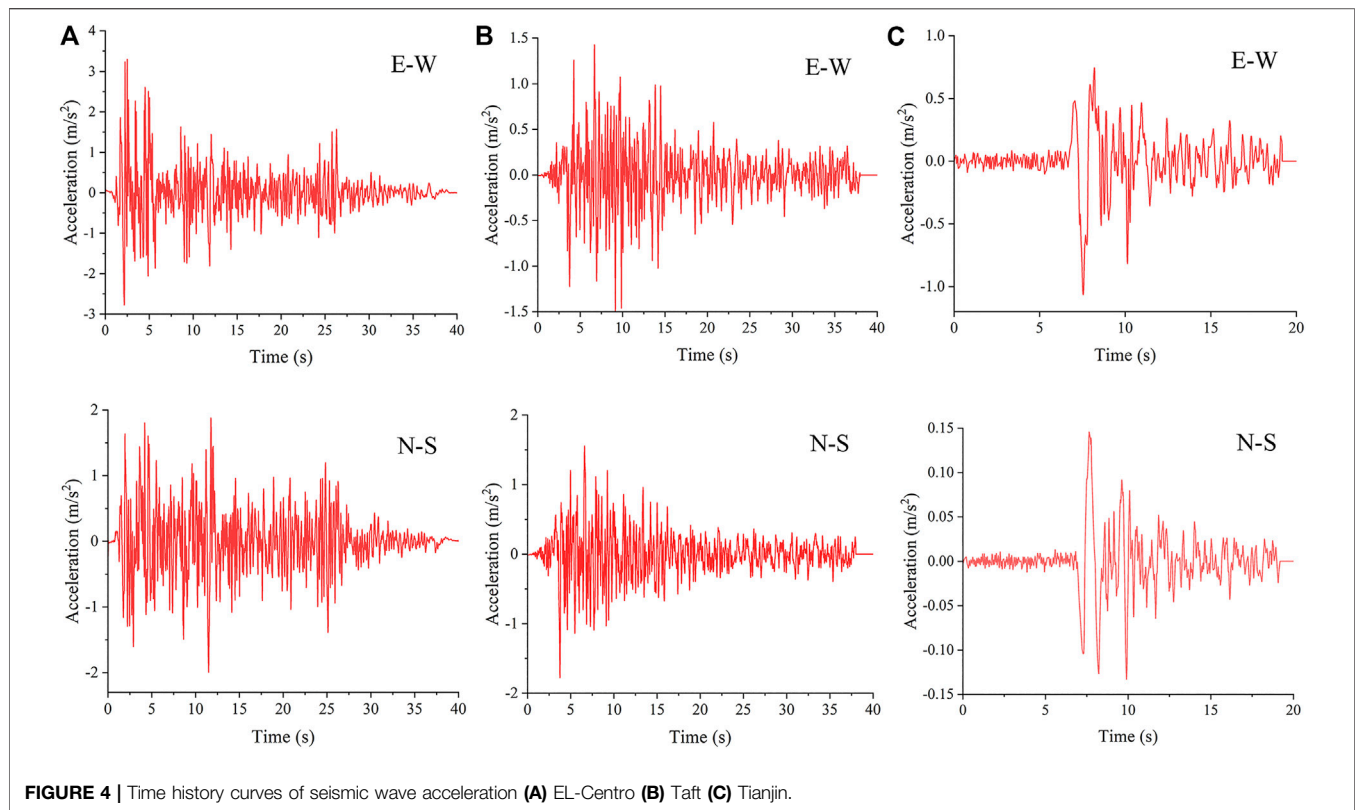


TABLE 4 | Natural period and modal participation coefficient of the original model.

Modal	Frequency (Hz)	Period (s)	Participation coefficient		
			X-direction	Y-direction	Z-direction
1	6.62	0.151	213.6	0.1	0.077
2	7.74	0.129	-56.3	-0.43	-0.48
3	7.99	0.125	-1.58	5.84	43.2
4	8.08	0.124	-2.75	1.64	-37
5	8.16	0.123	2.88	1.56	5.19
6	8.21	0.122	-9.19	-2.86	-2.3

features of the main modes of the structure in a certain susceptible frequency range, the actual vibration response generated by external or internal vibration sources in this frequency band can be inferred (Qu et al., 2017; Qu et al., 2018). In ADINA, by calculating the participating coefficients of each mode in the X, Y, and Z directions, the size relation of the influence coefficient of each mode in each direction is judged. Based on the modal frequency response theory, the dynamic stiffness of the response point is the superposition and coupling of the displacement of each mode to the point. The contribution of the modal to the displacement of the point is the modal participation factor. Through the frequency response analysis, we can find out the peak of some frequencies. Modal participation factor analysis can identify which main modal responses are superimposed at the peak frequency, and output several modes with large modal contribution according to the requirements, and

optimize the design according to the modal shapes. **Tables 4–6** respectively show the natural vibration period and modal participation coefficient of the first six modes of the three types of working condition models.

Yang et al. (1982) present the following empirical formula for the natural period of masonry structure:

$$T_1 = 0.0168(H_0 + 1.2) \quad (4)$$

Where T_1 is the basic period and H_0 is the height of the structure. According to the formula, $T_1 = 0.0168 \times (7.4 + 1.2) = 0.144$ s, which is close to the numerical simulation result of 0.151 s with an error of less than 5%, proving that the numerical simulation model is reasonable to a certain extent. Unlike other structures, the shaking table tests of the brick-wood structure are rare, and the numerical results in this study are only compared with the theoretical solution of the basic period of the masonry structure to verify the model.

TABLE 5 | Natural period and modal participation coefficient of the traditional strengthening model.

Modal	Frequency (Hz)	Period (s)	Participation coefficient		
			X-direction	Y-direction	Z-direction
1	6.68	0.150	0.193	1.05	17.1
2	6.74	0.148	-2.72	-1.44	-22.9
3	6.75	0.148	0.081	0.69	11.0
4	6.76	0.148	2.08	0.56	12.08
5	6.77	0.148	0.097	1.56	5.19
6	6.78	0.147	0.11	0.67	9.15

TABLE 6 | Natural period and modal participation coefficient of the new strengthening model.

Modal	Frequency (Hz)	Period (s)	Participation coefficient		
			X-direction	Y-direction	Z-direction
1	8.200	0.122	0.085	37.27	1.15
2	8.230	0.122	0.95	-59.1	5.91
3	8.280	0.121	3.15	-0.92	-1.29
4	8.283	0.121	1.98	25.6	-1.60
5	8.297	0.121	-2.93	-13.8	-0.39
6	8.300	0.120	-15.8	-45.2	1.13

The modal analysis result of the original structure model shows that it was more inclined to X-direction vibration. This may be because the structure has fewer longitudinal walls, and the top of the gable is constrained only by wooden purlins. Therefore, the X-direction vibration of the structure occurred before the Y-direction vibration, indicating that the X-direction stiffness of the structure is less than the Y-direction stiffness.

From the modal analysis of the traditional strengthening model, the vibration of the model was found to be more inclined to the Z-direction. This shows that the method has better X- and Y-direction constraints on the structure.

From the modal analysis of the new strengthening model, the Y-direction participation coefficient was shown to be greater than that of the X-direction, indicating that adding rubber vibration isolation pad constraints at the junction of the wooden purlin and gable can improve the X-direction's stiffness. Although the new strengthening method is not as comprehensive as the traditional in terms of improving the seismic performance of the structure, the installation of the damping-limit device is simpler and the construction is more convenient.

Displacement Response Analysis

Under the action of seismic waves, the displacement responses of the three structural models were analyzed separately, and the effect of reinforcement was analyzed by comparing the displacement changes with time and height. The model showed the same rule under the action of the three seismic waves. Due to space constraints, some of the diagrams take only the EL-Centro wave as an example to analyze the results.

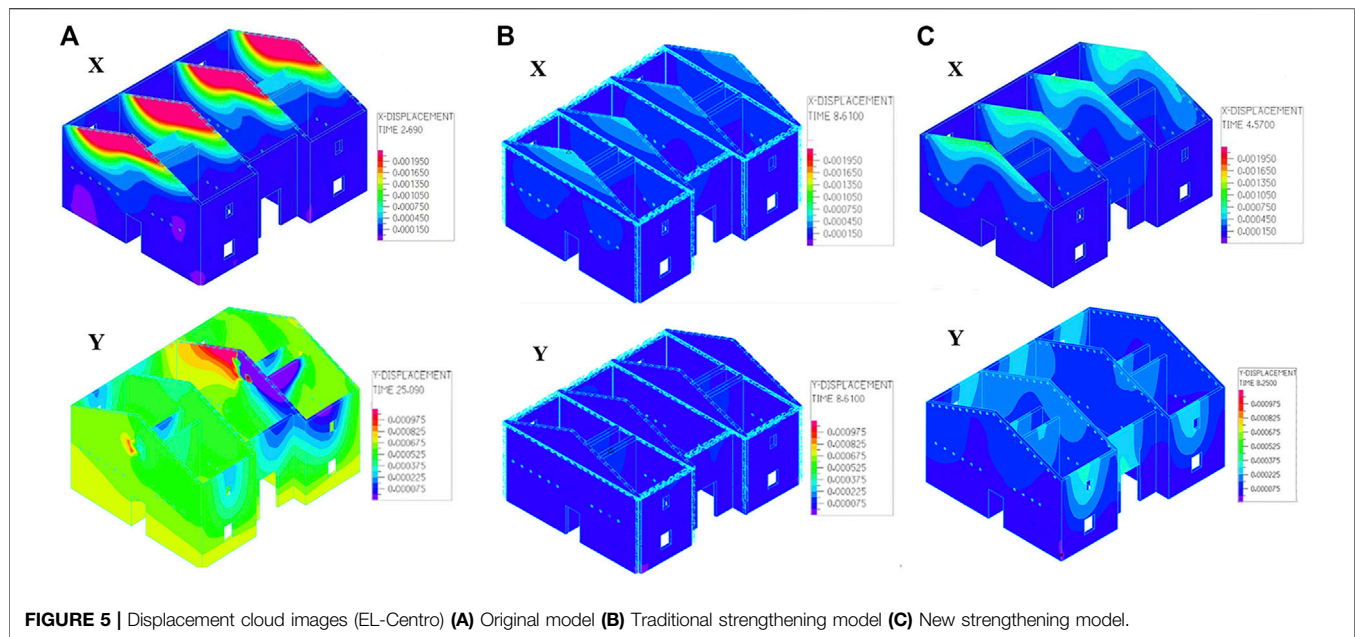
Figure 5 shows the displacement cloud images of the three types of models extracted from ADINA when the maximum displacement occurred in two directions. The figure shows that

the peak values of X-direction displacement of the three structures all appeared at the top of the gable, indicating that the out-of-plane stiffness of the top gable is smaller than that of the lower wall, which was most obvious in the original structure. The displacement image of the new strengthening model was similar to that of the original structure, but the value was much lower than that of the original one. In general, the effect of traditional reinforcement on displacement was the best.

Owing to the increase of the stiffness of the gable after the traditional reinforcement and the energy dissipation effect of the damping-limit device, the excessive displacement of the gable was significantly improved. At the moment of peak displacement, four nodes with larger displacements were selected: the highest node of the left and the middle gable, the cornice node of the front facade, and the highest node of the inner longitudinal wall. We then study the changes in their displacement time history under three conditions.

The displacement curves along the time of the four positions were studied sequentially, as shown in Figure 6. In a bi-directional earthquake, the peak of the gable of the original structure had a large deformation. The displacement time history image shows that the structural displacement tended to be stable after 30 s of ground motion. The lateral displacement of the structure tended to zero in the later stage of the time, and the cornice part remained elastic. Nevertheless, the longitudinal displacement was still vibrating at about 1 mm and did not tend to zero. Compared with the original structure, the longitudinal displacement of the traditional model was reduced about sixfold, and that of the new model was reduced fourfold.

The reasons for this phenomenon are as follows: The gable wall is high, and the cross-sectional area of the wall is greatly reduced. However, the traditional residential structure does not



provide consolidation measures at the gable, rigidity is considerably weakened. The longitudinal rigidity of the original structure is supported only by the wooden purlins, and the inertial force causes the gable to move too much out of the plane. As a result, some of the walls undergo plastic deformation at the later stage of the ground motion, and thus cannot be restored to their initial position. After traditional reinforcement, cement mortar surface layers are added on both sides of the top of the gable. The cement mortar is stronger than brick masonry, which can absorb seismic energy well and increase the out-of-plane stiffness of the gable. In the new strengthening model, the purlin passes through rubber and steel plates, which can increase its contact area with the wall. Moreover, rubber can dissipate the energy generated by seismic inertia force, improve the stress condition of components, and reduce the displacement of the peak of the gable.

Extract the corresponding data to draw the displacement envelope graph as shown in **Figure 7** and the inter-story drift angle as shown in **Table 7**. It was found from the figure that the X-direction displacement of the wall below 5 m of the original structure did not change significantly along with the height, but that of the top of the gable increased suddenly. This is because of the substantial stiffness of the lower part of the cross wall, and the limited displacement under the support of the longitudinal wall, which is more resistant to seismic force. After retrofitting, the displacement of the wall at the whole height, especially at the top, was clearly reduced. In addition, judging by the inter-story drift angle (Jiang et al., 2018), the original structure is close to a moderately damaged state, and the two reinforced structures are in good condition.

Principal Tensile Stress Analysis

To explore the mechanical characteristics of the brick-wood structure under seismic action, the principal tensile stress

cloud image was extracted from ADINA, and the mean principal tensile stress at the peak of the gable was calculated, as shown in **Figure 8** and **Table 8**.

The cloud images show that the stress concentration of the original structure was obvious at the junction of longitudinal and cross walls, the overlap between the purlins and the walls, and the peak of the gable. Some of the walls had exceeded the failure load of the material by 0.33 MPa and are in a state of failure. Among them, the top of the right cross wall in the middle was almost completely destroyed and there was a risk of collapse. The stress response of the lower part of the wall was good, and there was only slight damage at the corner of the window. After the traditional reinforcement, the stress concentration at the junction of the longitudinal and cross walls was significantly improved, and only slight wrecks occurred at the junction of the internal wall. After the strengthening of the damping-limit devices, the stress concentration at the top of the gable was also significantly improved, only minor damage occurred at the overlap of the purlins and the gable, the junction of the walls, and the surrounding of the opening. **Table 8** shows that under the action of the three seismic waves, the mean value of the principal tensile stress at the gable peak of the traditional strengthening model is reduced by about 60% compared with the original structure, while that of the new strengthening model is reduced by about 40%. Both methods reduce the tensile stress at the peak of the gable. Of the two, the improvement effect of the traditional one is more significant, but considering factors such as cost and construction period, the damping-limit device is preferable.

Shear Stress Analysis

Figure 9 and **Table 9** show the shear stress cloud images extracted from ADINA, and the mean value of the shear

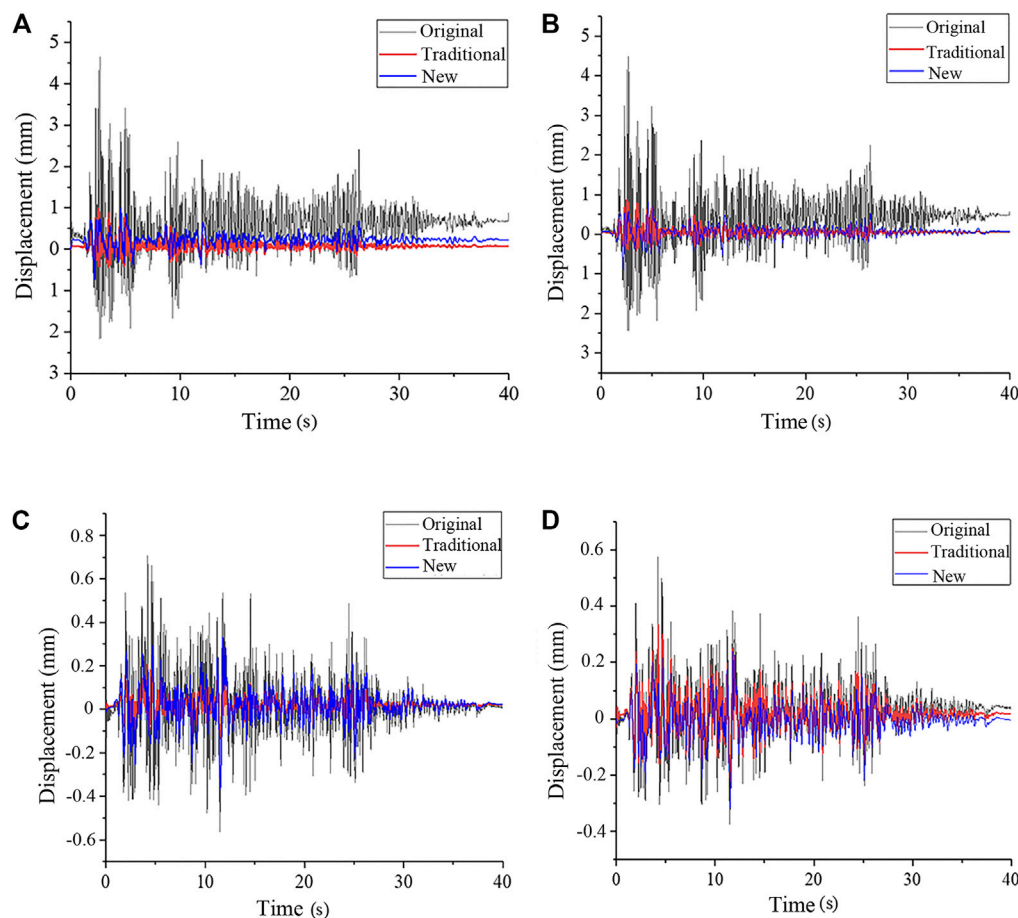


FIGURE 6 | Displacement time history curves of four typical positions (EL-Centro) **(A)** X-displacement of the left gable peak **(B)** X-displacement of the middle gable peak **(C)** Y-displacement of the front facade cornice **(D)** Y-displacement of the inner longitudinal wall peak.

stress at the bottom of the wall under the action of three seismic waves, respectively. The study found that in the original structure, the shear stress concentration at the bottom of the walls, the junction of the longitudinal and cross walls, and the peak of the gable was obvious, especially the peak and the bottom of the right cross wall in the middle had been damaged, and there was a risk of collapse. As the duration of the seismic wave increases, the plastic development became more obvious, and the damaged area at the junction of the walls showed an obvious downward trend. After the traditional reinforcement, only the junction of the internal walls and the openings were slightly damaged, which alleviated the excessive shear stress of the walls, and the mean value of the bottom shear stress was reduced by about 70%. After the new reinforcement, the top of the gable, the junction of the walls, and the openings were slightly damaged, and there was no plastic development phenomenon relative to the original structure. However, the reduction in the mean value of the bottom shear stress was very small, and the shear stress concentration had not been significantly improved compared to the original structure, indicating that the method has a limited effect on the lower part of the wall.

Acceleration Response Analysis

The magnitude of the acceleration reflects the dynamic response of the house under the action of an earthquake. The greater the acceleration, the faster the speed change, and the more unfavorable the structural safety. Draw the acceleration time history curve of the three points A, B, and C, as shown in **Figure 10**.

The X-direction acceleration of the original structure was increased by about 3.6 times compared with the amplitude-modulated seismic wave. The acceleration response was strong, and the range of change was large, which does serious damage to the structure. The traditional reinforcement failed to greatly reduce the acceleration response of the structure in the X-direction, indicating that although the displacement of the top gable was small, the swing speed changed rapidly. The new reinforcement significantly reduced the acceleration response of the wall. The maximum acceleration of the wall in the X-direction was only 1.1 m/s^2 , 50% lower than the acceleration of the seismic wave after amplitude modulation, which has a good shock absorption effect. This is because rubber can cushion the impact and the inertial force of the purlin on the wall. On the longitudinal wall, the acceleration response was far

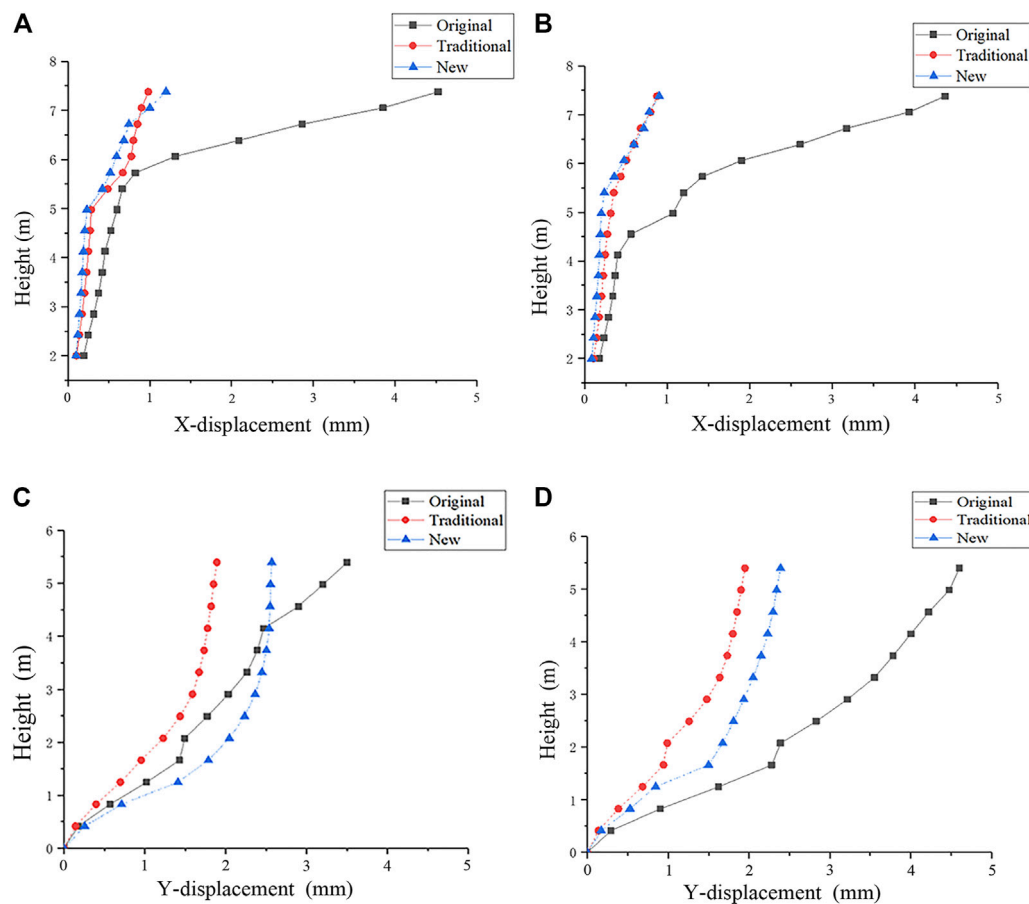


FIGURE 7 | Envelope graphs of wall displacement (EL-Centro) **(A)** X-displacement of the left gable **(B)** X-displacement of the middle gable **(C)** Y-displacement of the front longitudinal wall **(D)** Y-displacement of the inner longitudinal wall.

TABLE 7 | Maximum inter-story drift angle.

Model type	El-centro	Taft	Tianjin
Original	1/518	1/479	1/593
Traditional	1/3984	1/5025	1/8065
New	1/2571	1/1350	1/3745

less intense than that of the horizontal wall. The Y-direction acceleration at the cornice was 1.6 m/s^2 , and the acceleration response was good.

Among the three seismic waves, the EL-Centro wave had the most violent response and the Tianjin wave had the least violent. The X-direction accelerations of the gable peak under the action

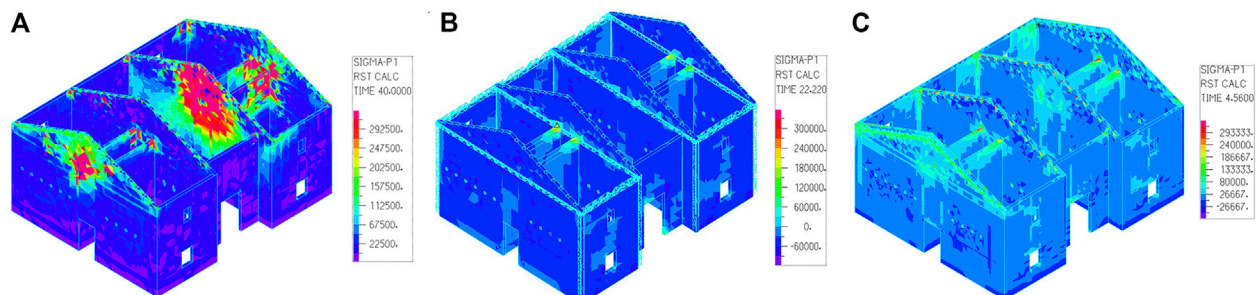
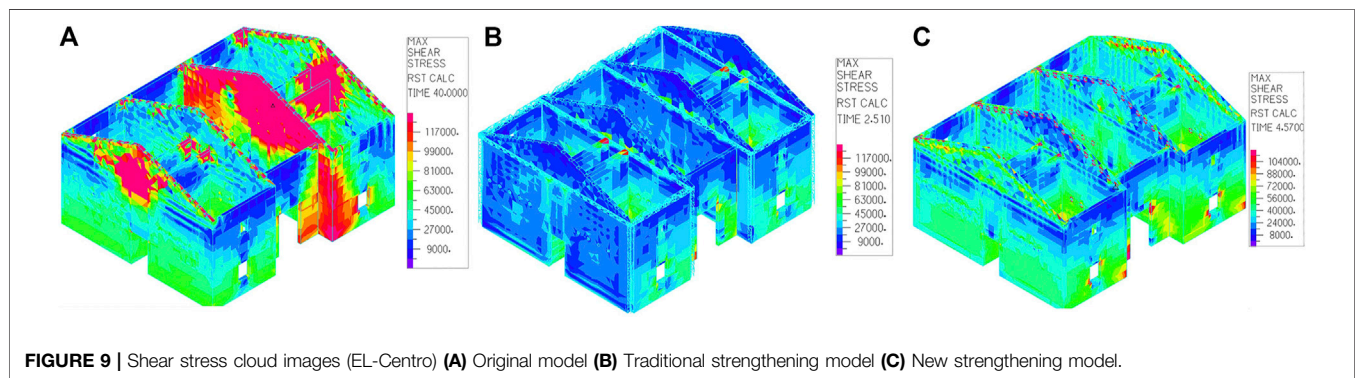


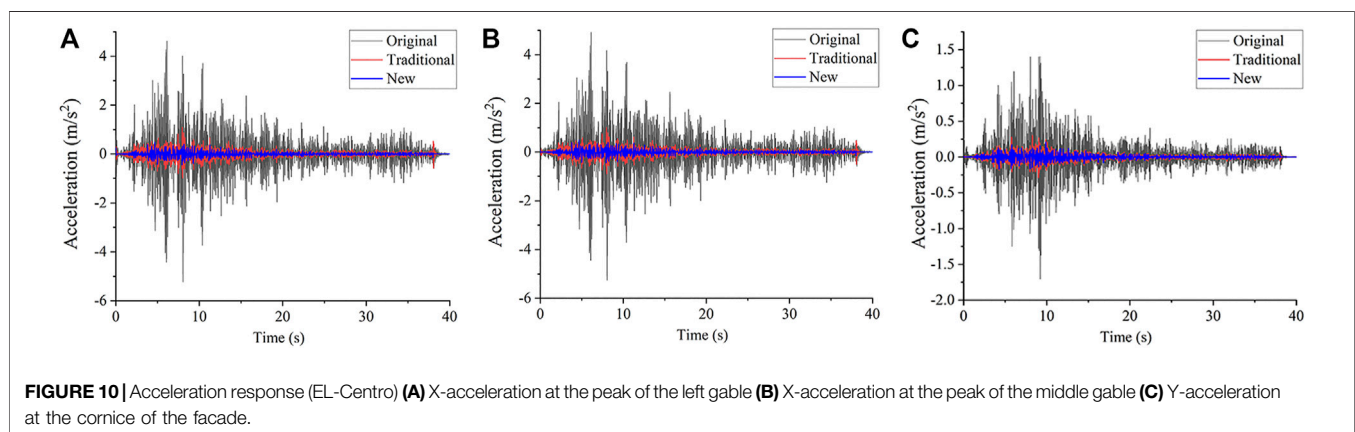
FIGURE 8 | Principal tensile stress cloud images (EL-Centro) **(A)** Original model **(B)** Traditional strengthening model **(C)** New strengthening model.

TABLE 8 | Mean principal tensile stress of the gable peak.

Model type	Seismic wave	Mean principal tensile stress (MPa)	Reduction compared to the original model
Original	EL-Centro	0.36	—
	Taft	0.32	—
	Tianjin	0.27	—
Traditional	EL-Centro	0.13	64%
	Taft	0.13	59%
	Tianjin	0.11	59%
New	EL-Centro	0.21	42%
	Taft	0.19	41%
	Tianjin	0.15	44%

**TABLE 9** | Mean shear stress at the bottom of the wall.

Model type	Seismic wave	Mean shear stress (MPa)	Reduction compared to the original model
Original	EL-Centro	0.081	—
	Taft	0.071	—
	Tianjin	0.067	—
Traditional	EL-Centro	0.027	67%
	Taft	0.021	70%
	Tianjin	0.015	78%
New	EL-Centro	0.072	11%
	Taft	0.066	7%
	Tianjin	0.063	6%



of three seismic waves were 8, 4.3, and 3.1 m/s², respectively. The magnifications were 3.64, 1.86, and 2.58, respectively.

CONCLUSION

In this study, numerical simulation was used to research the seismic performance and reinforcement effect of the brick-wood structure with purlin roof. Three types of models were established by finite element analysis software ADINA: the original structure, the strengthening model using the traditional method, and the strengthening model using the novel damping-limit device. The earthquake responses of the three models were compared, and the main conclusions are as follows:

- 1) The novel damping-limit device proposed in this paper can resolve the anti-seismic defects of the purlin roof structure. First, the device can limit the displacement of the purlins and prevent them from falling. In addition, the stress concentration phenomenon at the connection position of the wooden purlins and the walls was alleviated, and the average value of the main tensile stress at the peak of the gable was reduced by more than 40% compared with the original structure. The displacement and cracking of the gable peak had also been significantly improved, and the longitudinal displacement of this part had been reduced by four times compared with the original model.
- 2) The device has an obvious effect not only on the local but also on the seismic response of the structure. After the new method was used to strengthen the structure, the maximum inter-story drift angle of the structure under the action of the three seismic waves was only 23.8% of the original structure on average. The maximum acceleration of the wall in the X-direction was only 1.1 m/s², about 50% lower than that of the seismic wave after amplitude modulation, indicating that the device also has a good control effect on the acceleration response of the walls. However, it has no obvious influence on the shear stress of the lower part of the walls.
- 3) The study found serious defects in the seismic performance of the unreinforced original structure. The walls, especially the peak of the gables, are prone to excessively large out-of-plane displacement in an earthquake. The maximum inter-story drift angle was 1/479, which has reached a moderately damaged state. Meanwhile, there was obvious stress concentration at the junction of longitudinal and cross walls, the bottom of the walls, and the peak of the gables, all of which are prone to local damage or even collapse.
- 4) The traditional strengthening method has a better effect on reducing the seismic response of structural walls such as displacement and acceleration. Nevertheless, this technique also has obvious disadvantages of being costly and time-consuming. Moreover, most of the work is done by small local engineering teams without construction qualifications, so the quality of reinforcement cannot be guaranteed.
- 5) Since the damping-limit device is developed to reduce the stress concentration at the gable peak and to prevent purlins from falling, it does not increase the stiffness and strength of the bearing walls. Therefore, the control of the stress at the foot of the house and the displacement of the walls is limited, and the reduction of the cracking of the cross walls is also lower than that of the traditional method. However, this method is convenient for construction and it is easy to ensure the quality of reinforcement, which is more suitable for seismic strengthening of rural houses. If this method is combined with local wall strengthening, the overall seismic performance of the structure can be greatly improved. Furthermore, with the development of new building materials, it is possible to consider using materials such as nylon plates instead of steel plates to further reduce the cost and facilitate application.

DATA AVAILABILITY STATEMENT

The raw data supporting the conclusion of this article will be made available by the authors, without undue reservation.

AUTHOR CONTRIBUTIONS

BC conceived the study and designed the research method. BJ wrote the paper and drew the charts. MW made constructive comments on the study. XL build the models and analyzed the data.

FUNDING

This work was financially supported by the National Natural Science Foundation of China (grant number 51868048); China Earthquake Administration Basic Research Project (grant number 2018D18).

REFERENCES

- An, X., and Li, D. (2020). Typical Earthquake Damage Analysis of Ludian Earthquake with Ms 6. 5. *Build Struct.* 50 (7), 28–36. doi:10.19701/j.jzjg.2020.07.004
- Başı, Y., and Itskov, M. (1998). Finite Element Formulation of the Ogden Material Model with Application to Rubber-like Shells. *Int. J. Numer. Meth Engng* 42 (7), 1279–1305. doi:10.1002/(sici)1097-0207(19980815)42:7<1279::aid-nme437>3.0.co;2-i
- Basili, M., Vestroni, F., and Marcari, G. (2019). Brick Masonry Panels Strengthened with Textile Reinforced Mortar: Experimentation and Numerical Analysis. *Constr Build Mater.* 227, 117061. doi:10.1016/j.conbuildmat.2019.117061
- Beda, T. (2005). Optimizing the Ogden Strain Energy Expression of Rubber Materials. *J. Eng. Mater. Technol.* 127 (3), 351–353. doi:10.1115/1.1925282
- Borri, A., Castori, G., and Corradi, M. (2011). Shear Behavior of Masonry Panels Strengthened by High Strength Steel Cords. *Constr Build Mater.* 25 (2), 494–503. doi:10.1016/j.conbuildmat.2010.05.014
- Chen, B., Wang, D., Chen, S., and Hu, S. (2021). Influence of Site Factors on Offshore Ground Motions: Observed Results and Numerical Simulation. *Soil Dyn. Earthq Eng.* 145, 106729. doi:10.1016/j.soildyn.2021.106729
- Deng, M., Li, T., and Zhang, Y. (2020a). Compressive Performance of Masonry Columns Confined with Highly Ductile Fiber Reinforced Concrete (HDC). *Constr Build Mater.* 254, 119264. doi:10.1016/j.conbuildmat.2020.119264

- Deng, M., Zhang, W., and Yang, S. (2020b). In-plane Seismic Behavior of Autoclaved Aerated Concrete Block Masonry Walls Retrofitted with High Ductile Fiber-Reinforced Concrete. *Eng. Struct.* 219, 110854. doi:10.1016/j.engstruct.2020.110854
- Derakhshan, H., Walsh, K. Q., Ingham, J. M., Griffith, M. C., and Thambiratnam, D. P. (2020). Seismic Fragility Assessment of Nonstructural Components in Unreinforced Clay Brick Masonry Buildings. *Earthquake Eng. Struct. Dyn.* 49, 285–300. doi:10.1002/eqe.3238
- Ding, Y. (2015). *Study on Seismic Performance of Brick and Wood Structure Buildings in Western Villages* (Xi'an (CHN): Xi'an University of Architecture and Technology). dissertation/master's thesis.
- ElGawady, M. A., Lestuzzi, P., and Badoux, M. (2006). Aseismic Retrofitting of Unreinforced Masonry Walls Using FRP. *Compos. Part. B* 37, 148–162. doi:10.1016/j.compositesb.2005.06.003
- Jiang, L., Wang, Z., and Zhang, F. (2018). Damage Degree and Inter-Story Drift Angle Limit of Multi-Story Masonry Structures. *J. Build Struct* 39 (S2), 263–270. doi:10.14006/j.jzjgxb.2018.S2.036
- Kim, B., Lee, S. B., Lee, J., Cho, S., Park, H., Yeom, S., et al. (2012). A Comparison Among Neo-Hookean Model, Mooney-Rivlin Model, and Ogden Model for Chloroprene Rubber. *Int. J. Precis Eng. Man.* 13 (5), 759–764. doi:10.1007/s12541-012-0099-y
- Korkmaz, H. H., Korkmaz, S. Z., and Donduren, M. S. (2010). Earthquake Hazard and Damage on Traditional Rural Structures in Turkey. *Nat. Hazards Earth Syst. Sci.* 10 (3), 605–622. doi:10.5194/nhess-10-605-2010
- Liu, G. (2005). “Study on Basic Mechanical Performance of Masonry Structure,” (Changsha (CHN): Hunan University). dissertation/master's thesis.
- Ma, G., Hao, H., and Lu, Y. (2001). Homogenization of Masonry Using Numerical Simulations. *J. Eng. Mech.* 127 (5), 421–431. doi:10.1061/(asce)0733-9399(2001)127:5(421)
- Masi, A., Santarsiero, G., Lignola, G. P., and Verderame, G. M. (2013). Study of the Seismic Behavior of External RC Beam–Column Joints through Experimental Tests and Numerical Simulations. *Eng. Struct.* 52, 207–219. doi:10.1016/j.engstruct.2013.02.023
- Mendes, N., Lourenço, P. B., and Campos-Costa, A. (2014). Shaking Table Testing of an Existing Masonry Building: Assessment and Improvement of the Seismic Performance. *Earthq Engng Struct. Dyn.* 43 (2), 247–266. doi:10.1002/eqe.2342
- National Standards of the People's Republic of China (2010). *Code for Seismic Design of Buildings (GB 50011-2010)*. Beijing, China: China Architecture & Building Press.
- Park, J., Towashiraporn, P., Craig, J. I., and Goodno, B. J. (2009). Seismic Fragility Analysis of Low-Rise Unreinforced Masonry Structures. *Eng. Struct.* 31 (1), 125–137. doi:10.1016/j.engstruct.2008.07.021
- Qu, C., Yi, T., Li, H., and Chen, B. (2018). Closely Spaced Modes Identification through Modified Frequency Domain Decomposition. *Measurement* 128, 388–392. doi:10.1016/j.measurement.2018.07.006
- Qu, C., Yi, T., Yang, X., and Li, H. (2017). Spurious Mode Distinguish by Eigensystem Realization Algorithm with Improved Stabilization Diagram. *Struct. Eng. Mech.* 63 (6), 743–750. doi:10.12989/sem.2017.63.6.743
- Saleem, M. U., Numada, M., Amin, M. N., and Meguro, K. (2016). Shake Table Tests on FRP Retrofitted Masonry Building Models. *J. Compos. Constr* 20 (5), 04016031. doi:10.1061/(asce)cc.1943-5614.0000684
- Shabdin, M., Zargaran, M., and Attari, N. K. A. (2018). Experimental Diagonal Tension (Shear) Test of Un-reinforced Masonry (URM) Walls Strengthened with Textile Reinforced Mortar (TRM). *Constr Build Mater.* 164, 704–715. doi:10.1016/j.conbuildmat.2017.12.234
- Varum, H., Dumar, R., Furtado, A., Barbosa, A. R., Gautam, D., and Rodrigues, H. (2018). “Seismic Performance of Buildings in Nepal after the Gorkha Earthquake,” in *In Impacts and Insights of the Gorkha Earthquake*. Editors D. Gautam and H. Rodrigues (FL: Elsevier Inc Press), 47–63.
- Wang, X., Zhao, W., and Kong, J. (2020). Numerical Investigation on the Influence of In-Plane Damage on the Out-Of-Plane Behavior of Masonry Infill Walls. *Adv. Civ Eng.* 2020, 1–16. doi:10.1155/2020/6276803
- Xuan, W., Wu, G., Zuo, X., and Qian, X. (2016). Construction Technology and Engineering Application of Masonry Structure with Posted-Prefabricated Ring Beams and Constructional Columns. *Constr Technol.* 45 (16), 69–74. doi:10.7672/sjgs2016160069
- Yang, Y., Yang, L., Gao, Y., Yang, Y., Lu, X., and Yang, G. (1982). Method of Damage Prediction for Existing Multi-Story Brick Buildings and its Reliability. *Earthq Eng. Eng. Vib* 2 (3), 75–86. doi:10.13197/j.eeev.1982.03.006
- Zhu, Y., Xie, J., Zhong, X., and Yin, Y. (2016). Prospect of Research on Seismic Countermeasures Based on Village Buildings Situation. *Earthq Resist. Eng. Retrofit* 38 (2), 150–158. doi:10.16226/j.issn.1002-8412.2016.02.022

Conflict of Interest: The authors declare that the research was conducted in the absence of any commercial or financial relationships that could be construed as a potential conflict of interest.

Publisher's Note: All claims expressed in this article are solely those of the authors and do not necessarily represent those of their affiliated organizations, or those of the publisher, the editors and the reviewers. Any product that may be evaluated in this article, or claim that may be made by its manufacturer, is not guaranteed or endorsed by the publisher.

Copyright © 2021 Chen, Jia, Wen and Li. This is an open-access article distributed under the terms of the Creative Commons Attribution License (CC BY). The use, distribution or reproduction in other forums is permitted, provided the original author(s) and the copyright owner(s) are credited and that the original publication in this journal is cited, in accordance with accepted academic practice. No use, distribution or reproduction is permitted which does not comply with these terms.



Holistic Design of Energy Pile Bridge Deicing System With Ontology-Based Multiobjective Decision Making

Peng Zhang¹, Chunyi Cui^{1*}, Chaoji Li¹, Cheng Zhang² and Hailong Liu¹

¹Department of Civil Engineering, Dalian Maritime University, Dalian, China, ²Department of Civil Engineering, Xi'an Jiaotong-Liverpool University, Suzhou, China

OPEN ACCESS

Edited by:

Yunlai Zhou,
Universidade Lusófona, Portugal

Reviewed by:

Enzo Martinelli,
University of Salerno, Italy
Pavlo Maruschak,
Ternopil Ivan Puluj National Technical
University, Ukraine

*Correspondence:

Chunyi Cui
cuichunyi@dlmu.edu.cn

Specialty section:

This article was submitted to
Structural Materials,
a section of the journal
Frontiers in Materials

Received: 20 May 2021

Accepted: 16 July 2021

Published: 23 August 2021

Citation:

Zhang P, Cui C, Li C, Zhang C and
Liu H (2021) Holistic Design of Energy
Pile Bridge Deicing System With
Ontology-Based Multiobjective
Decision Making.
Front. Mater. 8:710404.
doi: 10.3389/fmats.2021.710404

Even though the energy piles have been applied for the bridge deicing system, the traditional design approach is commonly a single-domain and objective-oriented method and is consequently lacking means to comprehensively consider all the relevant factors, such as life-cycle cost, investment payback cycle, carbon emissions, etc. This paper presents a holistic design scheme for the energy pile deicing system of bridge decks. In this paper, a holistic designing tool, namely, OntoBDDS, was developed based on ontology method and SWRL rules. It can automatically provide financial, safety, and heat flux information for designers to evaluate and optimize the design scheme of a deicing system in the early design stage of a bridge. After semantic and syntactical validation of the OntoBDDS system, a case study was also conducted to demonstrate how to leverage knowledge query to provide a series of design alternatives autonomously through considering different design parameters. This case study also verified the practicability and feasibility of the OntoBDDS holistic decision-making system and indicated its potential to be applied for other engineering problems when dealing with multiobjective holistic design making.

Keywords: ontology, holistic design, energy pile, deicing, bridge

INTRODUCTION

Snow and icing are serious hazards that may severely influence the safety and the normal operation of a transportation system. A slippery road surface may cause accidents (Lee et al., 2014) and huge maintenance costs. Taking the United States as an example, the annual expense of ice and snow removal is more than 2.3 billion US dollars, accounting for 20% of the US Department of Transportation (DOT) winter road maintenance budget (Han and Yu, 2017). Therefore, how to remove the ice and snow of bridge safely and effectively has become an important issue to ensure the safe and efficient running of the transportation system.

Traditionally, the snow and ice on the pavement can be removed physically or chemically. The physical method, by which the snow and ice are removed by specially designed vehicles or shovels, is a labor-intensive yet low efficient method. The chemical methods also suffer from drawbacks such as corrosion to the bridge structure, pollution to the environment, and limited working scenario; most chemical ice removers are only effective below 3.9°C (Balbay and Esen, 2010). The energy pile system (Morino and Oka, 1994) provided another safe and efficient solution to the deicing problem. **Figure 1** demonstrates the schematic of the energy pile-based deicing system (EPBDIS) for a bridge deck. It utilizes energy piles to extract geothermal heat from underground and then pumps the heat into the exchange tubes beneath the bridge deck for deicing. Compared with the traditional methods, the EPBDIS is labor-free and ecofriendly (Miyamoto and Takeuchi, 2005; Brandl, 2006), which makes it promising in field applications.

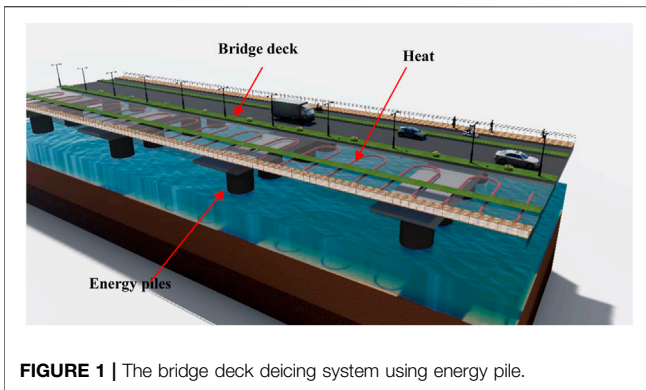


FIGURE 1 | The bridge deck deicing system using energy pile.

During the past decades, energy piles have been extensively studied theoretically and experimentally. In terms of thermal performance, a variety of numerical methods were proposed to study the heat transfer performance of the energy pile bridge deicing system and to verify its feasibility (Yari and Javani, 2010; Dupray et al., 2014; Han and Yu, 2017). Besides, many experimental studies and field tests were carried out to further validate the effectiveness of the energy piles. In Liu et al. (2007) and Balbay and Esen (2010), the authors conducted on-site experiments on the heat transfer performance of the energy pile bridge deck deicing system with a heat pump and verified its feasibility. Kong et al. (2019) and Bowers and Olgun (2015) studied and verified the thermal energy characteristics and feasibility of heat pump-free deicing systems based on field experiments. In addition, considering that the energy pile may cause temperature stress among the bridge structure, the influence of the energy pile on the bearing capacity was investigated by many researchers. In Laloui (2011) and Bourne-Webb et al. (2009), the effect of heat exchange on the bearing capacity of pile foundation was discussed. Subsequently, Amatya et al. (2012) and Ozudogru et al. (2015) discussed the response of energy pile's thermal performance with different end constraints and ground conditions. Loveridge and Powrie (2013) and Jeong et al. (2014) identified the key factors affecting the thermal-mechanical interaction of energy piles.

An optimal design of the energy piles shall comprehensively consider every related aspect, including the thermal exchange efficiency, load capacity, final cost, and environmental impacts. However, previous studies mainly focus on a specific aspect of the energy pile, neglecting the influence of other factors. For example, Nagai et al. (2009) developed a numerical simulation program to predict the temperature field of the system and evaluate the system performance. Liu et al. (2018) considered the heat transfer performance of the system and its economy and verified the feasibility of the system in Canada. In addition, due to the technical complexity of the ground source heat pump system, the relevant information is distorted and misunderstood when it is transmitted between different professions and departments, causing unnecessary losses (Zhang and Liao, 2015), which means that the rational use of systems requires an accurate and recognized domain of knowledge to ensure the accuracy of information transfer.

As a new semantic web technology, ontology can construct accurate domain knowledge and has been widely applied for knowledge sharing and exchange in different fields (Ahmed et al., 2007). Ontology's interdisciplinary features enable interrelated domains to be considered together, and its semantic structure, logical reasoning capabilities, and other characteristics provide an effective method for cross-domain integrated design. More importantly, its language could be recognized by both humans and computers. The ontology has been widely applied in relevant fields of energy pile bridge deicing systems such as pile engineering, bridge engineering, and ground source heat pump system. Specifically, Yurchyshyna and Zarli (2009) proposed a framework for consistency checking in buildings based on ontology. Zhang and Liao (2015) presented an ontology framework for describing ground source heat pump systems, providing guidance for constructing different ground source heat pump systems. Ren et al. (2019) proposed an ontology framework for bridge maintenance. The above provides the methodology and guidance for constructing the ontology framework of the energy pile bridge deck deicing system.

Based on the aforementioned works, it is necessary to use ontology to develop a designing tool for the energy pile bridge deck deicing system, which can comprehensively consider the heat flux, bearing capacity, and a total investment of the system to achieve optimal design. This research developed a comprehensive design decision-making tool named OntoBDDS (ontology of bridge deck deicing system using energy pile) for the holistic design of energy pile bridge deck deicing system in the early design stage. The remaining of the paper is organized as follows: *Development of OntoBDDS for Multiobjective Holistic Design* describes the development and validation of OntoBDDS; *Case Study* presents a case study to demonstrate how the engineers can use this tool to design the deicing system.

DEVELOPMENT OF ONTOLOGY OF BRIDGE DECK DEICING SYSTEM FOR MULTIOBJECTIVE HOLISTIC DESIGN

Determination of the Primary Indicators for the Energy Pile-Based Bridge Deck Deicing System

The key design parameters of the energy pile bridge deck deicing system include equipment cost, the vertical bearing capacity, heat flux, etc.

The Equipment Cost

The total cost of equipment and facilities includes the cost of the heat transfer tubes of the foundation and the deck and cost of the heat pumps. The cost of heat transfer tubes of the foundation can be calculated by the following equation:

$$C^{PT} = \sum_{i=1}^n C_i^{PT} \times L_i^{PT} \times N_i \quad (1)$$

in which i represents the i^{th} type of pile; L_i^{PT} denotes the length of the i^{th} type of pile; C_i^{PT} is the price of heat exchanger tube (RMB) per unit length of the i^{th} pile type; N_i is the number of the i^{th} pile type.

The cost of the heat transfer tubes imbedded in the bridge deck is expressed as

$$C^{\text{BT}} = \sum_{j=1}^n C_j^{\text{BT}} \times L_j^{\text{BT}} \times N_j \quad (2)$$

where j represents the j^{th} type of bridge deck; C_j^{BT} is the price of the heat transfer tube per unit length; L_j^{BT} is the length of the heat transfer tube of the j^{th} type of bridge deck; N_j is the number of the j^{th} type of bridge deck and C^{BT} is the total cost of the heat transfer tubes in the bridge deck.

The cost of the heat pumps can be easily attained by

$$C^{\text{P}} = \sum_{k=1}^m C_k^{\text{P}} \times N_k^{\text{P}} \quad (3)$$

in which k represents the k^{th} heat pump; C_k^{P} is the price of the k^{th} type of heat pump; N_k^{P} is the number of the k^{th} type of heat pump and C^{P} denotes the total cost of heat pump.

The total cost of equipment is expressed as

$$C^{\text{E}} = C^{\text{PT}} + C^{\text{BT}} + C^{\text{P}} \quad (4)$$

in which C^{PT} is the cost of the heat transfer tubes inside the foundation (in a unit of RMB); C^{BT} denotes the cost of the heat transfer tubes; C^{P} is the cost of the heat pumps and C^{E} is the total cost of all facilities.

Heat Flux

The heat extracted by the energy piles can be obtained by

$$Q_{\text{source}} = \sum_{i=1}^n q_i^{\text{pile}} \times L_i^{\text{pile}} \times N_i \quad (5)$$

where i indicates the i^{th} type of pile; q_i^{pile} denotes the heat attained by a unit length of the i^{th} type of pile; L_i^{pile} is the length of the i^{th} type of pile; N_i is the number of the i^{th} type of pile and Q_{source} is the total heat extracted by energy piles.

According to Han and Yu (2017), the available heat for the deicing system can be calculated by

$$Q_{\text{heat}} = \frac{COP}{COP - 1} \times Q_{\text{source}} \quad (6)$$

in which COP is the coefficient of performance of the heat pumps (Self et al., 2013), Q_{source} is the total energy extracted by energy piles from underground; Q_{heat} is the heat available for deicing.

The heated area of the bridge deck is expressed as

$$A_{\text{heat}} = \sum_{j=1}^n a_j^{\text{heat}} \times N_j \quad (7)$$

where j represents the j^{th} type of bridge deck; a_j^{heat} is the area of j^{th} type bridge deck heated by energy pile deicing system; N_j is the number of j^{th} type bridge deck and A_{heat} denotes the total area heated by the deicing system.

Therefore, the heat flux of the bridge deck without an additional heat pump is

$$q = \frac{Q_{\text{source}}}{A_{\text{heat}}} \quad (8)$$

where Q_{source} is the total energy; A_{heat} is the heated area and q is the heat flux provided by the energy pile system without a heat pump.

Similarly, the heat flux of the bridge deck with a heat pump is as follows:

$$q_{\text{pump}} = \frac{Q_{\text{heat}}}{A_{\text{heat}}} \quad (9)$$

where Q_{heat} is the total heat provided by the deicing system; A_{heat} is the heated area and q_{pump} represents the heat flux of the deicing system with heat pump.

Vertical Bearing Capacity

The bearing capacity provided by the energy piles can be obtained by

$$Q = \sum_{i=1}^n \frac{Q_i^{\text{vk}}}{K} \times N_i \quad (10)$$

in which i is the i^{th} type file; Q_i^{vk} is the vertical bearing capacity of the i^{th} type file; K is a safety factor; N_i is the number of the i^{th} type file and Q denotes the total vertical bearing capacity.

Evaluation

The evaluation of a deicing system is conducted *via* a comparison between provided heat flux and required heat flux q_0 . Grades and criteria are listed in Table 1.

Design and Development of Ontology of Bridge Deck Deicing System

The System Framework and User Guides of Ontology of Bridge Deck Deicing System

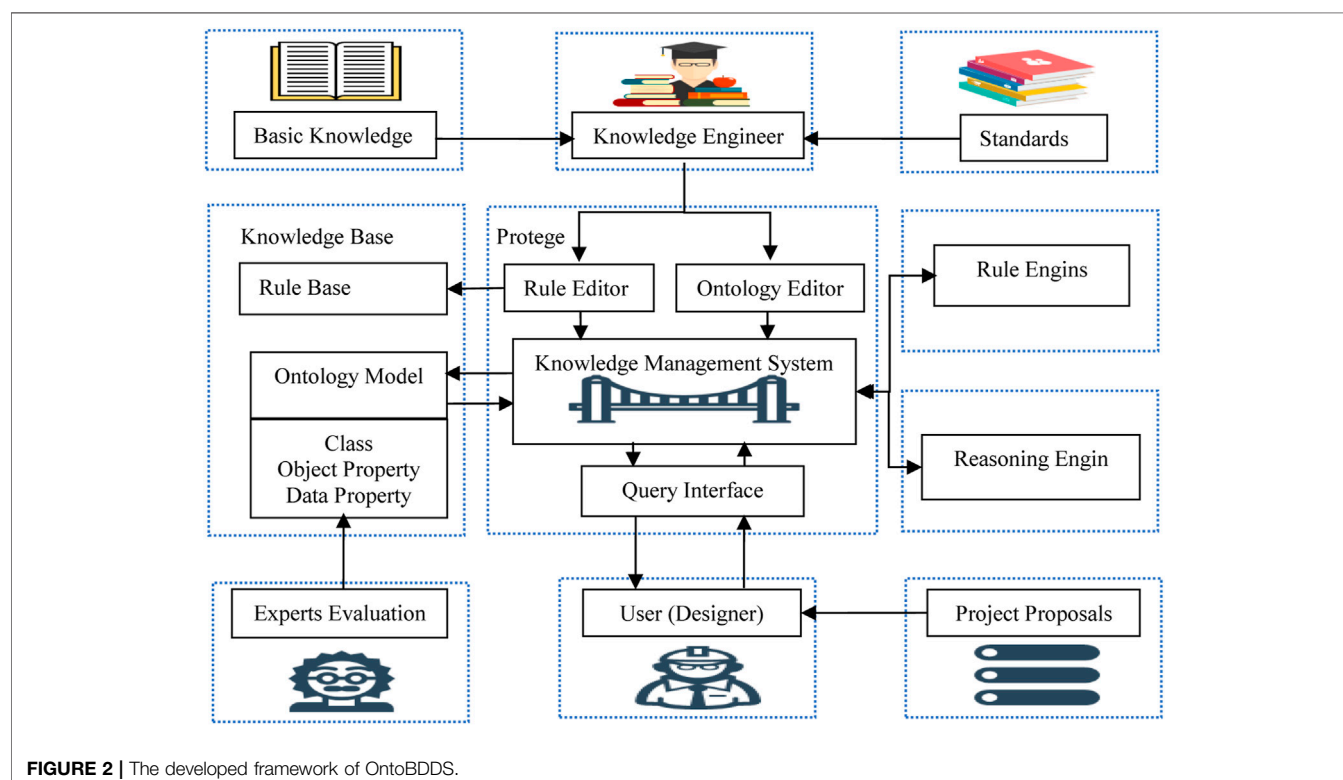
The proposed designing tool, OntoBDDS, consists of four major components: the database, the management system of ontologies, the editing system of rules, and the querying interface, as illustrated in Figure 2. Of these four parts, the database provides a foundation of all functions. All data and ontologies of the energy piles and information of the deicing system are saved in the database in OWL (ontology web language) format. The management system of ontologies is the core part of OntoBDDS, and in this study, it is developed by Protégé 5.2. The editing system of rules can offer a reasoning function with SWRL (semantic web rule language), to realize the holistic design of energy pile deicing system. Moreover, engineers can use the querying interface to obtain feasible solutions to the designing problem. The essential components of the ontology system, OntoBDDS, are specified as follows:

Ontology editor

Protégé-OWL 5.2 provides a platform to create and update ontologies, which is compatible with most OWL files and has various plug-ins for a user to select.

TABLE 1 | The evaluation of the energy pile deicing system for bridge deck.

Evaluation	Expression	Description
Good	$q \geq q_0$	The energy pile deicing system can satisfy the heat flux requirement without a heat pump
Feasible	$q_{\text{pump}} \geq q_0 \geq q$	The energy pile deicing system can satisfy the heat flux requirement with a heat pump
Not feasible	$q_0 > q_{\text{pump}}$	The energy pile deicing system cannot satisfy the heat flux requirement

**FIGURE 2** | The developed framework of OntoBDDS.

Ontology reasoner

Pellet is an OWL reasoning engine that implements the services of basic reasoning and consistency checking for OWL ontologies.

Plug-ins

SWRLTab is a Protégé-OWL plug-in that edits the SWRL rules, while SQWRLTab is a plug-in that edits SQWRL rules for querying.

Based on OntoBDDS, engineers can conduct a holistic design of the energy pile deicing system following the process illustrated in **Figure 3**.

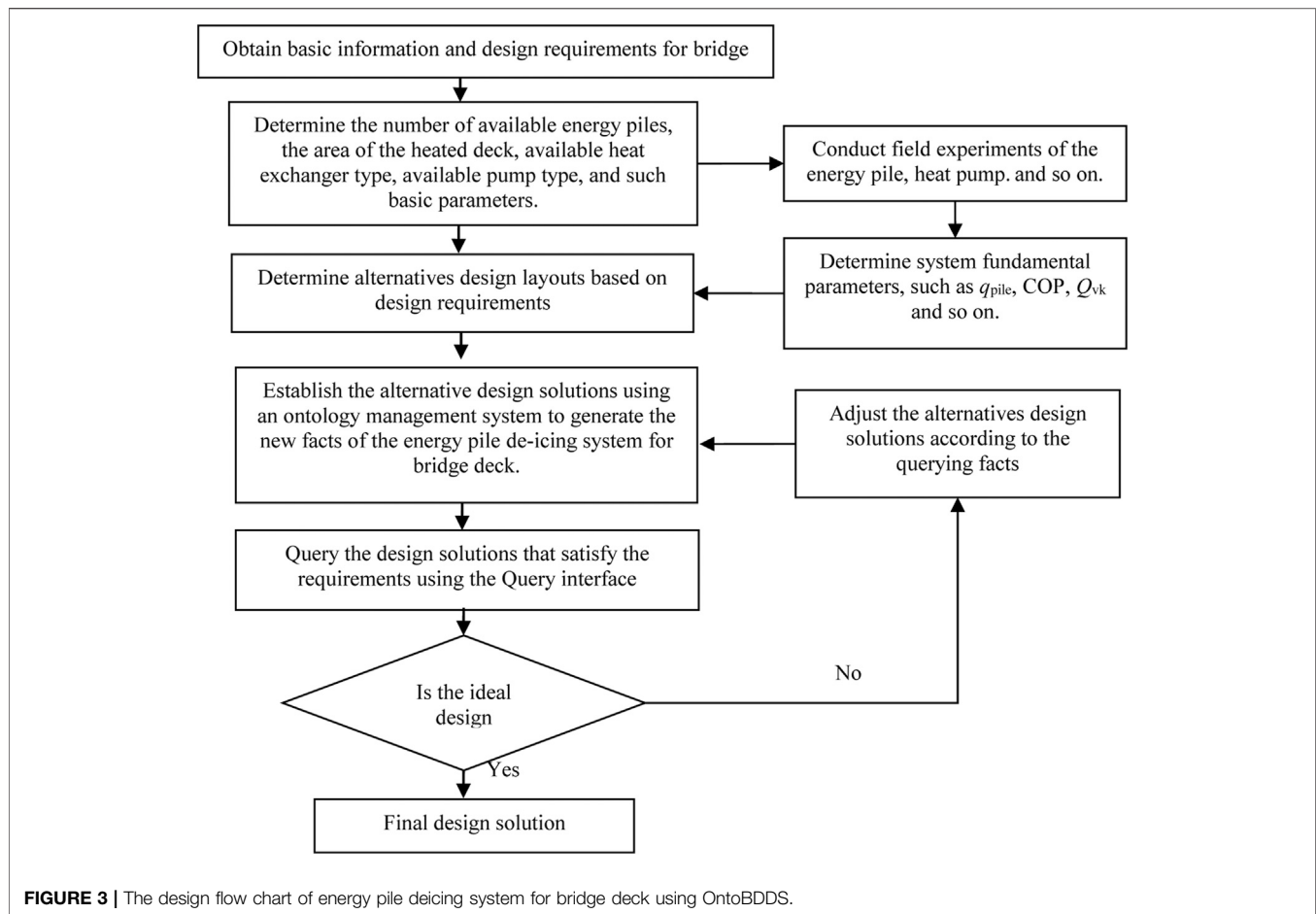
The Development of the Ontology of Bridge Deck Deicing System

The establishment of the OntoBDDS follows three major steps: Knowledge Identification, Knowledge Specification, and Knowledge Refinement. In the Knowledge Identification, the scope and the aim of the energy pile-based deicing system were determined on the basis of the function of the

OntoBDDS and ontology models established previously. In the step of Knowledge Specification, a specification of the knowledge model is constructed by establishing a semiformal ontology model, which can be further refined by engineers according to their designing purpose. In the last step, the Knowledge Refinement step, the ontology model is validated and refined to reassure the accuracy and conciseness of the system.

In this study, the scope of the ontology model includes pile foundation engineering, bridge engineering, bridge deicing, and geothermal pump system. Heat flux, cost, and safety of the bridge structure are the major issues to be considered in holistic design. The key concepts and terms of the OntoBDDS follow the IFC standard and relative ontology models established previously (Ren et al., 2019). The key concepts and terms are shown in **Figure 4** using UML (Unified Modeling Language).

In this study, the Ontology Development 101 (Noy and McGuinness, 2001) is utilized to develop the OntoBDDS. The Ontology Development 101 is a methodology widely accepted for establishing ontology systems because of its efficiency and simplicity. The detailed steps are illustrated in **Figure 5**. It can be further explained as follows:



Step 1: The relevant domain and scope of the ontology are determined based on basic questions (BQ) and competency questions (CQ).

Step 2: IFC framework of the building SMART is adopted as the main development standard for the exchanging and sharing of Building Information, which facilitates the concept development of information ontologies for the holistic design of energy pile system (Horrocks et al., 2004).

Step 3: A dictionary of key concepts and terms regarding the deicing systems is established, which includes maintenance, safety, financial cost, mechanical property, etc.

Step 4: According to the dictionary established in Step 3, general classes of the OntoBDDS are established as shown in **Figure 6A**.

Step 5: There are mainly two types of properties to describe the relevant classes, namely, object properties and data properties, which define the relationships between classes and represent the characteristics of class instances, respectively, as illustrated in **Figures 6B,C**.

Step 6: In this step, specific instances are created. Each instance represents a unique design solution of the energy pile-based deicing system.

Step 7: SWRL rules for the holistic design of energy pile system are defined to improve the ontology's flexibility for calculating and reasoning. There are four types of atoms for SWRL rules, i.e., Class atoms, Individual Property atoms, Data Valued Property atoms, and Built-in atoms. In addition, the symbols of SWRL rules include the connection symbol '~', the implication symbol '→', and the question mark '?' (Guizzardi et al., 2008). The specific SWRL rules for the calculation of equipment cost of energy pile system is illustrated as follows:

Equation	$C^E = C^{PT} + C^{BT} + C^P$
----------	-------------------------------

SWRL:	De-icing_system(?DS)Pile_heat_exchanger_tube_cost(?DS, ?pile_tube_cost)Bridge_deck_heat_exchanger_tube_cost(?DS, ?deck_tube_cost)Pump_cost(?DS, ?pump_cost)swrlb:add(?total_cost, ?pile_tube_cost, ?deck_tube_cost, ?pump_cost) -> Total_cost(?DS, ?total_cost)
-------	---

Step 8: User can query design solutions by inputting SQWRL rules in SQWRLQueryTab of the Protégé query interface. An example of cost query for energy pile system is illustrated as follows:

SQWRL De-icing_system(?DS)Total_cost(?DS,?total_cost)Q(?DS,?bearing_capacity)q0(?DS,?q_0) q(?DS,?q_)q_pump(?DS,?q_heat_pump)Evaluation(?DS,?evaluation)has_pump(?DS,?pump_type)->sqwrl:select(?DS,?total_cost,?bearing_capacity,?pump_type,?q_0,?q_,?q_heat_pump,?evaluation)

compare the ontology model with existing models, while the other method is to establish a new ontology model by expanding the existing one (Green et al., 2002). In this study, the OntoBDDS is developed based on IFC and existing ontology models (Ren et al., 2019). Therefore, the semantic

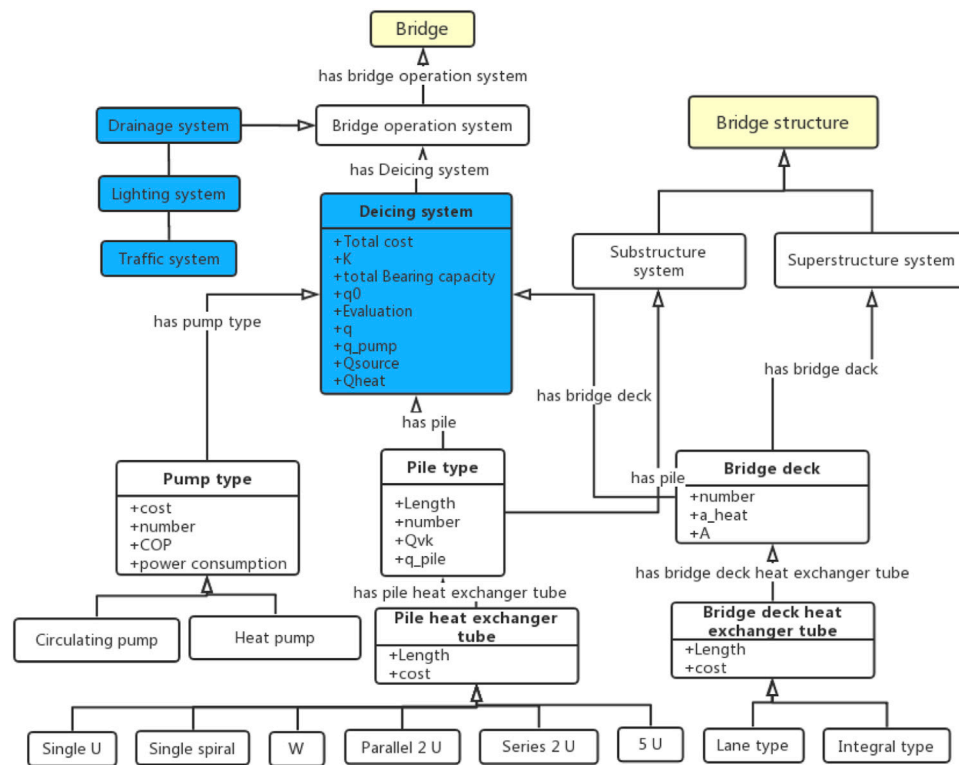


FIGURE 4 | Flowchart of UML classes for the key concepts of OntoBDDS ontology.

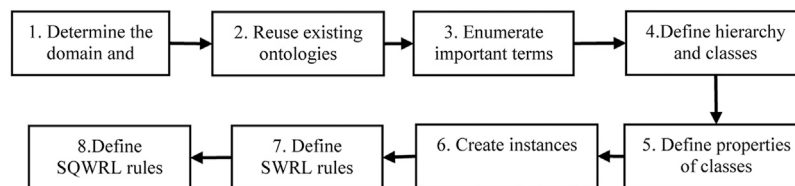


FIGURE 5 | Eight-step methodology.

Ontology Validation

Validation of the OntoBDDS system was performed to assure its accuracy and ability to provide the expected design function. The validation includes semantic correctness, syntactic correctness, and rules validation.

Semantic Validation

There are two methodologies to assure the semantic correctness of an ontology model. One method is to

correctness of the key concepts and terms is automatically validated.

Syntactical Validation

Syntactical validation can be conducted by reasoning engines. In this study, the OntoBDDS is developed using Protégé-OWL 5.2. The pellet reasoner embedded in Protégé-OWL 5.2 can be used to detect syntactical errors of OntoBDDS. Figure 7 shows the log of running pellet plug-in for completed consistency checking of the OntoEPS.

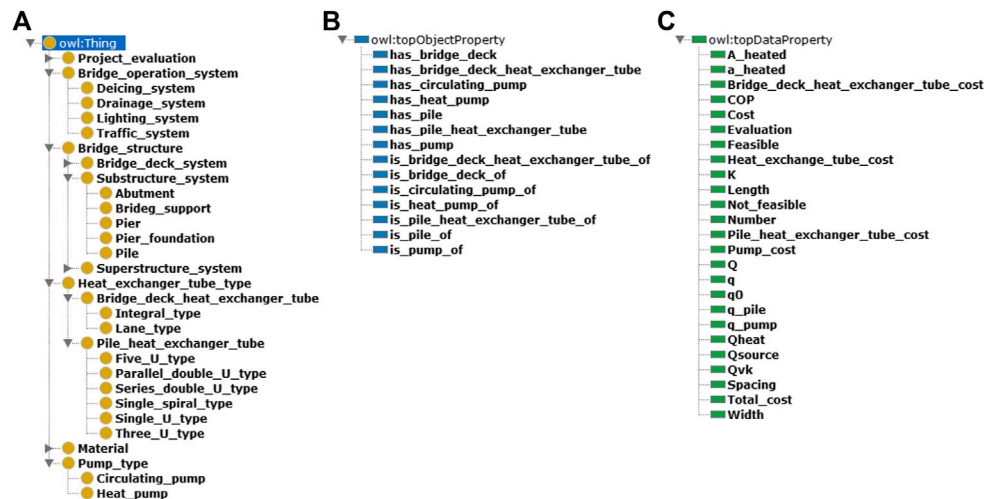


FIGURE 6 | The development ontology in the Protégé-OWL 5.2.

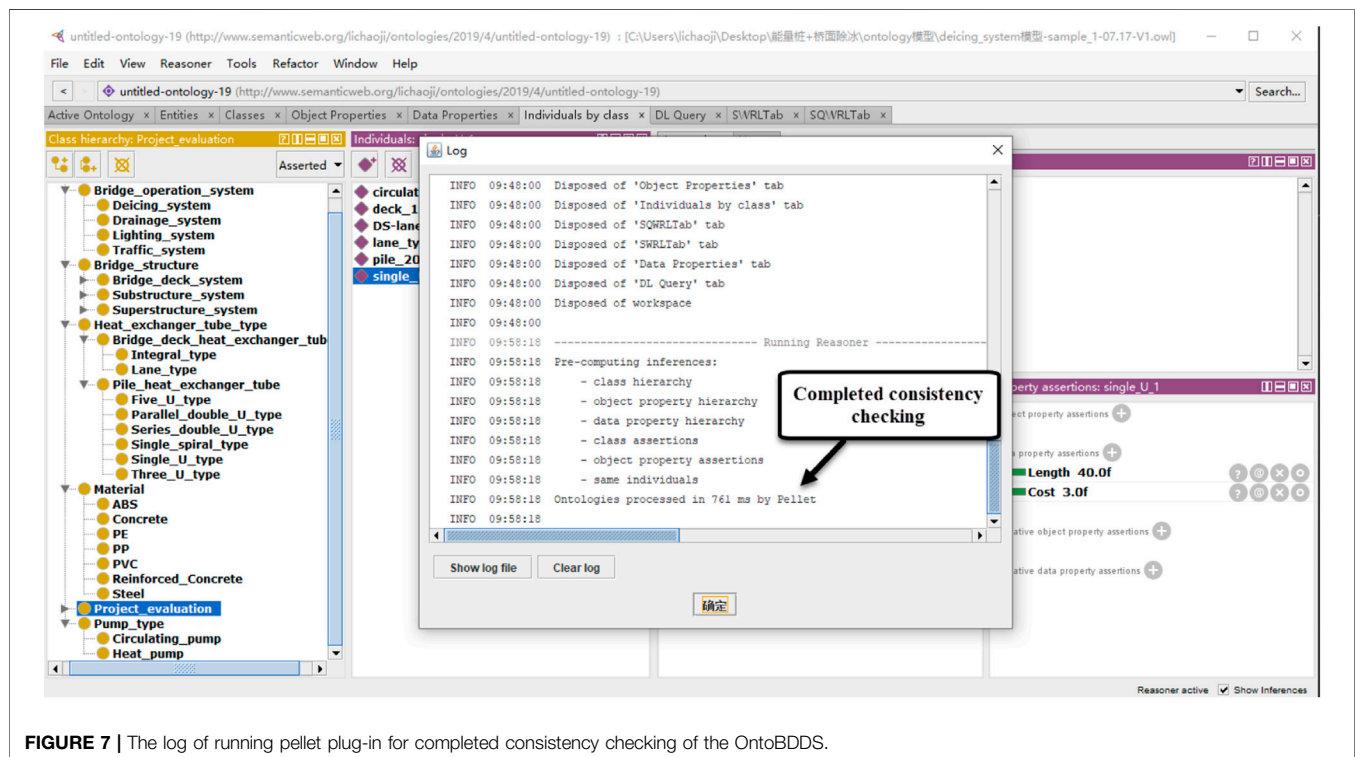


FIGURE 7 | The log of running pellet plug-in for completed consistency checking of the OntoBDDS.

Rules Validation

In this study, a plug-in called SWRLTAB is utilized to validate the rules preliminarily, as shown in Figure 8.

Then, in *Case Study*, a case study will be presented to further verify the effectiveness and feasibility of all the rules of OntoBDDS.

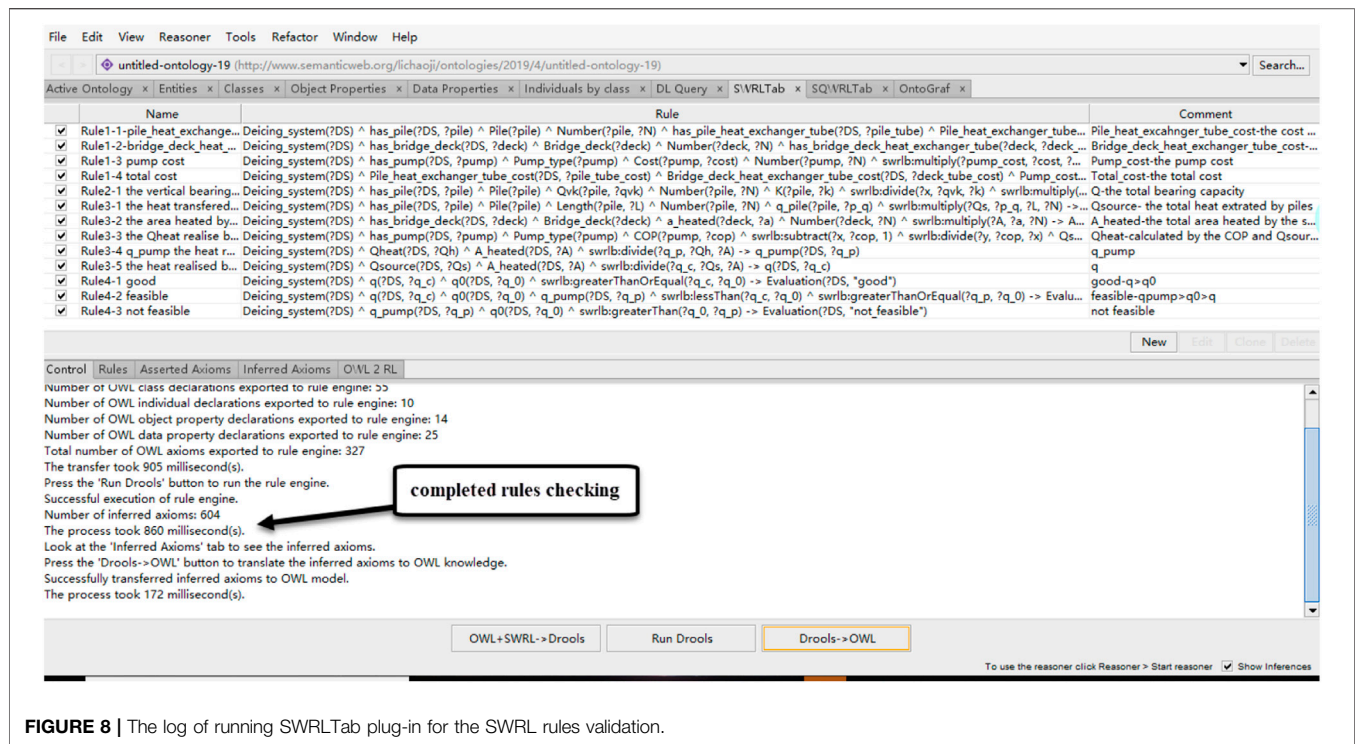


FIGURE 8 | The log of running SWRLTab plug-in for the SWRL rules validation.

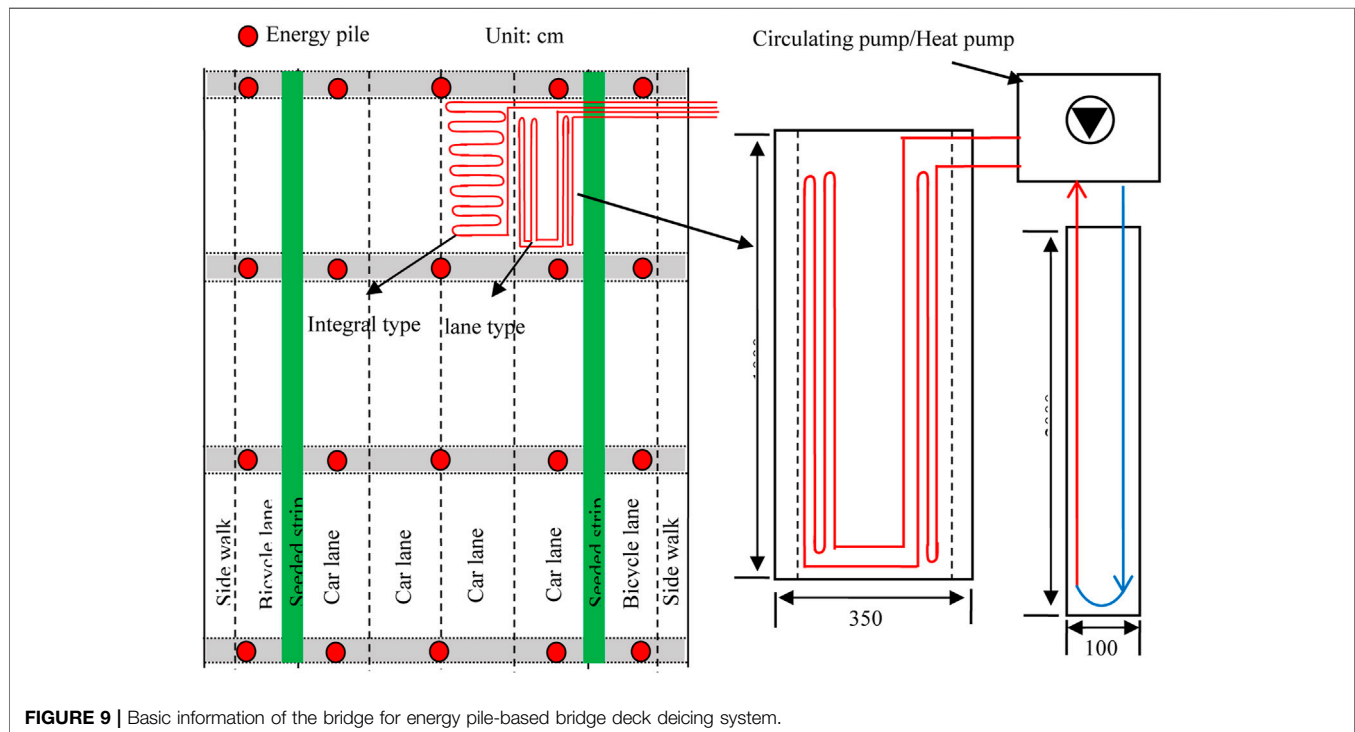


FIGURE 9 | Basic information of the bridge for energy pile-based bridge deck deicing system.

CASE STUDY

Case Study Description

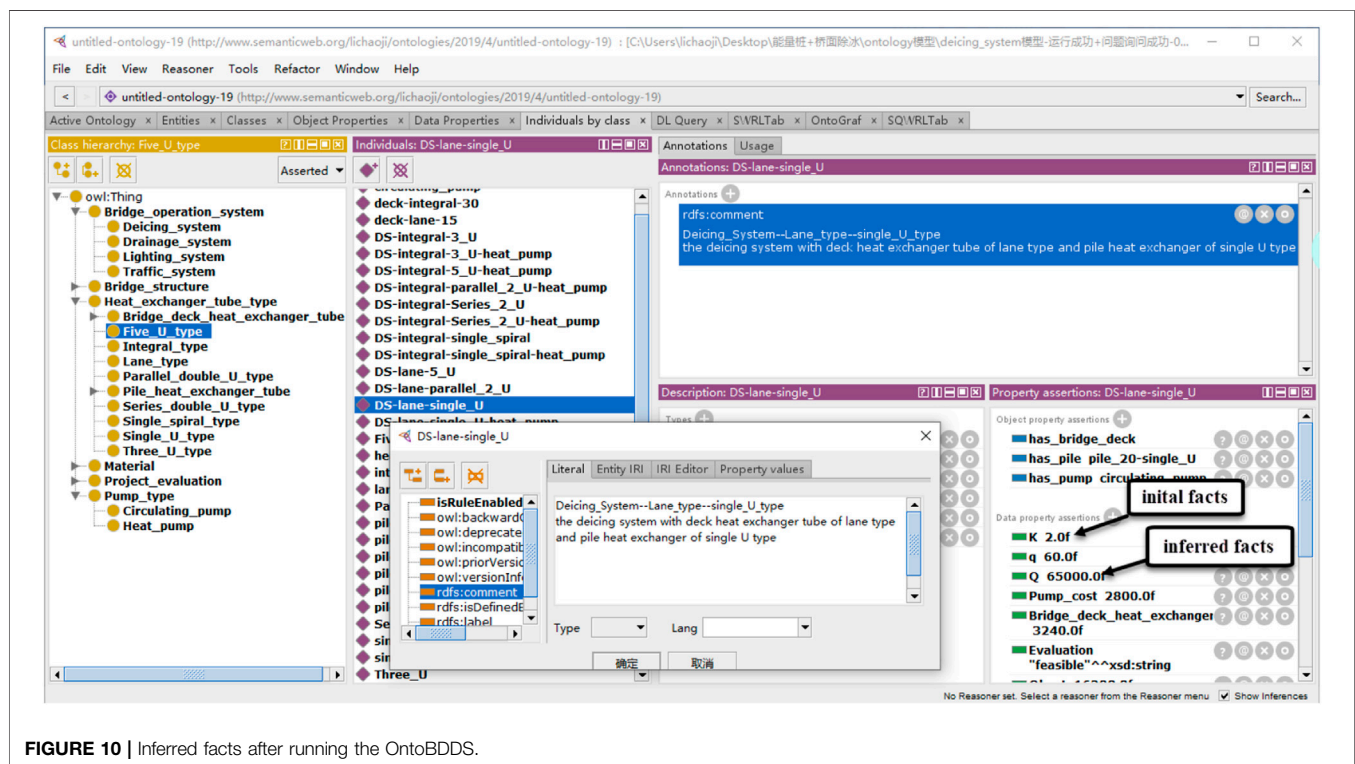
In this section, an energy pile-based deicing system for a bridge deck is designed to demonstrate the main functions of the

OntoBDDS software. The prototype bridge is a three-span beam bridge constructed in Jiangyin of Jiangsu Province. Its configuration is illustrated in Figure 9.

As shown in Figure 9, the size of the bridge deck allows for no more than 20 energy piles to be constructed. Moreover, heat

TABLE 2 | The detail of the design solution.

Design solutions	Pile		Pump				Bridge deck		Pile heat exchanger tube			Bridge deck heat exchange tube		
	Q _{pile} (w/m)	Q _{vk} (kN)	Type	COP	Cost (RMB)	Number	A (m ²)	Number	Type	Length (m)	Cost (RMB)	Type	Length (m)	Cost (RMB)
DS-lane-single_U	27	6,500	Circulating pump	---	2,800	1	15	12	Single U	40	3	Lane type	90	3
DS-lane-single_U-heat pump	27	6,500	Heat pump	3	16,000	1	15	12	Single U	40	3	Lane type	90	3
DS-lane-P_2_U	31.5	6,430	Circulating pump	---	2,800	1	15	12	Parallel 2 U	80	3	Lane type	90	3
DS-integral-P_2_U-heat_pump	31.5	6,430	Heat pump	3	16,000	1	30	12	Parallel 2 U	80	3	Integral type	150	3
DS-integral-S_2_U	36	6,400	Circulating pump	---	2,800	1	30	12	Series 2 U	80	3	Integral type	150	3
DS-integral-S_2_U-heat_pump	36	6,400	Heat pump	3	16,000	1	30	12	Series 2 U	80	3	Integral type	150	3
DS-integral-3_U	45	6,300	Circulating pump	---	2,800	1	30	12	3 U	120	3	Integral type	150	3
DS-integral-3_U-heat_pump	45	6,300	Heat pump	3	16,000	1	30	12	3 U	120	3	Integral type	150	3
DS-lane-5_U	54	6,250	Circulating pump	---	2,800	1	15	12	5 U	200	3	Integral type	150	3
DS-integral-5_U-heat_pump	54	6,250	Heat pump	3	16,000	1	30	12	5 U	200	3	Lane type	90	3
DS-integral-spiral	63	6,200	Circulating pump	---	2,800	1	30	12	Single spiral	250	3	Integral type	150	3
DS-integral-spiral-heat_pump	63	6,200	Heat pump	3	16,000	1	30	12	Single spiral	250	3	Integral type	150	3

**FIGURE 10** | Inferred facts after running the OntoBDDs.**TABLE 3** | SWRL rules to calculate bearing capacity.

Rule 1	<p>Calculating the bearing capacity: $Q = \sum_{i=1}^n \frac{Q_{vk}}{K} \times N_i$</p> <p>De-icing_system(?DS)has_pile(?DS, ?pile)*Pile(?pile)*Qvk(?pile, ?qvk)*Number(?pile, ?N)*K(?DS, ?k)^swrlb:divide(?x, ?qvk, ?k)^swrlb:multiply(?Q0, ?x, ?N) -> Q(?DS, ?Q0)</p>
--------	---

TABLE 4 | SWRL rules to calculate the total cost.

Rule 1	$C^{PT} = \sum_{i=1}^n C_i^{PT} \times L_i^{PT} \times N_i$ De-icing_system(?DS)has_pile(?DS,?pile)Pile(?pile)Number(?pile,?N)has_pile_heat_exchanger_tube(?pile,?pile_tube) Pile_heat_exchanger_tube(?pile_tube)Cost(?pile_tube,?cost) Length(?pile_tube,?L)swrlb:multiply(?pile_tube_cost,?cost,?L,?N)->Pile_heat_exchanger_tube_cost(?DS,?pile_tube_cost)
Rule 2	$C^{BT} = \sum_{j=1}^n C_j^{BT} \times L_j^{BT} \times N_j$ De-icing_system(?DS)has_bridge_deck(?DS,?deck)Bridge_deck(?deck)Number(?deck,?N) has_bridge_deck_heat_exchanger_tube(?deck,?deck_tube)Bridge_deck_heat_exchanger_tube(?deck_tube)Cost(?deck_tube,?cost) Length(?deck_tube,?L)swrlb:multiply(?deck_tube_cost,?N,?L,?cost)->Bridge_deck_heat_exchanger_tube_cost(?DS,?deck_tube_cost)
Rule 3	$C^P = \sum_{k=1}^m C_k^P \times N_k^P$ De-icing_system(?DS)has_pump(?DS,?pump)Pump_type(?pump)Cost(?pump,?cost)Number(?pump,?N)swrlb:multiply(?pump_cost,?cost,?N)->Pump_cost(?DS,?pump_cost)
Rule 4	$C^E = C^{PT} + C^{BT} + C^P$ De-icing_system(?DS)Pile_heat_exchanger_tube_cost(?DS,?pile_tube_cost)Bridge_deck_heat_exchanger_tube_cost(?DS,?deck_tube_cost)Pump_cost(?DS,?pump_cost)swrlb:add(?total_cost,?pile_tube_cost,?deck_tube_cost,?pump_cost)->Total_cost(?DS,?total_cost)

TABLE 5 | SWRL rules to calculate heat flux.

Rule 1	$Q_{source} = \sum_{i=1}^n q_i^{pile} \times L_i^{pile} \times N_i$ De-icing_system(?DS)has_pile(?DS,?pile)Pile(?pile)Length(?pile,?L)Number(?pile,?N)q_pile(?pile,?p_q)swrlb:multiply(?Qs,?p_q,?L,?N)->Qsource(?DS,?Qs)
Rule 2	$Q_{heat} = \frac{COP}{COP-1} \times Q_{source}$ De-icing_system(?DS)has_pump(?DS,?pump)Pump_type(?pump)COP(?pump,?cop)swrlb:subtract(?x,?cop,1)swrlb:divide(?y,?cop,?x)Qsource(?DS,?Qs)swrlb:multiply(?Qh,?y,?Qs)->Qheat(?DS,?Qh)
Rule 3	$A_{heat} = \sum_{j=1}^n a_j^{heat} \times N_j$ De-icing_system(?DS)has_bridge_deck(?DS,?deck)Bridge_deck(?deck)a_heated(?deck,?a)Number(?deck,?N)swrlb:multiply(?A,?a,?N)->A_heated(?DS,?A)
Rule 4	$q = \frac{Q_{source}}{A_{heat}}$ De-icing_system(?DS)Qsource(?DS,?Qs)A_heated(?DS,?A)swrlb:divide(?q_c,?Qs,?A)->q(?DS,?q_c)
Rule 5	$q_{pump} = \frac{Q_{heat}}{A_{heat}}$ De-icing_system(?DS)Qheat(?DS,?Qh)A_heated(?DS,?A)swrlb:divide(?q_p,?Qh,?A)->q_pump(?DS,?q_p)

TABLE 6 | SWRL rules for evaluation.

Rule 1	Evaluation: good De-icing_system(?DS)q(?DS,?q_c)q0(?DS,?q_0)swrlb:greaterThanOrEqualTo(?q_c,?q_0)->Evaluation(?DS,"good")
Rule 2	Evaluation: feasible De-icing_system(?DS)q(?DS,?q_c)q0(?DS,?q_0)q_pump(?DS,?q_p)swrlb:lessThan(?q_c,?q_0)swrlb:greaterThanOrEqualTo(?q_p,?q_0)->Evaluation(?DS,"feasible")
Rule 3	Evaluation: not feasible De-icing_system(?DS)q_pump(?DS,?q_p)q0(?DS,?q_0)swrlb:greaterThan(?q_0,?q_p)->Evaluation(?DS,"not_feasible")

TABLE 7 | SQWRL rules to query total cost, bearing capacity, q0, qpump, and evaluation.

SQWRL	De-icing_system(?DS)Total_cost(?DS,?total_cost)Q(?DS,?bearing_capacity)q0(?DS,?q_0)q(?DS,?q_)q_pump(?DS,?q_heat_pump)Evaluation(?DS,?evaluation)has_pump(?DS,?pump_type)->sqwrl:select(?DS,?total_cost,?bearing_capacity,?pump_type,?q_0,?q_,?q_heat_pump,?evaluation)
-------	--

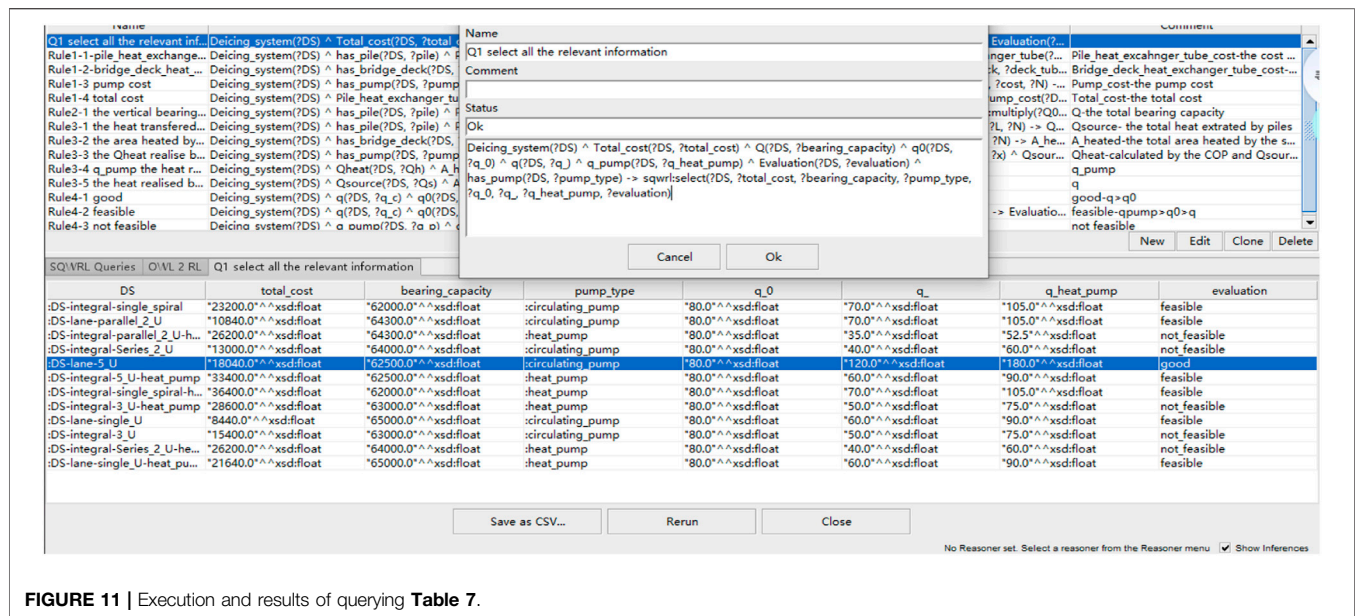


FIGURE 11 | Execution and results of querying Table 7.

TABLE 8 | SPARQL rules to query total cost less than 20,000 RMB.

SPARQL

De-icing_system(?DS) ^ Total_cost(?DS, ?total_cost) ^ Q(?DS, ?bearing_capacity) ^ q0(?DS, ?q_0) ^ q(?DS, ?q) ^ q_pump(?DS, ?q_heat_pump) ^ Evaluation(?DS, ?evaluation) ^ has_pump(?DS, ?pump_type) ^ swrlb:lessThan(?total_cost, 20,000) -> sqwrl:select(?DS, ?total_cost, ?bearing_capacity, ?pump_type, ?q_0, ?q, ?q_heat_pump, ?evaluation)

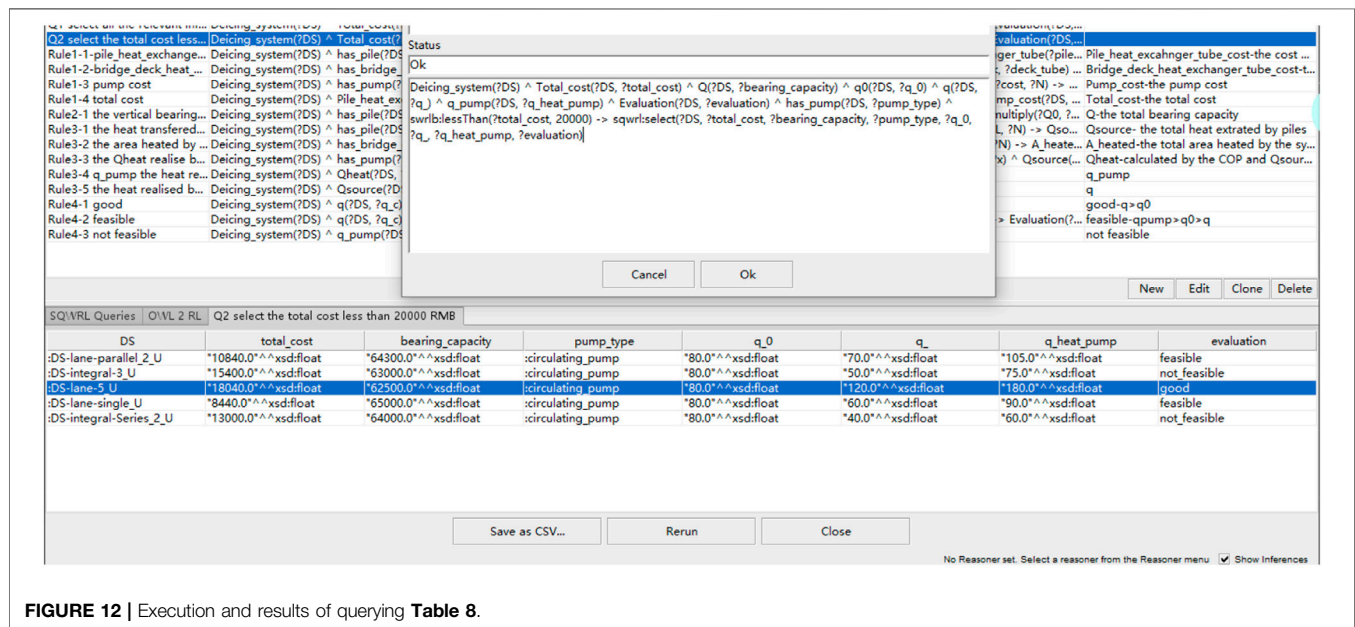


FIGURE 12 | Execution and results of querying Table 8.

transfer tubes will be embedded under the 12 pieces of bridge deck under car lanes. The bridge deck under the bicycle lanes or the sidewalk will not be heated by thermal tubes. Considering the heated area and the volume of circulating water, COP is set to 3, according to Self et al. (2013). Based on several different types of

heat exchangers and heat pumps, 12 design solutions are offered by OntoBDDS. The details of each design solution are presented in Table 2.

Thereafter, OntoBDDS can generate new facts based on the ontology model and the 12 aforementioned designing solutions. The

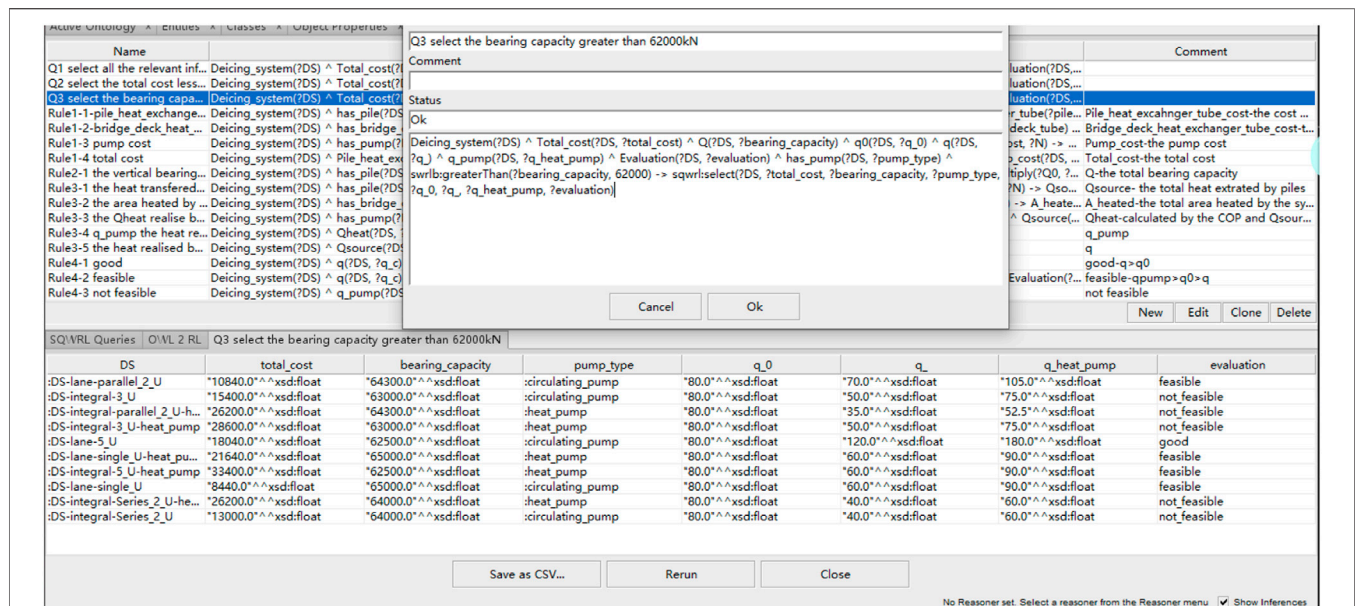


FIGURE 13 | Execution and results of querying **Table 9**.

TABLE 9 | SQWRL rules to query bearing capacity greater than 62,000 kN.

SQWRL De-icing_system(?DS)Total_cost(?DS,?total_cost)Q(?DS,?bearing_capacity)q0(?DS,?q_0) q(?DS,?q_j)q_pump(?DS,?q_heat_pump)Evaluation(?DS,?evaluation)has_pump(?DS, ?pump_type)swrlb:greaterThan(?bearing_capacity,62000)->sqwrl:select(?DS, ?total_cost, ?bearing_capacity, ?pump_type, ?q_0, ?q_, ?q_heat_pump, ?evaluation)

TABLE 10 | SQWRL rules to query feasible design solutions whose total cost is less than 20,000 RMB.

SQWRL

```
De-icing_system(?DS)^Total_cost(?DS, ?total_cost)^Q(?DS, ?bearing_capacity)^q0(?DS, ?q_0)^q(?DS, ?q_1)^q_pump(?DS, ?q_heat_pump)^ Evaluation(?DS, ?evaluation) has_pump(?DS, ?pump_type)swrlb:lessThan(?total_cost,20,000)swrlb:greaterThan (?q_heat_pump,?q_0)->sqwrl:select(?DS, ?total_cost, ?bearing_capacity, ?pump_type, ?q_0, ?q_1, ?q_heat_pump,?evaluation)
```

facts include the cost, heat flux, and bearing capacity among other features of each design solution. **Figure 10** demonstrates the interface after running the ontology model and reasoning rules. The reasoning rules are also presented from **Table 3–6**. Thereafter, engineers can use a plug-in called SQWRLQueryTAB to inquire the generated facts and make a comparison of each design solution.

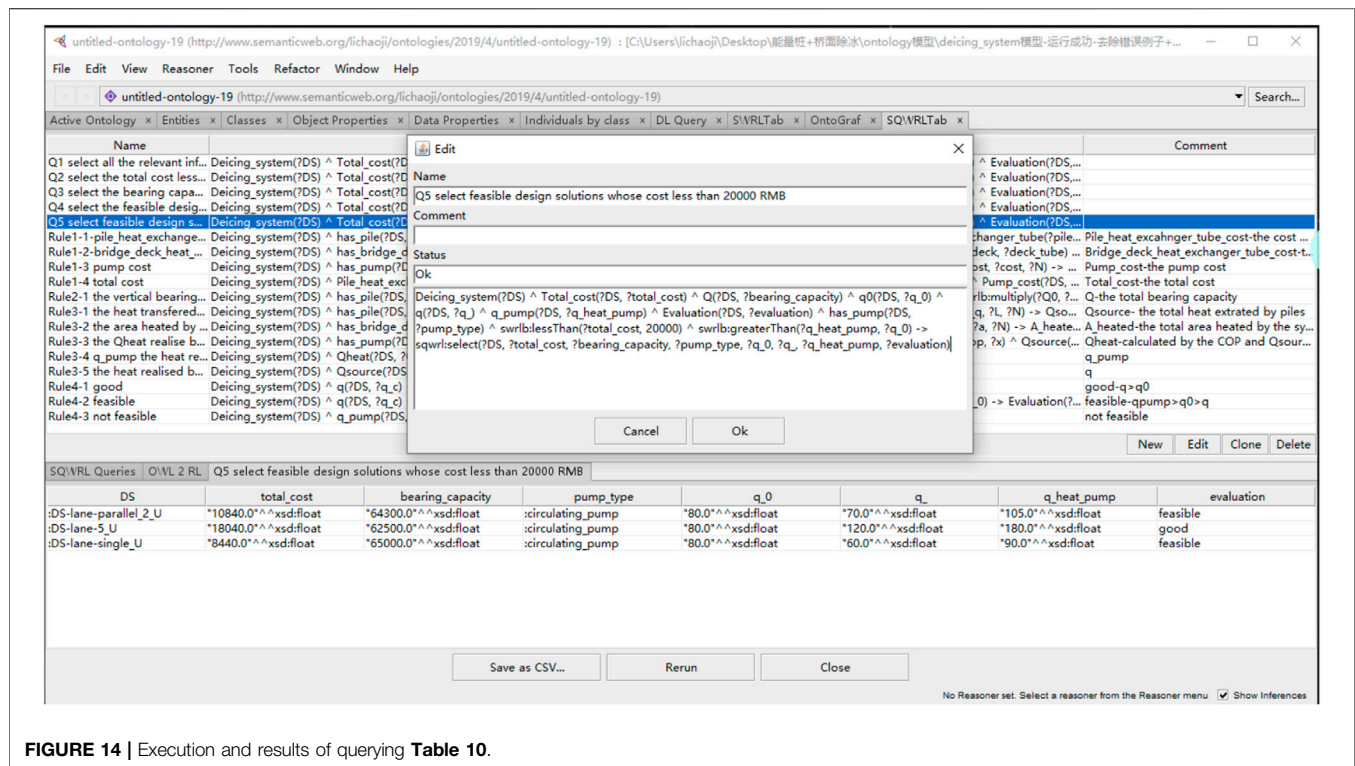
Application

This section demonstrates how engineers can use OntoBDDS to perform inquiry designing solutions of bridge deck deicing system in accordance with specified requirements. The inquiries can be conducted through inputting SQWRL commands in the SQWRLTab. For example, the total cost, bearing capacity, and heat flux can be obtained by the command shown in **Table 7** and the querying results are illustrated in **Figure 11**. Engineers can compare each design and make preliminary decisions.

Specialized design requirements can also be easily satisfied by SQWRL querying. **Table 8** shows the SQWRL querying command to filter design results with a total cost below 20,000 RMB. The querying results are illustrated in **Figure 12**. It can be seen that five designs satisfy this requirement and only three are graded as feasible.

Figure 13 illustrates the running results of **Table 9**, which aims to find design solutions with bearing capacity larger than 62,000 kN. It is shown that ten solutions are satisfying this requirement. Furthermore, the bearing capacities of all those filtered design solutions are of the same order of magnitude, which implies that the OntoBDDS can provide reasonable design solutions.

Hear flux and cost are also two major indicators of the deicing system. **Table 10** demonstrates the SQWRL command to filter design solutions of a cost less than 20,000 RMB and acceptable heat flux. The querying results are illustrated in **Figure 14**. It can be seen that there are three acceptable design solutions. The solution with heat pump and 5-U type heat



transfer tube offers the least cost and highest heat flux and therefore is the optimal solution.

CONCLUSION AND FUTURE WORK

Based on the ontology modeling method and the SWRL language, this paper establishes an integrated design system for energy pile bridge deck deicing systems. The OntoBDDS system is developed and provides designers with a simple and easy-to-use optimization design tool. The system provides designers with indicators on the economy, heat flux, and safety aspects of the design plan, so that the designer can choose and optimize the plan.

At the same time, this article uses a design example to demonstrate how engineers should use this system to optimize the design of the energy pile bridge deck deicing system when considering different design requirements. The example also shows the feasibility of the system. This ontology model is also developed based on the IFC standard and an existing, verified ontology model. The correctness of its semantics, grammar, and rules have also been verified. At the same time, the example shows how the system can be used when focusing on different design priorities, such as cost, safety, and heat flux to achieve the optimal system configuration and satisfy engineering requirements.

The concept of using OntoBDDS tools and an ontology framework as illustrated in this article can also be applied to other energy pile projects, such as energy tunnels, integrated design of building energy pile systems, etc. In future work, this ontology-based integrated design

concept can be extended to all aspects of engineering, and further efforts will be placed on developing knowledge acquisition methods involving more semantic explication (such as during cross-disciplinary interaction in a large-scale numerical analysis). Further development in this area can help basic or cross-domain reasoning in practical scenarios.

DATA AVAILABILITY STATEMENT

The data used to support the findings of this study are available from the corresponding author upon request.

AUTHOR CONTRIBUTIONS

PZ, CC, CL, and CZ conceived and designed the research work. PZ, CL, and HL analyzed the data. PZ, CL, and HL prepared original draft. CC and CZ reviewed and edited the paper. All authors contributed to the article and approved the submitted version.

FUNDING

This research was funded by the National Natural Science Foundation of China (NSFC), Grant no. 51808092, and United Navigation Foundation of Liaoning Province, Grant no. 2020-HYLH-48.

REFERENCES

- Ahmed, V., Pathmeswaran, R., and Aouad, G. (2007). A Generic Framework for the Development of Standardised Learning Objects within the Discipline of Construction Management. *J. Educ. Built Environ.* 2, 115–135. doi:10.11120/jebe.2007.02020115
- Amatya, B. L., Soga, K., Bourne-Webb, P. J., Amis, T., and Laloui, L. (2012). Thermo-mechanical Behaviour of Energy Piles. *Géotechnique* 62, 503–519. doi:10.1680/geot.10.p.116
- Balbay, A., and Esen, M. (2010). Experimental Investigation of Using Ground Source Heat Pump System for Snow Melting on Pavements and Bridge Decks. *Sci. Res. Essays* 5, 3955–3966. doi:10.1029/2009JG001147
- Bourne-Webb, P. J., Amatya, B., Soga, K., Amis, T., Davidson, C., and Payne, P. (2009). Energy Pile Test at Lambeth College, London: Geotechnical and Thermodynamic Aspects of Pile Response to Heat Cycles. *Géotechnique* 59, 237–248. doi:10.1680/geot.2009.59.3.237
- Bowers, G. A., and Olgun, C. G. (2015). *Experimental Investigation of Bridge Deck Deicing Using Energy Piles*. San Antonio, TX: Geotechnical Special Publication, 1628–1637.
- Brandl, H. (2006). Energy Foundations and Other Thermo-Active Ground Structures. *Géotechnique* 56, 81–122. doi:10.1680/geot.2006.56.2.81
- Dupray, F., Li, C., and Laloui, L. (2014). Heat-exchanger Piles for the De-icing of Bridges. *Acta Geotech.* 9, 413–423. doi:10.1007/s11440-014-0307-2
- Green, R., Bean, C. A., and Myaeng, S. H. (2002). The Semantics of Relationships. *Inf. Sci. Knowledge Manage.* 3, 325–327. doi:10.1007/978-94-017-0073-3
- Guizzardi Giancarlo, H., Terry, V., Johanna, V., Denny, S., and York (2008). AEON – an Approach to the Automatic Evaluation of Ontologies. *Appl. Ontol.* 3 (12), 41–62. doi:10.3233/O-2008-0048
- Han, C., and Yu, X. (2017). Feasibility of Geothermal Heat Exchanger Pile-Based Bridge Deck Snow Melting System: A Simulation Based Analysis. *Renew. Energy* 101, 214–224. doi:10.1016/j.renene.2016.08.062
- Horrocks, I., Patel-Schneider, P. F., Boley, H., Tabet, S., Grosz, B., Boley, H., et al. (2004). *SWRL: A Semantic Web Rule Language Combining OWL and RuleML*. doi:10.1145/988672.988771
- Jeong, S., Lim, H., Lee, J. K., and Kim, J. (2014). Thermally Induced Mechanical Response of Energy Piles in Axially Loaded Pile Groups. *Appl. Therm. Eng.* 71, 608–615. doi:10.1016/j.applthermaleng.2014.07.007
- Kong, G., Wu, D., Liu, H., Laloui, L., Cheng, X., and Zhu, X. (2019). Performance of a Geothermal Energy Deicing System for Bridge Deck Using a Pile Heat Exchanger. *Int. J. Energy Res.* 43, 596–603. doi:10.1002/er.4266
- Laloui, L. (2011). “In-situ Testing of a Heat Exchanger Pile,” in *Geo-Frontiers 2011: Advances in Geotechnical Engineering - Proceedings of the Geo-Frontiers 2011 Conference*, Location Dallas, Texas, March 13–16, 2011 (American Society of Civil Engineers ASCE). doi:10.1061/41165(397)43
- Lee, W.-K., Lee, H.-A., Hwang, S.-s., Kim, H., Lim, Y.-H., Hong, Y.-C., et al. (2014). A Time Series Study on the Effects of Cold Temperature on Road Traffic Injuries in Seoul, Korea. *Environ. Res.* 132, 290–296. doi:10.1016/j.envres.2014.04.019
- Liu, X., Rees, S. J., and Spitler, J. D. (2007). Modeling Snow Melting on Heated Pavement Surfaces. Part II: Experimental Validation. *Appl. Therm. Eng.* 27, 1125–1131. doi:10.1016/j.applthermaleng.2006.07.029
- Liu, H., Maghoul, P., Bahari, A., and Kavgi, M. (2018). Feasibility Study of Snow Melting System for Bridge Decks Using Geothermal Energy Piles Integrated with Heat Pump in Canada. *Renew. Energy* 136, 1266–1280. doi:10.1016/j.renene.2018.09.109
- Loveridge, F., and Powrie, W. (2013). Pile Heat Exchangers: thermal Behaviour and Interactions. *Proc. Inst. Civil Eng. - Geotech. Eng.* 166, 178–196. doi:10.1680/jeng.11.00042
- Miyamoto, S., and Takeuchi, M. (2005). Snow-Melting System on Road Using Seasonal Energy Storage Through Foundation Piles for Bridge. *Doboku Gakkai Ronbunshu* 2005, 51–797. doi:10.2208/jscej.2005.797_51
- Morino, K., and Oka, T. (1994). Study on Heat Exchanged in Soil by Circulating Water in a Steel Pile. *Energy and Buildings* 21, 65–78. doi:10.1016/0378-7788(94)90017-5
- Nagai, N., Miyamoto, S., Tsuda, T., and Yamahata, S. (2009). “Experimental Demonstrations and Optimal Design Conditions of Snow-Melting System Using Geothermal and Solar Energy,” in *Asme Heat Transfer Summer Conference Collocated with the Interpack09 & Energy Sustainability Conferences*, Location Dallas, Texas, March 13–16, 2011. doi:10.1115/ht2009-88181
- Noy, N. F., and McGuinness, D. L. (2001). *Ontology Development 101: A Guide to Creating Your First Ontology*. And San Antonio, TX: Stanford Medical Informatics.
- Ozudogru, T. Y., Olgun, C. G., and Arson, C. F. (2015). *Analysis of Friction Induced Thermo-Mechanical Stresses on a Heat Exchanger Pile in Isothermal Soil*. San Antonio, TX: Geotechnical&Geological Engineering.
- Ren, G., Ding, R., and Li, H. (2019). Building an Ontological Knowledgebase for Bridge Maintenance. *Adv. Eng. Softw.* 130, 24–40. doi:10.1016/j.advengsoft.2019.02.001
- Self, S. J., Reddy, B. V., and Rosen, M. A. (2013). Geothermal Heat Pump Systems: Status Review and Comparison with Other Heating Options. *Appl. Energy* 101, 341–348. doi:10.1016/j.apenergy.2012.01.048
- Yari, M., and Javani, N. (2010). Performance Assessment of a Horizontal-Coil Geothermal Heat Pump. *Int. J. Energy Res.* 31, 288–299. doi:10.1002/er.1230
- Yurchyshyna, A., and Zarli, A. (2009). An Ontology-Based Approach for Formalisation and Semantic Organisation of Conformance Requirements in Construction. *Automat. Constr.* 18, 1084–1098. doi:10.1016/j.autcon.2009.07.008
- Zhang, K., and Liao, P.-C. (2015). Ontology of Ground Source Heat Pump. *Renew. Sust. Energy Rev.* 49, 51–59. doi:10.1016/j.rser.2015.04.021

Conflict of Interest: The authors declare that the research was conducted in the absence of any commercial or financial relationships that could be construed as a potential conflict of interest.

Publisher’s Note: All claims expressed in this article are solely those of the authors and do not necessarily represent those of their affiliated organizations, or those of the publisher, the editors, and the reviewers. Any product that may be evaluated in this article, or claim that may be made by its manufacturer, is not guaranteed or endorsed by the publisher.

Copyright © 2021 Zhang, Cui, Li, Zhang and Liu. This is an open-access article distributed under the terms of the Creative Commons Attribution License (CC BY). The use, distribution or reproduction in other forums is permitted, provided the original author(s) and the copyright owner(s) are credited and that the original publication in this journal is cited, in accordance with accepted academic practice. No use, distribution or reproduction is permitted which does not comply with these terms.



Research on the Failure Evolution Process of Rock Mass Base on the Acoustic Emission Parameters

Xiaohui Liu^{1,2}, Xiaoping Zhao^{3*}, Shishu Zhang³, Ran Congyan³ and Rui Zhao¹

¹Key Laboratory of Fluid and Power Machinery, Xihua University, Ministry of Education, Chengdu, China, ²Key Laboratory of Deep Earth Science and Engineering, Sichuan University, Ministry of Education, Chengdu, China, ³Chengdu Hydroelectric Investigation and Design Institute Corporation, Chengdu, China

OPEN ACCESS

Edited by:

Yunlai Zhou,
Universidade Lusófona, Portugal

Reviewed by:

Srutarshi Pradhan,
Norwegian University of Science and
Technology, Norway
Tao Lai,
Nanjing Tech University, China
Ferenc Kun,
University of Debrecen, Hungary

*Correspondence:

Xiaoping Zhao
2013012@chidi.com

Specialty section:

This article was submitted to
Interdisciplinary Physics,
a section of the journal
Frontiers in Physics

Received: 30 November 2020

Accepted: 07 July 2021

Published: 24 August 2021

Citation:

Liu X, Zhao X, Zhang S, Congyan R
and Zhao R (2021) Research on the
Failure Evolution Process of Rock
Mass Base on the Acoustic
Emission Parameters.
Front. Phys. 9:635306.
doi: 10.3389/fphy.2021.635306

Fracture mechanics behavior and acoustic emission (AE) characteristics of fractured rock mass are related to underground engineering safety construction, disaster prediction, and early warning. In this study, the failure evolution characteristics of intact and fracture (e.g., single fracture, parallel fractures, cross fractures, and mixed fractures) coal were studied and contrasted with each other on the basis of the distribution of max amplitude of AE. The study revealed some meaningful results, where the value of b (i.e., the distribution characteristic of max amplitude of AE) could represent the failure evolution process of intact and fractured coal. The maximum amplitude distribution of AE events was characterized by Gaussian normal distribution, and the probability of the maximum amplitude of AE events corresponding to 35~50 dB was the largest. In the stress range of 60~80%, AE events and maximum amplitude increased rapidly, and the corresponding b value decreased. The energy of AE events showed a downward trend after reaching the maximum value at about 80% stress level. Under the same stress level, the more complex the fracture was, the larger the b value of coal-rock mass was, and the stronger the inhibition effect on the fracture expansion caused by the internal fracture distribution was. Due to the anisotropy of coal-rock mass with a single crack, the distribution of the b value was more discrete, while the anisotropy of coal-rock mass with mixed crack decreased, and the dispersion of the b value decreased. The deformation of cracked coal mainly caused by the adjustment of cracks during the initial loading b value experienced a trend of decreasing first, then increasing, and then decreasing in the loading process. When the load reached 0.8 times of the peak strength, the b value had a secondary decreasing trend, indicating the macroscopic failure of the sample, which could be used as a precursor criterion for the complete failure of coal-rock mass.

Keywords: fractured coal-rock mass, failure evolution, acoustic emission, maximum amplitude, distribution regularity

INTRODUCTION

As an important strategic resource in China, coal plays a very important role in primary energy consumption. In the National Energy Development Strategy (2030~2050), it was predicted that China's coal output will reach 3.4~4 billion tons in 2020~2030. In 2030 and 2050, coal will maintain about 55 and 50% of China's primary energy structure, respectively, so coal will remain the main

energy resource in China for a long time in the future. Due to the influence of geological structure and mining, fracture development occurs in the surrounding rock mass. Compared with the intact rock mass, the fractured rock mass has become very sensitive to blasting or mechanical disturbance load. Therefore, the study on the instability evolution characteristics of fractured coal–rock mass has important practical significance for efficient coal mining.

In general, the problem of rock mechanics was the mechanical behavior of fracture rock mass in the engineering scale, especially characters of strength, deformation, and failure of fracture rock mass. And the mechanical behavior of fracture rock mass was always a hotspot and difficult problem in rock mechanical field, where the hotspot was its strong application value and the difficulty lay in obtaining the fracture rock mass specimens. At present, the primary research methods for the fracture rock mass were fastened on the physical simulating test [1–5], numerical analysis [6, 7], *in situ* test, and others. Many achievements have been acquired through those methods, but their drawbacks are also obvious. For the physical simulation experiment, similar material and prefabricated crack were used to simulate the fracture rock mass specimens. But compared with the rock materials, the differences of similar material in the internal crystal structure, composition, and cementing material led to the essential difference on crack enlargement. Numerical methods were effective ways to study the mechanical behavior of fracture rock mass in recent years; however, the inhomogeneity of rock materials, parameter selection, and the failure criterion were problems that cannot be ignored. For the *in situ* test, the main problems were as follows: expensive, time consuming, and others. In this study, the fractured rock mass specimens were obtained through preloading the intact specimens to avoid the difficulty of obtaining fractured rock mass.

However, the fracture rock mass was cut by all kinds of structural surfaces, such as primary structural plane and secondary structural plane. This is bound to make the failure mechanism of fracture rock mass different with the intact rock. It must be more complex and diverse. It is very important to analyze this problem more reasonably and effectively. With the development of science, new technologies were also used in the research on rock mechanics, such as CT and AE [8–11]. Especially, since the AE technology was introduced into the field of rock mechanics by Goodman in the 1960s, the AE technique had become an indispensable methodology to study rock behaviors.

At present, there are many studies on the AE response of the rock failure process [12–16]. Chen [17] and Zhang [18] discussed the application of AE technology in rock mechanics research. Li et al. [19] studied the fracture development of intact shale in the fracturing process by using the AE ring number ratio and energy rate, and determined the damage evolution law of shale according to the AE ring number, and characterized the shale degradation behavior. Zhou [20], Zhang [21], and Xu et al. [22] by using AE monitoring system, such as breaking process of rock, studied the AE response of different stress stages. In particular, the AE b value is one of the important parameters; studying the characteristics of rock AE can reflect the change of micro-cracks on rock internal

scale, and the b value of mutations usually could be used as rock macroscopic failure precursors [23–25]. Lei et al. [26] showed that the sudden drop of the b value indicated that the interaction between the cracks inside the rock was enhanced, indicating that the rock was about to be unstable and might be destroyed soon. Yang et al. [27] found that the AE b value was relatively small at the early stage of loading, indicating the rock crack compaction behavior. The b value gradually increased in the elastic stage, indicating the elastic deformation behavior of the rock crack. When the stress level reaches 70% in the late loading period, the sudden drop of the b value corresponded to the crack propagation behavior. When the stress level reaches 90%, the low level of the b value indicated the macroscopic failure of rock. Xue et al. [28] found that the b value was abnormal in the early loading stage and was at a high value in the early loading stage. When the stress reached about 80% in the plastic stage, the b value began to decrease rapidly, indicating the rapid development of the number of large-scale cracks. Zha et al. [29] and Zhang et al. [30] believed that in the process of uniaxial compression of rock, the b value dropped sharply with the increase of stress at the late loading period, indicating the fracture of the rock. Lisjak et al. [31] obtained through numerical results that the b value of rock dropped sharply twice in the process of failure. The first time was at the pre-peak stress level of 75%, and the second time was at the pre-peak stress level of 97%. The decrease of the b value indicated that the crack on the main fracture plane was transformed from diffusion nucleation to crack coalescence.

However, the existing studies on AE response and the b value of rock are basically focused on intact rock mass, and there are few studies on AE characteristics during deformation and failure of fractured rock mass. In this study, the fractured coal–rock mass was acquired by preloading the intact coal rock. According to the different combinations of cracks in the fractured coal–rock mass, the specimens could be divided into single fracture, parallel fracture, cross fracture, and mixed fractured coal–rock mass, statistically. Based on rock material with the acoustic emission phenomenon in the failure process under loading, the maximum amplitude of AE events (i.e., the b value) was used to study the failure evolution process of the intact coal rock, the single fracture, parallel fracture, cross fracture, and mixed fractured coal–rock mass, and then, the failure evolution characteristics and difference between intact rock and fracture rock mass were studied.

TEST SPECIMENS AND EQUIPMENT

Feasibility Analysis and Scheme of Preparation of Fractured Coal–Rock Mass Technical and Test Equipment Feasibility

Fracture mechanical behavior of rock mass plays an important role in engineering practice. The fracture rock mass specimens were mainly obtained by direct or indirect methods presently. Affected by factors such as sampling and specimen processing, the direct method used to obtain fracture rock mass specimens during manufacturing was difficult. And so, the indirect method was the main method to obtain fracture rock mass specimens.

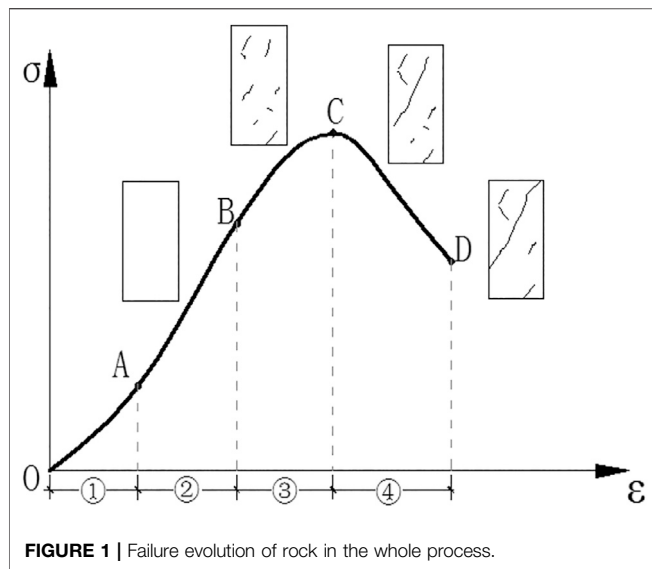


FIGURE 1 | Failure evolution of rock in the whole process.

As the anisotropic materials controlled by the structural plane, the fractured rock mass was obviously different from that of the conventional rock. In order to obtain the fractured rock mass by the loading of conventional rock, it was necessary to analyze and classify the deformation and failure process. For general rock materials, due to their relatively high strength, they had brittle fracture characteristics, most of which were “II” deformation and failure curves. The damage was severe, and the process from cracking to penetrating the specimen was very short. The success rate of obtaining fractured rock specimens was low. For the soft coal rock, the deformation and damage severity were relatively low, showing the “I” type deformation failure curve (**Figure 1**). It was feasible to stop the loading before the cracks penetrated the test piece to obtain the fractured rock specimen.

Based on it, the method for obtaining the fractured rock mass specimens was as follows: considering the failure process of coal-rock mass as the development and expansion of internal micro-cracks, and the process of macro-cracking through the test piece. Then by preloading the intact rock specimens, the fracture rock specimens could be obtained by stopping the loading process before cracks penetrated the specimens (**Figure 2**).

As mentioned above, it was feasible to obtain fracture rock mass on a laboratory scale when the test equipment loading system could stop loading after the max loading point and before the destruction point, and then, rock mass specimens with fracture and without destruction could be obtained. In this study, the early prefabricated and later loading of the fracture rock mass specimens were conducted by MTS815 rock mechanics test system (**Figure 3**) from Sichuan University. The testing system has a higher integral rigidity and electro-hydraulic servo control system, which can achieve a variety of control conditions such as stress, strain, and transformation. The testing system could also be made to stop loading before rock specimens are destroyed completely. Therefore, indoor prefabricated fractured rock specimens are also feasible on the test equipment. In order to avoid other influence of the fracture

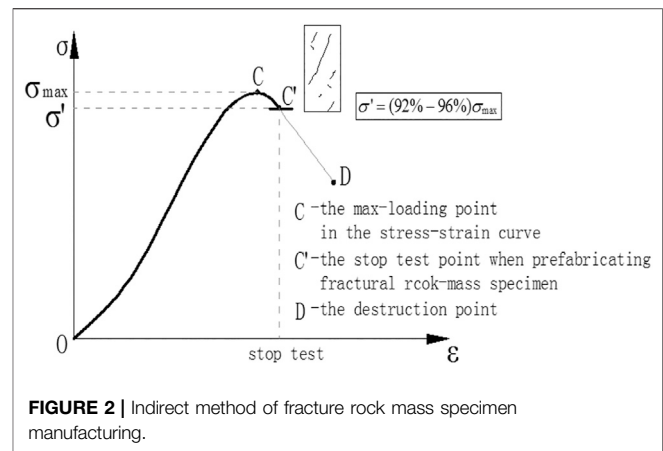


FIGURE 2 | Indirect method of fracture rock mass specimen manufacturing.

rock mass on failure evolution, uniaxial compression loading scheme to the specimens was adopted, with the axial loading rate of 10 kN/min before the loading arrived at the peak, and then, lateral deformation control was used after max loading point with the rate of 0.02 ~ 0.04 mm/min. In addition, in order to capture AE space location points, a total of 8 AE sensors were arranged on the upper and lower parts of the samples in the direction of vertical diameter.

Therefore, whether it was technical feasibility or the requirements of the test equipment, it was feasible to obtain the samples of the fractured coal-rock mass by loading the intact coal rock by laboratory test means.

Preparation Scheme of Fractured Coal-Rock Mass

Based on the MTS815 rock mechanics test system, different loading methods were used to perform fractured coal-rock mass samples of Pingdingshan and Tashan intact coal rock. The loading methods include uniaxial, conventional triaxial, and three different mining methods (the caving, no pillar, and protective layer mining). The relevant loading schemes are as follows [32]:

1) Uniaxial loading test

The axial compression was loaded to the peak load at a rate of 10 kN/min, and the post-peak stage was controlled by transverse deformation. The loading was stopped after the set stress value ($\sigma' = (92\% - 96\%) \sigma_{\max}$) was loaded at a rate of 0.02~0.04 mm/min.

2) Conventional triaxial loading test

It mainly included two stages: adding confining pressure stage, in which the internal confining pressure was loaded to 25 MPa at a rate of 3 MPa/min; in the axial compression stage, when the confining pressure was loaded to 25 MPa, the axial compression was loaded to the peak stage at a rate of 30 kN/min. After the peak, the lateral deformation control was adopted, and the loading was stopped at a rate of 0.02~0.04 mm/min to the preset stress value ($\sigma' = (92\% - 96\%) \sigma_{\max}$).

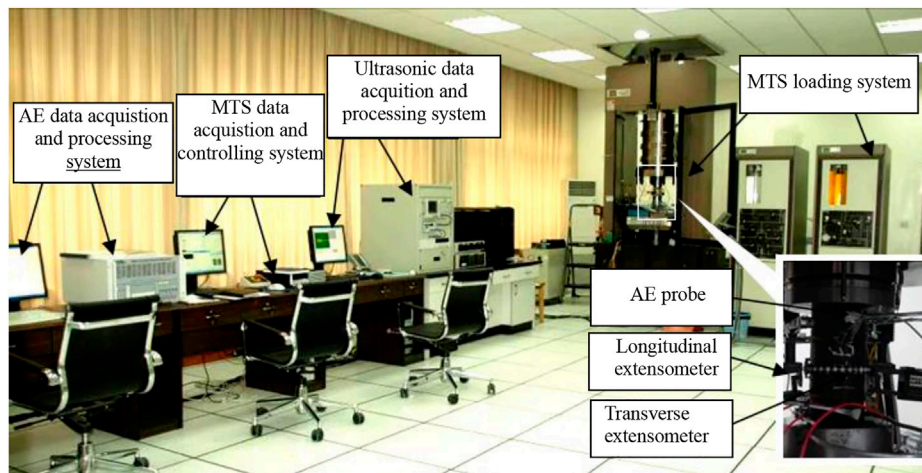


FIGURE 3 | MTS815 rock mechanics test system.

3) Indoor simulation loading of three mining methods in coal mine

There were mainly three stages: confining pressure loading stage, in which the confining pressure was loaded to 25 MPa at a rate of 3 MPa/min. In the first stage of confining pressure unloading, the confining pressure was unloaded at a rate of 1 MPa/min, and the axial load was loaded to 37.5 MPa at a loading rate of 2.25 MPa/min. In the second stage of confining pressure unloading, the confining pressure continues to be unloaded at a rate of 1 MPa/min. The axial load was loaded at a rate of 2.25, 3.5, and 4.75 MPa/min, respectively, according to the three mining methods of protective layer, top coal caving, and no coal pillar, until the peak. After the peak, the lateral deformation control was adopted. Loading was performed at a rate of 0.02~0.04 mm/min to the preset stress value ($\sigma' = (92\% - 96\%) \sigma_{\max}$) and then stopped.

Through the above indirect method, fractured coal-rock mass specimens could be obtained and classified, and then the failure evolution and difference of intact rock and fracture rock mass could be studied.

Fractured Rock Mass Classification

For the sake of better research on the failure evolution of the fracture rock mass, the fracture rock mass could be divided into single fracture, parallel fracture, cross fracture, and mixed fracture rock mass in the statistical sense based on the space composition and complexity of fracture in rock mass by pre-casting. And the typical specimen photos, CT scans, and their classification of the intact coal and fractured coal-rock mass specimens with different compositions are shown in **Table 1**. For distinguishing the intact coal and fractured coal-rock mass specimens conveniently, specimen number F represents the specimens were fractured coal-rock mass after pre-casting.

In order to avoid the deviation of the analysis results caused by different rock types, the hard rock and soft rock samples were, respectively, collected from Tashan coal mine and Pingdingshan

coal mine, and the fractured rock samples were prefabricated. The physical characteristics and microscopic composition are shown in **Table 2**. On this basis, the study carried out experimental research through 26 effective specimens, including six intact coal-rock specimens, five single fracture rock masses, three parallel fracture rock masses, five cross fracture rock masses, and seven mixed fracture rock masses.

THE QUANTITATIVE DESCRIPTION OF THE MAXIMUM AMPLITUDE DISTRIBUTION OF ACOUSTIC EMISSION

The maximum amplitude of a single AE event was analyzed during the loading process. For a single AE event, analyzing its maximum amplitude was meaningless, but the significance lies in the distribution of all the maximum amplitude of AE events during the failure process, which could reveal the failure evolution regularities and difference of fracture rock mass. As rock materials, Katsuyama [33] represented the distribution of maximum amplitude of AE through the following **Eq. 1**.

$$n(a) = k \cdot a^{-m} da, \quad (1)$$

where a is the maximum amplitude of AE events in the process of damage, and its unit is dB (0 dB is equivalent to 100 μ V, 100 dB is equivalent to 10 V).

$n(a)$ —the frequency distribution of maximum amplitude of a , between the amplitude increased from a to $a + da$ on the amount of AE events.

k, m —constants.

Through **Eq. 1**, amount of $N(A)$ which was greater than the maximum amplitude of A could be infinite integrals by **Eq. 1** as follows:

$$N(A) = \int_A^{+\infty} k \cdot a^{-m} da. \quad (2)$$

TABLE 1 | Photos and CT scans of typical specimens and their classification.


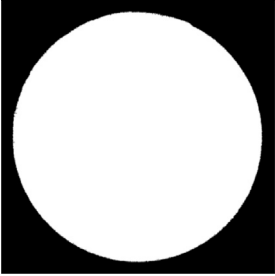
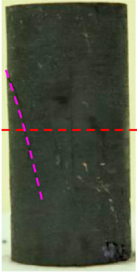

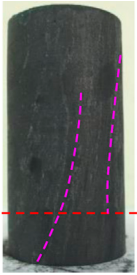
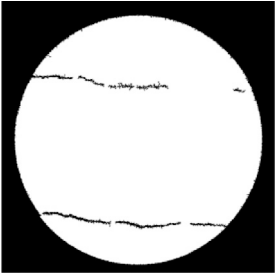



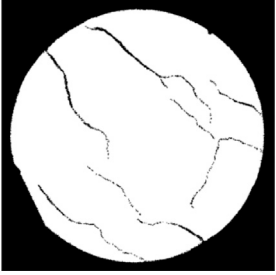
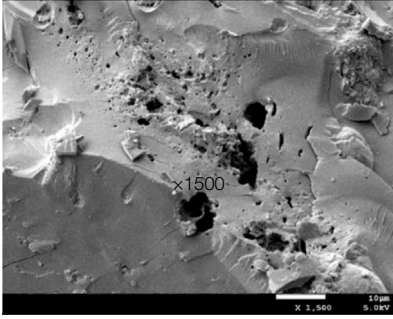
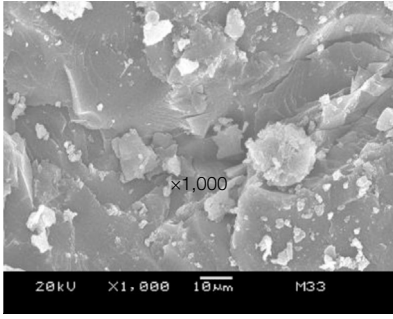
The fracture type	Crack images	CT scan	The geometric description
Intact coal (1–3)			No fractures
Single fractured coal-rock mass (F1-31)			A single fracture
Parallel fractured coal-rock mass (F1-72)			Two or more parallel fractures
Cross fractured coal-rock mass (F1-38)			Two intersecting fractures or Y-shaped fractures
Mixed fractured coal-rock mass (F1-35)			The random combination of the above fracture types

TABLE 2 | Physical and microscopic features of rock specimens.

Rock type	Scanning electron microscope	Average wave speed (m/s)
Pingding Shan coal rock		988.2
Tashan coal rock		2,606.2

Therefore,

$$N(A) = \frac{k}{1-m} \cdot A^{-(m-1)} = t \cdot A^{-(m-1)}. \quad (3)$$

where A is the maximum amplitude of AE events during the failure process, dB.

$N(A)$ is the amount of AE events that was greater than (include) the maximum amplitude in the process of failure.

t -constant, $= k/(1-m)$ -constant, its physical meaning was equivalent to the probability of hindering to specimen damage, and when the distribution density of blockage was higher, the probability of hindering to specimen damage was greater with the higher value of m .

When letting $b = m - 1$, Eq. 3 could be converted to Eq. 4 as follows:

$$N(A) = t \cdot A^{-b}. \quad (4)$$

Then, log on both sides of Eq. 4:

$$\log(N(A)) = \log(t) - b \log(A). \quad (5)$$

Therefore, by collecting AE events during the process of failure evolution, Eq. 5 could be used to obtain a quantitative description index (i.e., the value of b) of maximum amplitude distribution of AE events, where the b value was equivalent to the probability of hindering to the specimen failure. As a quantitative evaluation index, this parameter

was used to analyze the failure evolution regularities and difference of fracture rock mass.

TEST RESULT AND ANALYSIS

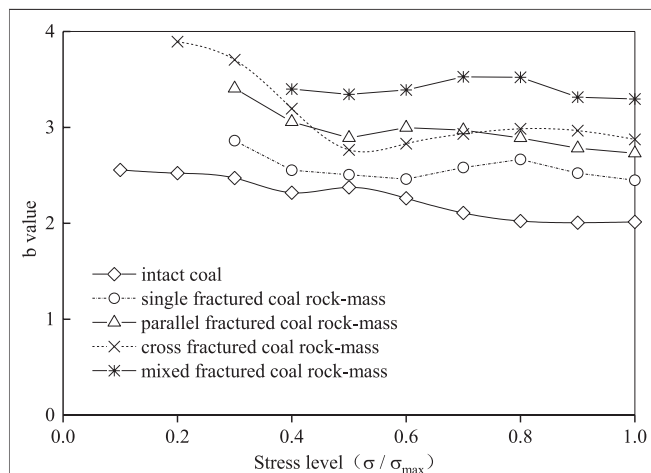
Based on the uniaxial loading condition, the maximum amplitude distribution characteristics of intact coal rock and four different fractured rock mass were analyzed.

Amplitude Variation Regularities Under Different Stress Levels

As a quantitative description of the maximum amplitude distribution characteristics of AE events in the loading failure process of rock, the b value could reflect the change of crack scale inside rock. In order to explore the similarities and differences in the crack evolution process of coal-rock mass with different fracture degrees in the loading failure process, the amplitude distribution of intact, single fracture, parallel fractures, cross fractures, and mixed fractures coal under different stress levels in the uniaxial loading process is listed in Table 3. Using the above method to calculate the b value, the fitting correlation coefficient under different stress levels was above 0.8, and part could reach 0.9, which showed that the b value error was small, to meet the requirements of the error [34]. Due to the length of the

TABLE 3 | Results of the b value under different stress levels of fractured coal-rock mass.

Stress level (σ/σ_{\max})		0.1	0.2	0.3	0.4	0.5	0.6	0.7	0.8	0.9	1.0	The average of R^2
Intact coal (1–3)	b value	2.556	2.523	2.472	2.319	2.374	2.261	2.108	2.023	2.006	2.014	0.917
Single fractured coal-rock mass (F1-31)		–	–	2.861	2.553	2.506	2.461	2.581	2.666	2.523	2.448	0.881
Parallel fractured coal-rock mass (F1-72)		–	–	3.406	3.057	2.891	2.997	2.971	2.890	2.782	2.731	0.967
Cross fractured coal-rock mass (F1-38)		–	3.893	3.705	3.195	2.765	2.830	2.932	2.985	2.966	2.875	0.879
Mixed fractured coal-rock mass (F1-35)		–	–	–	3.399	3.344	3.390	3.527	3.522	3.315	3.296	0.846

**FIGURE 4** | Distribution of the b value under different stress levels of fractured coal rock mass.

article and considering the small difference of the correlation coefficient of the value at different stress levels, the average correlation coefficient of various coal-rock masses at different stress levels is listed in **Table 3**. Due to the few AE events in the initial loading stage of individual samples, the b value was partially missing. The results showed that the b value was lower when the stress level was higher, which meant that the b value tended to decrease with the increasing of stress levels.

The distribution regularity of the b value for the intact coal and four kinds of fractured coal-rock mass under different stress levels is shown in **Figure 4**, where σ_{\max} represents the peak strength, namely, the failure point of the sample; σ is the actual stress. On the whole, the b value tended to decrease with the increasing of stress levels, where the illustrated maximum amplitude of distribution regularity was that AE events with large amplitude were increasing under the condition of the same amount of AE events, the physical meaning was that the propagation extent of internal cracks had a trend of increasing, and the scale of those cracks was becoming larger on the microcosmic with the increasing of uniaxial loading. From the local of the curve from **Figure 4**, the b value of both intact coal and fractured rock mass had a stage of increasing first and then decreasing, and the stress levels of this stage that appeared in fractured coal-rock mass were obviously higher than those in intact coal; for example, the stress levels of this stage in intact

coal were 40 ~ 60% of the peak, while the fractured coal-rock mass was about 50 ~ 90%. At this stage, the amount of AE events with large amplitude trended to decreasing, which revealed that the crack extension was restrained during the process of failure. Then, with the increasing of stress levels, AE events with large amplitude increased, but the b value was decreased fleetly. Comparing the b value of intact coal with that of fractured coal-rock mass (**Figure 4**) at this stage, the more complex fracture contained inside the coal-rock mass, the b value was increased more obviously, and the b value of the fractured coal-rock mass increased significantly higher than that of the intact coal. The b value of intact coal, single fracture, parallel fracture, cross fracture, and mixed fractured coal-rock mass was increased by 0.055, 0.085, 0.106, 0.155, and 0.178, respectively.

The more complex the fracture (i.e., in sequence of intact, single fracture, parallel fractures, cross fractures, and mixed fractures coal) in coal-rock mass, the greater b value it was under the same stress level. For example, when the loading reached the peak, the b value of the fracture rock mass from complex to simple was 3.296, 2.875, 2.731, and 2.448, respectively, while the b value of the intact coal was 2.014. In addition, compared with the results of distribution regularity of the b value for the intact coal, single fracture, parallel fracture, cross fracture, and mixed fractured coal-rock mass had a similar trend during the process of failure evolution at the stress level from 0 to the peak.

In conclusion, the characteristic parameter b of maximum amplitude distribution of AE events changing regularities under different stress levels showed that the damage of intact coal and fractured coal-rock mass were embodied as the increasing scale of cracks inside on the microscopic and increasing AE events with large amplitude. During the changing process, the growth of micro-cracks was restrained when the stress had increased to a certain level, and then, micro-cracks inside started to propagate until the stress reached the peak strength. In addition, the b value decreased before the specimen reached instability, which was also consistent with the existing literature reports [35–37]. The decrease of the b value represented the large-scale development of high-energy acoustic emission events. Before the failure, the b value dropped sharply, indicating that the proportion of high-energy large-scale micro-cracks increased gradually, and the development of micro-cracks changed from disorder to order. When the micro-crack size distribution was relatively constant, the b value gradually

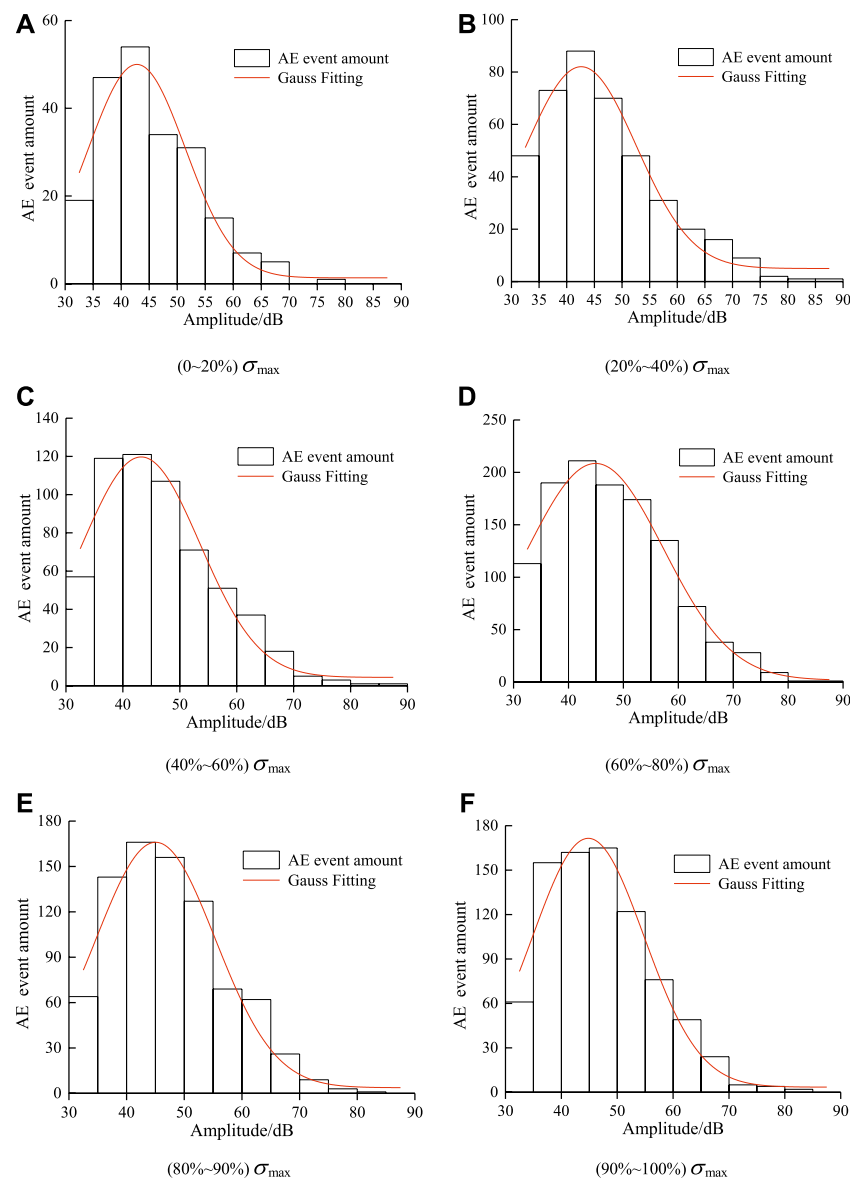


FIGURE 5 | Maximum amplitude distribution frequency and probability distribution curves of AE in different stress intervals of intact coal-rock mass (1-3).

tended to be stable. Finally, crack penetration led to specimen instability and failure.

The Frequency of Amplitude Distribution in Different Stress Intervals

Due to similar changing regularities of the characteristic parameter b of AE events in intact coal and fractured coal-rock mass during the failure evolution process, in order to study furthermore, the intact coal specimens 1-3# were used as an example to analyze the failure evolution process reflected by the b value in different stress intervals. During the uniaxial loading, the frequency of maximum

amplitude distribution of AE events in different intervals is shown in **Figure 5**.

Combined with the b value of intact coal rock in **Table 2**, when the stress level was in the interval of 0 ~ 20%, there was few of AE events with maximum amplitude about 35 ~ 45 dB mainly. As the stress level was loaded to the interval of 20 ~ 40%, the amount of AE events and amount of AE events with larger amplitude had increased, where the maximum amplitude was about 35 ~ 50 dB primarily, and the value b was reduced comparing with the previous interval. When the stress level was in the interval of 40 ~ 60%, the amount of AE events continued to increase, and the increasing of the low amplitude of the events was faster than that with larger amplitude, which suggested that the propagation of

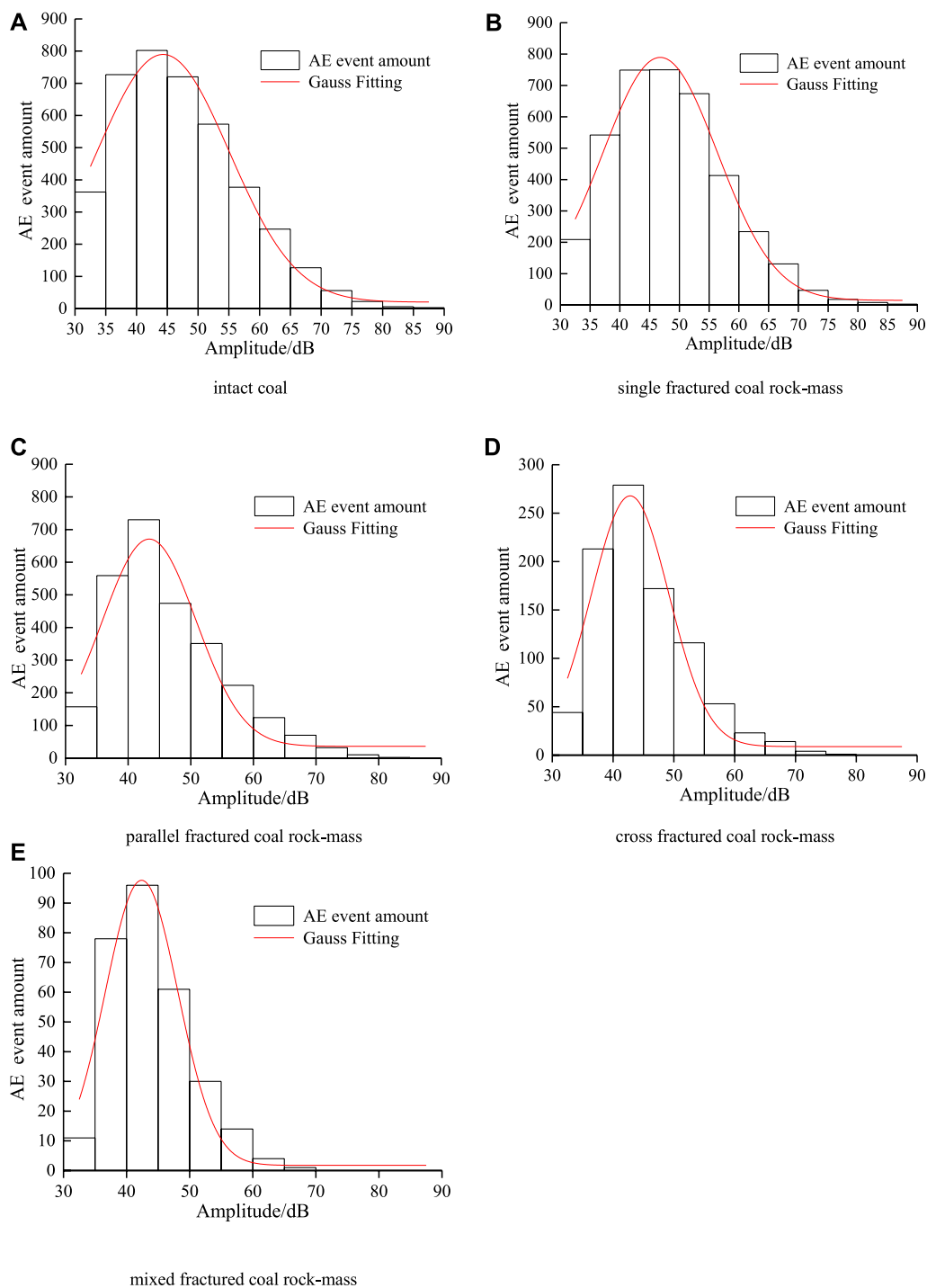


FIGURE 6 | Maximum amplitude distribution frequency and probability distribution curves of AE events from 0 to peak of intact coal and fractured coal-rock mass.

micro-cracks in this interval was restrained, and reflected with the increasing b value. When the stress level was in the interval of 60 ~ 80%, the amount of AE events with large amplitude had increased rapidly compared with the previous interval, especially the AE events with maximum amplitude about 50 ~ 60 dB, which embodied that the large scale of cracks were developing rapidly

on the microscale, and reflected with the reducing b value. After loading the stress level to the interval of 80 ~ 100%, the growth of AE events with maximum amplitude was getting to be stable, and the reducing of the b value was also gently. And comparing with the previous interval with larger scale of cracks developed, the crack development was dominated by adjustment and began

TABLE 4 | Gaussian normal distribution function of frequency distribution of AE maximum amplitude in different stress zones of intact coal-rock mass (1–3).

Stress level	The Gaussian normal distribution function	R^2
(0~20%) σ_{\max}	$g(x) = 1.34 + 48.66 \times e^{-2 \times [(x-42.80)/17.30]^2}$	0.931
(20~40%) σ_{\max}	$g(x) = 4.99 + 77.05 \times e^{-2 \times [(x-42.62)/19.99]^2}$	0.973
(40~60%) σ_{\max}	$g(x) = 4.38 + 115.35 \times e^{-2 \times [(x-43.21)/20.65]^2}$	0.953
(60~80%) σ_{\max}	$g(x) = 1.77 + 206.76 \times e^{-2 \times [(x-44.94)/24.75]^2}$	0.982
(80~90%) σ_{\max}	$g(x) = 3.74 + 162.25 \times e^{-2 \times [(x-45.04)/20.67]^2}$	0.963
(90~100%) σ_{\max}	$g(x) = 3.49 + 167.97 \times e^{-2 \times [(x-44.83)/19.92]^2}$	0.965

to expand along the existing large scale of cracks on the microscale.

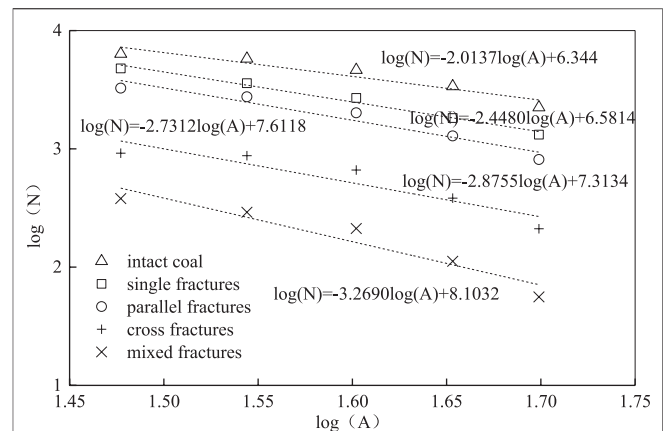
In order to better reflect the amplitude distribution characteristics of coal-rock mass, the Gaussian normal distribution function " $g(x) = y_0 + [a/(w \times \sqrt{\pi/2})] \times e^{-2 \times [(x-x_0)/w]^2}$ " was selected to perform statistical probability fitting for the maximum amplitude of AE events, and the Gaussian normal distribution curve as shown in Figure 6 was obtained. Its distribution function and degree of fitting are shown in Table 4. AE events with amplitude distribution have good Gaussian normal distribution characteristics, such as high fitting degree. In different stress regions, the probability of AE events concentrated in the range of maximum amplitude from 35 to 50 dB is the largest.

In summary, the quantitative evaluation index b value could reflect very well in the distribution regularities of maximum amplitude of AE events during the failure evolution process of coal, and the maximum amplitude of AE events could directly reflect the expanding intensity of cracks in the coal. Therefore, the characteristic parameter b of AE events could describe the failure evolution process of coal well. In addition, the stress interval with a large amplitude increase could be used as a precursor to the peak of the specimen through the maximum amplitude distribution frequency of the AE event. Then, the b value that characterizes the maximum amplitude distribution of the AE event was drastically reduced to the stress level when it was gradual as a pre-destruction.

The Variation Regularities of Maximum Amplitude Between Different Fractured Rock Mass

The maximum amplitude distribution frequency of AE events for intact coal and fractured coal-rock mass during the stress level from 0 to the peak loading is shown in Figure 6.

As shown in Figure 6, the distribution frequency of maximum amplitude of intact coal was more "full" than that in fractured

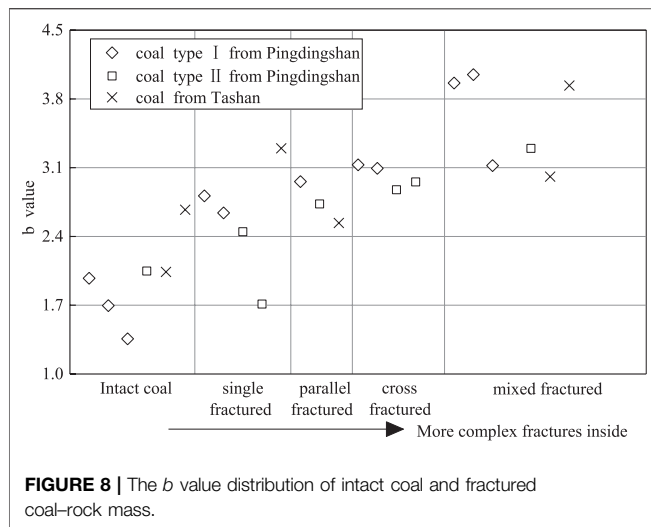
**FIGURE 7 |** The b value of intact coal and fractured coal-rock mass at the peak loading ($\sigma = \sigma_{\max}$).

coal-rock mass from the distribution shape, where it was more "slender" in fractured coal-rock mass. And comparing the shape in different fracture rock mass, the more complex the fracture (i.e., in sequence of intact coal, single fracture, parallel fractures, cross fractures, and mixed fractures) in coal-rock mass, the more "slender" it was. Based on the distribution characteristics of maximum amplitude of AE events, the intact coal had more AE event amount and more distribution range, where the amplitude of AE events was distributed mainly in the interval of 35 ~ 55 dB, and there were 87 AE events with amplitude more than 70 dB. For the fractured coal-rock mass with more complex fracture, the decrease of AE event amount was more obvious, and the AE events with large amplitude reduced more. Taking mixed fracture of coal-rock mass as an example, the maximum amplitude of AE events was mainly from 35 to 45 dB, where the amount of AE events declined steeply when the amplitude was larger than 45 dB, and there were no AE events with amplitude greater than 70 dB. So, compared with intact coal and fractured coal-rock mass, the more complex the fracture (i.e., in sequence of intact coal, single fracture, parallel fracture, cross fracture, and mixed fractured coal-rock mass), the more reduction of the total AE events and the amount with large amplitude of AE events. The reason for this was that with more complex fracture inside, the internal cracks could expand along the existed fracture more easily, and the cracks expanding with large scale were reduced more for the low bearing capacity of rock bridge cut by fractures.

In order to better reflect the amplitude distribution characteristics, through statistical probability fitting of the distribution frequency of

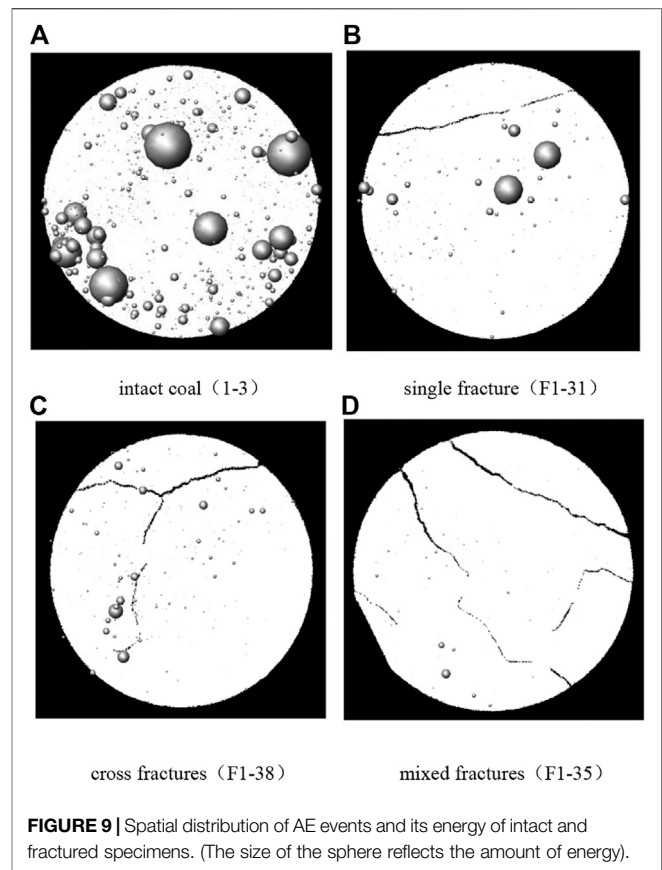
TABLE 5 | Gaussian normal distribution function of maximum amplitude distribution frequency of intact coal and fractured coal-rock mass.

The type of rock mass	The Gaussian normal distribution function	R^2
Intact coal (1–3)	$g(x) = 20.13 + 769.48 \times e^{-2 \times [(x-44.32)/21.53]^2}$	0.976
Single fractured coal-rock mass (F1-31)	$g(x) = 14.93 + 774.60 \times e^{-2 \times [(x-46.78)/19.29]^2}$	0.985
Parallel fractured coal-rock mass (F1-72)	$g(x) = 36.04 + 639.27 \times e^{-2 \times [(x-43.37)/14.96]^2}$	0.910
Cross fractured coal-rock mass (F1-38)	$g(x) = 8.82 + 259.06 \times e^{-2 \times [(x-42.81)/12.78]^2}$	0.936
Mixed fractured coal-rock mass (F1-35)	$g(x) = 1.76 + 95.89 \times e^{-2 \times [(x-42.38)/11.55]^2}$	0.953



the maximum amplitude, the Gaussian normal distribution law of the maximum amplitude distribution frequency with a high degree of fit can be obtained. **Table 5** shows the Gaussian normal distribution function and fitting degree of coal-rock mass with different fracture combinations. It was observed that the probability of the maximum amplitude event of AE occurred at about 45 dB was the largest.

Based on the characterization of the maximum amplitude distribution at the range from 0 to the peak loading, the b value characteristics at the peak stress of coal-rock mass with different fractures were further analyzed. As shown in **Figure 7**, under uniaxial loading, the b value at the peak stress of intact coal, single fracture, parallel fracture, cross fracture, and mixed fractured coal-rock mass was 2.014, 2.448, 2.731, 2.876, and 3.269, respectively. Thus, the b value of intact coal was the smallest, while the b value of coal-rock mass with mixed fractures with the most complex fractures was the largest. Thus, the more complex the primary fractures were, the greater the b value was, where the physical meaning was that the more complex the fracture inside, the more barriers existed to restrain crack propagation caused by internal crack distribution. On the microscale, the main reason for this was that the more the fractures existed in the coal-rock mass, the lower the capacity of bearing the load and storing less energy inside, and the cracks could be better adjusted during the crack propagation for the more the fractures existed, which led that the more complex the fractures inside, the less scale cracks happened. In addition, as shown in **Figure 8**, the b value distribution of single fracture coal-rock mass was more discrete, where the reason was that the bearing capacity of single fractured rock mass was influenced by the direction between the load and fracture, and the characteristics of anisotropic were reflected. For mixed fractured coal-rock mass, the discrete degree of the b value was lower than the single fracture inside, where it was shown that the effects were reduced which was caused by the direction between the loading and fracture with lower characteristics of anisotropic.



Temporal and Spatial Distribution Characteristics of Acoustic Emission Events

In order to reflect the relationship between the evolution of internal fractures and the degree of main fractures in the process of coal-rock failure, the spatial distribution of AE events and energy in the process of failure evolution of intact coal and coal-rock mass with different fractures is shown in **Figure 9**. By correcting the accuracy of the AE positioning system in the test process, the experiment was carried out under the condition that the absolute errors of the AE source in X direction, Y direction, and Z direction were all less than 2 mm. As for the energy of AE events, the energy and quantity of AE events in the failure process of intact coal rock were the largest. Compared with the coal-rock mass with different combinations of fractures, the amount of AE events and its energy had shown a trend of decrease when the fractures were more complex. Compared with fractured coal-rock mass, the spatial distribution of AE events in intact coal rock was discrete, and the crack propagation was random, which would not be affected by fracture. However, the spatial distribution of AE events reflected the correlation between the spatial location of fractures and AE events. Taking single, cross, and mixed fractured coal-rock mass as examples, under the condition of uniaxial loading, the expansion of the micro-cracks was controlled by the existing fractures, which led that the AE events were mainly distributed along the penetration

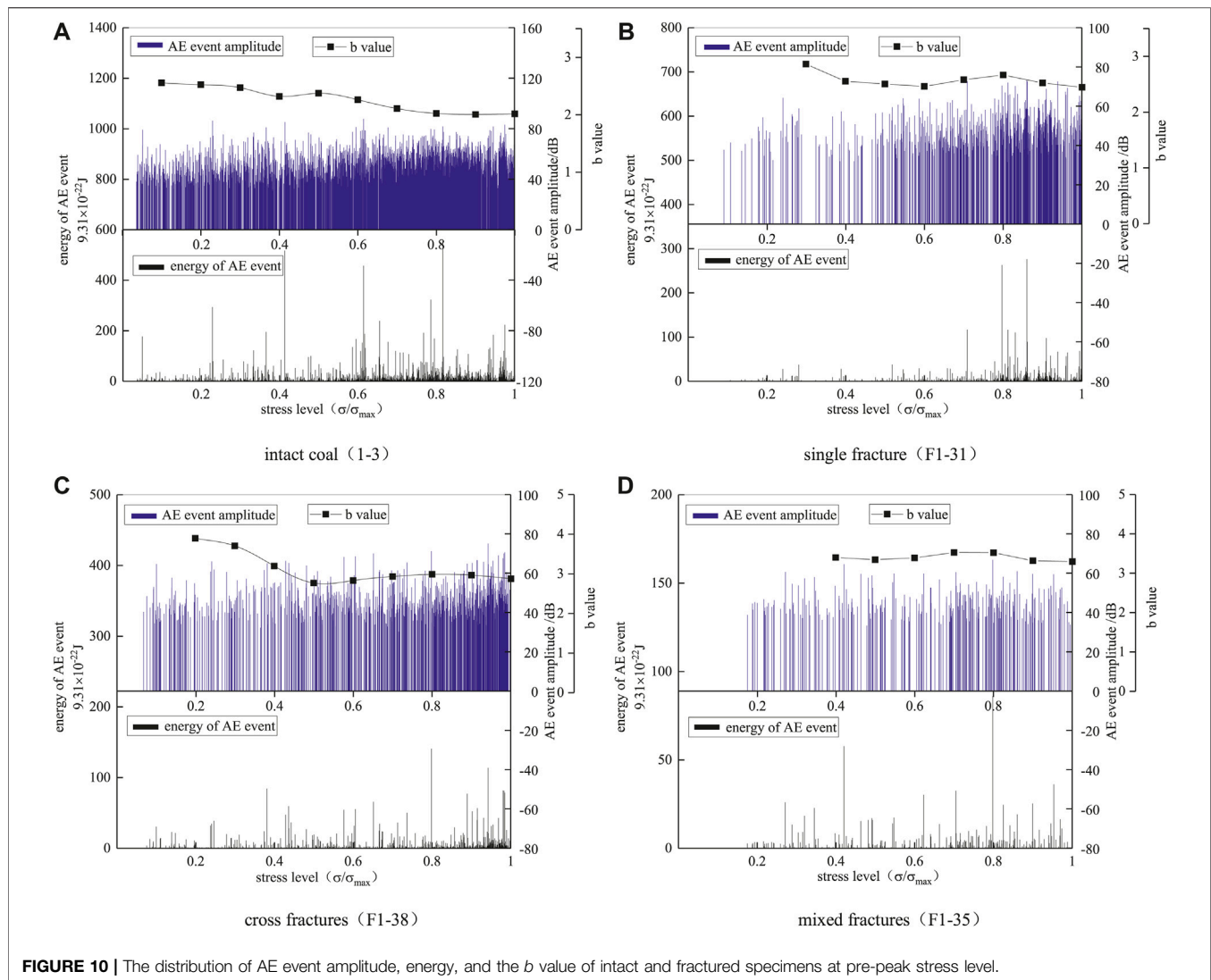


FIGURE 10 | The distribution of AE event amplitude, energy, and the b value of intact and fractured specimens at pre-peak stress level.

failure surface presenting with concentrated distribution on the macroscale. For single fracture coal-rock mass, the AE events were mainly distributed along the surface of existing fracture, while for cross and mixed fractured coal-rock mass, the AE events were mainly distributed in the locked segment.

The amplitude, energy, and the b value of AE events were combined to reflect the failure evolution process of intact coal and coal-rock mass with different fracture combinations and the relationship between the parameters. The relationship among AE event amplitude, energy, and the b value in different stress levels of intact coal and fractured coal-rock mass with different fracture combinations under uniaxial loading is shown in **Figure 10**.

As shown in **Figure 10**, the energy of AE events in intact coal-rock mass was greater than that in fractured coal-rock mass significantly, and the more complex the fracture was, the lower the AE energy was. At the low stress level, the more complex the fracture was, the deformation in the failure process was mainly adjusted along the existing fracture, and the lower the energy of acoustic emission event was. When the stress level was loaded to

0.6~0.8 times of the peak strength (σ_{\max}), the distribution of AE events with large energy was relatively concentrated, caused by cracks extending in special direction. During the stress level of 0.8 ~ 1, both the AE amplitude and AE energy increased and then decreased. Based on the AE amplitude and energy distribution of intact coal and fractured coal-rock mass, the variation trend of AE amplitude was consistent with that of AE energy, and when the energy value was large, the AE amplitude increased. Comparing with the distribution in intact coal, because of the effect of the existed fractures, AE events with large energy in fractured coal-rock mass were mainly distributed along the failure fracture during the whole loading process, which mainly happened at the stress level about 0.8, while the intact coal-rock mass occurred at 0.6~0.8 times. The amplitude of intact coal varied continuously during the test, while the amplitude of fractured coal and rock mass changed from disperse to continuity, and the amplitude frequency was high when the stress level was 0.6~1. The results of this study were consistent with those of Meng et al. [38, 39]. In the compaction and

elastic stages, the amplitude of AE energy was relatively low, and new micro-cracks could not be formed under low stress. When the stress entered the plastic stage, the internal structure of coal rock was damaged, and the amplitude of AE energy increased gradually.

As shown in **Figure 10**, no matter how intact coal or fractured coal-rock mass occurred with different fracture combinations, the energy of AE events showed a decreased trend after reaching the maximum value during the failure evolution process, and it indicated that the failure evolution was dominated by development and extension of cracks with smaller size and breakthrough the rock bridge between cracks after the AE event with maximum energy arrived. In general, the acoustic wave was the external macroscopic representation of crack extension in rock material during its failure process, where the maximum amplitude of the AE event was positively related to its energy. Combined with the distribution of the b value at different stress levels, the b value of AE events showed an increased trend at the stress level of 0.6–0.8 in fractured coal-rock mass, and it showed that the amount of AE events with large amplitude was decreasing and the internal energy was accumulating during this stress interval. When the stress level was loaded up to about 0.8, the b value was reducing obviously, where the amount of AE events with large amplitude was increasing conspicuously, and it was in accordance with the energy of AE event distribution in this stress level. After the stress level was about 0.8, the failure evolution was dominated by development and extension of cracks with smaller size, and the b value represented the distribution regularities of AE events were decreasing gradually and trending to be gentle finally. Therefore, based on the characteristics during the failure evolution process in fractured coal-rock mass, some regularities could be presented, where the b value would decrease and then increase and then decrease in the pre-peak phase, and the stress level could be considered as the precursor of the b value occurred. For intact coal, internal cracks were extended randomly under uniaxial loading caused by no constraint of existed fractures and higher strength inside, and the AE events with large energy were distributed during the whole failure process, where the b value was decreased on the whole and distinguished from fractured coal-rock mass. When the stress level was loaded up to about 0.8, the b value trended to be gentle after the AE event with largest energy happened, which was in accordance with fractured coal-rock mass. So, based on the variation regularity of the b value reflected and the maximum amplitude distribution of AE events in intact coal and fractured coal-rock mass during the failure evolution process, it could be considered that the second decrease and flattening of the b value is the premonitory criterion of failure.

CONCLUSION

As we know, one of the difficulties in studying the mechanical behavior of fractured rock mass was on how to obtain the fractured rock mass specimens. In this study, the fractured rock mass specimens were obtained by preloading intact rock

(coal) in the rock mechanic rigidity servo testing system (MTS815). Then through the acoustic emission phenomenon of rock during loading failure and the maximum amplitude distribution law of the AE event, the failure evolution process of intact rock and fractured rock mass specimens under uniaxial loading condition was studied on the basis of the maximum amplitude distribution of AE events. The main characteristics during the failure process could be concluded as follows:

- 1) Based on the quantity and spatial distribution of fractures, the fractured rock mass could be categorized into four types from simple to complex, such as single fracture, parallel fractures, cross fractures, and mixed fractures successively in the statistical sense.
- 2) The b value which represented the characteristics of the maximum amplitude distribution of AE events could be used to reflect the failure evolution process of the rock mass, where the more the fractures inside, the more obvious damage effect and the larger b value were.
- 3) Under different stress levels, the b value of intact rock and fractured rock mass showed a decreasing trend with the increase of load on the whole. Under the condition of the same stress level, the more complex the fractures inside, the larger the b value was. That is, the value b of intact coal rock < single fractured rock mass < parallel fractured coal-rock mass < cross fractured rock mass < mixed fractured coal-rock mass.
- 4) During the uniaxial loading, the cracks inside intact rock were extended randomly, and the distribution of AE events was discrete, where the AE events of the cracks inside fractured rock mass were concentrated under the influence of existed fractures.
- 5) Before the loading reached the peak value, in the process of failure evolution of intact rock mass and fractured rock mass, the b value decreased, then increased and then decreased, and finally tended to be flat. The feature that the b value decreased for the second time and gradually flattened out could be regarded as an early warning signal that the loading reached the peak.

DATA AVAILABILITY STATEMENT

The original contributions presented in the study are included in the article/Supplementary Material; further inquiries can be directed to the corresponding author.

AUTHOR CONTRIBUTIONS

All authors listed have made a substantial, direct, and intellectual contribution to the work and approved it for publication.

FUNDING

This article was financially supported by the Key Scientific Research Fund of Xihua University (Grant No: Z17113), the Key Project of Sichuan Education Department (Grant No:

18ZA0457), the Opening Fund of Key Laboratory of Deep Earth Science and Engineering Ministry of Education of Sichuan University (Grant No: DESE202003), and Chengdu Engineering Corporation Limited (CHIDI), POWERCHINA.

REFERENCES

- Singh M, Rao KS, and Ramamurthy T. Strength and Deformational Behaviour of a Jointed Rock Mass. *Rock Mech Rock Engng* (2002) 35(1):45–64. doi:10.1007/s006030200008
- Lajtai EZ. Shear Strength of Weakness Planes in Rock. *Int J Rock Mech Min Sci Geomech Abstr* (1969) 6(7):499–515. doi:10.1016/0148-9062(69)90016-3
- Savilahti T, Nordlund E, and Stephansson O. Shear Box Testing and Modeling of Joint Bridges. *Int J Rock Mech Min Sci Geomech Abstr* (1990) 28:295–300. doi:10.1016/0148-9062(91)92236-r
- Zhu WS, Liang ZY, Wang P, and Caizhao z. Research on Strength Behavior of Jointed Rock Mass by Numerical and Physical Simulation. *Proc of the Intern Conf on Mechanics of Jointed and Faulted Rock, Vienna* (1990) 29:389–397. doi:10.1016/0148-9062(92)93749-a
- Reyes O, and Einstein H. Failure Mechanism of Fracture Rock – A Fracture Coalescence Model. In: *Proceedings 7th International Congress of Rock Mechanics*; 16–20 Sep 1991; Germany, Aachen: Balkema Publishers (1991). p. 333–40.
- Min K-B, and Jing L. Numerical Determination of the Equivalent Elastic Compliance Tensor for Fractured Rock Masses Using the Distinct Element Method. *Int J Rock Mech Mining Sci* (2003) 40(6):795–816. doi:10.1016/S1365-1609(03)00038-8
- Shi GH. *Discontinuous Deformation Analysis: A New Numerical Model for the Statics and Dynamics of Block System*. Berkeley: University of California at Berkeley (1988).
- Ge XR, Ren JX, Pu YB, Ma W, and Zhu Y. A Real in Time CT Triaxial Testing Study of Meso-Damage Evolution. *Chin J Rock Mech Eng* (1999) 18(5):497–502. doi:10.3321/j.issn:1000-6915.1999.05.001
- Kawakata H, Cho A, Kiyama T, Yanagidani T, Kusunose K, and Shimada M. Three-dimensional Observations of Faulting Process in Westerly Granite under Uniaxial and Triaxial Conditions by X-ray CT Scan. *Tectonophysics* (1999) 313:293–305. doi:10.1016/S0040-1951(99)00205-x
- Labuz JF, and Bialzi L. Experiments with Rock: Remarks on Strength and Stability Issues. *Int J Rock Mech Mining Sci* (2007) 44(4):525–37. doi:10.1016/j.ijrmms.2006.09.005
- Feng X-T, Chen S, and Zhou H. Real-time Computerized Tomography (CT) Experiments on sandstone Damage Evolution during Triaxial Compression with Chemical Corrosion. *Int J Rock Mech Mining Sci* (2004) 41:181–92. doi:10.1016/S1365-1609(03)00059-5
- Kim J-S, Lee K-S, Cho W-J, Choi H-J, and Cho G-C. A Comparative Evaluation of Stress-Strain and Acoustic Emission Methods for Quantitative Damage Assessments of Brittle Rock. *Rock Mech Rock Eng* (2015) 48(2):495–508. doi:10.1007/s00603-014-0590-0
- Wang C, Chang X, and Liu Y. Experimental Study on Fracture Patterns and Crack Propagation of Sandstone Based on Acoustic Emission. *Adv Civil Eng* (2021) 2021:1–13. doi:10.1155/2021/8847158
- Wang J, Xie L, Xie H, Ren L, He B, Li C, et al. Effect of Layer Orientation on Acoustic Emission Characteristics of Anisotropic Shale in Brazilian Tests. *J Nat Gas Sci Eng* (2016) 36:1120–9. doi:10.1016/j.jngse.2016.03.046
- Zhang G, Li H, Wang M, Li X, Wang Z, and Deng S. Crack-induced Acoustic Emission and Anisotropy Variation of Brittle Rocks Containing Natural Fractures. *J Geophys Eng* (2019) 16(3):599–610. doi:10.1093/jge/gxz031
- Zhang H, Lu C-P, Liu B, Liu Y, Zhang N, and Wang H-Y. Numerical Investigation on Crack Development and Energy Evolution of Stressed Coal-Rock Combination. *Int J Rock Mech Mining Sci* (2020) 133:104417. doi:10.1016/j.ijrmms.2020.104417
- Chen Y. Application of Acoustic Emission Techniques to Rock Mechanics Research. *J Mech Strength* (1977) 05:312–22. (in chinese).
- Zhang BQ. Principle and Application of Acoustic Emission. *Petro-chemical Equipment* (1980)(06) 47–57.
- Li Y, Xue L, and Wu X. Study on Acoustic Emission and X-ray Computed-Tomography Characteristics of Shale Samples under Uniaxial Compression Tests. *Environ Earth Sci* (2019) 78(5):173. doi:10.1007/s12665-019-8185-4
- Zhou HW, Wang ZH, Ren WG, Liu ZL, and Liu JF. Acoustic Emission Based Mechanical Behaviors of Beishan Granite under Conventional Triaxial Compression and Hydro-Mechanical Coupling Tests. *Int J Rock Mech Mining Sci* (2019) 123:104125. doi:10.1016/j.ijrmms.2019.104125
- Zhang Y, Feng X-T, Yang C, Zhang X, Sharifzadeh M, and Wang Z. Fracturing Evolution Analysis of Beishan Granite under True Triaxial Compression Based on Acoustic Emission and Strain Energy. *Int J Rock Mech Mining Sci* (2019) 117:150–61. doi:10.1016/j.ijrmms.2019.03.029
- Xu J, Liu Y, and Peng S. Acoustic Emission Parameters of Three Gorges Sandstone during Shear Failure. *Acta Geophys* (2016) 64(6):2410–29. doi:10.1515/ageo-2016-0094
- Liu X, Gu Q, Tan Y, Ning J, and Jia Z. Mechanical Characteristics and Failure Prediction of Cement Mortar with a Sandwich Structure. *Minerals* (2019) 9(3):143. doi:10.3390/min9030143
- Zhang Q, and Zhang X-P. A Numerical Study on Cracking Processes in limestone by the B-Value Analysis of Acoustic Emissions. *Comput geotechnics* (2017) 92:1–10. doi:10.1016/j.compgeo.2017.07.013
- Zhou Z, Wang H, Cai X, Chen L, E Y, and Cheng R. Damage Evolution and Failure Behavior of Post-Mainshock Damaged Rocks under Aftershock Effects. *Energies* (2019) 12(23):4429. doi:10.3390/en12234429
- Lei X, Kusunose K, Rao MVMS, Nishizawa O, and Satoh T. Quasi-static Fault Growth and Cracking in Homogeneous Brittle Rock under Triaxial Compression Using Acoustic Emission Monitoring. *J Geophys Res* (2000) 105(B3):6127–39. doi:10.1029/1999JB900385
- Yang J, Mu Z-L, and Yang S-Q. Experimental Study of Acoustic Emission Multi-Parameter Information Characterizing Rock Crack Development. *Eng fracture Mech* (2020) 232:107045. doi:10.1016/j.engfracmech.2020.107045
- Xue Y, Dang F, Cao Z, Du F, Ren J, Chang X, et al. Deformation, Permeability and Acoustic Emission Characteristics of Coal Masses under Mining-Induced Stress Paths. *Energies* (2018) 11(9):2233. doi:10.3390/en11092233
- Zha E, Zhang R, Zhang Z, Ai T, Ren L, Zhang Z, et al. Acoustic Emission Characteristics and Damage Evolution of Rock under Different Loading Modes. *Energies* (2020) 13(14):3649. doi:10.3390/en13143649
- Zhang L, Yang D, and Chen Z. Deformation and Failure Characteristics of Weathered Granite under Uniaxial Compression. *AIP Adv* (2019) 9(7):075222. doi:10.1063/1.5113661
- Lisjak A, Liu Q, Zhao Q, Mahabadi OK, and Grasselli G. Numerical Simulation of Acoustic Emission in Brittle Rocks by Two-Dimensional Finite-Discrete Element Analysis. *Geophys J Int* (2013) 195(1):423–43. doi:10.1093/gji/ggt221
- Zhao XP. *Study on Mechanics Behavior of Fractured Coal Rock-Mass*. Chengdu: Sichuan University (2013).
- Katsuyama K. *Application of AE Techniques*. Beijing: China Metallurgical Industry Press (1996). Translated by Feng Xiating.
- Liu XL, Liu Z, Li XB, and Si HM. Acoustic Emission B-Values of limestone under Uniaxial Compression and Brazilian Splitting Loads. *Rock Soil Mech* (2019) 40(S1):267–74.
- Kong X, Wang E, Hu S, Shen R, Li X, and Zhan T. Fractal Characteristics and Acoustic Emission of Coal Containing Methane in Triaxial Compression Failure. *J Appl Geophys* (2016) 124:139–47. doi:10.1016/j.jappgeo.2015.11.018
- Su G-s., Gan W, Zhai S-b., and Zhao G-f. Acoustic Emission Precursors of Static and Dynamic Instability for Coarse-Grained Hard Rock. *J Cent South Univ* (2020) 27(10):2883–98. doi:10.1007/s11771-020-4516-6

ACKNOWLEDGMENTS

The authors wish to acknowledge the significant contributions to this study by all colleagues of Sichuan University and CHIDI who provided large amounts of original data.

37. Triantis D. Acoustic Emission Monitoring of marble Specimens under Uniaxial Compression. Precursor Phenomena in the Near-Failure Phase. *Proced Struct Integrity* (2018) 10:11–7. doi:10.1016/j.prostr.2018.09.003
38. Meng H, Yang Y, Wu L, Wang F, and Peng L. Study of Strength and Deformation Evolution in Raw and Briquette Coal Samples under Uniaxial Compression via Monitoring Their Acoustic Emission Characteristics. *Adv Civil Eng* (2020) 2020:1–16. doi:10.1155/2020/8868754
39. Ding X, Xiao X, Lv X, Wu D, and Xu J. Mechanical Properties of Bump-Prone Coal with Different Porosities and its Acoustic Emission-Charge Induction Characteristics under Uniaxial Compression. *Adv Civil Eng* (2019) 2019:1–18. doi:10.1155/2019/7581061

Conflict of Interest: XZ, SZ, and RC were employed by Chengdu Hydroelectric Investigation and Design Institute Corporation.

The remaining authors declare that the research was conducted in the absence of any commercial or financial relationships that could be construed as a potential conflict of interest.

Publisher's Note: All claims expressed in this article are solely those of the authors and do not necessarily represent those of their affiliated organizations, or those of the publisher, the editors and the reviewers. Any product that may be evaluated in this article, or claim that may be made by its manufacturer, is not guaranteed or endorsed by the publisher.

Copyright © 2021 Liu, Zhao, Zhang, Congyan and Zhao. This is an open-access article distributed under the terms of the Creative Commons Attribution License (CC BY). The use, distribution or reproduction in other forums is permitted, provided the original author(s) and the copyright owner(s) are credited and that the original publication in this journal is cited, in accordance with accepted academic practice. No use, distribution or reproduction is permitted which does not comply with these terms.



A Novel Piezoceramic-Based Sensing Technology Combined With Visual Domain Networks for Timber Damage Quantification

Haibei Xiong, Lin Chen, Cheng Yuan and Qingzhao Kong*

Department of Disaster Mitigation for Structures, Tongji University, Shanghai, China

OPEN ACCESS

Edited by:

Liqiang Wang,
Shanghai Jiao Tong University, China

Reviewed by:

Yiming Zhang,
Hebei University of Technology, China
Jie Li,
Xian Aeronautical Polytechnic Institute,
China

*Correspondence:

Qingzhao Kong
qkong@tongji.edu.cn

Specialty section:

This article was submitted to
Structural Materials,
a section of the journal
Frontiers in Materials

Received: 21 April 2021

Accepted: 31 July 2021

Published: 25 August 2021

Citation:

Xiong H, Chen L, Yuan C and Kong Q
(2021) A Novel Piezoceramic-Based
Sensing Technology Combined With
Visual Domain Networks for Timber
Damage Quantification.
Front. Mater. 8:688594.
doi: 10.3389/fmats.2021.688594

Early detection of timber damage is essential for the safety of timber structures. In recent decades, wave-based approaches have shown great potential for structural damage assessment. Current damage assessment accuracy based on sensing signals in the time domain is highly affected by the varied boundary conditions and environmental factors in practical applications. In this research, a novel piezoceramic-based sensing technology combined with a visual domain network was developed to quantitatively evaluate timber damage conditions. Numerical and experimental studies reveal the stress wave propagation properties in different cases of timber crack depths. Through the spectrogram visualization process, all sensing signals in the time domain were transferred to images which contain both time and frequency features of signals collected from different crack conditions. A deep neural network (DNN) was adopted for image training, testing, and classification. The classification results show high efficiency and accuracy for identifying crack conditions for timber structures. The proposed technology can be further integrated with a fielding sensing system to provide real-time monitoring of timber damage in field applications.

Keywords: timber beam crack, stress wave-based sensing, piezoelectric transducer, computer vision, deep neural network

INTRODUCTION

Timber structures have been increasingly utilized in building construction due to their excellent seismic performance and environmental friendliness, which mean flexible building function, especially with the improvement of engineering wood products (Cao et al., 2019; Chen et al., 2020; Sun et al., 2020). A variety of novel structural systems have been designed and built into landmarks. Wood cracking is an inevitable issue for timber structures because of the variation of temperature and humidity (Li et al., 2013; Dietsch and Winter 2018). Wood cracks could cause potential safety hazards and increase maintenance costs. Therefore, a reliable crack detection technology for extensive in-service and newly constructed timber structures is of great importance to ensure the safety of timber structures.

Existing approaches for timber cracks detection mainly include resistance drilling measurement and scanning image technique (Wei et al., 2011; Brites et al., 2012; Tannert et al., 2014; Kloiber et al., 2015; Zhang et al., 2015; Mol et al., 2020). Drilling measurement is a conventional method to assess the internal condition of timber members (Mol et al., 2020). However, this method is semi-destructive, and the results are highly affected by the test personnel. The scanning image method

utilizes different levels of absorbance between crack and health wood for external waves, such as microwaves (Baradit et al., 2009), X-rays (Wei et al., 2011; Pease et al., 2012; Sandak et al., 2015a), and infrared rays (Sandak et al., 2010; Sandak et al., 2015b), to obtain visualized information of the scanning section. However, this method is a qualitative assessment and limited to relatively high cost for real projects.

Compared to the existing wave-based inspection technology, the stress wave shows potential for timber crack detection since stress wave-based inspection is easy to perform with portable devices for *in situ* assessment. According to frequency bands, stress wave-based approaches can be divided into acoustic tomography (low frequency) (Dackermann et al., 2014a; Riggio et al., 2014; El-Hadad, 2017) and ultrasonic echo method (high frequency exceeds 20 kHz) (Puaad et al., 2014; Koca et al., 2018; Linke et al., 2019). The detection principles, equipment, and applications have been well demonstrated in the literature (Dackermann et al., 2014b; Krause et al., 2015). Conventional data processing for stress wave-based crack detection measures the change of wave velocity in timber structures. However, wave velocity is highly affected by various factors, such as moisture content, wood species, and orientation of growth rings. All mentioned factors bring uncertainties to detection results. Furthermore, wave velocity is normally obtained by the measurement of time-of-flight of the time-domain probing signal. The influences of damage on the frequency domain of the probing signal cannot be investigated (Lee and Shin, 2002).

For obtaining frequency features to achieve high accuracy in damage identification, time-frequency technologies have been widely applied in radar signal recognition (Ahmad et al., 2020), equipment fault detection (Ulloa and Barbieri, 2018), and non-destructive testing (Obuchowski et al., 2014; Dorafshan and Azari, 2020; Li et al., 2020). Gong et al. (Gong et al., 2020) proposed an algorithm for the automatic extraction of the stress wave reflection period based on image processing to measure the different lengths of buried metal piles in soil. Le et al. (Li et al., 2020) adopted time-frequency analysis to extract the instantaneous frequency of a vehicle-bridge interaction system and evaluated the bridge state. Hui et al. (Bao et al., 2018) used the deep learning neural network to identify different time-series images of signal faults in bridge health monitoring. However, there is still no study using time-frequency analysis combined with visual domain networks to detect the timber cracks.

In this paper, the authors propose a novel piezoceramic-based sensing technology combined with the vision classification algorithm for timber crack detection. The proposed visual domain method replaces the conventional way (i.e., damage index) of quantifying the variation of the stress wave signal in the time domain. The received stress wave signal was transformed into spectrograms using the short-time Fourier transform (STFT). Then, the dataset of each case with the label of crack depths was fed into a deep learning network for classification. Numerical simulation was performed to illustrate the stress wave propagation properties when passing through timber cracks in different depth cases. A series of experimental investigations, including a total of three timber beam specimens with seven crack

depth conditions in each, were conducted to validate the feasibility and accuracy of the proposed technology.

METHODOLOGY

The proposed approach consists of three major steps, as detailed in **Figure 1**: 1) data pre-processing by conducting joint time-frequency analysis; 2) data augmentation for expanding the dataset and simulating environmental uncertainties in operation; and 3) deep neural network (DNN) training for crack depth classification. Spectrograms of different crack depths are obtained in data pre-processing using the short-time Fourier transform (STFT). Three data augmentation methods include adding white noise to wave data in the time series, adding Gaussian noise to the spectrum, and jittering spectrograms, which will not change the main characteristics of signals from the statistical perspective (Tanner, 2014). After data augmentation, seven spectrum image datasets with the label of crack depths are fed into the proposed DNN to train a model and consequently identify damage severity.

Stress Wave-Based Sensing Technology Using Piezoelectric Transducers

Piezoelectric materials, such as lead zirconate titanate (PZT), have attracted increasing attention in real-time monitoring of structural damage for their high stability, small size, great linearity, and piezoelectric effects (Yang et al., 2018; Yuan et al., 2020). The feasibility, applicability, and reliability of PZT sensors have been widely validated in the past decade (Dansheng et al., 2016; Zhang et al., 2018a; Zhang et al., 2018b; Han et al., 2019). PZT-based detection mainly includes stress wave sensing and electro-mechanical impedance (EMI) method (Huo et al., 2017; Zhang et al., 2021), while the high-cost equipment requirement impedes practical applications of the EMI method. Furthermore, because of the larger range of perception and the indirect and the direct piezoelectricity of the PZT material, stress wave sensing is adopted in this research, in which PZT-based transducers can function as both actuators and sensors.

In this study, a pair of PZT patches (an actuator and a sensor) is mounted on the timber surface to generate and detect stress waves, respectively. **Figure 2** shows the stress wave propagation mechanism when a crack occurs on timber. The propagation property is affected by the internal condition in the wave path. The existence of cracks in the timber beam could transform the propagation path and wave pattern. When a crack is present, stress waves will reflect and diffract at the damage interface, causing the energy drop-down on the other side of the crack. In **Figure 2**, it is obvious that the stress wave energy attenuates due to reflection and diffraction at crack interfaces.

Generation of Spectrum Image Data

The time-series signal received by piezoelectric transducers only contains information of the time domain, which does not consider the influence of cracks on frequency components.

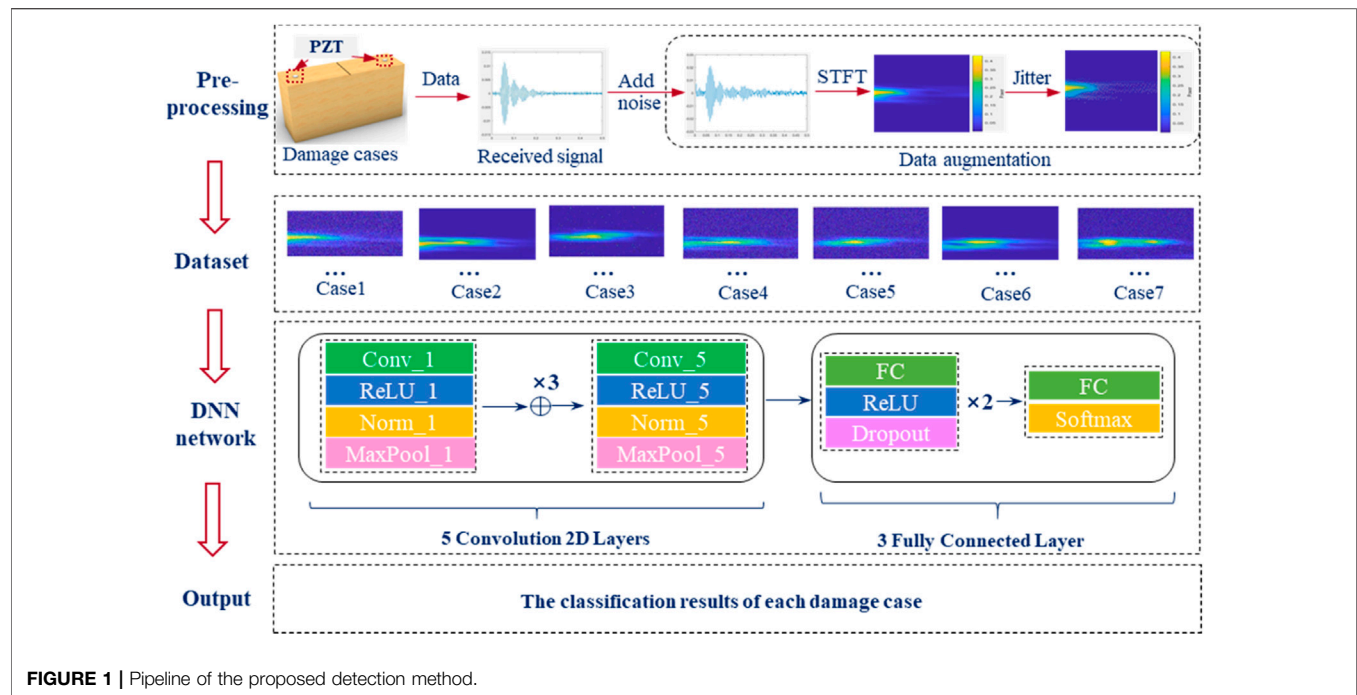


FIGURE 1 | Pipeline of the proposed detection method.

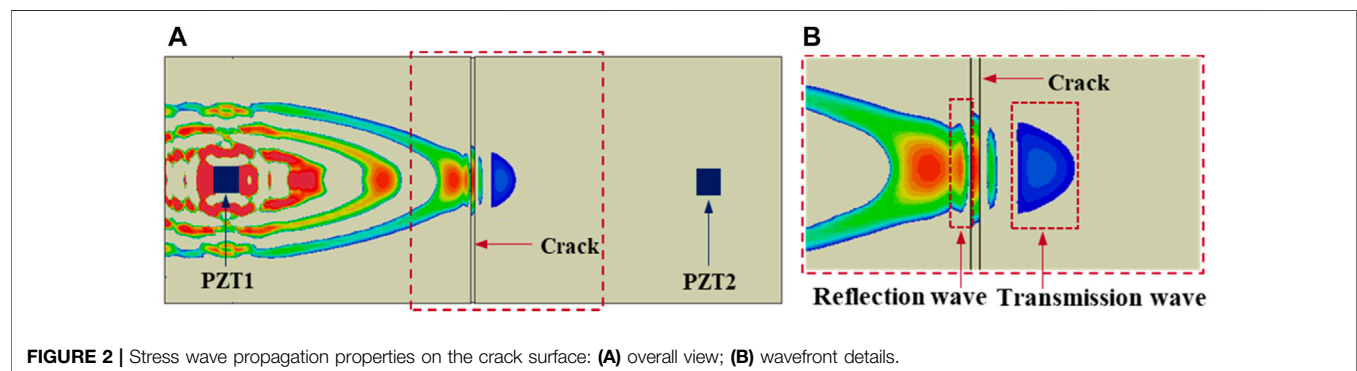


FIGURE 2 | Stress wave propagation properties on the crack surface: (A) overall view; (B) wavefront details.

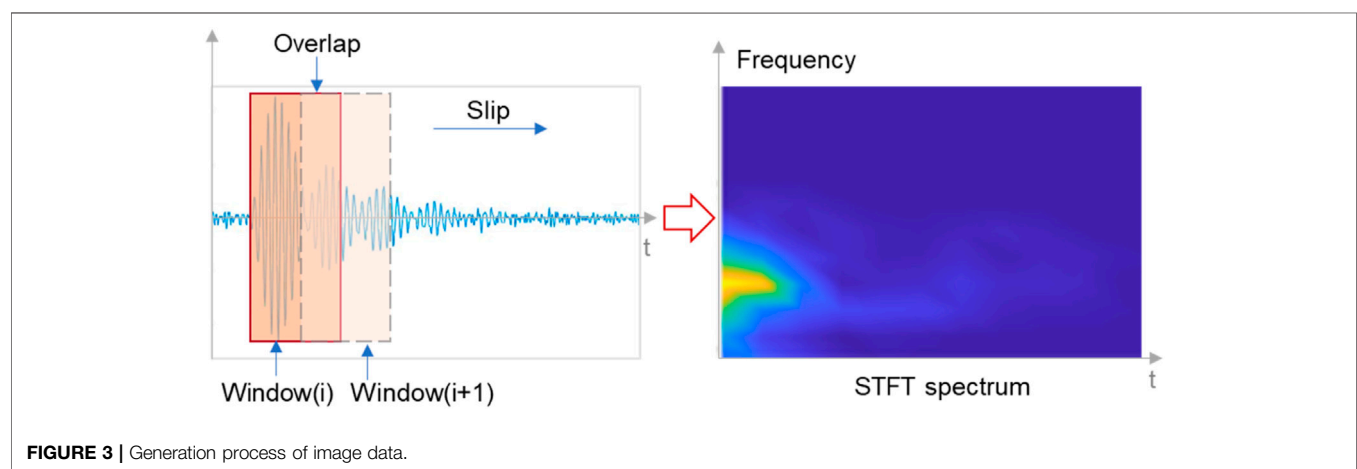
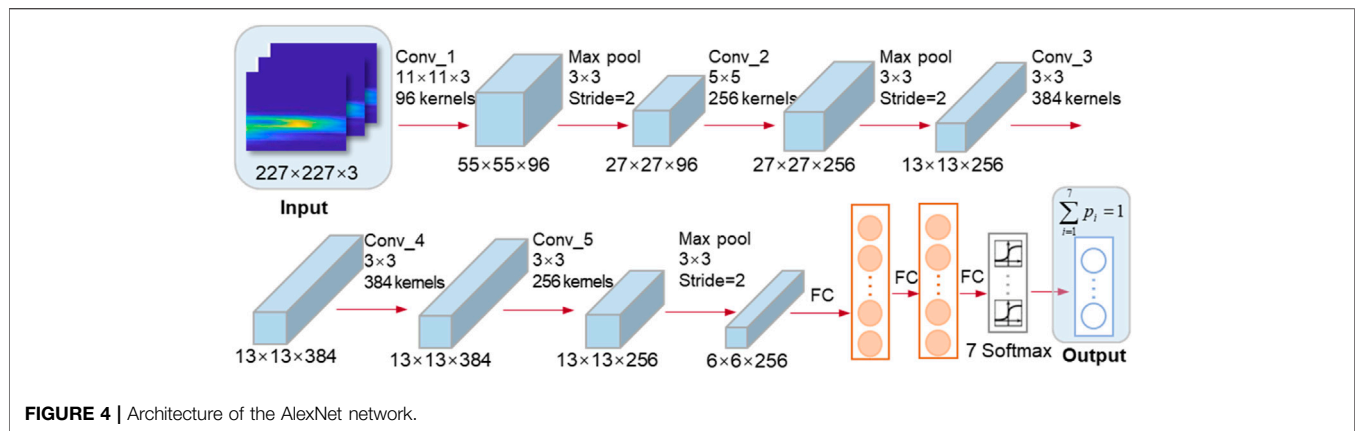


FIGURE 3 | Generation process of image data.



Thus, time–frequency analysis including both time and frequency information of the received signal is utilized in this research to obtain spectrum images of the received signal.

In this generation process of image data, time series from tests are transformed into frequency spectrums by using short-time Fourier transform (STFT). For an original discrete signal sequence $x(n)$, a pre-determined window function is used to divide the time series into many segments, and it is assumed the signal is pseudo-stationary over a short interval, and then Fourier transform is carried out on each window length (Bendory et al., 2017; Rashid and Louis, 2020). The transform process of STFT is shown in **Figure 3**. Both time- and frequency-domain characteristics of timber cracks are contained in STFT spectrums; thus, more damage features can be learned in the training process of the neural network. The calculation of STFT is shown in the following equation:

$$F(m\Delta t, f) = \sum x(n)g(n - m\Delta t)e^{-j\omega n} \quad (1)$$

where $F(m\Delta t, f)$ is a two-dimensional complex matrix representing STFT results, $g(n)$ is the length of the window function (chosen as the Hamming window), and Δt is the hop size in samples between successive discrete Fourier transforms.

Process of Classification Training

STFT spectrum images contain multi-domain feature information of each damage case. Since the DNN has validated significant performance in the classification of images (Shukla and Piratla, 2020), the timber crack detection is conducted using a transferred DNN. The AlexNet network is transferred in this study to imitate the human decision-making process for a deep understanding of the characteristics of STFT spectrums in different crack conditions. The AlexNet network consists of eight layers, including five convolution (Conv) layers and three fully connected (FC) layers (Krizhevsky et al., 2012), as shown in **Figure 4**.

As shown in **Figure 4**, damage spectrums are firstly normalized to the size of $227 \times 227 \times 3$ pixels in the input layer, and then 96 kernels are used to extract edge features in the first convolutional layer. The feature map obtained from the former convolutional layer is then put into the ReLU layer and is

mapped non-linearly using activation function (i.e., rectified linear unit, ReLU). The ReLU layer's output then gets into the pooling layer, in which salient features are extracted by the max-pooling algorithm. These steps are repeatedly conducted in the following four convolutional layers with different kernels and padding sizes. With the increase of convolutional layers, the extracted feature number is significantly increased. After that, feature maps are connected to FC layers. The dropout layer can avoid the occurrence of overfitting. The classification results can be obtained in the output layer using softmax function to normalize possibility in each class.

NUMERICAL STUDY

Model Setup

Numerical simulations were performed in Abaqus. The mechanical properties of timber were set as orthotropic, and detailed constants are listed in **Table 1**. The parameter E represents the elastic modulus, G is the shear modulus, and μ is Poisson's ratio. The indexes L , R , and T represent the longitudinal direction, radial direction, and tangential direction, respectively.

The material properties of PZT patches were adopted values in official documents of Abaqus¹. The dielectric constant, engineering constants, and piezoelectric coupling matrix are listed in **Table 2**.

The interfaces between timber and PZT patches were set as the connection type of tie. The solid element C3D8R was adopted for the timber beam, and the solid element C3D8E with piezoelectric effects was used for PZT patches. The excitation signal was produced by setting different electrical potentials at the top and bottom surfaces of PZT patches. In particular, the electrical potential at the bottom surface was set as zero, and at the top surface, ten voltages with a pre-determined amplitude were set. The excitation load is a one-cycle sine wave with a frequency of 190 kHz.

¹[http://wufengyun.com:888/books/exa/default.htm\(n.d.\)](http://wufengyun.com:888/books/exa/default.htm(n.d.)).

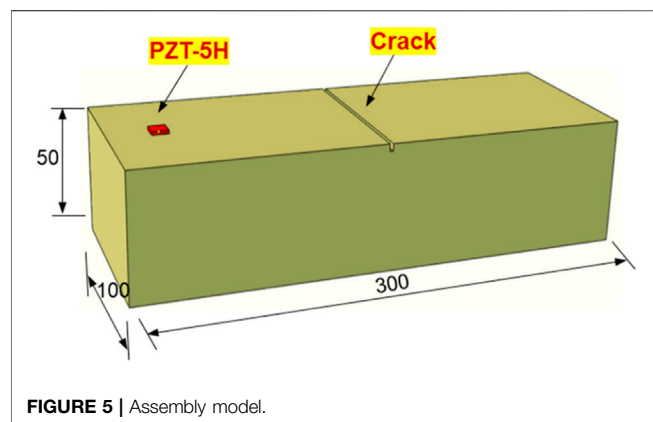
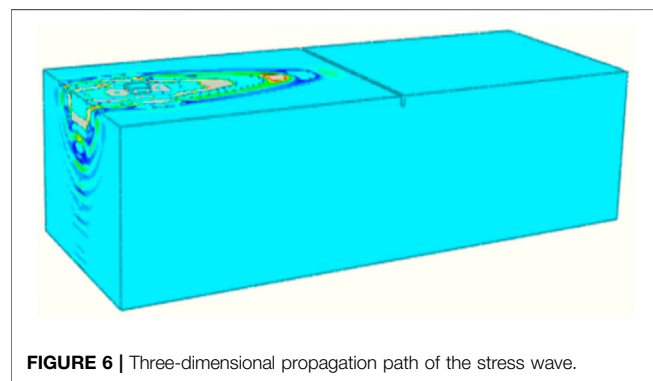
TABLE 1 | Mechanical properties of the timber material used in Abaqus.

Density (g/cm ³)	Moisture content (%)	E_L	E_R	E_T /MPa	G_{LR}	G_{LT}	G_{TR}	μ_{LR}	μ_{LT}	μ_{RT}
0.39	12	11,583	896	496	758	690	39	0.37	0.47	0.43

TABLE 2 | Material properties of PZT patches used in Abaqus.

Engineering constants (GPa)			Piezoelectric coupling matrix (m/volt) $\times E-10$	
E1	60.61		d311	-2.74
E2	60.61		d322	-2.74
E3	48.31		d333	5.93
v12	0.289		d112	7.41
v13	0.512		d223	7.41
			Dielectric matrix (farad/meter) $\times E-08$	
v23	0.512			
G12	23.5		D11	1.505
G13	23		D22	1.505
G23	23		D33	1.301

Note: numbers 1, 2, 3 refers to the direction. Direction 1 represents the length direction of PZT patch, direction 2 refers to the width direction of PZT patch, and direction 3 refers to the thickness direction of PZT patch.

**FIGURE 5** | Assembly model.**FIGURE 6** | Three-dimensional propagation path of the stress wave.

The implicit dynamic solver was used with a time period of 0.0001 s, and the time iteration was $1e-7$. **Figure 5** shows specimen dimensions and PZT locations in the established model. **Figure 6** depicts a three-dimensional propagation path of stress waves.

Effects of the Crack on Stress Wave Propagation

To investigate the effect of cracks on stress wave propagation, four crack depths were performed. **Figure 7** shows wavefronts of four damage cases in the 220th iteration step. Reflections are observed at the left and side boundaries, and wavefronts show the same pattern before passing through cracks, which means incident waves into the crack interface have same properties and differences as received signals that are only caused by cracks.

Figure 8 shows strain contours when stress waves are passing through the crack interface in the 400th iteration step. Reflection waves caused by the crack are obvious in all damage cases. The transmission wave is only observed at the crack depth of 4 mm, which indicates wave velocity decays when the stress wave passes through cracks.

After passing through cracks, the characteristics of stress waves show extreme differences (as depicted in **Figure 9**). At the same time in the 470th iteration step, the wavefronts drop down rapidly with the increase of crack depths, representing the attenuation of wave velocities. At the same position of the transmission wave, the stress wave intensity reduces significantly with the increase of crack depths.

EXPERIMENTAL VERIFICATION

Laboratory Test Specimen

Three timber specimens (pine wood) with the same dimensions (300 mm \times 100 mm \times 50 mm) were prepared at the State Key Laboratory of Tongji University. For simulating timber cracks, 2-mm-width cracks within seven different depths, listed in **Table 3**, were cut off on the top surface perpendicular to the

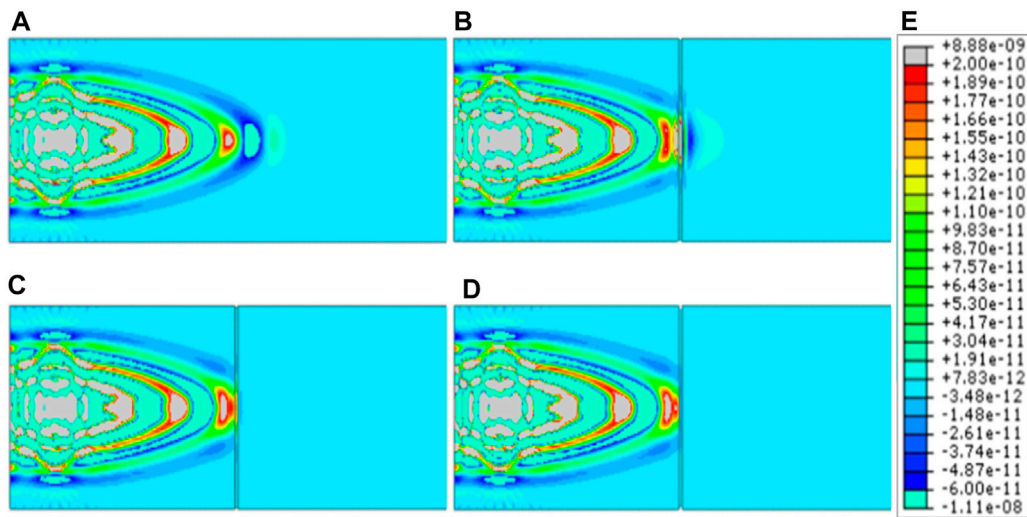


FIGURE 7 | Strain contours of the stress wave in the 220th iteration step: **(A)** crack depth of 0 mm; **(B)** crack depth of 4 mm; **(C)** crack depth of 10 mm; **(D)** crack depth of 20 mm; **(E)** stress wave intensity.

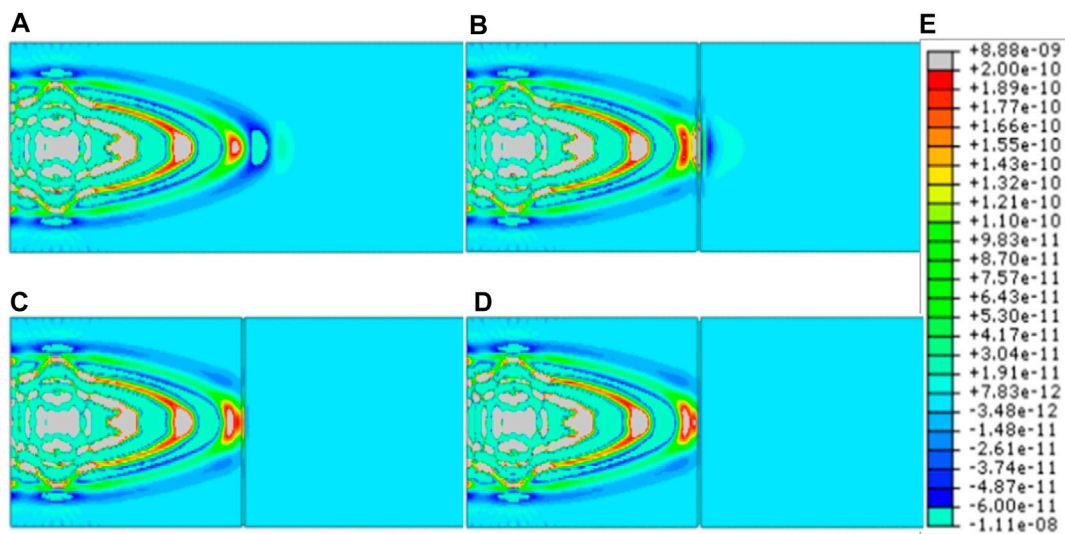


FIGURE 8 | Strain contours of the stress wave in the 400th iteration step: **(A)** crack depth of 0 mm; **(B)** crack depth of 4 mm; **(C)** crack depth of 10 mm; **(D)** crack depth of 20 mm; **(E)** stress wave intensity.

grain direction. Two PZT patches were mounted at predetermined locations using adhesive (Comix super glue B2695), and the distance is 50 mm from two adjacent ends of the timber specimen, as shown in **Figure 10**. The dimensions of PZT patches are 10 mm, 10 mm, and 2 mm in length, width, and depth, respectively.

Experimental Setup

The experimental apparatus includes timber specimens, a data acquisition system, and a monitoring visualization system, as depicted in **Figure 11**. Timber specimens are

fixed by two fixtures for simulating the boundary conditions in real cases. On the top surface of specimens, two PZT patches were used for transmitting and receiving signals. One PZT patch, excited by a one-cycle sine wave with a frequency of 190 kHz, is connected to the acquisition system with 2 MS/s sampling frequency. The data acquisition system consists of an acquisition card (NI USB 6366) and a signal power amplifier (Trek model 2100HF). The other PZT connected to the acquisition system is used to receive stress waves and displace the signal response in the visualization system.

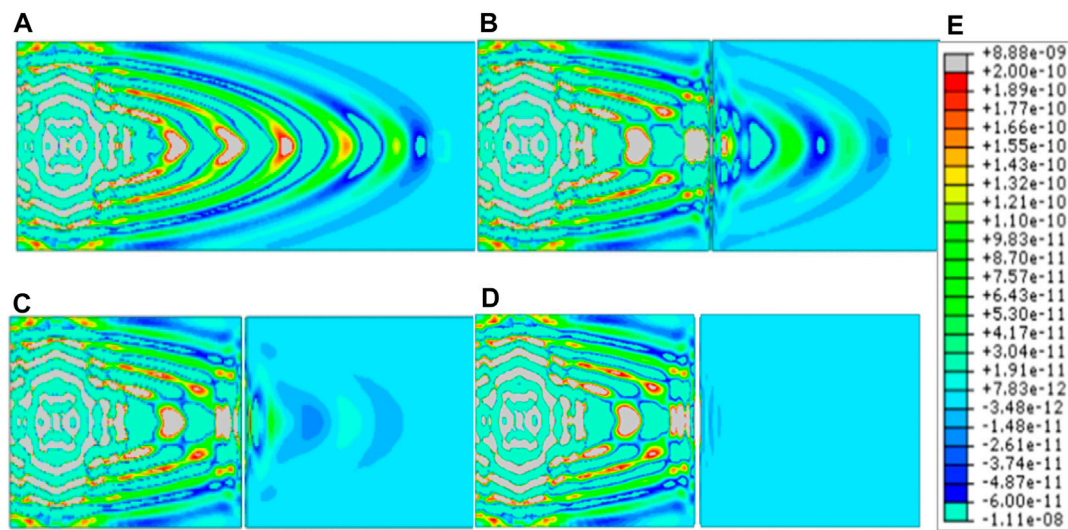


FIGURE 9 | Strain contours of the stress wave in the 470th iteration step: **(A)** crack depth of 0 mm; **(B)** crack depth of 4 mm; **(C)** crack depth of 10 mm; **(D)** crack depth of 20 mm; **(E)** stress wave intensity.

TABLE 3 | Seven cases of crack condition.

Case	1	2	3	4	5	6	7
Crack depth (mm)	0	2	4	6	8	10	20
Crack width (mm)	2	2	2	2	2	2	2

RESULTS AND DISCUSSION

Time-Domain Signal Collection

The time-domain probing signals for three specimens are shown in **Figure 12**. The time duration of each specimen is 0.5 ms. A general trend of all the test specimens shows two significant wave packets in time response. The first wave packet is the signal directly received from the probing signal, and the second wave packet is the signal received from boundary reflections. The signal amplitudes decrease with the increase of crack depth in the first wave packet. The second wave packet has no similar trend due to the multi-boundary reflection effects. Because of the large material dispersion of timber, time-domain signals are very difficult to process and classify the damage cases. Thus, time-frequency spectrums in terms of images are established from each time-domain signal for training the developed DNN.

Data Training Process

Since original signals from tests are limited to training neural networks, three data augmentation methods are used to expand datasets in both the time domain and the frequency domain. Gaussian noises with certain signal-to-noise ratios were added to raw data, and all raw data were transformed into frequency spectrums by STFT. In addition, salt and pepper noises were added into spectrum images of original signals, and spectrum images were jittered into 8 channels and 16 channels, respectively. Each original signal was expanded to 27 images after data augmentation. Spectrums from different specimens but for the same crack depth were mixed into a separate dataset. A total of 567 images were obtained in this research, as shown in **Figure 13**.

Classification Results

Visual domain network-based image identification for the spectrum dataset was conducted. Seven datasets with 567 images are mixed and fed into the transferred AlexNet network. The learning rate is set as 0.0001, and a total of 200 epochs are set. In each epoch, images are randomly split into the training set and validation set. As shown in **Figure 14**, the training dataset accounts for 70% of the total images, and the validation dataset accounts for 30%. As shown in **Figure 15**, the

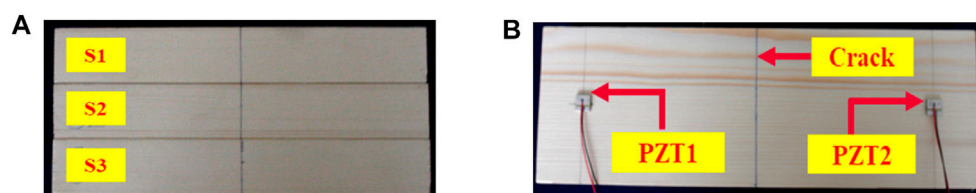


FIGURE 10 | Timber specimens: **(A)** side view; **(B)** top view of PZT configuration.

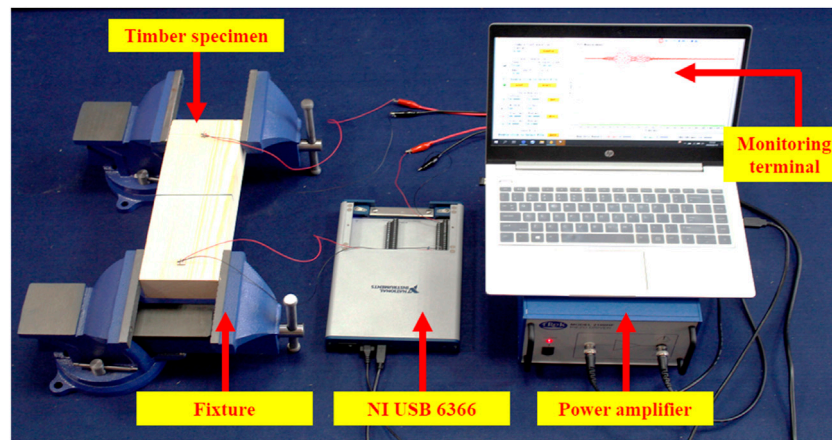


FIGURE 11 | Experimental apparatus.

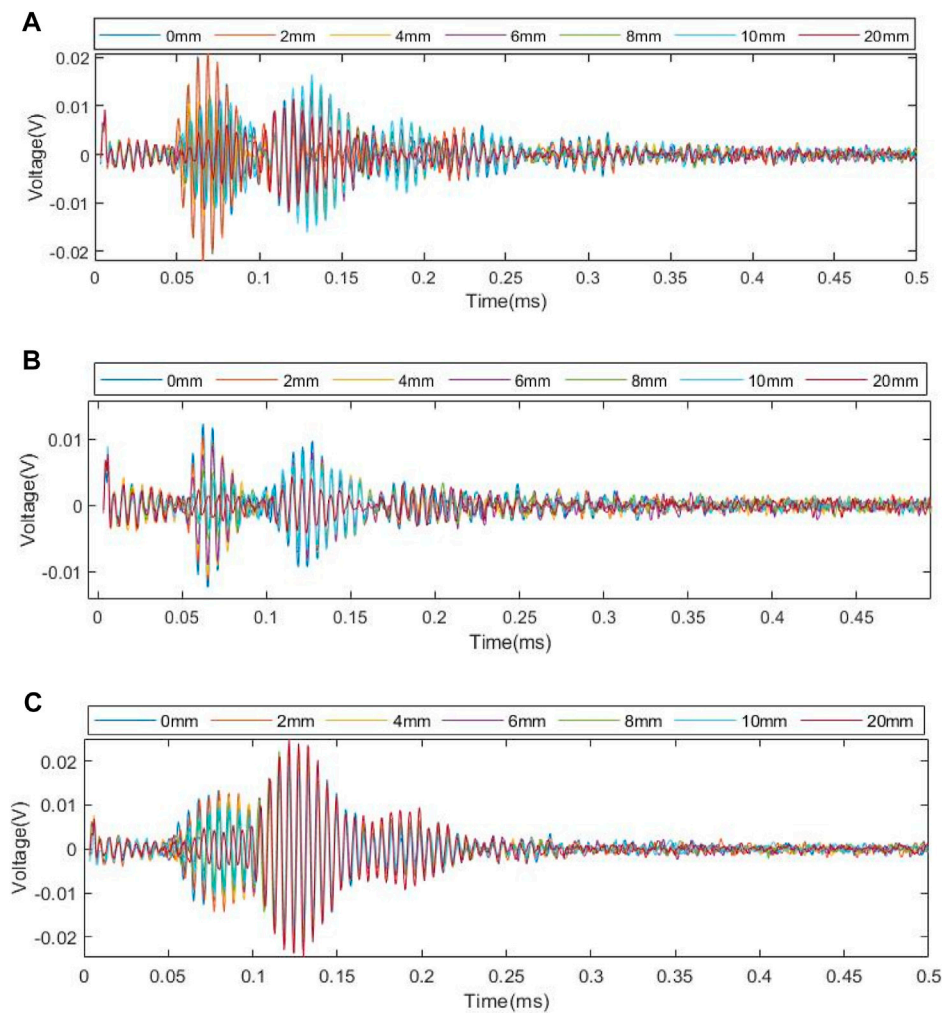


FIGURE 12 | Received signals: (A) specimen 1; (B) specimen 2; (C) specimen 3.

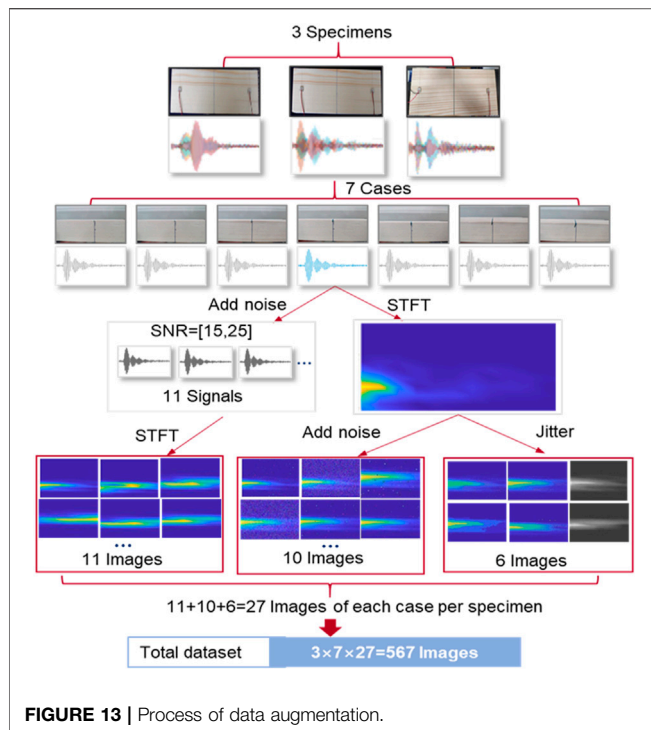


FIGURE 13 | Process of data augmentation.

predicted accuracy rapidly increases with the addition of iterations. When the number of iterations exceeds 2,000, the prediction accuracy approaches a constant value of 95.83%.

Figure 16 illustrates the confusion matrix regarding the classification accuracy of the validation dataset. The average accuracy rate is 95.8%. The crack depth of 8 mm has the highest accuracy of 100%. The crack depths of 0 mm, 2 mm, 4 mm, and 10 mm have the same accuracy with a 4.3% probability of wrong predictions, and the crack depth of 20 mm has a lower accuracy of 91.7%.

Discussions

The classification results from the transferred DNN show the feasibility of the proposed technology to identify timber crack severity. Compared with traditional signal processing of the

stress wave method, the proposed method based on STFT spectrums and computer vision technique shows the advantage in generality and the extensibility of the dataset. However, adopting this approach in field applications still faces a few challenges. In particular, four aspects should be considered in the future work: 1) The detection accuracy is highly limited to the size of the training dataset, which requires continuously expending the current dataset to improve the stability and adaptability of the developed DNN-based classification. 2) Only timber beam elements are investigated in the experimental study, whereas the boundary conditions and dimensional features may be different from other timber structural components, such as columns, wood slab, and timber connections. All mentioned factors may influence the reflection pattern of stress waves. 3) The performance of the proposed method in identifying cracks in propagation is not clear. Therefore, one possible solution is to collect stress wave signals over the whole loading process and then divide these raw data and their corresponding STFT spectrums into different stages according to crack propagating severity and then use the computer vision approach to identify crack propagation. 4) The form of sensor used in this research is surface-mounted patches, whose performance is easily affected by environmental variations and service life. Proper sensor protection should be considered to ensure its long-time service for structural health monitoring of timber structures.

CONCLUSIONS

This research proposes a novel piezoceramic-based sensing technology combined with visual domain networks for timber crack detection. Surface-mounted piezoelectric transducers were utilized to transmit and receive stress waves in both numerical simulations and experiments. The numerical and experimental results reveal the wave propagation properties in different cases of crack depths. A total of 567 images were reconstructed by transferring the time-domain signal to time-frequency spectrums. Respective labels from the dataset were trained through the transferred DNN, and the predicted

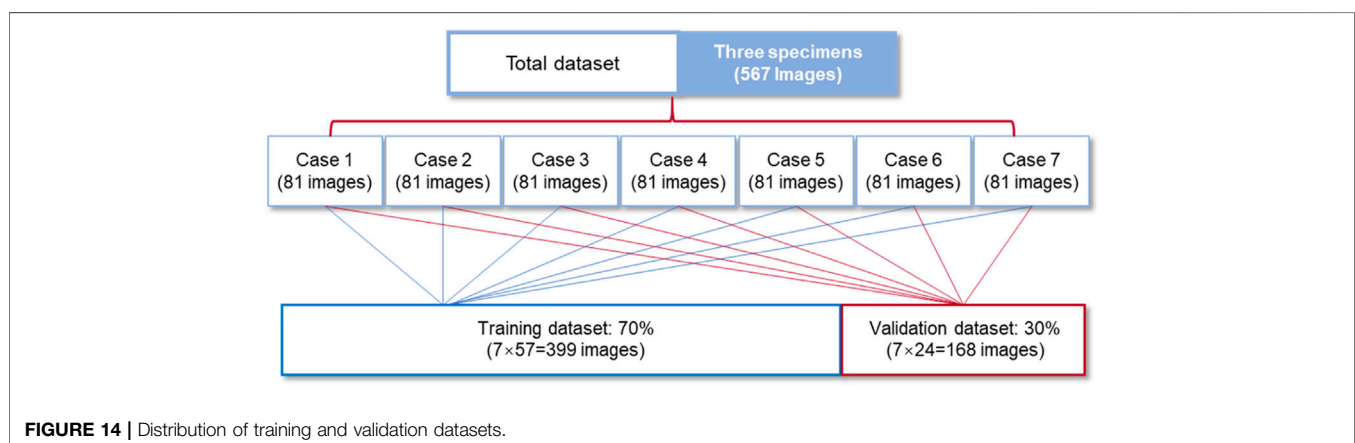


FIGURE 14 | Distribution of training and validation datasets.

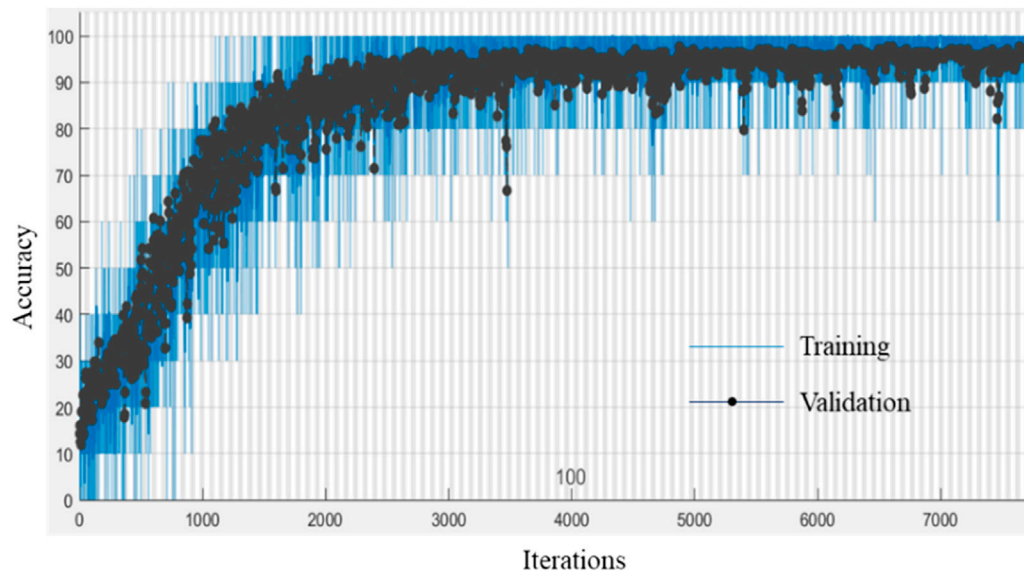


FIGURE 15 | Training process of accuracy.

Output Class	0mm	10mm	20mm	2mm	4mm	6mm	8mm	
0mm	23 13.7%	1 0.6%	0 0.0%	1 0.6%	0 0.0%	1 0.6%	0 0.0%	88.5% 11.5%
10mm	0 0.0%	23 13.7%	0 0.0%	0 0.0%	0 0.0%	0 0.0%	0 0.0%	100% 0.0%
20mm	0 0.0%	0 0.0%	22 13.1%	0 0.0%	0 0.0%	0 0.0%	0 0.0%	100% 0.0%
2mm	1 0.6%	0 0.0%	0 0.0%	23 13.7%	0 0.0%	0 0.0%	0 0.0%	95.8% 4.2%
4mm	0 0.0%	0 0.0%	0 0.0%	0 0.0%	23 13.7%	0 0.0%	0 0.0%	100% 0.0%
6mm	0 0.0%	0 0.0%	2 1.2%	0 0.0%	1 0.6%	23 13.7%	0 0.0%	88.5% 11.5%
8mm	0 0.0%	0 0.0%	0 0.0%	0 0.0%	0 0.0%	0 0.0%	24 14.3%	100% 0.0%
	95.8% 4.2%	95.8% 4.2%	91.7% 8.3%	95.8% 4.2%	95.8% 4.2%	95.8% 4.2%	100% 0.0%	95.8% 4.2%
	0mm	10mm	20mm	2mm	4mm	6mm	8mm	
	Target Class							

FIGURE 16 | Confusion matrix of the validation dataset.

outputs show an average accuracy of 95.8% for crack condition identification. The proposed technology has great potential for

achieving real-time monitoring of timber damage in engineering projects when expanding the training samples from *in situ* timber damage cases.

DATA AVAILABILITY STATEMENT

The raw data supporting the conclusions of this article will be made available by the authors, without undue reservation.

AUTHOR CONTRIBUTIONS

HX involved in data analysis. LC wrote the paper. CY contributed to FEM modeling. QK provided the idea and revised the paper.

FUNDING

The authors greatly appreciate the funding support from the National Natural Science Foundation of China (Grant numbers 51978507, 52020105005, and 51978502) and Science and Technology Commission of Shanghai Municipality (Grant numbers 19DZ1201200, 19DZ1202502).

REFERENCES

- Ahmad, A. A., Lawan, S., Ajiya, M., Yusuf, Z. Y., and Bello, L. M. (2020). Extraction of the Pulse Width and Pulse Repetition Period of Linear FM Radar Signal Using Time-Frequency Analysis. *J. Adv. Sci. Eng.* 3, 1–8. doi:10.37121/jase.v3i1.69
- Bao, Y., Tang, Z., Li, H., and Zhang, Y. (2018). Computer Vision and Deep Learning-Based Data Anomaly Detection Method for Structural Health Monitoring. *Struct. Health Monit. Int. J.*, 147592171875740.

- Baradit, E., Aedo, R., and Aguilera, C. (2009). Imaging Processing for Knot Detection in wood Using Microwaves. *Wood Res.* 54, 55–60.
- Bendory, T., Eldar, Y. C., and Boumal, N. (2017). *Non-Convex Phase Retrieval from STFT Measurements*. IEEE Trans. Inf. Theor.. doi:10.1109/icassp.2017.7953062
- Brites, R. D., Lourenço, P. B., and Machado, J. S. (2012). A Semi-destructive Tension Method for Evaluating the Strength and Stiffness of clear wood Zones of Structural Timber Elements In-Service. *Construction Building Mater.* 34, 136–144. doi:10.1016/j.conbuildmat.2012.02.041

- Cao, J., Xiong, H., and Chen, L. (2019). Procedure for Parameter Identification and Mechanical Properties Assessment of CLT Connections. *Eng. Struct.* 203, 109867.
- Chen, J., Xiong, H., Wang, Z., and Yang, L. (2020). Experimental Buckling Performance of Eucalyptus-Based Oriented Oblique Laminated Strand Lumber Columns under Centric and Eccentric Compression. *Construction Building Mater.* 262, 120072. doi:10.1016/j.conbuildmat.2020.120072
- Dackermann, U., Crews, K., Kasal, B., Li, J., Riggio, M., Rinn, F., et al. (2014). *In Situ* assessment of Structural Timber Using Stress-Wave Measurements. *Mater. Struct.* 47, 787–803. doi:10.1617/s11527-013-0095-4
- Dackermann, U., Skinner, B., and Li, J. (2014). Guided Wave-Based Condition Assessment of *In Situ* Timber Utility Poles Using Machine Learning Algorithms. *Struct. Health Monit.* 13, 374–388. doi:10.1177/1475921714521269
- Dansheng, W., Qinghua, W., Hao, W., and Hongping, Z. (2016). Experimental Study on Damage Detection in Timber Specimens Based on an Electromechanical Impedance Technique and RMSD-Based Mahalanobis Distance. *Sensors* 16, 1765.
- Dietsch, P., and Winter, S. (2018). Structural Failure in Large-Span Timber Structures: A Comprehensive Analysis of 230 Cases. *Struct. Saf.* 71, 41–46. doi:10.1016/j.strusafe.2017.11.004
- Dorafshan, S., and Azari, H. (2020). Evaluation of Bridge Decks with Overlays Using Impact echo, a Deep Learning Approach. *Automation in Construction* 113, 103133. doi:10.1016/j.autcon.2020.103133
- Ei-Hadad, A. (2017). *Using Acoustic Emission Technique with Matlab® Analysis to Detect Termites in Timber-In-Service*. Melbourne: The university of Melbourne.
- Gong, P., Luo, M., Zhou, L., Jiang, L., and Chen, X. (2020). An Image Processing Method for Extraction of the Stress Wave Reflection Period. *Appl. Sci.* 10, 3486. doi:10.3390/app10103486
- Han, F., Jiang, J., Xu, K., and Wang, N. (2019). Damage Detection of Common Timber Connections Using Piezoceramic Transducers and Active Sensing. *Sensors* 19, 2486. doi:10.3390/s19112486
- Huo, L., Chen, D., Liang, Y., Li, H., Feng, X., and Song, G. (2017). Impedance Based Bolt Pre-load Monitoring Using Piezoceramic Smart Washer. *Smart Mater. Struct.* 26, 057004. doi:10.1088/1361-665x/aa6a8e
- Kloiber, M., Drdác, M., Machado, J. S., Piazza, M., and Yamaguchi, N. (2015). Prediction of Mechanical Properties by Means of Semi-destructive Methods: A Review. *Construction Building Mater.* 101, 1215–1234. doi:10.1016/j.conbuildmat.2015.05.134
- Koca, G., Dndar, T., and Nusret, A. S. (2018). Using the Ultrasonic Stress Wave Technique to Evaluate Structural Timber Members of an Old Masonry Building. *Kastamonu University Journal of Forestry Faculty* 18(3), 341–349. doi:10.17475/kastorman.499081
- Krause, M., Dackermann, U., and Li, J. (2015). Elastic Wave Modes for the Assessment of Structural Timber: Ultrasonic echo for Building Elements and Guided Waves for Pole and Pile Structures. *J. Civ. Struct. Health Monit.* 5, 1–29. doi:10.1007/s13349-014-0087-2
- Krizhevsky, A., Sutskever, I., and Hinton, G. (2012). ImageNet Classification with Deep Convolutional Neural Networks. *Adv. Neural Inf. Process. Syst.* 25.
- Lee, U., and Shin, J. (2002). A Frequency Response Function-Based Structural Damage Identification Method. *Comput. Structures* 80, 117–132. doi:10.1016/s0045-7949(01)00170-5
- Li, J., Zhu, X., Law, S. S., and Samali, B. (2020). Time-varying Characteristics of Bridges under the Passage of Vehicles Using Synchroextracting Transform. *Mech. Syst. Signal. Process.* 140, 106727.1–106727.19. doi:10.1016/j.ymssp.2020.106727
- Li, P., Yang, N., and Wang, Y. (2013). Research on Structural Present State and Damage Reasons of Ancient Tibetan Buildings. *Amm* 351–352, 1652–1656. doi:10.4028/www.scientific.net/amm.351-352.1652
- Linke, G., Rug, W., and Pasternak, H. (2019). “Strength Grading of Structural Timber in Existing Structures with the Ultrasonic Time-Of-Flight Measurement,” in 5th Int. Conf. Struct. Health Assess (Guimaraes, Portugal: Timber Struct.).
- Mol, A., Cabaleiro, M., Sousa, H. S., and Branco, J. M. (2020). HBIM for Storing Life-Cycle Data Regarding Decay and Damage in Existing Timber Structures. *Autom. Constr.* 117. doi:10.1016/j.autcon.2020.103262
- Obuchowski, J., Wyłomańska, A., and Zimroz, R. (2014). The Local Maxima Method for Enhancement of Time-Frequency Map and its Application to Local Damage Detection in Rotating Machines. *Mech. Syst. Signal. Process.* 46, 389–405. doi:10.1016/j.ymssp.2014.01.009
- Pease, B. J., Scheffler, G. A., and Janssen, H. (2012). Monitoring Moisture Movements in Building Materials Using X-ray Attenuation: Influence of Beam-Hardening of Polychromatic X-ray Photon Beams. *Construction Building Mater.* 36, 419–429. doi:10.1016/j.conbuildmat.2012.04.126
- Puaad, M. B. F. M., Ahmad, Z., and Azlan, H. M. (2014). *Ultrasonic Wave Non-destructive Method for Predicting the Modulus of Elasticity of Timber*. Springer Singapore.
- Rashid, K. M., and Louis, J. (2020). Activity Identification in Modular Construction Using Audio Signals and Machine Learning. *Automation in Construction* 119, 103361. doi:10.1016/j.autcon.2020.103361
- Riggio, M., Anthony, R. W., Augelli, F., Kasal, B., Lechner, T., Muller, W., et al. (2014). *In Situ* assessment of Structural Timber Using Non-destructive Techniques. *Mater. Struct.* 47(5), 749–766.
- Sandak, A., Sandak, J., and Riggio, M. (2015a). Estimation of Physical and Mechanical Properties of Timber Members in Service by Means of Infrared Spectroscopy. *Construction Building Mater.* 101, 1197–1205. doi:10.1016/j.conbuildmat.2015.06.063
- Sandak, A., Sandak, J., and Riggio, M. (2015b). *Multivariate Analysis of Multi-Sensor Data for Assessment of Timber Structures: Principles and Applications*. Constr. Build. Mater.
- Sandak, J., Sandak, A., and Negri, M. (2010). Mechanical Testing of wood Assisted by Infrared Spectroscopy and thermal Imaging, 11th World Conf. Trentino, Italy. *Timber Eng.* 3, 2081–2085.
- Shukla, H., and Piratla, K. (2020). Leakage Detection in Water Pipelines Using Supervised Classification of Acceleration Signals. *Autom. Constr.* 117.
- Sun, X., He, M., and Li, Z. (2020). Novel Engineered wood and Bamboo Composites for Structural Applications: State-Of-Art of Manufacturing Technology and Mechanical Performance Evaluation. *Constr. Build. Mater.* 249.
- Tannert, A., Rw, K., Kloiber, P., Riggio, R., and Widmann, Y. (2014). *In Situ assessment of Structural Timber Using Semi-destructive Techniques*. Mater. Struct. 47(5), 767–785.
- Ulloa, F., and Barbieri, G. (2018). “Bearing Fault Detection through Machine Learning: Time-Domain vs Time-Frequency Analysis for Feature Extraction,” in *First EAGE Workshop High Perform. Comput. Upstream* (Santander, Colombia: Lat. Am.). doi:10.3997/2214-4609.201803075
- Wei, Q., Leblon, B., and La Rocque, A. (2011). On the Use of X-ray Computed Tomography for Determining wood Properties: a review. This Article Is a Contribution to the Series the Role of Sensors in the New Forest Products Industry and Bioeconomy. *Can. J. For. Res.* 41, 2120–2140. doi:10.1139/x11-111
- Yang, W., Kong, Q., Ho, S. C. M., Mo, Y. L., and Song, G. (2018). *Real-Time Monitoring of Soil Compaction Using Piezoceramic-Based Embeddable Transducers and Wavelet Packet Analysis*. IEEE Access. 6, 5208–5214.
- Tanner, M. A. (2014). *Data Augmentation*. Hoboken: John Wiley. doi:10.1002/9781118445112.stat00409
- Yuan, C., Kong, Q., Chen, W., Jiang, J., and Hao, H. (2020). Interfacial Debonding Detection in Externally Bonded BFRP Reinforced Concrete Using Stress Wave-Based Sensing Approach. *Smart Mater. Struct.* 29, 035039 (13pp). doi:10.1088/1361-665x/ab7111
- Zhang, C., Yan, Q., Wang, X., Panda, G. P., Vipulanandan, C., and Song, G. (2021). Measurement and Evaluation of Soft Soil Strength Development during Freeze-Thaw Process Based on Electromechanical Impedance Technique. *Meas. Sci. Technol.* 32 (14pp), 025113 (14pp). doi:10.1088/1361-6501/abb7a1
- Zhang, J., Huang, Y., and Zheng, Y. (2018). A Feasibility Study on Timber Damage Detection Using Piezoceramic-Transducer-Enabled Active Sensing. *Sensors* 18, 1563. doi:10.3390/s18051563
- Zhang, J., Li, Y., Huang, Y., Jiang, J., and Ho, S. C. (2018). A Feasibility Study on Timber Moisture Monitoring Using Piezoceramic Transducer-Enabled Active Sensing. *Sensors* 18, 3100. doi:10.3390/s18093100

Zhang, J., Xu, Q.-f., Xu, Y.-x., and Zhang, M. (2015). Research on Residual Bending Capacities of Used wood Members Based on the Correlation between Non-destructive Testing Results and the Mechanical Properties of wood. *J. Zhejiang Univ. Sci. A*. 16, 541–550. doi:10.1631/jzus.a1400276

Conflict of Interest: The authors declare that the research was conducted in the absence of any commercial or financial relationships that could be construed as a potential conflict of interest.

Publisher's Note: All claims expressed in this article are solely those of the authors and do not necessarily represent those of their affiliated organizations, or those of

the publisher, the editors, and the reviewers. Any product that may be evaluated in this article, or claim that may be made by its manufacturer, is not guaranteed or endorsed by the publisher.

Copyright © 2021 Xiong, Chen, Yuan and Kong. This is an open-access article distributed under the terms of the Creative Commons Attribution License (CC BY). The use, distribution or reproduction in other forums is permitted, provided the original author(s) and the copyright owner(s) are credited and that the original publication in this journal is cited, in accordance with accepted academic practice. No use, distribution or reproduction is permitted which does not comply with these terms.



Experimental Evaluation of Miniature Impedance Board for Loosening Monitoring of the Threaded Pipe Connection

Yabin Liang^{1,2,3,4†}, Yixuan Chen^{1,2†}, Zuocai Zhang^{1,2,3,4} and Qian Feng^{1,2,3,4*}

¹Institute of Seismology, CEA, Wuhan, China, ²Hubei Key Laboratory of Earthquake Early Warning, Wuhan, China, ³Hubei Earthquake Administration, Wuhan, China, ⁴Wuhan Institute of Earthquake Engineering Co. Ltd., Wuhan, China

OPEN ACCESS

Edited by:

Yang Zhang,
Dalian University of Technology, China

Reviewed by:

Tianyong Jiang,
Changsha University of Science and
Technology, China
Kai Xu,
Wuhan University of Science and
Technology, China

*Correspondence:

Qian Feng
qfengwh@foxmail.com

[†]These authors have contributed
equally to this work and share first
authorship

Specialty section:

This article was submitted to
Interdisciplinary Physics,
a section of the journal
Frontiers in Physics

Received: 10 June 2021

Accepted: 12 July 2021

Published: 31 August 2021

Citation:

Liang Y, Chen Y, Zhang Z and Feng Q
(2021) Experimental Evaluation of
Miniature Impedance Board for
Loosening Monitoring of the Threaded
Pipe Connection.
Front. Phys. 9:723260.
doi: 10.3389/fphy.2021.723260

Electromechanical impedance (Electromechanical impedance)-based methods as potential nondestructive evaluation (NDT) techniques have been widely used in the field of structural health monitoring (SHM), especially for the civil, mechanical, and aerospace engineering fields. However, it is still difficult to apply in practical applications due to the limitations of the impedance measurement hardware, which is usually expensive, bulky, and heavy. In this paper, a small, lightweight, and low power consumption EMI-based structural health monitoring system combined with the low-cost miniature impedance board AD5933 was studied experimentally to investigate its quantifiable performance in impedance measurement and structural damage identification. At first, a simple impedance test with a free PZT patch was introduced to present the impedance calibration and measurement procedure of AD5933, and then its calibration performance was validated by comparing the signature with the one measured by a professional impedance analyzer (WK6500B). In order to further validate the feasibility and effectiveness of the AD5933 board in practical applications, a threaded pipe connection specimen was assembled in the laboratory and then connected with the AD5933 to acquire its impedance signatures under different loosening severities. The final results demonstrated that the impedance measured by the AD5933 show a good consistency with the measurements by the WK6500B, and the evaluation board could be successfully utilized for the loosening severities identification and quantitatively evaluation.

Keywords: electromechanical impedance, miniature impedance board, AD5933, threaded pipe connection, loosening monitoring

INTRODUCTION

Electromechanical impedance (EMI)-based structural health monitoring as a NDT technique was first proposed by [1]; and exhibits great potential in the field of structural health monitoring [2–4]. In recent years, the EMI technique had been employed by researchers to assess structures in various fields and of various materials: aerospace and aircraft structures [5], concrete structures [6–8], steel structures [9–11], jacket-type offshore structures [12], and polymer and reinforced composite structures [13]. The basic principle of the EMI-based damage detection technique is to track the electrical impedance of a PZT (lead zirconate titanate) transducer, which was surface bonded onto the host structure. Owing to the

interactive electromechanical coupling properties of the PZT transducer, slight changes in the physical characteristics of the host structure can be captured by detecting the changes in the electrical impedance of the PZT transducer. Thus, the health condition and service status of the host structure can be effectively evaluated by measuring the electrical impedance of the PZT transducer and comparing it with baseline data.

Though EMI-based techniques have received great attention in the area of structural health monitoring and damage identification, they still face many challenges during practical application. One of the biggest challenges is the nature of impedance measurement hardware, which is usually very expensive, bulky, and heavy, such as the professional precious impedance analyzer (WK6500B, Wayne Kerr Electronics Co., United Kingdom) with a price of approximately 10,000 USD, a mass of approximately 14 kg, and the dimensions 190 mm × 440 mm × 525 mm. With these disadvantages, it becomes very difficult for EMI-based techniques to be applied in field use for online SHM, and therefore seriously limits its wider adoption in the future.

In recent years, an AD5933 evaluation board manufactured by Analog Devices Co. (Norwood, MA, United States) has received a lot of attention in the field of SHM due to its excellent impedance measurement ability. The board is very cheap (approximately 60 USD), and is characterized by its low weight (approximately 240 g) and small dimensions (80 mm × 80 mm). The evaluation board can measure the impedance signatures up to 100 kHz with 512 maximum data points. Due to these distinguishing advantages, much research had been published around this low-cost, on-board SHM system [14–19]. For example [20], investigated the influence of the calibration process of the AD5933 on impedance measurements and validated its damage detection ability in carbon fiber reinforced polymer CFRP panels suffering delamination [21]. Successfully applied the AD5933 board to detect common defects of the glass fiber composite plates, such as delamination and cracking. All the published research showed that impedance measurement by the AD5933 board provides good consistency with measurements obtained from a professional impedance analyzer. Therefore, some researchers have demonstrated that a mini-impedance measuring board such as the AD5933 is likely to be a key part of future sensor systems, especially in the next generation of EMI-based SHM systems.

On the other hand, threaded connections have been widely utilized in pipeline engineering due to their distinguishing advantages of flexibility (aiding in assembly and disassembly), excellent bearing capacity for large axial force, good interchangeability, and reusability [22, 23]. However, in practical application this type of connection is always subjected to variable external loads and environmental pollution, which may induce cracks or loosen the connection during its service period. In this situation, it becomes necessary to guarantee a sealed and secure connection and thus reduce potential leakage risk. With the development of SHM techniques [24–26], many novel methods have been proposed by researchers in recent years to deal with this issue. For example, a distributed temperature

sensing system (DTS), combined with optical fibers, has been successfully employed to detect and locate leakage along the pipelines by monitoring variations in the surrounding temperature of the pipe [27, 28]. In addition, the piezoceramic-based active sensing method combined with the time reversal technique has also been utilized to identify when the connection becomes loose and evaluate the severity of the looseness [29]. In 2018 [30], tried to apply an EMI-based technique to monitor the health condition of threaded pipe connections in real time, but the impedance signatures in this research were acquired by a professional impedance analyzer.

In this paper, the miniature impedance board AD5933 was employed as an EMI-based SHM system, and its performance in impedance measurement and damage detection was experimentally investigated. Firstly, a free PZT impedance test was carried out to present in detail the impedance calibration and measurement procedure of the AD5933, and its impedance calibration performance was also investigated by comparing the results with a professional impedance analyzer (WK6500B). Then, a threaded pipe connection was assembled in the laboratory as a test specimen and experimentally investigated to further validate the feasibility and effectiveness of the AD5933 board, especially in its damage identification ability under several different connection-loosening severities. During the experiments, all the impedance measurements taken by the AD5933 board were compared with the ones measured by the WK6500B.

ELECTROMECHANICAL IMPEDANCE PRINCIPLE

In 1994 [1], first proposed the concept of electromechanical impedance-based techniques and tried to apply them in the field of structural health monitoring. EMI takes full advantage of the dual functions of the piezoelectric patches it utilizes, which can act as both the actuator and sensor simultaneously. These unique interactive electromechanical coupling properties provide the piezoelectric patches with the potential to be employed to detect the slightest alterations in frequency response functions for the host structure. In this way, structural health condition and service status can be effectively identified.

Normally, the small sized piezoelectric transducer (lead zirconate titanate-PZT) is surface bonded onto the host structure by the high-strength adhesive, and is powered by voltage or current. Thus, for the PZT–host structure coupling system, its integrated electro-mechanical characteristics may be electrically represented by the PZT electrical impedance, which is always directly affected by the dynamics of the PZT patch and the host structure. Among them, the mechanical impedance of the PZT patch, denoted by $Z_a(\omega)$, can be always defined as the ratio of a harmonic input voltage $V(\omega)$ to the current response $I(\omega)$, in which ω is the angular frequency of the driving voltage. Therefore, the electrical admittance of the PZT patch, denoted by $Y(\omega)$ (i.e., inverse of the electrical impedance $Z(\omega)$), can be expressed in the following equation:

$$Y(\omega) = \frac{I(\omega)}{V(\omega)} = i\omega a \left(\bar{\epsilon}_{33}^T (1 - i\delta) - \frac{Z_s(\omega)}{Z_s(\omega) + Z_a(\omega)} d_{3x}^2 \hat{Y}_{xx}^E \right) \quad (1)$$

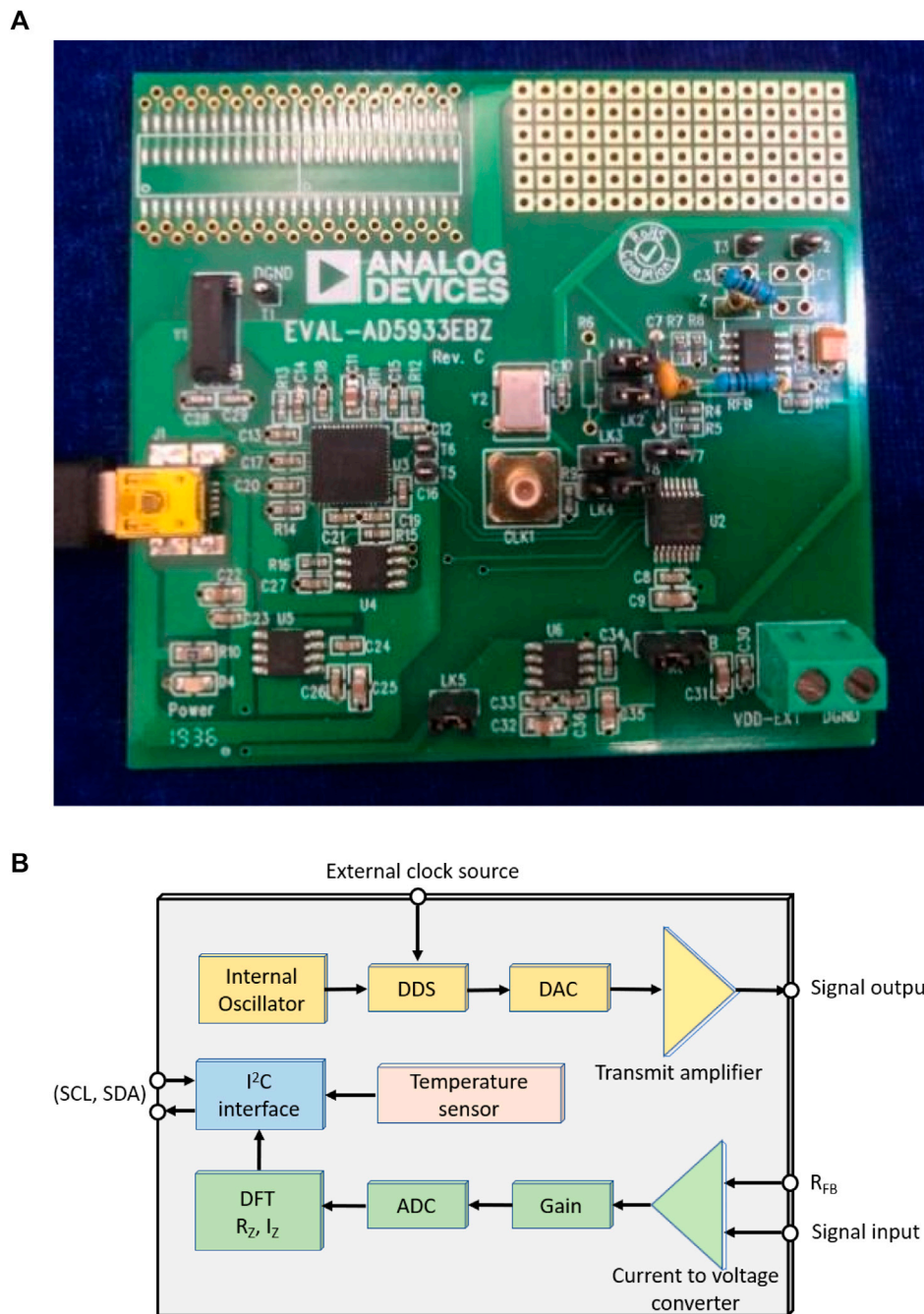


FIGURE 1 | AD5933 evaluation board **(A)** photo **(B)** block diagram.

where $Z_s(\omega)$ denotes the mechanical impedance of the host structure, a is the geometric constant of the PZT patch, \hat{Y}_{xx}^E is the complex Young's modulus within zero electric field, $\hat{\epsilon}_{33}^T$ is the dielectric constant at zero stress, and δ is the dielectric loss tangent of the PZT patch, d_{3x} is the piezoelectric coupling constant in the arbitrary x direction at zero stress.

With the help of this formula, the electrical impedance of the PZT patch before and after a damage occurrence for the host structure can be calculated and compared, thus the health

condition and service status of the host structure can be evaluated.

MINIATURE IMPEDANCE BOARD AD5933

As shown in **Figure 1A**, the AD5933, as a miniature electronic board developed by Analog Devices Co., has the ability to measure impedance across a limited frequency, ranging from a few Hertz

TABLE 1 | Technical specification for AD5933.

Parameters	Values
Frequency ranges	Up to 100 kHz
Measured parameters	Z as real and imaginary parts, other parameters need to be calculated
Accuracy	±0.5%
Maximum measured points	512
Communication interfaces	1. chip-I ² C 2. evaluation board-USB
Power supply	2.7–5.5 V DC, <1 W
Dimensions	80 mm × 80 mm
Mass	237 g
Operating temperature range	–40°C~125°C

up to 100 kHz. The evaluation board receives information, communication, and power via USB cable when connected to a laptop which has been pre-installed with the supporting software provided by Analog Devices. As shown in **Figure 1B**, the AD5933 board includes an internal oscillator, signal generator (direct digital synthesizer, DDS), digital-to-analog converter (DAC), transmit amplifier, current-to-voltage converter, gain control block, analog-to-digital converter (ADC), discrete Fourier transform (DFT), digital signal processing engine, and I²C bus controller. The detailed technical specification for AD5933 is presented as **Table 1**.

For the impedance measurement, the DDS and DAC work together to generate an analog frequency sweep signal, which is then amplified and sent out as an output signal to excite the measured impedance. Then, working together with the current obtained from gain resistor R_{FB} , the response signal in the form of electric current is converted to voltage by current-to-voltage converter, and then processed by the ADC and DFT engine after gain. In this way, the real and imaginary data of the impedance can be calculated by the DFT engine and then sent to the I²C controller, and finally transmitted to the laptop via USB cable.

It should be noted that the evaluation board also has a high performance trimmed 16 MHz surface-mount crystal that can be used as a system clock for the AD5933 when needed. Communication and interfacing to the AD5933 board is via a USB cable connected to a laptop, which controls and generates the I²C signals. With the help of the pre-installed dedicated software developed by Analog Devices, some related work can be done on the laptop, including setting working parameters (the frequency and gain etc.), reading the temperature from the internal sensor, performing calibration, and conducting and storing the measurements.

CALIBRATION PROCEDURE AND PERFORMANCE FOR AD5933

Calibration Procedure

For evaluation of the AD5933 board, a proper calibration before measurement is of critical importance and directly influences the accuracy of the final measurement. Calibration

of the AD5933 evaluation board is required each time the software or hardware is restarted or reset. In this research, in order to present the calibration procedure in detail and investigate the calibration performance of the AD5933 board, a free PZT patch was employed to connect to the AD5933 board and conduct the calibration and impedance measurement test.

According to the documentation [31], the calibration gain factor can be calculated in two different ways, i.e., mid-point or multi-point frequency calibration. In this study, the mid-frequency point calibration method combined with a resistor with known resistance value was selected because of convenience, and the influences to the impedance measurement stemming from different calibration methods can be further studied in future works. In this situation, it should be noted that this calibration approach works correctly only for measurements related to electronic elements like resistors with purely resistance characteristics. Therefore, the detailed calibration procedure can be summarized as following:

1) Obtaining the referential measurements

First, a professional impedance analyzer was connected with the free PZT patch, and a wide frequency excitation was applied to the patch. Then, the corresponding impedance signature of the PZT patch was measured and analyzed to select the sensitive frequency band. In addition, the minimal and maximal impedance magnitude was also obtained.

2) Selection of R_{CAL} and R_{FB}

According to the application note report published by [32], the value of the calibration resistor R_{CAL} should be equal to:

$$R_{CAL} = \frac{Z_{min} + Z_{max}}{3} \quad (1)$$

where Z_{min} , Z_{max} denote the minimal and maximal impedance of the measured PZT element, respectively. Based on the pre-test results of step (1) (Z_{min} , Z_{max}), the calibration resistor R_{CAL} was first determined, and then the referential resistor R_{FB} was also selected as $R_{FB} = R_{CAL}$ (in the pure resistance case).

3) Calibration

After the R_{CAL} and R_{FB} resistors were determined and then connected to the AD5933 board at the desired position, the related evaluation parameters of the board could be set by the evaluation software dashboard. After that, an impedance measurement can be conducted, and thus several related parameters can be respectively, calculated by the acquisition of the real R_Z and imaginary I_Z datasheet, for example, the magnitude M , the gain factor GF , and the phase φ_{AD5933} .

When the real and imaginary data of the impedance have been obtained by AD5933, the magnitude of the known resistance R_{CAL} can be calculated as:

$$M = \sqrt{R_Z^2 + I_Z^2} \quad (2)$$

Based on the calculated magnitude M , the gain factor GF could be obtained by following the formula:

$$GF = \frac{Y_{CAL}}{M} = \frac{\frac{1}{Z_{CAL}}}{M} = \frac{1}{R_{CAL}} \quad (3)$$

where Y_{CAL} , Z_{CAL} refer to calibration admittance and impedance, respectively. In this study, calibrating resistor R_{CAL} is utilized instead of impedance Z_{CAL} .

On the other hand, the phase φ_{AD5933} was calculated using the general formula:

$$\varphi_Z = \tan^{-1}\left(\frac{I_Z}{R_Z}\right) \quad (4)$$

4) Measurement

Measurement was taken by removing the R_{CAL} resistor from the board and connecting it to the free PZT patch instead, then conducting an impedance measurement using the AD5933 board, and acquiring the real and imaginary data for the impedance. In this situation, the impedance magnitude of the free PZT patch can be achieved following the equation:

$$Z_{PZT} = \frac{1}{GF \cdot M_{PZT}} \quad (5)$$

where M_{PZT} is the impedance magnitude for the piezoelectric transducer calculated based on Eq. 2. At the same time, the phase φ_{sys} was also calculated following Eq. 4.

5) Calibration for the measurement

Based on the phase φ_{AD5933} in step 4) and the phase φ_{sys} in step (5), the corrected phase φ_{PZT} for the PZT patch can be calculated by following the equation:

$$\varphi_{PZT} = \varphi_{sys} - \varphi_{AD5933} \quad (6)$$

6) Extraction of the real and imaginary data

Based on the corrected Z_{PZT} in step 4) and the phase φ_{PZT} in step (5), the real R_{PZT} and imaginary X_{PZT} of the PZT impedance can be calculated as:

$$R_{PZT} = |Z_{PZT}| \cdot \cos(\varphi_{PZT}) \quad (7)$$

$$X_{PZT} = |Z_{PZT}| \cdot \sin(\varphi_{PZT}) \quad (8)$$

$$\theta_{PZT} = -\varphi_{PZT} \quad (9)$$

where θ_{PZT} is phase angle between real and imaginary part of admittance.

Calibration Performance

In this calibration test for a free PZT patch, the sweep frequency band was selected as 10–30 kHz following the calibration procedure in step 1) of the last section, and the calibration resistor R_{CAL} was selected as 10 kΩ. Then, the real and

imaginary part of the PZT impedance can be calculated with the AD5933 board following the above calculation procedures. On the other hand, in order to further validate the calibration performance, a professional impedance analyzer (WK6500B) was employed here to measure the PZT impedance as the reference.

Characteristics measured by the WK6500B and AD5933 boards with the calibration resistance 10 kΩ are presented in **Figure 2**. From the figure, it is clear that the impedance signal measured by the calibrated AD5933 board presents a good consistency with the result measured by the WK6500B, especially for the imaginary part. For the real part of impedance, these characteristics remain similar, however differ a little considering their values, but the frequencies corresponding to peaks are almost the same.

Based on the results, it can be concluded that the AD5933 evaluation board has the potential to be utilized as an impedance analyzer to acquire the electromechanical impedance signal of the host structures after proper calibration.

On the other hand, it should be noted that many factors, such as the A/D conversion and the inherent electrical impedance of the internal chips, may induce the difference between the impedance signatures measured by the AD5933 and the professional impedance analyzer. In addition, the calibration process of AD5933 will also significantly influence the measurement result, for example, the selection of R_{CAL} and R_{FB} resistor, the selection of calibration method (mid-point frequency or multiple point frequency calibration), the number of sampling points, and the calculation of the gain factor. The temperature sensor of AD5933 requiring to measure and compensate for temperature also contributes to the differences. However, it does not seem to cause significant problems for SHM, because the impedance-based SHM is based on the relative difference between two normalized signals: the healthy condition and the test conditions [15, 33].

EXPERIMENTAL PREPARATIONS

In the above section, the detail calibration procedures of AD5933 have been discussed, its impedance measurement performance after calibration had also been verified by a free PZT transducer, and finally a good, consistent result was observed. In this section, in order to further validate the impedance measurement performance of the AD5933 evaluation board, especially in practical application, a threaded pipe connection was assembled in the laboratory and then the board experimentally investigated for its damage detection ability.

Experimental Setup

As shown in **Figure 3**, a pipeline connection specimen was assembled in the laboratory from two pipe segments and a threaded coupling part, and then fixed to the ground by a steel fixture. A PZT-5H patch was bonded onto the surface of the threaded connection by epoxy adhesive. **Table 2** presents the

TABLE 2 | The parameters of the specimen and the PZT patch.

	Parameters	Values	Unit
PZT-5H	Dimension	$\varnothing 12 \times 0.5$	mm
	Density	7800	kg/m ³
	Young's modulus	46	Gpa
	Poisson's ratio	0.3	-
	Structural damping	3×10^{-9}	-
	Piezoelectric strain coefficients d_{31} , d_{32} / d_{33} / d_{24} , d_{15}	-2.10/5.00/5.80	10^{-10} m/V or 10^{-10} C/N
	Mechanical loss factor	0.001	-
Steel specimen	Dielectric loss factor	1.75/2.12	10^{-8} F/m
	Electric permittivity ϵ_{11}^T , $\epsilon_{22}^T/\epsilon_{33}^T$	$\varnothing 48$ ($\varnothing 42$)*	mm
	Diameter (pipe part)	$\varnothing 60$ ($\varnothing 45$)*	mm
	Diameter (coupling part)	7900	kg/m ³
	Density	206	Gpa
	Poisson's ratio	0.3	-
	Static friction coefficient (steel-steel)	0.15	-

Note: The value in the bracket donates the inner diameter.

detailed geometric and material parameters of the specimen and the PZT patch.

The complete experimental setup consists of the pipeline test specimen, the AD5933 evaluation board, and a laptop, as shown in **Figure 3**. The surface mounted PZT patch in the specimen was connected with the AD5933 board via a USB cable. The corresponding software provided by Analog Devices Co. was pre-installed on the laptop to pre-set the acquisition parameters and control the board for the impedance measurement during the test. In addition, a professional impedance analyzer, WK6500B, was employed here for result comparison.

Experimental Procedure

In the experiment, in order to quantitatively indicate the changes in the contact area of the threaded connection during the process of loosening occurring and developing, the relative rotation circles between the coupling and the pipe segment were introduced as a monitoring variable. Therefore, seven different looseness severities were established and investigated, from tightest to loosest for the contact region of the pipe connection, by rotation of the pipe segment. At the beginning of the experiment, the initial tightest status was regarded as the health baseline for the connection. Then, six loosening severities were introduced by rotating the pipe segment from one circle to six circles with the step-increase of one circle for each level of severity. **Figure 4** presents the four different loosening severities of the threaded pipe connection during the experiment. Thus, a total of seven service statuses for the threaded pipe connection were implemented and investigated in this study.

Calibration and Acquisition Procedure

In the experiment, the AD5933 evaluation board was utilized to acquire the impedance data of the test specimen under different loosening severities. As per the above description in section four, the calibration was necessary for the AD5933 board before it could be properly utilized for the impedance measurement. Therefore, based on the description on Section 4.1, the detailed calibration and measurement procedure for this AD5933-based loosening monitoring experiment can be conducted as following:

- 1) Firstly, a sweep frequency excitation test with the frequency range of 10–100 kHz was conducted by a professional impedance analyzer, the WK6500B. Then, the related impedance measurements including the magnitude $|Z|$ and phase θ were obtained, and thus the calibration and reference resistors for AD5933 were determined as $R_{CAL} = R_{FB} = 2 \text{ k}\Omega$. In addition, the impedance-sensitive frequency range of the test specimen was also determined as from 20 to 60 kHz.
- 2) Secondly, the calibration resistor R_{CAL} and the reference resistor R_{FB} were installed on the AD5933 board in the desired positions. Then, the related measurement parameters of the board were pre-set by the control software on the laptop. Thus, a sweep excitation with the frequency range from 20 to 60 kHz and the voltage amplitude of 1 V was applied to the calibration resistor, and therefore its corresponding impedance response, including the magnitude and phase, were obtained. Finally, the gain factor GF and the phase φ_{AD5933} were calculated, respectively.
- 3) Thirdly, replacing the calibration resistor R_{CAL} with the PZT patch which was surface bonded onto the host structure. Then, a sweep frequency excitation test was conducted to the pipeline specimen using the AD5933 board with the same preset parameters as in step (2); thus the real and imaginary data of the impedance signal of the PZT patch could be obtained.
- 4) Fourthly, calibrating the impedance measurement in step 3) with the calculated calibration parameters, including the gain factor GF and the phase φ_{AD5933} , which were obtained from step 2) above. After that, the true impedance response of the test specimen could be calculated.

It should be noted that even though both the real and imaginary part of the impedance signatures could be measured by the AD5933 board, only the real impedance measurements will be presented and analyzed in this study. This is because some literature [34–36] has reported that the imaginary part of the impedance is dominated by the capacitive response of the PZT patch itself and less sensitive to the changes in the mechanical properties of the structure. Thus, a conclusion had been drawn that the real part (i.e., resistance R) of

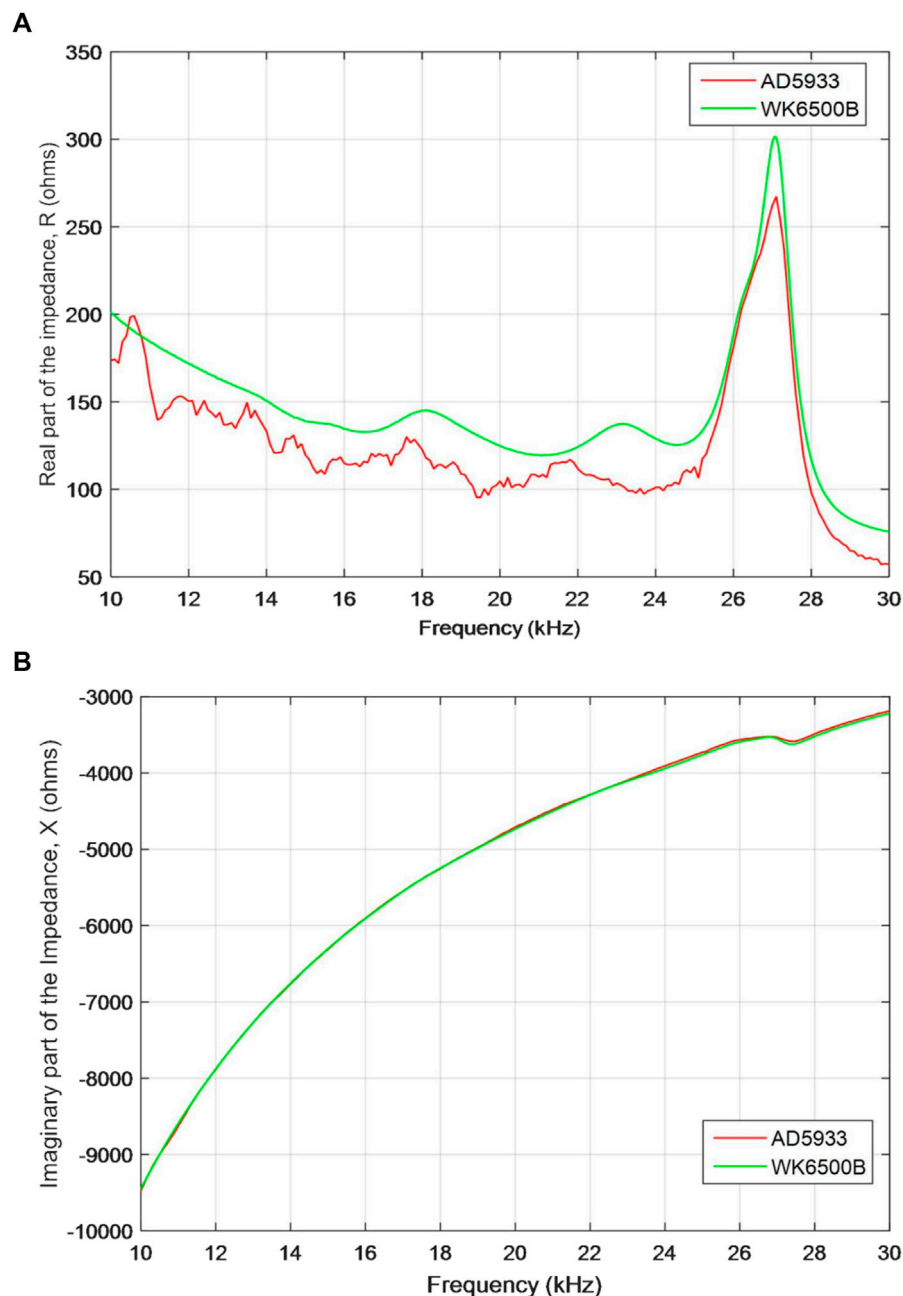


FIGURE 2 | Comparison of impedance measurements for WK6500B and AD5933: **(A)** the real part, and **(B)** the imaginary part of the impedance.

the impedance signature is more sensitive to changes in the structural mechanical properties compared with the imaginary part of the impedance (i.e., the reactance X).

In this study, the real part of the impedance signals, measured by WK6500B and AD5933 respectively, were presented and compared as shown in **Figure 5**. In the figure, it is clear that the impedance signal measured by the professional equipment has a smoother curve, but more burr phenomenon can be found in the measurements of the evaluation board. Even so, both results share the same change trend and peak position, which are

more important and meaningful in the procedures of SHM and damage detection. Therefore, it can be concluded that the AD5933 evaluation board has the possibility to obtain the key information and parameters of the impedance measurement of the host structure, and has significant potential in the field of SHM and damage detection.

During the experimental procedure, each loosening severity was investigated to acquire the impedance signal following that step (4), then the real and imaginary part of the measurement impedance could be obtained by the AD5933 board.

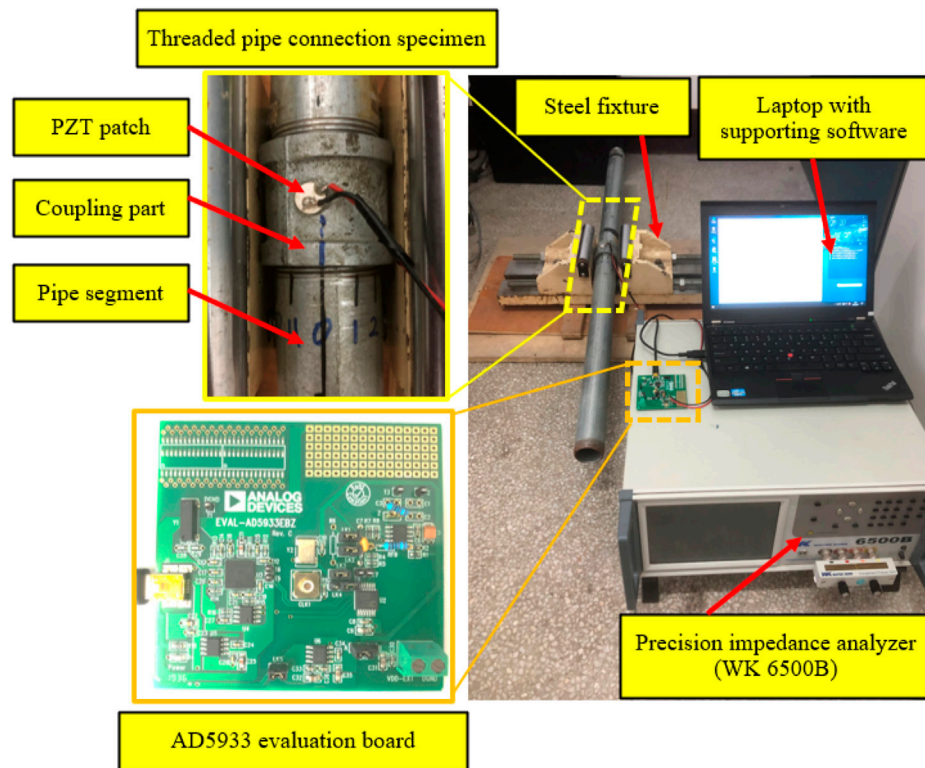


FIGURE 3 | Experimental setup.

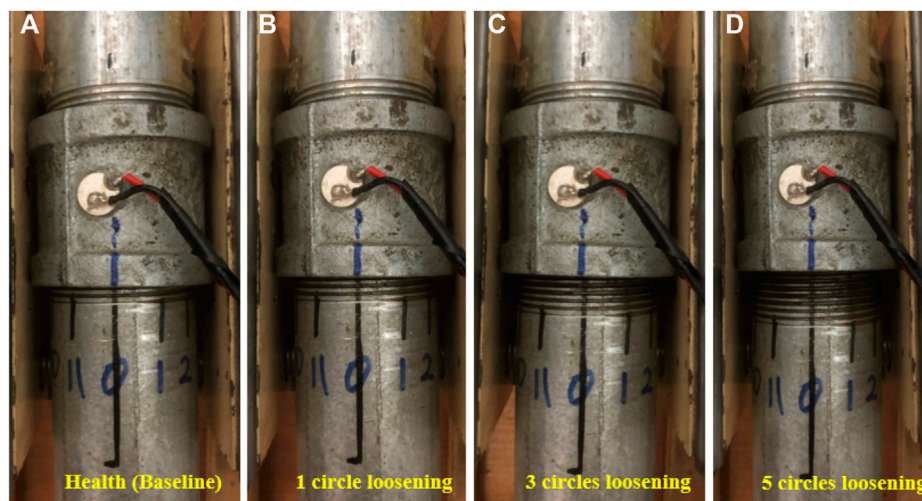


FIGURE 4 | Several loosening severities for (A) health (baseline), (B) one circle, (C) three circles and (D) five circles of loosening.

EXPERIMENTAL RESULT ANALYSIS AND DISCUSSION

Experimental Results and Analysis

Following the calibration and measurement procedure described above for the AD5933 evaluation board, the real

part of the electrical impedance signatures of the PZT patch, which was surface bonded onto the host structure, was successfully obtained, as shown in Figure 6. From the figure, it is observed that the real part of the impedance measurement under different loosening severities presents a significant difference. This phenomenon proves that the

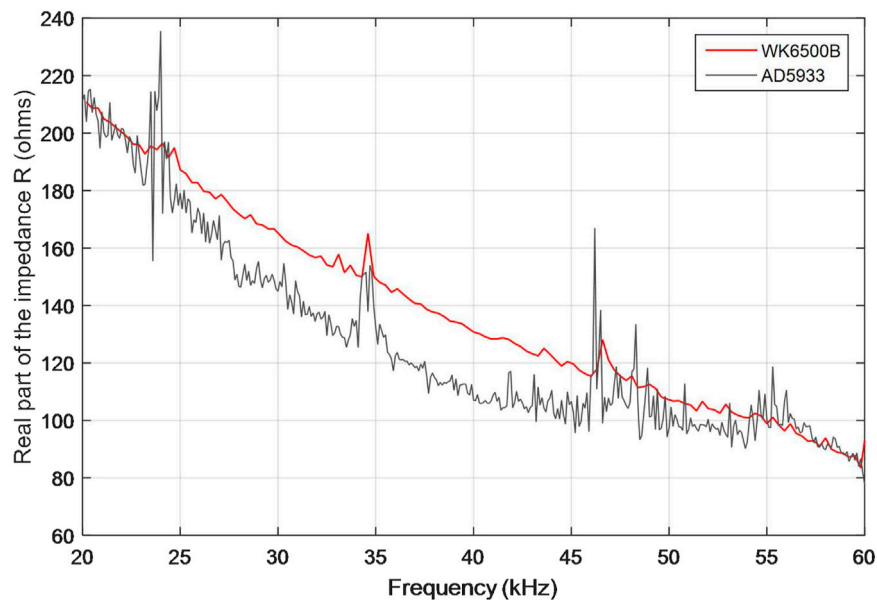


FIGURE 5 | Comparison of impedance from WK6500 and AD5933 for the pipeline specimen.

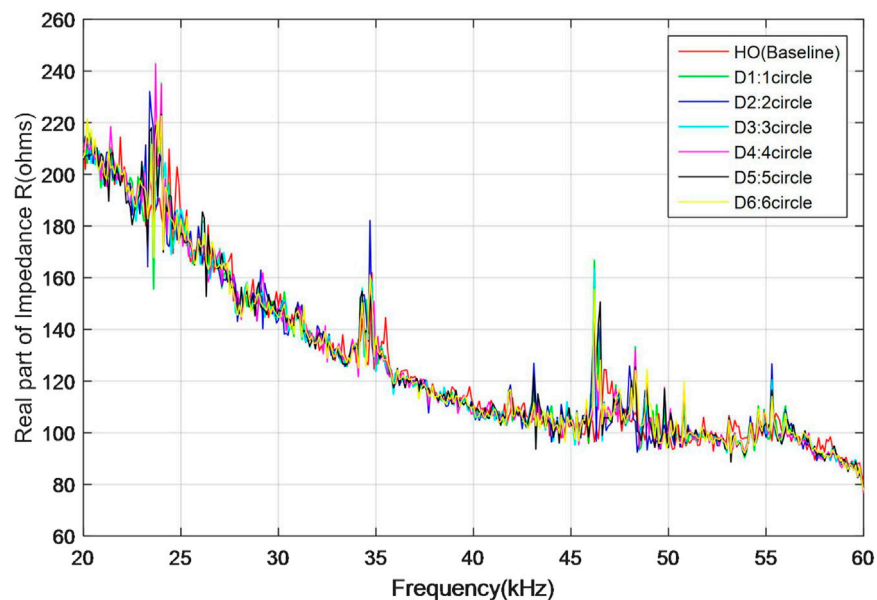
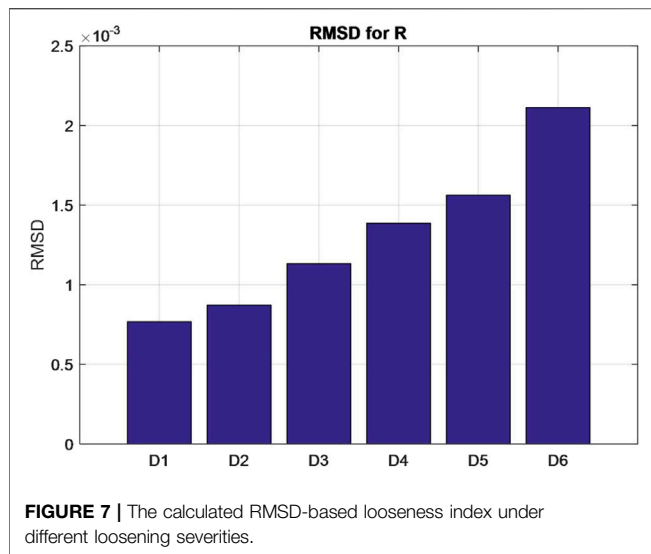


FIGURE 6 | Measured electrical impedance signatures of the PZT patch by AD5933.

mechanical impedance changes in the pipeline connection due to the occurrence and development of loosening could be effectively captured by the electrical impedance of the PZT patch using the AD5933 board.

In order to quantitatively distinguish the differences, the root-mean-square distance (RMSD) algorithm was employed here to help to build a looseness detection index, thus the final identification

result was presented in **Figure 7**. In the figure, it is observed that the RMSD-based looseness detection index increases in line with the increasing looseness severity of the connection. Based on the above analysis, it can be concluded that the AD5933 impedance evaluation board has an excellent ability to acquire the impedance signature of the host structure, and presents great potential for defect identification and hazard assessment.



DISCUSSION

In this research, a cheap impedance evaluation board—AD5933—manufactured by the Analog Device Co., was experimentally studied to investigate its impedance calibration and measurement performance. At first, a simple impedance acquisition test for a free PZT patch was conducted to help to introduce the detail calibration procedure. Meanwhile, the PZT impedance signature measured by AD5933 was compared with the result measured by the professional impedance analyzer, WK6500B, and the final comparison result presents good consistency. Then, in order to further investigate the feasibility and effectiveness of AD5933 when applied in the real SHM field, especially for practical applications, a looseness disease detection test for a threaded pipeline connection was conducted, and the final results proved that the impedance measurement by AD5933 can be successfully utilized for the identifying loosening.

However, it should be noted that even though a free PZT patch and a loosening threaded pipe connection were experimentally investigated in this study, it is still necessary and meaningful to further validate the impedance measurement performance of the AD5933 board on more complex structures and in more practical applications. This related research will be conducted in our next work.

On the other hand, similar to the professional impedance analyzer, the accuracy and precision of the impedance measurement for the AD5933 board will also be significantly influenced by some external factors, including ambient temperature, moisture, environmental pressure, etc. For example, several researchers [37, 38] had experimentally verified that changing temperature will induce difference in EMI-based detection results, including magnitude changes or frequency shifts in measured impedance signatures.

Even so, it still did not affect the ability and potential of EMI to be utilized as an impedance measurement device in the SHM and damage detection fields, especially for practical application.

In its current state, due to space limitation, the study is focused on verifying the feasibility of using the AD5933 board to acquire an impedance signature and realize damage identification for a host structure, especially detecting loosening in a threaded pipe connection.

CONCLUSION

In this study, a miniature impedance evaluation board, AD5933, was studied in detail to investigate its impedance calibration and measurement performance. Compared with the professional impedance analyzer, the AD5933 is much cheaper, has smaller dimensions and a much lower weight. In this research, a simple impedance measurement for a free PZT patch was investigated, and the acquisition signatures of the AD5933 presented a good consistency with the ones measured by the professional impedance analyzer. In addition, a threaded pipe connection specimen was assembled and tested in the laboratory to further validate the feasibility and effectiveness of the AD5933 board, especially performance in damage identification. The final results proved that the AD5933 board can be successfully utilized for loosening severity identification and quantification. Based on the above research, all the investigation results demonstrated that the AD5933 board has excellent ability in impedance measurement after proper calibration, and presents great potential in the area of structural health monitoring and damage detection, especially in practical application.

DATA AVAILABILITY STATEMENT

The original contribution presented in the study are included in the article/Supplementary Material, further inquiries can be directed to the corresponding authors.

AUTHOR CONTRIBUTIONS

All authors discussed and agreed upon the idea and made scientific contributions. YL developed the original idea, YL and QF designed the experiments, YL, YC, and ZZ conducted the experiments, YL and YC analyzed the data, YL and QF wrote the original draft. QF made critical revision to the paper.

FUNDING

The research was partially supported by the National Natural Science Foundation of China (Grant No. 51708520). The authors would like to thank for them for their financial support.

REFERENCES

- Liang C, Sun FP, and Rogers CA. An Impedance Method for Dynamic Analysis of Active Material Systems. *J Vibration Acoust* (1994) 116(1):120–8. doi:10.1115/1.2930387
- Hu X, Zhu H, and Wang D. A Study of concrete Slab Damage Detection Based on the Electromechanical Impedance Method. *Sensors* (2014) 14(10):19897–909. doi:10.3390/s141019897
- Armstrong TW, and Sevostianov I. Electrical Impedance Changes Due to Cracks in Planar Conductive Structural Elements. *Struct Health Monit* (2015) 14(5):489–501. doi:10.1177/1475921715596221
- Wang D, Song H, and Zhu H. Electromechanical Impedance Analysis on Piezoelectric Smart Beam with a Crack Based on Spectral Element Method. *Math Probl Eng* (2015) 2015:713501. doi:10.1155/2015/713501
- Selva P, Cherrier O, Budinger V, Lachaud F, and Morlier J. Smart Monitoring of Aeronautical Composites Plates Based on Electromechanical Impedance Measurements and Artificial Neural Networks. *Eng Structures* (2013) 56:794–804. doi:10.1016/j.engstruct.2013.05.025
- Liang Y, Li D, Parvasi SM, Kong Q, Lim I, and Song G. Bond-slip Detection of concrete-encased Composite Structure Using Electro-Mechanical Impedance Technique. *Smart Mater Struct* (2016) 25(9):095003. doi:10.1088/0964-1726/25/9/095003
- Narayanan A, Kocherla A, and Subramaniam KVL. Understanding the Coupled Electromechanical Response of a PZT Patch Attached to concrete: Influence of Substrate Size. *Measurement* (2018) 124:505–14. doi:10.1016/j.measurement.2018.04.055
- Liang Y, Ye Z, and Feng Q. Axial Load Monitoring for concrete Columns Using a Wearable Smart Hoop Based on the Piezoelectric Impedance Frequency Shift: a Feasibility Study. *Adv Civil Eng* (2020) 2020:1329516. doi:10.1155/2020/1329516
- Liang Y, Li D, Parvasi SM, and Song G. Load Monitoring of Pin-Connected Structures Using Piezoelectric Impedance Measurement. *Smart Mater Struct* (2016) 25(10):105011. doi:10.1088/0964-1726/25/10/105011
- Huo L, Chen D, Liang Y, Li H, Feng X, and Song G. Impedance Based Bolt Pre-load Monitoring Using Piezoceramic Smart Washer. *Smart Mater Struct* (2017) 26(5):057004. doi:10.1088/1361-665x/aa6a8e
- Liang W, Zhang L, Xu Q, and Yan C. Gas Pipeline Leakage Detection Based on Acoustic Technology. *Eng Fail Anal* (2013) 31:1–7. doi:10.1016/j.engfailanal.2012.10.020
- Min J, Yi J-H, and Yun C-B. Electromechanical Impedance-Based Long-Term SHM for Jacket-type Tidal Current Power Plant Structure. *Smart structures Syst* (2015) 15(2):283–97. doi:10.12989/sss.2015.15.2.283
- Na W, Koh KH, Lee AS, Cho S, Ok B, Hwang S-W, et al. Binder-less Chemical Grafting of SiO₂ Nanoparticles onto Polyethylene Separators for Lithium-Ion Batteries. *J Membr Sci* (2019) 573:621–7. doi:10.1016/j.memsci.2018.12.039
- Park S, Yun CB, and Inman DJ. Wireless Structural Health Monitoring Using an Active Sensing Node. *Int J Steel Struct* (2006) 6:361–8.
- Min J, Park S, Yun CB, and Song B. Development of a Low-Cost Multifunctional Wireless Impedance Sensor Node. *Smart Structures Syst* (2010) 6(5–6):689–709. doi:10.12989/sss.2010.6.5_6.689
- Lin TH, Lu YC, and Hung SL. Locating Damage Using Integrated Global-Local Approach with Wireless Sensing System and Single-Chip Impedance Measurement Device. *ScientificWorldJournal* (2014) 2014:729027. doi:10.1155/2014/729027
- Wandowski T, Malinowski P, and Ostachowicz W. Calibration Problem of AD5933 Device for Electromechanical Impedance Measurements. In: *EWSHM-7th European Workshop on Structural Health Monitoring*. Nantes, France: Nantes, France: Université de Nantes (2014).
- Kaur N, Bhalla S, Shanker R, and Panigrahi R. Experimental Evaluation of Miniature Impedance Chip for Structural Health Monitoring of Prototype Steel/RC Structures. *Exp Tech* (2016) 40(3):981–92. doi:10.1007/s40799-016-0097-6
- Guo Z, Huang T, and Schröder K-U. Development of a Piezoelectric Transducer-Based Integrated Structural Health Monitoring System for Impact Monitoring and Impedance Measurement. *Appl Sci* (2020) 10(6):2062. doi:10.3390/app10062062
- Wandowski T, Malinowski PH, and Ostachowicz WM. Improving the EMI-Based Damage Detection in Composites by Calibration of AD5933 Chip. *Measurement* (2021) 171:108806. doi:10.1016/j.measurement.2020.108806
- Tawie R, Park HB, Baek J, and Na WS. Damage Detection Performance of the Electromechanical Impedance (EMI) Technique with Various Attachment Methods on Glass Fibre Composite Plates. *Sensors* (2019) 19(5):1000. doi:10.3390/s19051000
- Van Wittenberghe J, De Pauw J, De Baets P, De Waele W, Ost W, De Roeck G, et al. Fatigue Investigation of Threaded Pipe Connections. *Ijssmed* (2010) 1(1):182–9. doi:10.21825/scad.v1i1.20424
- Van Wittenberghe J. *Experimental Analysis and Modelling of the Fatigue Behaviour of Threaded Pipe Connections*. [Doctoral dissertation]. Ghent (Belgium): Ghent University (2011).
- Qu C-X, Yi T-H, Zhou Y-Z, Li H-N, and Zhang Y-F. Frequency Identification of Practical Bridges through Higher-Order Spectrum. *J Aerosp Eng* (2018) 31(3):04018018. doi:10.1061/(asce)as.1943-5525.0000840
- Qu CX, Yi TH, and Li HN. Mode Identification by Eigensystem Realization Algorithm through Virtual Frequency Response Function. *Struct Control Health Monit* (2019) 26(10):e2429. doi:10.1002/stc.2429
- Parvasi SM, Ji Q, and Song G. Structural Health Monitoring of Plate-like Structures Using Compressive/Shear Modes of Piezoelectric Transducers. *Earth and Space* (2016) 1033.
- Mishra A, and Soni A. Leakage Detection Using Fibre Optics Distributed Temperature Sensing. In: 6th Pipeline Technology Conference (2011); New Delhi, India. engineers india limited (2011).
- Zuo J, Zhang Y, Xu H, Zhu X, Zhao Z, Wei X, et al. Pipeline Leak Detection Technology Based on Distributed Optical Fiber Acoustic Sensing System. *IEEE Access* (2020) 8:30789–96. doi:10.1109/access.2020.2973229
- Liang Y, Feng Q, and Li D. Loosening Monitoring of the Threaded Pipe Connection Using Time Reversal Technique and Piezoceramic Transducers. *Sensors* (2018) 18(7):2280. doi:10.3390/s18072280
- Liang Y, Feng Q, Li D, and Cai S. Loosening Monitoring of a Threaded Pipe Connection Using the Electro-Mechanical Impedance Technique-Experimental and Numerical Studies. *Sensors* (2018) 18(11):3699. doi:10.3390/s18113699
- Analog Device. *Evaluation Board for the 1 MSPS, 12-Bit Impedance Converter, Network Analyzer, AD5933 DataSheet*. Norwood, MA, USA: Analog Devices Inc. (2008).
- Analog Device. *AN-1252 Application Note*. Norwood, MA, USA: Analog Devices Inc. (2013).
- Overly TGS, Park G, Farinholt KM, and Farrar CR. Development of an Extremely Compact Impedance-Based Wireless Sensing Device. *Smart Mater Struct* (2008) 17(6):065011. doi:10.1088/0964-1726/17/6/065011
- Ayres JW, Lalande F, Chaudhry Z, and Rogers CA. Qualitative Impedance-Based Health Monitoring of Civil Infrastructures. *Smart Mater Struct* (1998) 7(5):599–605. doi:10.1088/0964-1726/7/5/004
- Park G, Sohn H, Farrar CR, and Inman DJ. Overview of Piezoelectric Impedance-Based Health Monitoring and Path Forward. *Shock vib Dig* (2003) 35(6):451–63. doi:10.1177/05831024030356001
- Park G, and Inman DJ. Structural Health Monitoring Using Piezoelectric Impedance Measurements. *Phil Trans R Soc A* (2007) 365(1851):373–92. doi:10.1098/rsta.2006.1934
- Baptista F, Budoya D, Almeida V, and Ulson J. An Experimental Study on the Effect of Temperature on Piezoelectric Sensors for Impedance-Based Structural Health Monitoring. *Sensors* (2014) 14:1208–27. doi:10.3390/s140101208
- Wandowski T, Malinowski PH, and Ostachowicz WM. Delamination Detection in CFRP Panels Using EMI Method with Temperature Compensation. *Compos Structures* (2016) 151:99–107. doi:10.1016/j.compstruct.2016.02.056

Conflict of Interest: YL, ZZ, and QF were employed by the company Wuhan Institute of Earthquake Engineering Co., Ltd.

The remaining authors declare that the research was conducted in the absence of any commercial or financial relationships that could be construed as a potential conflict of interest.

Publisher's Note: All claims expressed in this article are solely those of the authors and do not necessarily represent those of their affiliated organizations, or those of the publisher, the editors, and the reviewers. Any product that may be evaluated in this article, or claim that may be made by its manufacturer, is not guaranteed or endorsed by the publisher.

Copyright © 2021 Liang, Chen, Zhang and Feng. This is an open-access article distributed under the terms of the Creative Commons Attribution License (CC BY). The use, distribution or reproduction in other forums is permitted, provided the original author(s) and the copyright owner(s) are credited and that the original publication in this journal is cited, in accordance with accepted academic practice. No use, distribution or reproduction is permitted which does not comply with these terms.



Old - New Concrete Interfacial Bond Slip Monitoring in Anchored Rebar Reinforced Concrete Structure Using PZT Enabled Active Sensing

Jian Jiang^{1,2,3}, Yixuan Chen² and Junwu Dai^{1*}

¹Institute of Engineering Mechanics, China Earthquake Administration, Key Laboratory of Earthquake Engineering and Engineering Vibration, China Earthquake Administration, Harbin, China, ²Hubei Key Laboratory of Earthquake Early Warning, Institute of Seismology, China Earthquake Administration, Wuhan, China, ³Wuhan Institute of Earthquake Engineering Co. Ltd., Wuhan, China

OPEN ACCESS

Edited by:

Qingzhao Kong,
Tongji University, China

Reviewed by:

Venu Gopal Madhav Annamdas,
Continental, Germany
Ping Zhao,
University of Minnesota Twin Cities,
United States

*Correspondence:

Junwu Dai
junwu@iem.ac.cn

Specialty section:

This article was submitted to
Smart Materials,
a section of the journal
Frontiers in Materials

Received: 11 June 2021

Accepted: 13 September 2021

Published: 27 September 2021

Citation:

Jiang J, Chen Y and Dai J (2021) Old -
New Concrete Interfacial Bond Slip
Monitoring in Anchored Rebar
Reinforced Concrete Structure Using
PZT Enabled Active Sensing.
Front. Mater. 8:723684.
doi: 10.3389/fmats.2021.723684

Post-installed anchor technology is widely used for structural strengthening and for retrofitting existing constructions. The old-new concrete interface associated with using this technology is of great significance in the shear capacity of concrete structural member under shear forces. For such members, interface failures usually occur with bond slip. In this paper, an application of a piezoceramic enabled active sensing technique is put forward to monitor Old - New concrete interfacial bond slip. Three concrete specimens (S1, S2, and S3) are fabricated and each specimen consists of two parts. Each part is made of concrete poured at different times, and both are bonded with an anchored rebar embedded inside the specimen. Two PZT aggregates bonded to opposing sides of the concrete specimen helped to realize active sensing. During the shear loading test, both the load values and the signals from sensors are acquired every 20 s. The test durations of S1, S2 and S3 lasted 960, 1,120, and 1,110 s, respectively. Furthermore, the received signal energies are quantified through wavelet packet analysis to monitor the Old - New concrete interfacial bond slip process. The experimental results show that the change of WPEI in the received signals has a direct relation with the severity of the Old - New concrete interfacial bond slip. Moreover, the PZT-based active sensing approach is feasible to monitor the shear-induced bond slip in Old - New concrete interfaces.

Keywords: anchored rebar, bond slip, lead zirconate titanate transducer, active sensing, structural health monitoring

INTRODUCTION

Post-installed anchor technology has been commonly applied in terms of structural strengthening and retrofitting of existing constructions. A post-installed anchor in general is composed by a rebar imbedded in a hole drilled in hardened concrete with structural bonding agent (Cook, 1992; Cook et al., 1993; Ronald and Robert, 2001). Currently, epoxy acts as an universal structural adhesive due to its excellent properties (Wang et al., 2015). Since the rebars can be installed in nearly all the expected position in hardened concrete, the post-installed anchors are able to increase the whole

framework's bearing capacity by integrating the new concrete member with the original concrete member (Wörle, 2014).

As the post-installed anchor technique serves as a connection method of high efficiency in terms of structural reconstruction and expansion, now it has been widely applied in practice and has also attracted much research attention. Much of the reported research literature focus on interfaces in rebar, epoxy, and concrete systems (Mahrenholtz et al., 2016; González et al., 2018; Muciaccia et al., 2018). Bouazaoui and Li (2008) used pull out tests to investigate the interfacial adhesion quality between rebar and concrete as well as to measure the apparent shear stress between anchored rebar and concrete. Barnaf et al. (2012) carried out the pull out tests and numerical simulations so as to determine both the behavior and bonding strength of industrial adhesives which are adopted for anchor bonding. Bajer and Barnat (2012) conducted researches over both the bond quality and the concrete-bond failure of a bonded anchor loaded by tensile forces. The pull-out test is commonly introduced to check the bonding strength between concrete and anchored rebar systems; nevertheless, pull-out tests are detrimental (Yilmaz et al., 2013; Brencich, 2015). Nondestructive evaluation (NDE) methods are generally required for the purpose of performing *in-situ* assessment over epoxy bonded anchors. Rizzo et al. (2010) studied the adoption of acoustic emission (AE) to evaluate the structural stability of concrete strengthened and underpinned by chemically bonded anchors.

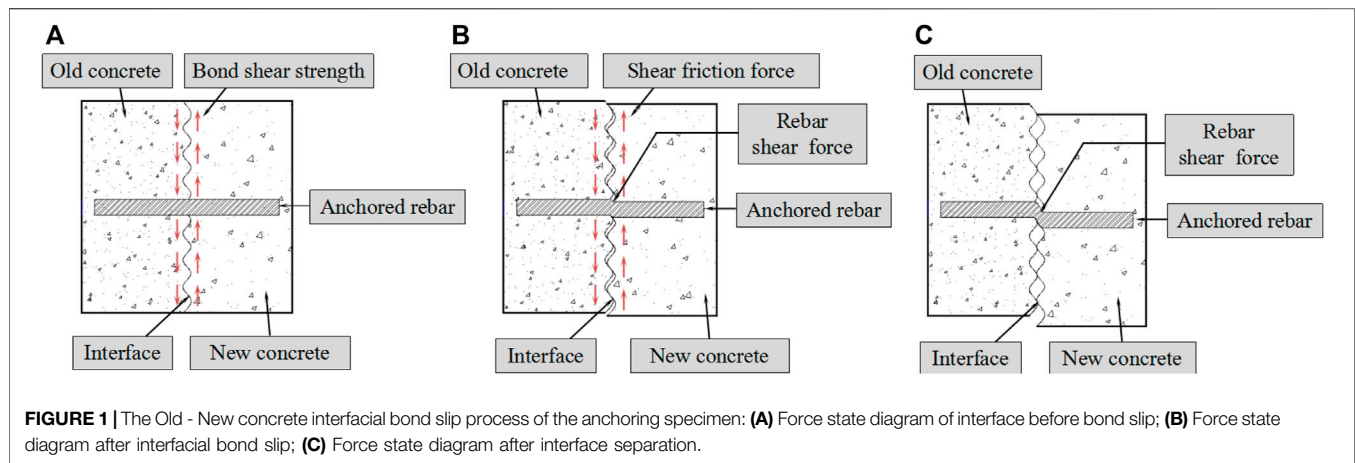
Moreover, the PZT-enabled active sensing approach was introduced by Jiang et al. (2019) to demonstrate the development of bonding strength along the interface layer between the concrete and the bonded rebar. The AE parameters including the amplitude, duration, and signal strength were employed to characterize the stage of concrete bond deterioration (Abouhussien and Hassan, 2017b). Hou et al. (2009) discussed the feasibility of OTDR optical fiber technology to monitor the debonding of FRP reinforced concrete structure. Zhou et al. (2008) used BOTDR(A) technology to evaluate the bond slips between steel bars and concrete in reinforced concrete beams. In addition, electro-mechanical impedance (EMI) method was employed to detect the bond-slip in the concrete-encased composite structure (Liang et al., 2016).

However, the shear bearing capacity of a strengthened member is collectively assumed by the concrete and the anchored rebars when the member is under shear load. The interface between the new and old concrete is relatively weak due to the discontinuous aggregate particles in the Old - New concrete interface caused by the different pouring time (Maili and Jing, 2018). Therefore, the Old - New concrete interface plays a crucial role in determining the shear bearing capacity; specifically, interface failures usually occur with bond slip. To prevent the brittle and sudden failure of strengthened concrete structures, it is of practical significance and great research value to monitor the bond slip at the Old - New concrete interface when a strengthened structural member is under shear load. Most studies mainly focus on the effect of shear force on the interfacial bond slip of new-old concrete. In Wang's research, theoretical and experimental research was performed to evaluate the mechanical

performance of new and old concrete beams under sustained loads (Wang et al., 2011). As to find out the influencing factors on the bond slip, the age difference (Song et al., 2015), normal stresses (Al-Fasih et al., 2021) and curing condition (Mirmoghataei et al., 2015) were considered. Many studies have also shown that the concrete type has a certain influence on the interfacial bond slip between the Old - New concrete. In their researches, concrete types include: reinforced concrete (Abouhussien and Hassan, 2017), high-strength concrete (Qasim, 2020), ultra-high-strength (Hyun-Soo Youm and Changbin, 2021), composite ceramist lightweight aggregate concrete (Liu et al., 2020), and reactive powder concrete (Ju et al., 2020). In addition, the influence of compressive strength on the bond slip of the old-new concrete were evaluated and the optical compressive strength were concluded (Júlio et al., 2006; Diab et al., 2017). Recently, the scanning electron microscopy (SEM) were employed to evaluate the interfacial bond properties of self-expanding polymer and concrete under the shear load (Fang et al., 2021).

In recent years, the piezoelectric-based technique has been commonly accepted and applied as an effective form of structural health monitoring (SHM) technique (Bhalla and Kaur, 2018; Feng and Ou, 2018; Hu et al., 2018; Xu et al., 2019). Serving as one of the most commonly recognized piezoelectric materials, Lead Zirconate Titanate (PZT) has the advantages of low costs, quick response, and wide bandwidth (Zhu et al., 2017; Zhou et al., 2020), and can be easily fabricated in different geometries (Zeng et al., 2015; Wang et al., 2020a). Because of the piezoelectric effect, PZT patches can be used as either sensors or actuators for structural damage detection and condition monitoring (Nicassio et al., 2020). Most of the early applications of PZT-based techniques are based on impedance analysis and active sensing. For example, impedance analysis was adopted in order to evaluate debonding between fiber-reinforced polymer rebar and fiber-reinforced polymer rebar (Li et al., 2017), preload monitoring in bolted connections (Lee, 2021), load monitoring (Annamdas and Soh, 2017), damage monitoring in pin connection (Fan et al., 2018), and monitoring the status of a composite panel (Dziendzikowski et al., 2018). The active sensing technique was used for cement hydration monitoring (Kong and Song, 2017), impact localization (Coles et al., 2020), monitoring of bolted spherical joint connections (Xu et al., 2018a), timber crack monitoring (Wang et al., 2020b) and cyclic crack monitoring (Qin et al., 2015).

Active sensing technology was also applied for detecting and monitoring the structural bond slip, which includes but not limited to the bond slip detection between concrete and a steel plate (Xu et al., 2018b; Feng and Ou, 2015), the bond slip between concrete and GFRP/steel bars (Hong et al., 2018; Zhang et al., 2020), and the debonding detection in hidden frame supported glass curtain walls (Kong et al., 2016). However, to the authors' best knowledge, no literature is available about active sensing-based monitoring of Old - New concrete interfacial bond slip in post-installed anchor reinforced structures. Therefore, this paper conducts experiments to detect the Old - New concrete interfacial bond slip using the method of PZT-based active sensing. To demonstrate whether the PZT enabled active sensing approach is



feasible or not, three testing specimens are fabricated, with each specimen containing two sections of concrete that are respectively poured at two different times. An anchored rebar is installed in both the new and the old concretes. Two PZT aggregates severed as an actuator-sensor active sensing pair to monitor the Old - New concrete interface bond slip when the specimens experienced shear loads applied a by test machine. The experimental results show the development of bond slip at the interface between the new and old concrete with the shear loading procedure, and that the bond slip influences the interface shearing capacity and the stress wave propagation. The comparison between the load-time curve and the WPEI - time curve demonstrates that the active sensing method is an effective approach to detect the bond slip processes in Old - New concrete interfaces.

PRINCIPLES

Analysis of Old - New Concrete Interfacial Shear Mechanism

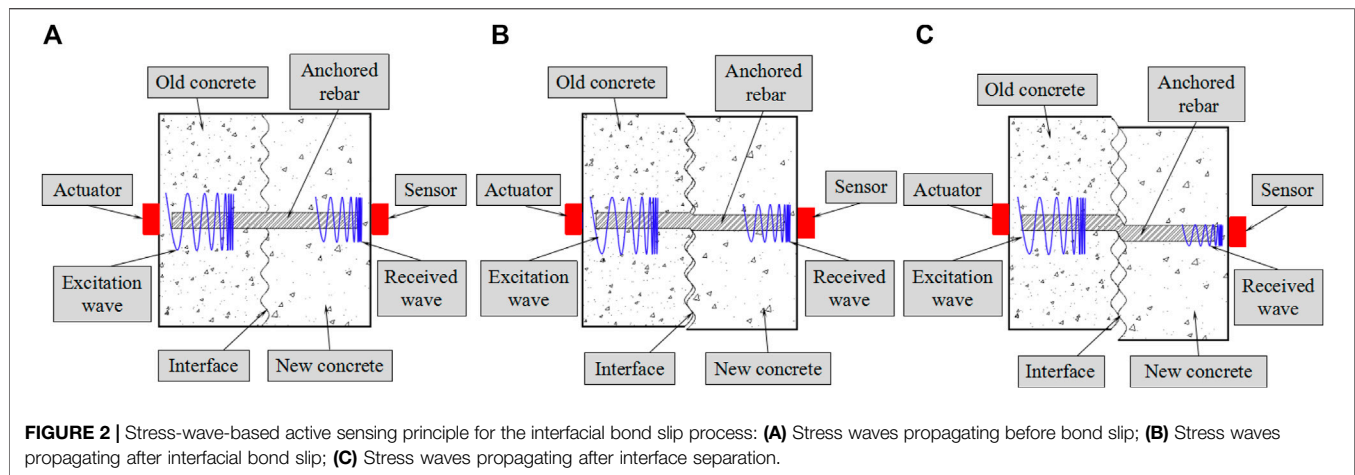
The Old - New concrete interfacial bond slip mechanism of the anchoring specimen can be segmented into three stages as seen in **Figure 1**. As shown in **Figure 1A**, from the beginning of loading until the occurrence of Old - New concrete interfacial bond slip, the shear capacity attributes to the adhesive force of the concrete. At this stage, the bond is composed by van der Waals forces, the chemical strength of the cement base, and the mechanical bite ability of the Old - New concrete aggregate (Maili and Jing, 2018). When a sufficiently strong shear force occurs, the interfacial bond slip can be witnessed, which begins as a small crack at the interface. With the continuously increasing shear force, the crack continues to grow until it spans the entire interface, as shown in **Figure 1B**. At this stage, the anchored rebar begins to partake remarkably during the interfacial shear process. The interfacial shear capacity mainly stems from the frictional force of concrete as well as the shear force of the anchored rebar. After the interface is separated, as shown in **Figure 1C**, the bite force of the Old - New concrete interface is observed a decline to zero, and the shear capacity is entirely born by the pinned rebar.

Piezoceramic-Based Active Sensing Method

Figure 2 illustrates the active sensing method for monitoring Old - New concrete interfacial bond slip within an anchored rebar reinforced concrete structure during the shearing test process. Two PZT aggregates are attached on the new and old concrete surfaces, respectively. One PZT aggregate participates as an actuator and another plays a role as a sensor. The propagation of the stress wave originated from the actuator can be clearly witnessed from the old concrete to the new concrete through the interface and the anchored rebar. The sensor is capable of detecting the stress waves propagating from the new concrete since concrete participates significantly as a desirable conduit for the propagation of the stress wave. During the interfacial bond slip monitoring test, the stress waves propagation is highly dependent upon the bond condition of the Old - New concrete interface. From the beginning of loading until the initiation of the interfacial bond slip, the performance of the new-old concrete bond is pretty excellent. The stress wave can easily travel through both sections of concrete and be received by the sensor with minimal distortion. when the shear force increases to a specific high level and relative interfacial sliding occurs, the crack between new and old concrete will exert a direct influence on the propagation of the stress wave. With further interfacial bond slip, the stress wave energy spread from the old concrete to the new one continues to attenuate. The stress wave energy decreases towards a steady state as the crack completely separates the interface. When the interface is completely separated, only a minimal amount of stress wave energy is propagated through the anchor rebar still connecting the two sections of concrete. With the analysis of the received signals' energy, the Old - New concrete interfacial bond slip process can be monitored.

Wavelet Packet-Based Energy Index

The wavelet packet-based energy index (WPEI) is an effective analysis technique that has been widely used to quantitatively evaluate structural changes. In this study, the stress-wave energy transmission from the old concrete to the new concrete is sensitively correlated to the performance of interface bond; thus, the energy response which is observed and noted at the



sensor can indicate and gauge the bond condition and even the bond slip process. In order to monitor the stress waves' energy recorded at PZT sensors, WPEI analysis is introduced herein to compute the energy values of the signal at PZT sensors. Because the received sensor signal is a frequency rich wave that is correlated to the actuator's production, the sweep sine wave excitation signal, WPEI analysis can be utilized in the decomposing of the recorded wave into a series of frequency bands. The total energy of the received stress wave signal can be estimated by the summation of energies across all the frequency bands.

The PZT sensor signal that represents the propagation stress wave is decomposed through wavelet packet decomposition. Here a n -level decomposition is assumed, which will result in 2^n signal sets $\{X_1, X_2, \dots, X_{2^n}\}$. Furthermore, j is assumed to be the frequency band, with $j = 1, 2, \dots, 2^n$ and $n = 5$ in this study. Each decomposed signal from the original signal X_j can be further defined as following:

$$X_j = [x_{j,1}, x_{j,2}, \dots, x_{j,m}] \quad (1)$$

where m refers to the number of samples. Thus, the decomposed signal energy E_j can be specifically expressed as:

$$E_j = \sum_{k=1}^{k=m} x_{j,k}^2 \quad (2)$$

The total energy of the stress wave signal E can be summarized by all the decomposed signals and expressed as:

$$E = \sum_{j=1}^{2^n} E_j \quad (3)$$

The recorded signal can be characterized based on the WPEI analysis. In this experiment, the Old - New concrete interface bond condition at the beginning of the shear loading test is recognized as the original state. The received signal energy decreases with the worsening of interfacial bond slip, and the WPEI computes the changes in the received signal energy during the shear loading test.

EXPERIMENTAL SETUP AND PROCEDURE

Specimen Fabrication

In the experiment, three specimens (S1, S2, and S3) with the same dimensions and materials were fabricated. Each specimen consists of three parts: old concrete, new concrete and an anchored rebar. **Figure 3** details the fabrication process and the dimensions of the specimens. Firstly, the first (i.e., old) layer of class C25 concrete with the dimensions $160 \text{ mm} \times 160 \text{ mm} \times 80 \text{ mm}$ was poured. In the specimen, the part of old concrete is first poured and set for 28 days. Then, the rebar was implanted into a hole drilled into the old concrete and secured in place using epoxy. After the epoxy completely solidified for few hours, the new concrete of class C35 was poured over the old concrete. After the new concrete has solidified with another 28 days, the specimens are formed and conducted the experiments. The dimensions, strength grade and implanted length of the rebar are $\Phi 14 \text{ mm} \times 140 \text{ mm}$, HRB 335 and 70 mm, respectively.

As vividly illustrated in **Figure 4**, two PZT aggregates are firmly adhered to the surfaces of new and old concrete. One of them participated as the actuator and the other one worked as the sensor in the monitoring test. The aggregate is composed by inserting a PZT patch with electric wire into two cylindrical marble blocks. The dimensions of the cylindrical smart aggregate and the PZT patch are $\Phi 25 \text{ mm} \times 20 \text{ mm}$ and $15 \text{ mm} \times 15 \text{ mm} \times 0.3 \text{ mm}$, respectively. The material properties of the experimental specimens and PZT aggregates are listed in **Table 1**.

Experimental Setup

Figure 5 illustrates the experimental setup for the monitoring of the Old - New concrete interfacial bond slip. The setup includes the specimens (S1, S2, and S3) with PZT aggregates, a power amplifier, a data acquisition and control system, and a laptop computer. To excite the PZT actuator, a swept sine wave signal is initially produced by the data acquisition and control system and then augmented by the power amplifier with a gain of 50. Then the amplified swept sine signal is fed into the actuator to produce the stress wave, and the sensor detected the propagating wave

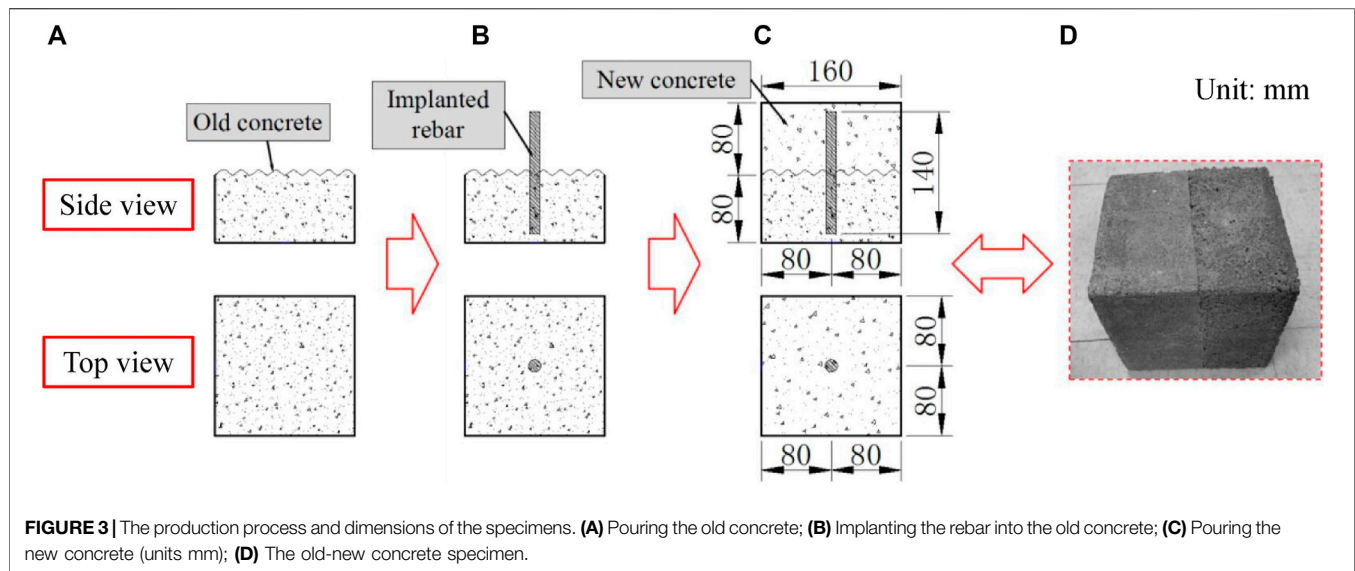


FIGURE 3 | The production process and dimensions of the specimens. (A) Pouring the old concrete; (B) Implanting the rebar into the old concrete; (C) Pouring the new concrete (units mm); (D) The old-new concrete specimen.

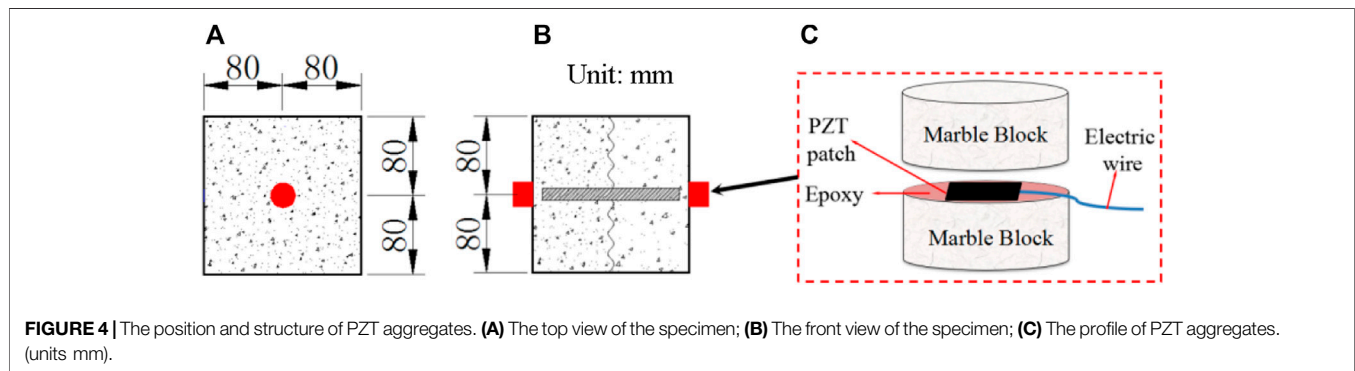


FIGURE 4 | The position and structure of PZT aggregates. (A) The top view of the specimen; (B) The front view of the specimen; (C) The profile of PZT aggregates. (units mm).

TABLE 1 | The material properties of the experimental specimens.

Materials	Parameters	Value	Units
Concrete	Density	2,400	kg/m ³
	Young's modulus	33	Gpa
	Compression strength	40.3	Mpa
Rebar	Density	7,900	kg/m ³
	Yield strength	350	Mpa
	Tensile strength	530	Mpa
	Elongation	19	%
Epoxy	Tensile strength	14	Mpa
	Compressive strength	65	Mpa
	Flexure strength	53	Mpa
	Bonding strength	17	Mpa
PZT aggregates	Dimension	Φ25 × 20	Mm
	Piezoelectric strain coefficients (−d31/d33/d15)	1.75/4.00/5.90	10−10 C/N

from concrete. For the swept sine signal, the frequency range is 1,000 Hz–300 kHz, the amplitude is 3 V, and the time interval is 1 s. The sampling frequency of the data acquisition and control system is 2 MS/s.

In the experiment, the axial compressive load adopted upon the specimen is under the control of a universal material test

machine under the displacement control mode, as shown in **Figure 5**. In order to apply a uniform stress to the specimen, two thick steel plates were placed at the upper and lower ends of the specimen, respectively. Furthermore, two steel blocks and two wood blocks were placed between the test specimen and thick steel plates, and the specific position of the blocks are shown in

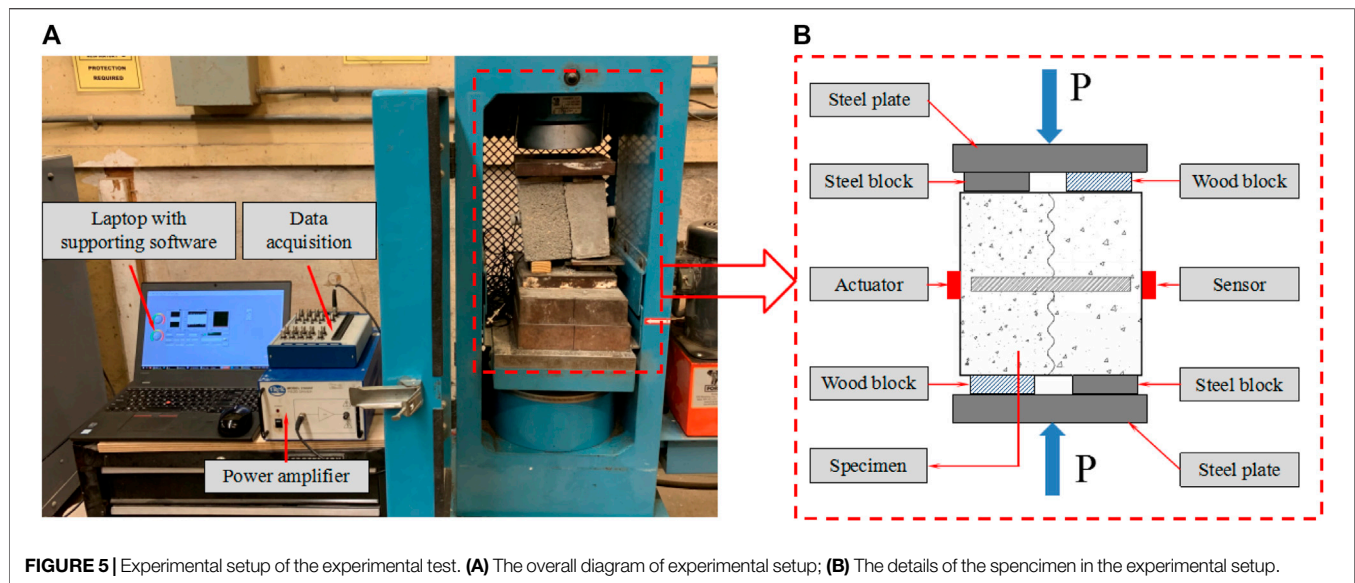


FIGURE 5 | Experimental setup of the experimental test. **(A)** The overall diagram of experimental setup; **(B)** The details of the specimen in the experimental setup.

Figure 5. It is noted that the position of wood blocks and steel blocks in the upper and lower ends of the test specimen is different. When the vertical load was set upon the central position of the steel plate by the hydraulic machine, compressive stress is applied to the old-new concrete specimens through the wood and iron blocks. Due to different Young's modulus between the wood and iron blocks, they will produce different compression deformation. Different deformations of the blocks can lead to different vertical displacement of old and new concrete, resulting in shear forces at the Old - New concrete interface. Before the concrete interface is stripped, the specimen is not deformed, two thick steel plates have a strong binding force at the upper and lower ends of the test specimen, resulting in good shear force conduction at the interface.

In terms of both the PZT-enabled active sensing and pressure gauge, the load value and received signal were collected every 20 s. During each experiment, the Old - New concrete interfacial bond slip would be eventually accompanied by a visible crack and a shear displacement, meanwhile, there would be a plunge in the loading time history. When this happened, the experiment was terminated.

EXPERIMENTAL RESULTS AND DISCUSSIONS

Figure 6 shows the specimens after the shear loading test. A visible crack can be observed in each specimen. The loading time histories of S1, S2, and S3 are respectively represented by the red, black, and blue curves in **Figure 7**. The load in **Figure 7** is the compressive force from the testing system. As explained in *Experimental Setup*, the process of applying compressive stress in the specimens result in the interfacial bond slip between the old/new concrete. Therefore, the time history curve of the compressive force was employed to reflect the interfacial bond

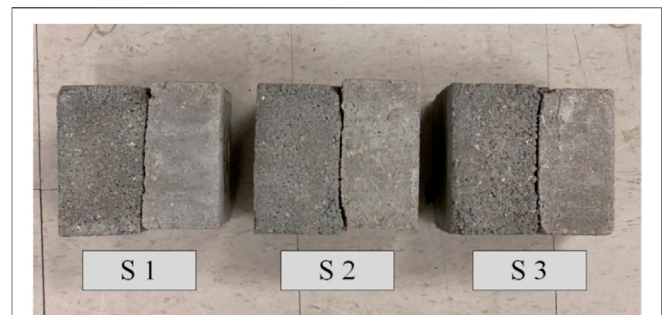


FIGURE 6 | Specimens after shear loading test.

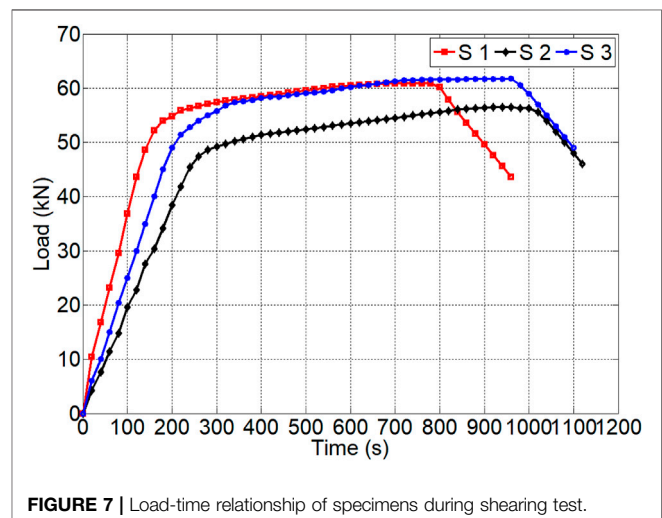


FIGURE 7 | Load-time relationship of specimens during shearing test.

slip process of the old/new concrete. The test durations of S1, S2, and S3 are respectively 960, 1,120, and 1,110 s. It is clearly illustrated from the red curve that there are three stages in the

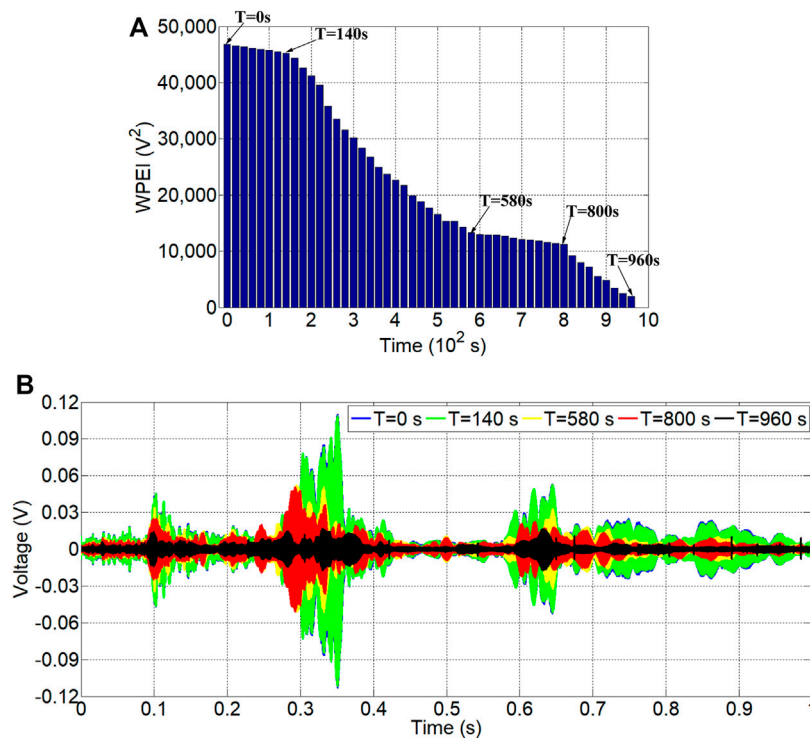


FIGURE 8 | WPEIs and received signal of S1: **(A)** WPEIs of the received signal; **(B)** the received stress wave signal.

loading process. From 0 s to 140 s, the shear strength of the new-old concrete interlayer is generated by the concrete's bond strength. In this stage, the load value increases rapidly and linearly with time. From 140 s to 800 s, the interfacial shear capacity is significantly produced by both the concrete frictional force of the concrete and shear force of anchored rebar. At this point, the load rate slowed down significantly. From 580 s to 800 s the load value remained almost a constant value. From 800 s to 960 s, visible cracks appeared in the interface between old and new concrete. In this stage, the interlayer shear strength is mostly generated by the shear force of anchored rebar and the load value drops rapidly. The maximum load value of S1 is 60.42 kN. S2 and S3 can also be divided into three stages of the same trend (black curve at 0–240 s, 240–1,020 s, and 1,020–1,120 s; blue curve at 0–220 s, 220–980 s, and 980–1,110 s). The maximum load of S2 is 56.50 and 61.74 kN for S3.

The received signal was recorded every 20 s during the experiment. **Figure 8A** shows the WPEIs of received signals of S1 during the shear loading process. The WPEIs can be divided into four stages over time: 0–140 s, 140–580 s, 580–800 s, and 800–960 s. **Figure 8B** demonstrates the time domain signal collected in S1 at 0, 140, 580, 800, and 960 s. Each curve acts as a representation of the received signal by sensor over a 1 s duration (i.e., the length of the swept sine signal). The received signals at 0 and 140 s are almost identical as indicated by the blue curve and green curve in **Figure 8B**. The WPEI experiences only a slight change in this stage, suggesting that bond slip has not yet

occurred and the Old - New concrete interface bond strength can bear the shear load. From 140 to 580 s, the WPEI experiences a notable decrease with time elapsed. The decrease in WPEI is mirror by the drop in the amplitude of the received signals between 140 and 580 s, as seen in the green and yellow curves in **Figure 8B**. The signal strength reduction means that the Old - New concrete interfacial bond slip has occurred and is worsening. From 580 to 800 s, there is little change of in WPEI while the amplitude of the received signals has slight reduction. The lack of significant changes means that the interfacial bond slip has spread throughout the entire interface, but the Old - New concrete interface is not completely separated. From 800 to 960 s, the WPEI continues to decrease towards a very low value. As shown in **Figure 8B**, this stage is represented by the black curve, and the amplitude of the recorded signal at 960 s is greatly reduced to less than 0.01 V. In this stage the Old - New concrete interface is beginning to separate, and the stress wave can only propagate through the rebar, explaining the weak received signal. **Figures 9, 10** present that the behavior of the WPEIs and time domain signals of S2 and S3 remain almost the same as that of S1. The WPEIs and the amplitude of the received stress wave signals vary with the deterioration of Old - New concrete interface bond condition.

The relationship between the load and the WPEIs of S1, S2, and S3 are shown in **Figure 11**. The blue curve represents the load value during the shear loading test and the red curve represents the WPEI of the recorded signals. As clearly illustrated in **Figure 11A**, in first 140 s, the load value increases linearly and

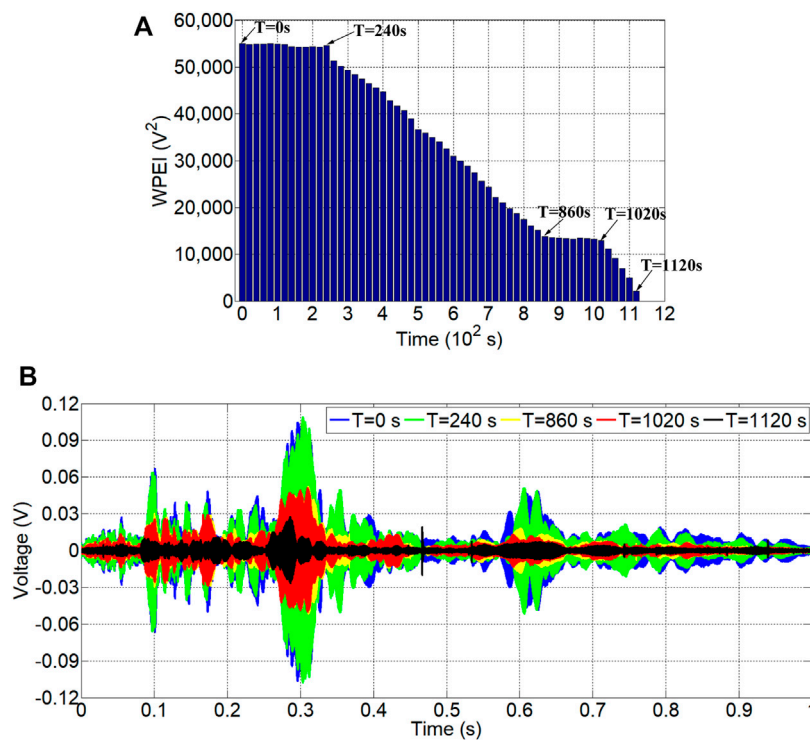


FIGURE 9 | WPEIs and received signal of S2: **(A)** WPEIs of the received signal; **(B)** the received stress wave signal.

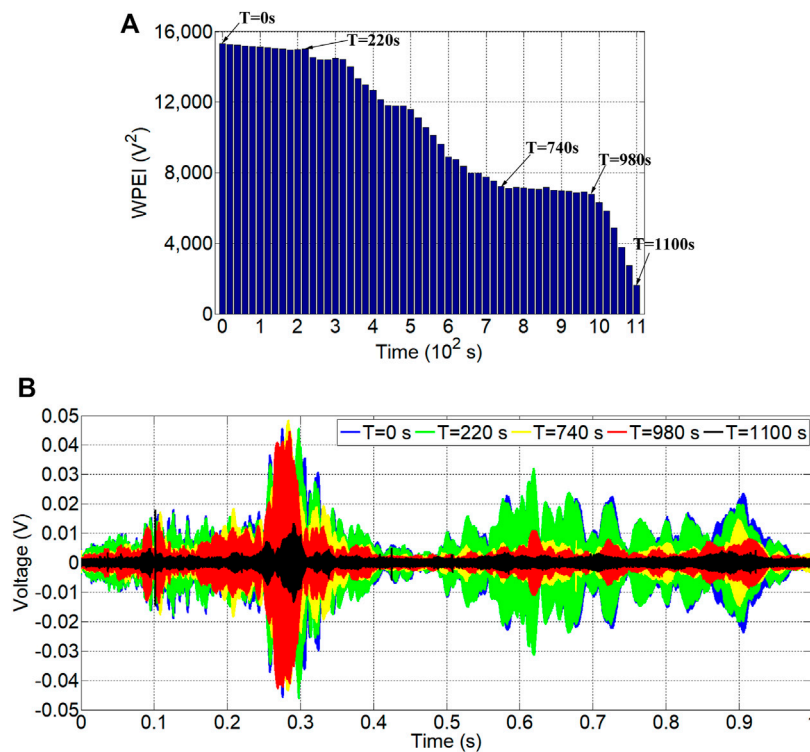


FIGURE 10 | WPEIs and received signal of S3: **(A)** WPEIs of the received signal; **(B)** the received stress wave signal.

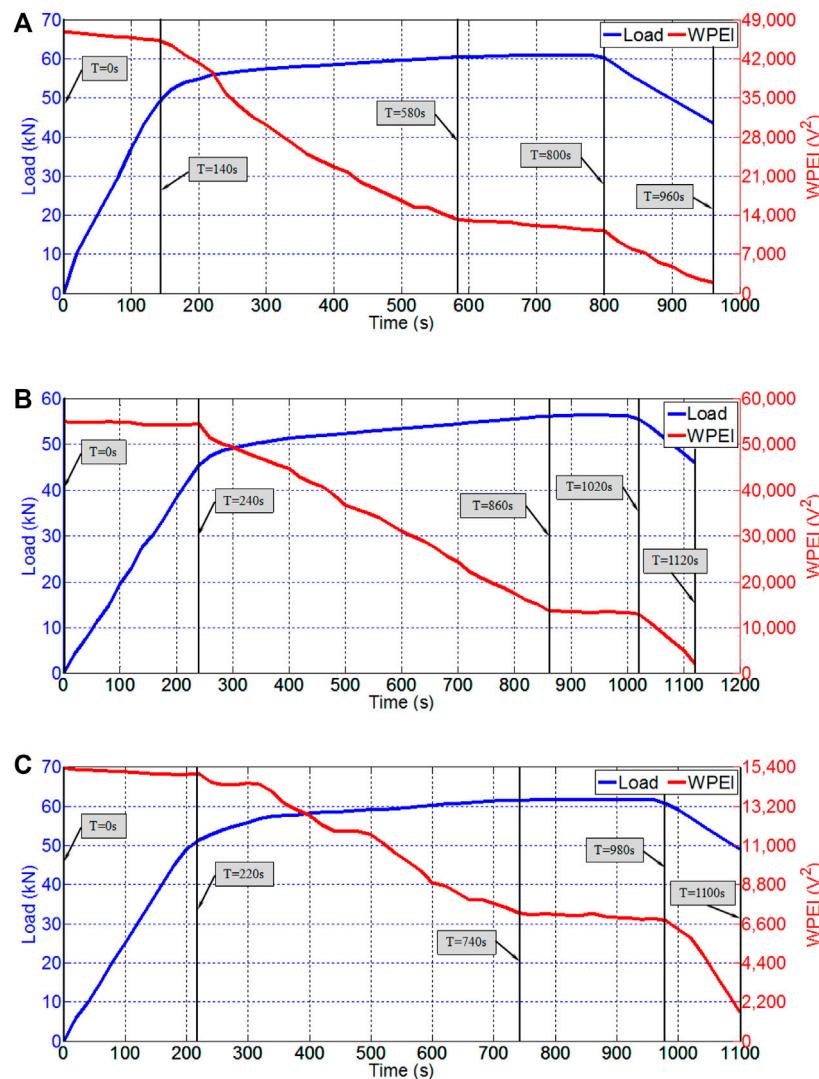


FIGURE 11 | The relationship between load and WPEIs for the three different specimens: **(A)** The relationship between load and WPEIs of S1; **(B)** The relationship between load and WPEIs of S2; **(C)** The relationship between load and WPEIs of S3.

the WPEI value changes slightly, which means that in this stage there is no bond slip at the interface and that the shear capacity is generated by the Old - New concrete bond strength. From 140 to 580 s, the load value increases nonlinearly, and the growth rate decreases. The WPEI decreases significantly in this stage. These changes show that the Old - New concrete interfacial bond slip has initiated and is continuing to develop. In this stage, the anchored rebar begins to play an important role in the shear process of the interface, and the interfacial shear capacity mainly originates from the shear force of anchored rebar and the frictional force of concrete. From 580 to 800 s, the load value reaches a steady-state value and the WPEI value decreases slightly. In this stage, the bond slip continues to develop, and the crack runs throughout the entire interface. However, the Old - New concrete interface is not completely separated, and the shear force is shared by both the frictional force of concrete and the shear force of anchored rebar. From 800 to 960 s, both the load

and the WPEI experiences an obvious reduction. In this stage, a visible crack and shear displacement in the S1 can be observed. The interface of Old - New concrete began to separate, and the bite force of the interface is reduced to zero. The interfacial shear capacity mainly depends on the shear force of the anchored rebar. Therefore, the stress wave can only travel through the rebar, and the WPEI drops rapidly.

In **Figures 11B,C**, the load-time curve and WPEI-time curve show share a similar trend as the one shown in **Figure 11A**. As the Old - New concrete interface is the weakest parts of all the specimens during the shear loading test, the interfacial bond condition varies with increases in applied shear force. The interfacial bond slip occurs when shear force is bigger than the interface bond strength, and stress wave propagation will change. The Old - New concrete interfacial bond slip process can be tracked by the analysis of the collected signal, which illustrates that the method of active sensing is able to effectively detect the

Old - New concrete interfacial bond slip development in real time during the shear loading process.

In the experiment process, when the interfacial bond slip occurs and concrete tilted, compressive loads may take place at the interface as well. Nevertheless, this paper mainly attempts to employ the piezoelectric active sensing method to monitor the process of interfacial bond slip between the new-old concrete reinforced by the anchored rebar. Although it is likely to result in the compressive loads when the bond slip happened in the new-old concrete, the active sensing could effectively characterize the process of the old-new concrete interfacial bond slip. Different from the concrete cube in this paper, the main load-bearing components in the actual project are beams or columns. Therefore, the anchoring form of the steel bar in the new concrete and the layout of the transducers in practical project will also be different from the experimental studies. However, the paper is an exploratory experiment which explore the feasibility of the active sensing method to monitor Old - New concrete interfacial bond slip in the anchored rebar reinforced concrete structure.

CONCLUSION AND FUTURE WORK

The Old - New concrete interface is the weakest link of concrete structures reinforced with post-installed anchors, especially when under shear loads. Interface failure often initiates with bond slip, and it is necessary to monitor the Old - New concrete interfacial bond slip to avoid the brittle and sudden failure of strengthen concrete structures. A PZT-based active sensing method was developed for the real time monitoring of Old - New concrete interfacial bond slip in a post-installed anchor reinforced concrete structure. To verify the proposed approaches, experiments were conducted upon specimens consisting of two parts of concrete which were poured at different times. The new and old concrete parts were connected with an anchored rebar. Two PZT aggregates were adhered to the two opposing ends of the concrete specimen to realize the active sensing approach. A shear loading test was conducted in which the load value and received signal were collected every 20 s. A comparison of the wavelet packet-based energy index (WPEI) with the load value clearly shows that the interfacial bond condition changes with the shear force development. Interfacial bond slip occurs when shear force is larger than the interface bond strength. Bond slip can

greatly influence the interfacial shear capacity and the propagation of the stress wave in the Old - New concrete. The change of WPEI in the received signals is in direct relation to the severity of the Old - New concrete interfacial bond slip, and demonstrates whether the PZT-based active sensing method is feasible or not in terms of monitoring shear-induced Old - New concrete interfacial bond slip.

In future studies, the authors will design better loading methods to ensure that the shear load can be better applied during the whole experiment process. And the Old - New interfacial bond slip of real engineering components including the beams and columns will be further researched in detail. In addition, the influence of different ages, composite stress states, and steel anchoring forms on Old - New concrete interfacial bond slip would be considered. Moreover, the active sensing method combined with the method of big data, artificial intelligence would be employed to achieve intelligent monitoring of old-new concrete interfacial bond slip.

DATA AVAILABILITY STATEMENT

The original contributions presented in the study are included in the article/Supplementary Material, further inquiries can be directed to the corresponding author.

AUTHOR CONTRIBUTIONS

JJ developed the original idea. JD and JJ designed the experiments. YC and JJ conducted the experiments. JJ and YC analyzed the data. JJ and YC wrote the original draft. JD made critical revision to the paper.

FUNDING

This research was financially supported by the National key research and development program “Search and rescue techniques for earthquake casualties in catastrophic municipal urban areas” (PID: 2018YFC1504404) and Science for Earthquake Resilience of China Earthquake Administration (Grant No. XH19043Y and XH20040YSX).

REFERENCES

- Abouhussien, A. A., and Hassan, A. A. (2017). Acoustic Emission Monitoring for Bond Integrity Evaluation of Reinforced concrete under Pull-Out Tests. *Adv. Struct. Eng.* 20 (9), 1390–1405. doi:10.1177/1369433216678864
- Abouhussien, A. A., and Hassan, A. A. (2017). Application of Acoustic Emission Monitoring for Assessment of Bond Performance of Corroded Reinforced concrete Beams. *Struct. Health Monit.* 16 (6), 732–744. doi:10.1177/1475921716681460
- Al-Fasih, M. Y., Mohamad, M. E., Ibrahim, I. S., Ahmad, Y., Ariffin, M. A. M., Sarbini, N. N., et al. (2021). Experimental and Numerical Evaluations of Composite concrete-to-concrete Interfacial Shear Strength under Horizontal

and normal Stresses. *PLoS ONE* 16 (5), e0252050. doi:10.1371/journal.pone.0252050

- Annanddas, V. G. M., and Soh, C. K. (2017). Load Monitoring Using a Calibrated Piezo Diaphragm Based Impedance Strain Sensor and Wireless Sensor Network in Real Time. *Smart Mater. Struct.* 26 (4), 045036. doi:10.1088/1361-665x/aa5f40
- Bajer, M., and Barnat, J. (2012). The Glue-concrete Interface of Bonded Anchors. *Construction Building Mater.* 34, 267–274. doi:10.1016/j.conbuildmat.2012.02.030
- Barnaf, J., Bajer, M., and Vyhnanekova, M. (2012). Bond Strength of Chemical Anchor in High-Strength Concrete. *Proced. Eng.* 40, 38–43. doi:10.1016/j.proeng.2012.07.052
- Bhalla, S., and Kaur, N. (2018). Prognosis of Low-Strain Fatigue Induced Damage in Reinforced concrete Structures Using Embedded Piezo-Transducers. *Int. J. Fatigue* 113, 98–112. doi:10.1016/j.jfatigue.2018.04.002

- Bouazaoui, L., and Li, A. (2008). Analysis of Steel/concrete Interfacial Shear Stress by Means of Pull Out Test. *Int. J. Adhes. Adhesives* 28 (3), 101–108. doi:10.1016/j.jadhadh.2007.02.006
- Brencich, A. (2015). A post-installed Insert for Pull-Out Tests on concrete up to 70 MPa. *Construction Building Mater.* 95, 788–801. doi:10.1016/j.conbuildmat.2015.07.055
- Coles, A., de Castro, B. A., Andreades, C., Baptista, F. G., Meo, M., and Ciampa, F. (2020). Impact Localization in Composites Using Time Reversal, Embedded PZT Transducers, and Topological Algorithms. *Front. Built Environ.* 6 (27). doi:10.3389/fbuil.2020.00027
- Cook, R. A., Dorrer, G. T., and Klingner, R. E. (1993). Bond Stress Model for Design of Adhesive Anchors. *Sj* 90 (5), 514–524. doi:10.14359/3945
- Cook, R. A. (1992). Load-Deflection Behavior of Cast-In-Place and Retrofit Concrete Anchors. *Sj* 89 (6), 639–649. doi:10.14359/4134
- Diab, A. M., Abd Elmoaty, A. E. M., and Tag Eldin, M. R. (2017). Slant Shear Bond Strength between Self Compacting concrete and Old concrete. *Construction Building Mater.* 130, 73–82. doi:10.1016/j.conbuildmat.2016.11.023
- Dziendzikowski, M., Niedbala, P., Kurnyta, A., Kowalczyk, K., and Dragan, K. (2018). Structural Health Monitoring of a Composite Panel Based on PZT Sensors and a Transfer Impedance Framework. *Sensors* 18 (5), 1521. doi:10.3390/s18051521
- Fan, S., Li, W., Kong, Q., Feng, Q., and Song, G. (2018). Monitoring of Pin Connection Loosening Using Eletromechanical Impedance: Numerical Simulation with Experimental Verification. *J. Intell. Mater. Syst. Structures* 29 (9), 1964–1973. doi:10.1177/1045389X18754354
- Fang, H., Su, Z., Li, X., Wang, F., and Fu, Y. (2021). Interfacial Bond Performance between Self-Expansion Polymer and concrete. *Construction Building Mater.* 270, 121459. doi:10.1016/j.conbuildmat.2020.121459
- Feng, Q., and Ou, J. (2018). Self-Sensing CFRP Fabric for Structural Strengthening and Damage Detection of Reinforced Concrete Structures. *Sensors* 18 (12), 4137. doi:10.3390/s18124137
- González, F., Fernández, J., Agranati, G., and Villanueva, P. (2018). Influence of Construction Conditions on Strength of post Installed Bonded Anchors. *Construction Building Mater.* 165, 272–283. doi:10.1016/j.conbuildmat.2017.12.144
- Hong, X., Liu, Y., Liufu, Y., and Lin, P. (2018). Debonding Detection in Hidden Frame Supported Glass Curtain Walls Using the Nonlinear Ultrasonic Modulation Method with Piezoceramic Transducers. *Sensors* 18 (7), 2094. doi:10.3390/s18072094
- Hou, S., Cai, C. S. S., and Ou, J. (2009). “FRP Debonding Monitoring Using OTDR Techniques.” in Proceedings of the Second International Conference on Smart Materials and Nanotechnology in Engineering, Weihai, China, July 8–11 2009. 7493. doi:10.1117/12.843559
- Hu, G., Tang, L., and Das, R. (2018). General Framework for Modeling Multifunctional Metamaterial Beam Based on a Derived One-Dimensional Piezoelectric Composite Finite Element. *J. Aerosp. Eng.* 31 (6), 04018088. doi:10.1061/(ASCE)AS.1943-5525.0000920
- Hyun-Soo Youm, W. Y. L. S. G. H., and Changbin, J. (2021). Interface Shear Strength between Ultra-high-performance Concrete and Normal-Strength Concrete. *Sj* 118 (2). doi:10.14359/51729350
- Jiang, J., Hei, C., Feng, Q., and Jiang, J. (2019). Monitoring of Epoxy-Grouted Bonding Strength Development between an Anchored Steel Bar and Concrete Using PZT-Enabled Active Sensing. *Sensors* 19 (9), 2096. doi:10.3390/s1906137710.3390/s19092096
- Ju, Y., Shen, T., and Wang, D. (2020). Bonding Behavior between Reactive Powder concrete and normal Strength concrete. *Construction Building Mater.* 242, 118024. doi:10.1016/j.conbuildmat.2020.118024
- Júlio, E. N. B. S., Branco, F. A. B., Silva, V. D., and Lourenço, J. F. (2006). Influence of Added concrete Compressive Strength on Adhesion to an Existing concrete Substrate. *Building Environ.* 41 (12), 1934–1939. doi:10.1016/j.buildenv.2005.06.023
- Kong, Q., Robert, R., Silva, P., and Mo, Y. (2016). Cyclic Crack Monitoring of a Reinforced Concrete Column under Simulated Pseudo-dynamic Loading Using Piezoceramic-Based Smart Aggregates. *Appl. Sci.* 6 (11), 341. doi:10.3390/app6110341
- Kong, Q., and Song, G. (2017). A Comparative Study of the Very Early Age Cement Hydration Monitoring Using Compressive and Shear Mode Smart Aggregates. *IEEE Sensors J.* 17 (2), 256–260. doi:10.1109/JSEN.2016.2624799
- Lee, J.-W. (2021). An Experimental Study on Bolt Looseness Monitoring Using Low-Cost Transfer Impedance Technique. *Int. J. Steel Struct.* 21 (1), 349–359. doi:10.1007/s13296-020-00442-1
- Li, W., Fan, S., Ho, S. C. M., Wu, J., and Song, G. (2017). Interfacial Debonding Detection in Fiber-Reinforced Polymer Rebar-Reinforced concrete Using Electro-Mechanical Impedance Technique. *Struct. Health Monit.* 17 (3), 461–471. doi:10.1177/1475921717703053
- Liang, Y., Li, D., Parvasi, S. M., Kong, Q., Lim, I., and Song, G. (2016). Bond-slip Detection of concrete-encased Composite Structure Using Electro-Mechanical Impedance Technique. *Smart Mater. Struct.* 25 (9), 095003. doi:10.1088/0964-1726/25/9/095003
- Liu, X., Liu, Y., Wu, T., and Wei, H. (2020). Bond-slip Properties between Lightweight Aggregate concrete and Rebar. *Construction Building Mater.* 255, 119355. doi:10.1016/j.conbuildmat.2020.119355
- Mahrenholtz, P., Eligehausen, R., Hutchinson, T. C., and Hoehler, M. S. (2016). Behavior of Post-Installed Anchors Tested By Stepwise Increasing Cyclic Load Protocols. *ACI Struct. J.* 113 (5), 997–1008. doi:10.14359/51689023
- Maili, C., and Jing, M. (2018). Experimental Study on Shear Behavior of the Interface between New and Old Concrete with Reinforced. *KSCE J. Civ Eng.* 22 (5), 1882–1888. doi:10.1007/s12205-017-2007-6
- Mirmoghtadai, R., Mohammadi, M., Ashraf Samani, N., and Mousavi, S. (2015). The Impact of Surface Preparation on the Bond Strength of Repaired concrete by Metakaolin Containing concrete. *Construction Building Mater.* 80, 76–83. doi:10.1016/j.conbuildmat.2015.01.018
- Muciaccia, G., Consiglio, A., and Rosati, G. (2018). *Creep Behavior of Bonded Anchor under High Sustained Loading at Long Term Temperature*. (Cham, Switzerland: Springer International Publishing), 956–964. doi:10.1007/978-3-319-59471-2_111
- Nicassio, F., Carrino, S., and Scarselli, G. (2020). Non-linear Lamb Waves for Locating Defects in Single-Lap Joints. *Front. Built Environ.* 6 (45). doi:10.3389/fbuil.2020.00045
- Qasim, O. A. (2020). Different Concrete Types Affecting the Bond Strength and Interfacial Joints between New and Old Concrete. *IOP Conf. Ser. Mater. Sci. Eng.* 745, 012169. doi:10.1088/1757-899x/745/1/012169
- Qin, F., Kong, Q., Li, M., Mo, Y. L., Song, G., and Fan, F. (2015). Bond Slip Detection of Steel Plate and concrete Beams Using Smart Aggregates. *Smart Mater. Struct.* 24 (11), 115039. doi:10.1088/0964-1726/24/11/115039
- Rizzo, P., Spada, A., Degala, S., and Giambanco, G. (2010). Acoustic Emission Monitoring of Chemically Bonded Anchors. *J. Nondestruct Eval.* 29 (1), 49–61. doi:10.1007/s10921-010-0065-5
- Ronald, A. C., and Robert, C. K. (2001). Factors Influencing Bond Strength of Adhesive Anchors. *Sj* 98 (1). doi:10.14359/10149
- Song, X., Wu, Y., Gu, X., and Chen, C. (2015). Bond Behaviour of Reinforcing Steel Bars in Early Age concrete. *Construction Building Mater.* 94, 209–217. doi:10.1016/j.conbuildmat.2015.06.060
- Wang, D., Wu, D., He, S., Zhou, J., and Ouyang, C. (2015). Behavior of post-installed Large-Diameter Anchors in concrete Foundations. *Construction Building Mater.* 95, 124–132. doi:10.1016/j.conbuildmat.2015.07.129
- Wang, F., Chen, Z., and Song, G. (2020a). Monitoring of Multi-Bolt Connection Looseness Using Entropy-Based Active Sensing and Genetic Algorithm-Based Least Square Support Vector Machine. *Mech. Syst. Signal Process.* 136, 106507. doi:10.1016/j.ymssp.2019.106507
- Wang, W.-w., Dai, J.-g., Li, G., and Huang, C.-k. (2011). Long-Term Behavior of Prestressed Old-New Concrete Composite Beams. *J. Bridge Eng.* 16 (2), 275–285. doi:10.1061/(ASCE)BE.1943-5592.0000152
- Wang, Y., He, M., Sun, L., Wu, D., Wang, Y., and Zou, L. (2020b). Improved Kalman Filtering-Based Information Fusion for Crack Monitoring Using Piezoelectric-Fiber Hybrid Sensor Network. *Front. Mater.* 7 (300). doi:10.3389/fmats.2020.00300
- Wörle, P. (2014). Enhanced Shear Punching Capacity by the Use of post Installed concrete Screws. *Eng. Structures* 60, 41–51. doi:10.1016/j.engstruct.2013.12.015
- Xu, J., Wang, C., Li, H., Zhang, C., Hao, J., and Fan, S. (2018a). Health Monitoring of Bolted Spherical Joint Connection Based on Active Sensing Technique Using Piezoceramic Transducers. *Sensors* 18 (6), 1727. doi:10.3390/s18061727
- Xu, K., Ren, C., Deng, Q., Jin, Q., and Chen, X. (2018b). Real-Time Monitoring of Bond Slip between GFRP Bar and Concrete Structure Using Piezoceramic

- Transducer-Enabled Active Sensing. *Sensors* 18 (8), 2653. doi:10.3390/s18082653
- Xu, Y., Luo, M., Liu, Q., Du, G., and Song, G. (2019). PZT Transducer Array Enabled Pipeline Defect Locating Based on Time-Reversal Method and Matching Pursuit De-noising. *Smart Mater. Struct.* 28 (7), 075019. doi:10.1088/1361-665x/ab1cc9
- Yilmaz, S., Özen, M. A., and Yardim, Y. (2013). Tensile Behavior of post-installed Chemical Anchors Embedded to Low Strength concrete. *Construction Building Mater.* 47, 861–866. doi:10.1016/j.conbuildmat.2013.05.032
- Zeng, L., Parvasi, S. M., Kong, Q., Huo, L., Lim, I., Li, M., et al. (2015). Bond Slip Detection of concrete-encased Composite Structure Using Shear Wave Based Active Sensing Approach. *Smart Mater. Struct.* 24 (12), 125026. doi:10.1088/0964-1726/24/12/125026
- Zhang, L., Zheng, Y., Hu, S., Yang, J., and Xia, L. (2020). Identification of Bond-Slip Behavior of GFRP-ECC Using Smart Aggregate Transducers. *Front. Mater.* 7 (165). doi:10.3389/fmats.2020.00165
- Zhou, L., Zheng, Y., Huo, L., Ye, Y., Chen, D., Ma, H., et al. (2020). Monitoring of Bending Stiffness of BFRP Reinforced concrete Beams Using Piezoceramic Transducer Enabled Active Sensing. *Smart Mater. Struct.* 29 (10), 105012. doi:10.1088/1361-665x/ab936d
- Zhou, Z., He, J., Huang, Y., and Ou, J. (2008). “Experimental Investigation of RC Beams Using BOTDA(R)-FRP-OF.” in Proceedings of the 19th International Conference on Optical Fibre Sensors, April 15–18 2008, Perth, WA, Australia (Perth, WA, Australia: Proc. SPIE 7004). doi:10.1117/12.787120
- Zhu, J., Ho, S. C. M., Patil, D., Wang, N., Hirsch, R., and Song, G. (2017). Underwater Pipeline Impact Localization Using Piezoceramic Transducers. *Smart Mater. Struct.* 26 (10), 107002. doi:10.1088/1361-665x/aa80c9

Conflict of Interest: Author JJ was employed by the company Wuhan Institute of Earthquake Engineering Co., Ltd.

The remaining authors declare that the research was conducted in the absence of any commercial or financial relationships that could be construed as a potential conflict of interest.

Publisher’s Note: All claims expressed in this article are solely those of the authors and do not necessarily represent those of their affiliated organizations, or those of the publisher, the editors and the reviewers. Any product that may be evaluated in this article, or claim that may be made by its manufacturer, is not guaranteed or endorsed by the publisher.

Copyright © 2021 Jiang, Chen and Dai. This is an open-access article distributed under the terms of the Creative Commons Attribution License (CC BY). The use, distribution or reproduction in other forums is permitted, provided the original author(s) and the copyright owner(s) are credited and that the original publication in this journal is cited, in accordance with accepted academic practice. No use, distribution or reproduction is permitted which does not comply with these terms.

Advantages of publishing in Frontiers



OPEN ACCESS

Articles are free to read
for greatest visibility
and readership



FAST PUBLICATION

Around 90 days
from submission
to decision



HIGH QUALITY PEER-REVIEW

Rigorous, collaborative,
and constructive
peer-review



TRANSPARENT PEER-REVIEW

Editors and reviewers
acknowledged by name
on published articles

Frontiers

Avenue du Tribunal-Fédéral 34
1005 Lausanne | Switzerland

Visit us: www.frontiersin.org

Contact us: frontiersin.org/about/contact



REPRODUCIBILITY OF RESEARCH

Support open data
and methods to enhance
research reproducibility



DIGITAL PUBLISHING

Articles designed
for optimal readership
across devices



FOLLOW US

@frontiersin



IMPACT METRICS

Advanced article metrics
track visibility across
digital media



EXTENSIVE PROMOTION

Marketing
and promotion
of impactful research



LOOP RESEARCH NETWORK

Our network
increases your
article's readership